



Development of a non-animal bioinspired biomaterials for tissue engineering and regenerative medicine

Mathilde Stricher

► To cite this version:

Mathilde Stricher. Development of a non-animal bioinspired biomaterials for tissue engineering and regenerative medicine. Biomaterials. Université de Technologie de Compiègne, 2022. English. NNT : 2022COMP2706 . tel-04064094

HAL Id: tel-04064094

<https://theses.hal.science/tel-04064094>

Submitted on 11 Apr 2023

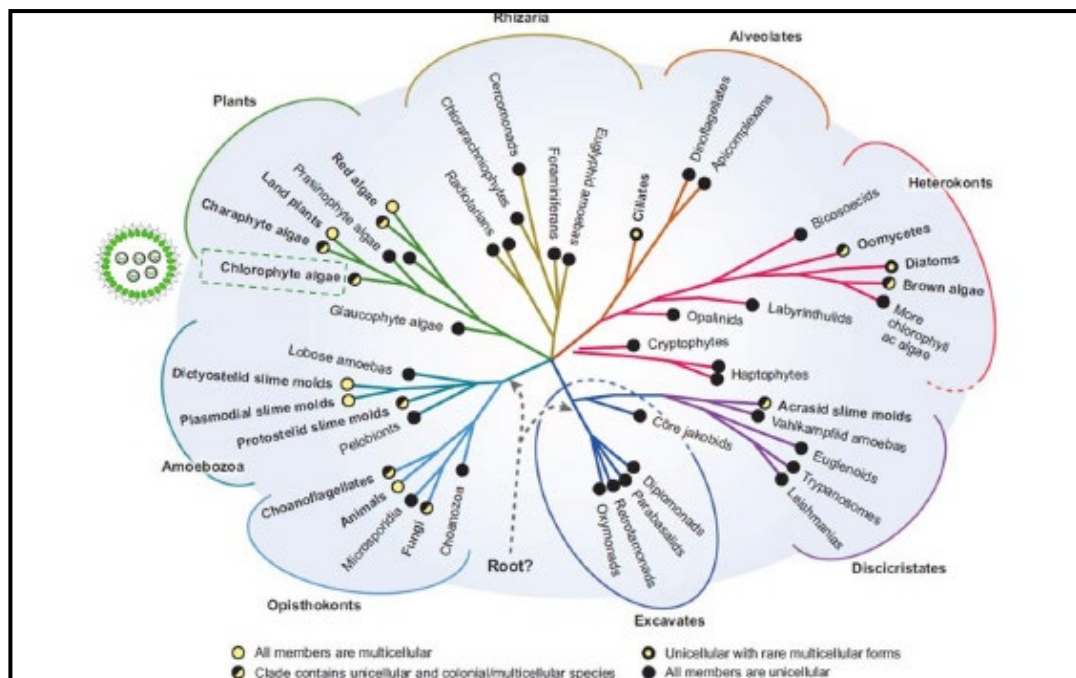
HAL is a multi-disciplinary open access archive for the deposit and dissemination of scientific research documents, whether they are published or not. The documents may come from teaching and research institutions in France or abroad, or from public or private research centers.

L'archive ouverte pluridisciplinaire **HAL**, est destinée au dépôt et à la diffusion de documents scientifiques de niveau recherche, publiés ou non, émanant des établissements d'enseignement et de recherche français ou étrangers, des laboratoires publics ou privés.

Par **Mathilde STRICHER**

*Développement de biomatériaux bioinspirés
non animaux pour l'ingénierie tissulaire :
application en médecine régénérative*

Thèse présentée
pour l'obtention du grade
de Docteur de l'UTC



Soutenue le 15 novembre 2022

Spécialité : Bioingénierie : Unité de Recherche en
Biomécanique et Bioingénierie (UMR-7338)

D2706



THÈSE DE DOCTORAT

École doctorale 71 : Sciences pour l'ingénieur

Spécialité : Bioingénierie

Développement de biomatériaux bioinspirés non animaux pour l'ingénierie tissulaire : application en médecine régénérative

Présentée et soutenue publiquement par

Mathilde STRICHER

le 15 novembre 2022

Pour obtenir le grade de docteur de
UNIVERSITÉ DE TECHNOLOGIE DE COMPIÈGNE

Directeurs de thèse : Dr. Christophe EGLES, Dr. Frédéric DELBECQ

Laboratoire de BioMécanique et BioIngénierie (BMBI)
Equipe Cellules Biomatériaux Bioréacteurs (CBB)
CNRS UMR 7338

Unité de recherche Transformations Intégrées de la Matière Renouvelable
(TIMR) Equipe Chimie organique et technologies alternatives (OCAT)
TIMR UTC-ESCOM

Jury :

Fouzia Boulmedais	DR CNRS, Institut Charles Sadron, Université de Strasbourg	Rapportrice
Emmanuel Pauthe	Pr, Laboratoire ERRMECe, Université de Cergy-Pontoise	Rapporteur
Sophie Gangloff	Pr, EA 4691 BIOS, Université de Reims Champagne-Ardenne	Examinatrice
Julien Payen	Co-fondateur & CEO, Lattice Medical	Examineur
André Pauss	Pr, TIMR, UTC-ESCOM	Examineur
Claude-Olivier Sarde	Pr, TIMR, UTC-ESCOM	Membre invité
Christophe Egles	Pr, UMR CNRS 7338, UTC	Directeur de thèse
Frédéric Delbecq	Pr, TIMR, UTC-ESCOM	Directeur de thèse

Acknowledgements - Remerciements

J'exprime ma sincère reconnaissance à l'ensemble des membres du jury pour avoir accepté d'évaluer mon travail pour l'obtention du grade de docteur en Bioingénierie de l'Université de Technologie de Compiègne, Fouzia Boulmedais et Emmanuel Pauthe en tant que rapporteurs et Sophie Gangloff pour la présidence de ce jury. Je remercie Julien Payen, CEO de Lattice Medical pour l'intérêt qu'il porte à mon travail et son applicabilité du point de vue industriel. Je remercie Erwann Guénin d'avoir suivi avec bienveillance mes travaux de thèse de bout en bout ainsi que Cécile Mias Vigouroux et Sophie Catoire pour les riches échanges que nous avons pu avoir dans le cadre de mon comité de suivi annuel.

Je tiens à exprimer mes plus sincères remerciements aux professeurs Christophe Egles et Frédéric Delbecq pour leur confiance, encadrement et enthousiasme vis à vis de mes travaux de thèse. Ce projet m'a permis de laisser libre court à ma créativité, d'exercer mon esprit critique et d'approfondir mes connaissances tout particulièrement en médecine régénérative et science des matériaux. Je remercie ma marraine et mon parrain de Volvox, Pascale Vigneron et Claude-Olivier Sarde de m'avoir transmis leur passion pour cette algue et son incroyable potentiel.

Je tiens également à remercier l'ensemble du laboratoire BMBI, tout particulièrement Cécile Legallais et Muriel Vayssade, respectivement en tant que responsable du laboratoire BMBI et responsable de l'équipe CBB, d'avoir fait en sorte que je puisse poursuivre mes travaux de thèse dans les meilleures conditions notamment dans les heures les plus sombres du COVID, du télétravail et des confinements successifs. Je remercie l'ensemble des chercheurs, personnels permanents et post-docs du laboratoire, particulièrement Timothée Baudequin, Ulysse Pereira, Claire de Lartigue, Nathalia Muniz Oderich et Pascale Vigneron, qui ont indéniablement contribué à l'évolution et la maturation de ce projet que ce soit au détour d'une conversation dans le cadre des journées scientifiques du laboratoire, d'un café ou de manipulations montées sur un coin de paillasse. Je remercie Anne Le Goff et Quentin Dermigny pour leur support dans la production et le traitement de données de caractérisation mécanique de mes matériaux. Je tiens à remercier Vanessa Bleicher pour son appui technique notamment en histologie. Je remercie Catherine Lacourt et Alexandra Cousin pour leur soutien logistique dans approvisionnement du laboratoire, l'élaboration des journées scientifiques et l'organisation de mes participations en congrès.

Je remercie également l'ensemble des personnels du laboratoire TIMR et de l'équipe OCAT, chercheurs, permanents et doctorants de m'avoir accueilli dans vos rangs pendant ces 3 ans. Je remercie tout particulièrement Erwann Guénin pour son accompagnement, Cristina

Belda Marin, Franco Otaola, Yancie Gagnon et Nadim Ayoub pour leur bienveillance et leur aide lors de mes passages au laboratoire.

Je remercie les personnels du SAPC, notamment Frédéric Nadaud et Caroline Lefebvre pour leur accueil et support en microscopie électronique à balayage et microscopie confocale.

Je tiens à remercier chaleureusement l'ensemble des doctorants de l'équipe CBB, les doctorants qui m'ont ouvert la voie par leur exemple, Augustin, Mattia, Lilandra, Mégane et tout particulièrement Sabrina, Manon et Antoine qui ont fait la traversée à mes côtés. Votre soutien m'a porté jusqu'ici, je vous en remercie et je vous souhaite le meilleur pour la suite. Enfin, je souhaite encore bien du courage aux doctorants qui vont suivre Taha, Lisa, Rosa, Nicolas et ceux qui se sont lancés tout récemment. Claire je suis ravie que tu prennes ma succession, je serai bien sûr présente pour toi à chaque fois que tu en ressentiras le besoin.

Plus personnellement, je remercie Bastien et nos familles respectives pour leur bienveillance, leurs encouragements et les chaleureux moments partagés pendant ces trois dernières années. Je remercie avec beaucoup d'émotions particulièrement ma maman pour son soutien sans faille tout au long de ma scolarité. Lors de la JPO en 2014, nous étions entrées, déterminées par une issue de secours, nous glissant entre deux arbres décoratifs destinés à la condamner pour rejoindre sans sourciller les rangs des visiteurs. Après 8 ans passés dans cette université, aujourd'hui, promis, je connais la sortie. L'UTC m'a beaucoup apporté sur le plan académique, professionnel mais aussi personnel. J'en profite pour remercier chaleureusement mes amis de la première heure, Manon, Yann, Guillaume, Emmanuelle, Camille, Elodie, Frédérique, Axel, Romane, Linda et Louise pour leur fidélité et les mémorables moments que l'on a partagé ensemble à Compiègne et en dehors depuis.

Enfin, je remercie mon sujet d'étude, ma muse, Volvox Carteri. Après 3 ans d'étude intensive, nier la personnification serait un mensonge, merci.

Scientific communications

CONGRESS

Stricher M., Vigneron P., Sarde. C.-O., Delbecq F., Egles C., "Volvox carteri, a versatile and promising material for tissue engineering" - Oral presentation
1st Annual Meeting of GDR 2088, October 2020, Nice, France

Stricher M., Vigneron P., Sarde. C.-O., Delbecq F., Egles C., "Volvox carteri as an innovative, versatile, promising biomaterial for tissue engineering" - Oral presentation
6th TERMIS world congress, November 2021, Maastricht, The Netherlands

PUBLICATIONS

Published:

M. Stricher, C-O. Sarde, E. Guénin, C. Egles, F. Delbecq, "Cellulosic/polyvinyl alcohol composite hydrogel: Synthesis, characterization and applications in tissue engineering," *Polymers*, vol. 13, no. 20, p. 3598, Oct. 19, 2021, ISSN: 2073-4360. DOI: [10.3390/polym13203598](https://doi.org/10.3390/polym13203598).

P. Quantin, M. Stricher, S. Catoire, H. Ficheux, C. Egles, "Dermatokinetics: Advances and Experimental Models, Focus on Skin Metabolism." [published online ahead of print, 2022 May 17], *Curr Drug Metab*, vol. 23, n° 5, p. 340-354, avr. 2022, DOI: [10.2174/1389200223666220517114004](https://doi.org/10.2174/1389200223666220517114004).

S. Ji, M. Stricher, F. Nadaud, E. Guenin, C. Egles, F. Delbecq, "Solvent-Free Production by Extrusion of Bio-Based Poly(glycerol-co-diacids) Sheets for the Development of Biocompatible and Electroconductive Elastomer Composites", *Polymers*, 14, 18, pp. 3829, sept. 2022, DOI: [10.3390/polym14183829](https://doi.org/10.3390/polym14183829).

In preparation:

M. Stricher, P. Vigneron, F. Delbecq, C-O. Sarde, Egles C., "The microalga V. Carteri promotes histogenesis and adipogenesis through the modular self-assembly of living building blocks in soft-tissue regeneration and augmentation"

Abstract

V. carteri f. *nagariensis* is an established model for the study of the genetic basis underlying the acquisition of mechanisms of multicellularity and cellular differentiation. This microalga constitutes, in its most simplified form, a sphere built around and stabilised by a form of primitive extracellular matrix. Based on its structure and its ability to support surface cell adhesion most likely induced by the composition of its extracellular matrix, we have developed a modular approach to soft tissue engineering by compact-stacking of *V. carteri* colonies. *V. carteri* suspension demonstrated cytocompatibility, histogenesis promoting properties, and no induction of an inflammatory response *in vitro*, which allowed us to consider the use of *V. carteri* suspension colonies for soft tissue augmentation and to initiate the study of its *in vivo* biocompatibility. *V. carteri* exhibited cellular fate-directing properties, causing fibroblasts to take on an alkaline phosphatase⁺ stem-cell-like phenotype and both human adipose-derived stem cells and mouse embryonic stem cells to differentiate into pre-adipocytes to adipocytes. The ability of *V. carteri* to support histogenesis and adipogenesis was also observed *in vivo* by subcutaneous tissue augmentation of athymic mice, highlighting the potential of *V. carteri* to support or influence tissue regeneration.

The potential identified in *V. carteri* inspired us to develop other alternatives materials including plant-based polymers in the form of a cellulose and polyvinyl alcohol based composite hydrogel that we extensively characterised with the same intent of application as a substitute for soft tissue augmentation. We finally pursued the biomimetic approach by studying the feasibility of developing plant-based and *V. carteri*-based materials that would display its microsphere morphology and, additionally, its protein content.

Our conclusion presents *V. carteri* as an innovative and inspiring biomaterial for tissue engineering and soft tissue regeneration. Its strategies in terms of shape, structure, and composition can be central in the design of a new generation of bio-inspired heterogeneous biomaterials, recapitulating more appropriately the complexity of the body tissues when guiding their regeneration.

Keywords: Microalgae, Composite hydrogel, Microsphere, Sphere packing, Tissue Engineering, Regenerative medicine, Soft tissue.

Résumé

L'ingénierie tissulaire est considérée comme l'une des plateformes scientifiques de la médecine régénérative, qui vise à réparer, remplacer ou régénérer des cellules, des tissus ou des organes pour rétablir une fonction déficiente [100]. Ce domaine est continuellement alimenté par de nouveaux modèles et de nouvelles solutions thérapeutiques, principalement basés sur des produits d'origine animale. Dans le cadre de cette thèse, nous avons souhaité prendre l'approche inverse et repousser la règle des 3R (c.-à-d. Replacement, Reduction, et Refinement) en projetant notre objectif vers la proposition de matrices végétales alternatives et innovantes dans une approche de bio-inspiration pour l'ingénierie tissulaire et le développement de solutions thérapeutiques pour le traitement et la régénération des défauts des tissus mous. Nous avons par ailleurs l'intention de développer des caractérisations structurelles, chimiques et biologiques approfondies de nos matériaux pour évaluer leur potentiel et identifier les applications les plus appropriées.

L'importante biofonctionnalité des solutions d'ingénierie tissulaire est permise par l'acquisition d'une tridimensionnalité obtenue par l'association spécifique de cellules, biomolécules et éventuellement biomatériaux. Développer une démarche de bio-inspiration autour de l'ingénierie tissulaire revient donc à s'intéresser à la manière dont les organismes ont acquis cette tridimensionnalité. L'évolution est marquée par des événements définis impliquant de profondes innovations décrites par Szathmáry et Smith [1], dans le cadre des transitions majeures dans l'évolution (MTE). Celles-ci expliquent la structure hiérarchique de la vie sur Terre - des gènes aux chromosomes, des chromosomes aux cellules, de la complexification des cellules (des cellules procaryotes aux cellules eucaryotes), des cellules individuelles aux organismes multicellulaires, et des organismes aux sociétés - et de sa constante complexification.

Le passage d'organismes unicellulaires à des organismes multicellulaires s'est produit des dizaines de fois indépendamment et simultanément dans l'évolution de la vie sur Terre, menant au développement des algues rouges, des algues brunes, des plantes terrestres, des animaux et des champignons. La multicellularité acquise par les algues vertes volvocines est l'une des plus étudiées et sert de modèle pour le fondement génétique sous-jacent à l'acquisition de la multicellularité et de la différenciation cellulaire [8]. Les *Volvocaceae*, nommées par Ehrenberg en 1834 [10], sont des algues biflagellées et photosynthétiques, comprenant huit genres (*Chlamydomonas*, *Tetrabaena*, *Gonium*, *Astrephomene*, *Pandoria*, *Eudorina*, *Pleodorina* et *Volvox*), et une soixantaine d'espèces. La force des algues volvocines en tant que système modèle évolutif réside dans la proposition de deux systèmes extrêmes en taille et complexité, l'algue unicellulaire *Chlamydomonas reinhardtii* unicellulaire et sous

forme de colonie multicellulaire *Volvox carteri*, ainsi qu'un large spectre d'espèces intermédiaires dont la dimension, le degré de structuration et la spécialisation cellulaire varient considérablement établissant un continuum entre les deux [12]. L'acquisition progressive de processus fondamentaux qui ont conduit à des espèces multicellulaires et de plus en plus complexes de *Volvocaceae* a été défini par le biais d'une analyse phylogénomique par Kirk [13]. Ces processus fondamentaux décrivent une complexification progressive permise par une structuration aux niveaux cellulaire - par acquisition de mécanismes d'attachement, polatisation, différenciation cellulaire - et matricielle par la formation et l'expansion d'une matrice extracellulaire. Le genre le plus évolué *Volvox* a donc été sélectionné comme objet de bio-inspiration, dans son espèce et forme les plus documentés dans la littérature, *Volvox carteri* f. *nagariensis*.

Tout d'abord, nous avons mis en place une stratégie dans la partie C autour de l'utilisation de la microalgue *V. carteri* comme biomatériau pour l'ingénierie tissulaire et une application en médecine régénérative. Dans le chapitre C1, la production, la conservation, et les caractérisations structurelle et biologique de cette algue ont été entreprises afin de considérer l'intégration de celle-ci en culture de cellules de mammifères et lever progressivement les réserves liées à son utilisation inhabituelle. L'enceinte de culture incluant un contrôle de la température et l'alternance de phases d'illumination et d'obscurité a permis de standardiser la production de l'algue *V. carteri*. Une production satisfaisante en conditions stériles de $11,34 \pm 2.7$ millions de colonies de *V. carteri* par phase de 21 jours de culture a été maintenue pendant plus de trois ans fournissant la quantité d'algues nécessaire pour étudier l'utilisation de *V. carteri* comme biomatériau innovant pour l'ingénierie tissulaire. Une production maximale de 45.36 ± 10.8 millions de colonies de *V. carteri* par phase de 21 jours de culture a été estimée, principalement limitée par les dimensions de la chambre de culture. Bien que notre dispositif puisse être suffisant pour les études précoces et précliniques, des investissements supplémentaires et une optimisation de la culture seraient nécessaires pour assurer l'évaluation clinique, l'industrialisation et la commercialisation. La fixation à l'éthanol 70% des algues garantit une conservation à long terme de l'algue par préservation de la morphologie de l'algue permettant une gestion de la production indépendante des manipulations en culture cellulaire. Cette fixation permet la déflagellation partielle de la surface de l'algue et l'extraction des molécules solubles et actives. Simplifiée dans sa composition interne et surfacique, l'algue peut ainsi être ramenée à sa structure primaire et macroscopique, une microsphère de matrice extracellulaire particulièrement mis en évidence par la révélation des glycoprotéines α -D- Mannose et Glucose par histochimie au moyen de la lectine Concanavalin A. Les colonies préservées en éthanol 70% se sont avérées être adaptées pour un emploi en culture cellulaire. Stable en conditions de culture, à 37°C et 5% CO₂, l'innocuité de notre matériel préservé et de ses composés solubles et libérés par sonication ont démontré la cytocompatibilité globale de *V. carteri* au regard de la norme ISO 10993-5 [310]. Le secrétome de monocytes/macrophages murins J774.2 induit par *V. carteri*

sous de multiples conditions a montré l'absence de réponse pro-inflammatoire, ce qui témoigne de la non-activation des macrophages à 48 heures d'exposition démontrant les propriétés non inflammatoires et non immunogènes de notre matériau confortant l'hypothèse de biocompatibilité. De multiples types cellulaires dont les fibroblastes murins L929 et humains HDFn, et les cellules endothéliales HUVEC ont démontré des capacités d'adhésion à la surface des colonies de *V. carteri* nous permettant d'envisager une approche d'ingénierie tissulaire par association de modules cellularisés appelés living building blocks.

Le modèle modulaire basé sur l'auto-empilement de colonies précellularisées a ainsi été décrit et développé en Chapitre C2. La démarche de développement tissulaire a ainsi pu être démontré *in vitro*, par emploi de living building blocks construit par la cellularisation de colonies de *V. carteri* par les HDFn. Une caractérisation morphologique de la suspension saturée d'algue a permis de mettre en évidence son adéquation pour une utilisation en culture cellulaire. La suspension présente des algues de diamètre normalement distribué entre 150 et 300 μm générant un haut compactage à saturation de $74.8 \cdot 10^3$ colonies/mL (57%V/V), offrant une surface de culture de 65 cm^2 par insert de culture de 12 puits, multipliant ainsi par un facteur 72 la surface de culture initiale. Ce système a démontré une certaine malléabilité tout en maintenant l'interconnectivité, la compaction augmentant par déformation progressive des colonies quantifiée par la modification de leur circularité. Les HDFn ont été en mesure de proliférer sur cette surface comme le montre l'augmentation progressive de l'activité mitochondriale mesurée tout au long des 21 jours de culture combinée à la densification cellulaire observée entre les colonies d'algue. Par ailleurs, en culture à la surface de *V. carteri*, les HDFn ont également montré une activité phosphatase alcaline significative observable à partir du jour 2, alors qu'étalées sur la surface de culture, aucune activité enzymatique n'a été détectée. Ceci témoigne d'une potentielle capacité de modification du comportement cellulaire de la culture dans ce système, ici une redirection vers un phénotype de type cellules souches qui présentent une activité phosphatase alcaline significativement augmentée. A l'issue de la culture, un tissu cohésif pouvait être obtenue. Par étude histologique et précouplage des colonies à la rhodamine, nous avons été en mesure d'observer la distribution homogène de nombreux fibroblastes sur l'ensemble de l'épaisseur du tissu associé à une capacité à de production de néosynthèse, révélé par la coloration au safran de collagène néoformé. L'ensemble de ces résultats démontre les capacités de soutien de l'histogénèse *in vitro* par *V. carteri* et l'efficacité de ce système par auto-empilement de living building blocks, nous permettant d'envisager son intégration dans le contexte de l'augmentation des tissus mous. L'implantation en sous-cutané de cette structure tissulaire a donc été réalisée sur modèle de souris nude athymique, présentant un système immunitaire amoindri permettant l'observation de la réponse inflammatoire liée à la réponse à un corps étranger. Un volume de tissu gélatineux d'environ 150 mm^3 a été injecté directement sous la peau de la souris en utilisant une seringue en raison de sa fragilité, créant ainsi un implant apparent visible de l'extérieur. L'expansion de volume créée par l'injection est restée détectable et inchangée en taille et en forme pendant toute la durée de l'expérience. Une injection de gel de collagène bovin a été utilisée comme condition contrôle. Bien que

la même quantité de matériau ait été initialement injectée, le témoin de collagène bovin a pratiquement disparu, laissant une structure à peine détectable sous la peau de la souris un mois après l'implantation. En revanche, l'implant du tissu à base d'HDFn et *V. carteri* présentait une grande structure de type tissu mésenchymateux pénétrée par les vaisseaux sanguins environnants. Cette structure identique a également été observée deux mois après l'implantation, suggérant sa stabilité *in vivo*. Ce tissu fibreux cellularisé de façon homogène présentait, lors de la coloration histologique à l'hématoxyline-éosine, des restes de structures sphériques attribuables à la dégradation des colonies de *V. carteri*. Les analyses histologiques des échantillons de biopsie du HDFn de *V. carteri* injecté ont montré que ce tissu d'augmentation était mésenchymateux, épais et ne présentaient, comme ses tissus environnants, aucun signe d'inflammation démontrant son intégration un mois après l'implantation. Ceci est conforté par la synthèse et la vascularisation du néotissu démontrant une colonisation incontestable des espaces interstitiels *in situ*. Il s'agit d'une preuve de concept pour la formation de tissus tridimensionnels par association de living building blocks de *V. carteri* et son application à la régénération tissulaire *in vivo*. L'empilement compact des colonies de *V. carteri* offre une surface de culture étendue, unique et intégralement interconnectée, adaptée à la cellularisation et à la diffusion dans tout le matériau. Modulant le confinement, le comportement et l'hétérogénéité cellulaires, la suspension de *V. carteri* représente une matrice d'origine végétale innovante pour de telles utilisations permettant l'adhésion, la prolifération et la sécrétion de la matrice avec d'éventuelles propriétés de différenciation.

Comme nous avons précédemment identifié que *V. carteri* pouvait avoir un impact sur le phénotype cellulaire en étant capable de faire évoluer les fibroblastes dermiques humains néonataux vers la synthèse de la phosphatase alcaline, nous nous sommes demandé si ce système de culture pouvait à lui seul diriger la différenciation des cellules souches de quelque manière que ce soit. En plus du stimulus moléculaire, la mécanique et la topographie du substrat pourraient diriger une telle différenciation. Nous l'avons donc vérifié en Chapitre C3. Des cellules souches mésenchymateuses humaines et des cellules souches embryonnaires murines ont été ensemencées sur notre système de blocs de construction vivants *V. carteri* et cultivées jusqu'à 3 semaines sans aucune supplémentation induisant l'adipogénèse. La morphologie des cellules et leur engagement dans la voie adipogénique ont été suivis par la coloration de leur contenu lipidique avec de l'Oil Red O contre coloré avec de l'hémalum ou à la phalloïdine/DAPI pour révéler leur cytosquelette d'actine leur noyau cellulaire pour une observation en microscopie optique ou confocale. Les cellules souches mésenchymateuses dérivées du tissu adipeux humain (hASC) ont été capables en quelques heures d'adhérer, de s'étendre et de recouvrir partiellement la surface de *V. carteri*, en développant des protubérances membranaires similaires à celles présentées lors de la culture en 2D sur des surfaces traitées par culture. Tout en restant adhérentes et en grappes à la surface des colonies de *V. carteri*, certaines hASC sont devenues plus rondes en 48 heures, s'écartant de la morphologie caractéristique des cellules mésenchymateuses, présentant la condensation de leur cytosquelette d'actine autour de leur noyau. Nous avons observé la

formation de dizaines de microgouttelettes lipidiques de 1 à 3 μm de diamètre, typiques de la voie adipogénique. Les hASC se sont également polarisées en rapprochant leurs noyaux de la membrane cellulaire, concentrant les gouttelettes lipidiques en position centrale, signe d'une maturation adipocytaire avancée. La rondeur du noyau cellulaire semble également être modifiée. *V. carteri* en tant que substrat a généré au moins la différenciation et le maintien des hASC en préadipocytes. Alors que le volume de chaque gouttelette lipidique individuelle ne semblait pas évoluer de manière significative entre J2 et J21, le volume global des préadipocytes formés a augmenté, concentrant de plus en plus de gouttelettes lipidiques. Ce résultat a été confirmé sur les cellules embryonnaires murines C3H/10T1/2 qui ont montré des capacités d'adhésion à la surface de *V. carteri* sous la forme d'une structure de type sphéroïde tout en accumulant des microgouttelettes lipidiques d'environ 1 μm de diamètre dès 48h, démontrant une fois de plus l'induction adipogénique des cellules souches par culture sur colonies de *V. carteri*. Des gouttelettes lipidiques d'un diamètre de 2, 6,5 et 8 μm ont pu être identifiées respectivement à 7, 14 et 21 jours de culture. Les C3H/10T1/2 ont montré une concentration et une expansion des gouttelettes lipidiques tout en maintenant des points d'ancrage à la surface de la colonie. Certaines cellules C3H/10T1/2 se sont finalement avérées être complètement rondes, atteignant une différenciation adipocytaire avancée. La culture en modèle d'auto-empilement de *V. carteri* a généré une synthèse massive et un maintien de gouttelettes lipidiques pendant la durée de la culture tant sur C3H/10T1/2 que sur hASC, démontrant indéniablement la capacité de l'algue à promouvoir l'adipogenèse sans ajout de facteurs d'induction supplémentaires. Ces propriétés adipogéniques sont de manière très probablement due à des facteurs morphologiques et biomécaniques.

V. carteri fournit un substrat sphérique avec une rigidité globale d'environ 3 kPa, stable quels que soient le diamètre de la colonie et le stade de développement, démontrant l'homogénéité des propriétés mécaniques offertes par la suspension. L'uniformité de la rigidité des colonies de *V. carteri* résulte des mécanismes actifs, complexes et efficaces de membrane et de matrice extracellulaire qui assurent l'intégrité de l'algue tout au long de son développement. *V. carteri* présente une rigidité semblable à celle des adipocytes et des tissus adipeux, dont les modules de Young varient entre 0,5 à 2 kPa [393], [404], [405]. La faible résistance à la déformation de la colonie *V. carteri* peut être attribuée à la quantité élevée de proline hydroxylée conférée par la prédominance de la phérophorine dans la MEC. En effet, il a été démontré que l'hydroxylation de la proline améliore l'élasticité du collagène [406]. Le mimétisme biomécanique des adipocytes et tissus adipeux de *V. carteri* pourrait induire la différenciation adipocytaire des cellules souches mésenchymateuses *in vitro*. En effet, il a été montré que la recreation *in vitro* de la rigidité de tissu adipeux peut stimuler l'adipogenèse des cellules souches mésenchymateuses dérivées de l'adipose humaine sans l'utilisation d'additifs chimiques dans le milieu [177]. *V. carteri* s'inscrit parfaitement dans la plage de 2 à 4 kPa de rigidité optimale et estimée pour l'induction mécanique de l'adipogenèse [403]. Les cellules souches mésenchymateuses cultivées sur un substrat flexible réduisent significativement leur surface cellulaire et leur rapport d'aspect en raison d'une faible contractilité du

cytosquelette [407], influençant la différenciation des adipocytes via la signalisation ERK [408], favorisant l'upregulation de l'expression génique des trois marqueurs adipogéniques (c'est-à-dire PPAR γ , CEBP α et aP2) et l'accumulation de lipides [177]. La dynamique de réorganisation du cytosquelette d'actine affecte également la rondeur du noyau pendant la différenciation des adipocytes [409].

Par ailleurs, comme il a été démontré que l'implantation de tissu mésenchymateux à base de *V. carteri* permettait de maintenir avec succès le volume expansé *in vivo* malgré le remodelage de l'implant, nous avons donc cherché à évaluer la part de ce processus intrinsèquement liée à *V. carteri* par implantation en sous-cutané par injection d'une suspension saturée d'algue uniquement. Une analyse histopathologique de l'implant intégré a été réalisée par rapport à un témoin non implanté, un mois après l'implantation. Tout d'abord, nous avons observé une réduction significative du volume d'injection dans les premiers jours suivant l'implantation. Cette réduction était principalement liée au drainage du fluide résiduel et à la reconfiguration de l'empilement des sphères d'algues, car nous avons identifié que notre injectable pouvait encore contenir du tampon à 44 %V/V. La suspension de colonies de *V. carteri* n'a pas montré de dispersion particulière dans les tissus, car les deux points d'injection très rapprochés sont restés distincts tout au long de l'implantation. En ne considérant que la fraction solide, nous avons noté une réduction de 3,5 à 4 fois du volume de l'implant 1 mois après l'implantation. Pourtant, une structure tissulaire translucide remodelée restait visible à ce stade. Aucun signe clinique d'inflammation (ex: rougeur, gonflement) n'a été détecté pendant la période d'implantation. L'étude anatomopathologique a montré le remplacement de la suspension de *V. carteri* par un tissu de type mésenchyme à 1 mois post-implantation. Ce tissu remodelé de 500 μ m d'épaisseur présentait une matrice extracellulaire homogène, une infiltration cellulaire et une intégration dans une capsule fibreuse structurellement similaire au tissu conjonctif interstitiel superposé aux couches tissulaires standard de l'épiderme, du derme, du tissu adipeux blanc dermique et du panniculus carnosus sans altération visible ni infiltration algale. Les souris athymiques ne développent qu'un poil réduit "abortif" [389] mais présentent encore de nombreux follicules pileux intégrant les structures associées telles que les glandes sébacées et les réserves de cellules souches. Aucune structure vasculaire n'a été correctement visualisée dans le tissu remodelé. Cependant, des vaisseaux sanguins ont été trouvés dans le tissu interstitiel environnant, montrant que le tissu remodelé doit être infiltré et alimenté par des systèmes capillaires que nous n'avons pas pu observer. La matrice extracellulaire développée ne présentait aucune structure algale résiduelle, mais comprenait de nombreux macrophages et fibroblastes spumeux, ce qui indique que la dégradation des matériaux et le remodelage de la matrice peuvent encore se poursuivre dans des conditions d'inflammation légère.

Ce tissu mésenchymateux présentait des niches d'une dizaine d'adipocytes en croissance répartis sur l'ensemble de l'implant, en particulier dans sa partie inférieure. Alors que le tissu mésenchymateux généré par *V. carteri* a montré un développement tissulaire au même degré que celui observé après 4 semaines d'implantation d'implants à base de collagène,

y compris des faisceaux de collagène matures et une néovascularisation à la périphérie de l'implant [448], il a également montré un développement avancé de la niche du tissu adipeux. L'adéquation de la rigidité de *V. carteri* avec la rigidité du tissu adipeux doit avoir favorisé le développement de la niche du tissu adipeux. La rigidité du tissu doit avoir favorisé la différenciation adipocytaire des cellules MSC et progénitrices infiltrées, car il a été démontré que le conditionnement mécanique et biochimique était à la fois équivalent et suffisant pour permettre une différenciation adipocytaire radicale. Équivalents et suffisants pour stimuler considérablement l'adipogénèse *in vivo* [449]. En effet, l'adipogénèse *in vivo* ont été précédemment induites avec succès par voie biochimique en déclenchant l'activation de gènes adipogéniques par l'intermédiaire d'un mécanisme de médiation. L'activation des gènes adipogéniques médiée par PPAR- γ via le chargement de matériel avec la rosiglitazone [449], de pioglitazone [450], [451] ou d'insuline et d'IGF I [452]. Les matériaux décellularisés à base de matrice dermique [453], de membrane basale [454] et de tissu adipeux [455] suscitent également un grand enthousiasme, car ces matrices complexes contiennent une grande variété de protéines structurales (par exemple COL I, COL III) et adipogènes (par exemple COL IV, COL VI, laminine), tout en fournissant une source de facteurs de croissance (par exemple FGF2). Ces matrices complexes qui contiennent une grande variété de protéines structurales (par exemple COL I, COL III) et adipogéniques (par exemple COL IV, COL VI, laminine) tout en fournissant des sources de facteurs de croissance (par exemple FGF2, VEGF-A, IGF I) ont montré leur capacité à soutenir efficacement l'adipogénèse *in vitro* et *in vivo*. Cependant, ce type d'induction nécessite souvent une prédifférenciation *in vitro* avant l'implantation [456]. Nos recherches préliminaires ont montré que *V. carteri* pouvait rapidement induire une différenciation adipogénique simultanément à la réponse inflammatoire, permettant le développement de niches adipocytaires. La simultanéité de ces processus souligne comment *V. carteri* peut être un compromis approprié pour promouvoir la régénération de tissus mous en équilibrant les impacts bénéfiques et négatifs de la réponse inflammatoire.

V. carteri est un biomatériau qui favorise l'adipogénèse. Ses effets adipogéniques, démontrés *in vitro* et *in vivo*, sont directement liés à sa capacité à imiter le tissu adipeux structurellement, mécaniquement et moléculairement, car nous le soupçonnons de délivrer des signaux biochimiques primitifs de la matrice extracellulaire, de l'adhésion cellulaire et de l'accumulation de lipides.

Pour contrebalancer la complexité structurelle et moléculaire de *V. carteri*, nous nous sommes également engagés dans le développement de matériaux bioinspirés de l'algue à des fins d'ingénierie tissulaire, qui seraient chimiquement et structurellement entièrement caractérisés. chimiquement et structurellement entièrement caractérisés. Par analogie avec *V. carteri*, que nous avons utilisé comme bloc structurel dans le développement de nos tissus, nous avons mis au point des matériaux bioinspirés de l'algue. Nous avons produit dans un premier temps un hydrogel composite basé sur la cellulose, l'unité structurelle végétal dans le chapitre D1 qui correspond à l'article publié : M. Stricher, C.-O. Sarde, E. Guénin, C. Egles,

and F. Delbecq, "Cellulosic/polyvinyl alcohol composite hydrogel: Synthesis, characterization and applications in tissue engineering," *Polymers*, vol. 13, no. 20, p. 3598, Oct. 19, 2021, ISSN: 2073-4360. DOI: [10.3390/polym13203598](https://doi.org/10.3390/polym13203598).

Notre méthodologie de synthèse nous a permis d'obtenir une pâte de cellulose microcristalline dialdéhyde (DMCC) et alcool polyvinylique (PVA) prête à l'emploi pouvant être déclinée sous de multiples formes, membrane, scaffold ou billes réalisées par moulage, fabrication additive, extrusion ou électrospinning principalement pour des applications biomédicales. Des hydrogels composites cellulose/PVA peuvent être synthétisés en contrôlant le degré d'oxydation du DMCC, le ratio DMCC/PVA et sa porosité par l'ajout d'agents porogènes. La caractérisation physique de nos hydrogels révèle l'homogénéité du réseau micrométrique interconnecté, l'incorporation de fibres de cellulose microcristalline, ainsi que la bonne intégration d'une porosité supplémentaire. En modulant le ratio DMCC-/PVA, nous constatons que la cellulose rigidifie l'hydrogel au niveau macrométrique, très probablement par l'intermédiaire des microfibrilles de cellulose cristalline. Le degré d'oxydation de la cellulose étant largement lié à la taille des particules, un impact sur les propriétés mécaniques de l'hydrogel au niveau macroscopique est observé lorsque celui-ci varie. Nous supposons que la rigidité supérieure observée pour les échantillons à 9% et 18% est certainement liée à la dimension plus importante des particules de cellulose microcristalline par rapport à la DMCC 36% qui a davantage subi l'hydrolyse et la fragmentation. Au niveau nanométrique les matériaux à base de DMCC à 9% et 36% présentent un module de Young similaire d'environ 40 kPa, tandis qu'à 18%, on obtient un module de Young nettement inférieur. Ces observations sont très certainement liées à l'organisation du réseau DMCC/PVA, à la nature et à la densité des interactions et des liaisons associées. Nos hydrogels ont des propriétés mécaniques similaires à celles des tissus mous dont les modules de Young varient de 0,1kPa à 1MPa. Par cellularisation, les matrices tendent à se rigidifier comme cela a été précédemment observé par le dépôt, le remodelage et la réticulation des protéines de la matrice extracellulaire notamment le collagène [482].

Pour envisager toute application biomédicale, une étude rigoureuse de l'acceptabilité biologique de ce matériau a été entreprise. Les milieux de relargage des hydrogels DMCC/PVA montrent une viabilité décroissante des L929 au fur et à mesure que le degré d'oxydation du DMCC augmente jusqu'à 18% d'oxydation du DMCC, en conformité avec la norme ISO 10993-5. Le PVA étant connu pour être totalement biocompatible, la cytotoxicité indirecte observée sur les L929 est due à la libération de particules de dialdéhyde de cellulose. Ce même effet a déjà été observé sur la lignée de fibroblastes NIH/3T3 où la viabilité cellulaire chute à 70% pour 1,74 mmol/10 g de PVA de groupes CHO [483]. Malgré sa faible oxydation, le DMCC prédomine dans la composition de notre hydrogel, atteignant un minimum de 23,38 mmol/10 g PVA à 9%. L'absence de toxicité observée sous 18% reflète le plein engagement des groupes aldéhydes dans des liaisons stables non délétères au niveau cellulaire. Lorsqu'elles sontensemencées à la surface du matériau, l'interaction cellule-DMCC/PVA montre une corrélation entre la viabilité cellulaire des HDF et les propriétés

mécaniques du matériau au niveau nanométrique. matériau au niveau nanométrique. En effet, les HDFs présentent une viabilité cellulaire plus forte pour le DMCC 9% et 36% que pour le DMCC 18% , montrant un module de Young respectivement de 23, 27 et 13 kPa. Bien que peu de données soient disponibles sur les hydrogels DMCC/PVA, de nombreuses études montrent l'impact positif en 2D et 3D des hydrogels montrent l'impact positif en 2D et 3D de la rigidité de la matrice sur l'activité des fibroblastes en termes de adhésion cellulaire, de prolifération et de migration [484], [485]. La matrice DMCC 9%/PVA (2:1) semble être le matériau le plus approprié pour une utilisation *in vitro*.

Étant donné que les matériaux DMCC/PVA ont des micro-environnements sensiblement identiques dans leur composition, des résultats très similaires sont ensuite obtenus pour les matériaux DMCC 9%, 18% et 36% pendant la culture à long terme. Comme une infiltration homogène et totale du matériau poreux est obtenue, l'induction de la porosité avec une granularité contrôlée du sel s'avère efficace et suffisante dans notre cas. Après 3 semaines de culture, les fibroblastesensemencés s'organisent en agrégats cellulaires de type sphéroïde. En effet, en tant que polymère biologiquement inerte, le PVA montre une incapacité à engager des interactions avec les protéines ECM telles que la fibronectine, le collagène, la laminine et donc à s'associer avec les récepteurs intégrines cellulaires. L'incorporation de cellulose microcristalline dans notre hydrogel offre des points d'ancrage pour ces agrégats cellulaires. En effet, sur les surfaces de cellulose, les HDFs peuvent établir des adhésions cellulaires et développer des filopodes car les HDF peuvent établir des adhésions cellulaires et développer des filopodes car les nombreux groupes hydroxyles à la surface de la cellulose permettent l'adsorption des protéines nécessaires à l'adhésion cellulaire par interactions électrostatiques et liaisons hydrogènes [486], [487]. Par fonctionnalisation chimique, oxydation, phosphorylation ou greffage chimique spécifique, ces interactions peuvent être favorisées pour remédier à la supplémentation en facteur de croissance ou en FBS [488]. Les fibroblastes confinés mécaniquement ont montré leur capacité à se reprogrammer en cellules souches et à rajeunir [382], [383]. Dans la littérature, le PVA et la cellulose bactérienne ont également démontré des propriétés de formation de sphéroïdes et de maintien à long terme des cellules souches [489]-[491]. Le potentiel de ces structures de type sphéroïde à la surface de notre matériau DMCC/PVA est très élevé, fournissant un environnement récapitulant la complexité *in vivo* mieux que les cultures traditionnelles en 2D ou en 3D. La fonctionnalité de ces cellules est plus représentative de la prédictivité des modèles pharmacologiques et présente des propriétés de régénération prometteuses pour les applications d'ingénierie tissulaire et de médecine régénérative. Les hydrogels DMCC/PVA implantés présentent une stabilité complète après un mois d'implantation, une légère inflammation caractérisée par une infiltration importante de neutrophiles et de macrophages et la formation d'une fine capsule fibreuse à la périphérie de l'implant. En induisant une porosité dans l'implant, la surface de contact est augmentée et l'infiltration cellulaire est facilitée, ce qui semble augmenter le score inflammatoire augmentant apparemment le score inflammatoire. Une telle inflammation indique une réaction à

un corps étranger, une réaction clé pour évaluer la sécurité d'un échafaudage dans les applications d'ingénierie tissulaire. En effet, une fois implanté, notre matériau interagit avec son environnement, par l'infiltration de fluides, de protéines et de cellules. Constitué de cellulose et de PVA, l'implant est reconnu comme un non-soi, et l'organisme entreprend des processus inflammatoires visant à sa destruction ou à son isolement du reste du corps [492]. Dans le cas des hydrogels à base de cellulose, une légère inflammation a également été observée à 4 semaines, puis a disparu à 8 semaines, la capsule fibreuse entourant l'implant s'affinant [493], [494]. En l'absence d'une cellulase équivalente à la rupture de la liaison β -(1 \rightarrow 4) glycosidique *in vivo*, la cellulose démontre une lente dégradation *in situ* via la phagocytose des macrophages des particules. Les matériaux cellulosiques peuvent persister sous la forme cristalline cristalline jusqu'à 5 mois après l'implantation [495].

Dans le chapitre précédent, nous avons pu mettre au point un hydrogel cellulosique dont la rigidité se situe dans la gamme des matrices de tissus mous, correspondant spécifiquement à la rigidité des tissus fibreux tels que le derme, le tissu musculaire lisse ou le tissu mammaire. La combinaison des deux polymères, cellulose et PVA, démontre la capacité de notre matériau à soutenir une adhésion cellulaire modérée tout en favorisant une structure cellulaire de type sphéroïde telle que *V. carteri* la génère lorsqu'elle est en contact avec diverses lignées cellulaires telles que les fibroblastes dermiques humains ou les cellules souches embryonnaires murines C3H/10T1/2. Nous avons étudié ici la possibilité de synthétiser des micro sphères basées sur cette combinaison de polymères afin de poursuivre la réplication d'un matériau qui se rapproche structurellement de *V. carteri* dans sa structure la plus basique, une sphère déformable.

Dans cette preuve de concept, nous nous sommes attachés à établir la faisabilité de la génération de microsphères cellulosiques. Nous avons synthétisé ici un hydrogel composite cohésif à base de cellulose et de PVA en adaptant la technique de dégénération/régénération NMP/LiCl décrite dans le chapitre D1 à l'utilisation de la cellulose nanocristalline (NCC). La coloration spécifique au Calcofluor White a démontré une diminution significative de la taille des particules de cellulose présentes dans ce matériau par rapport à l'hydrogel à base de DMCC. La XDR a montré une augmentation de la cristallinité de la NCC par rapport au MCC, ce qui est la conséquence de l'absence de tout contenu amorphe. Cette haute cristallinité a été préservée après l'oxydation, ce qui montre que la structure cristalline de l'hydrogel a été préservée. En effet, les fonctions dialdéhyde sont ajoutées aux extrémités de la chaîne et donc à la périphérie des particules. Les interactions et liaisons stabilisant le réseau polymérique DNCC/PVA ont été confirmées (c'est-à-dire les liaisons hydrogène, acétal et hémiacétal). Cependant, des ajustements supplémentaires de la formulation seraient nécessaires dans un premier temps pour créer un biomatériau qui présente des propriétés mécaniques, d'adsorption des protéines et d'adhésion cellulaire comparables à celles de *V. carteri*. Alors que des microsphères à l'échelle millimétrique ont été produites, les paramètres d'extrusion par flux d'air coaxial (c'est-à-dire l'augmentation du débit d'air, la réduction

du taux d'extrusion de la pâte polymère ou le diamètre de l'aiguille) devraient être optimisés pour obtenir un diamètre optimal des microsphères de 100 à 350 μm . Enfin, une caractérisation structurale, physicochimique et mécanique supplémentaire serait nécessaire pour étudier l'influence de la forme sphérique des microsphères et produire une caractérisation finale du matériau. La MCC, la MFC et la NCC séchées présentent des modules de Young d'environ 25, 100 et 130 GPa, respectivement [511], [512]. Les particules de NCC sont généralement mises en œuvre comme agent de renforcement dans les compositions de films secs composites à base de polymères synthétiques et naturels tels que le PVA [505], [513], l'alginate [514], le chitosan [515]-[517] ou la gélatine [497]. Néanmoins, les fibres cellulodiques représentent un polymère mécaniquement versatile car leur capacité de rétention d'eau, directement liée à leur forte teneur en -OH, entraîne une diminution significative de la rigidité des fibres cellulodiques lorsque le niveau d'humidité augmente [518]. Les fibres cellulodiques sous forme de MCC et de NCC incorporées dans la formulation d'hydrogels à forte teneur en eau, tels que les hydrogels à base de PVA, ont permis de produire des hydrogels relativement souples avec des modules d'Young ajustables allant de 1 à 70 kPa [519]-[522]. Jayaramudu et al. [523] ont précisément réduit le module de Young d'un hydrogel de PVA de 82 kPa à 7 kPa en améliorant la capacité d'absorption d'eau de l'hydrogel en augmentant le rapport CNC/PVA. La CNC fait preuve d'une biocompatibilité élevée, ce qui la rend pertinente pour diverses applications biomédicales, notamment les pansements, les implants et les systèmes d'administration de médicaments [504], [509], [524], [525]. Nous sommes donc convaincus qu'un hydrogel d'une rigidité d'environ 2 kPa peut être produit à la fois sous forme d'hydrogel cylindrique plat et de microsphères en utilisant cette combinaison de polymères et ce processus de réticulation. De tels matériaux bio-inspirés pourraient d'abord représenter un biomatériau alternatif pour le remplacement des tissus mous qui serait plus facilement caractérisé et donc plus facilement et rapidement commercialisable. De plus, ce type de matériau nous permettrait d'étudier les mécanismes d'action d'un modèle d'empilement de sphères de l'algue *V. carteri*, en particulier l'impact sur les cellules du système d'empilement de sphères, l'influence de la courbure de la surface, et la rigidité de l'hydrogel.

Afin de poursuivre notre stratégie de création de modèles analogues de *V. carteri* initiée au chapitre D2, visant finalement à étudier les mécanismes impliqués dans les propriétés biologiques de *V. carteri* (c'est-à-dire l'adhésion cellulaire, la prolifération et l'adipogénèse), nous avons prévu d'incorporer une composante moléculaire directement issue de *V. carteri*. Compte tenu de l'expertise de notre équipe en matière d'extrusion coaxiale par flux d'air et de greffage de protéines ou de peptides sur l'alginate, nous avons choisi d'utiliser ce polymère pour examiner la faisabilité du greffage de protéines de *V. carteri*. Nous pourrions ainsi proposer un matériau alternatif entièrement végétal qui reproduirait structurellement, mécaniquement et moléculairement une colonie de *V. carteri*.

Les composants solubles de *V. carteri* ont été séparés des débris végétaux par sonication rapide, centrifugation et filtration sur une membrane de cellulose d'une porosité de 1 m. La

solution algale concentrée contenait des glycoprotéines, des polysaccharides et des molécules plus petites comme des pigments ou des molécules actives. La fraction soluble a montré des capacités d'auto-assemblage puisqu'un matériau de type éponge s'est formé après lyophilisation, témoignant au moins de l'implication de faibles forces électrostatiques/de liaison entre les polymères de *V. carteri*. En effet, certaines glycoprotéines de *V. carteri* (c'est-à-dire les phéroporines DZ1 et DZ2) ont déjà démontré des capacités d'auto-assemblage autocatalytique [94]. Ici, nous avons démontré la faisabilité de la fonctionnalisation de l'alginate avec des extraits de protéines de *V. carteri*, car l'analyse FTIR et le test BCA ont montré des preuves du greffage. Des ajustements de formulation devront être effectués pour déterminer le rapport approprié entre l'alginate et les extraits de *V. carteri* afin d'assurer une bonne gélification de l'alginate et de confirmer un effet bénéfique observable de l'inclusion des protéines de *V. carteri* sur l'adhésion cellulaire. La réticulation EDC/NHS de l'extrait soluble de *V. carteri* et de l'alginate est basée sur l'association des fonctions carboxyliques de l'alginate avec tout composé possédant des amines primaires. Cette réticulation constitue donc une sélection grossière de la composition protéique de *V. carteri*. Le procédé de réticulation EDC/NHS ou NHS-sulfo est l'une des méthodes les plus utilisées pour la fonctionnalisation biologique des polymères et la conjugaison des protéines sur des matériaux polymères. La force de ce système réside dans sa simplicité, son efficacité et sa polyvalence en raison de l'omniprésence des fonctions carboxyle dans de nombreux polymères et des fonctions amine dans les séquences protéiques. Cette méthode a été largement utilisée pour la fonctionnalisation de polymères naturels (par exemple, collagène, gélatine et alginate) ainsi que de polymères synthétiques (par exemple, Polycaprolactone, Poly(L-lactide)) en greffant des protéines entières (par exemple, fibronectine, collagène) ou des peptides (par exemple, épitope de la fibronectine, G4RGDSP, épitope de la laminine, IKVAV, et peptide d'adhésion, YIGSR) principalement pour améliorer l'adhésion cellulaire, la prolifération cellulaire pour favoriser la colonisation cellulaire *in vitro*, l'intégration tissulaire *in vivo*, et la biocompatibilité des matériaux [531]-[535]. Ce système a montré des possibilités de stabilisation des matrices de collagène, d'amélioration de leurs propriétés physicochimiques, notamment la résistance thermique et enzymatique, et de modulation de leurs propriétés rhéologiques soit en augmentant leur contrainte de cisaillement par homo-réticulation, soit en les diminuant par l'introduction de L-lysine [536], [537]. D'autres polymères et protéines alternatives réticulent, en ciblant des acides aminés spécifiques tels que les résidus lysine en utilisant le réticulant 5,5-bisvanilline [538] ou les résidus cystéine en profitant de sa thiol-réactivité au maléimide pour générer une liaison thiosuccinimide [539]-[542]. La réticulation des glycoprotéines de *V. carteri* et la mise en forme de microsphères nous permettent d'évaluer le rôle des glycoprotéines algales dans les capacités des extraits solubles de *V. carteri* pour l'adhésion cellulaire, le développement tissulaire et l'induction de l'adipogenèse observés dans les chapitres C1, C2 et C3. La mise en œuvre de la stratégie de rigidification des colonies de *V. carteri* pourrait être envisagée en réticulant leur matrice extracellulaire afin d'élargir son champ d'action et de mieux s'adapter aux cellules contractiles (par exemple, les fibroblastes, les myocytes). Un modèle d'environnement multi-mécanique basé sur *V. carteri* pourrait ainsi être développé en combinant une faible rigidité d'environ

2 kPa pour la différenciation des adipocytes et une plus grande rigidité à ajuster (10-50 kPa) pour l'expansion des cellules contractiles. Alternativement, un tel modèle pourrait être reproduit en utilisant la réticulation de l'alginate et des glycoprotéines *V. carteri*, car le module de Young d'un hydrogel d'alginate peut varier de 1 à 500 kPa en modulant la proportion d'acide β -D-mannuronique et d'acide α -L-gulonurique, la concentration en alginate et les paramètres de gélification (par exemple, la nature et la concentration des cations, la vitesse et la durée de gélification) [543]-[545]. Ceci représente un travail préliminaire vers le développement de microsphères semblables à *V. carteri* pour combiner les composants morphologiques, mécaniques et moléculaires de *V. carteri* en utilisant l'alginate pour mieux comprendre les mécanismes d'adhésion cellulaire médiés par *V. carteri*. Cependant, ce matériau purement végétal présente également un intérêt en tant que matériau bio-inspiré alternatif pour l'ingénierie tissulaire.

Dans le cadre de mon travail de thèse, nous avons pu illustrer, à travers les capacités biologiques observées dans notre principal objet d'étude, la micro-algue *V. carteri*, l'intérêt des matrices et matériaux d'origine végétale comme alternatives aux matériaux d'origine animale, encore principalement employés en ingénierie tissulaire pour la production de modèles de recherche toxicologique, de modèles pathologiques à des fins de criblage pharmacologique, ou de biomatériaux pour la régénération tissulaire. Dans ce travail de thèse, nous avons établi la polyvalence de *V. carteri* en tant que matrice d'intérêt pour l'ingénierie tissulaire et la régénération tissulaire, en mettant en évidence ses capacités de construction de tissus. Le potentiel des extraits de *V. carteri* ou de composés spécifiques (c'est-à-dire les phéoporines, les protéines de type collagène ou laminine) n'a été qu'effleuré ici. Ces polymères dérivés de *V. carteri* pourraient être utilisés pour favoriser l'adhésion des cellules à des surfaces peu bioactives ou même pour former des environnements semblables à des membranes basales par réticulation chimique ou même par électrofilage. Bien que l'empilement de sphères ne soit probablement pas physiologique en termes absolus pour le développement de tissus, *V. carteri* en tant que modèle de développement pour l'acquisition multicellulaire et pour l'établissement d'une MEC sur laquelle tout repose nous a incités à développer un schéma alternatif pour la construction de tissus. Bien qu'un grand nombre d'incertitudes et d'inconnues demeurent autour des mécanismes expliquant les capacités de *V. carteri* partiellement explorées dans ce manuscrit, *V. carteri* représente certainement un matériau à fort potentiel pour l'ingénierie tissulaire et la médecine régénérative.

Contents

Acknowledgements - Remerciements	3
Scientific communications	5
Abstract	7
Résumé	9
Abbreviations	35
 Part A - General context	 39
A1 <i>Volvox carteri</i> f. <i>nagariensis</i>, an established model for developmental and evolutionary biology	39
A1.1 The volvocine green algae family, a phylogenetic perspective on unicellularity to multicellularity transition	39
A1.1.1 The major transitions in evolution framework	39
A1.1.2 The <i>Volvocaceae</i> , a model for the development of multicellularity . . .	40
A1.1.3 The <i>Volvocaceae</i> , knowledge gaps and challenges	42
A1.2 Fundamental knowledge on <i>V. carteri</i>	44
A1.2.1 Natural habitat and sampling	44
A1.2.2 Structuration of an adult <i>V. carteri</i> colony	45
A1.2.3 Asexual life cycle of <i>V. carteri</i>	46
A1.2.4 Sexual life cycle of <i>V. carteri</i>	49
A1.2.5 <i>V. carteri</i> 's reproductive cycle handling in lab culture	50
A1.2.6 <i>V. carteri</i> extracellular matrix architecture	51
 A2 Tissue engineering strategies based on <i>V. carteri</i>'s development	 55
A2.1 Top-down vs. bottom-up approaches to tissue engineering	55
A2.1.1 The traditional approach	56
A2.1.2 The modular approach	58
A2.2 The volvocine algae – analogies with the formation of living building blocks .	59
A2.2.1 The significance of cell attachment and adhesion mechanisms	60
A2.2.1.1 Algal cell attachment and ECM based-cellular membranes – milestone for multicellular development	60

A2.2.1.2 Cell adhesion – key parameter for the living building blocks shaping	61
A2.2.2 The significance of the extracellular matrix on cell differentiation . . .	64
A2.2.2.1 Impact of the ECM on algal differentiation	64
A2.2.2.2 Impact of the ECM on cell differentiation in mammal cells . .	65
A3 Context of soft-tissue augmentation and regeneration	67
A3.1 Towards the proposal of soft tissue fillers	67
A3.1.1 Context of soft tissue augmentation	67
A3.1.1.1 Soft tissue	67
A3.1.1.2 Soft tissue defect	67
A3.1.2 Soft tissue augmentation, from synthetic non degradable materials to integrated tissue substitutes	68
A3.1.2.1 Soft tissue augmentation	68
A3.1.2.2 Traditional approach	69
A3.1.2.3 Regenerative approach	69
A3.2 Biological mechanisms implied in soft tissue augmentation	70
A3.2.1 Host tissue response	70
A3.2.2 The inherent role of inflammation, managing the foreign body reaction	72
A3.2.2.1 Anticipate the foreign body reaction from the conception phase	72
A3.2.2.2 Evaluate the foreign body reaction both <i>in vitro</i> and <i>in vivo</i> .	75
A3.2.2.3 Opportunities provided by soft tissue-based substitutes and grafts	77
A4 Thesis research project: <i>V. carteri</i> living building blocks-based stacking model and bioinspiration for biomaterial design	81
A4.1 Thesis objectives	81
A4.2 Development of the thesis research project	82
Part B - Material and methods	87
B1 <i>V. carteri</i> culture	87
B1.1 Culture maintenance	87
B1.2 Algal enumeration and observation	88
B1.3 Algal deflagellation	88
B1.4 Production of <i>V. carteri</i> raw extract	89
B2 <i>V. carteri</i> inspired material synthesis	91
B2.1 PVA/Cellulose-based material synthesis	91
B2.1.1 Sodium periodate-mediated cellulose oxidation	91
B2.1.2 Cellulose/PVA coupling via LiCl/NMP system	91
B2.1.3 Formation of cellulose/PVA hydrogels	92
B2.1.4 Microbeads extrusion	93

B2.2	<i>V. carteri</i> like-microbeads synthesis	94
B2.2.1	Covalent cross-linking of alginate and <i>V. carteri</i> proteins and polysaccharides	94
B2.2.2	Microbeads synthesis	94
B3	Characterisations of <i>V. carteri</i>, <i>V. carteri</i> inspired and derivative materials	95
B3.1	Biomaterial physico-chemical characterisation	95
B3.1.1	Fourier-Transform Infrared Spectroscopy (FTIR)	95
B3.1.2	Quantification of the Dialdehyde Content (DC %)	95
B3.1.3	X-ray Diffraction Analysis (XDR)	96
B3.2	Microstructural analysis	96
B3.2.1	Environmental Scanning Electron Microscopy (ESEM)	96
B3.2.2	<i>V. carteri</i> flagella observation using confocal microscopy	96
B3.2.3	<i>V. carteri</i> cell wall observation using confocal microscopy	96
B3.2.3.1	Chitin and cellulose staining using Calcofluor White staining	96
B3.2.3.2	Amyloid content staining using Congo Red	97
B3.2.3.3	F-actin staining using Phalloidin	97
B3.2.3.4	Mucous content staining via Periodic acid–Schiff (PAS) reaction	97
B3.2.3.5	Lipophilic content staining using Oil red O	97
B3.2.4	<i>V. carteri</i> polysaccharides and glycoproteins observation using lectin histochemistry	97
B3.2.4.1	Concanavalin A α -D-mannosyl and α -D-glucosyl staining . .	98
B3.2.4.2	Wheat Germ Agglutinin sialic acid and N-acetylglucosaminyl residues staining	98
B3.2.5	DMCC hydrogels physical characterisation	98
B3.2.5.1	Cellulose observation using Calcofluor White staining	98
B3.2.5.2	Pore Connectivity, Water Content and Swelling Ratio	98
B3.3	Mechanical characterisation	99
B3.3.1	Uniaxial compressive test	99
B3.3.2	Nanoindentation test	99
B3.4	Cell culture on <i>V. carteri</i> microalgae, inspired and derivative materials	100
B3.4.1	Primary cells and lineage culture maintenance	100
B3.4.1.1	Mouse fibroblast cell line L929 (L929)	100
B3.4.1.2	Mouse BALB/c monocyte macrophage J774.2 (J774.2)	100
B3.4.1.3	Mouse embryo cell line C3H/10T1/2, Clone 8 (C3H10)	100
B3.4.1.4	Primary Neonatal Human Dermal Fibroblasts (HDFn)	100
B3.4.1.5	Human Adipose tissue-derived mesenchymal Stem Cells (ASC)	101
B3.4.1.6	Human Umbilical Vein Endothelial Cells (HUVECs)	101
B3.4.2	Pseudo-tissue construction using <i>V. carteri</i> as a living building block basic material	102
B3.5	Biochemical and biological analysis	102
B3.5.1	Total protein content determination	102

B3.5.2	<i>V. carteri</i> <i>in vitro</i> deformability	103
B3.5.3	Cytotoxicity testing following the ISO 10993-5 standards [310]	103
B3.5.4	<i>In vitro</i> inflammation investigation	104
B3.5.5	Cell adhesion evaluation	104
B3.5.6	Cell viability estimation	105
B3.5.7	Cell proliferation evaluation	105
B3.5.8	Histological analysis	106
B3.5.8.1	Observation of HDFn self-organisation in Rhodamine pre-coupled <i>V. carteri</i> based pseudotissue	106
B3.5.8.2	Hemalun Eosin Safran (HES) staining procedure	106
B3.5.8.3	Adipogenic differentiation monitoring	106
B3.6	Implantation in an Athymic Mice Model	107
B3.7	Statistical analyses	108

Part C - *Volvox carteri*, a versatile and innovative biomaterial for tissue engineering and regenerative medicine **111**

C1 The *V. carteri* micro-algae evidences great potential as a biomaterial for tissue engineering **111**

C1.1	<i>V. carteri</i> material specificity	111
C1.1.1	Lab scale production of <i>V. carteri</i> microalgae	111
C1.1.2	<i>V. carteri</i> preculture modification	113
C1.1.2.1	Algal structural preservation	113
C1.1.2.2	Algal surface modification	113
C1.2	<i>V. carteri</i> suitability for <i>in vitro</i> 3D cell culture	115
C1.2.1	<i>V. carteri</i> L929 cytocompatibility study	115
C1.2.2	<i>V. carteri</i> inflammation potential	116
C1.2.3	Formation of <i>Volvox carteri</i> cellularised building blocks	118
C1.3	Investigation of <i>V. carteri</i> cell adhesion properties	119
C1.3.1	<i>V. carteri</i> extract adhesiveness study	119
C1.3.2	Apprehension of <i>V. carteri</i> segmentation from cytoskeleton, cell wall to mucosal contents.	120
C1.4	Discussion	126
C1.4.1	Scaling-up <i>V. carteri</i> microalgae supply	126
C1.4.2	Reducing <i>V. carteri</i> to a sphere-like state	127
C1.4.3	<i>V. carteri</i> , a flexible cell-carrier biomaterial	127
C1.4.4	Investigating <i>V. carteri</i> cell adhesion properties	129
C1.5	Conclusion	130

C2 Engineering reconstructed tissue for tissue filling using *V. carteri* living building block approach - proof of concept **131**

C2.1	Morphological analysis of <i>V. carteri</i> cell carrying system	131
------	--	-----

C2.1.1 Particle size analysis of <i>V. carteri</i> saturated suspension	131
C2.1.2 <i>In vitro</i> deformability of <i>V. carteri</i> analysis	133
C2.2 Production of a mesenchymal tissue by <i>V. carteri</i> living building block technique	133
C2.3 Early <i>in vivo</i> biocompatibility investigation of <i>V. carteri</i> -based three-dimensional tissue filler	135
C2.4 Discussion	136
C2.4.1 Vegetal material suitability for tissue engineering and regeneration . .	136
C2.4.2 Forming mesenchymal tissues using <i>V. carteri</i> living building block approach	137
C2.4.3 <i>V. carteri</i> -based mesenchymal tissues application as soft-tissue filling and regeneration	138
C2.5 Conclusion	139
C3 <i>V. carteri</i> alone promotes adipogenesis without the use of any adipocyte differen- tiation cocktail	141
C3.1 Evaluation of the mechanical properties of <i>V. carteri</i> colonies	141
C3.2 Phenotypic outcome of stem cells introduced into <i>V. carteri</i> compact packing culture system	142
C3.2.1 Impact of <i>V. carteri</i> living building block culture on human mesenchy- mal stem cells	142
C3.2.2 Impact of <i>V. carteri</i> living building block culture on mouse embryonic stem cells	146
C3.3 Early investigation of the <i>in vivo</i> outcome of a <i>V. carteri</i> only-based injectable for tissue filling and regeneration	147
C3.4 Discussion	149
C3.4.1 <i>V. carteri</i> promote both C3H/10T1/2 and hASC adipogenesis <i>in vitro</i> .	150
C3.4.2 <i>V. carteri</i> provide stiffness in the range of soft tissues	150
C3.4.3 Potential impacts of <i>V. carteri</i> structural and molecular components . .	152
C3.4.3.1 Providing an ECM-like to basal membrane-like micro-environment	152
C3.4.3.2 Stimulating adipogenesis hormonally	155
C3.4.4 <i>V. carteri</i> promote tissue regeneration and adipogenesis <i>in vivo</i>	155
C3.5 Conclusion	157
Part D - <i>Volvox carteri</i> bioinspired material, plant-based alternatives for tissue engineering and regenerative medicine	161
D1 Cellulosic/Polyvinyl alcohol composite hydrogel: synthesis, characterization and applications in tissue engineering	161
D1.1 Impact of the oxidation level on the DMCC particle size	161
D1.2 Strategy for producing the DMCC/PVA scaffolds	162
D1.3 Structural characterization of the DMCC/PVA scaffolds	164

D1.4 Investigation of DMCC/PVA scaffold potential use for tissue engineering, im- plantable matrices	166
D1.5 Discussion	168
D1.6 Conclusion	172
D2 The miniaturisation of a cellulose-based composite hydrogel for the production of <i>V. carteri</i> bio-inspired microspheres: proof of concept	173
D2.1 Adaptation of the DMCC/PVA hydrogel synthesis process to nano-crystalline cellulose	173
D2.2 Preliminary physico-chemical analysis of the DNCC/PVA hydrogel	174
D2.3 DNCC/PVA hydrogel microsphere extrusion feasibility	175
D2.4 Discussion	175
D2.5 Conclusion	178
D3 Production of <i>V. carteri</i>-like microspheres containing <i>V. carteri</i> content based on alginate cross-linked material: Proof of concept	179
D3.1 <i>V. carteri</i> polymer separation from a raw extract	179
D3.2 <i>V. carteri</i> polymer and alginate cross-linking	180
D3.3 Examining the efficacy of the cross-linking	181
D3.4 Discussion	182
D3.5 Conclusion	184
Conclusion and perspectives	185
Bibliography	189
Appendix	239

List of Figures

A1.1	The consensus phylogenetic distribution of multicellularity among eukaryotes.	40
A1.2	Examples of volvocine species sorted by size and complexity.	41
A1.3	Volvox and volvocine algae.	42
A1.4	Bibliometric analysis of <i>V. carteri</i> research.	43
A1.5	Body plan, cell types and structural features of an adult <i>V. carteri</i> colony. .	46
A1.6	Asexual life cycle of <i>V. carteri</i>	47
A1.7	Embryo inversion in <i>V. carteri</i>	48
A1.8	Sexual life cycle of <i>V. carteri</i>	50
A1.9	Schematic diagram of ECM in <i>V. carteri</i>	51
A1.10	Schematic cross-section of a <i>V. carteri</i> colony with the localization of known extracellular matrix (ECM) glycoproteins.	53
A2.1	Bottom-up vs. top-down approaches in tissue engineering.	56
A2.2	Fibrous, porous, and hydrogel-based scaffolds.	57
A2.3	An overview of bottom-up tissue engineering strategies.	58
A2.4	Analogies between volvocine algae multidimensional evolution and living building blocks development.	59
A2.5	Embryogenesis to organoid formation.	61
A2.6	Cell sheet engineering.	62
A2.7	Cell fibres engineering.	62
A2.8	Commonly used methods for the formation of spheroids.	64
A2.9	Role of mechanosensing/mechanotransduction signalling on stem cell fate. .	65
A3.1	Mechanical properties of different human tissues.	68
A3.2	Phases of host tissue leading to a foreign body reaction.	71
A3.3	Design of advanced anti-foreign body reaction materials.	74
A3.4	<i>In vitro</i> and <i>in vivo</i> evaluation of the post-implantation host response . .	76
A3.5	Schematic of organ decellularization and tissue decellularization approaches. .	77
A3.6	Liposuction, fat grafting and the components of adipose tissue.	78
A4.1	<i>V. carteri</i> -based and <i>V. carteri</i> -bioinspired material approaches for tissue engineering and regenerative medicine	81
A4.2	<i>V. carteri</i> living building blocks-based model composed of the compaction of preseeded <i>V. carteri</i> colonies	82
B1.1	<i>V. carteri</i> micro-algae culture system.	88

B2.1	MCC/PVA hydrogel reaction scheme.	92
B2.2	Production of cellulosic composites materials from porous macro cylindrical hydrogels to microbeads.	93
B2.3	<i>V. carteri</i> bio-inspired microbeads extrusion.	93
B2.4	Sodium alginate– <i>V. carteri</i> protein grafting	94
B3.1	Primary cells and cell lineages culture observed under phase-contrast microscopy.	101
B3.2	Experimental procedure to generate <i>V. carteri</i> living building blocks-based pseudotissue.	102
C1.1	Characterisation and optimisation of the <i>V. carteri</i> culture.	112
C1.2	Harvesting and preservation of <i>V. carteri</i> microalgae.	113
C1.3	<i>V. carteri</i> state of deflagellation.	114
C1.4	<i>V. carteri</i> cytotoxicity evaluation adapted from the ISO 10993 standards.	115
C1.5	J774.2 murine macrophages secretome upon exposition to <i>V. carteri</i> (VX).	116
C1.6	Principal component analysis (PCA) of J774.2 macrophages secretome upon 24h-exposition to <i>V. carteri</i>	117
C1.7	Cellular adhesion to the surface of <i>V. carteri</i> colonies.	118
C1.8	<i>V. carteri</i> (VX) extract adhesiveness.	119
C1.9	<i>V. carteri</i> actin content.	120
C1.10	<i>V. carteri</i> mucus labelling.	121
C1.11	<i>V. carteri</i> N-acetyl-D-glucosamine (GlcNAc) or Sialic acid glycoproteins labelling.	122
C1.12	Stage 2 <i>V. carteri</i> α -D-Mannose & Glucose glycoproteins labelling.	124
C1.13	Stage 4 <i>V. carteri</i> α -D- Mannose & Glucose glycoproteins labelling.	125
C2.1	Characterisation of <i>V. carteri</i> suspension under <i>in vitro</i> culture conditions.	132
C2.2	<i>V. carteri</i> HDFn-based building blocks <i>in vitro</i> culture.	133
C2.3	<i>V. carteri</i> scaffold induce HDFn phosphatase alkaline activity.	134
C2.4	Reconstructed pseudotissue based of <i>V. carteri</i> HDFn-based building blocks.	135
C2.5	<i>V. carteri</i> HDFn pseudotissue early <i>in vivo</i> physical stability and biocompatibility study.	136
C3.1	<i>V. carteri</i> stiffness determination (n=95).	142
C3.2	Production of Adipose-derived stem cells <i>V. carteri</i> living building blocks.	143
C3.3	Adipose-derived stem cells adipogenic differentiation upon culture in a <i>V. carteri</i> living building blocks environment.	144
C3.4	Adipose-derived stem cells adipogenic differentiation upon culture in a <i>V. carteri</i> living building blocks environment.	145
C3.5	Adipose-derived stem cells mitochondrial activity upon culture in a <i>V. carteri</i> living building blocks environment.	146
C3.6	C3H/10T1/2 murine embryonic cells adipogenic differentiation upon culture in a <i>V. carteri</i> living building blocks environment.	147

C3.7	1-month <i>in vivo</i> integration of a <i>V. carteri</i> suspension only injectable. . . .	148
C3.8	Sequence homology screening using BlastP [434], [435] based on EuKaryotic Orthologous Groups (KOG) annotation analysis of <i>V. carteri</i> [26] focusing on extracellular matrix and lipogenesis analogues.	154
C3.9	Suggested mechanism of <i>in situ</i> soft tissue regeneration mediated by <i>V. carteri</i> saturated suspension injection	156
D1.1	Morphological analysis of dialdehyde (DMCC) and non-oxidised microcrystalline cellulose (MCC) particules.	162
D1.2	MCC hydrogel synthesis.	163
D1.3	PVA and DMCC-based composite scaffolds physico-chemical analysis. . .	164
D1.4	Structural analysis of MCC DMCC based scaffold.	165
D1.5	DMCC/PVA hydrogels mechanical properties	166
D1.6	DMCC/PVA hydrogels cytocompatibility.	167
D1.7	DMCC/PVA hydrogels biocompatibility	168
D2.1	Physico-chemical characterisation of the DNCC/PVA hydrogels	176
D2.2	Production of NCC/PVA-based composite hydrogel microbeads	176
D3.1	<i>V. carteri</i> extraction	180
D3.2	Production of <i>V. carteri</i> -like microbeads	181
D3.3	Alginate and <i>V. carteri</i> soluble extract cross-linking efficiency	183
D3.4	Knowledge provided by this thesis work for the use of <i>V. carteri</i> as a biomaterial for tissue engineering and application in regenerative medicine. .	186
D3.5	Development perspectives around <i>V. carteri</i> material.	188

List of Tables

A1.1 <i>V. carteri</i> main strains available in algal culture collections.	44
A3.1 FDA-approved dermal filling treatments.	69
B1.1 Composition of <i>V. carteri</i> Culture Medium (VT medium)	87
B3.1 <i>V. carteri</i> cell wall staining confocal microscopy excitation and emission spectrum range	97
B3.2 Nanoindentation probe properties	99
B3.3 PHANTAST plugin parameters for confluency estimation	105
D1.1 DNPH/Hydroxyproline CHO dosage.	162

Abbreviations

μm : Micrometre	GAG: Glycosaminoglycans
AF: Alexa fluor	GBP: Glycan-binding proteins
Algal-CAM: Algal-cell adhesion molecule	GH: Growth hormone
AP: Alkaline phosphatase	HBSS: Hanks' balanced salt solution
ASC: Adipose-derived stem cells	HDFn: Neonatal human dermal fibroblasts
BCA: Bicinchoninic acid assay	HE: Hematoxylin-eosin
BZ: Boundary zone	HES: Hematoxylin-eosin-safran
C3H10: Mouse embryo cell line	HRGP: Hydroxyproline rich glycoproteins
C3H/10T1/2, Clone 8	HUVEC: Human umbilical vein endothelial cells
COL: Collagen	IBMX: 3-isobutyl-1-methylxanthine
Con A: Concanavalin A	IFN γ : Interferon γ
CRISPR— Cas9: Clustered regularly interspaced short palindromic repeats and CRISPR-associated protein 9	IGF: Insulin-like growth factor
CZ: Cellular zone	IL: Interleukin
DAPI: 4,6-diamidino-2-phenylindole	IP-10: Interferon γ -induced protein 10
DEX: Dexamethasone	iPSC: Induced pluripotent stem cells
DMCC: Dialdehyde microcrystalline cellulose	J774.2: Mouse BALB/c monocyte macrophage J774.2
DMEM: Dulbecco's modified eagle medium	KOG: Eukaryotic orthologous groups
DNA: Deoxyribonucleic acid	L929: Mouse fibroblast cell line L929
DNCC: Dialdehyde nanocrystalline cellulose	LAM: Laminin
DNPH: 2,4-dinitrophenylhydrazine	LPS: Lipopolysaccharide toxin
DZ: Deep zone	M1: Pro-inflammatory macrophage
ECM: Extracellular matrix	M2: Anti-inflammatory macrophage
EDC: 1-Ethyl-3-(3-dimethylaminopropyl) carbodiimide	MCC: Microcrystalline cellulose
ETI: Evolutionary transitions in individuality	MIP-3 α : Macrophage inflammatory protein-3 α
FBR: Foreign body reaction	mKC: Mice keratinocytes-derived chemokine
FBS: Fetal bovine serum	MSC: Mesenchymal stem cells
FTIR: Fourier-transform infrared spectroscopy	MTE: Major transitions in evolution
FZ: Flagellar zone	MTS: 3-(4,5-dimethylthiazol-2-yl)-5-(3-carboxymethoxyphenyl)-2-(4-sulfophenyl)-2H-tetrazolium
	MWDO: Molecular weight cutoff

NANOG: Homeobox protein	PLA: Poly(lactic acid)
NCC: Nanocrystalline cellulose	PLGA: Poly(lactic-co-glycolic acid)
NHS: N-Hydroxysuccinimide	PLLA: Poly-L-Lactic Acid
NIES: National institute for environmental studies	PMMA: Poly(methyl methacrylate)
NMP: 1-methyl-2-pyrrolidone	PRP: Platelet-rich plasma
OCT4: Octamer-binding transcription factor 4	PS: Polystyrene
ON: Overnight	PVA: Polyvinyl alcohol
PFA: Paraformaldehyde	RCF: Relative centrifugal force
PBS: Phosphate-buffered saline	RGD: Arginylglycylaspartic acid
PCA: Principal component analysis	RNA: Ribonucleic acid
PCL: Poly(ϵ -caprolactone)	RT: Room temperature
PDMS: Polydimethylsiloxane	SEM: Standard error to the mean
PEG: Polyethylene glycol	SOX2: Sex determining region Y-box 2
PGA: Poly(glycolic acid)	TNF α : Tumor necrosis factor α
ph : Pherophorin	UTEX: University of texas culture collection
phS: Pherophorin-S	VEGF: Vascular endothelial growth factor
	WGA: Wheat germ agglutinin
	XDR: X-ray diffraction analysis

Part A - General context

Chapter A1

Volvox carteri f. nagariensis, an established model for developmental and evolutionary biology

A1.1 The volvocine green algae family, a phylogenetic perspective on unicellularity to multicellularity transition

A1.1.1 The major transitions in evolution framework

Evolution is marked by well-defined events involving profound innovations. To explain the hierarchical structure of life on Earth — genes to chromosomes, chromosomes to cells, cell complexification (i.e., prokaryotic cells to eukaryotic cells), individual cells to multicellular organisms, and organisms within societies — and the acquisition of an overall increase in complexity throughout evolution, Szathmáry and Smith [1] suggested the major transitions in evolution (MTE) framework, also referred to as evolutionary transitions in individuality (ETI) [2].

Major evolutionary transitions are characterized by (1) transition in individuality, and (2) by the emergence of a novel inheritance system, notably driven by selective forces (ecological or efficiency benefits) requiring cooperation, division of labor, communication, mutual dependence, and negligible within-group conflict [3], [4]. While the question of the criterion of the emergence of a new level of individuality for the classification of significant developmental milestones as MTE, like the emergence of the genetic code, language, nervous, or immune systems, is still up for debate within the evolutionist community, the acquisition of multicellularity is, on the contrary, the subject of consensus [4]–[7]. Indeed, the transition from unicellular to multicellular life clearly reflects the gain in complexity and the creation of a new form of individuality in the transition from lower-level individuals into new higher-level individuals.

The transition from unicellular to multicellular organisms has occurred dozens of times independently and simultaneously in the evolution of life on Earth (Fig. A1.1), in the development of red algae, brown algae, land plants, animals, and fungi. Yet, the multicellularity acquired by volvocine green algae has been one of the most thoroughly investigated and

serves as a model for the genetical foundation of multicellularity and cellular differentiation [8].

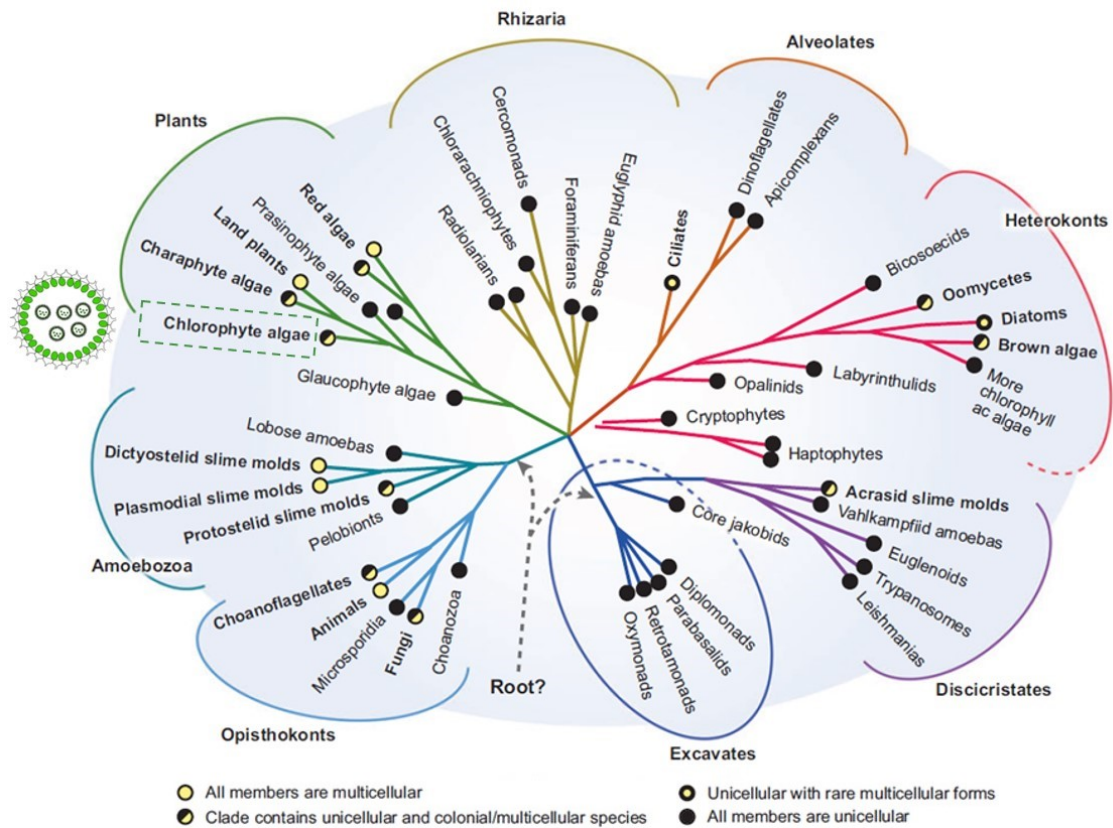


Figure A1.1: The consensus phylogenetic distribution of multicellularity among eukaryotes. Multicellularity also occurred in multiple ways in prokaryotes, as evidenced by the simultaneous appearance of unicellular representatives transitioning to multicellular organisms across the phylogenetic distribution. As chlorophyte algae, the volvocine algae and *Volvox carteri* algae are part of the phylogenetic branch which is associated to the evolution of land plants. This figure adapted with permission from [9].

A1.1.2 The *Volvocaceae*, a model for the development of multicellularity

The *Volvocaceae*, named by Ehrenberg in 1834 [10], are biflagellated, photosynthetic algae comprising eight genera (i.e., *Chlamydomonas*, *Tetrabaena*, *Gonium*, *Astrephomene*, *Pandoria*, *Eudorina*, *Pleodorina*, and *Volvox*), including around sixty different species of which a fraction is depicted in Fig. A1.2 [11]. The strength of the volvocine algae as an evolutionary model system lies in the proposal of two major models representing size, and complexity extremes, the unicellular *Chlamydomonas reinhardtii* and the multicellular *Volvox carteri* forma *nagariensis*, as well as a wide range of intermediate species establishing an evolutionary continuum [12]. Volvocine algae are thus both unicellular in the form of *C. reinhardtii* (Fig. A1.2A) and colonial (Fig. A1.2B-O) (e.g., *Gonium pectorale*, *Eudorina elegans*, and *Volvox gigas*), with substantially variability in dimension, degrees of structuration and cellular specialization. Kirk [13] first defined via phylogenomic analysis a gradual acquisition of fundamental processes that have led to increasingly multicellular and complex forms of *Volvocaceae* (Fig. A1.3). His

hypothesis has received a broad consensus and has been continuously refined ever since with the inclusion of new knowledge [14]–[19]. Although this evolutionary pattern excludes a significant amount of *Volvocaceae* diversity, this lineage hypothesis is nevertheless thought to be a reasonable approximation of volvocine algae evolutionary connections [15].

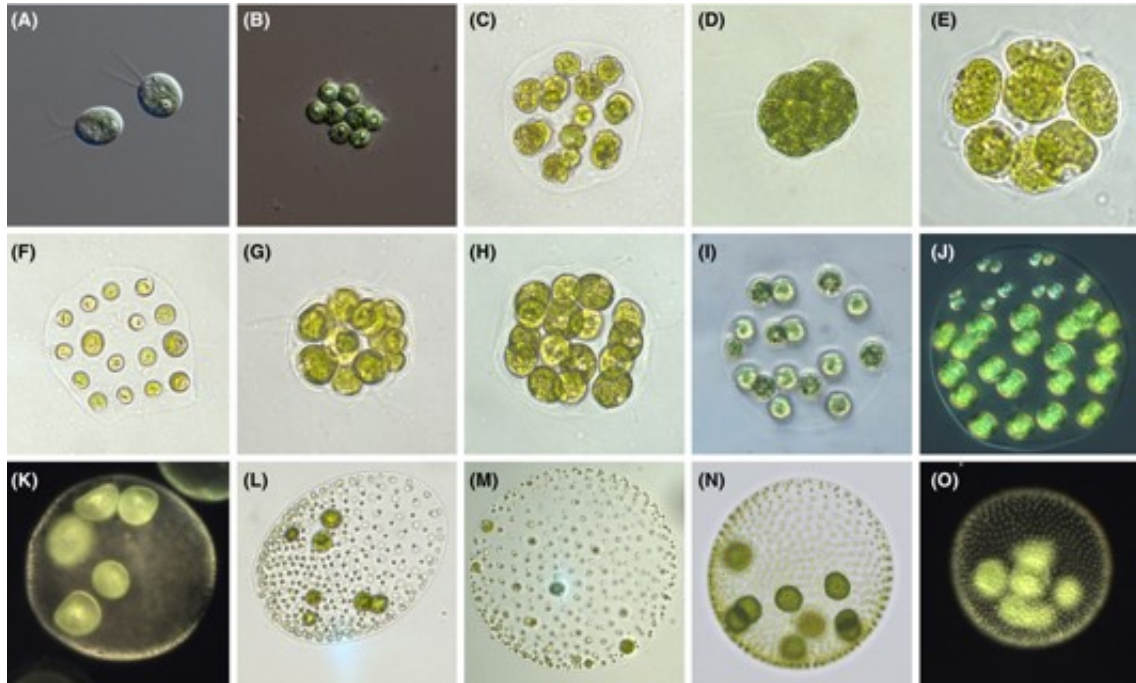


Figure A1.2: Examples of volvocine species sorted by size and complexity. A. *Chlamydomonas reinhardtii*, B. *Gonium pectorale*, C. *Astrephomene gubernaculiferum*, D. *Pandorina morum*, E. *Volvulina compacta*, F. *Platydictyria caudata*, G. *Yamagishiella unicocca*, H. *Colemanosphaera charkowiensis*, I. *Eudorina elegans*, J. *Pleodorina starrii*, K. *Volvox barberi*, L. *Volvox ovalis*, M. *Volvox gigas*, N. *Volvox aureus*, O. *Volvox carteri*. This figure was reproduced with permission from [12].

The establishment of genetic control of cell number, cell attachment mechanisms via incomplete cytokinesis, basal body orientation and the transformation of cell walls into extracellular matrix (ECM) were allowed the cohesion of the first forms of multi-cellular organisms, such as *Tetrabaena socialis*, consisting of the assembly of unicellular *Chlamydomonas reinhardtii*-like cells [16]. Additional adaption, coordination, and structural optimisation mechanisms, including organismal polarity, partial inversion has evolved as organisms grow more cells like *Gonium pectorale* [17]. Embryonic inversion mechanisms, which consist on turning the spherical embryo completely inside out via temporal and spatial regulation of cell shape changes and cytoplasmic bridges relocations [18], first appeared in *Pandorina morum*, allowed organisms deriving from *Eudorina elegans* to retain the formation and expansion of an ECM, which has been subsequently responsible for holding the cells together.

For a long time, *Pleodorina starrii* was considered to be the first anisogamous organism, showing non-identical gametes. However, recently, Takashi Hamaji et al. [19] discovered a reduced male sexual chromosomal region, shifting the attribution of this innovation to *Eudorina elegans*. Formerly, the algal growth pattern was divided between biflagellate and

non-mobile reproductive stages. Cell specialization through germ-soma cell differentiation evolved gradually in *Pleodorina starrii* until it was completed in *Volvox carteri* with the support of joint asymmetric cell division and a bifurcated cell cycle mechanism. This germ-soma dichotomy represents a division of labour between the somatic cells, which are responsible for colony motility via phototropism, ensuring the feeding function, and the gonidia, which are focused on reproductive functions. Finally, a sexual reproduction mechanism, involving a small motile male gamete and a large less motile female gamete, was introduced to complement asexual reproduction by ordinary cell division, which allowed algal species' prosperity up to then.

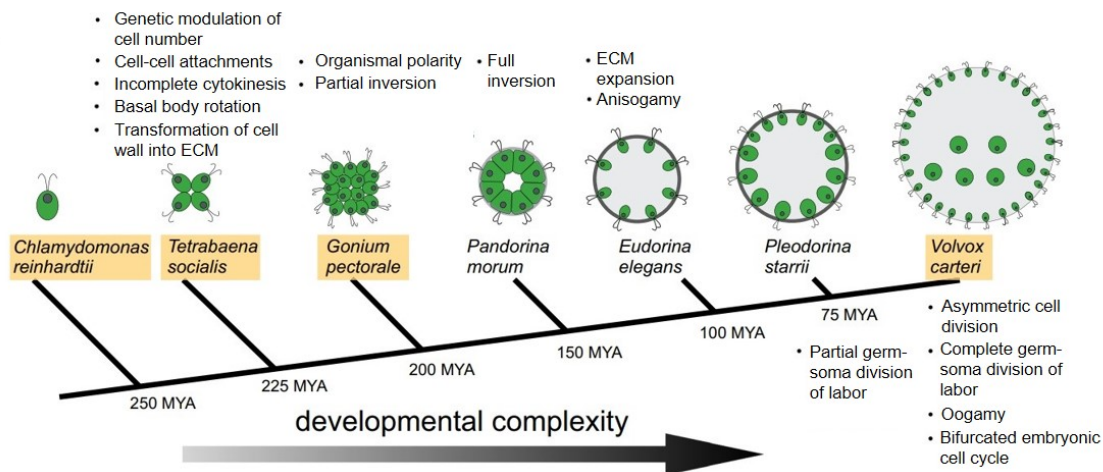


Figure A1.3: Volvox and volvocine algae. Simplified cladogram of selected volvocine species from representative genera shown in cartoon form with successive cellular and developmental innovations indicated by bulleted descriptions above or below the node in which they arose. Volvocine algal cells are polarized with an apical pair of flagella just above the nucleus and a single large chloroplast located basally. Species with published sequenced genomes have names in tan boxes. Light grey shading depicts extracellular matrix (ECM) that occupies increasing amounts of spheroid volume in successive genera. Estimated divergence times provided in million years ago (MYA) at each node are based on data in [20]. This figure was initially adapted from [21], [22].

A1.1.3 The Volvocaceae, knowledge gaps and challenges

Although the *Volvocaceae* are an established model for developmental and evolutionary biology, significant disparities in scientific knowledge exist across their genera and species, *C. reinhardtii* and *V. carteri* being the most studied organisms. While Ehrenberg described the genus *Chlamydomonas* in 1833 [23], *Volvox* was discovered in a ditch-water sample at the very beginning of 1700, so to say more than 100 years before *C. reinhardtii*, by Antony Van Leeuwenhoek in a letter to Sir Hans Sloane, delivering a very accurate sketch and description of it as 'a very pleasant sight, green round particles of the bigness of sand-grains seeming to move of themselves by a rolling motion'.

In the past fifty years, knowledge around *V. carteri* has been growing, as shown by the increasing number of publications referenced on the Pubmed database (Fig. A1.4) under

'*Volvox carteri*' with an average number of about 50 publications per decade and the holding since 2011 of a biennial International Volvox Conference meeting [24] on the model of the biennial International Chlamydomonas meeting organized since 1983 [25]. *V. carteri* is being studied as a model organism for the development of sex and multicellularity as well as cellular differentiation, bringing together a research community from genomics, biological physics, hydrodynamics, and social evolution. *V. carteri*, which has only been cultured in a dozen laboratories around the world [22], is still understudied in comparison to *C. reinhardtii*, its unicellular phylogenetic relative that has been the subject of 320 publications in 2021 alone, and 2500 publications in the last decade.

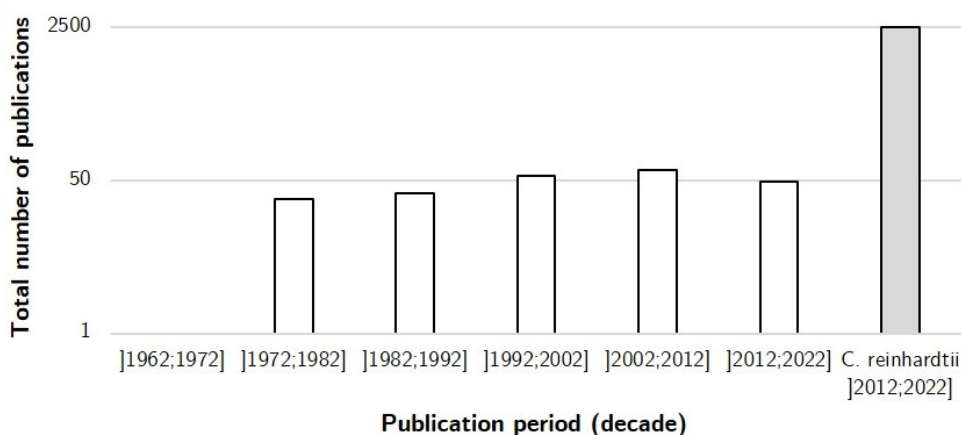


Figure A1.4: Bibliometric analysis of *V. carteri* research. Tracking the number of articles by decade (log scale) registered on the Pubmed platform as of September 9th 2022, and reported under the query search for '*Volvox carteri*'. For comparison, the number of papers noted under the '*Chlamydomonas reinhardtii*' search was determined from 2012 to 2022.

Despite fundamental differences in organismal complexity, *V. carteri* and *C. reinhardtii* share a substantial amount of their genome, with the exception of a few highly specific proteins (e.g., pherophorins (ph), volvox matrix metalloproteases, and D cyclins), indicating an overall comparable protein-coding potential [26]. The development of a high level of complexity in *V. carteri*, as described above, is intrinsically linked to equally complex mechanisms resulting from developmental innovation and adaptation.

V. carteri research is affected by technical difficulties in the development of research methodologies related to algal strain conservation (e.g., cryopreservation [27]–[29], culture maintenance [30], culture synchronization [31], sexuality maintenance [32]), to the routine adaptation of genomic, transcriptomic, and proteomic techniques (e.g., DNA and RNA sequencing [33]–[35], DNA transformation [36], RNA interference-mediated knockdowns [37], CRISPR–Cas9 genome editing [38]), and the development of specific bioinformatic tools [26] (e.g., constitution of large databases, modelling of protein structure, assignment of biological function). These technical limitations are being reduced as improved genomic, transcriptomic, and proteomic resources are becoming more easily accessible, adapted, and implemented. The continuous providence of knowledge about *V. carteri* could help arouse more

interest, especially outside the genomic community, thereby favouring the deployment of additional resources to improve the understanding of *V. carteri* evolutionary and developmental mechanisms, its complete characterization, and identification of potential applications for its exploitation.

A1.2 Fundamental knowledge on *V. carteri*

A1.2.1 Natural habitat and sampling

V. carteri, like other green algae, can be found worldwide, particularly in low-turbulent, low-turbidity, high-alkalinity, and nutrient-rich freshwater ecosystems [39], [40]. Most volvocaceans inhabit small shallow water bodies of temperate climate zones (28°C–30°C), flourishing in ephemeral puddles, pools, and ponds, especially in agricultural fields [41]. Volvocaceans typically appear in late spring or early summer and proliferate through asexual reproduction. As climate conditions deteriorate, the algae are capable of switching to sexual reproduction, forming zygospores, or to dormant forms sinking to the bottom. As favourable conditions return the following year, volvocaceans reappear.

Rice fields constitute an especially favourable environment for the proliferation of volvocine algae, which explains the large number of *V. carteri* strains originating from India and Japan, stored in two algal collections, the National Institute for Environmental Studies (NIES) in Japan and the University of Texas Culture Collection (UTEX) in the USA. A non-exhaustive list of the most commonly used *V. carteri* strains, preserved and available in the NIES and UTEX collections, is provided in Table A1.1. Algal strains can be directly isolated from water sampling as a colony or germinating zygospores capable of withstanding long periods of drought and heat by collecting dried soil samples from nearby water bodies [42]. *V. carteri* male-female pair HK9 and HK10 (a.k.a. Adm and Eve), which were originally germinated by Richard Starr [43], remain the standard strains for *V. carteri* research in most laboratories for developmental mutant isolation [44], [45], genome sequencing [26], and editing [38].

Table A1.1: *V. carteri* main strains available in algal culture collections. The genus *V. carteri* includes several forms (*f.*), the most researched of which is *f. nagariensis*, named after one of its collection site, the River Nagari near Tirupati in South India. *V. carteri* main strains have been preserved in two large algal collections, the National Institute for Environmental Studies (NIES) in Japan, and the University of Texas Culture Collection (UTEX) in the United States, *V. carteri f. nagariensis* male-female pair HK9 and HK10 being the gold standard (F: female mating-type, M: male mating-type).

Strain name	Sex-type	Geographical origin	Isolation date	References
<i>f. nagariensis</i>				
—	—	Chennai, India	1916	[46]
UTEX 1885	F	Kobe, Hyogo, Japan	Before 1964	[43], [45], [47], [48]
HK10/Eve				
UTEX 1886	M	Kobe, Hyogo, Japan	Recombinant	[43], [49]

Table A1.1 – continued from previous page

Strain name	Sex-type	Geographical origin	Isolation date	References
HK9/Adm			of HK10	
UTEX 2903	F	Poona, India	1973	[50], [51]
UTEX 2908	F	Kobe, Hyogo, Japan	Before 1973	[52], [53]
NIES 397	F	Ichinomiya, Achi, Japan	N.A	[51], [54], [55]
NIES 398	M	Ichinomiya, Achi, Japan	N.A	[51], [54], [55]
NIES 4205	F	Taiwan	25-05-2016	[56]
NIES 4207	M	Taiwan	10-06-2016	[56]
<i>f. kawasakiensis</i>				
NIES 580	F	Kawasaki, Japan	30-01-1984	[54], [56]
NIES 581	M	Kawasaki, Japan	11-11-1990	[54], [56]
NIES 732	F	Kawasaki, Japan	01-1984	[55]–[58]
NIES 733	M	Kawasaki, Japan	25-02-1984	[55]–[58]
<i>f. weismannia</i>				
UTEX 1875	M	Waterford, Australia	Before 1968	[55]
UTEX 1876	F	Waterford, Australia	Before 1968	[55]
UTEX 2180	M	—	Before 1974	[49]
UTEX 2904	F	Lawrence, Kansas, USA	Before 1974	[49]

A1.2.2 Structuration of an adult *V. carteri* colony

An adult *V. carteri* (Fig. A1.5) colony represents a 100 to 500 μm sphere comprising an outer sheet, consisting of a monolayer of ~ 2000 – 4000 equidistant biflagellate *Chlamydomonas*-like somatic cells, and enclosing ~ 16 much larger reproductive aflagellated gonidia cells.

Somatic cells are responsible for the colony's overall organismal movement via the coordination of their flagellar beats, directed outside the colony. The structure and dynamics of flagella beat, as well as flagella-driven flows, have been extensively characterized and modelled [41], [59], [60]. *V. carteri* phototaxis is primarily based on an asymmetry of flagellar activity between the illuminated and shaded sides of the colony's anterior part. The flagellar beat decelerates in the presence of illumination and accelerates in the absence of illumination. This phenomenon is temperature dependent and reverses itself below 16°C [61].

Gonidia cells contained within individual embryonic vesicles connected to the somatic cells sheet, pass through several phases of development, including cell multiplication and differentiation, which will lead to the formation of new young adult colonies. Both terminally differentiated somatic cells and gonidia reproductive cells are embedded in an extremely structured, crosslinked, clear extracellular matrix, enabling complete cohesion of the algal structuration within and at the surface of the colony [43].

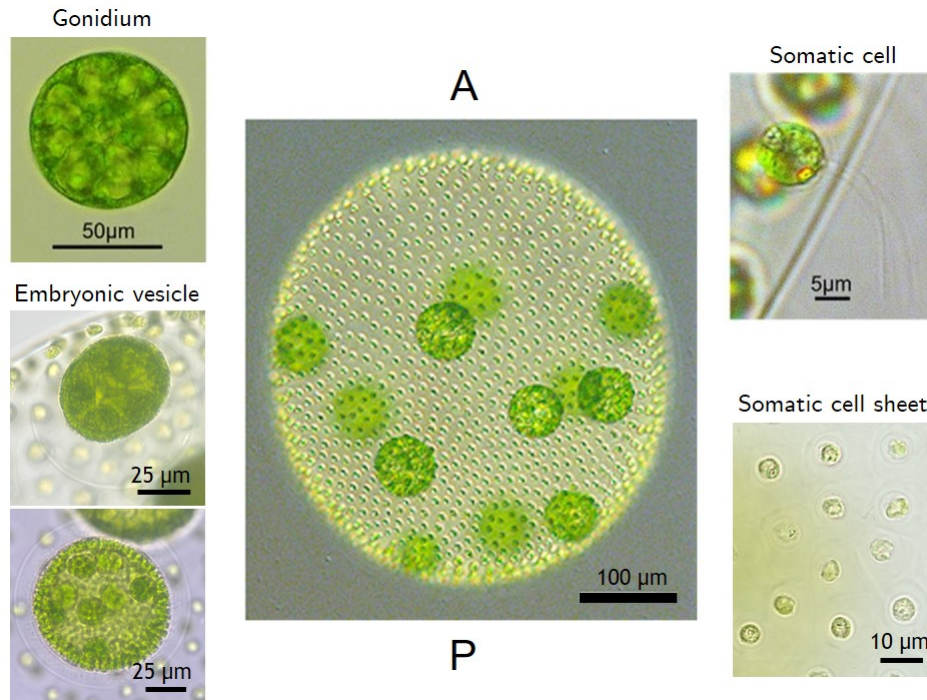


Figure A1.5: Body plan, cell types and structural features of an adult *V. carteri* colony. An adult *V. carteri* colony present two distinct cell types: ~2000 small, flagellated somatic cells and ~16 large, aflagellate germ cells called gonidia. Somatic cells are on the outer surface of the colony with flagella oriented towards the exterior. Gonidia are just beneath the somatic cell layer in the posterior hemisphere contained into embryonic vesicles connected to the colony surface until reaching the final colony maturity requirements including somatic cell flagellation. All cells are embedded within a clear, compartmentalized extracellular matrix. Anterior (A) and posterior (P) poles of the spheroid are labeled. This figure was modified from [8].

A1.2.3 Asexual life cycle of *V. carteri*.

V. carteri vegetative reproduction (Fig. A1.6), also known as the asexual reproduction cycle, occurs in a haploid phase (1n). Mature pre-cleavage adults display unicellular gonidia that shortly initiate embryogenesis, demonstrating rapid and synchronous cleavage divisions without growth [62]. Cleavage occurs via incomplete cytokinesis, which forms cytoplasmic bridges between each cell, providing a continuum that holds the embryo together [63]. Embryonic cell cleavage proceeds symmetrically up to the fourth cycle of division. At the 5th cleavage, a sequence of asymmetric cleavage divisions that mark the first apparent step of germ-soma differentiation forms large embryonic cells that will become future gonidia cells and smaller cells that will become terminally differentiated somatic cells. The somatic precursors and all cells from the posterior hemisphere continue to cleave symmetrically until the completion of a total of 11–12 divisions, resulting in the ~2000 somatic cells and a single anterior-posterior axis [64]. The gonidial precursors then temporarily stop any cleavage activity. Using specific mutants, three sets of gene loci have been identified as key players in germ-soma differentiation: *gls* genes ('gonidia less') act in the embryo to shift cell-division planes, allowing asymmetric divisions; ('late gonidia') genes act in the large gonidial initials to prevent somatic differentiation; and *regA* genes ('somatic regenerator') act in the small somatic initials to prevent reproductive development [48], [65]–[67]. Cheng

et al. [68] demonstrated that Hsp70A and GlbA function as chaperone partners, regulating asymmetric division with a relative abundance of Hsp70A alone in asymmetrically dividing blastomere cells. At this stage, the embryo is in a rather inconvenient configuration as all somatic precursors are present in the inner part and the gonidial precursor faces the outer part of the embryo. Therefore, the embryo must be turned itself completely inside out to reposition the soon-to-be somatic cells on the outside and the gonidia on the inside. This process, known as full inversion, demonstrates process variety within the genus *Volvox*.

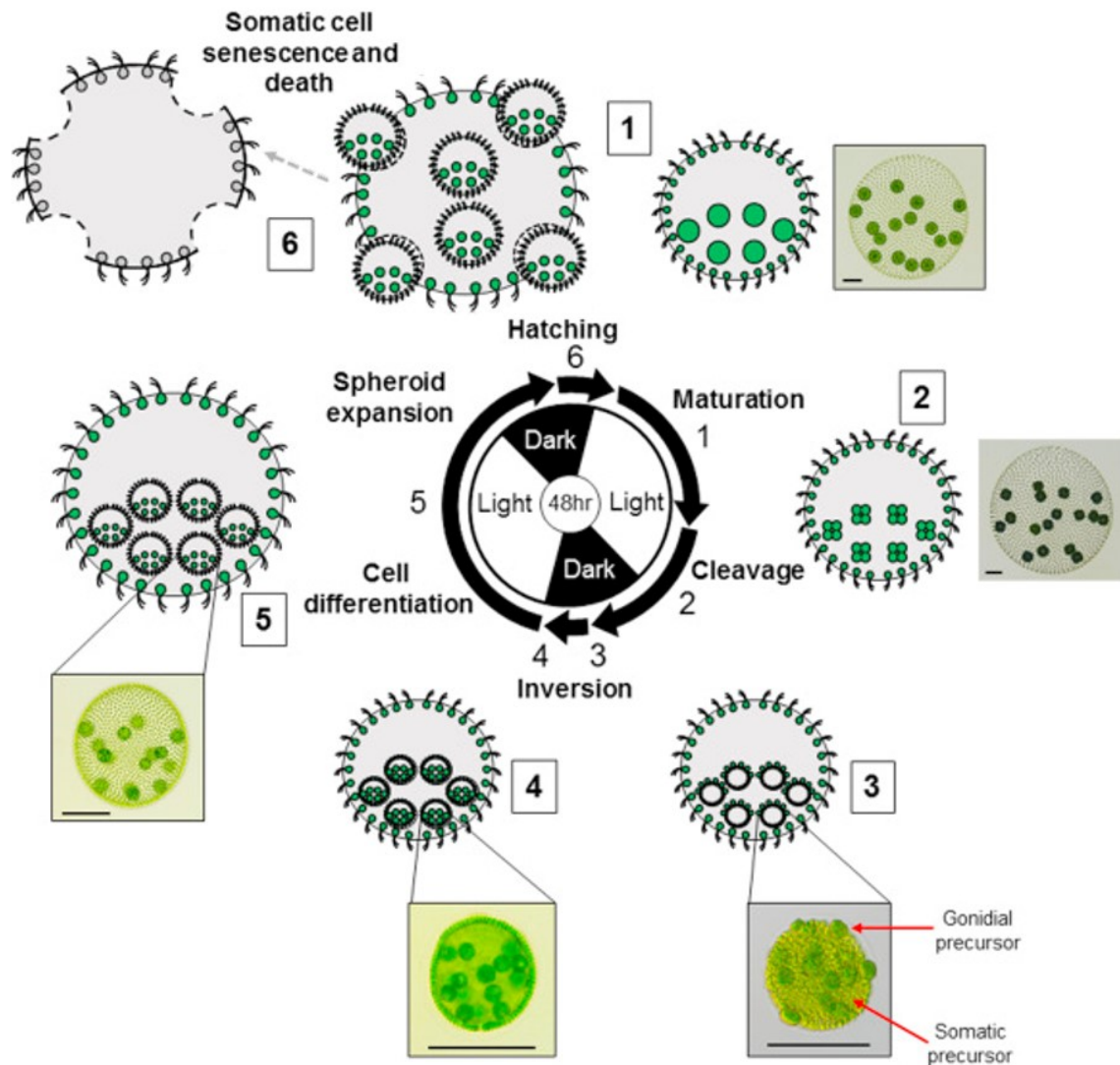


Figure A1.6: Asexual life cycle of *V. carteri*. Stages of vegetative reproduction are depicted clockwise with cartoons and micrographs of selected stages, showing a 48-hour diurnal regime used to synchronize their life cycle with alternating 16 hours-light and 8 hours-dark periods. Arrows represent the approximate duration of each phase (1: Mature adult spheroid with pre-cleavage gonidia (large green circle) and flagellated somatic cells (small green circle) embedded within extracellular matrix (grey), 2: Adult mother spheroid with four-cell stage embryos derived from gonidia, 3: Adult mother spheroid with post-cleavage embryos prior to inversion. Note the large gonidial precursor cells on the exterior surface, 4: Adult mother spheroid with post-inversion juveniles, 5: Adult mother spheroid with differentiated and expanded juveniles, 6: Late stage juveniles hatching from their mother spheroid. The somatic cells from the mother spheroid undergo senescence and death). This figure was modified from [8].

The *V. carteri* inversion (Fig. A1.7) process have been widely studied, characterised [62], [69]–[73] and more recently modelled [74], [75]. The embryo first detaches from the surrounding glycoprotein vesicle wall by an initial contraction caused by somatic cell precursor elongation into spindle-shaped cells, reducing their lateral dimension by about *sim*40%. [69], [70]. The embryo's detachment from the vesicular wall releases tensile tension at the phialopore opening, the unique embryonic region of *V. carteri* that lacks cytoplasmic bridges, allowing the phialopore lips to fold and curve along the embryo until full reversal completion. The reversion of cellular sheet curvature is driven by cellular contractions and majorly impelled by the counter-pressure provided by the cytoplasmic-bridge system in a kinesin-dependent manner [62], [71]. The phialopore is finally positioned on the posterior pole of the embryo. By convention the anterior—posterior polarity of the spheroid is reversed at the same time that the inside—outside polarity is reversed by inversion, ultimately coinciding with the direction in which adult colonies will eventually swim [72], [73]. During inversion, flagella begin to emerge from somatic cells and continue to elongate [72]. As the extracellular matrix quickly accumulates, the embryo's precursor cells eventually differentiate. When the inversion is complete, the cytoplasmic bridges vanish, and the newly created ECM takes up the role of holding the organism together [62].

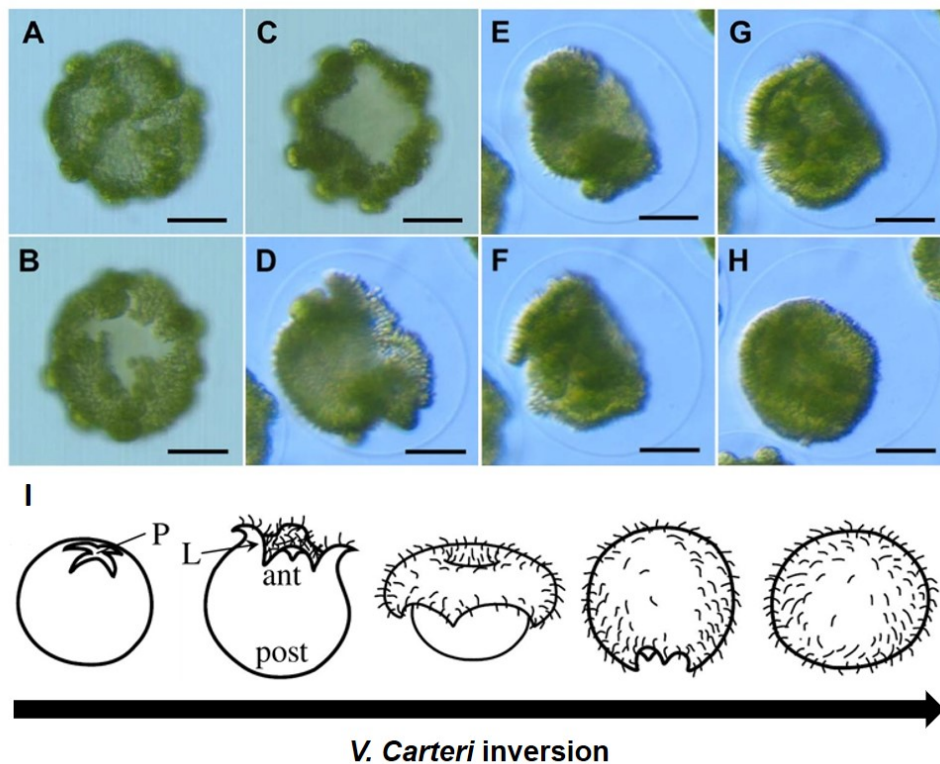


Figure A1.7: Embryo inversion in *V. carteri*. A–H: Successive steps of embryo inversion (scale bar = 25 μm). *V. carteri* embryo inversion occurs within a glycoprotein vesicle and is initiated by the widening of a swastika-shaped opening (A–B), known as phialopore (P), present on the anterior (ant) pole of the embryo, forming four lips (L) that begin to fold outward (C–D), progressively curl further onto the surface of the embryo (E–F), until full inversion is complete and the phialopore is presented on the posterior (post) pole of the embryo (G–H). I. Diagram of the *V. carteri* inversion process, known as type-A inversion. This figure was adapted from [72], [74].

Soma-germ-specific transcriptome patterns were highlighted by both Klein et al. [35] and Matt et al. [76], who performed extensive transcriptomic analysis. While gonidia cells and precursors primarily demonstrated transcripts with only reproductive connotated functions (e.g., asymmetric cell division gls and Hsp70A, and embryonic cell-cell adhesion protein Algal-CAM (i.e., Algal-Cell Adhesion Molecule)), somatic cells presented transcripts related to a more altruistic role. Indeed, in addition to the essential function of colony orientation, somatic cells are exclusively responsible for the synthesis and glycosylation of ECM glycoproteins as well as ECM remodelling agents, including Volvox matrix metalloproteases and soluble pherophorin. By deposition of ECM, somatic cells enable cohesion and massive expansion of both mother and daughter colonies of *V. carteri*. The mother colony hatches once daughter colonies have reached a critical threshold of cellular development and global volume. A recent study [77] has shown that pH₂S diffuses massively from the mother somatic cells to the embryonic vesicle throughout the development of the daughter colonies and highly accumulates around the pre-hatch daughter colonies, allowing the hatching and release of the juvenile colonies from the inner vesicles toward the outer membrane.

A1.2.4 Sexual life cycle of *V. carteri*.

As previously stated, *V. carteri* transitions to sexual reproduction (Fig. A1.8) in reaction to the onset of unfavourable climatic conditions accompanied by their home ponds drying up in midsummer and fall. The rise in temperature in these shallow waters thus represents a precursor to the high drought-, heat-, and cold-resistant zygospores' formation by sexual reproduction. The sexual cycle of *V. carteri* shows some variability depending on the form. The instance of *V. carteri f. nagariensis* is presented here. Male strain spermatozoa stimulated by heat spontaneously synthesize sex-inducing glycoprotein (SI), which converts asexually growing males and females to the sexual pathway [78]–[80]. SI phytohormone causes the embryo's cellular differentiation into somatic cells and gonidia to be delayed, resulting in the differentiation of female stem embryos into egg cells and male stem embryos into somatic cells and sperm cells in the form of sperm packets, also known as androgonidia. Male sex spheroids of *V. carteri f. nagariensis* show a ratio of 1:1 to > 50:1 between somatic cells and androgonidia [56], [81]. This sexual dimorphism of males and females results from the haploid system of UV sex chromosomes [57]. In this system, which is widespread in eukaryotes, particularly in red, green, and brown algae, females and males respectively carry a U chromosome and a V chromosome [82]. Sperm packets are released by mature male strains, swim to the female strain, enter it, and fertilize its female egg. Upon fusion of the female and male cells, diploid zygotes are formed. The fertilised adult female colony matures and releases thick-walled, dormant orange-red zygospores. Exposure of the zygospores to light and nutrients initiates germination and meiosis to produce four haploid progeny (two of each asexual mating type) that re-enter the vegetative life cycle [83].

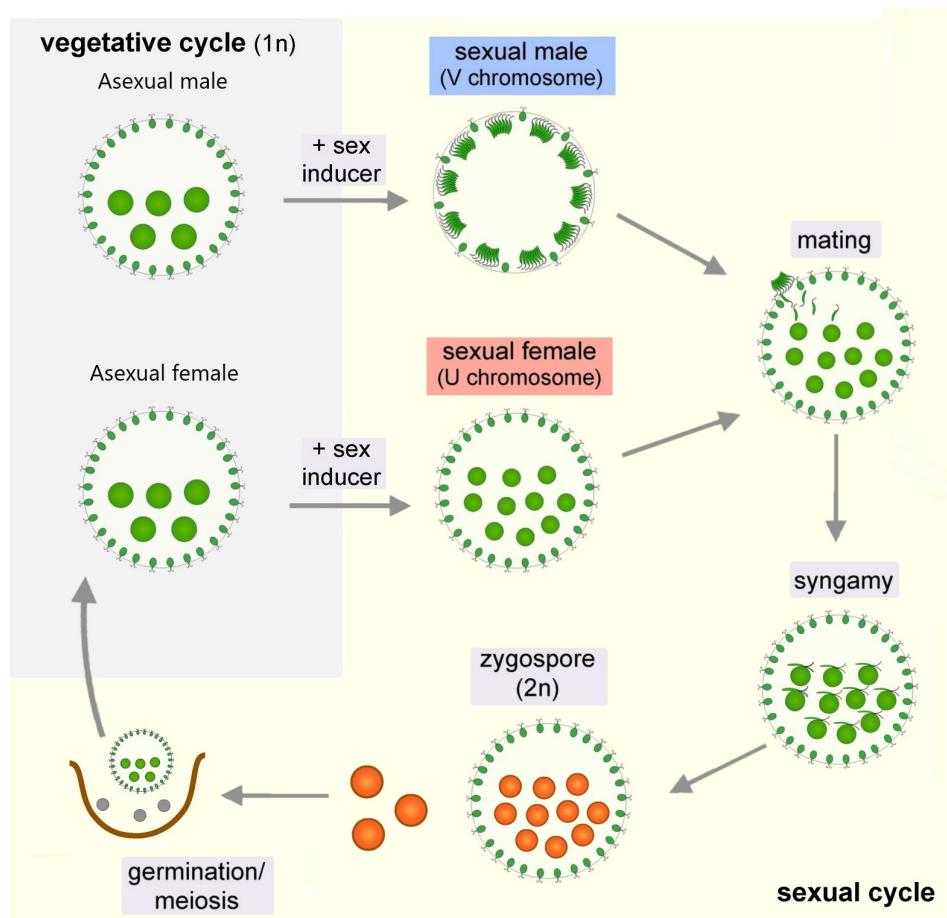


Figure A1.8: Sexual life cycle of *V. carteri*. Vegetative reproduction (grey shaded region) occurs in a haploid phase (1n) while sexual reproduction (pale yellow region) occurs in a diploid phase (2n). Sexual development is triggered by exposure to sex inducer and leads to gonidia undergoing modified embryogenesis and development into adult sexual egg-bearing females or adult sexual sperm-packet-bearing males. Sperm packets are released and swim to females where mating takes place with internal fertilization (syngamy), resulting in formation of diploid zygospores. Meiosis occurs upon germination and produces three polar bodies and one haploid progeny that re-enters the vegetative life cycle. This figure was adapted from [22], [84].

A1.2.5 *V. carteri*'s reproductive cycle handling in lab culture

The sexual reproduction can be artificially stimulated via SI or induction of its synthesis in a male strain via a brief rise in temperature. Yet, female *V. carteri* strains (e.g., Eve, NIES 397) are preferred for routine studies that do not involve the sexual cycle [22]. Indeed, male strains can spontaneously undergo sexual differentiation, leading to the irreversible development of sexual male colonies unable to reproduce on their own and thus leading to the extinction of the population [41]. In addition, the asexual cycle is extremely convenient since it can be readily synchronised by exposure to a predefined light-dark cycle (16:8 light-dark diurnal regime). Indeed, juveniles with putative somatic and reproductive cells are formed during darkness, but these cells do not differentiate until light returns [85]. Every 48 hours, a complete reproductive cycle is completed.

A1.2.6 *V. carteri* extracellular matrix architecture

V. carteri produces a considerable amount of ECM, accounting for up to 99% of its total volume [41], representing a continuum, primarily composed of negatively charged fibrous hydroxyproline rich glycoproteins (HRGP) [86], which is responsible for the colony's global cohesion, protecting the gonidia transitioning to juvenile forms while maintaining the monolayer of somatic cells tight, allowing an effective direction of colony displacement [73]. While being extremely complex, ECM demonstrate regularity in its structure, including several region-specific morphological components [41]. Kirk [87] has precisely documented, defined, and established nomenclature for the inner compartmentalisation of the extracellular matrix of *V. carteri* f. *nagariensis* based on light and electron microscopy observations (Fig. A1.9 [26]). A *V. carteri* colony can be broken down into four main zones, which are, from the outside in, the flagellar zone (FZ), the boundary zone (BZ), the cellular zone (CZ), and finally, the deep zone (DZ). Each zone can be subdivided into 3 to 4 subzones based on specific molecular features.

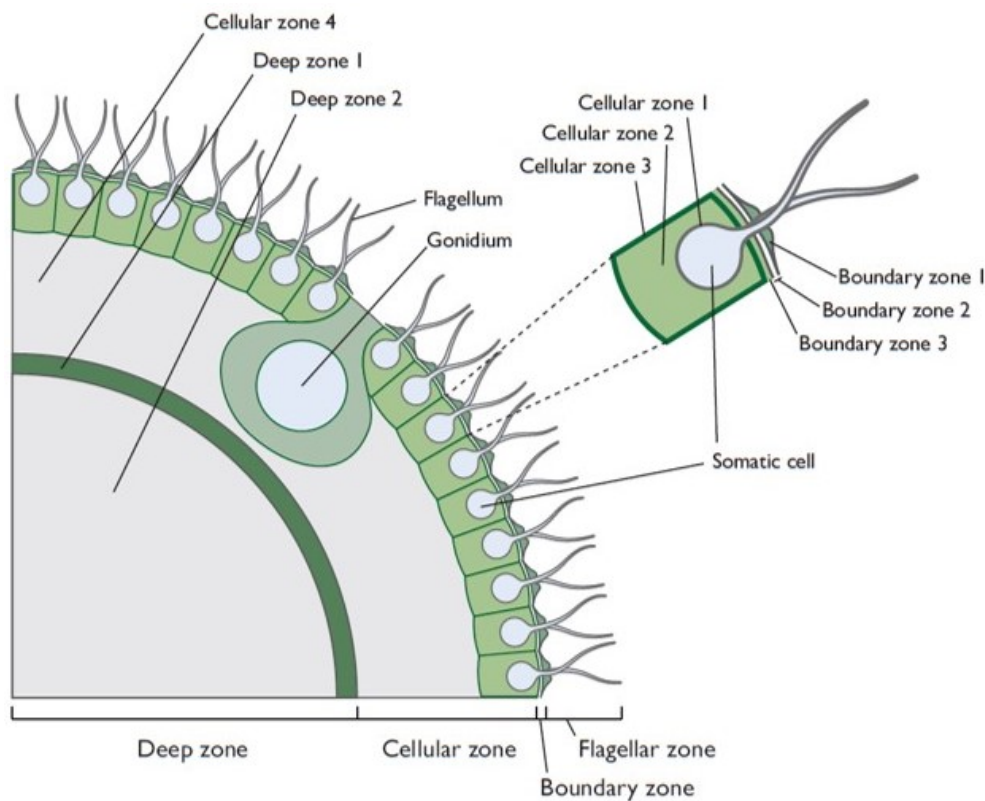


Figure A1.9: Schematic diagram of ECM in *V. carteri*. In this schematic cross-section of a *V. carteri* adult colony, the elaboration of the ECM into deep, cellular and boundary and flagellar zones is shown, with the three subzones of the cellular and boundary zones surrounding a single zoomed in somatic cell. Fibrous cellular zone 1 is attached to the somatic cell body plasmalemma, cellular zone 2 is relatively amorphous; fibrous cellular zone 3 forms compartments around the somatic cells. The boundary zone is continuous except where interrupted by flagella, the dense fibrous boundary zones 1 and 3 flank the tripartite boundary zone 2. Deep zone 1 is an band of filaments and surrounds the amorphous deep zone 2. This figure was reproduced with permission from [26].

The boundary zone (BZ) covers the whole surface of the sphere, except in parts disrupted by flagellar structures (FZ). BZ comprises a crystalline layer (BZ2), surrounded on its outer and inner sides by thick fibrous layers (BZ1 and BZ3). The cellular zone displays a thin coherent network of ECM filaments (CZ1) tightly applied to the plasmalemma of each cell body, as well as an equally coherent network of filaments (CZ3) underlying BZ3, passing halfway between and under neighbouring cells to form enclosed chambers. Those chambers are filled with a much looser meshwork of filaments (CZ2) that appears to be partly entangled with CZ1 or CZ3 at the extremities of the mesh, retaining the somatic cell bodies. The CZ1 layer is frequently referred to as the vesicle in the case of the gonidium, the embryo, and the juvenile colonies derived from it. DZ denotes all of the ECM components lying underneath the cell zone, including (DZ1), a fibrous layer that surrounds DZ2, which is composed of relatively amorphous compounds that fill the deeper parts of the spheroid [41], [87].

By isolation of the various proteic fractions corresponding to the zones mentioned above, it has been possible to identify and localise the different HRGPs constituting the ECM of *V. carteri* (Fig. A1.10) [77]. These identifications were often carried out under sexual life cycle induction by SI, as it has been shown to promote ECM remodelling [88]–[90].

SSG185, a highly sulfated HRGP, was the first ECM glycoprotein to be studied and identified as the main precursor of the CZ3 filament network [91]. Next, ISG, initially found to be transiently expressed in inverting embryos or sperm packets, was demonstrated to accumulate at the base of flagella and in BZ. ISG is assumed to hold somatic cells in an adaptive orientation and to act as the scaffold upon which the rest of the ECM is subsequently assembled [92], [93]. Sumper termed the first "pherophorins" (phI and phII) as these insoluble ECM glycoproteins that were induced by SI phytopheromone [90]. From then on, the *V. carteri* ECM glycoproteins discovered were mostly termed pherophorins. *V. carteri* ECM exhibits significant remodelling plasticity, as a complete self-healing mechanism can regenerate the integrity of the colony upon rupture, combining volvox metalloproteinase-mediated ECM deconstruction, continuous glycoprotein deposition, and glycoprotein autocatalytic reticulation capacities [89], [94]. Pherophorin-S (phS) is a notable example of ECM remodeling plasticity. Unlike most pherophorins, phS is soluble and was found to only accumulate in DZ [88]. Pherophorin-S has recently been demonstrated [77] to be able to migrate to the surface, soften and disintegrate the ECM with the coordination of ECM lytic enzymes, allowing for the release of juvenile colonies.

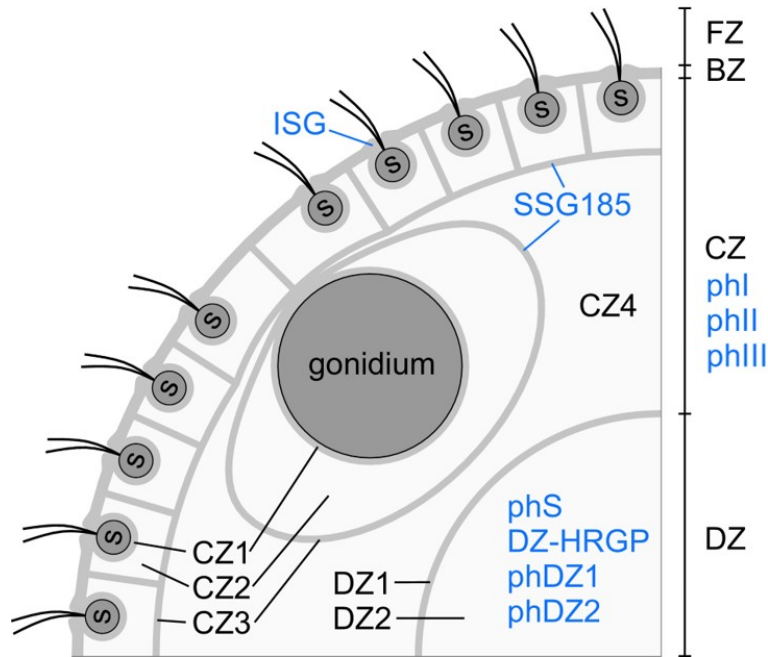


Figure A1.10: Schematic cross-section of a *V. carteri* colony with the localization of known extracellular matrix (ECM) glycoproteins. The alleged or proven localization of the ECM glycoproteins is indicated (*blue*). Further details can be found in the corresponding publications: ISG [93], SSG185 [91], phI [90], phII [90], phIII [95], phS [88], DZ-HRGP [96], phDZ1 [94] and phDZ2 [94]. This figure modified from [77].

Chapter A2

Tissue engineering strategies based on *V. carteri*'s development

Volvox carteri f. nagariensis is a known model for developmental and evolutionary biology, as described in Chapter A1. The volvocine algae family sets an example of the gradual acquisition of multicellularity, one of the major evolutionary transitions that have led to the complexity and refinement of biological systems. To reach the level of complexity displayed by *V. carteri*, these organisms have developed several mechanisms and strategies echoing those employed in tissue models and substitute engineering via the modular approach. Some of these strategies will be addressed in this chapter.

Tissue engineering was primarily introduced in the 1980s as the use of prosthetic devices and the surgical manipulation of tissue. Yet, as a modern scientific discipline, tissue engineering is centred around the application of engineering, physics and medicine principles to produce functional substitutes that can mimic, enhance or replace native tissues [97]–[99]. Tissue engineering is considered one of the scientific platforms of regenerative medicine, which aims to repair, replace, or regenerate cells, tissues, or organs to restore impaired function [100]. The other platforms are cell therapies (i.e., transplantation of cells) and gene therapies (i.e., genetic modification of cells). Many tissues or organs, including corneal tissue [101], skin [102], lung barriers [103], cartilage [104], and bone [105], can be partially or fully reproduced in their structure and/or functions using tissue engineering strategies.

A2.1 Top-down vs. bottom-up approaches to tissue engineering

Biological tissues can be engineered by adopting either a top-down or bottom-up approach (Fig. A2.1. The top-down approach is the traditional one, consisting of cellularising, fully formed or forming, three-dimensional polymeric networks. A tissue aspect can be obtained as cells proliferate, deposit their own extracellular matrix, and eventually remodel the material in the case of a partially to fully degradable material. Conversely, the modular approach, that emerged more recently, consists of developing individual living building blocks with or without the use of a supporting matrix, which are later combined to form a larger unit, ultimately producing a cohesive pseudotissue.

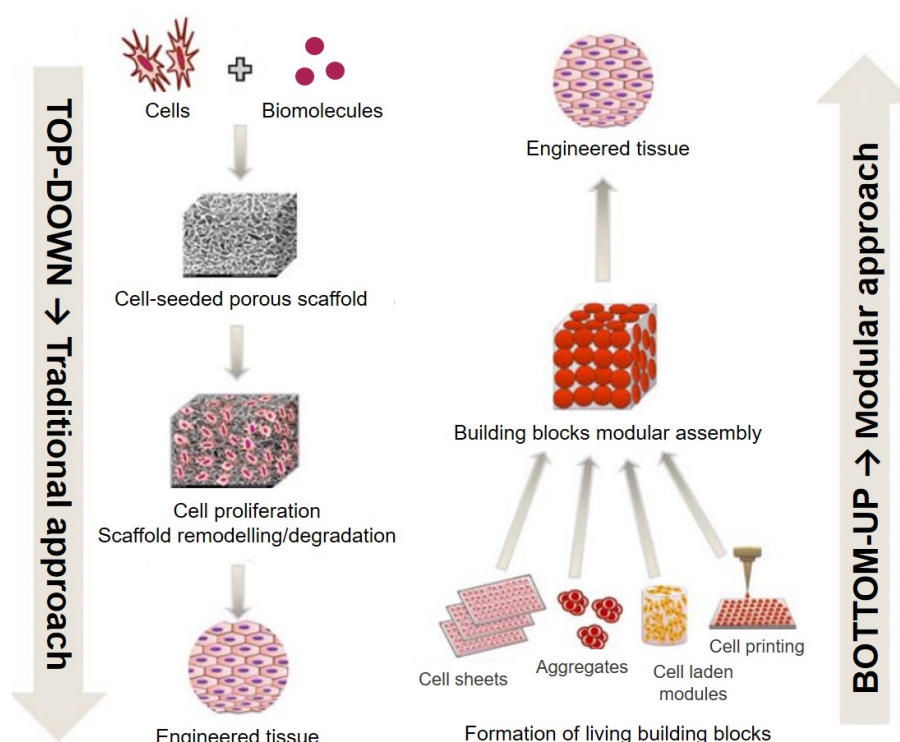


Figure A2.1: Bottom-up vs. top-down approaches in tissue engineering. The traditional, top-down approach (left) involves seeding cells into full sized porous scaffolds to form tissue constructs. This approach poses many limitations such as slow vascularization, diffusion limitations, low cell density and non-uniform cell distribution. In contrast, the modular or bottom-up approach (right) involves assembling small, non-diffusion limited, cell-laden modules to form larger structures and has the potential to eliminate the shortcomings of the traditional approach. This figure modified from [106].

A2.1.1 The traditional approach

The top-down approach derives from early tissue engineering constructs designed prospectively to allow for appropriate cell release upon final implantation [107]. Scaffolds, as an extension of the principles of 2D cell culture, serve primarily as a culture substrate. These constructs were produced by modulating the nature, concentration, compaction level, and organization of polymers to confine various cell types on scaffolds that mimic a wide range of extracellular matrix environments. Scaffold design aims at providing a well-balanced environment between mechanical properties, high specific surface area, good diffusivity, and interconnectivity to support and sustain cell functions [108].

Tissue-engineered scaffolds can be classified structurally as fibrous, porous, or hydrogel-based scaffolds (Fig. A2.2). Fibrous scaffolds display nanoscale and microscale interconnecting textile-like structures. These structures mimic the fibrous nature of native ECM, which consists of nanoscale structural and adhesive protein fibres, including collagen, elastin, fibronectin, and laminin [109], [110]. Porous scaffolds are produced by inducing tunable porosity within the matrix during the polymeric network's development, allowing for better control of gas, nutrient, and cell diffusion. Various porosity induction methods (e.g.,

solvent casting, particle leaching, gas foaming, phase separation, and freeze drying) can be used to accommodate a large variety of polymers and formulations [108], [111]. Finally, hydrogel-based scaffolds are three-dimensional networks of cross-linked hydrophilic polymers, which can retain large amounts of water in a swollen scaffold. Hydrogels better mimic the ECM environment of soft tissues, combining a similar level of hydration, elastic behaviour, and a easily tunable interconnected porosity [112].

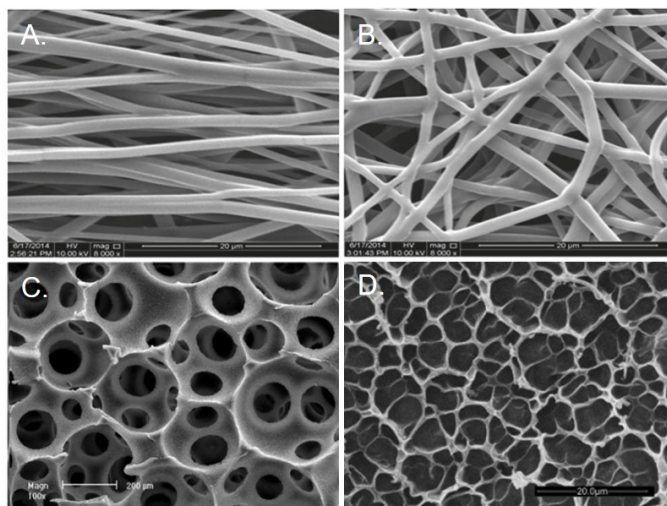


Figure A2.2: Fibrous, porous, and hydrogel-based scaffolds. Scanning electron micrographs of electrospun polyurethane-based with aligned (A.) and random (B.) fibrous microstructures, C. Poly-L-lactic acid macroporous scaffolds produced by phase separation and sugar-leaching, D. freeze dried methacrylated gelatin-based hydrogel. This figure was adapted from [113]–[115].

This top-down approach, which is suited for single-phase matrices development on a small scale, quickly reaches its limits when scale-up and complexity are attempted. As the primary intention of a scaffold is to ensure cellular functions within the matrix, two key antagonistic parameters must be precisely optimised: porosity and mechanical properties (i.e., high stiffness and stability of the polymeric network). A trade-off exists between achieving the high porosity required for efficient mass transfer (i.e., oxygen, nutrients, growth factors, and cell diffusion) and sufficient uniform cellularisation and maintaining good mechanical properties. Indeed, optimising positivity requires pore size and density increases to limit closed pores and promote pore interconnectivity, which in turn alters the density and polymeric network structure, thereby affecting the stability and rigidity of the material [116]. While scaffolds with poor porosity fail to support cellular activity due to a lack of vital supply, scaffolds with low stiffness fail to support cellular adhesion. Although seeding optimisation approaches are being proposed (e.g., sequential seeding [117], modification of media density and viscosity [118], bioreactor-mediated seeding [119], it remains a challenge to seed and maintain cells on large-scale scaffolds with uniform distribution and at densities that correspond to native tissue. Indeed, in conventionally produced scaffolds, cell colonisation and viability *in vitro* and *in vivo* are often limited to a few hundred microns in thickness [120], [121].

Further challenges arise when seeking to generate spatially organised multicellular structures, such as including the establishment of innate vascular structure that becomes imperative for supplying large engineered tissue grafts or the development of other complex tissue features (e.g., neural junctions, zonal or gradient seeding, and transition regions) [122].

A2.1.2 The modular approach

The modular approach, also referred to as bottom-up, is an emerging alternative approach consisting of forming tissues from living building blocks. Those living building blocks are produced using cells, together with optional biomaterials and biomolecules, via self-assembly, directed assembly, and remote assembly principles, ranging from 1D to 4D units, in the form of cell fibres, cell sheets, cell spheroids, and cell organoids. The combination of these living building blocks that may differ will then be merged into more or less complex tissue constructs. This approach, the techniques applied, and the resulting construct presented in Fig. A2.3, have been extensively detailed in this recent review [122].

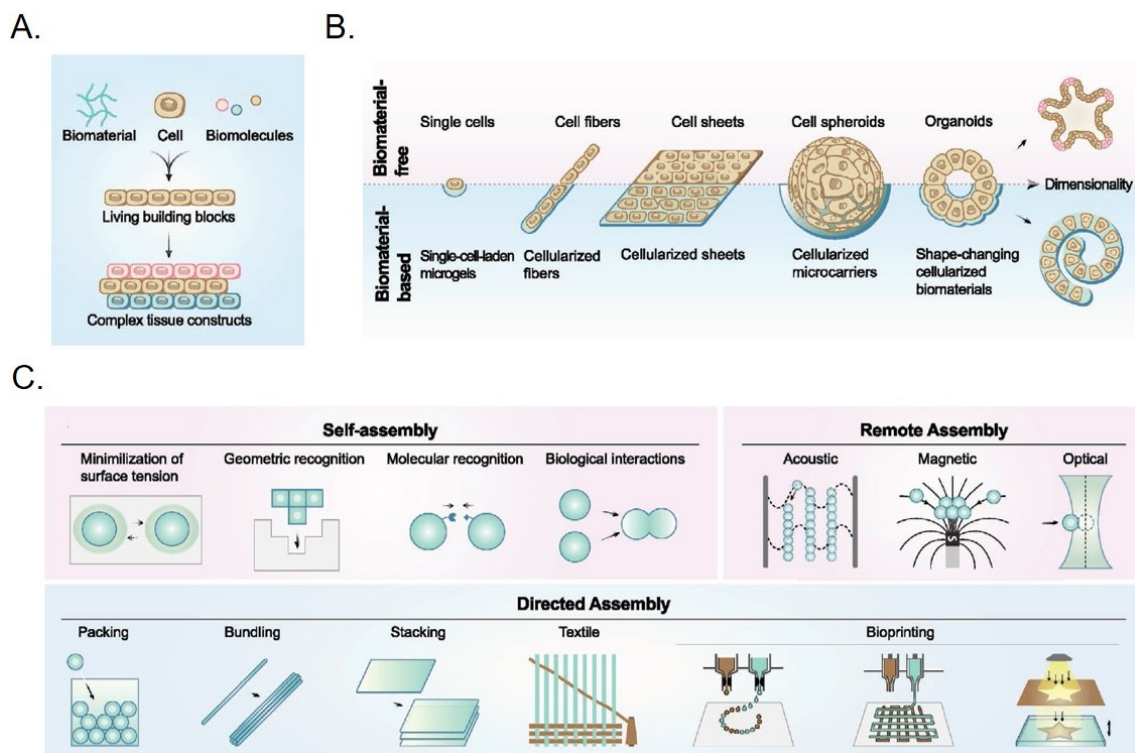


Figure A2.3: An overview of bottom-up tissue engineering strategies. A. Living building blocks are fabricated using cells, together with optional biomaterials and biomolecules, and then assembled into complex tissue constructs, B. An illustration of the different multidimensional living building blocks, ranging from 0D single cell units to 4D dynamic multicellular units. Biomaterial-free and biomaterial-based categories are indicated, C. A schematic of representative techniques for living building block assembly, categorized into self-assembly, directed assembly, and remote assembly. This figure reproduced with permission from [122].

This modular approach, in contrast to the rigid framework imposed by the traditional scaffolding approach, enables the easy and controlled introduction of the previously mentioned

forms of complexity — heterogeneity (e.g., zonal or gradient seeding and substrate transitions) and complex structuration (e.g., vascular network, neural network) — through modulation of cell types and densities or the molecular and mechanical environment provided by the introduced biomaterial. The techniques used to produce such tissue models will not be described further in this section. Yet, various living building block structures will now be put into perspective with the progressive multicellularity acquired in the phylogeny of Volvocine algae and during the development of *V. carteri*.

A2.2 The volvocine algae – analogies with the formation of living building blocks

Volvocine algae phylogeny presents morphological analogies with the multicellular structures developed in tissue engineering (Fig. A2.4). Similarly to the volvocine microalgae, living building blocks result from the assembly of unicellular units into multicellular forms, displaying various levels and patterns of structuration. A wide range of living building blocks can be produced by tissue engineering, mainly by affecting cell adhesion, the associated ECM and/or cell specialisation through cell combination and differentiation. These strategies echo, respectively, cell attachment processes, the development and expansion of an algal ECM, and a division of labour by cell specialisation.

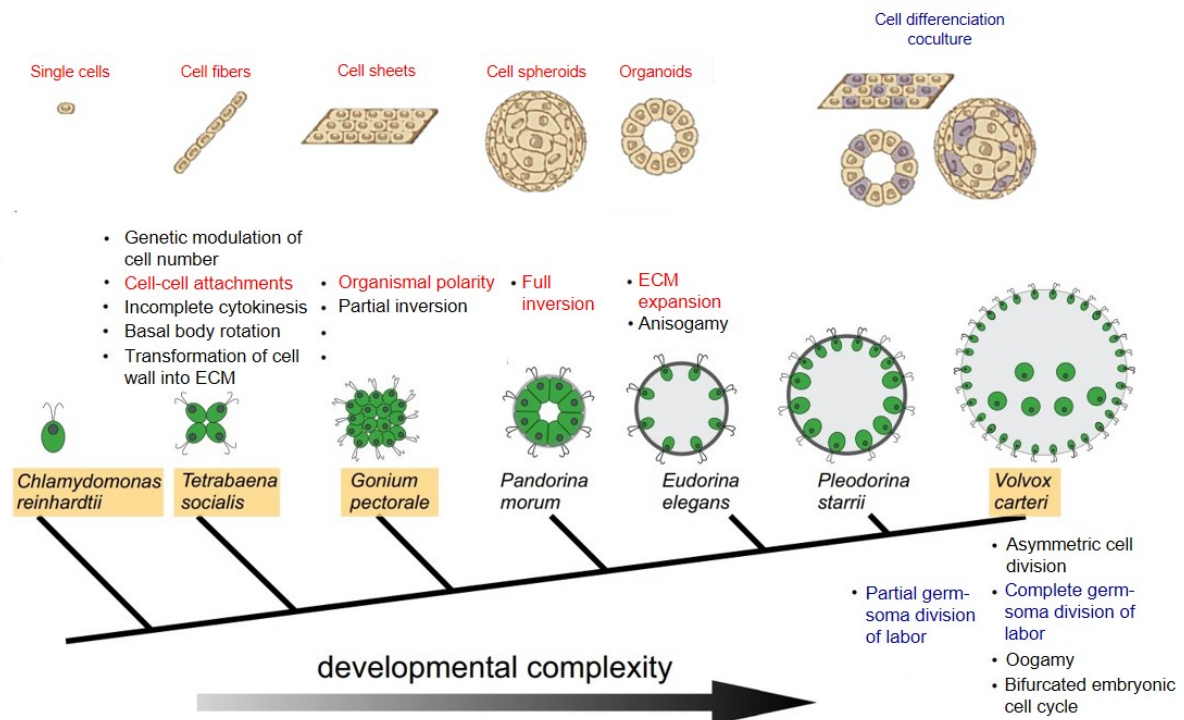


Figure A2.4: Analogies between volvocine algae multidimensional evolution and living building blocks development. Identification of the biological mechanisms that have allowed the acquisition of a progressive and increasingly complex multidimensionality of volvocine algae, analogies with living building blocks formation strategies. This figure was adapted from [21], [22] and [122].

A2.2.1 The significance of cell attachment and adhesion mechanisms

A2.2.1.1 Algal cell attachment and ECM based-cellular membranes – milestone for multicellular development

While mammal cells interact via membrane cell adhesion molecules (CAM) (e.g., integrins and cadherins) and often use ECM as an attachment substrate, volvocine algae develop multicellularity by embedding their cells in a shared ECM [123]. Indeed, the emergence of multicellular organisms in volvocine has been conditioned by the need to develop cellular attachment systems to ensure the cohesion of these organisms throughout their developmental cycle and their resistance to the hydrodynamic constraints of their natural environment. Starting from *T. socialis*, an early form of volvocine colonial organism, cellular attachment is ensured by cytoplasmic bridges established by incomplete cytokinesis and reinforced by an external thin layer of ECM [16]. Volvocine cell-cell adhesion mechanisms have evolved gradually but are marked by two milestones: the early transformation of cell walls into ECM proteins and the emergence of ECM accumulation capacities [13], [72], [87], [124]. This intermediate form of cell attachment provided by both bridges and ECM incorporation evolved with the development of more and more cellularized forms of volvocine algae [125]. These cytoplasmic bridges persist even in late Volvocines forms, finally disappearing once the volume and cohesiveness of the ECM are sufficient to maintain the organism's cohesion. Cytoplasmic bridges are still extant in some Volvox species (e.g., *Volvox globator*, *Volvox rousseletii*), but disappear immediately after the embryonic inversion process in species such as *Volvox carteri* or *Volvox tertius* [62], [126], [127].

Cell adhesion has been shown to be crucial from the earliest stages on, functioning at different scales to organise cells, tissue, and the overall embryo morphogenesis [128], [129]. *V. carteri* is one of the first models of embryogenesis [8]. In addition to the membrane developments constituted by cytoplasmic bridges, cell adhesion molecules are thought to be involved in *V. carteri* embryonic cell-cell adhesion, cell differentiation, and morphogenetic movements, as has been widely reported in numerous embryogenesis processes. The identified membrane-associated protein algal-CAM represents one of the first plant homologs of animal adhesion proteins as it demonstrated analogies with fasciclin I, a cell adhesion molecule involved in the neuronal development of *Drosophila* [130]. The morphological similarity of *V. carteri* embryos and those of mammals like mice deeply emphasises the conservation and fundamental significance of cell adhesion processes during tissular development, of which embryogenesis is the most outstanding example [131], [132]. These adhesion processes are also employed for the formation of complex tissue constructs evolving from simple cellular aggregates to structurally and/or functionally reproducing individual organs (Fig. A2.5) [133]–[137].

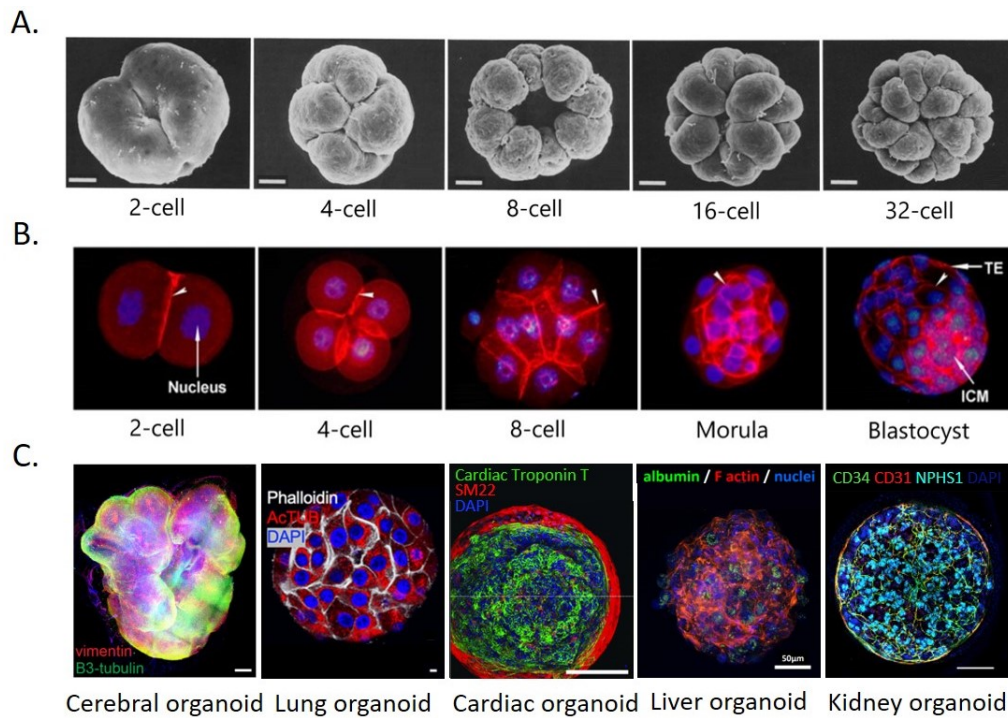


Figure A2.5: Embryogenesis to organoid formation. A. Five preliminary stages of embryogenesis in *V. carteri*, B. Early stages of murine embryogenesis from 2-cell embryo to blastocyte stage, C. Organoid engineering. This figure was adapted from [131]–[137]

A2.2.1.2 Cell adhesion – key parameter for the living building blocks shaping

As demonstrated by volvocine microalgae, cell-adhesion mechanisms are crucial for the development of multicellular structures and greatly impact their shape. The modulation of cell adhesion (i.e., cell-cell and cell-substrate) is one of the most widely used strategies to influence the formation of most forms of the living building blocks from cell fibers, cell sheets, cells spheroid to organoids.

Cell adhesion can be highly targeted to induce cell spreading and surface colonisation to form cell sheets upon reaching full confluency. To promote cell spreading on a surface, topographic (i.e., increased roughness), mechanical (i.e., increased stiffness), and chemical (i.e., surface energy enhancement by vapour plasma-treatment, surface charge modification by polyelectrolyte multilayer deposition, and adhesive peptide grafting) modifications can be used [138]–[141]. Upon confluency, cell sheets acquire cohesiveness through cell-cell, cell-neo synthesised ECM adhesion, and can be released by manually or by controlled separation from the material using intelligent surface treatment (Fig. A2.6 [142]). Electrical-responsive polyelectrolyte multilayers and thermoresponsive N-isopropyl acrylamide coatings are particularly employed for this purpose [141]. Cell sheets can be used to partially model tissues or improve healing and regeneration when altered [143]. While single-cell sheet layers are sufficient to reproduce the corneal tissue and the bladder wall, cell sheets can be staked as homo or hetero constructs to develop prevascular mesenchyme [144], epidermis [145], ligament [146], and cardiac wall substitutes [147].

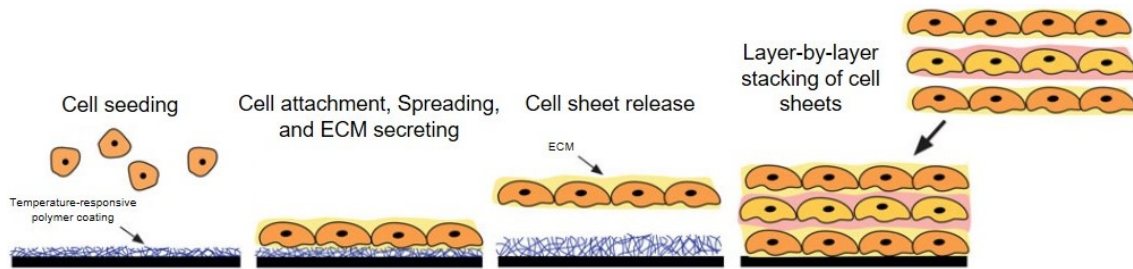


Figure A2.6: Cell sheet engineering. Cells are initially seeded on a “releasable” cell culture dish with a temperature-responsive polymer coating that guides attachment, spreading, and extracellular matrix (ECM) secretion. By changing temperature, the intact cell monolayer is released, which can be subsequently stacked with similar or dissimilar cell sheets to form a three-dimensional cellular construct. This figure was adapted from [142].

Cell-cell and cell-substrate adhesion can be specifically uniaxially oriented by forming elongated fibre-like structures. Surface patterning, microfluidics, and bioprinting technologies are applied to generate fibrous living building blocks that, when combined, can generate three-dimensional fibrous tissue constructs (Fig. A2.8 [148]). Sousa et al. [149] designed fibre-like materials by combining a superhydrophobic surface patterned with elongated wettable channels with hanging drop technology to drive by gravity the aggregation of single cells into a fibre-like material-free construct in which the vascularisation architecture was easily developed through endothelial cell co-culturing.

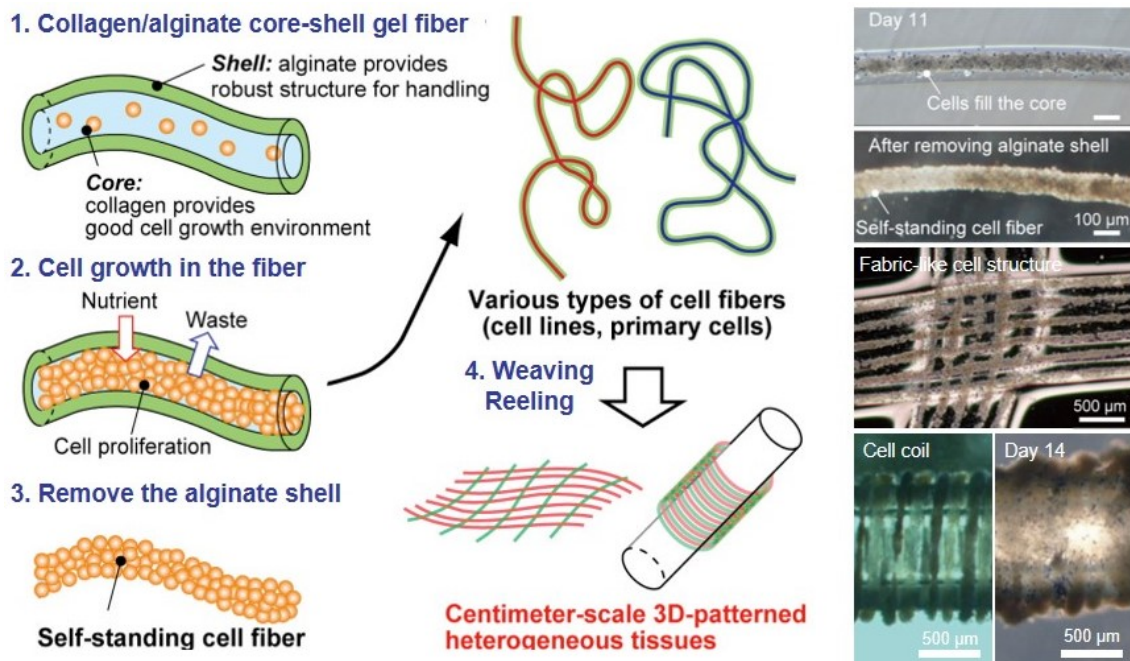


Figure A2.7: Cell fibres engineering. Centimetre-scale 3D heterogeneous tissues assembly made of material-free synthesised cell fibres. HepG2-based fibres can be formed in collagen and alginate core-shell fibres. These cell fibres can retain their shape after the removal of the alginate shell and can be processed into fabric-like or coil-like structures. This figure was adapted from [148].

Microfluidic technologies are widely used to produce micro-and nanoscale structures of various shapes, including fibres and tubes, solidifying polymers through photopolymerisation or ionic cross-linking processes [150]. Using the gelation and degelation properties of alginate [151], [152], combined or not with adhesive molecules (e.g., gelatin [153], collagen [148]) or biostimulant polymers (i.e., chitosan [154]), cells can be easily encapsulated and cultured in tubular guidance structures. Alginate can then be degelled once the cell fibre's cohesion is stabilised by cell-cell and cell-matrix interaction mechanisms, and can be processed into fabric-like or coil-like structures to form 3D tissues.

Finally, cell-cell adhesion can be selectively promoted at the expense of cell-ECM adhesion to produce an aggregation of adherent cells into compact spheroids. Spheroids provide a three-dimensional environment that is physiologically more representative of a native tissue environment than traditional two-dimensional substrate culture. These aggregates allow for growing structural complexity and are readily incorporated into microfluidic devices. Spheroids are thus used in many medical fields, including cancer research, tissue engineering, tissue repair, and regeneration [155], [156].

A wide range of methods for the formation of spheroids has been developed based on biomaterial-based or biomaterial-free approaches. These methods are founded on the principle of promoting cell-cell adhesion by inducing cell agglutination (i.e., suspended drop method [157], microwell method [158], magnetic force drive method [159], microfluidic entrapment method [160], encapsulation [161]) and/or on limiting the establishment of strong cell-matrix adhesion by inhibiting contact with possible deposited ECM molecules or the biomaterial (i.e., superhydrophobic anti-adhesive surface [162], extremely soft material [163], constant agitation of the suspension [164]). The modification of the expression of adhesion surface receptors from primarily integrin-mediated focal adhesion to cadherin-mediated tight junctions promotes these cell clusters and compactions impacting by mechanotransduction mechanism cell functions and metabolism [165]–[169]. Indeed, cell detachment results in the upregulation of cadherin expression, which has been shown to be crucial for successful spheroid formation by actively promoting cell cluster formation [170], [171]. Yet, cell-ECM integrin-mediated adhesion persists as ECM molecules (e.g., collagen I, fibronectin, laminin) are synthesised within the spheroid and participate in the cohesion and physiological representation of this formed 3D microenvironment [172].

The connection between cell-cell adhesion and ECM thus appeared very early in the development of multicellular organisms, as evidenced by the fact that the cell membrane of Volvocine algae is itself an early form of ECM (e.g., CAM of algae, pherophorins in developing and adult *V. carteri* colonies, respectively). Indeed, in mammalian cells, the cross-talk between cell-cell and cell-ECM adhesion modulates the mechanical landscape of the cell, impacting its functionality [173]. The coordination of cell-cell and cell-extracellular matrix adhesions has been shown to be essential for tissue formation and morphogenesis, both *in vitro* and *in vivo*, as a driving force of complex cell differentiation processes [156].

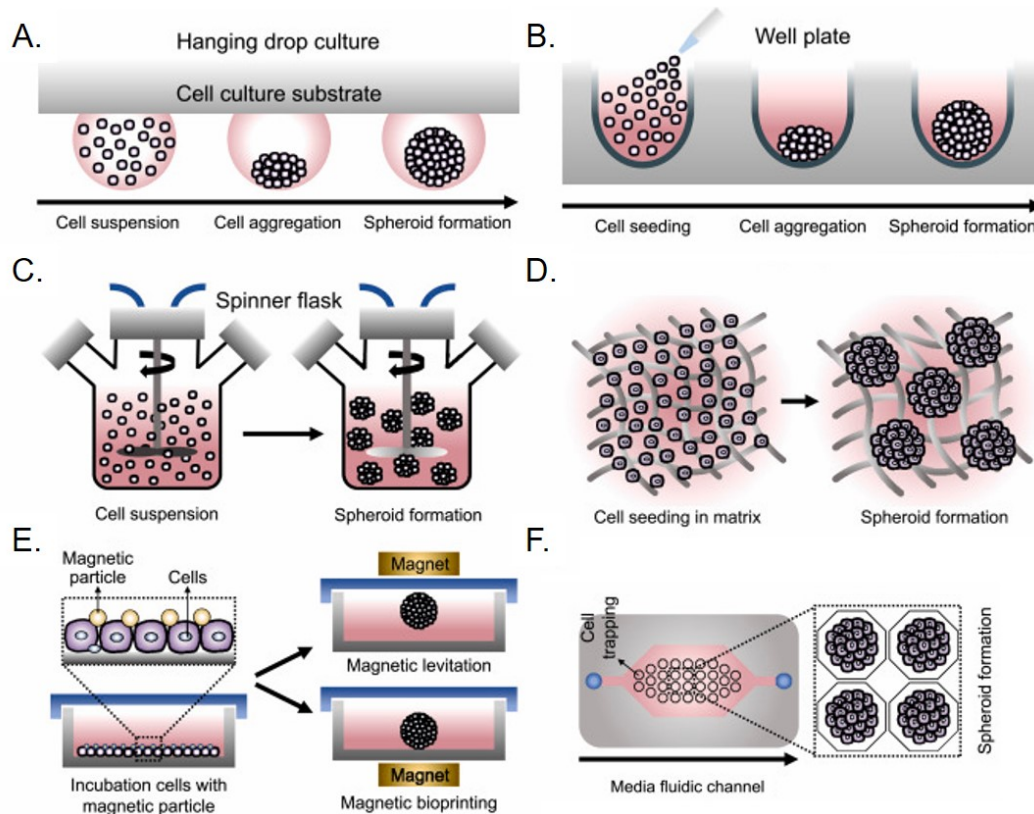


Figure A2.8: Commonly used methods for the formation of spheroids. Representative schematic of various spheroid formation methods A. hanging drop culture, B. micro-well plate method, C. the spinner flask levitation culture D. Hydrogel matrix, E. Magnetic force-derived formation, F. Microfluidic chip-based formation. This figure was adapted from [156].

A2.2.2 The significance of the extracellular matrix on cell differentiation

A2.2.2.1 Impact of the ECM on algal differentiation

By observation of the phylogeny of Volvocine algae, we note the sequentiality in the development and complexification of the ECM (i.e., shifting from cellular membrane to a form of ECM surface, formation of a circular organism by inversion capable of containing the expansion of an ECM), which ultimately allowed partial to complete cellular differentiation in *P. Starri* and *V. carteri* [21], [22].

V. carteri is considered to be a good model for cell differentiation as it has only 2 cell types: large germ cells called gonidia and small terminally differentiated somatic cells, whose already distinct functions could be identified [76]. During the development of the alga *V. carteri* from the embryonic stage to the juvenile colonies, the ECM appears quickly to be very crucial. Indeed, the synthesis of ECM proteins (e.g., Algal CAM, and pherophorins) is triggered long before the inversion process, allowing the desintegration of the cytoplasmic bridges very quickly at the end of it. The ECM network guarantees the cohesion of the organism and continuously support the full maturation of its two cell types analogically to mammal ECM architecture [62], [174].

A2.2.2.2 Impact of the ECM on cell differentiation in mammal cells

As previously stated, cell adhesion processes initiate and influence tissue formation and morphogenesis mechanisms [156], [173]. Cells interact with and are influenced by their microenvironment (i.e., the surrounding ECM) by constantly sensing mechanical and chemical cues and converting them into biochemical signals to orchestrate major cellular processes (i.e., cell polarization, migration, or differentiation) and influence tissue modelling *in vitro* and remodelling *in vivo* [175].

For that matter, in the context of tissue engineering, biomaterials are therefore specifically designed to represent a wide range of tissue microenvironments and thus offer multiple combinations of ECM mechanical and molecular features. The targeted differentiation of pluripotent stem cells represents a major example of the ability to modulate the functionality of a cell by modifying its mechanical or molecular environment (Fig. A2.9).

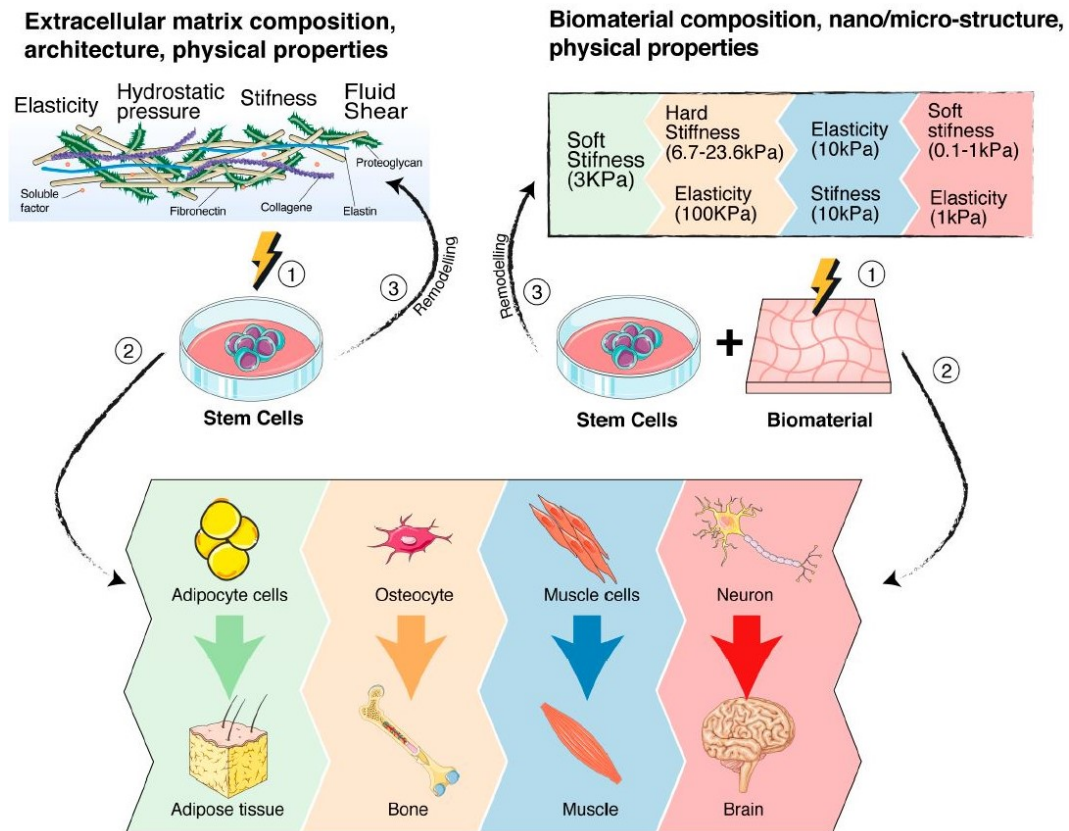


Figure A2.9: Role of mechanosensing/mechanotransduction signalling on stem cell fate. From left to right, stem cells-extracellular matrix (ECM) and stem cells-biomaterials cross-talks. (1,2) Cartoon summarizes of the the different mechanical properties of ECM and biomaterials on driving the stem cell differentiation process toward specific differentiation lineage. The colours correlate the mechanical property with the differentiation lineage [176]–[180]. (3) Cartoon also shows the active reciprocal role of stem cells on remodelling the ECM or the biomaterials. This figure was reproduced with permissions from [181].

Just as we can reprogram any differentiated cells into induced Pluripotent Stem Cells (iPSC) by transfection of embryonic transcription factors (i.e., Oct3/4, Sox2, c-Myc, and Klf4) [182], [183], we can even more easily induce a specific cellular differentiation modifying cell signalling through biochemical stimulation. As an example, adipogenesis (i.e., the process of cell differentiation into adipocytes) can be induced by an induction cocktail mainly composed of insulin, dexamethasone, 3-isobutyl-1-methylxanthine (IBMX), and/or rosiglitazone [184]. In addition to contributing to the delivery of biochemical signals, the mechanical properties of the ECM represent equally important signals. Indeed, by modifying the mechanical properties (i.e., stiffness and elasticity) of the matrix or the biomaterial provided to stem cells, certain differentiation pathways ranging from nerve cells to bone cells can be induced [176]–[181]. Thus, when forming living building blocks, even by a scaffold-free approach, the synthesis of a neoECM is particularly required as, on the one hand, the stability and cohesion of the tissue construct could not be ensured by cell-cell adhesions alone, and on the other hand, the phenotypic stability and viability of the cells could not be guaranteed in the long-term either.

The example provided by volvocine algae, in particular, *V. carteri* as a model for the development of multicellularity through the introduction and refinement of adhesion, extracellular matrix synthesis, and differentiation processes, has led us to consider its use in a modular approach for soft tissue engineering with applications in regenerative medicine.

Chapter A3

Context of soft-tissue augmentation and regeneration

A3.1 Towards the proposal of soft tissue fillers

A3.1.1 Context of soft tissue augmentation

A3.1.1.1 Soft tissue

"Soft tissue" is a general term that refers to various groups of tissues in the body that are neither hardened (i.e., bones and teeth) nor organs. Soft tissues can be divided into connective tissues (e.g., tendons, ligaments, fascia, fibrous tissues, fat, and synovial membranes) and non-connective tissues (e.g., muscles, nerves, and blood vessels) [185]. The primary physiological functions of soft tissues are to connect, support, and surround the organs and other structures of the body [186]. Despite their fundamental structural, mechanical, and functional diversity, all soft tissues constitute a hydrated cellularised environment built upon an extensive composite network of ECM proteins (i.e., collagen, elastin, proteoglycans, and glycosaminoglycans) [187]. The ECM network, through its composition and structuring, largely contributes to the broad spectrum of mechanical properties observed in soft tissues (Fig. A3.1) [188]–[190]. The ultimate pathological alterations of the ECM (e.g., stiffening by collagen accumulation) deeply affect the mechanical functionality of soft tissue, which in turn affects reciprocally its global biological functionality [191].

A3.1.1.2 Soft tissue defect

Just as soft tissue encompasses a broad spectrum of tissues, so too can it be damaged. Indeed, due to their supporting and protecting functions, these tissues are continuously exposed to damage, injury, and loss due to trauma, burns, infections, tumour removals, and degenerative or autoimmune diseases. The broad definition of soft tissue creates ambiguity in the terminology used in their respective alterations. Indeed, while "soft tissue injuries" only qualify for the specific alteration of muscles, tendons, or ligaments due to trauma or overuse, "soft tissue defects" refer as much to a loss of integrity of the skin (ranging from small lacerations to large avulsive injuries) as to a multitude of tissue volume losses (e.g., gingival recession, decrease in mass of subcutaneous tissue, and necrotic tissue or tumour

resections) [192]–[197]. From now on, the loss of volume of subcutaneous fibrous tissue will only be discussed and referred to as a soft tissue defect or tissue loss.

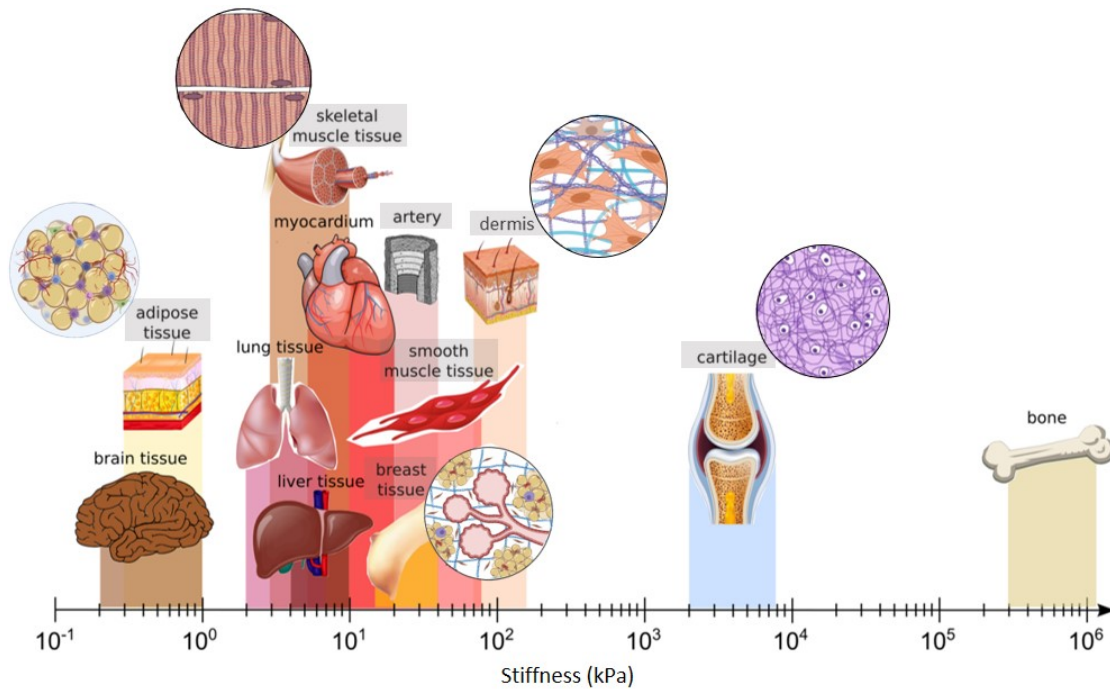


Figure A3.1: Mechanical properties of different human tissues. The stiffness of soft tissue ranges from 0.2 to 1 kPa for adipose tissue to 2 to 8 MPa for cartilage. Soft tissues are highlighted by shaded boxes. This figure was modified from [188], [198]–[202].

A3.1.2 Soft tissue augmentation, from synthetic non degradable materials to integrated tissue substitutes

A3.1.2.1 Soft tissue augmentation

Soft tissue augmentation refers to all techniques used in aesthetic, cosmetic, and regenerative medicine that aim to create volume in the body or face through the use of grafts or biomaterial fillers. A suitable biomaterial for soft tissue volume increase requires two properties : (i) a satisfactory volume stability over a period of time, and (ii) a satisfactory biological behavior for modeling and remodeling procedures [203].

Soft tissue augmentation can be used to fill in pathologically lost tissue volume as well as to shape the contours of the body or face for aesthetic preferences, including age-related concerns. In the United States alone, which, along with Brazil, has the highest rate of aesthetic/cosmetic procedures (i.e., an estimated 19% of total procedures performed worldwide) [204], the recourse to soft tissue augmentation by injection or minimally invasive implantation accounts for 7.8 million procedures, i.e., 50% of the procedures performed for a market worth more than 4.7 billion US dollars [205]. Treatments used and approved by the U.S. Food and Drug Administration (FDA) for dermal filling are provided in the Table A3.1 as a representative example of available options for soft tissue augmentation.

A3.1.2.2 Traditional approach

As the primary objective is to provide a stable augmented volume to compensate for volume loss, the traditional approach, which is still widely used, consists of developing and implanting bioinert, non-degradable, and synthetic materials. In the field of facial injection, the use of Botulinum toxin (Botox®) remains extensively employed as a standard face filler (i.e., used in 44% of total procedures) [205]–[207]. Despite the controversy surrounding their ruptures, leaks, and various side effects, and with the evolution of their internal composition (silicone and saline-based liquid gel fill to cohesive "gummy bear" gel fill), external composition (i.e., smooth to textured), and morphology (i.e., round to anatomical shape), silicone implants remain the gold standard implant for very large volume augmentation, including breast or calf augmentation [208]–[212].

A3.1.2.3 Regenerative approach

The second regenerative approach aims to recreate a tissue-like physiological environment. Tissue regeneration could be initiated by grafting or injecting synthetic bioactive biomaterials (e.g., poly-L-lactic acid and poly(methyl methacrylate) [213]–[219] or ECM-based material mainly to promote collagen production and remodelling in the form of decellularised dermal or adipose ECM [220]–[225], or unique ECM compounds (e.g., acid hyaluronic [226]–[228], and calcium hydroxylapatite [229], [230]). Mini-invasive procedures, such as autologous adipose tissue injection, can be performed for the same intent, having higher bioactivity due to being freshly harvested and cellularised and biocompatibility than commercial options. More recently, the injection of platelet-rich plasma (PRP), also known as platelet-rich growth factors, initially used for its anti-inflammatory and cell proliferation properties in sports-related musculoskeletal injuries, has found many applications in the dermatology field, promoting wound healing, tissue regeneration for scar revision, and overall skin rejuvenation [231], [232].

Table A3.1: FDA-approved dermal filling treatments.

Synthetic dermal fillers		
Botulinum Toxin	Botox®, Dysport® Xeomin®, Jeuveau®	[206], [207]
Poly-L-Lactic Acid (PLLA) microparticles	Sculptra®	[213], [214]
Poly(methyl methacrylate) (PMMA) microspheres	Bellafill®, Artefill®	[215]–[219]
Natural dermal fillers		
Acellular Dermal Matrix Allograft	AlloDerm®, DermaMatrix® FlexHD®, AlloMax®	[220]–[223]
Adipose Matrix Allograft	Leneva®, Renuva®	[224], [225]
Calcium hydroxylapatite	Radiesse®	[229], [230]

Table A3.1 – continued from previous page

Synthetic dermal fillers		
Hyaluronic acid	Juvéderm Ultra™, Perlane™	[226]–[228]
	Restylane™, Belotero®	
Autografts		
Autologous adipose tissue injection	–	[233]
Platelet Rich Plasma (PRP)	–	[231]

A3.2 Biological mechanisms implied in soft tissue augmentation

A3.2.1 Host tissue response

Any injection or implantation of material generates, to some extent, a local or systemic host tissue response. The body unavoidably reacts to the detection of an induced tissue discontinuity, whether the material is synthetic or natural, by initiating a well-known and characterised specific inflammatory process that can lead to a foreign body reaction (FBR)(Fig. A3.2).

Injection or implantation generates an injury to the vascularised connective tissue, triggering an inflammatory response leading to changes in vascular flow and permeability, resulting in the leakage of blood, fluid, and proteins (e.g., albumin, immunoglobulin and fibrinogen) to the injury site in a process known as exudation [234]. These proteins contained in these surrounding invading fluids adsorb non-specifically to the surface of the implant, a process known as biofouling, forming a transient blood-based provisional matrix. A protein coating that will allow immune recognition, mediating subsequent adhesion of platelets and macrophages to the surface of the implanted materials [235]. The subsequent recruitment of neutrophils and mononuclear cells (i.e., monocytes and lymphocytes) by chemotaxis characterises the acute and chronic stages of the inflammatory response, respectively. In parallel, proteases and oxygen free radicals are released from lysosomes to degrade the material [235]. The monocytes will differentiate into pro-inflammatory macrophages (M1) releasing Tumor Necrosis Factor α (TNF α), and Interleukins IL-1 β , IL-6, and IL8 [236], [237] that will attempt to phagocyte the material and will initiate angiogenesis by releasing angiogenic stimulators including vascular endothelial growth factor (VEGF), leading to the development of an immature capillary-based vascular network [238]. Upon continuous monocyte recruitment, others specific anti-inflammatory and pro-regenerative macrophage populations (i.e., M2a and M2c) will differentiate and activate [239], [240]. The coordination of M1 and M2 macrophages induces the recruitment of endothelial cells and fibroblasts, forming a granulation tissue by orchestrating matrix deposition and vascularisation [239]. In addition, the collaboration of macrophages is also manifested by their ability to undergo fusion to enhance their phagocytic efficiency and form multi-nucleated giant cells, known as foreign body giant cells [241]. This phase, characterised by the presence of both macrophages and

foreign body giant cells, is termed the "foreign body reaction" [235]. The deposition of collagen and plasma fibronectin ultimately forms a fibrous capsule that isolates the biomaterial from the rest of the body [242].

The host tissue response (Fig. A3.2) can terminate at any time upon full degradation or encapsulation of the implant. Hence, we can easily comprehend how non-phagocytic synthetic compounds inducing a foreign body reaction are ultimately encapsulated, guaranteeing the augmentation volume, while ECM-based substitutes, although less immunogenic and inflammatory, are easily phagocytosed, leading to a more or less progressive reduction in the volume of the implant, requiring repeated implantation procedures. The severity of the foreign body reaction (e.g., intensity level and persistence of the triggered inflammation and thickness of the associated fibrous capsule) and its interference with the implant function determine the device's biocompatibility. An implant failure would qualify as an implant impaired in its function or integrity. In the case of a biosensor, for example, the formation of a fibrous capsule would significantly delay the inward diffusion of key analytes such as glucose, compromising device functionality. Whereas breast implant failure would refer to an alteration in the implant's integrity caused by degradation during inflammatory phases or contracture resulting from the development of an overly thick fibrous capsule.

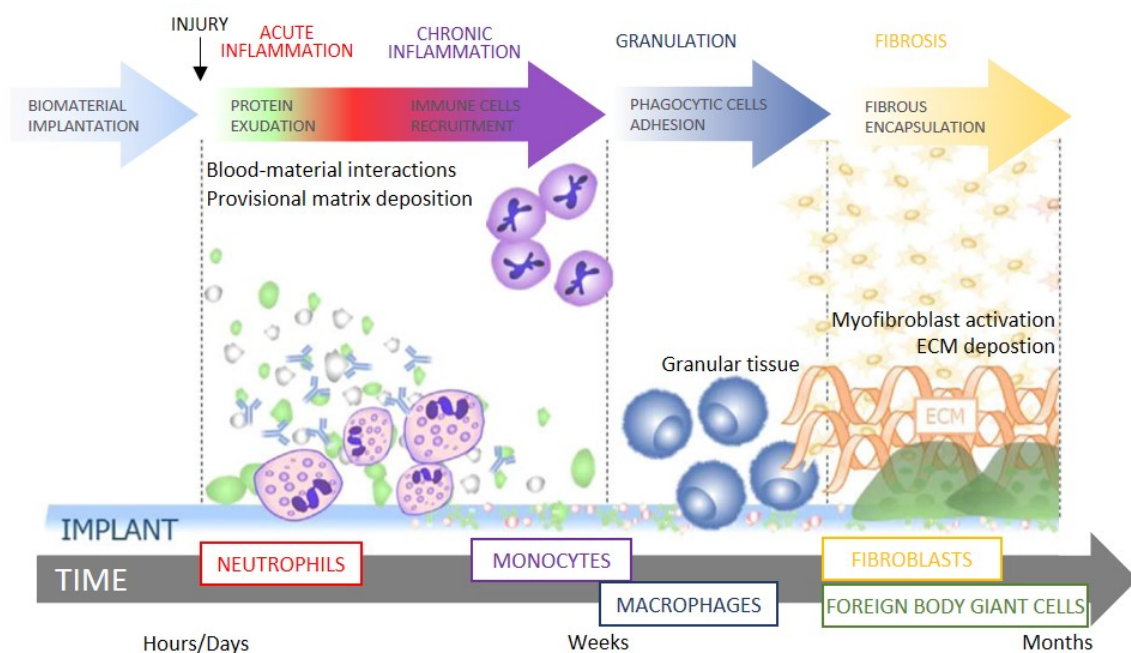


Figure A3.2: Phases of host tissue leading to a foreign body reaction. Upon implantation, the surrounding wound fluid proteins non-specific adsorption coat the biomaterial as inflammatory cells including neutrophils and monocytes reach the wound site. The monocyte population sequentially differentiate into macrophages M1, then M2 and finally fuse into foreign body giant cells, leading to the recruitment of fibroblasts. Fibroblasts then start to wall the implant off from the surrounding tissue by depositing massive amounts of collagen, resulting in the formation of a thick fibrous capsule that isolates the implant from the rest of the body. This figure was modified from [243].

A3.2.2 The inherent role of inflammation, managing the foreign body reaction

Soft tissue augmentation aims to produce a volume that would incorporate as much fibrous connective tissue as possible to ensure structural continuity between the implant and the surrounding tissues and would ultimately include non-connective structures (i.e., blood vessels, nerves). Such a construct will ensure the physiological functionality of the host tissue, both mechanically and bioactively. This degree of tissue integration would require monitoring of the foreign body reaction throughout the process of biomaterial design, implantation procedure, post-implantation tissue host reaction and remediation, as well as eventual biomaterial remodeling *in situ*.

As inflammation is inevitably induced upon implantation and that the process of tissue repair and regeneration is intrinsically connected to inflammation, the management and evaluation of the foreign body reaction is a major opportunity to achieve optimal fusion between the implant and the surrounding tissue.

A3.2.2.1 Anticipate the foreign body reaction from the conception phase

Choosing the core biomaterial components

To fulfil the intended usage, the material must be chosen with full awareness of its strengths and drawbacks. This choice is critical for establishing a host tissue response management strategy.

Synthetic polymers (e.g., poly(ϵ -caprolactone) (PCL), poly(lactic acid) (PLA), poly(glycolic acid) (PGA), poly(lactic-co-glycolic acid) (PLGA), and polyvinyl alcohol (PVA)) are often utilised for tissue engineering and medical device manufacturing applications. Synthetic polymers display high chemical functionality, which allows for a wide range of shaping options (e.g., hydrogel, foam, and sheet) via various synthesis techniques (e.g., chemical crosslinking, repeated freezing and thawing, and electrospinning), often leading to tuneable and stable mechanical properties [244]–[246]. Most synthetic polymer-based materials, on the other hand, cause a typical FBR, which must be managed to reduce the risk of implant failure.

Natural polymers include polysaccharides (e.g., alginate, chitosan, glycosaminoglycans, and hyaluronan) and proteins (e.g., collagen, fibrin, and silk fibroin). Polysaccharides (e.g., alginate, chitosan, glycosaminoglycans, and hyaluronan) and proteins are examples of natural polymers (e.g., collagen, fibrin, and silk fibroin). Natural polymers tend to be preferred because of their resemblance to native tissues, particularly their ECM, which forms a hydrogel also structured by polysaccharides, glycoproteins, and proteins, giving them the propensity to produce reduced inflammation and foreign body reactions with minimal fibrosis while demonstrating remodelling capabilities. As a result, decellularized ECM appears to be a valuable biomaterial that provides a structure and composition closest to the host tissue [247]. However, natural polymers frequently exhibit poor mechanical properties and

repeatability due to variable sourcing, as well as high structural complexity and enzymatic degradability, which must be addressed in the implant design [248].

Material selection is thus critical for establishing an efficient foreign body reaction control approach. In the case of synthetic polymer materials, the focus will be put on decreasing inflammation by restricting upstream immune cell interactions and activation, hence minimising the foreign body reaction and subsequent encapsulation. The emphasis in the case of natural polymer-based materials will be put on preserving the material's physical and mechanical stability by reducing its degradation.

The development of composite materials that would combine the mechanical and biostability interests of synthetic compounds with the biofunctionalities of natural materials is considered an opportunity to achieve an adapted FBR response management.

Surface Modulation of Synthetic Polymeric Materials, from Bioinertness to Controlled Immunogenicity

Molecular and physical properties of the biomaterial interface influence cellular functions and activities such as adhesion, spreading, migration, proliferation, and differentiation by triggering specific molecular events, determining the outcome of the foreign body reaction [249]. Surface modifications allow bioactive change without sacrificing inner mechanical properties [250], [251]. Blood protein-biomaterial and cell-biomaterial interactions, as key initiators of the host tissue response, need to be investigated with great vigilance to better apprehend and control the generated FBR.

Molecular properties

The molecular environment developed on the surface of the implant is primarily determined by the nature of its core component but can subsequently be adapted by surface chemistry modulating its chemical functions, ionicity and hydrophobicity, or through polymeric coating and grafting..

An inert biomaterial is characterised by its lack of interaction with biological elements, whether proteinic or cellular. This property is typically provided by non-ionic (i.e., zwitterionic) very hydrophilic polymers, including polyvinyl alcohol, polyacrylamide, hyaluronic acid, dextran, and especially polyethylene glycol (PEG). This bioinertness limits the ability to undergo any FBR and tissular integration, which is required for soft tissue augmentation. Yet, this type of material is well suited for contexts requiring freedom from encapsulation interference and/or integration with surrounding tissue, including biosensor coatings, artificial vitreous fillers, drug delivery systems, and cell encapsulation therapies (Fig. A3.3) [252]–[254].

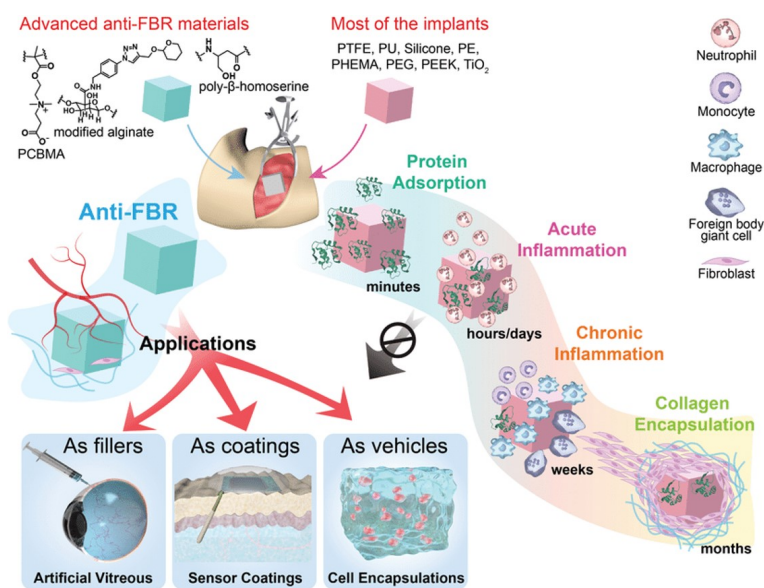


Figure A3.3: Design of advanced anti-foreign body reaction materials. Anti-FBR materials by their bioinertness prevent any involvement in the inflammatory process leading to an FBR, encapsulation and integration with surrounding tissues finding a variety of applications including as artificial vitreous, sensor coatings, and cell encapsulation therapies. This figure was reproduced with permission from [254].

In the context of soft tissue augmentation, controlled inflammation is preferred as tissue remodelling processes highly depend on inflammation. Three key events modulate FBR-related inflammation: (i) the non-specific adsorption of blood proteins leading to the recruitment of the cellular machinery, (ii) the subsequent adhesion of these immune cells (neutrophil, monocytes and macrophages) and (iii) the differentiation of monocytes into pro-inflammatory M1 or anti-inflammatory M2 macrophages.

These three events are triggers for a significant reduction in inflammation. In order to impair non-specific proteic binding, non-specific adsorption sites of synthetic polymers can be blocked by grafting of specific peptides (e.g., arginyl-glycyl-aspartic acid (RGD) and proteins (e.g., osteopontin), limiting the detection and adhesion of immune response initiators (neutrophil and monocyte) while promoting interactions with fibroblasts or/and with ECM through protein-protein interactions to stimulate integration with surrounding tissue [255], [256]. Hemoglobin preadsorption on polystyrene significantly reduces fibrinogen adsorption, which prevents macrophage adhesion-related acute inflammation and could lower the global FBR response [257]. This cellular cascade can also be modulated by local release or administration of anti-inflammatory drugs including dexamethasone, salicylic acid, pirfenidone, or pravastatin, which mitigates the FBR, limiting fibrous capsule formation and promoting angiogenesis [258]–[261].

Finally, immunoinstructive material (i.e., materials with the ability to modulate or mimic the function of immune cells) demonstrated the ability to orient macrophage phenotypes. Indeed, an untreated hydrophobic polystyrene (PS) surface and a hydrophilic O₂ plasma etched polystyrene surface (O₂-PS40) showed the ability to induce M2 anti-inflammatory

and M1 pro-inflammatory macrophage differentiation, respectively [262]. The identification of immunoinstructive polymers capable of controlling macrophage phenotype was demonstrated by library screening of hundreds of meth(acrylate) and meth(acrylamide) monomers, demonstrating that a balance between M1 and M2 macrophages was critical to limit FBR as a majority of either M1-like or M2-like macrophages produce fibrous encapsulation by the inflammatory mechanism or by exacerbating ECM deposition, respectively. This emphasises the level of precision required to address FBR management properly [263].

Physical properties

The physical properties of biomaterials (i.e., size, shape, roughness, surface topography, and mechanical strength) greatly influence protein adsorption and immune cell interactions and activations and thus constitute a strategic axis for the control of the FBR.

The size of micro- and nano-sized spheres and particles also affects the FBR, as nano-sized particles tend to increase the FBR [264], [265]. The incorporation of porosity has been shown to promote favourable tissue responses by limiting sharpness and mechanical property discrepancy while supporting cellular infiltration at the implant's periphery, promoting histogenesis and angiogenesis, modulating integration with surrounding tissue, and minimising fibrous encapsulation [266]. The surface topography of biomaterials is often used to modulate immune cell adhesion, spreading and activation. In addition, nanotopography has demonstrated a significant influence on the *in vitro* and *in vivo* FBR to PCL nanofiber scaffold as aligned fibres appeared to guide cellular penetration *in vivo*, subsequently minimising host response and enhancing tissue-scaffold integration [267]. Additionally, evidence supports physical and mechanical-mediated regulation of macrophage phenotype polarisation and activation [268]–[270].

A3.2.2.2 Evaluate the foreign body reaction both *in vitro* and *in vivo*

In vitro investigation of FBR key events

The high understanding of the nature and sequencing of the molecular and cellular events occurring during a host tissue response leading to FBR allows for the deployment, prior to an ultimate *in vivo* implantation, of a set of methodologies to anticipate and remedy this FBR.

The characterization of the biomaterial interactions with blood components is particularly focused on in the case of the evaluation of the FBR of synthetic and composite biomaterials. The quantification of the non-specific adsorptive capacities of proteins in the form of blood samples or isolated proteins (e.g., fibrinogen) and the characterization of the surface hydrophilicity and roughness are usually performed simultaneously as these factors influence the protein adsorption ([255]–[257], [271]. The ability to induce coagulation and complement activation that activates proteolytic cascades is also commonly studied [272]. An extensive

evaluation by various *in vitro* culture conditions of the biomaterial's ability to promote or inhibit adhesion and activation of key player immune cells (i.e., neutrophils, monocytes, and macrophages) by cytokine secretome analysis is typically carried out [273]. In particular, the propensity to induce targeted differentiation of monocytes into pro-inflammatory M1 or anti-inflammatory M2 macrophages and to support the proliferation and deposition of ECM are of particular interest in assessing the potential for tissue remodelling and tissue integration [262], [263]. The degradability of the material can also be anticipated by exposure to various conditions of enzymatic mimicking of the *in situ* degradability [274].

In vivo assessment of FBR

The selection of the host model in animal experiments is made based on high interspecies similarity to the phenomenon under study. The most common *in vivo* model of the FBR is implantation at subcutaneous or intraperitoneal sites in mice or rats, which allows for monitoring of the entire FBR process from inflammation to fibrosis (Fig.) [275]. Thymus deficient mice can be used for this purpose since T cells are not necessary for a normal foreign body reaction [276].

Assessment of FBR intensity is usually done on sequential follow-up at 1 week, 1 month, and 2+ months to study the initiation and resolution of the inflammatory process. On histological observations, read-out analysis consists of assessing the intensity and phase of inflammation reached by counting neutrophils, monocytes, macrophages (M1 or M2), and foreign body giant cells; and observing the aspect of the implant-surrounding tissue interface to attest to the absence or presence and thickness of the fibrous capsule and to evaluate tissue integration. Cytokine analysis of the secretome on biopsies can also be used to determine the intensity of inflammation [277].

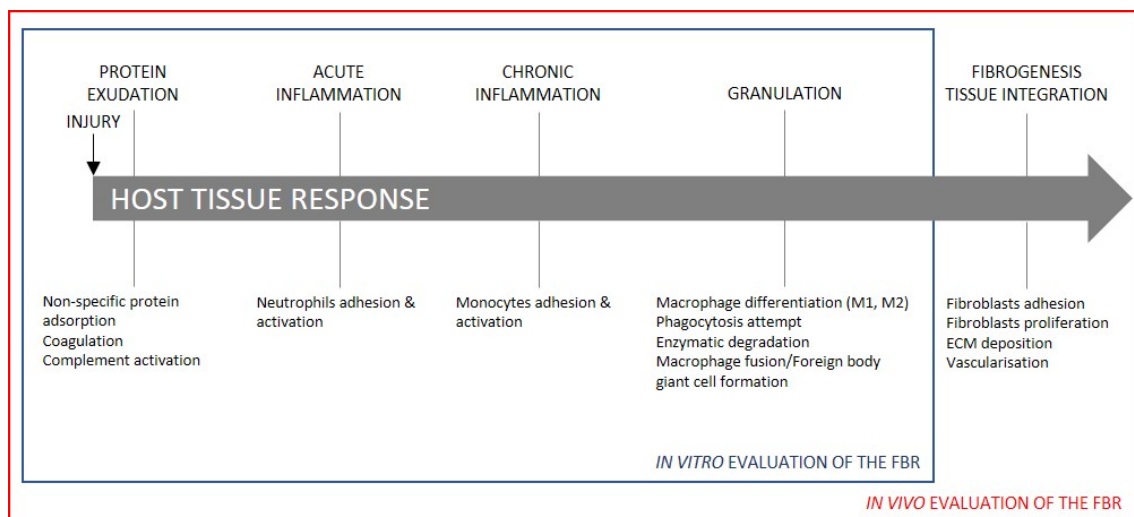


Figure A3.4: *In vitro* and *in vivo* evaluation of the post-implantation host response

A3.2.2.3 Opportunities provided by soft tissue-based substitutes and grafts

Benefits of ECM-based substitutes for the management of FBR

ECM-based biomaterials represent decellularised, lipid-free protein derivatives and purified protein extracts of previously living tissues or organs (Fig. A3.5). Decellularisation methods combine physical (e.g., freezing, and hydrostatic pressure), chemical (e.g., hypotonic and hypertonic solutions, alcohols, ionic detergents, non-ionic detergents, organic solvent chelates) and enzymatic (e.g., trypsin, and peptin) approaches to break down and disrupt cells to remove allogeneic or xenogeneic cell antigens [278]. Decellularisation methodologies inevitably induce physical and chemical damage to the ECM [279].

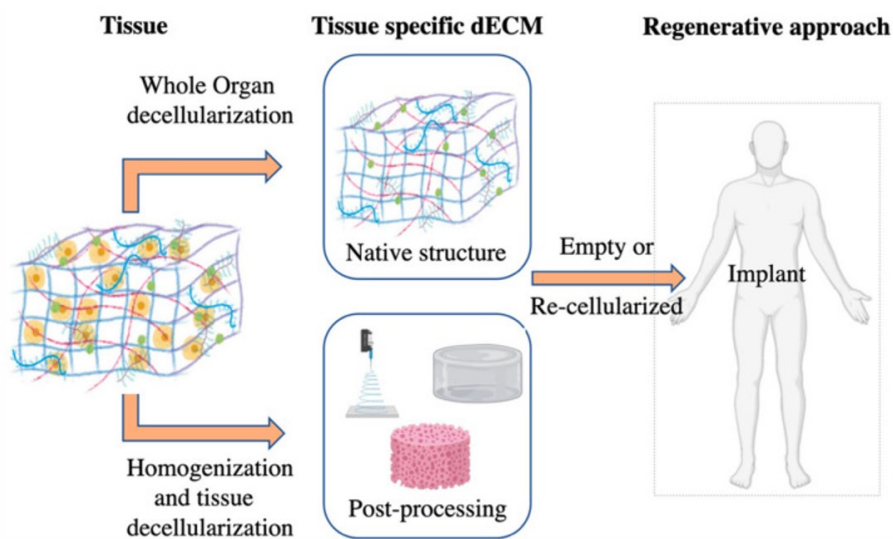


Figure A3.5: Schematic of organ decellularization and tissue decellularization approaches. This figure was reproduced with permission from [279].

ECM-based biomaterials for tissue augmentation are often extracted from decellularised dermis that shows the lowest structural complexity compared to other tissues or organs. Decellularised matrices are mainly composed of collagen and elastin, which serve as primary structural elements, supporting trace amounts of cell-engaging proteins (i.e., fibronectin, vitronectin, osteopontin, glycosaminoglycans (GAGs)) and growth factors. By presenting matrices that are physically and biochemically similar to native tissues, ECM-based biomaterials are proposed to restore healing signals, limit inflammation and foreign body reactions. While the natural origin of ECM bioscaffolds does not preclude the inevitable initiation of a host tissue response, these materials are expected to rapidly promote constructive tissue remodelling outcomes by degradation, releasing bioactive elements (e.g., chemoattractants, growth factors), and promoting subsequent deposition and remodelling of the matrix by endogenously recruited stem cells [280], [281]. Further research is still needed to improve the efficiency and reproducibility of decellularisation methods as well as their precise characterization to ensure the quality of the formed substitute anticipating the induced inflammation,

the structuring of the ECM to preserve its stability and mechanical properties, as well as the denaturation of ECM components due to the use of brutal decellularisation methods [282].

Benefits of autologous adipose tissue transplantation

Autologous fat grafts are a common procedure in aesthetic and reconstructive plastic surgery for tissue regeneration, such as burn healing [283], scar treatment [284], peripheral nerve surgery [285], soft tissue and breast reconstruction [286], [287], trunk [288], and lower limb volumes and contours deformities [289]. Soft tissue lipofilling injections (Fig. A3.6), easily harvested from the lower abdomen and inner thighs, improve the volume or contour of soft tissue [290]. Fat grafting is associated with unpredictable resorption of adipose tissue due to poor graft quality, which is related to the lack of standardised protocols for donor site preparation prior to harvesting, harvesting technique, processing (i.e., washing, centrifugation, filtration or isolation of adipose tissue-derived stem cells), and transplantation [291]. However, a large body of literature supports the efficiency of fat grafting in aesthetic and reconstructive cases [292].

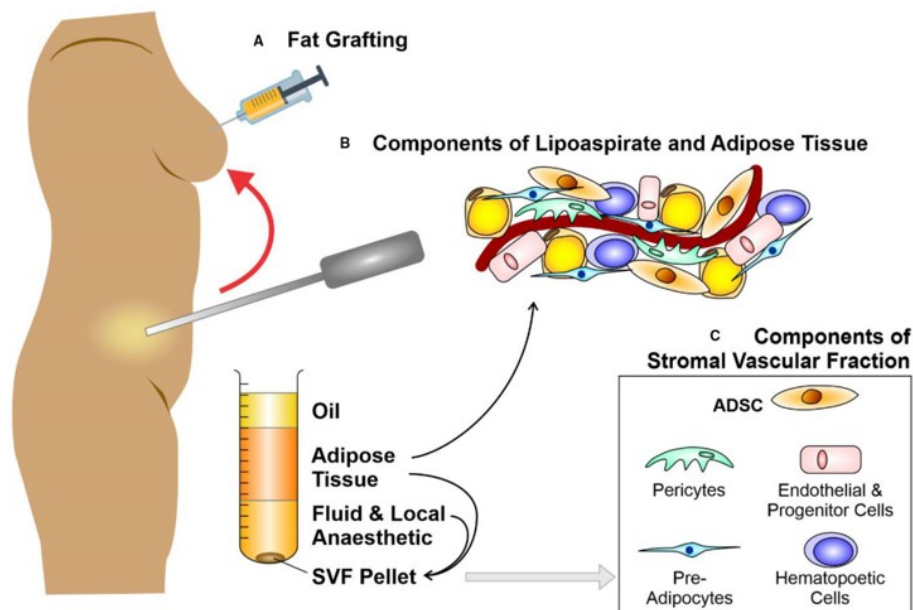


Figure A3.6: Liposuction, fat grafting and the components of adipose tissue. A. Schematic diagram depicting fat grafting after liposuction of subcutaneous fat from an abdominal donor site, B. The components of lipoaspirate separate into layers of oil (discarded), aspirated adipose tissue and infranatant (composed of blood, plasma, and local anesthetic), C. The components of adipose tissue and the key constituents of the stromal vascular fraction (SVF) pellet may be re-introduced to enhance the fat graft. Further processing of this adipose tissue with collagenase digestion and centrifugation allows the isolation of a SVF pellet. This figure was reproduced with permission from [290].

The efficiency of fat autologous graft lies in the supply of readily available and self-renewing multi-lineage pluripotent stem cells, the adipose-derived stem cells (ASCs) [293]. ASCs demonstrate multipotency for differentiation into mature bone, cartilage, and fat [294]. ASCs are now considered to orchestrate tissue regeneration through the paracrine effects of their

broad secretome (i.e., chemokines, cytokines, and protein growth factors) on driving angiogenesis, suppression of local immune/inflammatory responses, and reduction of fibrogenesis [290], [295]. With ASC, the stromal vascular fraction contains multiple cell types including pericytes, endothelial cells, endothelial cell progenitor cells and blood cells, promoting the rapid vascularisation required for graft stability and survival. Based on the success of autologous adipose tissue transplantation, adipose tissue engineering for soft tissue augmentation and replacement represents an opportunity to provide improved therapeutic modalities to precisely control tissue regeneration [296].

Chapter A4

Thesis research project: *V. carteri* living building blocks-based stacking model and bioinspiration for biomaterial design

A4.1 Thesis objectives

The tissue engineering field is continuously fueled by new models and new therapeutic solutions, mainly based on animal-derived products. In the context of my thesis, we wished to take the opposite approach and push the 3Rs rule (i.e., Replacement, Reduction, and Refinement) by projecting our objective towards the proposition of alternative and innovative plant-based matrices for tissue engineering and the development of therapeutic solutions for the treatment and regeneration of soft tissue defects (Fig.A4.1). We intended to develop in-depth structural, chemical, and biological characterizations of our materials to evaluate their potential and identify the most appropriate applications.

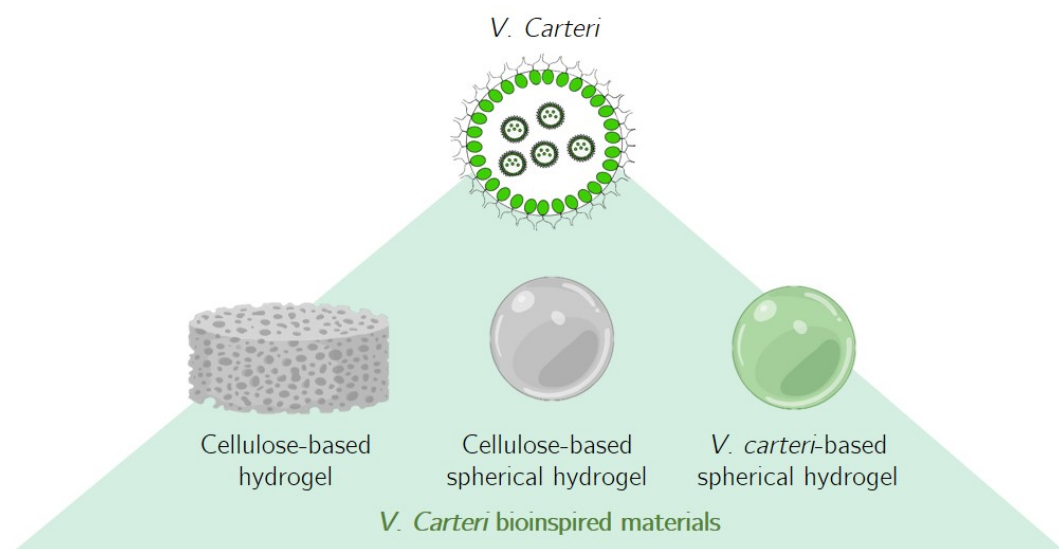


Figure A4.1: *V. carteri*-based and *V. carteri*-bioinspired material approaches for tissue engineering and regenerative medicine Created with BioRender.com.

A4.2 Development of the thesis research project

First, we set up a strategy in Part C around the use of the microalga *V. carteri* as a biomaterial. In chapter C1, the maintenance in discontinuous culture, the preservation of this alga, and its structural, mechanical, and biological characterization were undertaken to ensure that we were able to integrate it into mammalian cell culture and to progressively overcome the reservations related to the unusual use of an integral and complex microalga in human cell culture and to identify the most adapted bioengineering paths. Thus, several proofs of concept were proposed for *V. carteri*'s use in tissue engineering and regenerative medicine. *V. carteri* colonies consist of, in their more basic shape, spherical objects of variable diameter, able to form highly compact suspensions and able to make different cell types of both murine and human origin adhere to their surface.

The *V. carteri*-based living building block stacking model of tissue production (Fig. A4.2) suggested in this thesis work is a direct result of this. To overcome the difficulty of cell colonising matrices or scaffolds *in vitro*, we proposed using the bottom-up approach based on the development of cellularized structural bricks whose juxtaposition would create a sufficient culture surface to support cell adhesion, cell proliferation, and extracellular matrix expansion. In Chapter C2, starting from encouraging results initially observed using a murine fibroblast line, we first developed an *in vitro* model of dermal substitute based on human dermal fibroblasts. In this context, we characterised the matrix that *V. carteri* living building blocks-based stacking model represented, and its potential to promote cell adhesion and proliferation for homogeneous, cohesive, and reproducible *in vitro* tissue building.

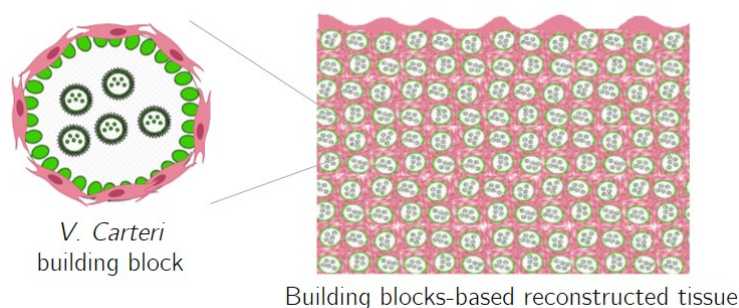


Figure A4.2: *V. carteri* living building blocks-based model composed of the compaction of preseeded *V. carteri* colonies Created with BioRender.com.

The flexibility provided by this tissue-building method *in vitro* also suggested that this type of system could be easily repopulated by cells *in vivo*. Indeed, implanted matrices and scaffolds often experience difficulties in the diffusion of cells and nutrients, which frequently result in decellularisation and devascularisation of implants, both in the short and long term. The structural bricks represented by *V. carteri* colonies, either un- or pre-cellularized, display a large surface area that is flexible in its assembly and fully interconnected. A preliminary subcutaneous implantation study was carried out *in vivo* on an athymic mouse model to test its degradability, biocompatibility, and ability to support histogenesis. Once these *in vitro* and *in vivo* parameters were investigated, we examined in Chapter C3 the ability of *V. carteri*

to direct the differentiation of stem cells.

V. carteri is a high-potential material that has demonstrated the potential of plant-based alternatives for tissue engineering applications. In Part D, we developed a second approach based on the bioinspiration of *V. carteri* for the development of alternative biomaterials. In Chapter D1, we focused on the synthesis, characterization, and application in tissue engineering of a composite hydrogel based on microcrystalline cellulose, the building block of plant life. In Chapter D2, we then pushed the bio-inspiration of *V. carteri* by studying the feasibility of reproducing its basic structure, a microsphere, by seeking to miniaturise our cellulose-based hydrogel to reach this scale. Finally, in Chapter D3, we chose to study the possibility of reproducing synthetic *V. carteri* in its spherical structure and protein content by forming alginate and *V. carteri* material-based microspheres.

Part B - Material and methods

Chapter B1

V. carteri culture

Unless specified otherwise all chemical reagents have been purchased from Sigma-Aldrich (St. Louis, MO, USA).

B1.1 Culture maintenance

V. carteri f. *nagariensis* was provided by National Institute for Environmental Studies (NIES-397) based in Tsukuba, Japan. This strain was grown continuously under sterile conditions in VT medium pH 7.5 (Table B1.1, [297], [298]) and maintained in the ST 5 Basic Smart growth chamber fitted with a 15000 lux light system (POL-EKO-APARATURA, Wodzisław Śląski, Poland)(Fig. B1.1A) at 25°C under an alternating day-night cycle of respectively 14h and 10h. On the 19th day of culture (Fig. B1.1B), the colonies of *V. carteri* were harvested by filtration using a 100 µm porosity sieve (Haver & Boecker oHG, Oelde, Germany). The algal suspension could be used fresh or preserved in 70% ethanol or 4% Paraformaldehyde (PFA).

Table B1.1: Composition of *V. carteri* Culture Medium (VT medium)

Medium components	CAS number	Concentration
Calcium nitrate tetrahydrate	13477-34-4	250 µM
Cobaltous chloride hexahydrate	7791-13-1	42 µM
Disodium β-glycerol phosphate pentahydrate	13408-09-8	82 µM
EDTA disodium dihydrate	6381-92-6	8 µM
Ferric chloride hexahydrate	10025-77-1	219 µM
Glycylglycine	556-50-3	3.784 mM
Magnesium sulfate heptahydrate	10034-99-8	81 µM
Manganese dichloride	7773-01-5	79 µM
Potassium chloride	7447-40-7	335 µM
Sodium molybdate dihydrate	10102-40-6	31 µM
Vitamin B1 hydrochloride	67-03-8	29,6 nM
Vitamin B7	58-85-5	2,3 nM
Vitamin B12	68-19-9	0,7 nM
Zinc sulfate heptahydrate	7446-20-0	23 µM

B1.2 Algal enumeration and observation

V. carteri were immobilised following immersion in a 167 mM acetic acid Phosphate-buffered saline (PBS) solution. The algal suspension was deposited in the 50 mm x 20 mm x 1 mm chamber of a Sedgewick Rafter S52 counting cell (Graticules Optics Ltd, UK) (Fig. B1.1C) presenting a total volume of 1 mL. The counting cell was observed using the Leica MDG41 microscope (Leica Microsystems, Wetzlar, Germany). Acquisitions were made for further processing using Image J [299] such as determining the diameter or stage of development of *V. carteri* colonies. For the observation of *V. carteri* colony microstructures, the Leica DM1000 LED microscope (Leica Microsystems, Wetzlar, Germany) was used.

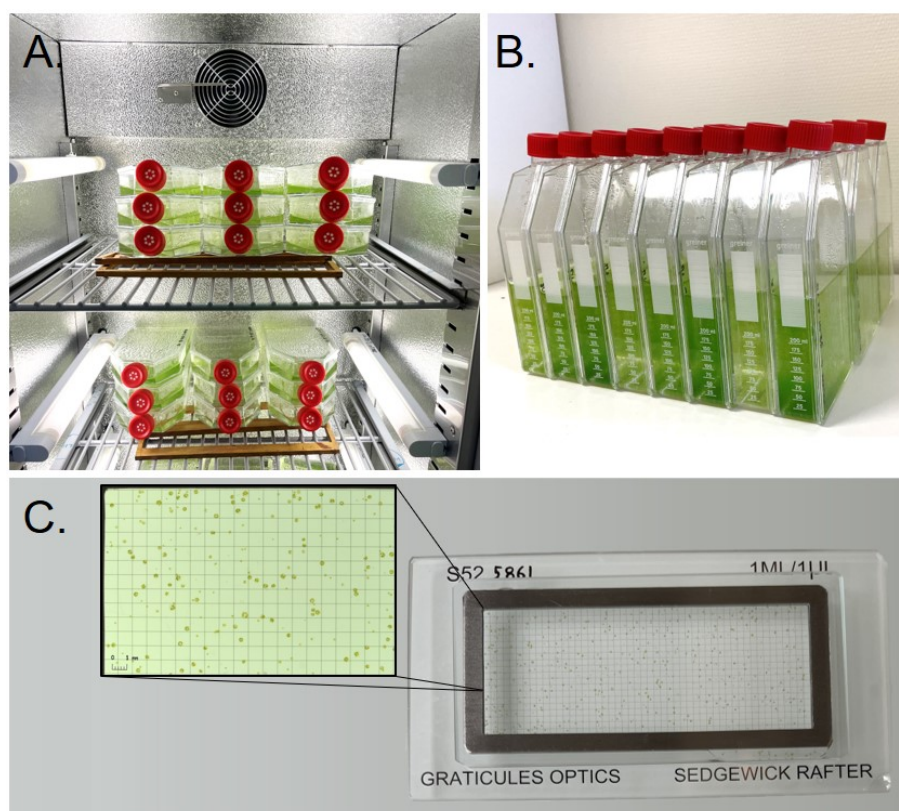


Figure B1.1: *V. carteri* micro-algae culture system. A. Growth chamber fitted with a 15000 lux light system (POL-EKO-APARATURA, Wodzisław Śląski, Poland), B. Algal suspension appearance upon harvest on day 19, C. Sedgewick Rafter S52 counting cell for micro-organism and phytoplankton enumeration (Graticules Optics, UK).

B1.3 Algal deflagellation

The effectiveness of *V. carteri* deflagellation by 70% ethanol fixation was compared to the pH shock deflagellation standard method ([300], [301]) established in the literature. To do so, 1mL of freshly harvested *V. carteri* saturated suspension was resuspended in PBS solution at pH 7 concentrated to 7% m/m glucose and 10 μ M Glycylglycine. The pH was then dropped to pH 4 for 90 seconds using a 1N acetic acid solution and quickly returned to pH 7 with

1N NaOH solution. Flagella present on the surface of the colonies could be observed using bright-field microscopy.

B1.4 Production of *V. carteri* raw extract

For future synthesis experiments, freshly harvested colonies of *V. carteri* saturated suspension were crushed on ice by ultrasound via 0.5 seconds cycles at 400W, 24kHz for 1 min using a UP400S ultrasonic device (Hielscher Ultrasonics, Teltow, Germany). The soluble fraction was collected following a 3871 Relative centrifugal force (RCF) centrifugation for 1 min and filtration on Grade 393 α -cellulose filter paper with a 1 μ m retention rate (Sartorius, Göttingen, Germany) in a Büchner system to remove any membrane and cell residues. The resulting raw extract was used in cell culture immediately or freeze-dried using the Alpha 1-2 LD plus freeze drier (Christ, Martin Christ Gefriertrocknungsanlagen GmbH, Osterode am Harz, Germany) and stored long-term at -80°C for subsequent chemical coupling. The reaction yield was determined from the dried product mass and the density and volume of the saturated suspension of *V. carteri*.

For future cell culture experiments, extracts were prepared using a 15 000 colonies/mL suspension in PBS. Upon the algal suspension rupture using ultrasound method, the soluble fraction was collected following a 3871 RCF centrifugation for 1 min and stored at -20°C until use.

Chapter B2

V. carteri inspired material synthesis

Unless specified otherwise all chemical reagents have been purchased from Sigma-Aldrich (St. Louis, MO, USA).

B2.1 PVA/Cellulose-based material synthesis

The chemical reactions corresponding to the dialdehyde microcrystalline cellulose (DMCC) oxidation and DMCC-PVA cross-linking are shown in Fig. B2.1. The various shaping options of these cellulosic materials are illustrated in Fig. B2.2.

B2.1.1 Sodium periodate-mediated cellulose oxidation

Extra pure microcrystalline cellulose (mean particles size: 90 μm , ACROS Organics, Carlsbad, CA, USA) was suspended with 6.25, 12.5 or 25% w/w sodium periodate (ACROS Organics, Carlsbad, CA, USA) in water for 4h reaction at 90°C under conventional thermal heating with stirring and reflux. Dried DMCC powders with theoretical molar dialdehyde content of 9, 18 and 36% were stored at RT.

To miniaturise the cellulose-based hydrogel for microsphere synthesis, nanocrystalline cellulose (NCC, CelluForce, Montreal, Quebec, Canada) was suspended with 6.25% w/w sodium periodate in water for 4h reaction at 90°C under conventional thermal heating with stirring and reflux. The dialdehyde nanocrystalline cellulose (DNCC) was then recovered by centrifugation at 3871 RCF for 15 min and washed twice in permuted H₂O to remove reaction residues. DNCC was then dried by lyophilization using Alpha 1-2 LD plus freeze drier (Christ, Martin Christ Gefriertrocknungsanlagen GmbH, Osterode am Harz, Germany) and stored at room temperature (RT) until use. The reaction yield was determined from the dried product mass.

B2.1.2 Cellulose/PVA coupling via LiCl/NMP system

For the formulation of DNCC/PVA (2:1) hydrogels, 3.2 g of DNCC and 1.6 g of fully hydrolysed PVA were suspended in 20 mL of concentrated 1-Methyl-2-pyrrolidone (NMP; 99.5% Extra Dry, ACROS Organics, Carlsbad, CA, USA) at 12% w/w Lithium chloride (LiCl; 99%,

ACROS Organics, Carlsbad, CA, USA) for 20 min reaction at 90°C under conventional thermal heating with constant stirring.

For microsphere formation, the DNCC/PVA formulation was modulated using 9% theoretically oxidised DNCC. 2.0 g of 9% DNCC were dispersed in 10 mL of deionised water with stirring at RT. The resulting gel was acidified for 30 min by pouring in 4-5 drops of 36%V/V HCl. Then, 1.0 g of PVA (80% hydrolysed; MW= 9000-10000) were added and the stirring was continued for 30-45 minutes. The product was then dried by acetone precipitation, filtration of the insoluble fraction and rapid drying at RT. The product was then dissolved in 25 mL of NMP (NMP; 99.5% Extra Dry, ACROS Organics, Carlsbad, CA, USA) containing 4.6%w/V of LiCl (99%, ACROS Organics, Carlsbad, CA, USA) by conventional heating for 15 min at 90°C on stirring until a homogeneous and pourable gel was obtained.

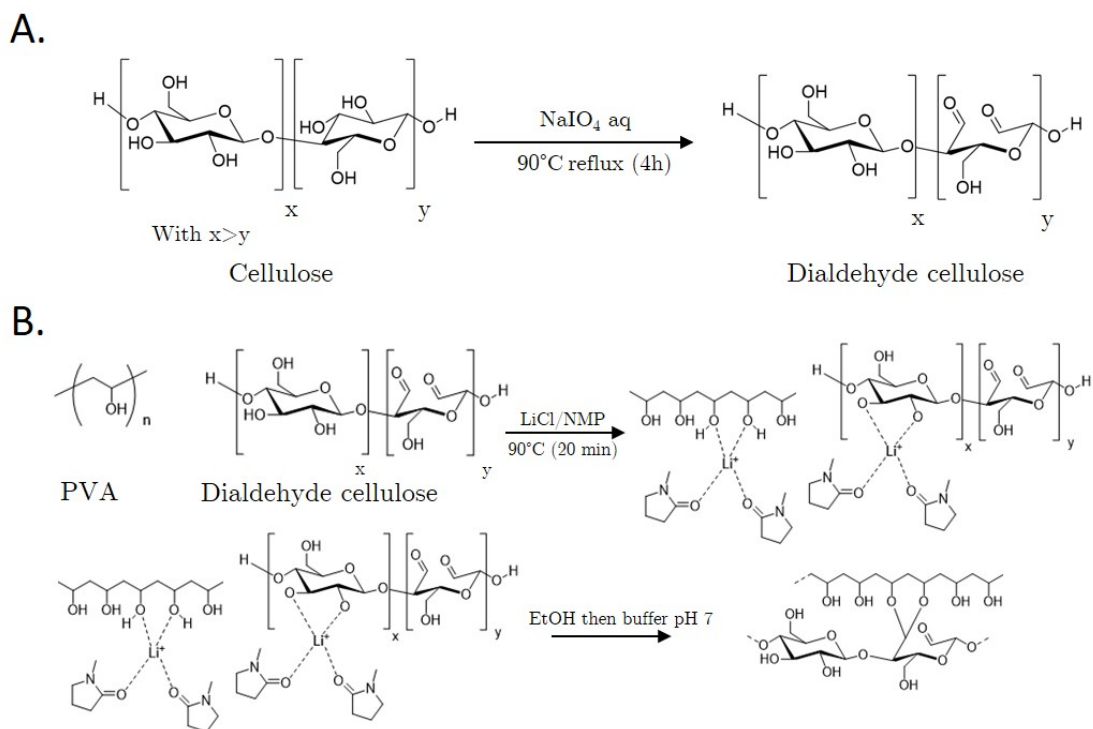


Figure B2.1: MCC/PVA hydrogel reaction scheme. Schematic representation of A. microcrystalline or nanocrystalline oxidation, B. Dialdehyde cellulose/PVA cross-linking via NMP/LiCl system. Figure modified from [302].

B2.1.3 Formation of cellulose/PVA hydrogels

The resulting paste was deposited in pre-made polydimethylsiloxane (PDMS) moulds forming cylindrical samples 16 mm in diameter and 3 mm thick following successive immersion in absolute ethanol (Fisher Bioreagents, Waltham, MA, USA) and ultra-pure water (Millipore, Burlington, MA, USA). DMCC/PVA ratio was also modulated to 1:1 and 1:2. Macroporosity is promoted by 1 g/mL NaCl (0–500 μm and 50–100 μm ; VWR Chemicals; Radnor,

PA, USA) addition before casting. Long-term storage of the resulted DMCC/PVA scaffolds was ensured in absolute ethanol at 4°C.

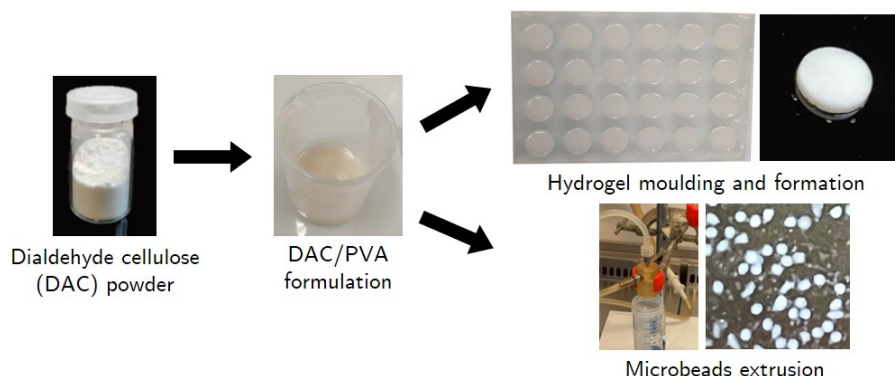


Figure B2.2: Production of cellulosic composites materials from porous macro cylindrical hydrogels to microbeads. This figure was modified from [302].

B2.1.4 Microbeads extrusion

9% DMCC/PVA (2:1) microbeads were formed with a homemade system based on a coaxial airflow extrusion method [303], [304]. As presented in B2.3A, the cellulosic solution was extruded through a 24 gauge needle using a 5 mL syringe mounted on a 100 series syringe pump (KdScientific, Holliston, MA, USA) under a extrusion flow rate of 1.7mL/min and a coaxial air flow rate of 3L/min. The droplets were projected into a gelation bath of absolute ethanol (Fisher Bioreagents, Waltham, MA, USA). Droplets produced were allowed to settle for 30 min in the gelation bath to ensure gel formation. After that, the microbeads were washed three times in deionised water. Long-term storage of the resulted DNCC/PVA beads was ensured in absolute ethanol at 4°C.

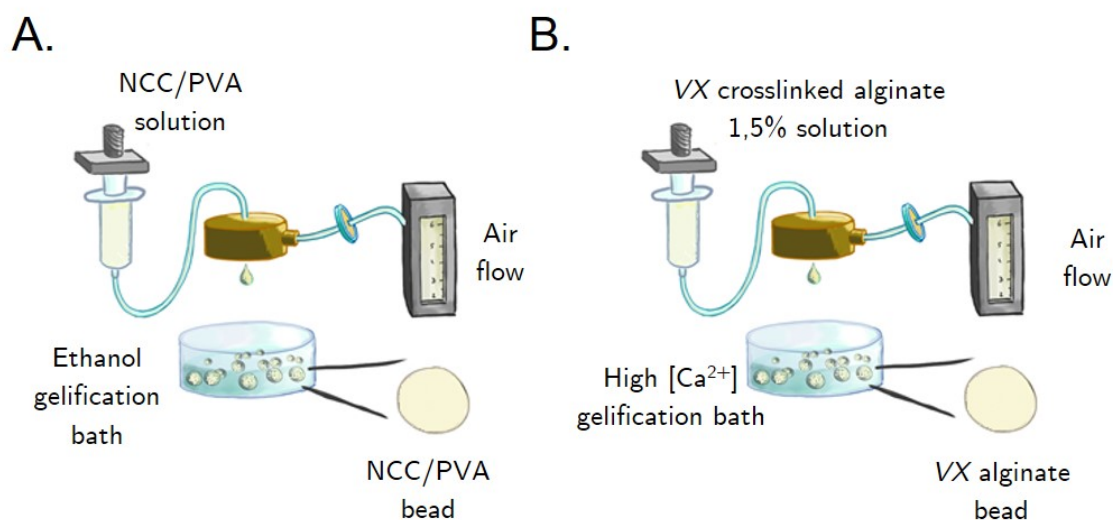


Figure B2.3: *V. carteri* bio-inspired microbeads extrusion. A. NCC/PVA microbeads extrusion principle, B. Volvox-like microbeads formation principle.

B2.2 *V. carteri* like-microbeads synthesis

B2.2.1 Covalent cross-linking of alginate and *V. carteri* proteins and polysaccharides

Sodium alginate (MANUCOL LKX, DuPont, Wilmington, DE, USA, Guluronic/Mannuronic ratio 30-70, viscosity Cps (1%) 60-170) was solubilised at 1.5%w/w in 0.5M MES buffer pH 6.5 and then additionally enriched with 0.06M 1-Ethyl-3-(3-dimethylaminopropyl)carbodiimide (EDC) hydrochloride and 0.12M N-Hydroxysuccinimide (NHS) for 3h reaction at RT. *V. carteri* raw extract was then added at 15%w/w to the alginate content and allowed to react at RT for 24 hours. The solution was then dialysed against water using a 12-14 kDa Molecular weight cutoff (MWDO) membrane. 4 water changes were performed in a total of 24h dialysis period. The solution was then lyophilised and stored at 4°C until use.

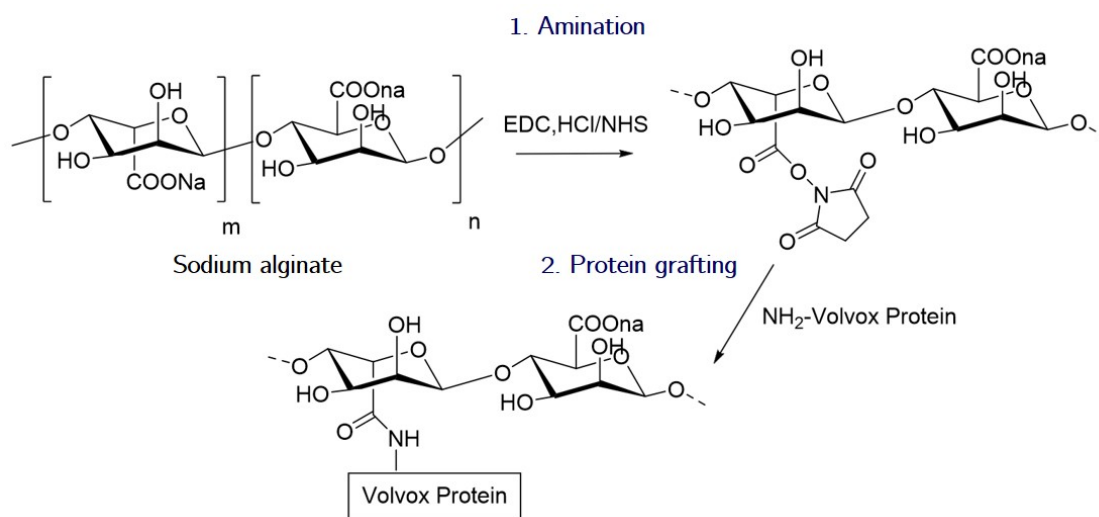


Figure B2.4: Sodium alginate-*V. carteri* protein grafting 1. Amination of alginate sodium using EDC/NHS, 2. *V. carteri* proteins grafting

B2.2.2 Microbeads synthesis

V. carteri cross-linked alginate 1.5%w/v were sterilised by successive filtrations on 0.8, 0.45 to 0.22 μm porous membranes. The microbeads were formed with a homemade system based on a coaxial airflow extrusion method [303], [304]. As presented in Fig. B2.3B, the alginate solution was extruded through a 24 gauge needle using a 5 mL syringe mounted on a 100 series syringe pump (KdScientific, Holliston, MA, USA) under an extrusion flow rate of 1.7mL/min and a coaxial air flow rate of 3L/min. The droplets were projected into a gelation bath (NaCl 154 mM, HEPES 10 mM and CaCl₂ 115 mM pH 7.4). Droplets produced were allowed to settle for 15 min in the gelation bath to ensure gel formation. After that, the microbeads were washed three times in cell culture medium and maintained at 4°C until use.

Chapter B3

Characterisations of *V. carteri*, *V. carteri* inspired and derivative materials

Unless specified otherwise all chemical reagents have been purchased from Sigma-Aldrich (St. Louis, MO, USA).

B3.1 Biomaterial physico-chemical characterisation

B3.1.1 Fourier-Transform Infrared Spectroscopy (FTIR)

FTIR spectra of various dried materials were recorded using an FT-IR 4000 (Jasco, Tsukuba, Japan) in a range of 400 to 4000 cm^{-1} operated at 4 cm^{-1} resolution using KBr method such as PVA, 9%, 18% and 36% (2:1) DMCC/PVA hydrogels, 9% (2:1) DNCC/PVA hydrogel, alginate powder and *V. carteri* cross-linked-alginate hydrogel.

B3.1.2 Quantification of the Dialdehyde Content (DC %)

For both DMCC and DNCC, the degree of oxidation was estimated following 2 distinct methods: 2,4-dinitrophenylhydrazine (DNPH) and hydroxylamine hydrochloride indirect dosing. For the DNPH method, 0.1 g of DAC to be tested were dissolved under stirring at RT for 4 h in 30 mL of 16.77 mM DNPH in acidified methanol solution. The reacted yellowed cellulose was filtered and washed with acetone before being dried and weighed. The filtrate was diluted in 400 mL of distilled water. Non-reacted DPNH solution absorbances were measured by UV spectroscopy at 350 nm. The dialdehyde content was thus determined using a calibration curve prepared with DNPH acidified methanol solutions varying from 2.0 to 17 mM. For the hydroxylamine method [305], 0.1 g of DAC to be tested were dissolved under stirring at RT for 3 h in 25 mL of 25 mM hydroxylamine hydrochloride ($\text{NH}_2\text{OH}\cdot\text{HCl}$) at initial pH of 3.4. Released hydrochloric acid acidifying the solution were then dosed back raising the pH to the initial one via a NaOH solution (0.1 M) under stirring and measurement with a pH meter. The dialdehyde content was thus determined as:

$$\text{DC}(\%) = \frac{V_{\text{NaOH}} \times C_{\text{NaOH}}}{m_{\text{sample}} \times m_w} \times \frac{1}{2} \times 100 \quad (\text{B3.1})$$

where M_w represents the molar weight of the dialdehyde cellulose unit ($160 \text{ g}\cdot\text{mol}^{-1}$).

B3.1.3 X-ray Diffraction Analysis (XDR)

XDR patterns were recorded on an X'pert MRD diffractometer (Pan Analytic/Philips, Eindhoven, the Netherlands; 40 Kv, 30 mA) using $\text{CuK}\alpha$ ($\lambda = 0.151418$ nm) radiation. Scans were performed over a 2θ range from 0 to 55, with a step size of 0.018° with a counting time per step of 5 s. The crystallinity index [306] of the cellulosic samples was calculated based on equation , where the crystalline I_{Cr} and the amorphous I_{Am} components are both defined as the peak intensity at 2θ of 22.7° and the minimum intensity around 2θ of 18° :

$$I = \frac{I_{Cr} \times I_{Am}}{I_{Cr}} \times 100 \quad (\text{B3.2})$$

B3.2 Microstructural analysis

B3.2.1 Environmental Scanning Electron Microscopy (ESEM)

Scanning electron microscopy (XL 30-ESEM FEG, Philips, Amsterdam, The Netherlands) was used to visualise the nano, microstructure and organisation of multiple samples such as dry DMCC powders, previously dehydrated DMCC/PVA hydrogels or freeze-dried raw extracts of *V. carteri*.

B3.2.2 *V. carteri* flagella observation using confocal microscopy

4% PFA or 70% ethanol preserved *V. carteri* were washed 3 times for 10 minutes in osmotic water, permeabilised in 5% Triton X100 for 10 minutes and then saturated for 15 minutes in 3% BSA solution. After a quick 10 minutes of rinsing in osmotic water, the colonies were incubated for 1h with a $1 \mu\text{g/mL}$ anti- β -tubulin mouse antibody solution (Abcam, Cambridge, UK). The algae were then rinsed once again and incubated with CYTM3 - conjugated goat anti-mouse IgG antibody at a 1:200 ratio (Jackson ImmunoResearch, Ely, UK) and DAPI at 1:1000. Once rinsed a final time, the colonies could be observed under fluorescence confocal microscopy (Zeiss LSM 710, Zeiss, Jena, Germany) with DAPI (Excitation: 405 nm, Emission: 410-495 nm) and CYTM3 (Excitation: , Emission:) filters.

B3.2.3 *V. carteri* cell wall observation using confocal microscopy

4% PFA preserved *V. carteri* colonies, thrice rehydrated in a 5-minute osmotic water dip were processed for all stainings. The incubations were performed at RT. All stainings were combined with a DAPI counterstaining executed at a concentration of $1 \mu\text{g/mL}$ and were observed employing confocal microscopy (Zeiss LSM 710, Zeiss, Jena, Germany) using emission and excitation spectrum displayed in Table B3.1.

B3.2.3.1 Chitin and cellulose staining using Calcofluor White staining

V. carteri colonies were stained for 15 min with a drop of Calcofluor White Stain and a drop of 10% potassium hydroxide. Once rinsed in large amounts of osmotic water, the cellulose or chitin content was directly imaged using confocal microscopy.

B3.2.3.2 Amyloid content staining using Congo Red

10 μ L of *V. carteri* suspension sample were immersed in 5 μ L of a 1%w/v Congo Red for 5 minutes and rinsed for an extra 15 minutes in 1N NaCl. Amyloid content of the colonies was finally observed via confocal microscopy.

B3.2.3.3 F-actin staining using Phalloidin

Preserved *V. carteri* were immersed in 300 μ L of 1X solution of Phalloidin-iFluor 488/DAPI (Abcam, Cambridge, UK) for 90 minutes. The coloured colonies were then rinsed thrice for 5 minutes in osmotic water and imaged using confocal microscopy.

B3.2.3.4 Mucous content staining via Periodic acid–Schiff (PAS) reaction

Preserved *V. carteri* were placed in a 0.5%w/v periodic acid solution for 5 minutes, in osmotic water for 5 minutes and then in Schiff's reagent (MERCK, Darmstadt, Germany) for 15 minutes. The colonies were rinsed thrice for one minute in tap water and counterstained with DAPI. Once stained, the colonies could be observed under bright-field or fluorescence confocal microscopy.

B3.2.3.5 Lipophilic content staining using Oil red O

Preserved *V. carteri* were immersed in an 18%w/v working solution of Oil Red O for 60 minutes. Once rinsed 3 times for 45 minutes in osmotic water, lipophilic content was revealed by confocal microscopy.

Table B3.1: *V. carteri* cell wall staining confocal microscopy excitation and emission spectrum range

Staining	Target	Excitation wavelength (nm)	Emission spectrum range (nm)
Calcofluor White	Chitin, Cellulose	505	463-580
Congo Red	Amyloid content	514	539-753
Phalloidin-iFluor 488	F-actin	488	495-630
Periodic acid–Schiff reaction	Mucus content	488	600-660
Oil Red O	Lipophilic content	543	576-750
DAPI	Nuclear DNA	405	410-495

B3.2.4 *V. carteri* polysaccharides and glycoproteins observation using lectin histochemistry

The sample preparation and observation procedures were identical for both lectin labellings. *V. carteri* colonies stored in 4% PFA were washed twice in PBS for 10 minutes, permeabilised in 5%V/V Triton X100 in PBS for 10 minutes, washed in PBS for 5 minutes and finally saturated 3%w/v Bovine serum albumin (BSA) in PBS for 15 minutes. The sample was then stained following the lectin-specific protocol as found below.

The colonies of *V. carteri* were finally imaged in imaging chamber coverslips (Ibidi, Gräfelting, Germany) with Alexa Fluor 488 (Excitation: 488 nm, Emission: 495-630 nm, Zeiss LSM 710, Zeiss, Jena, Germany) and DAPI (Excitation: 405 nm, Emission: 410-495 nm) acquisition parameters.

B3.2.4.1 Concanavalin A α -D-mannosyl and α -D-glucosyl staining

Alexa Fluor™ 488 Concanavalin A (Con A AF 488, Invitrogen™, Waltham, MA, USA) was stored at 9X (1 mg/mL) in 0.1M sodium bicarbonate pH 8.3 at -20°C. *V. carteri* colonies were then resuspended at 1X Con A AF 488 in 0.1M sodium phosphate action buffer 7.2, 0.15M NaCl, 0.1 mM Mn²⁺, 0.1 mM Ca²⁺) with DAPI at 1 μ g/mL at 37°C in the dark for 2 hours and then washed once for 10 minutes in PBS.

B3.2.4.2 Wheat Germ Agglutinin sialic acid and N-acetylglucosaminyl residues staining

Alexa Fluor™ 555 Wheat Germ Agglutinin (WGA AF 555, Invitrogen™, Waltham, MA, USA) was stored at 200X (1 mg/mL) in PBS at -20°C. *V. carteri* colonies were then resuspended at 1X WGA AF 555 in Hanks' Balanced Salt Solution (HBSS) with DAPI at 1 μ g/mL at 37°C in the dark for 2 hours and then washed once for 10 minutes in PBS.

B3.2.5 DMCC hydrogels physical characterisation

B3.2.5.1 Cellulose observation using Calcofluor White staining

To show the cellulosic content (meaning both nano and micro cellulose) of the samples were firstly rehydrated samples and stained for 15 min in a drop of Calcofluor White Stain and a drop of 10% potassium hydroxide. Cellulosic content of hydrogels was observed once rinsed with osmotic water at 433 nm using epifluorescence microscopy (Leica DMI6000 B, Leica Microsystems, Wetzlar, Germany).

B3.2.5.2 Pore Connectivity, Water Content and Swelling Ratio

DMCC/PVA composites hydrogels were weighted at several stages: hydrated m_h , dehydrated m_w gently wicked on absorbent paper to remove water entrapped into scaffold cavities and dried m_d under a laboratory hood for 24 h. The swelling ratio of the scaffold was recorded via mass measurement m_s upon rehydration into ultrapure water every 15 min for one hour and then regularly until no further mass fluctuations were observed. The degree of pore connectivity (PC), total water content (Q_w) and Swelling ratio (α) were calculated as:

$$PC(\%) = \frac{m_h - m_w}{m_h} \times 100 \quad (B3.3)$$

$$Q_w(\%) = \frac{m_h - m_d}{m_h} \times 100 \quad (B3.4)$$

$$\alpha = \frac{m_s}{m_d} \times 100 \quad (B3.5)$$

B3.3 Mechanical characterisation

B3.3.1 Uniaxial compressive test

Uniaxial compression tests were conducted on overnight (ON) rehydrated cylindrical DMCC/PVA hydrogels (16 mm diameter, 3 mm thick). The wet samples were compressed with a 22 N load cell at a rate of 0.6 mm/min to 35% strain using a Synergie 400 mechanical testing system (MTS system, Eden Prairie, MN, USA). The Young's modulus was obtained as the slope of the stress-strain curve between 10–20% deformation, avoiding any surface detection bias.

B3.3.2 Nanoindentation test

Nanoindentation assays were performed using a PIUMA CHIARO nanoindentation system (Optics11, Amsterdam, The Netherlands) on rehydrated DMCC/PVA hydrogels and Rehydrated Ethanol 70% preserved *V. carteri*. Before testing, calibration of the cantilever sensitivity was performed by indenting a hard surface (e.g., a Petri dish).

The load was measured following a 15,000 nm indentation at 3 nm/s. The properties of the colloidal probes for each sample are listed in Table B3.2. For rehydrated DMCC/PVA hydrogels, three separate samples were tested at five different locations. For rehydrated *V. carteri* preserved in 70% ethanol, 95 colonies were tested and their diameters determined simultaneously.

The Young's modulus, E , was determined between 1 and 3 μm of indentation using a python code developed in the laboratory (Anaconda3, Anaconda, Inc., Austin, TX, USA [307]) based on the Hertz sphere-sphere model [308], [309]. The Young's modulus was determined by the following equation:

$$F = \frac{4}{3}E \times \sqrt{R\delta^3}, \quad (\text{B3.6})$$

where F represents the load, δ the indentation and R the contact area radius with :

$$R = \left(\frac{1}{R_1} + \frac{1}{R_2} \right)^{-1}, \quad (\text{B3.7})$$

R_1 and R_2 being respectively the colloidal probe radius and spherical sample radius. In the specific configuration of a sphere and a plane, as applied to hydrogels, $R = R_1$, the colloidal probe radius.

Table B3.2: Nanoindentation probe properties

Sample	Colloidal probe diameter (μm)	Cantilever stiffness (N/m)
DMCC Hydrogels	28.5	0.47
<i>V. carteri</i>	24	0.48

B3.4 Cell culture on *V. carteri* microalgae, inspired and derivative materials

Unless stated otherwise all culture reagents were purchased from GibcoTM (Thermo Fisher Scientific, Waltham, MA, USA) and all primary cells and lineages (Fig. B3.1) were provided by ATCC (Manassas, VA, USA).

B3.4.1 Primary cells and lineage culture maintenance

The cells were maintained in the appropriate cell media and allowed to grow at 37 °C in a humidified 5% CO₂ atmosphere in a T-75 or T-175 cm² filter cap flask until 80% confluency was reached. The cells were then passaged using 0.05% trypsin and resuspended at the density required to run the experiment or to maintain the culture.

B3.4.1.1 Mouse fibroblast cell line L929 (L929)

The L929 cells are a fibroblast cell line derived from a clone of normal subcutaneous areolar and adipose tissue of a male C3H/An mouse (ATCC-CC1-1, Biosafety Level 1). The cells were maintained in Dulbecco's Modified Eagle Medium (DMEM, 1 g/L Glucose) completed with 10% decompemented fetal bovine serum (FBS), 2 mM of L-Glutamine (L-Glu), 100 units/ml of penicillin and 100 µg/ml of streptomycin.

B3.4.1.2 Mouse BALB/c monocyte macrophage J774.2 (J774.2)

The J774.2 cell line is a subclone derived from the reticulum cell sarcoma cell line, J774.1 Like mature macrophages (ECACC-85011428, Biosafety Level 1). The cells were maintained in DMEM completed with 10% decompemented FBS, 2 mM of L-Glu, 100 units/ml of penicillin and 100 µg/ml of streptomycin.

B3.4.1.3 Mouse embryo cell line C3H/10T1/2, Clone 8 (C3H10)

The C3H/10T1/2 cells are a fibroblast-like cell line isolated from a line of C3H mouse embryo cells (ATCC-CCL-226, Biosafety Level 1). The cells were maintained in DMEM completed with 10% decompemented FBS, 2 mM of L-Glu, 100 units/ml of penicillin and 100 µg/ml of streptomycin.

B3.4.1.4 Primary Neonatal Human Dermal Fibroblasts (HDFn)

HDFn are primary human dermal fibroblasts isolated from a neonatal foreskin and cryopreserved at the end of primary culture. Originally obtained from Invitrogen cell culture (Waltham, MA, USA, C-004-5C, Biosafety Level 2), HDFn were grown in DMEM containing 10% of decompemented characterised FBS (HyClone, Logan, UT, USA), 2 mM L-Glu, 100 units/ml penicillin and 100 µg/ml streptomycin, buffered using 0.01M HEPES.

B3.4.1.5 Human Adipose tissue-derived mesenchymal Stem Cells (ASC)

ASC52telo are hTERT immortalised human adipose-derived Mesenchymal stem cell lineage exhibiting a fibroblast-like morphology. ASC (ATCC SCRC-4000, Biosafety Level 2) was maintained in Mesenchymal Stem Cell Basal Medium for Adipose-derived MSCs enriched with MSC Supplement (ATCC, Manassas, VA, USA) plus 100 units/ml of penicillin and 100 $\mu\text{g}/\text{ml}$ of streptomycin.

B3.4.1.6 Human Umbilical Vein Endothelial Cells (HUVECs)

Primary Human Umbilical Vein Endothelial Cells (HUVEC) are isolated from a human umbilical vein and cryopreserved at the end of the primary culture. HUVECs (CRL-1730™, Biosafety Level 2) were cultivated in an M199 medium supplemented with 10% decomplexed FBS, 50 $\mu\text{g}/\text{mL}$ of heparin, 2 mM of L-Glu, 100 units/ml of penicillin and 100 $\mu\text{g}/\text{ml}$ of streptomycin.

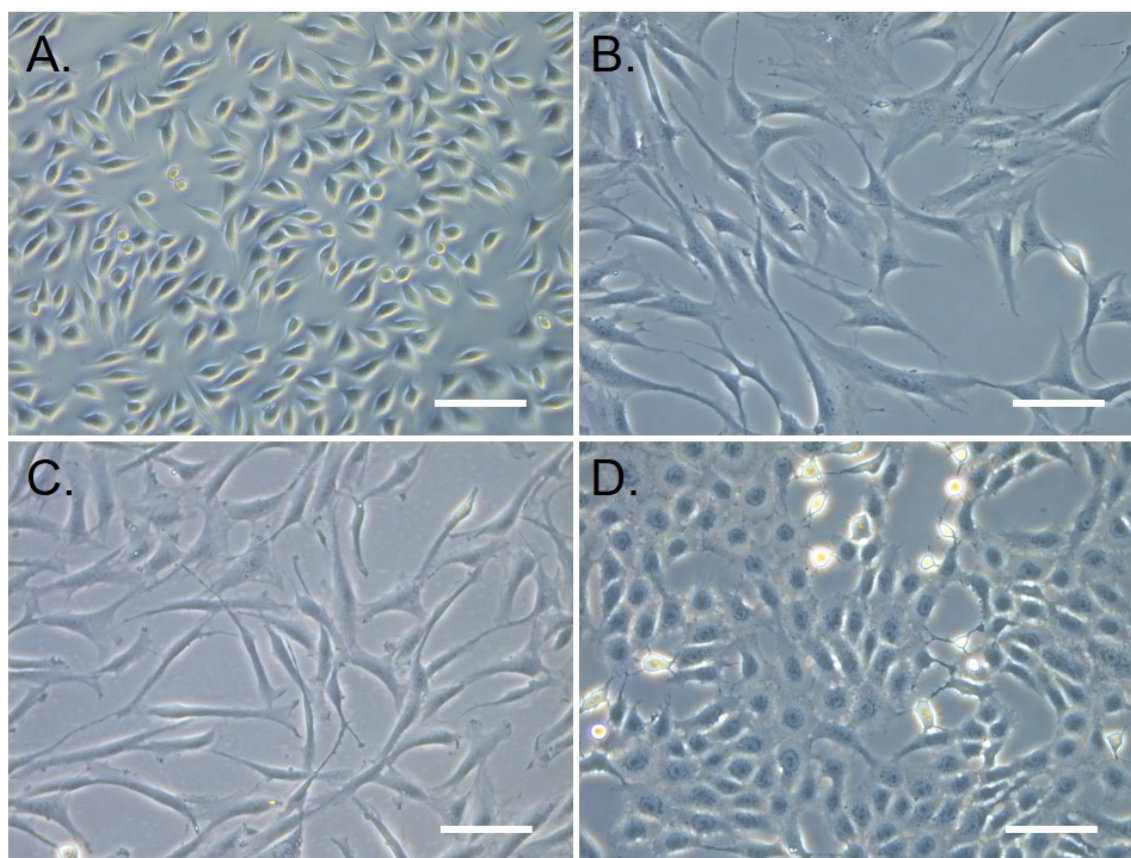


Figure B3.1: Primary cells and cell lineages culture observed under phase-contrast microscopy. A. Mouse fibroblast cell line L929, B. Primary Neonatal Human Dermal Fibroblasts (HDFn), C. Human Adipose tissue-derived mesenchymal Stem Cells (ASC), D. Human Umbilical Vein Endothelial Cells (HUVEC) (Scale bar: 100 μm).

B3.4.2 Pseudo-tissue construction using *V. carteri* as a living building block basic material

The culture method for *V. carteri* cell seeding and the generation of a pseudotissue following prolonged cell culture was standardised (Fig. B3.2), for all cell types: L929, HDFn, HUVEC, C3H10, and ASC.

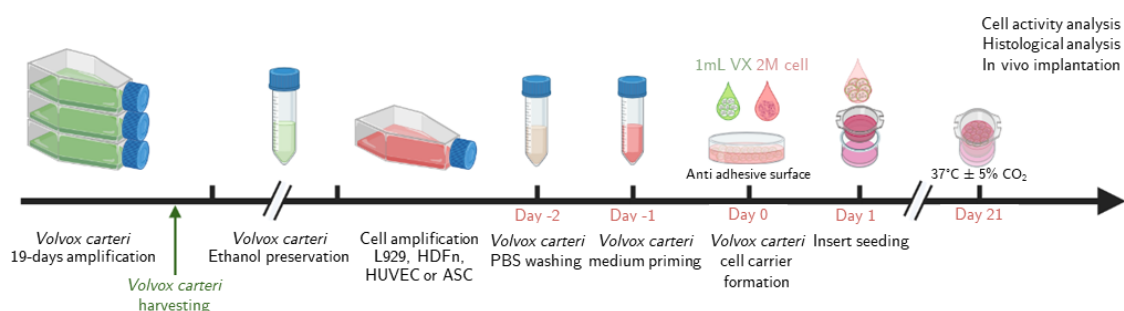


Figure B3.2: Experimental procedure to generate *V. carteri* living building blocks-based pseudotissue. Created with BioRender.com.

The ethanol 70% preserved *V. carteri* were washed twice in PBS, allowing them to sediment at 4°C in between washes. The algae were then primed ON with the relevant culture medium for the subsequent cell seeding.

V. carteri living building blocks were formed by seeding 1 mL of cellular suspension of density 2M cells/mL per mL of a saturated suspension of algae followed by a 45 min incubation in a 15 mL tube and then 4h on a non-adhesive surface: 3.5 cm diameter petri dish (Greiner Bio-One, Frickenhausen, Germany) or 6-well plate (Evergreen Scientifics, Vernon, CA, USA).

1 mL of *V. carteri* living building block homogenised suspension was transferred per 12-well culture insert. For the L929 lineage, culture inserts of 0.4 μm porosity were used (353180, FalconTM, Corning, NY, USA). Otherwise, a 3 μm porosity culture insert was used (353181, FalconTM, Corning, NY, USA). The 1 mL of basal culture medium was then changed daily for 2 days and then every 2-3 days for the remainder of the culture, usually until 21 days of culture. Depending on the analysis to be performed, the sample was either processed immediately or fixed with 4% PFA for 1h at 37°C.

B3.5 Biochemical and biological analysis

B3.5.1 Total protein content determination

The total protein content of the supernatant of a 50 000 *V. carteri* colonies/mL suspension, ultrasonically disrupted and briefly centrifuged at 3871 RCF, was determined using the Bicinchoninic Acid (BCA) Protein Assay following the manufacturer's instructions. 15 μL or 15 mg of the sample was mixed with 615 μL of BCA working solution consisting of 50 volumes

of Bicinchoninic Acid solution per volume of 4% Copper(II) sulfate solution. In parallel, BSA was used as the reference protein to establish the standard curve and positive control for the determination of the total protein content of the sample. The reaction proceeded for 30 minutes at 37°C. For quantification, the absorbance was read at 562 nm with a multimode microplate reader (Spark 10M, TECAN). For empiric demonstration of proteic content, the sample was observed macroscopically post-reaction. A purple turning material demonstrates protein component.

B3.5.2 *V. carteri* in vitro deformability

500 μ L of saturated algal suspension was placed in 12-well culture inserts (353181, FalconTM, Corning, NY, USA). The sample was maintained in the same way as cellularised samples in culture for 21 days with regular basal media changes.

The deformability of the algae was monitored by phase-contrast microscopy imaging on days 2, 7, 14 and 21. The circularity of each colony was determined using Image J [299] as follows:

$$Circularity = 4\pi \times \frac{Area}{Perimeter^2} \quad (B3.8)$$

A perfectly circular colony would provide a circularity index of 1.

B3.5.3 Cytotoxicity testing following the ISO 10993-5 standards [310]

This method was applied to evaluate the toxicity of the DMCC hydrogels, *V. carteri* colonies and extracts.

Extracts of sterile DMCC materials were formulated following the standards method. Briefly, latex, used as a positive control, was extracted at 6 cm²/mL and test cellulosic materials at 1.25 cm²/mL for 24h at 37°C on stirring in DMEM medium supplemented with 10% SVE, PenStrep (100 U/mL, 100 μ g/mL) and L-glutamine 2 mM.

To attest *V. carteri* colonies cytotoxicity, a pellet of about 1 mL of rinsed 70% ethanol fixed colonies was extracted for 24h in 1 mL of DMEM complete medium at 37°C under agitation.

V. carteri pellet were crushed on ice in 1mL of DMEM complete medium by ultrasound via 0.5 seconds cycles at 400W, 24kHz for 1 min using a UP400S ultrasonic device (Hielscher Ultrasonics, Teltow, Germany). Only the soluble fraction was subsequently used.

100 μ L of extracts were deposited on L929 mice fibroblast cell monolayers pre-cultured for 24h in 96-well plates and incubated for an additional 24h at 37°C in the presence of 5% CO₂. The medium was then substituted with 120 μ L of 3-(4,5-dimethylthiazol-2-yl)-5-(3-carboxymethoxyphenyl)-2-(4-sulfophenyl)-2H-tetrazolium (MTS) solution in a complete medium (1:5; Promega, Madison, WI, USA) for 2h at 37°C. The absorbance was read at 492

nm.

The viability percentage for each material was determined as the absorbance ratio to the untreated control. According to the standards, an extract inducing over 70% viability was considered non-toxic.

B3.5.4 *In vitro* inflammation investigation

To further investigate *V. carteri* alga cytocompatibility, J774 murine macrophage line inflammatory patterns were determined following a 24h-exposure to freshly harvested or ethanol-fixed *V. carteri* colonies as well as *V. carteri* extracts filtered at 0.8 μ m or not.

For this purpose, J774 macrophages were seeded at a density of 200 000 cells per well in a 12-well plate and incubated overnight. Then, 2X exposure solutions were added. For *V. carteri* samples and extracts, macrophages were exposed at a density of 15,000 cells/mL and equivalent. Negative and positive control conditions were generated through exposure to culture medium alone or concentrated at 20 μ g/mL of lipopolysaccharide toxin (LPS). Supernatants were recovered the following day and stored at -20°C. Concentrations of supernatants cytokines and chemokines (pg/mL) were quantified using the V-plex Proinflammatory panel 1, Cytokine panel 1, and Th17 Panel 1 kits from Meso Scale Diagnostics (MSD, MD, USA) according to the manufacturer's instructions, which included mKC, IFN- γ , IL-1 β , IL-2, IL-4, IL-5, IL-6, IL-10, IL-12p70, TNF- α , IL-9, IP10, IL-15, IL-17A/F, IL-27P28/IL-30, IL-33, MCP-1, MIP-1 α , MIP2, IL-23, IL-16, IL-17A, IL-17C, IL17E/IL-25, IL-21, IL-22, IL-31, MIP-3 α . In case of concentrations below or above the detection limits, these values were replaced by the threshold values respectively.

B3.5.5 Cell adhesion evaluation

The cell adhesion to several materials was investigated such as DMCC hydrogels (i.e., 9%, 18% and 36% dialdehyde-based), *V. carteri* colonies and extracts.

Cellulosic hydrogels were seeded with 250,000 HDFn cells by immersion in HDFn cell suspension. Cell adhesion was examined at 48h of culture on samples fixed for 15 min with 4% PFA, permeabilised for 5 min with 0.1% Triton X-100, saturated for 10 min with 1% BSA and stained for 30 min with phalloidin/DAPI (1/1000; 1/200) at room temperature in the dark. The nucleus and the actin cytoskeleton were respectively revealed by DAPI and Phalloidin (Ex/Em: 493/517 nm; Ex/Em: 340/488 nm) using confocal microscopy (Zeiss LSM 710, Oberkochen, Germany). To visualise long-term cell organisation within the matrix, seeded DAC/PVA scaffolds were maintained in culture for 3 weeks and then stained for DAPI/Phalloidin.

Cell adhesion on the surface of *V. carteri* colonies was observed for multiple cell types: L929, HDFn, HUVEC, and ASC. 24h seeded *V. carteri* living building blocks were produced as

presented in the section B3.4.2. Briefly, 2M cell/mL cell suspension was seeded per 1mL of *V. carteri* of saturated suspension, cultured for 45 minutes in 15 mL tubes and 3h on an antiadhesive surface. The culture on the antiadhesive surface was prolonged for 24h to evaluate the early adhesion of those cells on the *V. carteri* microalgae surfaces observing it using an contrast-phase light microscopy. The culture could also be rinsed in PBS, fixed at 3% glutaraldehyde in Rembaum buffer (pH 7.4) for 1h and be observed with environmental scanning electron microscopy.

To investigate the adhesive potential of *V. carteri* extracts, *V. carteri* extracts were produced by crushing a 50 000 *V. carteri* colonies/mL suspension in complete medium on ice by ultrasound via 0.5 seconds cycles at 400W, 24kHz for 1 min using a UP400S ultrasonic device (Hielscher Ultrasonics, Teltow, Germany). 1 mL of this extract per well was deposited in a non-adhesive 6-well plate for 1h (Evergreen Scientifics, Vernon, CA, USA). L929, HDFn or either HUVEC suspension were seeded at a density of 5 000 cell/cm² on a non-adhesive or *V. carteri* extract coated plate. Cell confluency was evaluated at 24h and 48h on contrast-phase light microscopic acquisitions using Image J [299] and the PHANTAST plugin [311] with σ and ϵ parameters established for each cell type as found in Table B3.3.

Table B3.3: PHANTAST plugin parameters for confluency estimation

Cell Type or lineage	σ	ϵ
L929	2	0.03
HDFn	5	0.03
HUVEC	5	0.02

B3.5.6 Cell viability estimation

The cell viability of HDFn seeded on DMCC-based hydrogels was obtained at 48h of culture by 30 min treatment with ViaQuantTM Far-Red Fixable Dead Cell Stain Kit (Genecopoeia, Rockville, MD, United States), followed by DAPI/Phalloidin staining procedure (B3.5.5). Living and dead cells could be visualised using epifluorescence microscopy (Leica DMI6000 B, Leica Microsystems, Wetzlar, Germany).

B3.5.7 Cell proliferation evaluation

Cellular proliferation within reconstructed pseudo-tissue using cellularised *V. carteri* living building block was estimated by monitoring the global mitochondrial activity of the human cells built-in at days 2, 7, 14 and 21. To do so, 24-well culture inserts (3 μ m porosity, 353104, FalconTM, Corning, NY, USA) seeded with living building block samples as described in the section B3.4.2 were firstly rinsed using PBS for 5 minutes and then incubated with 1.2 mL of MTS solution in a complete medium (1:5, Promega, Madison, WI, USA) for 2h at 37°C. The absorbance was read at 492 nm with a multimode microplate reader (Spark 10M, TECAN). In parallel, inverted phase-contrast microscopy observations were performed.

B3.5.8 Histological analysis

B3.5.8.1 Observation of HDFn self-organisation in Rhodamine pre-coupled *V. carteri* based pseudotissue

To discriminate human cells from the *V. carteri* colony carrier, the algal colonies were pre-coupled with rhodamine-NHS (Life technologies, Carlsbad, CA, USA). The 70% ethanol preserved colonies were pre-rinsed in 8.3 mg/mL sodium bicarbonate buffer pH 8.2 and filter sterilised. The *V. carteri* colonies were then placed in a 250 μ g/mL rhodamine-NHS sodium bicarbonate buffered solution for 3 hours at RT in the dark. The algae were then rinsed thoroughly with Milli-Q water. The rhodamine coupled algal suspension was then processed as usual for pseudotissue production using HDFn over a 21-day culture period as described previously in the section B3.4.2.

Once fixed for 1h in 4% PFA at 37°C, the sample was dehydrated, embedded in paraffin and cut using routine protocols. The sections were then deparaffinised in two xylenes 5-minute immersions and progressively rehydrated in consecutive 2-minute immersions in 100%, 95% and 70% ethanol followed by a 10-minute PBS soaking. Finally, a 1 μ g/mL DAPI solution was applied to the section for 30 min. Once rinsed, the sections were observed under an epifluorescence microscope (Leica DMI6000 B, Leica Microsystems, Wetzlar, Germany) to reveal DAPI-stained HDFn cells in the blue wavelength range and the *V. carteri* colonies in the red wavelength range.

B3.5.8.2 Hemalun Eosin Safran (HES) staining procedure

Once fixed for 1h in 4% PFA at 37°C, the samples were dehydrated, embedded in paraffin and cut using routine protocols. The sections were deparaffinised in two xylenes 5-minute immersions, progressively rehydrated in consecutive 2-minute immersions in 100%, 95% and 70% ethanol and fully rehydrated in PBS for 10-minutes. The samples were then stained in hematoxylin, blued in tap water for 5 minutes each and then quickly dipped for 2 minutes in eosin. Once rinsed for 6 minutes in osmotic water, the slices were dehydrated once again in 100% ethanol to proceed to a 2-minute safran staining. The sections were finally dipped twice in 100% ethanol for 1 minute and in xylene for 5 minutes. The slides were then mounted using Eukitt mounting medium. For Hemalun Eosin staining, the same procedure was applied except the dehydration step following eosin staining was continued to mounting.

B3.5.8.3 Adipogenic differentiation monitoring

Adipogenic differentiation was monitored on days 2, 7, 14 and 21 of culture on pseudotissues produced using either adipose-derived or C3H1 embryo stem cells-based living building blocks. A 3 mg/mL Oil Red O stock solution was prepared in isopropanol. 3 parts of the Oil Red O stock solution were diluted in 2 parts of osmotic water. The Oil Red O working solution was mixed, allowed to sit for 10 minutes at RT and then filtered through Whatman

paper number 42 (Whatman, Maidstone, UK) to remove crystallised staining.

All solutions were deposited in the basal compartment to avoid dispersion of the sample. Thermanox coverslips seeded at 5000 cell/cm² as a 2D control were also stained using the following procedure.

Once fixed for 1h in 4% PFA at 37°C, the sample was rinsed twice for 15 minutes in osmotic water and then incubated ON at RT with 1 mL of Oil Red O working solution. The residual dye has been rinsed out thoroughly. For bright-field Microscopy observation, the sample were counterstained following a 1-minute hematoxylin staining. For confocal microscopy observation, DAPI and Phalloidin counterstainings were performed to display both nuclear and cytoskeleton content. Once stained and rinsed, the sample was counterstained for 30 minutes in a 1 µg/mL DAPI solution at RT in the dark. The stain was then washed away via a 15-minute washing. The pseudotissues were then prepared for Phalloidin-iFluor 488 ON staining (1:1000, Abcam, Cambridge, UK) by successive 10-minute 0.1% triton X100 permeabilisation, 15-minute 3% BSA saturation and 15-minute rinsing using osmotic water.

Following final incubation and rinsing, the sample was isolated from the insert and the membrane cutting it using a scalpel. Once transferred on a standard microscope slide or an imaging chamber coverslip (Ibidi, Gräfelfing, Germany), the sample could then be observed using confocal microscopy (Leica DM1000 LED, Leica Microsystems, Wetzlar, Germany) using the following parameters: Oil Red O (Excitation: 543 nm, Emission: 576-750 nm), Phalloidin-iFluor (Excitation: 488 nm, Emission: 495-630 nm) and DAPI (Excitation: 405 nm, Emission: 410-495 nm).

B3.6 Implantation in an Athymic Mice Model

Pathogen-free 5-week-old male athymic mice (Rj: NMRI-Foxn1 nu/nu, JANVIER LABS, Le Genest-Saint-Isle, France; 30 g) were housed in polycarbonate cages, in a temperature and humidity-controlled room, and had food and water ad libitum. All the *in vivo* experiments were approved by the “Comité Régional d’Ethique en Matière d’Expérimentation Animale de Picardie” (CREMEAP; C2EA-96) and were done in compliance with European directive 2010-EU63.

Both ethanol sterilised DAC/PVA scaffolds and *V. carteri* HDFn cellularised suspensions were implanted subcutaneously on the backs of athymic mice. The animals were killed after one or two months and their skins at the implantation site were harvested, observed under a microscope and processed under classical histology procedures (Althisia, Troyes, France).

For DAC/PVA scaffolds, an anatomopathological study of the haematoxylin eosin-stained sections was performed by a veterinary pathologist and ranked as follows (SCIEMPATH BIO, Larcay, Belgium). Local inflammation scores at the implantation site were calculated

ranging from 0 (absent) to 4 (severe) following the ISO10993-6 considering the infiltration of cellular inflammation at the interface of the material, and the presence of fibrosis/fibrous capsule surrounding the injected filler, necrosis and tissue degeneration. A score of 0 designates that the absence of inflammatory reaction as the cellularity at the interface is similar to the non-injected adjacent dermis. Scores of 1 to 4 were respectively attributed when no inflammatory reaction, a low focal to a multifocal inflammatory reaction, moderate multifocal to diffuse inflammatory and severe inflammatory reaction showing extensive infiltrates, necrosis or fibrosis were observed at the implant interface.

B3.7 Statistical analyses

Data were depicted as mean \pm standard error to the mean (SEM) from at least three independent experiments, displayed as an individual dot. For large datasets ($N > 50$), a box plot was preferred, showing the median, 1st and 3rd quartiles. Statistical significance of differences was determined as indicated in figures using GraphPad Prism 5.03 (GraphPad Software Inc.). Unpaired t-tests or two-way ANOVAs with Bonferroni post hoc analysis were used to analyse differences between groups, as appropriate. Effects were designated significant at $p < 0.05$.

The normality of distribution was checked using the Shapiro-Francia Test, as appropriate for large datasets. The nearer W' to 1, the more normal the distribution tends to be.

To study the correlation between two continuous variables, the Pearson's correlation test was applied. The correlation coefficient, Pearson's r , ranges from -1 to 1 . A value of 0 implies that there is no linear dependence between the variables. A value of $+1$ indicates that Y increases linearly with X , and vice versa for -1 .

**Part C - *Volvox carteri*, a versatile and
innovative biomaterial for tissue
engineering and regenerative
medicine**

Chapter C1

The *V. carteri* micro-algae evidences great potential as a biomaterial for tissue engineering

The aim of this chapter was to investigate the potential of V. carteri as a biomaterial for tissue engineering, by anticipating its production, sterilisation and preparation for the purpose of in vitro cell culture, by examining adverse effects such as toxicity and inflammation induction, and by exploring the interaction of cells in contact with it in both native and extract forms.

C1.1 *V. carteri* material specificity

C1.1.1 Lab scale production of *V. carteri* microalgae

To provide a sufficient, continuous and regular supply of fresh microalgae for the duration of the thesis project, a 300 mL batch culture was maintained in a growth chamber. Punctual monitoring of the growth pattern of the culture was performed to control its constancy.

V. carteri batch growth curve (Fig. C1.1 A), firstly showed a latent phase from 0 to 7 days of culture characteristic of a metabolic adaptation phase inherent to batch culture. This metabolic adaptation induced by the passage from a nutrient impoverished to rich media was associated with an overall slowing down of the development of the algae, particularly of stages 3 to 4 and stages 4 to 1 colonies corresponding respectively to the expansion of their matrix and the hatching of the mother colonies. Indeed, an accumulation of colonies of developmental stages 3 and 4 was observed on day 3 of culture in Fig. C1.1 B. The growth phase was initiated at 7 days. During this entire phase, average distribution of stage 1 to 4 *V. carteri* colonies of respectively 75.1, 20.2, 3.4, and 1.2% was observed. This asymmetrical distribution demonstrated that these developmental phases occur within uneven timescales, with the division and cell differentiation phases of the gonidia being more time-consuming than the maturation and hatching phases of the daughter colonies. Between 14 and 19 days, the *V. carteri* culture expanded exponentially with an average doubling time of 2.3 days i. e. 55 hours. For optimal maintenance of the *V. carteri* batch culture, the reseedling and harvesting of *V. carteri* microalgae were carried out between D19 and D21. An average density of 2520 ± 604.8 VX/mL, i.e., production of 2.52 ± 0.61 M *V. carteri* colonies/L of medium

was obtained. A short stationary phase of 2 days was observed followed by a decline phase starting around 24 days of culture. During this period, the decreasing density of the suspension was combined with a significant decrease in chlorophyll A and B production and the disappearance of developmental stages 3 and 4.

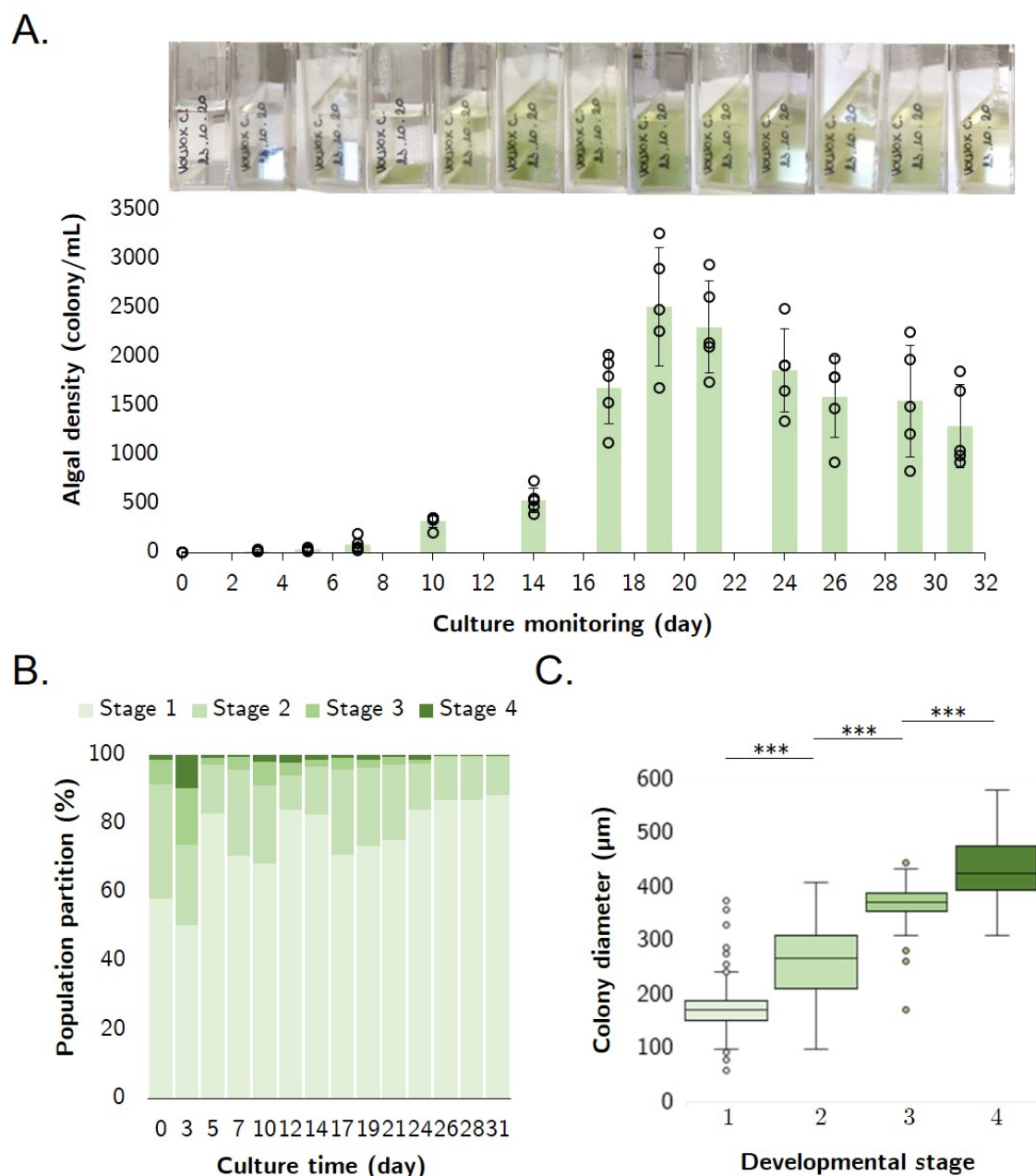


Figure C1.1: Characterisation and optimisation of the *V. carteri* culture. A. *V. carteri* growth curve in 300 mL batch culture (N=5), B. Partition of *V. carteri* developmental stage along the culture period (N=5), C. Distribution of *V. carteri* diameters within each developmental stage (N \geq 100 for each stage; two-way ANOVA with Bonferroni test post-hoc analysis (***: $p \leq 0.001$)).

Although a diameter increase is visible (Fig. C1.1C) as *V. carteri* colony matures, the colony developmental stage cannot be strictly discriminated by this criterion. Diameters varying respectively from 150 to 200, 200 to 300, 350 to 400 and 400 to 450 μm were recorded for

stages 1 to 4 colonies. Algal harvesting using a 100 μm sieve thus allowed the elimination of all membrane and cellular debris.

C1.1.2 *V. carteri* preculture modification

C1.1.2.1 Algal structural preservation

Such algae incorporation into mammal cell cultures as a material requires their fixation. Once cultivated and harvested, *V. carteri* colonies should be preserved to stop their proliferation, cellular and metabolic activities as quickly as possible, guaranteeing their structure and limiting the algal stress response.

4% PFA fixation seemed to maintain in whole the microalgae integrity, structure and composition. However, 4% PFA preserved *V. carteri* use was limited to the algae structural study as cytotoxic releases were observed despite successive washings of the fixed samples. On the other hand, the 70% ethanol fixation was thus preferred for subsequent cell culture applications for its rapidity, its overall preservation of the algal geometry and its ease of removal by multiple rinses. The discolouration observed in Fig. C1.2 caused by the 70% ethanol fixation showed that this solvent generated membrane permeabilization that inevitably led to the elimination of soluble compounds, of which chlorophyll was the most visible.

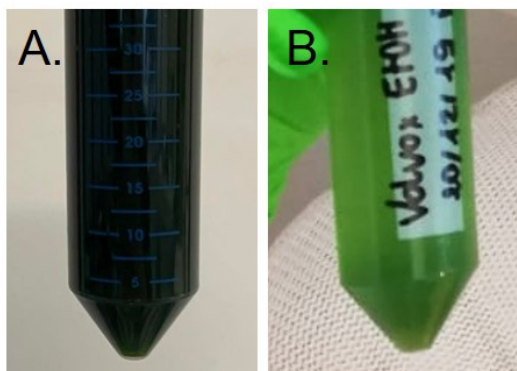


Figure C1.2: Harvesting and preservation of *V. carteri* microalgae. A. Photograph of a freshly harvested *V. carteri* suspension, B. Photograph of a 70% ethanol preserved *V. carteri* suspension.

C1.1.2.2 Algal surface modification

As 70% ethanol preservation impacted *V. carteri* membrane permeability, we wondered how it could also affect the colony surface, especially its flagellation pattern. While 4% PFA preservation maintained the integrity of the algae including its flagellum structure designated by black arrows in Fig. C1.3 A on both surface and cross-section observation, the pH shock deflagellation standard method [300], [301] (Fig. C1.3 C) a total deflagellation of the *V. carteri* colonies comprising any daughter colonies. Detached flagella were specified by red arrows. We observed in Fig. C1.3 B that 70% ethanol fixation generated a partial deflagellation of *V. carteri*. Some flagella were reduced in size, some were detached leaving two light reflecting anchor points and others remained on the colony surface.

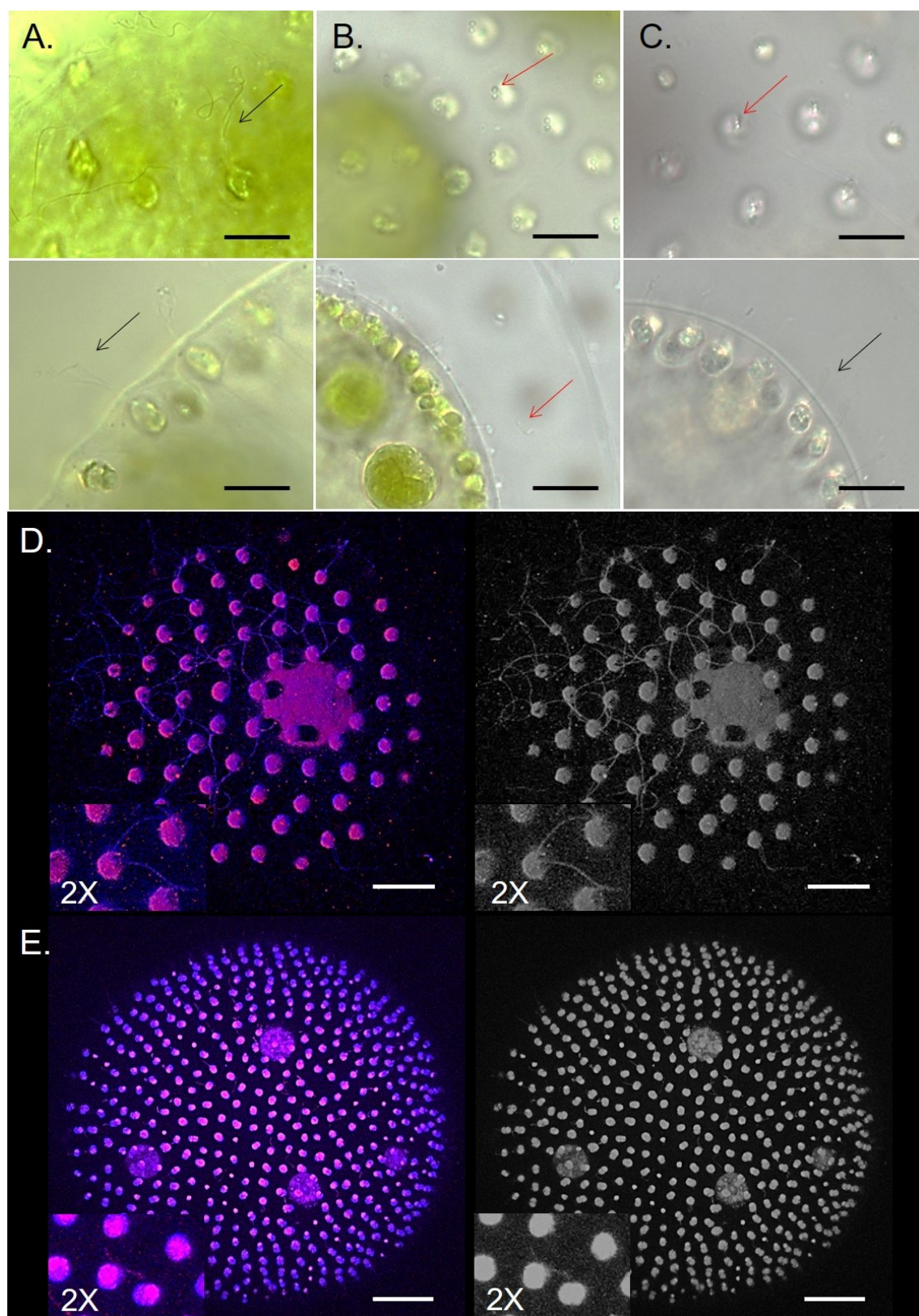


Figure C1.3: *V. carteri* state of deflagellation. Bright-field microscopy observation of A. 4% PFA-preserved *V. carteri* colonies showing the presence of visible flagella (black arrows), B. 70% ethanol-preserved *V. carteri* colonies demonstrating partial external deflagellation (red arrows), C. pH shock-deflagellated *V. carteri* demonstrating total external and partial internal flagella loss (scale bar: 10 μm), D. 4% PFA preserved *V. carteri* flagella, and E. 70% ethanol preserved *V. carteri* flagella immunolabeling for β -tubulin and DAPI counterlabelled provided with grayscale image (scale bar: 25 μm).

We attempted to quantify the deflagellation of *V. carteri* somatic cells by immunofluorescence labelling targeting the β -tubulin key flagellum component. A DAPI counterlabelling was performed to ensure the algal overall structure could be visualised. Biflagellated somatic cells could be identified on both 4% PFA and 70% ethanol preserved microalgae with confocal microscopy (Fig. C1.3 D-E). However, flagella remained difficult to observe consistently on a sufficient number of algae and a minimal surface of a single alga due to their dimension, curvature and spatial orientation. A flagellum dimension represents about ten micrometres in length and a few tens of nanometers in thickness [59]. While a deflagellation could be noticed, this prevented us from producing a reliable quantification.

C1.2 *V. carteri* suitability for *in vitro* 3D cell culture

To plan *V. carteri* use as a culture substrate, cellular reactivity was investigated by studying cellular activity and dynamics upon contact with the alga. A structural study was carried out by various staining and imaging to better understand the cellular behaviours observed and validated by the adhesiveness study of the formulated *V. carteri* extract.

C1.2.1 *V. carteri* L929 cytocompatibility study

V. carteri cytocompatibility was estimated on *V. carteri* primed or sonicated medium conditions under the ISO 10993-5 standard by determining L929 murine fibroblasts' cellular activity following a 24h-exposition. Cellular viability (Fig. C1.4) was expressed assuming the control medium condition to have the maximum cellular activity, i.e., 100% cellular viability. The test validity was reviewed by exposure to a known cytotoxic reagent.

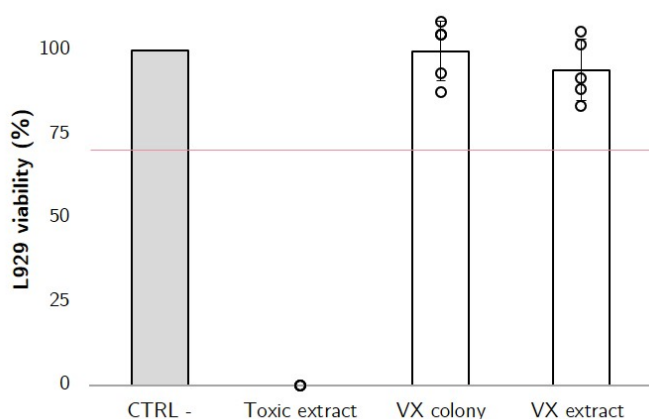


Figure C1.4: *V. carteri* cytotoxicity evaluation adapted from the ISO 10993 standards. Determination of L929 viability in contact with *V. carteri* primed medium and *V. carteri* extract normalised to the complete medium negative control (N=5).

For the medium primed with *V. carteri*, i.e., mimicking the contact with the surface of the alga, L929 viability of $99.8 \pm 8.8\%$ was obtained. For the sonicated condition, i.e., simulating total exposition to *V. carteri* compounds, both external and internal, L929 cell viability of

94.2 ± 9.3% was found. All *V. carteri* test conditions demonstrated an L929 viability above the 70% limit. According to ISO 10993 criteria, the *V. carteri* suspensions and extracts are considered therefore non-cytotoxic.

C1.2.2 *V. carteri* inflammation potential

To further investigate *V. carteri* biocompatibility, the murine J774.2 macrophages cytokine secretome heatmap (Fig. C1.5) was generated upon a 24h-exposure with various *V. carteri* samples in regards to untreated (CTRL-) and pro-inflammatory LPS-treated (CTRL+) controls. The supernatant cytokines quantification was performed by Meso Scale Discovery technique and expressed as Log 2-fold change of the untreated control. To identify the main axes of variance and different patterns within this multidimensional data set, the data was processed (Fig. C1.6), under principal component analysis following an autoscaling normalisation with the use of Metaboanalysis software [312].

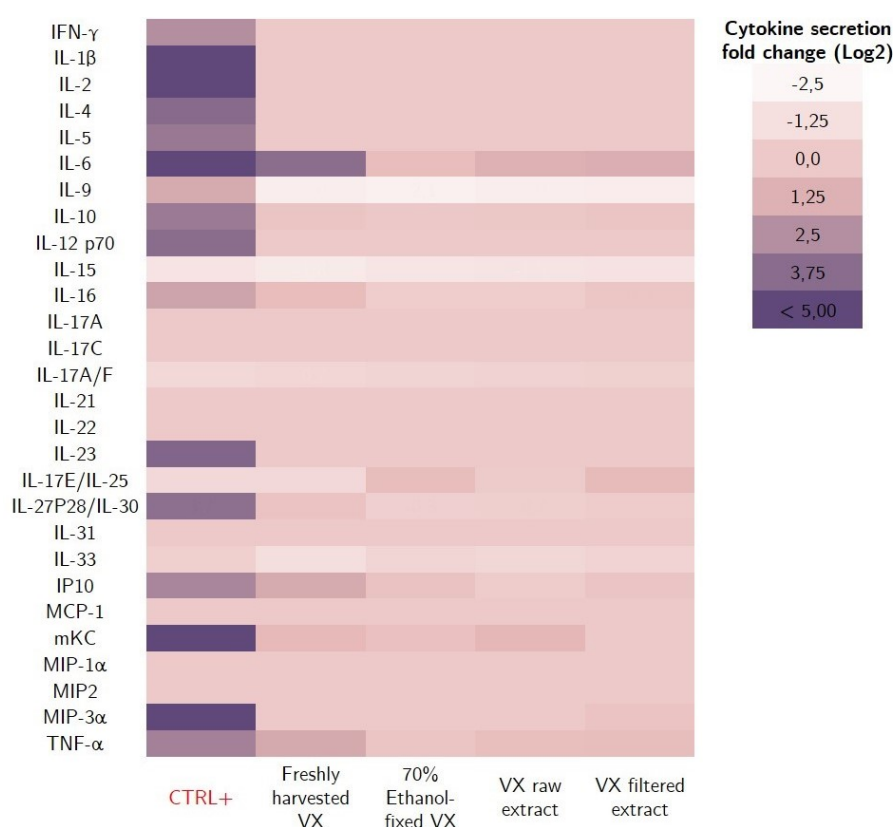


Figure C1.5: J774.2 murine macrophages secretome upon exposition to *V. carteri* (VX). The supernatant cytokines and chemokines concentration upon J774.2 macrophages 24h-exposition were measured by Meso Scale Discovery and expressed as Log 2-fold change of non-treated control (N=3). When below or above the detection range, the concentrations were replaced by the threshold values. A 2 µg/mL LPS solution was used as a positive control (CTRL+).

The secretome heatmap highlights an acute inflammation induced by 2 µg/mL LPS exposure through the significant secretion of numerous pro-inflammatory cytokines including interferon γ, TNF-α and a large set of interleukins, IL-1β, IL-2, IL-4, IL-5, IL-6, IL-10, IL-12, IL-23 and IL-30 as well as chemokines such as Interferon γ-induced protein 10 (IP-10),

mice keratinocytes-derived chemokine (mKC) and Macrophage Inflammatory Protein-3 α (MIP-3 α). This pro-inflammatory response was also evidenced through the application of principal component analysis (PCA), as the LPS treated condition (*red*) represents a cluster isolated from the untreated condition in Fig. C1.6 A.

V. carteri samples did not show pro-inflammatory cytokines and chemokines secretion to the extent induced by LPS as shown by the heatmap profiles and the aggregation of *V. carteri* samples around the negative control on the PCA. Only unfixed, freshly harvested *V. carteri* suspension induced moderate IL-6 and TNF- α secretions.

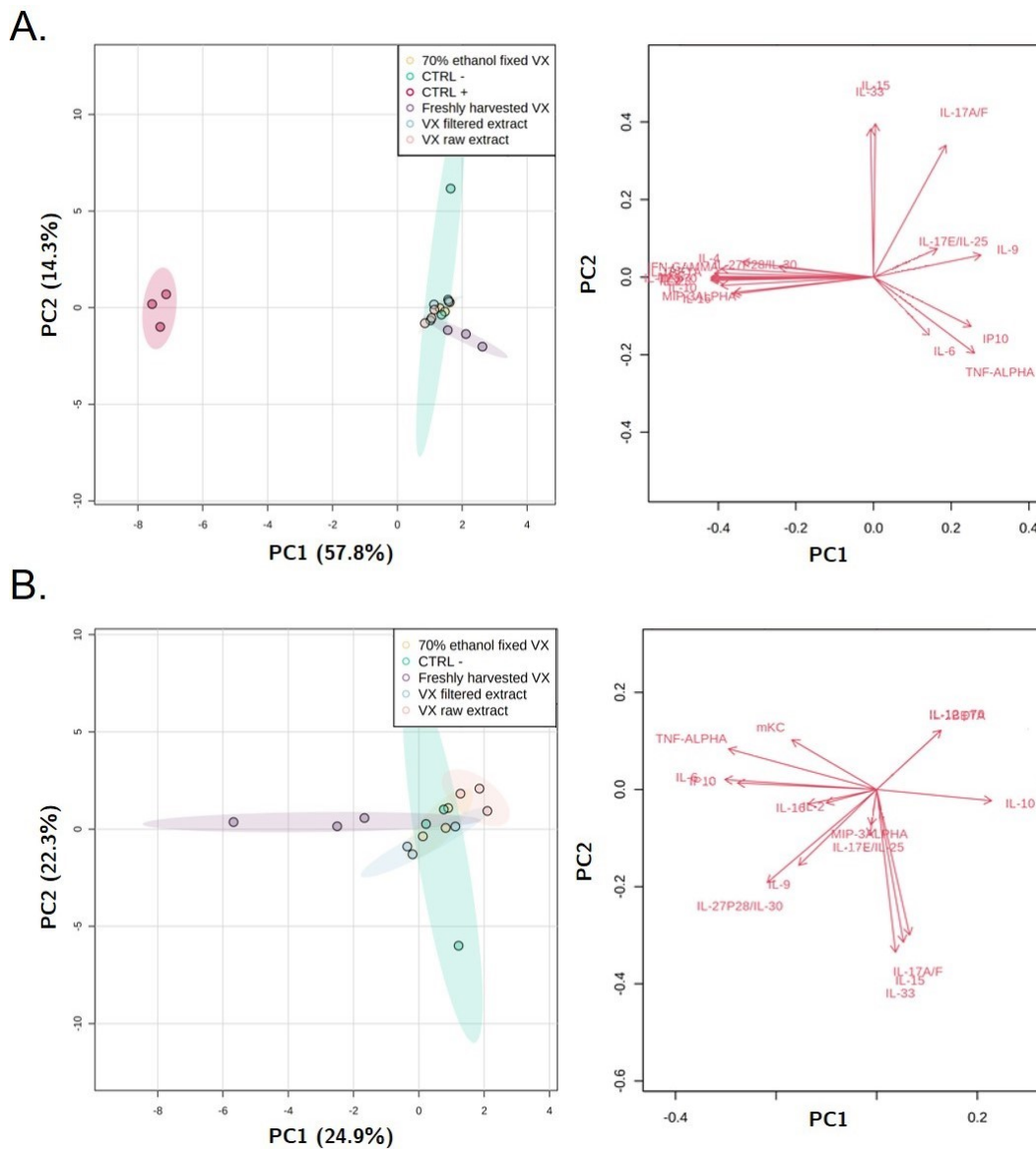


Figure C1.6: Principal component analysis (PCA) of J774.2 macrophages secretome upon 24h-exposition to *V. carteri*. A. PCA analysis of *V. carteri*-induced macrophage secretome in regards to both untreated (CTRL-) and treated (CTRL+) controls. B. PCA analysis of *V. carteri*-induced macrophage secretome in regards to the untreated (CTRL-) control. The supernatant cytokines and chemokines concentrations were determined by Meso Scale Discovery (N=3), processed for normalisation and PCA analysis with Metaboanalysis software [312].

To more precisely identify variations between *V. carteri* conditions, a principal component analysis was performed without LPS-induced acute inflammation condition. In the PCA (Fig. C1.6 B), a deviation of the unfixed and freshly harvested *V. carteri* group (purple) from the control reference group (green) was observed related to the moderate secretion of pro-inflammatory cytokines and chemokines, TNF- α , IL-6, IP-10 and mKC. Once these algae were fixed with 70% ethanol (yellow), a complete re-centring around the control group was denoted. A slight variation was also observed for the raw extract condition (pink) corresponding to the slight secretion of IL-6, IL-10, IL-12, mKC and TNF- α . By filtration of this raw extract at 0.8 μm (orange), a re-centration around the control group was also observed.

C1.2.3 Formation of *Volvox carteri* cellularised building blocks

When seeded together with a *V. carteri* saturated suspension on an anti-adhesive surface, the various cell types developed differing behaviours at its surface. Firstly, L929 murine fibroblasts demonstrated significant cell adhesion capabilities to the algal surface by phase contrast (Fig. C1.7 A) and scanning electron microscopy (Fig. C1.7 B) observations. Although some could remain isolated, the majority of cells attached to the surface developed by the algal suspension (white arrows). In contrast, human dermal fibroblasts (HDFn) in Fig. C1.7 C tended to organize into spheroids (black arrows) before adhering to the algal surface without covering it. Finally, human umbilical vein endothelial cells (HUVEC) showed an intermediate behaviour in that cells remained individualised forming small chains and some cells adhered to the algal surface without completely encircling it (red arrows, Fig. C1.7 D).

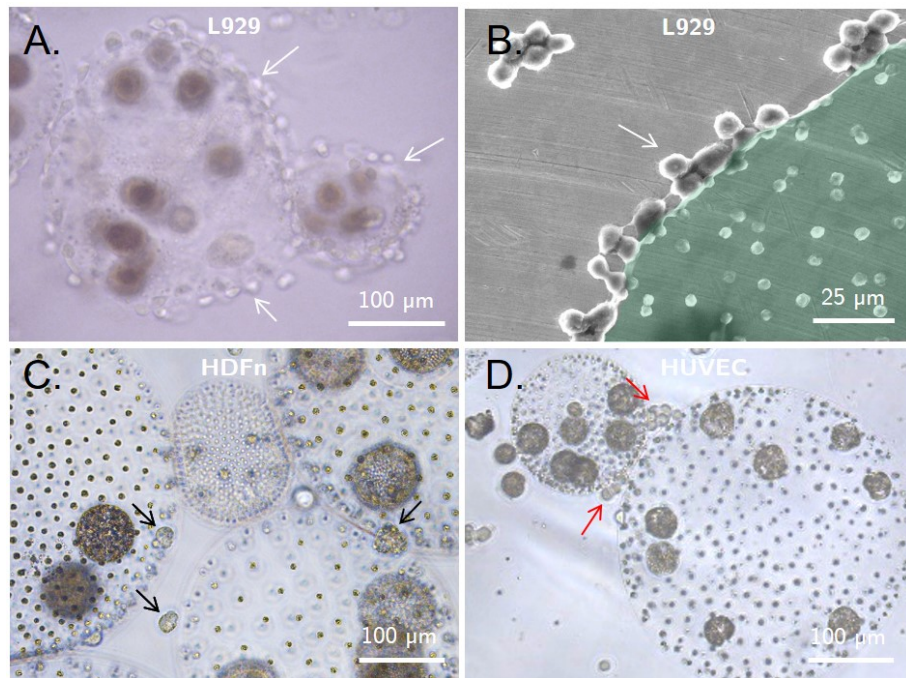


Figure C1.7: Cellular adhesion to the surface of *V. carteri* colonies. A. Contrast phase and B. ESEM observation of L929 adhered on the surface of *V. carteri* (white arrows), Contrast phase observation of C. HDFn spheroid like structures (black arrows) and D. HUVEC cell chains (red arrows) adhered to the surface of *V. carteri* microalgae.

C1.3 Investigation of *V. carteri* cell adhesion properties

C1.3.1 *V. carteri* extract adhesiveness study

To evidence cell adhesion properties developed by the *V. carteri* alga, a raw extract of a 15 000 colonies/mL algal suspension was produced by quick sonication. The solution was then filtered to remove any remaining membrane residue. An anti-adhesive plate was then coated using the extract. An anti-adhesive plate and an adhesive treated for culture were used respectively as negative (CTRL-) and positive (CTRL+) controls. The confluence status of the L929, HDFn and HUVEC cell types were determined following a 48h incubation and expressed as a proportion of the CTRL+ condition in Fig. C1.8.

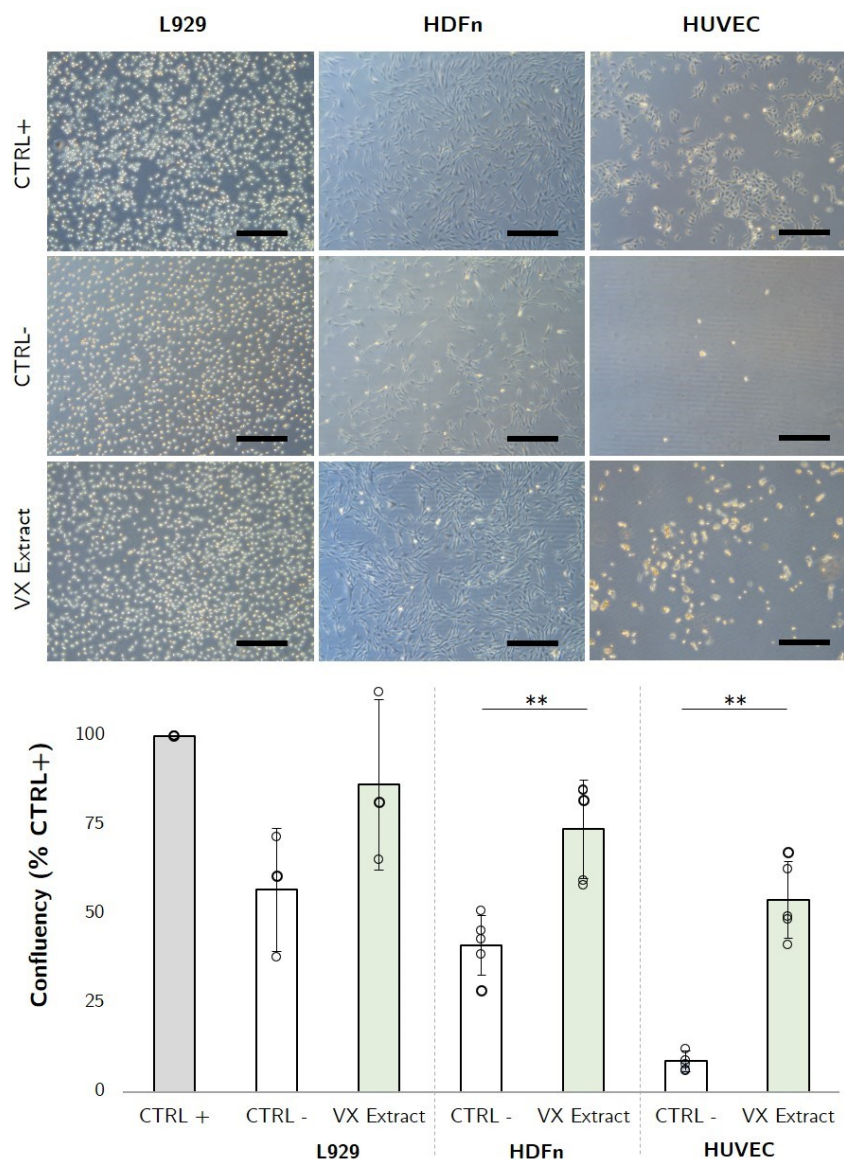


Figure C1.8: *V. carteri* (VX) extract adhesiveness. Contrast-phase observation of L929, HDFn, HUVEC cells upon 48h-seeding on culture treated, anti-adhesive or *V. carteri* extract coated surfaces (scale bar: 250 μ m). Cellular confluency was estimated using PHANTAST plug-in and Image J software [299], [311] ($n \geq 3$, Mann-Whitney U test (**: $p \leq 0.01$)).

We observed for each cell type a confluency dropping for the CTRL- condition while the raw extract pre-treated condition exhibited increased confluency. More specifically, for the murine L929 fibroblast lineage, the confluency decreased to $56.8 \pm 17.2\%$ in the CTRL- and recovered to $86.3 \pm 23.9\%$ with the *V. carteri* extract coating. This effect was reproduced with significance for human dermal fibroblasts, increasing from $41.3 \pm 8.4\%$ to $73.8 \pm 13.8\%$ of maximal confluency, and human HUVEC endothelial cells, increasing from $8.7 \pm 3.0\%$ to $53.9 \pm 10.7\%$ of maximal confluency. *V. carteri* raw extract components, most likely glycoproteins and glycans demonstrated cell adhesion promotion properties on both human mesenchymal and endothelial cell types.

C1.3.2 Apprehension of *V. carteri* segmentation from cytoskeleton, cell wall to mucosal contents.

Animal cells, microorganisms, and plants share common structural and functional compounds conserved throughout evolution. To investigate *V. carteri* colonies' structure and composition, we focused on such common cytoskeleton, cell wall, mucosal bodies. Significant structural distinctions only appeared at the transition from stage 2 to 3. Colonies of stages 1 and 3 exhibited similar features, respectively, to stage 2 and 4. Therefore, the following labellings compare stage 2 and 4 colonies with the aim to provide a representative morphology of the algae.

Firstly, *V. carteri* actin cytoskeleton was exhibited by phalloidin conjugation in Fig. C1.9.

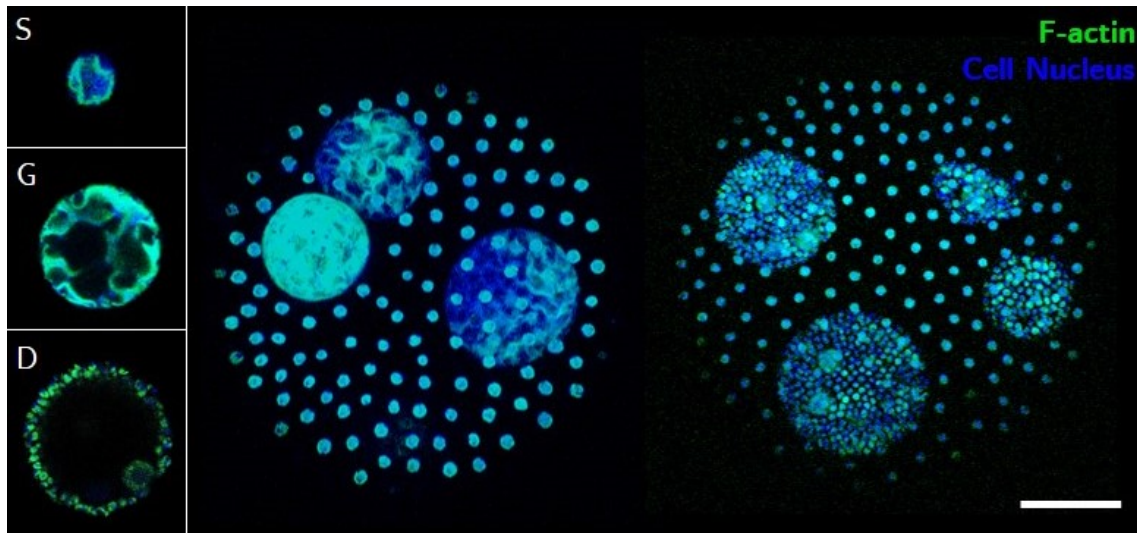


Figure C1.9: *V. carteri* actin content. From left to right, confocal microcopy observation of a stage 2 and stage 4 colonies of *V. carteri* whose F-actin was revealed by phalloidin staining and DNA content by DAPI (S: somatic cell, G: gonidia, D: daughter colony, scale bar: 50 μm).

It showed a limitation of the cytoskeletal content to somatic and gonidial cells attesting membrane significance in the assembly, compartmentalisation and support of the colony. This locality demonstrated the individuality of each somatic cells and the daughter colonies within them. While in stage 2, the cohesion of the gonidia seemed to be supported by a

dense F-actin network. Once the differentiation of the gonidia cells and the phenomenon of membrane inversion were finalised, this cytoskeleton must be disintegrated and reorganised to be solely limited to the somatic cells.

A specific feature of the *Volvocaceae* algae family relies in a complex extracellular matrix expansion. With the aim to localise this extracellular matrix, different stainings of the mucosal and lipophilic contents as well as glycoproteins labelling were undertaken.

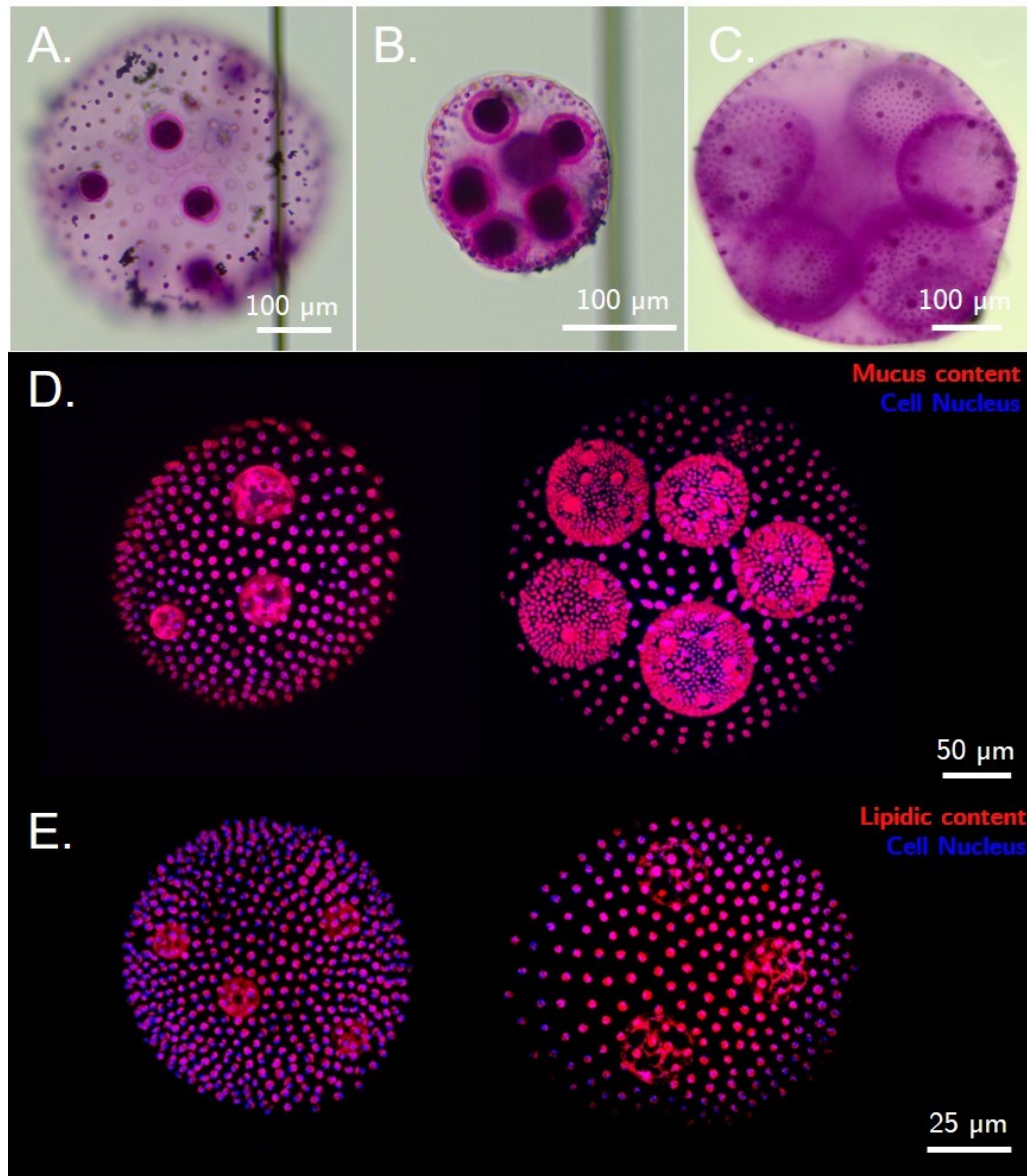


Figure C1.10: *V. carteri* mucus labelling. A-C. Bright-field microscopy observation of Periodic acid-Schiff stained *V. carteri* colonies stage 1, 2 and 4, D. From left to right, confocal microscopy observation of a stage 2 and 4 colonies of *V. carteri* whose mucus content was revealed by Periodic acid-Schiff staining and DNA content by DAPI, E. From left to right, confocal microscopy observation of a stage 2 and 4 colonies of *V. carteri* whose lipophilic content was revealed by Oil Red O and DNA content by DAPI.

Mucus consists of viscoelastic biological gels composed of water, sugars, proteins and lipids

[313]. *V. carteri* mucus-like content was detected by PAS staining (Fig. C1.10), as respectively violet and red stains under bright-field and confocal fluorescent microscopies. Such content clustered within cellular bodies, surrounding somatic cells and gonidia in Fig. C1.10 A-B. In addition, a secretion of mucosal content evidenced by bright violet staining enveloping the gonidia of stage 1 and 2 *V. carteri* colonies. This content was relocated and diffused (Fig. C1.10 C), within the whole colony upon membrane inversion occurring to reach stage 3 maturation. This diffusion was also visible on confocal microscopy observations (Fig. C1.10 D), in which the mucosal shell coating the gonidia disappeared and was limited to the somatic cells in stage 4 colonies.

The lipid content was stained using Oil red O lipophilic dye (Fig. C1.10 E). A somatic and gonidial distribution was observed as well for stage 2 colonies. A lipophilic matter remained present following membrane inversion, surrounding the somatic cells sheet of the stage 4 daughter colonies.

To examine the glycoproteins and glycans comprised in this mucosal content and more widely in *V. carteri* microalgae, glycosylations and sialylations were targeted by lectin histochemistry.

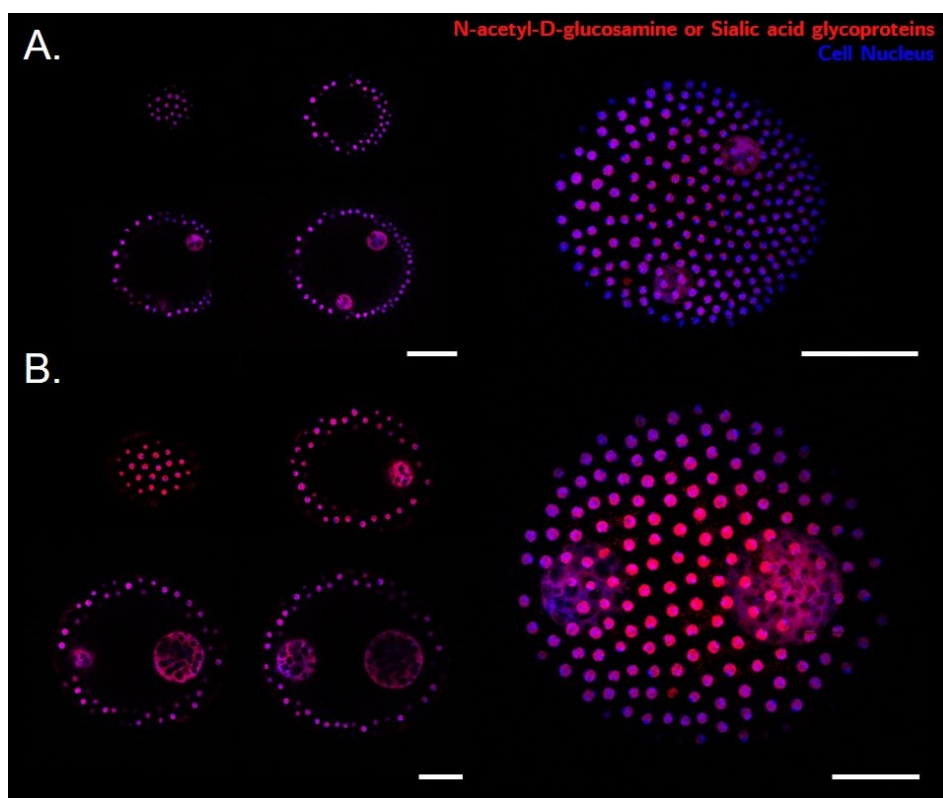


Figure C1.11: *V. carteri* N-acetyl-D-glucosamine (GlcNAc) or Sialic acid glycoproteins labelling. Representative Z-stack images and reconstructed 3D image of A. stage 2 and B. stage 4 colonies whose GlcNAc or Sialic acid glycoproteins residues were revealed by Wheat Germ Agglutinin and DNA content by DAPI labelling using confocal microscopy (Scale bar: 50 μm).

Wheat Germ Agglutinin (WGA) pairs with both N-acetyl-D-glucosamine (GlcNAc) and sialic-acid-containing glycoconjugates and oligosaccharides. This WGA labelling presented in Fig. C1.11 displayed a specific localization of such compounds within the cell bodies, somatic cells and gonidia. As for lipophilic substance staining, a polymeric mesh was visualised in the cell sheet of stage 4 colonies' daughter colonies.

Concanavalin A binds both α -D-mannose and glucose residues. Con A staining of stage 2 and 4 colonies highlighted in Fig. C1.12 and C1.13 the ubiquity of these glycans and glycosylated proteins in *V. carteri* microalgae within its cellular bodies, extracellular matrix and cytoplasmic membranes. Lectin staining allowed us to apprehend the entire complexity and compartmentation of the algae at all development stages. Thus, the structures highly based on membrane dynamics described in the literature and listed in Chapter A1 could be visualised all at once at early and late development stage.

The *V. carteri* mother colony has an external unicellular sheet and a mucous core in which cavities house gonidia, a heterogeneous bundle of self-organised DNA, proteins, glycans and lipids. The gonidia single-celled in stage 1 become multicelled at stage 2. Once the membrane inversion of the gonidia/daughter colonies has been achieved in stage 3, these cavities expand as the volume of the daughter colonies increases. Beyond a critical volume at stage 4, the mother colony hatching and the daughter colonies' release takes place. On the other hand, from a purely external point of view, once fixed in ethanol, the alga represents a flexible sphere of variable dimension at all stages covered with glycoproteins and glycans.

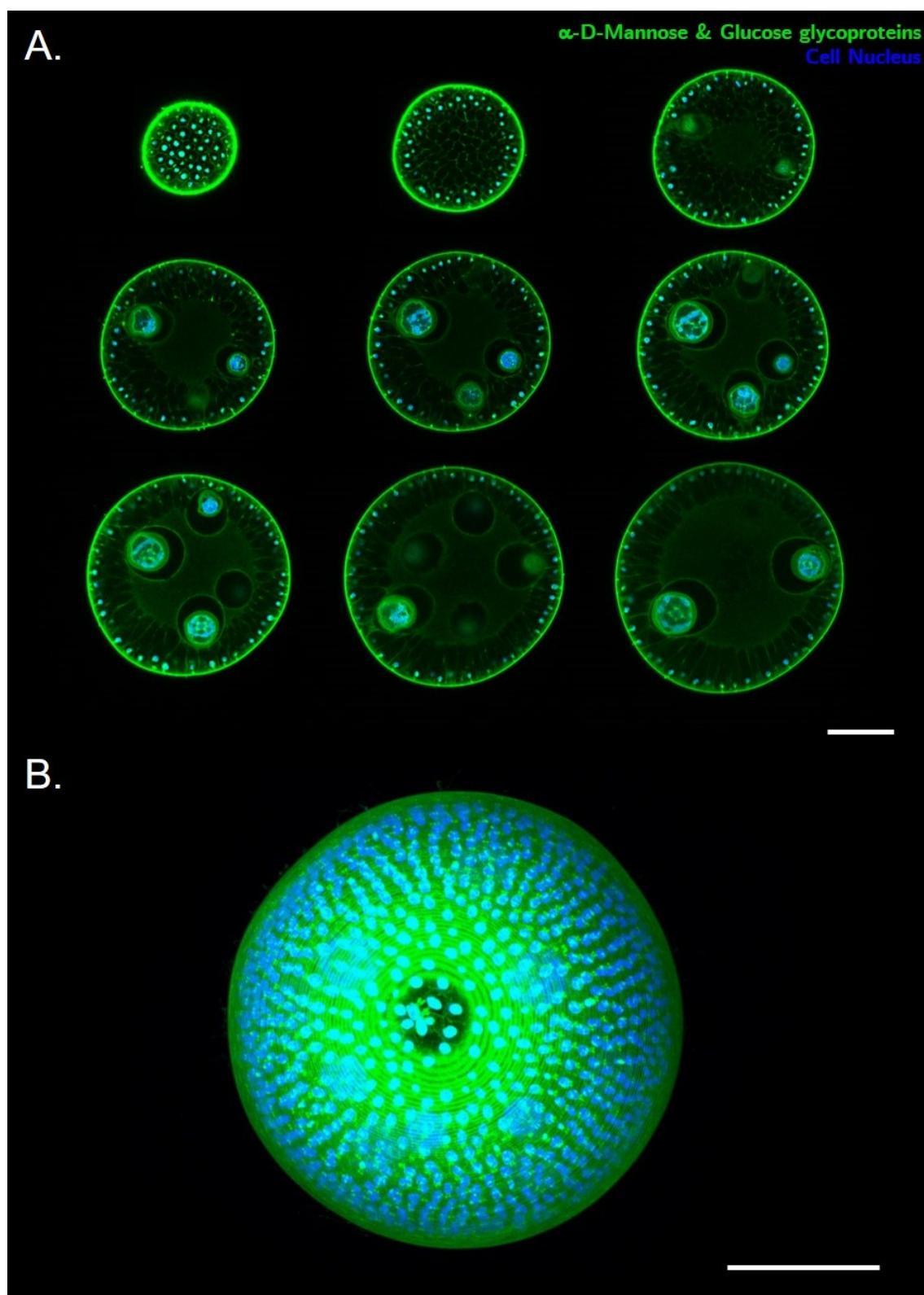


Figure C1.12: Stage 2 *V. carteri* α -D-Mannose & Glucose glycoproteins labelling. A. Representative Z-stack images of a stage 2 colony of *V. carteri* whose glycoproteins with α -D-Mannose & Glucose sugar groups were revealed by Concanavalin A and DNA content by DAPI were captured by confocal microscopy and B. a representative 3D image of the labelled microalgae was reconstructed using the Zeiss software (Scale bar: 50 μ m).

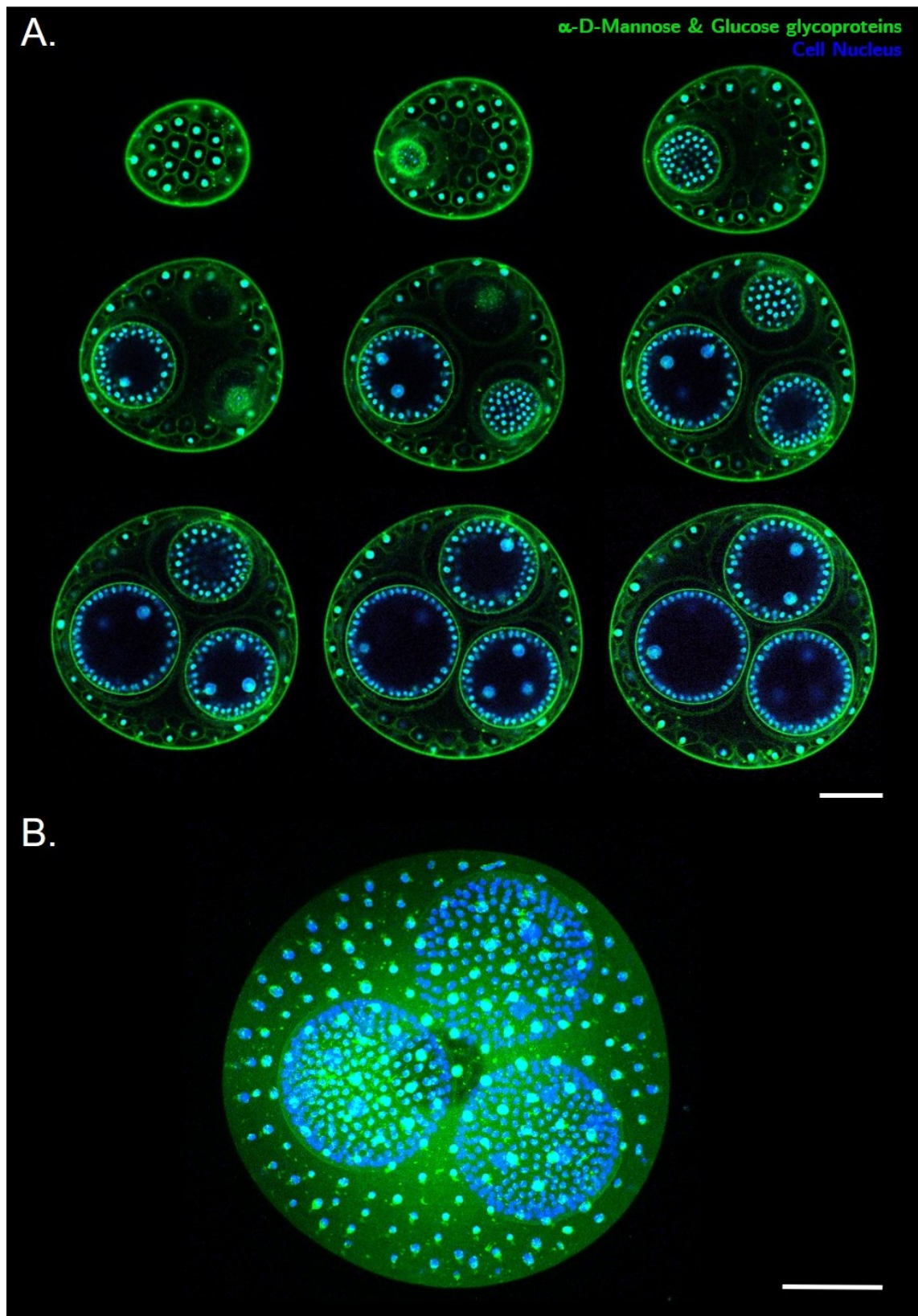


Figure C1.13: Stage 4 *V. carteri* α -D- Mannose & Glucose glycoproteins labelling. A. Representative Z-stack images of a stage 4 colony of *V. carteri* whose glycoproteins with α -D-Mannose & Glucose sugar groups were revealed by Concanavalin A and DNA content by DAPI were captured by confocal microscopy and B. a representative 3D image of the labelled microalgae was reconstructed using the Zeiss software (Scale bar: 50 μ m).

C1.4 Discussion

C1.4.1 Scaling-up *V. carteri* microalgae supply

The light-controlled thermostated culture system has allowed the standardization of the *V. carteri* alga production, as the previous homemade culture system was impacted mainly by the ambient temperature and illumination and would generate uncertain, irregular and seasonal harvests. It was possible to double the culture volume from 150 mL to 300 mL without impacting the quality of the algal suspension obtained. A satisfactory production of 11.34 ± 2.7 M colonies of *V. carteri* per 21 days has been maintained for over three years to provide the necessary quantity of algae to investigate *V. carteri* use as an innovative biomaterial for tissue engineering. Maximal production of 45.36 ± 10.8 M colonies of *V. carteri* per 21 days of culture has been estimated. It was mainly limited by the 300L capacity thermostatic chamber as 60 T-175 flasks could fit into the culture device. While our culture device could be sufficient for early to pre-clinical investigations, additional investments and culture optimisation would be necessary to ensure the clinical evaluation, industrialization and commercialization phases.

Over the past two decades, research and technologies related to microalgae culture on a commercial scale have been promoted by the fuel, chemical, pharmaceutical, and food industries that have identified flourishing microorganisms and derivatives [314]. At all scales, culture systems such as photobioreactors or outdoors race-way ponds focus on providing controlled light, temperature, nutrients and gas availability by stirring, semi-continuous to continuous feeding and harvesting, avoiding any stress response, with the aim to reach algal growth and productivity full capacities [315], [316]. While those culture systems are suitable for a broad spectrum of algae, adjusted abiotic parameters should accommodate every organism [317]. Although configuration is naturally required to reach high productivity, the up-scaling of the culture of *V. carteri* should not encounter any absolute limitation and should, on the contrary, benefit from the advances provided by the dynamics of these industries.

An injectable *V. carteri* product, similarly to hyaluronic acid or botulinic toxin substitutes, would be qualified as medical devices and should fulfill the related regulatory requirements. For future clinical use, we should aim to keep our material under sterile conditions at room temperature to 4°C. During our studies, we have highlighted the capacity of 70% ethanol-preserved algae gradually evaporated from the solvent at RT under a fume hood to regain its original shape by rehydration in PBS (data not shown). We can thus consider dry storage of our product and rehydration with a sterile solution upon use. Investigations will still be necessary to determine the optimum drying parameters for the algal morphology, mechanical properties and protein content preservations. Dry storage would present many advantages for the aseptic preservation and transportation of the injectable product. While 70% ethanol fixation has yet satisfied our aseptic constraints, regulatory procedures will have to be applied. The moist heat (ISO 17665, [318]–[320]), gamma or beta radiation

(ISO 11137, [321]–[323]) or ethylene oxide (ISO 11135, [324]) sterilization methodologies are mostly used in the case of medical devices or pharmaceutical products. As the gamma radiation method induces the mortality of microorganisms by targeting their DNA structure, it could thus be advantageous to ensure both asepsis and algal degradation. Ultimately the final sterilization method should allow for the preservation of the algal structure and the key properties related to its potential for tissue regeneration.

C1.4.2 Reducing *V. carteri* to a sphere-like state

Although the 4% PFA fixation was suitable for the structural study of the alga that we implemented later, the 70% ethanol preservation, a cleaner solvent, has also shown its efficiency in maintaining the morphology and the global integrity of the alga. A partial deflagellation of the colonies of *V. carteri* was obtained by preservation with 70% ethanol, thus freeing at least partly its surface. Indeed, the biflagellates of *V. carteri*'s somatic cells, about 20 μm apart each [325], constitute a surface hindrance. These flagella could thus be removed without using more harsh methods, either by pH dropping by means of acids [300], [301] or by intracellular Ca^{2+} increasing by means of chloral hydrate [326] or biosurfactants such as orfamide A [327].

The ethanol permeability of *V. carteri* membranes also allowed the diffusion and extraction of any soluble compounds, chlorophyll and carotenoid pigments, non-cross-linked small molecules like pherophorin-S and any active molecules as non-structural proteins, enzymes, phytohormones and metabolites. Only structural and cross-linked ECM would remain. Internally and externally stripped, the alga can thus be streamlined to its primary and macroscopic structure, a sphere.

C1.4.3 *V. carteri*, a flexible cell-carrier biomaterial

Both algal extracts respectively generated upon sonication at harvest and soaking following 70% preservation exhibited high levels of cell viability on the murine fibroblast L929 line. With regard to the ISO 10993-5 standards [310], the observed innocuity of our preserved material, and its soluble and sonication-released compounds demonstrated *V. carteri* global cytocompatibility.

Macrophages are highly phagocytic and release mediators modulating both inflammatory and immune responses. A balanced inflammation, i.e., not excessive in its intensity and duration, even stimulates tissue renewal allowing the formation or remodelling of neotissues. The inflammatory and immunogenic potential of *V. carteri* was thus globally evaluated *in vitro* through the different conditions of exposure and the determination of the associated J774.2 murine macrophages secretome. The pro-inflammatory LPS control condition induced the expected activation of macrophages through TLR4/CD14 receptors [328], [329] evidenced by distinctive increases in the expression of pro-inflammatory mediators, cytokines (TNF- α , IL-1 β , IL-6, IL-8, IL-12) and chemokines (IP10, mKC, MIP-3 α) [330]–[333].

As the immune response is subject to the regulation of both pro- and anti-inflammatory stimuli balance, the lack of secretion of MIP-1 α and MIP-2 chemokines at 48h of LPS exposure can be explained by the inhibition of their expressions by IL-10 and IFN- γ [334].

While few data are available on the possible pro- or anti-inflammatory effects of green algae in general, pro-inflammatory responses to algal products such as sulfated polysaccharides and glycosylated proteins are increasingly studied as their machinery is considered for the production of vaccine adjuvants and antigens [335]–[337]. *V. carteri*-induced J774.2 secretome showed the absence of global pro-inflammatory response indicating macrophage non-activation at 48h of exposure and non-pro-inflammatory and non-immunogenic resulting properties. Only exposure to living *V. carteri* algae generated a weak pro-inflammatory response that could be induced by toxins synthesised upon either or both algal stress and mortality. The algal flagella state should not have induced macrophage activation as algal flagella unlike bacterial flagella is covered by the cell membrane [59]. Schenck and al. [338] observed no significant inflammatory response to *C. reinhardtii*, *V. carteri* related unicellular alga, implantation in both athymic nude mice and zebrafish *in vivo* models. This photosynthetic graft also demonstrated that *C. reinhardtii* in the implanted scaffolds did not trigger any deleterious local or systemic immune responses in a 90 days follow-up, allowing full tissue regeneration in humans [339]. Although *V. carteri* will not be exempt from the need for such supplementary investigations, given their phylogenetic proximity plus *V. carteri* being used as an inactivated material, this allows for great confidence in the overall biocompatibility of the algae.

V. carteri filtered raw extract and preserved ethanol 70% materials demonstrated the overall *in vitro* non-immunogenicity of the algae as both did not induce any particular cytokine secretion and did not generate macrophage activation at 48h of exposure. On the contrary, the anti-inflammatory effect of the algae could be investigated, upon LPS-activation for instance, as a decrease in proinflammatory IL-9 and IL-15 were observed for all *V. carteri* treated conditions. Indeed, some phytochemicals such as polyphenols, polysaccharides, terpenes, fatty acids, pigments, proteins and several other bioactive are investigated in search of anti-inflammatory effects for use as food supplements mainly. Respectively used as dry biomass or extract, *C. debaryana*, and *P. japonica* have demonstrated their anti-inflammatory efficacy in the treatment of intestinal mucosa inflammation *in vivo* [340], [341]. Green algae phytochemicals such as hydroxylated fatty acids, chlorophyll-derived pheophorbides, carotenoids, and glycoglycerolipids showed anti-inflammatory effects decreasing nitric oxide intracellular levels [342], [343].

Both murine and human cells of mesenchymal and endothelial origins were able to develop cell adhesion to the algal surface. While developing variable adhesion strategies, these cellular abilities demonstrate *V. carteri* colonies' potential to be used as a cell carrier. The improvement of its surface adhesion properties, or alternatively the exploitation of its selective adhesion and anti-adhesion behaviours, could be sought.

C1.4.4 Investigating *V. carteri* cell adhesion properties

While *V. carteri* surface cell adhesion properties were previously described, *V. carteri* extract coating significantly increased cell adhesion of both human fibroblasts and endothelial cells to the anti-adhesive surface demonstrating the global cell adhesion potential of the algae. To comprehend and investigate algal composition, structuration and cell-adhesion properties origin, several stainings and labelling were performed by focusing on highly conserved structural components common to both plants and animals.

As in *C. reinhardtii*, the F-actin cytoskeleton of *V. carteri* supports the nucleus and organelles of adult somatic cells in the staking of distinct linear actin filaments [344]. In addition to this F-actin configuration, this gonidial structure was conjugated with similarly organised lipophilic and mucosal content. Actin filaments may play an active role in endocytosis, organelle and protein transportation in *V. carteri*

The cell adhesion properties of the *V. carteri* surface and extract are most likely to be conferred by glycoproteins, particularly pherophorins. Synthesised and secreted by somatic cells [76], pherophorins are predominant in the composition of *V. carteri*, contained and specific to each algal compartments from the cell walls, inner membranes to ECM meshes [345], [346]. As hydroxyproline-rich glycoproteins (HPRGs) with Ser((hydroxy-)Pro)_n repeats in the centred HR domains, pherophorins are classified as extensins. Similarly to lectins, pherophorins contain saccharide binding specificities in the A and B side domains [347]. These molecular specificities allow self-assembly and autocatalytic cross-linking of these glycoproteins producing an insoluble fibrous network, as observed for the deep zone pherophorins DZ1 and DZ2 [94]. Pherophorins as cross-linking proteins are analogous to animal collagen in the building of ECM architectures [174].

As most secreted molecules are glycosylated, the extracellular matrices of multicellular organisms are as well [348]. *V. carteri* shares a common pathway of N-glycosylation of glycoproteins with other eukaryotic species [349]. Plant HRGPs, and therefore *V. carteri* pherophorins, being rich in Pro, Thr, and Ser, highly glycosylated, and found in the extracellular matrix, have been considered functionally equivalent to mammalian proteoglycans such as mucins [350]. Importantly, however, O-linked glycosylation of mucins occurs through Ser and Thr residues rather than Hyp residues, which are rarely, if ever, glycosylated in animals [351]. *V. carteri* glycoprotein O-glycosylation patterns present long glycosylated chains, predominantly formed of arabinose and galactose sub-units [77], [88], [94], but can include mannose and glucose sub-units, as does the ISG glycoprotein [352]. Both ConA lectin and PAS labellings demonstrated the significance of glycosylation in *V. Carteri* essence. ConA lectin, specifically binding α -mannose/ α -glucose on N-glycans with little cross-reactivity [353], [354], allowed us to precisely map the structure of *V. carteri*.

Pherophorins-alleged adhesion properties might be associated with the presence of a adhesion binding motif that could consist in a primitive sequence analogous to the historical

animal collagen GFOGER or fibronectin RGD. This hypothetic sequence would definitely involve hydroxyproline considering its predominance in their protein sequence. Indeed, hydroxyproline is an essential compound of the fibrillar collagens, accounting for 14% of the total amount of imino and amino acids. Furthermore, in addition to the structural maintenance of the collagen I triple helix [355], [356], it has been shown that proline hydroxylation is essential for integrin binding, stabilisation and subsequent cell adhesion [357].

The glycosylated character of pherophorins could conversely confer direct cell anti-adhesive or adhesive properties. As analogous glycoproteins and cell surface barrier substances, mucins not only limit the binding of pathogens to epithelial cells by steric hindrance [358] but also prevent mammalian fibroblasts, myoblasts and epithelial cells adhesion on coated surfaces [359]. The collagen glycosylation pattern features O-glycosylated lysine and hydroxylysine (Hyl) residues comprising α -glucose and β -D-galactose biglycan. Collagen glycosylation level varies between the types and increases with age and in metabolic diseases [360]. Collagen IV glycosylations were found to modulate integrin interfering with both $\alpha 2\beta 1$ and $\alpha 3\beta 1$ integrins interactions [361]. Glycosylations modulate integrin-cell adhesion by masking cryptic sites and disrupting proteoglycan interactions [362]. The heat denaturation of collagen, commonly used in *in vitro* models, targets lysine and hydroxylysine residues glycosylations exposing cryptic binding sites for cell adhesion [363], [364]. However, N-glycans can be targeted by cell surface molecules to enhance cell-matrix attachment. In the case of plasma fibronectin, synergistic interactions of N-glycans with cell surface glycan-binding proteins improved integrin-mediated cell adhesion and wound healing migration [365]. Glycan-binding proteins (GBP) or lectins expressed by various cell types are capable of binding a wide variety of N and O-glycans, glycolipids and proteoglycans/glycosaminoglycans impacting cellular signalling, adhesion, differentiation as well as pathogenic processes including inflammation, tumorigenesis, metastasis, microbial, and parasitic pathogenesis [366]–[368]. Oligosaccharide-mediated cell adhesion strategies are developed to promote cell-biomaterial interaction through surface grafting of highly glycosylated proteins, also able to anchor cell surface glycans, such as conA and WGA lectins [369]. *V. carteri* pherophorins thus could mediate mammal cellular adhesion through direct interaction with surface binding receptors or indirectly entrapping or interacting with secreted ECM components.

C1.5 Conclusion

In this chapter we investigated the potential of *V. carteri* for tissue-engineered material development while ensuring the algal production, sterilization, preservation, cytocompatibility and *in vitro* non-immunogenicity, which led us to pursue our investigations. We were able to apprehend *V. carteri* high compartmentalisation and demonstrate its global cell adhesion properties that we assume are associated with its rich glycoprotein content, particularly the pherophorins that could modulate integrin-mediated cell adhesion to *V. carteri*-based materials.

Chapter C2

Engineering reconstructed tissue for tissue filling using *V. carteri* living building block approach - proof of concept

*Having demonstrated the suitability of *V. carteri* for in vitro cell culture and the possibility of using it as a cell carrier, we investigated the ability of *V. carteri* to support tissue growth in the form of cellularised building blocks providing a heterogeneous three-dimensional environment. Finally, we examined the in vivo outcome of such tissue for its application as a filler.*

C2.1 Morphological analysis of *V. carteri* cell carrying system

To construct three-dimensional tissues, we rely on the compact stacking of spheres as a scaffold. *V. carteri* colonies cellularised by mammal cells are used as a biomaterial in the form of a saturated algal suspension fixed in 70% ethanol, rehydrated and primed in culture medium. We firstly characterised this saturated suspension of *V. carteri* to determine the morphology of such scaffold and to verify its behaviour when maintained independently in *in vitro* culture conditions.

C2.1.1 Particle size analysis of *V. carteri* saturated suspension

For the production of cellularised building blocks, a saturated suspension of *V. carteri* was used at a ratio of 500 μL of saturated suspension per million mammal cells. The distribution of *V. carteri* colonies' diameter within this suspension was established on microscopic observation and displayed in Fig. C2.1.

The colonies presented a diameter normally distributed, as a W' of 0.9934 close to 1 was obtained from the Shapiro-Francia Test suitable for large data sets. The diameter of the colonies exhibited a centred distribution between 200 and 250 μm rising at 25% of total number of colonies. About 70% of the colonies had a diameter ranging between 150 and 300 μm . The removal of undesirable algae which could have clogged the culture insert pores was effective since algae with a diameter inferior to 100 μm constituted only 2.70% of the total algal suspension.

The saturated suspension exhibited a density of about $74.8 \cdot 10^3$ colonies/mL. $37.4 \cdot 10^3$ colonies of *V. carteri* were thus placed in suspension per million mammal cells. *V. carteri* colonies occupied 57.0% of the total volume of the suspension. Thus, $430 \mu\text{L}$ of residual medium were finally retained through sedimentation per mL of the saturated suspension. The surface area developed by the suspension of *V. carteri* per 12-well insert represents a surface area of about 65 cm^2 multiplying the available surface area to about 72 times the initial insert surface. Hence, the cells were seeded at a density of $15.5 \cdot 10^3$ cells/ cm^2 of *V. carteri* surface.

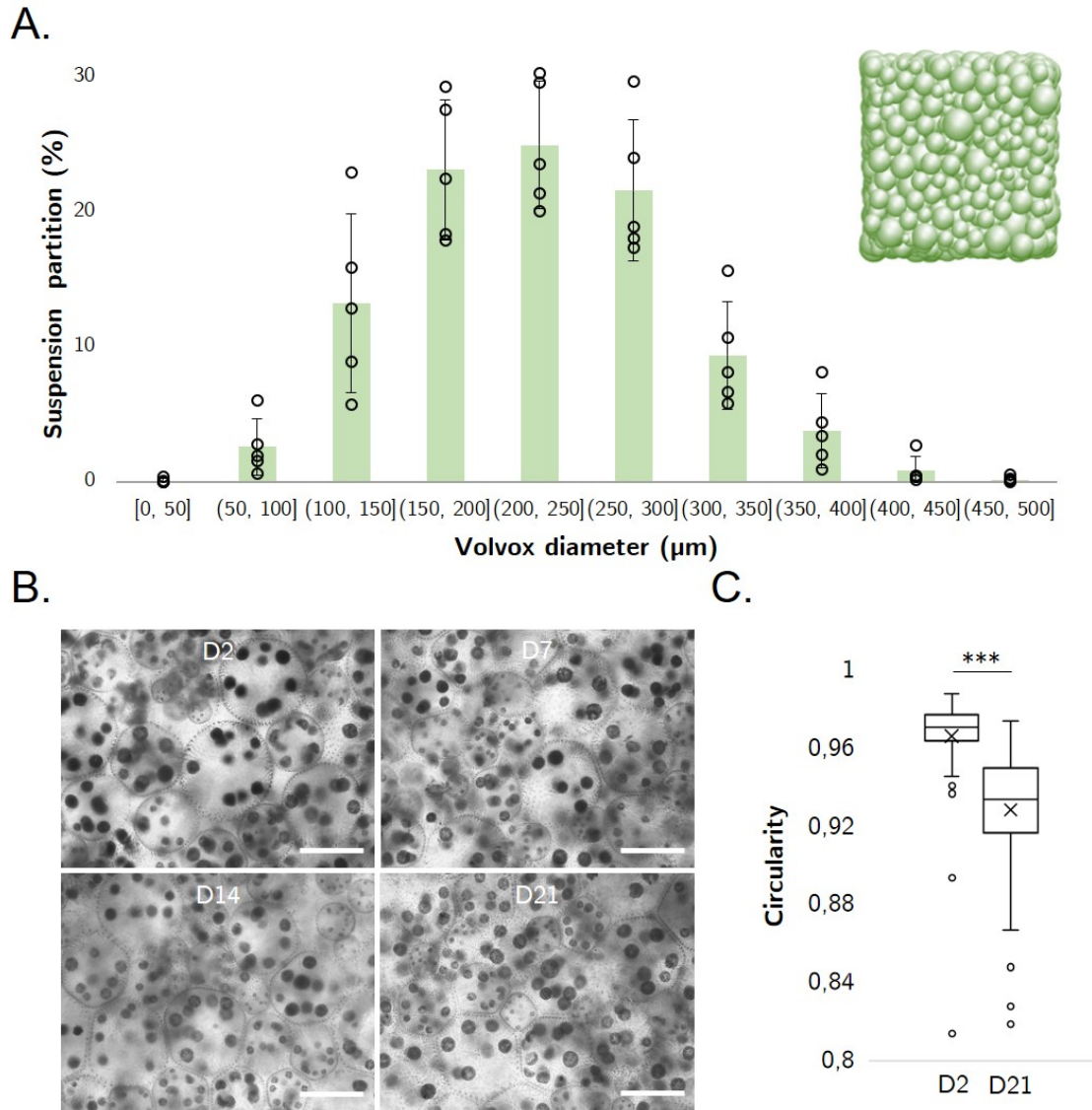


Figure C2.1: Characterisation of *V. carteri* suspension under *in vitro* culture conditions. A. Wide normal distribution of colonies diameter in a 70% ethanol fixed, PBS rehydrated and complete medium primed *V. carteri* saturated suspension (N=5; Shapiro-Francia Test; $W' = 0.9934$), B. *V. carteri* suspension contrast phase microscopy observation along *in vitro* culture duration (N=3, scale bar: $250 \mu\text{m}$), C. *V. carteri* circularity determination ($n \geq 75$, Welch t-test (**): $p \leq 0.001$)).

C2.1.2 *In vitro* deformability of *V. carteri* analysis

To investigate the impact of *in vitro* maintenance on *V. carteri* colonies' morphology, the algal suspension was maintained in standard insert culture conditions at 37°C and 5% CO₂ with regular basal medium changes for 21 days. At D2, the algal colonies were closely spaced, but gaps were created at their intersection. Then, the colonies' spacing was reduced by draining excess culture medium from the apical compartment. Between D7 and D21, the colonies were gradually deformed without any rupture until adopting hexagonal to square shapes by mechanical constraint of the continuous compact stacking of the spheres. A significant deformation was thus reported following 21 days of culture (C2.1 B). The circularity of the algae decreased significantly from 0.97 in the early days to 0.92 on completion of the culture ((C2.1 C).

C2.2 Production of a mesenchymal tissue by *V. carteri* living building block technique

Morphological, proliferation and histological studies have been performed with the aim to assess the generation of filler pseudotissue based on HDFn-cellularised *V. carteri* living building block maintained upon 3 weeks of culture.

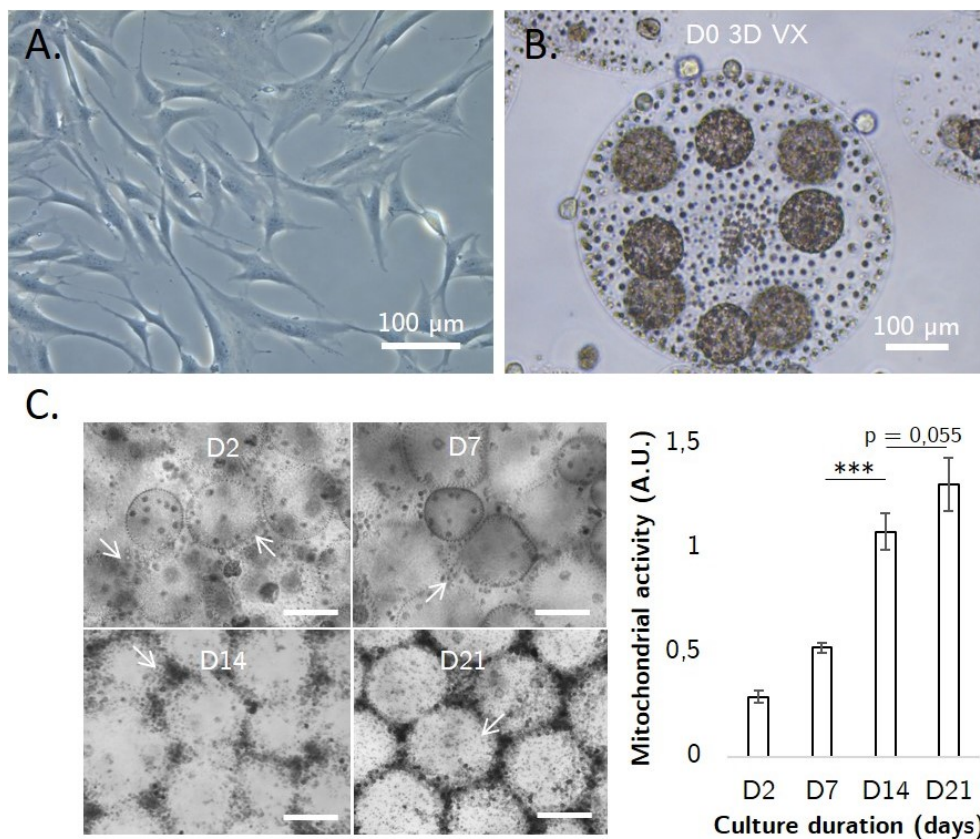


Figure C2.2: *V. carteri* HDFn-based building blocks *in vitro* culture. A. 2D culture of HDFn, B. Production of *V. carteri* HDFn-based living building blocks, C. Proliferation monitoring along the culture (Scale bar: 100 µm, N = 3, ANOVA analysis – Post Hoc Bonfferoni test (***: p < 0,001))

As shown in Fig. C2.2 and highlighted previously in Chapter C1, HDFn adhered to the surface of *V. carteri* in the form of sphere shaped aggregates while grown in 2D, HDFn expanded in a fusiform manner, developing structures like focal adhesions and filopodia. HDFn mitochondrial activity increased over the course of the culture. This activity was multiplied by 4.5 between days 2 and 21, going from 0.29 to 1.31. This rise in activity was associated with the creation and densification of fibroblasts-based tissue structures at the periphery of the colonies, marked by a white arrow in Fig. C2.2 A, demonstrating HDFn proliferation on the surface developed by the algal suspension.

While cultured onto *V. carteri* surface, HDFn also exhibited in C2.3 a significant alkaline phosphatase activity starting at day 2, whereas spread onto culture surface, no enzymatic activity was detected. As the previously noted tissue material on the surface of the colonies expanded, more and more fibroblasts were found to be positive for alkaline phosphatase expression.

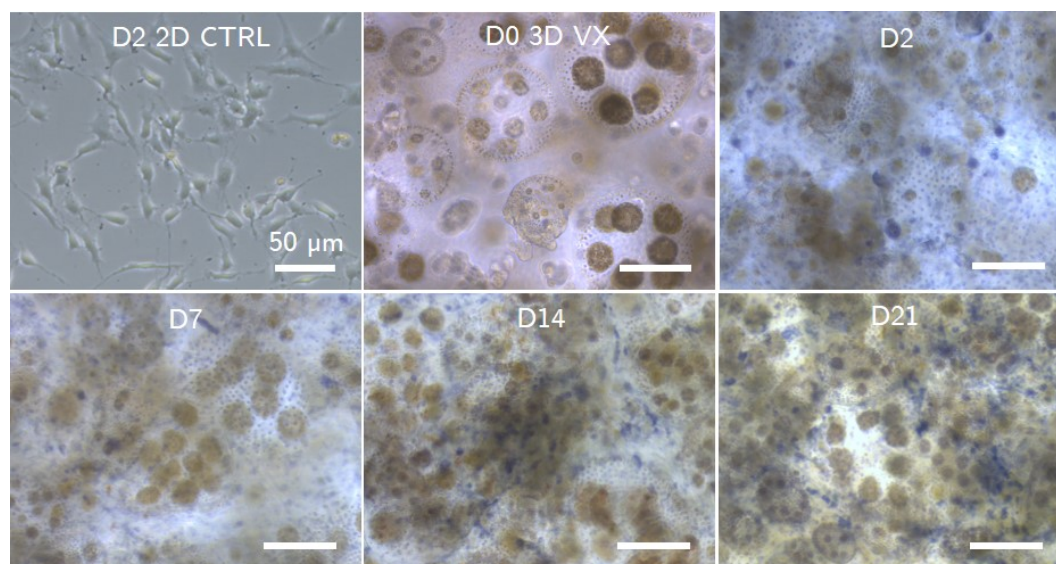


Figure C2.3: *V. carteri* scaffold induce HDFn phosphatase alkaline activity. Contrast-phase observation of *V. carteri* HDFn- based living building blocks treated to reveal any phosphatase activity, along 3 weeks of *in vitro* culture (scale bar: 250 µm)

Upon three weeks-culture completion, a pseudotissue with integrity, although flexible, fragile and difficult to manipulate, was obtained (Fig. C2.4 A). This approach, applied on a suspension of *V. carteri* coupled to Rhodamine in red, showed in Fig. C2.4 B a homogeneous distribution of fibroblasts in blue within the whole tissue thickness. However distorted, the *V. carteri* colonies remained complete and offered a surface on which the fibroblasts expanded. Cellular clusters were formed in the cavities resulting from the aggregation of multiple *V. carteri* colonies. Upon Hematoxylin-Eosin-Safran (HES) staining, this organization was recovered on an uncoupled sample (Fig. C2.4 C). The integrity of *V. carteri*, in bright pink, was observed. Its mucosal content was discernible as a thin pale pink to yellow veil. Finally, self-organised cell sheets and clusters, whose nuclei were coloured in purple, supported by a fibrous extracellular matrix, were seen in light pink to yellow.

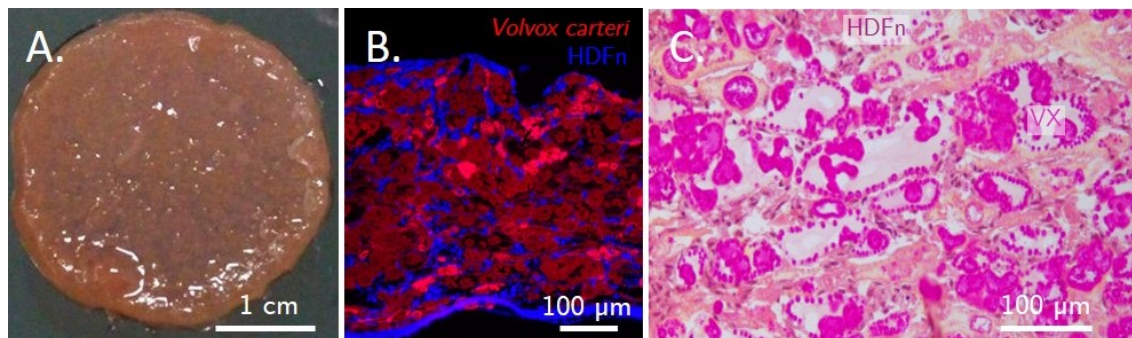


Figure C2.4: Reconstructed pseudotissue based of *V. carteri* HDFn-based building blocks. A. Photograph of the pseudotissue obtained after 21 days of culture, B. Epifluorescence observation of DAPI stained HDFn (blue) cellularised and Rhodamine cross-linked *V. carteri* (red) pseudotissue, C. Histological observation of Hematoxylin Eosine Safran stained pseudotissue

C2.3 Early *in vivo* biocompatibility investigation of *V. carteri*-based three-dimensional tissue filler

Finally, to ascertain the *in vivo* behaviour of the *V. carteri* HDFn-based living building block-based 3-weeks pseudotissue and its resulting body response, we implanted this three-dimensional system subcutaneously into athymic mice. To this end, the three-dimensional tissue was collected in a syringe due to its brittleness. A gelatinous suspension volume of about 150 mm³ was injected directly under the mouse skin, creating an externally visible protruding implant. The volume expansion created by the injection, indicated by an arrow in Fig. C2.5 A, remained detectable and unchanged in size and shape for the entire duration of the experiment. Bovine collagen gel injection was used as a comparison to create the same soft tissue augmentation as a control condition.

Animals were killed upon 1-month and 2-month of implantation. Necropsy and histological analysis of the biopsy specimens were performed and respectively displayed in Fig. C2.5 B and Fig. C2.5 C. Although the same amount of material was initially injected, the bovine collagen control mostly disappeared, leaving a small, barely detectable mass under the mouse skin at 1-month post-implantation. In contrast, the *V. carteri* HDFn-based building block implant exhibited a large mesenchymal tissue-like structure penetrated by the surrounding blood vessels. This identical structure was also observed on 2-month post-implantation necropsy (data not shown) suggesting its *in vivo* stability.

This homogeneously cellularised fibrous tissue showed, upon histological hematoxylin eosin staining, remnants of spherical structures attributable to the breakdown of *V. carteri* colonies, point out by a black arrow. Histological analyses of the injected *V. carteri* HDFn biopsy specimens showed that the accumulation of this thick mesenchymal tissue and the surrounding tissues showed no inflammation evidence one month after implantation, with the absence of eosinophils, neutrophils, and macrophages or other remaining inflammatory cells. Yet, neotissue's synthesis and vascularisation in the resulting tissue expansion at 1-month post-implantation demonstrated an inarguable colonization of the interstitial spaces by stromal

growths.

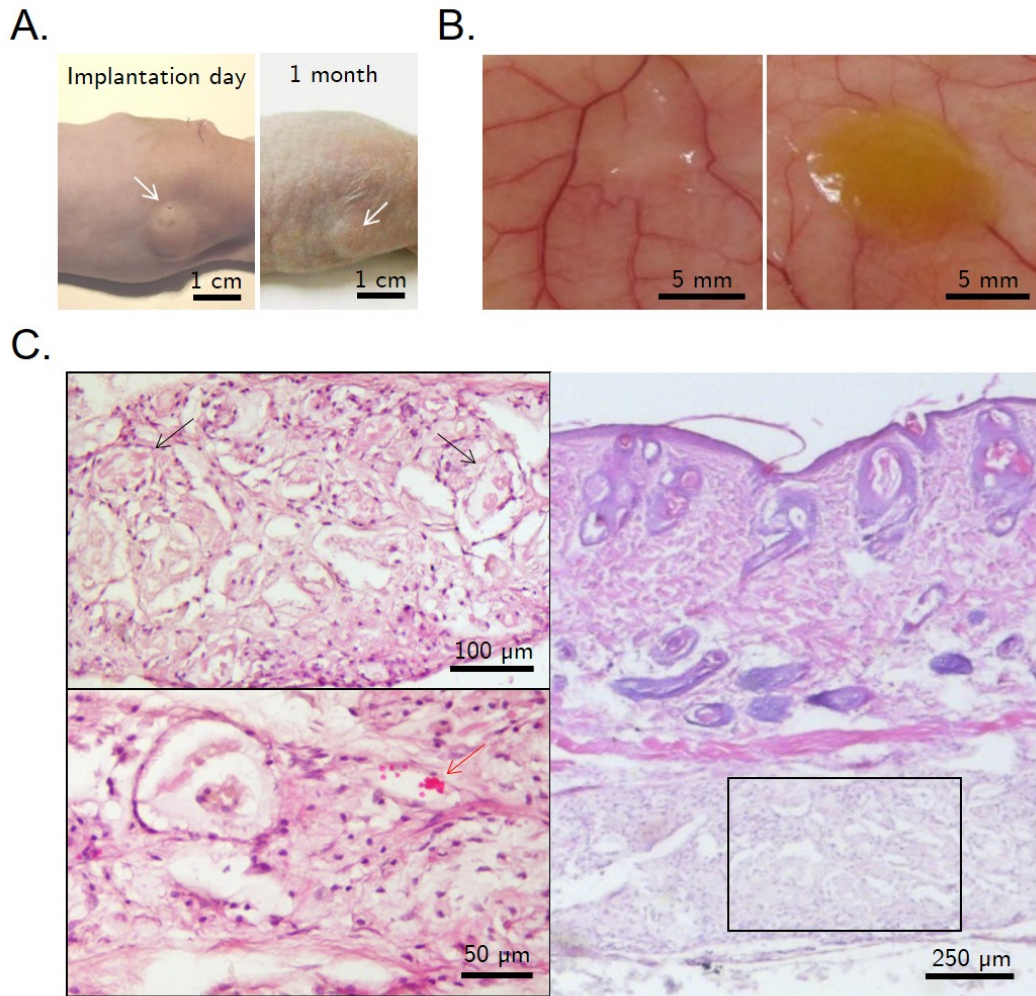


Figure C2.5: *V. carteri* HDFn pseudotissue early *in vivo* physical stability and biocompatibility study. A. Post-implant and 1-month follow-up photographs of the implant site (*white arrow*), B. From left to right, macroscopic aspect of the collagen and *V. carteri* HDFn pseudotissue implants at 1-month post implantation, C. Histopathological examination via HE staining of the implanted HDFn *V. carteri* (*black arrow*) based pseudotissue upon 1-month implantation showing signs of vascularisation (*red arrow*).

C2.4 Discussion

C2.4.1 Vegetal material suitability for tissue engineering and regeneration

Tissue engineering strategies generally converge towards the molecular, structural and mechanical reproduction of *in vivo* tissue microenvironments, seeking active cell adhesion, migration, proliferation and differentiation as well as ECM synthesis and remodelling in order to initiate, regulate and guide the regeneration process [370]. As integral parts of tissues, being structural and cell-engaging elements, usually, ECM-derived materials are favoured for scaffold formation. Yet, this does not prevent them from encountering challenges and

drawbacks in sustainably promoting tissue regeneration (i.e., matrix variability, tuneable complexity, poor mechanical properties, high degradability and variable immunological response) [282]. The search for alternative natural compounds analogous in composition, structure or function is an under-researched reserve and could help to provide new therapeutic solutions for tissue regeneration. Many researchers have now overcome the daunting task of crossing the kingdoms focusing on micro-algae and plant-based materials. As the main structural component of plants, cellulose has been used widely for regenerative medicine applications. Cellulosic materials have been selected respectively for their water absorption capacity in cartilage tissue engineering [371], [372], for their mechanical strength for bone tissue engineering [373], [374], and globally for their biocompatibility, stability and potential for wound healing both *in vitro* and *in vivo* [375], [376]. Interestingly, by taking advantage of similarities in the vascular structure of plant and animal tissues, Gershlak et al [377] were able to use a decellularised plant tissue as a vascularised scaffold for tissue engineering applications. Moreover, the incorporation of *Spirulina* in electrospun scaffolds has demonstrated improvement in cytocompatibility by providing a wide range of vital nutrients to the cells, thereby affecting their metabolism [378]. Similarly, living photosynthetic *C. reinhardtii* algae implanted in a wound defect effectively delivered oxygen *in situ* to limit hypoxia and promote wound healing [338], [339]. Here, we aimed to take advantage of *V. carteri*'s global structure and collagen-like ECM and surface marker to form 3D constructs for tissue filling.

C2.4.2 Forming mesenchymal tissues using *V. carteri* living building block approach

The *V. carteri* algal suspension represents an assembly of spheres normally distributed around 250 μm in diameter. This individual block stacking organisation offers an infinite malleability for multi-volume shaping and a drastically increased surface area developed by our material. The size dispersion of the preserved colonies allows for larger compaction of the spheres while creating niches at their intersection and an interstitial continuum, ensuring its full interconnectivity. As for conventional scaffold development, guaranteeing effective mass transport for nutrient supply (i.e., glucose, growth factors, etc.) and gas diffusion (i.e., oxygen, carbon dioxide) is highly challenging as the solid phase of the material acts as a diffusion barrier [379]. Indeed, the diffusion throughout this sphere compaction must be significantly decreased between D0 and D2 as diffusion coefficient studies in random packings of polydisperse hard spheres showed that the effective diffusion was mainly decreased with the increasing solid volume fraction. In other words, it can be easily understood that the decrease of the interstitial void space between spheres obstructs diffusive transport [380]. However, this high packing density and the progressive deformation without rupture of the algal spheres over the culture time should facilitate the cohesion of the created structure.

Moreover, fibroblasts being contractile cells and *V. carteri* exhibiting signs of deformability, these cells have been able to manage this interstitial volume drain by substituting it with extracellular matrix while proliferating as demonstrated by the increase of mitochondrial

activity and histological analysis. Based on our observations, cellularised *V. carteri* building blocks can be used to assemble three-dimensional tissues.

HDFn demonstrated positivity for alkaline phosphatase (AP) activity exclusively when grown in 3D, starting from D2 and sustainingly until D21. As a high level of AP correlates with pluripotency and undifferentiated pluripotent stem cell phenotypes [381], *V. carteri* could induce fibroblast dedifferentiation, forming fibroblasts aggregates and confining them into niches. Indeed, mechanically confined fibroblast has shown the ability to reprogram in stem-cell-like cells and rejuvenate, demonstrating phosphatase alkaline activity [382], [383]. Yet, while high AP is associated with pluripotency, AP is also ubiquitous and known to be actively produced in bone, liver, and kidney [384]. Further analysis including the determination of pluripotency transcription factors expression in HDFn seeded on *V. carteri* (i.e., OCT4 (octamer-binding transcription factor 4), SOX2 (sex determining region Y-box 2), and homeobox protein NANOG)) should be pursued to validate this statement. Altogether, we have demonstrated that this culture system is suitable to build a mesenchymal tissue showing an even distribution of cells and matrix secretion over the whole thickness of the created tissue.

C2.4.3 *V. carteri*-based mesenchymal tissues application as soft-tissue filling and regeneration

Soft tissues (i.e., fat, fibrous, muscular tissues) are continuously exposed to damage and loss due to trauma, burns, infections, tumour removals, and degenerative or autoimmune diseases. In 2022 alone, the soft tissue repair market was expected to grow by nearly 13%, rising from \$9.26 billion to \$10.46 billion, mainly because of the increase in sport-related injuries and injuries among the growing geriatric population [385]. While autologous fat and tissue transplantation remain the gold standard, such drafts still demonstrated shrinkage, poor stability and regeneration properties in the long-term. In addition to lost volume restoration using biomaterials, current advances in the field aim to strategically promote tissue healing by stimulating the body's regenerative mechanisms. We are progressively shifting from rather inert scaffolds, using biomaterials already approved by health agencies, mainly for minimal body reaction and resorption properties, toward templates that are actively designed (i.e., size, chemistry and architecture) to control the delivery of molecular and mechanical signals to specifically target cells, induce and control the regenerative process [370]. As unconventional as it can seem, *V. carteri* displays considerable molecular and structural complexity, as well as distinctive mechanisms of self-healing and self-regeneration [94] to represent exciting opportunities for animal and human tissue regeneration.

Here, we demonstrated that conversely to the collagen matrix, *V. carteri*-based mesenchymal tissue remained stable, highly cellularised, and vascularised for up to 2 months post-implantation. Indeed, as collagen is physiologically ubiquitous, collagen matrices exhibit a high degradability that impacts *in vivo* stability but facilitates *in situ* integration. However, the *in vivo* resorption rate of a collagen implant can be regulated by controlling its density and intermolecular cross-linking degree [386], it tends to generate foreign body response

[387]. Since no significant inflammation was observed during the degradation of *V. carteri* in these implantation conditions. It can be hypothesised that *V. carteri* was degraded *in vivo* by a fibroblast-dependent phagocytic mechanism related to homeostatic matrix remodelling [388]. Given that *V. carteri*-based mesenchymal tissue *in vivo* stability has been reported, further investigations should be undertaken to evaluate tissue ingrowth and remodelling within the implant by distinguishing murine and human fibroblasts. The tissular density, cellularisation and vascularisation should also be examined in the long term to confirm the potential of such a matrix for soft tissue regeneration.

C2.5 Conclusion

We realised a proof of concept for three-dimensional tissue formation using the *V. carteri* living building block method and its application for *in vivo* tissue regeneration. The compact packing of *V. carteri* colonies offers an extensive, unique, and integrally interconnected culture surface suitable for cellularisation and diffusion throughout the template. Modulating cellular guidance, containment and heterogeneity, the *V. carteri*-based template represents an innovative matrix of vegetal origin for such uses allowing adhesion, proliferation, and matrix secretion with possible differentiation properties.

Chapter C3

***V. carteri* alone promotes adipogenesis without the use of any adipocyte differentiation cocktail**

*As we previously identified that *V. carteri* could impact cellular phenotype by being able to shift neonatal human dermal fibroblasts into alkaline phosphatase synthesis, we questioned if this culture system alone would be able to direct stem cell differentiation in any way. In addition to molecular stimulus, the substrate mechanics and topography would drive such differentiation. The *V. carteri* mechanical characterization was thus performed. As the implantation of *V. carteri*-based mesenchymal tissue has been shown to successfully maintain the expanded volume in vivo despite remodelling of the implant, we seek to assess the part of this process intrinsically linked to *V. carteri* evaluating the capacity of a *V. carteri* suspension only implant to maintain the volume, cellularisation and vascularisation under the same implantation conditions.*

C3.1 Evaluation of the mechanical properties of *V. carteri* colonies

The *V. carteri* living building block culture system can grow soft mesenchymal tissues. However, mesenchymal tissues can develop variable stiffness ranging from kPa to MPa. In order to accurately defined the mechanical properties of our algal suspension at the cell level, the nanoscopic stiffness of rehydrated 70% ethanol fixed *V. carteri* colonies was assessed using nanoindentation. The load generated upon a 15 000 nm indentation at a speed of 3 nm/s was quantified using a 28 μm diameter colloidal probe arranged on a rigid 0.48 N/m cantilever. Simultaneously, the colony diameter was measured ($n = 95$). The load increased with indentation. The Young's modulus was determined as the slope of the linear part of the curve between 1 and 3 μm considering Hertz's sphere-sphere contact model.

The calculated Young's moduli were plotted in Fig. C3.1 as a function of the diameter of the colony. *V. carteri* colony Young's moduli ranging from 1.5 to 4 kPa for diameters ranging from 100 to 400 μm were obtained. *V. carteri* colonies presented an average Young modulus of 2.8 ± 0.5 kPa. The diameter of the colony did not seem to impact its mechanical properties since no correlation between colonies Young's modulus and diameter was observed (Pearson's correlation test; Pearson's $r = 0.063$).

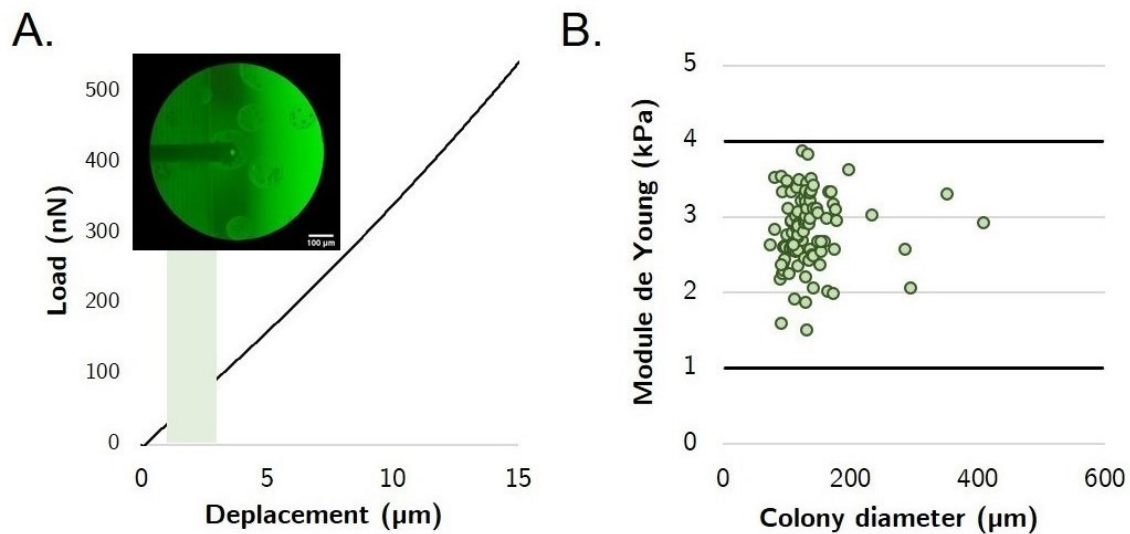


Figure C3.1: *V. carteri* stiffness determination (n=95). A. Mean load-displacement curve obtained upon 15,000 nm nanoindentation at a rate of 3 nm/s on *V. carteri* colony (Probe diameter: 28 μm , stiffness: 0.48 N/m), B. Distribution of Nanoscopic Young's modulus of *V. carteri* colonies as a function of their diameter (Pearson's correlation test; Pearson's $r = 0,063$).

C3.2 Phenotypic outcome of stem cells introduced into *V. carteri* compact packing culture system

Both human mesenchymal and murine embryonic stem cells were seeded onto our *V. carteri* living building block system and cultured for up to 3 weeks without any adipogenic inducing supplementation. Cell morphology and engagement on the adipogenic pathway were monitored by staining their lipid content with Oil Red O respectively counterstained with hemalun or counter-labelled with DAPI and phalloidin to reveal their cell nucleus and actin cytoskeleton for observation either by optic or confocal microscopy.

C3.2.1 Impact of *V. carteri* living building block culture on human mesenchymal stem cells

Human Adipose tissue-derived mesenchymal Stem Cells (hASC) were able within a few hours, as seen in Fig. C3.2, to adhere, spread and partially cover the surface of *V. carteri*, developing membrane protrusions similar to those exhibited when cultured in 2D on culture treated surfaces. While remaining adherent and in clusters on the surface of *V. carteri* colonies, some hASC became rounder within 48 hours, diverting from mesenchymal cells' characteristic morphology, as shown by the condensation of their actin cytoskeleton around their nucleus. We observed the formation of dozens of lipid microdroplets of 1 to 3 μm in diameter, typical of adipogenic pathway drift. hASC also polarised itself drawing its nuclei closer to the cell membrane, concentrating the lipid droplets in a central position, an advanced adipocytic maturation indication. The roundness of the cell nucleus also seemed to be altered.

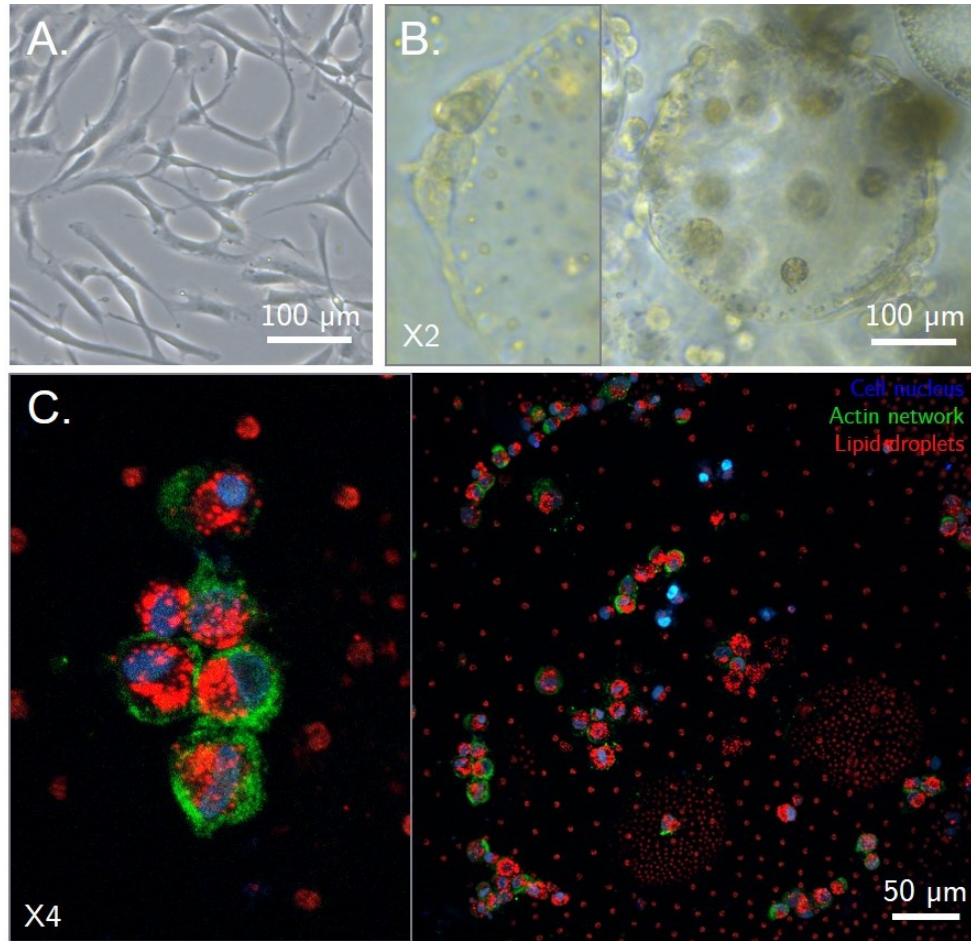


Figure C3.2: Production of Adipose-derived stem cells *V. carteri* living building blocks. A. 2D cultured hASC, B. 48h hASC seeded on and spread out around *V. carteri* colonies, C. 48h hASC seeded *V. carteri* showing hASC adhered onto the microalgae surface exhibiting nuclear content (blue), actin network stained with phalloidin (green) and numerous lipid droplets (red).

As we observed hASC differentiating rapidly, we wondered how far the adipogenic differentiation could get by continuing the culture. We, therefore, monitored hASC lipidic content until 21 days of culture by Oil Red O staining observed under light and confocal microscopy in Fig. C3.3 and C3.3.

hASC cultured in 2D spread out on the surface treated for adherent cell culture, developing a fusiform shape induced by the unidirectional orientation of its actin cytoskeleton. hASC only exhibited nanometric lipid droplets under bright-field microscopy once total confluency was reached. 2D grown hASC remained mesenchymal. On the other hand, both visualization methods revealed the appearance and maintenance of micrometric lipid droplets in hASC cultured in 3D on *V. carteri* living building block system for up to 21 days, confirming the adipocyte differentiation of the stem cells. *V. carteri* as a substrate generated at least differentiation and maintenance of hASC into preadipocytes. While the volume of each individual lipid droplet did not appear to evolve significantly between D2 and D21, the overall volume of the formed preadipocytes increased, concentrating more and more lipid droplets.

While confocal microscopy distinctively evidences the above-mentioned nucleus polarisation to the plasma membrane and shape modification, optic microscopy observation thus showed that although the cells cultured in 3D on *V. carteri* had a rounded cell body around the nucleus, hASC still developed very fine membrane protrusions spreading over the surface of *V. carteri* even at 21 days of culture. These protrusions must participate in supporting the obtained tissue cohesion, as it is essentially the juxtaposition of *V. carteri* colonies.

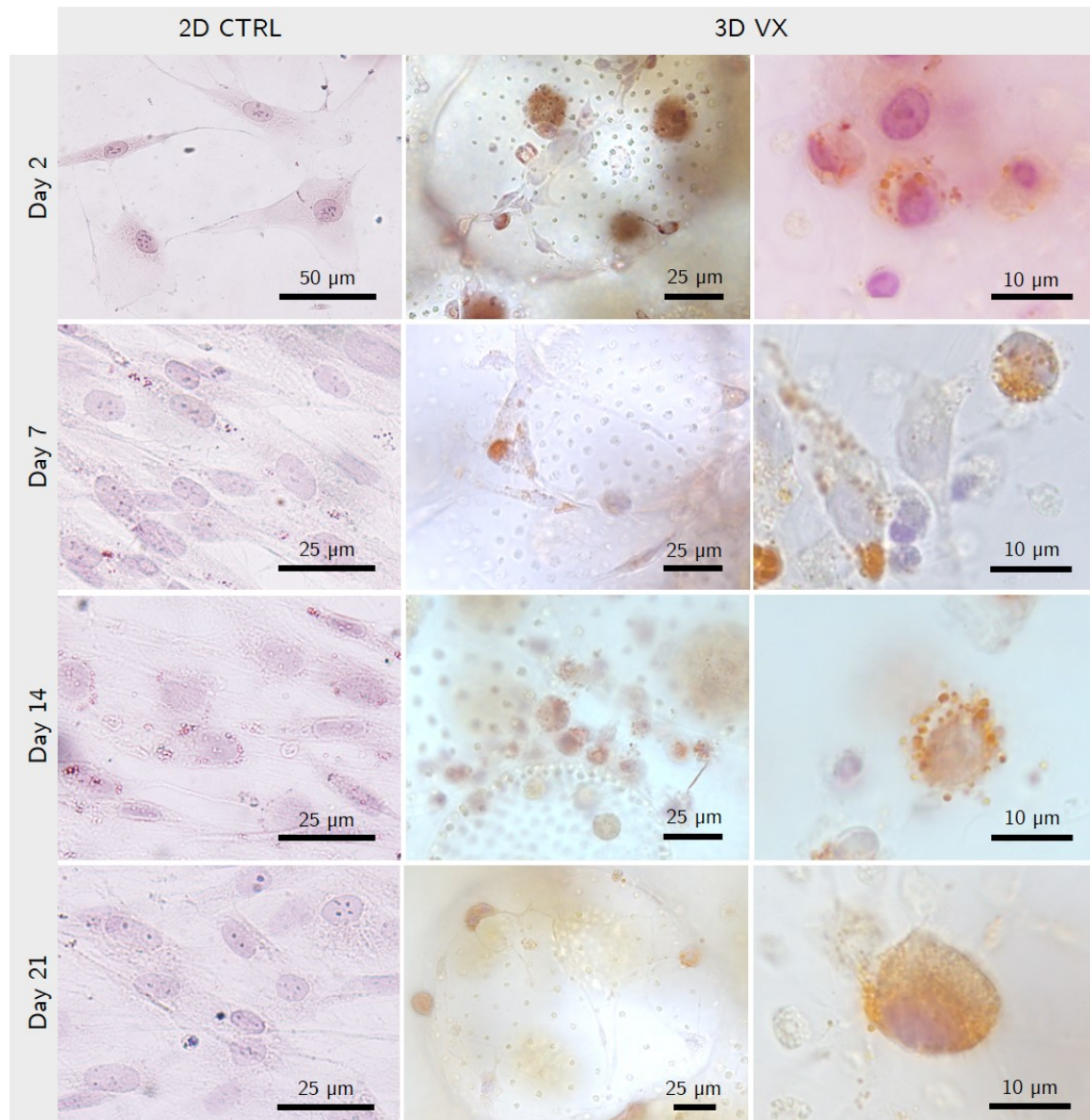


Figure C3.3: Adipose-derived stem cells adipogenic differentiation upon culture in a *V. carteri* living building blocks environment. Bright-field microscopy observation of hASC grown for up to 21 days using the *V. carteri* living building block technique, exhibiting oil red o stained-lipid microdroplets (red) and counterstained with hemalun to reveal the cell nucleus (purple).

Moreover, we monitored in Fig. C3.5 the overall morphological appearance of the formed tissue by phase contrast microscopy and simultaneously tracked hASC mitochondrial activity over the entire culture period.

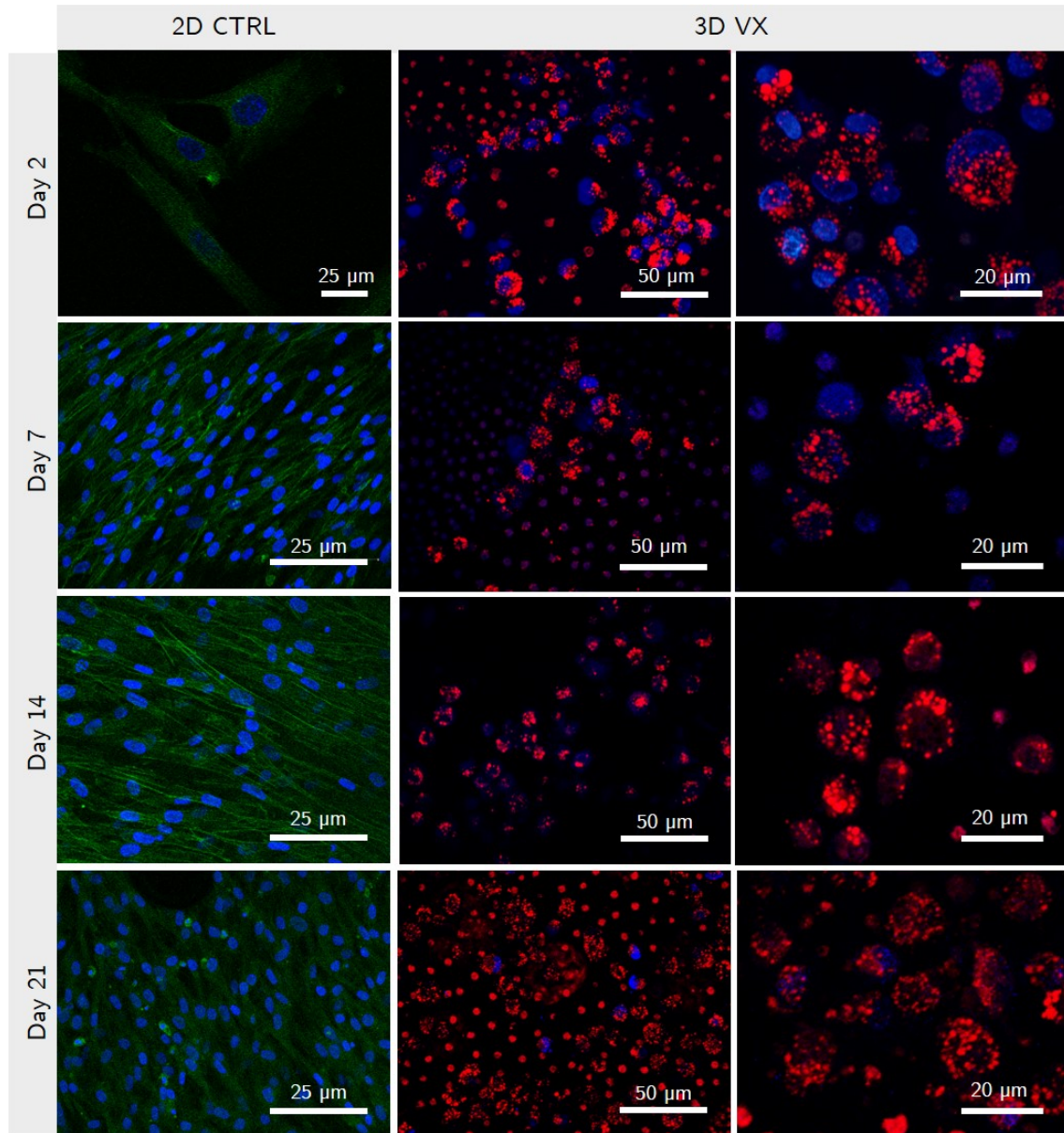


Figure C3.4: Adipose-derived stem cells adipogenic differentiation upon culture in a *V. carteri* living building blocks environment. Confocal microscopy observation of hASC grown for up to 21 days using the *V. carteri* living building block technique, exhibiting oil red o stained-lipid microdroplets (*red*), phalloidin-stained cytoskeleton (*green*) and counterstained with DAPI to reveal the cell nucleus (*blue*).

We observed an opacification of the cellular content at the interface between *V. carteri* colonies over 3 weeks of culture, which was characteristic of cellular proliferation since the cells could be distinctly visualised. This densification was even more noticeable in the niches created by the juxtaposition of three algal colonies. However, this was not directly linked as expected to the measurement of an overall increase in mitochondrial activity. The mitochondrial activity measured was almost non detectable throughout the culture in 5 independent experiments, while in 2 of them, a sudden increase in mitochondrial activity was detected as of D14. Yet, a highly cohesive tissue was obtained on completion of the culture.

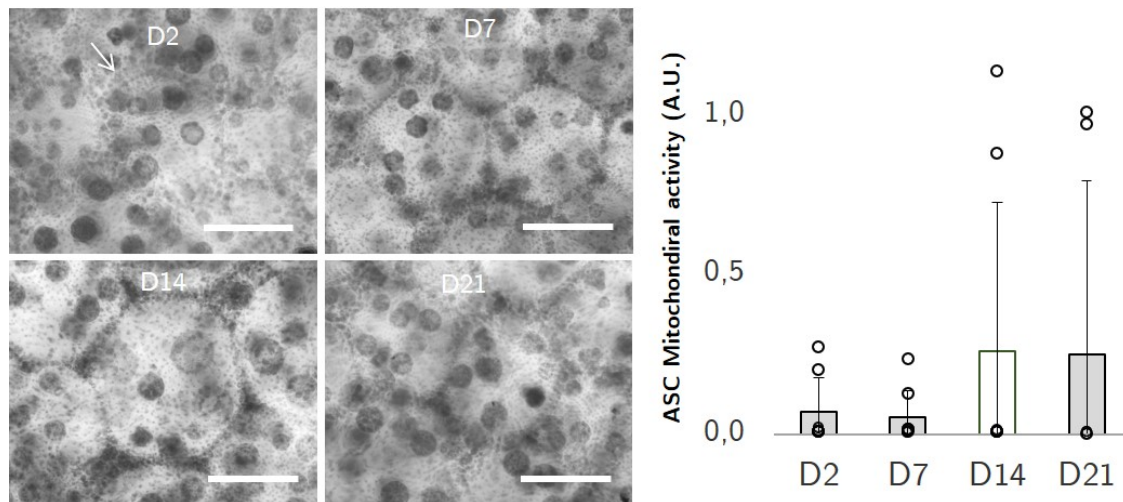


Figure C3.5: Adipose-derived stem cells mitochondrial activity upon culture in a *V. carteri* living building blocks environment. Contrast-phase microscopy observation and mitochondrial activity of hASC grown for up to 21 days using the *V. carteri* living building block technique showing densification of the interstitial tissue in between *V. carteri* colonies (scale bar: 250 μm).

C3.2.2 Impact of *V. carteri* living building block culture on mouse embryonic stem cells

To ensure the replicability of the effect observed with hASCs while broadening out the pluripotency of the cells used, we aimed to apply our culture system to C3H/10T1/2 murine embryonic stem cells.

We initially noted that C3H/10T1/2 adhered to the surface of *V. carteri* as spheroids-like structure (data not shown). The lipid content of C3H/10T1/2 monitored over the whole culture duration is provided in Fig. C3.6. C3H/10T1/2 grown in 2D on a surface treated for culture showed lipid nanodroplet formation once high cellular confluence was reached at 21 days of culture. Maintained in the *V. carteri* suspension on inserts, C3H/10T1/2 demonstrated lipid microdroplets formation of approximately 1 μm in diameter as early as 48h, demonstrating once again the adipogenic induction of stem cells by *V. carteri* template. Some cells were observed losing or having lost their nucleus (black arrows). While no increase in C3H/10T1/2 cell size was observed, their lipid droplets significantly expanded as the culture progressed. Lipid droplets with diameters of 2, 6.5 and 8 μm could be identified at 7, 14 and 21 days of culture, respectively. Yet, C3H/10T1/2 showed a concentration and expansion of the lipid droplets while maintaining anchorage points at the colony surface. Some C3H/10T1/2 were ultimately found to be fully round, achieving advanced adipocyte differentiation.

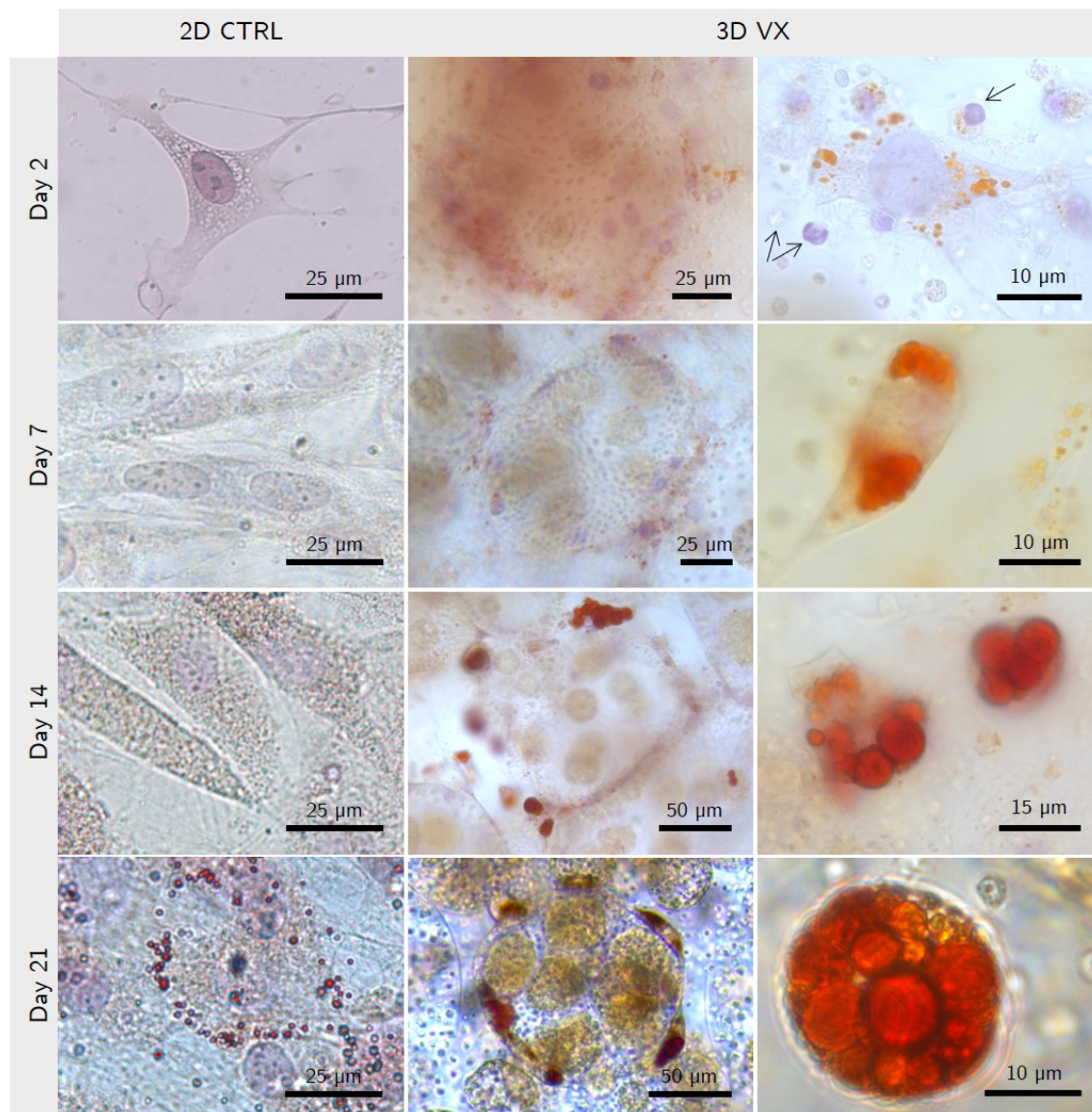


Figure C3.6: C3H/10T1/2 murine embryonic cells adipogenic differentiation upon culture in a *V. carteri* living building blocks environment. Bright-field microscopy observation of C3H/10T1/2 grown for up to 21 days using the *V. carteri* living building block technique, exhibiting oil red o stained-lipid microdroplets (red) and counterstained with hemalun to observe the cell nucleus (purple).

C3.3 Early investigation of the *in vivo* outcome of a *V. carteri* only-based injectable for tissue filling and regeneration

Given *V. carteri* suspension efficiency to induce tissue development and to influence cellular behaviour *in vitro*, we sought to explore the potential of an injectable composed exclusively of a suspension of rehydrated 70% ethanol-fixed *V. carteri* colonies. The *V. carteri* suspension was therefore injected subcutaneously into an athymic mice model. The overall appearance of the implant was observed upon harvesting 1-month post-implantation, as displayed in Fig. C3.7 A. Histopathological analysis of the integrated implant provided in Fig. C3.7 B-C was performed in opposition to a non-implanted control.

Firstly, we observed a significant reduction in the injection volume in the first few days following implantation. This reduction was mainly related to the drainage of residual fluid and the reconfiguration of the algal sphere packing, as we identified that our injectable could still comport 44%V/V buffer. The suspension of *V. carteri* colonies did not show any particular dispersion throughout the tissues as both closely spaced injection spots remained distinct throughout the implantation. While considering only the solid fraction, we noted a 3.5 to 4-fold reduction in implant volume 1-month post-implantation. Yet, a remodelled translucent tissular structure remained visible at this stage. No clinical signs of inflammation (i.e., redness, swelling) were detected during the implantation period.

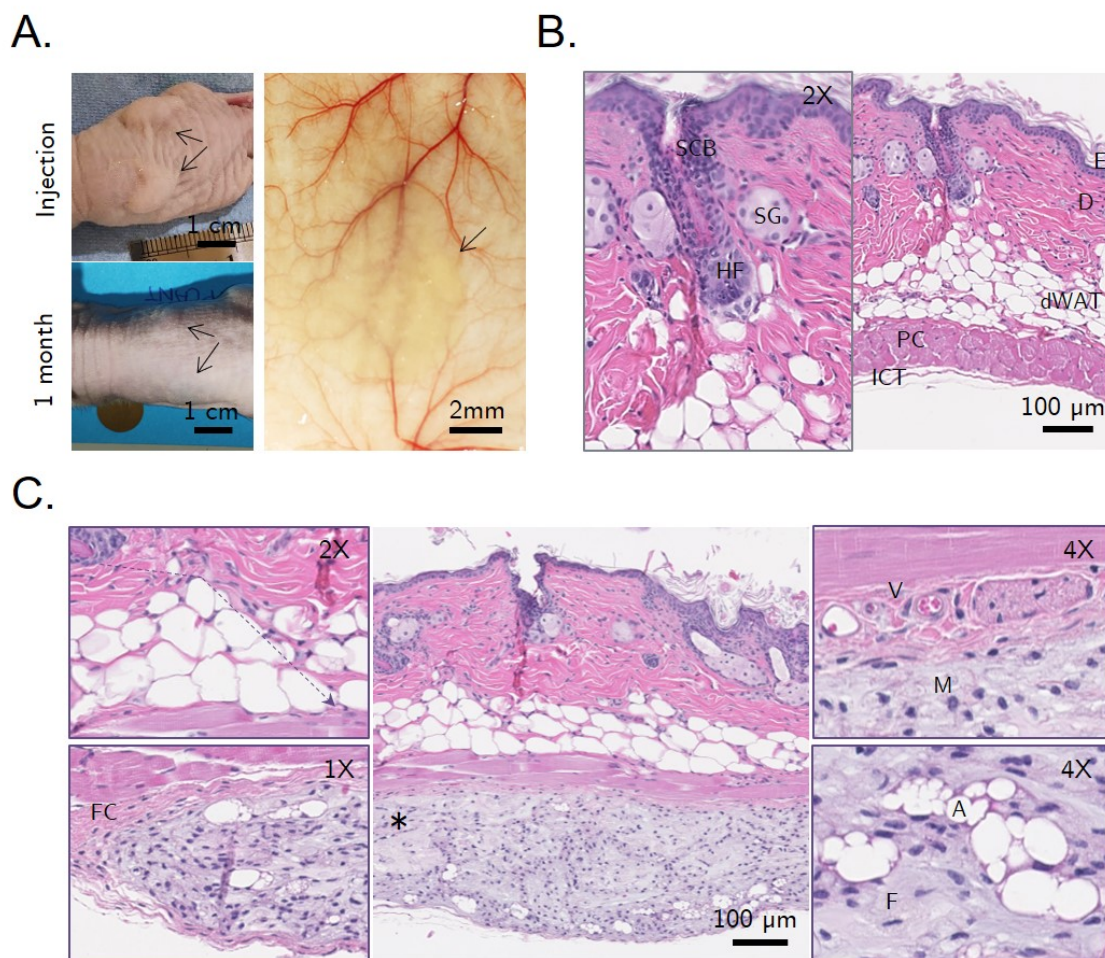


Figure C3.7: 1-month *in vivo* integration of a *V. carteri* suspension only injectable. A. Post and follow-up implantation photographs showing the volume evolution and macroscopic aspect of the implant (blacks arrows) at 1-month post-implantation, B. Histopathological examination of a control skin specimen exhibiting normal tissue structuration (E: epidermis, D: dermis, dWAT: dermis white adipose tissue, PC: panniculus carnosus, ICT: interstitial connective tissue) emphasizing the hair follicle significance in remodelling the cutaneous microenvironment (HF: hair follicle, SG: sebaceous glands, SCB: Stem cell bulge), C. Histopathological examination of *V. carteri* injectable implant (*: implant, FC: fibrous capsule, V: blood vessels, M: macrophages, A: adipocytes, F: Fibroblasts, purple arrow: cellular infiltration)

The anatomopathological study showed the replacement of the *V. carteri* suspension by a mesenchyme-like tissue at 1-month post-implantation. This 500 μm thick-remodelled tissue

presented a homogeneous extracellular matrix, cellular infiltration and integration in a fibrous capsule structurally similar to the interstitial connective tissue overlaid with standard tissue layers of epidermis, dermis, dermal white adipose tissue and the panniculus carnosus without visible alteration or algal infiltration. Athymic mice only grow an 'abortive' reduced hair [389] but still displays numerous hair follicles integrating associated structures such as sebaceous glands and stem cell bulge. No vascular structures were properly visualised in the remodelled tissue. However, blood vessels were found in the surrounding interstitial tissue, showing that the remodelled tissue must be infiltrated and supplied by capillary systems we were unable to observe. The developed extracellular matrix showed no remaining algal structures but comprised numerous foamy macrophages and fibroblasts, indicating that material degradation and matrix remodelling could still be ongoing under mild inflammatory conditions. Interestingly, this mesenchymal tissue displayed niches of about ten growing adipocytes distributed throughout the implant, particularly in its lower part.

C3.4 Discussion

Adipose tissue engineering has recently emerged as a growing field in regenerative medicine aiming to remedy adipose tissue lost upon severe trauma, burns or tumour resection. Unfortunately, the biomaterials currently available for adipose tissue substitution still face limitations guaranteeing long-term tissue regeneration. Natural constituents, being mostly extracellular matrix elements, are sensitive to remodelling, easily, and rapidly eliminated by the organism. In contrast, synthetically-derived materials display better volume preservation but lack naturalness to produce structural and functional soft tissue regeneration. Such material usually generates a foreign body response stabilizing the volume by isolating it from the rest of the body by encapsulation into a fibrous tissue [390],[177]. Recently, research efforts focus on the design of bioactive materials targeting specific regenerative mechanisms [370].

The *in vitro* adipogenesis aiming at differentiate mesenchymal stem cells into preadipocyte, with the ultimate goal to produce mature adipocytes, is commonly induced mainly with dexamethasone (DEX), isobutylmethylxanthine (IBMX), and insulin. Those chemicals trigger a series of transcription factors, including CREBP, KLF4, 5, and 9, CEBP β and δ that will subsequently activate the second wave of adipogenic gene inducers, PPAR γ , CEBP α and SREBP [391]. The duration, degree and type of adipogenic differentiation achieved differ according to the cell type (i.e., stem cell origin, primary pre-adipocyte) and the composition of the induction cocktail. Differentiation protocols generally require about 10 days of culture, without ultimately reaching the unilocular white adipocyte stage in 2D culture [184], [392], [393]. The morphological distinction between white, brown and beige adipocytes is very limited, especially at early developmental stages encountered *in vitro*. Type-specific transcript markers are usually necessary to distinguish them reliably [394]. Additionally, adipocytes have astonishing plastic properties demonstrating trans-differentiation capacities of fully mature adipocytes [391], [395]. While phenotyping determination is essential

apprehend adipogenesis mechanisms in the context of metabolic pathologies, in the context of soft tissue regeneration, the adipocyte differentiation efficiency is often limited to their ability to generate lipid droplets, regardless of the type of adipocytes formed.

C3.4.1 *V. carteri* promote both C3H/10T1/2 and hASC adipogenesis *in vitro*

V. carteri living building block culture generated a massive lipid droplets synthesis and maintenance in culture duration on both C3H/10T1/2 and hASC, undeniably demonstrating the capabilities of the alga as a material to promote adipogenesis without any addition of induction factors. hASC exhibited both cytoskeleton anisotropy as well as nucleus polarisation and roundness alteration as early as 48h, reflecting a significant shift towards the adipogenic pathway [393], [396]. By contrast, 2D adipogenic differentiation of both C3H/10T1/2 and hASC would necessitate 7 to 10 additional days of culture post-confluency in an adipogenic induction medium including at least insulin and thiazolidinedione-insulin sensitizers [397], [398]. While the number of microdroplets per cell for hASC increased as the culture progressed, no significant growth in lipid microdroplets size was observed. On the contrary, a distinct lipid microdroplet expansion could be observed for C3H/10T1/2. This differentiation limit can be explained by interspecies differences in their lipid accumulation mechanisms, especially regulated by PPAR γ . Unlike mouse adipose cells, human adipose cells cannot secrete *in vitro* endogenous PPAR γ ligands requiring a PPAR γ agonist supplementation into their adipogenic medium [399]. Under glucocorticoid responsiveness, a human-specific endogenous LMO3 transcript has been found to modulate human adipocyte differentiation by acting on PPAR γ , between the early and late phases of adipocyte differentiation [400]. To reach advanced adipocyte differentiation, *in vitro* exogenous sources of PPAR γ ligands could be added by supplementation in the medium or by establishing co-culture including PPAR γ ligands secreting cells such as human adipose tissue-derived microvascular endothelial cells [401]. To further assess the level and nature of the adipocyte differentiation induced by *V. carteri*-mediated culture, adipogenic genes and transcription factors expression levels, adipokines (e.g., adiponectin, leptin) as well as lipoprotein lipase secretion levels could be quantified. Moreover, type-specific and advancement-specific differentiation markers could be screened by immunostaining.

C3.4.2 *V. carteri* provide stiffness in the range of soft tissues

As 2D hormone-induced cultures have shown limitations for mesenchymal stem cells differentiation into fully mature adipocytes, biomaterials are engineered to employ stem cell mechanobiology to promote differentiation. As an example, hASCs can differentiate into neurons, adipocytes, myoblasts, or osteoblasts when cultured on substrates with stiffnesses of 0-1, 2-4, 8-10, and >30 kPa, respectively [177], [282], [402], [403].

V. carteri provided a spherical substrate with an overall stiffness of about 3 kPa, stable regardless of colony diameter and stage of development, demonstrating the homogeneity of the mechanical properties offered by the suspension. *V. carteri* colony stiffness uniformity

results from the active, complex and efficient membrane and extracellular matrix mechanisms ensuring optimal algal integrity throughout the algal development. *V. carteri* exhibits adipocyte to adipose tissue like-stiffness, commonly presenting Young moduli of 0.5-2kPa [393], [404], [405]. The poor resistance to deformation of the *V. carteri* colony may be attributed to the high quantity of hydroxylated proline conferred by perlecan predominance in the ECM, as proline hydroxylation has been shown to improve collagen elasticity [406]. *V. carteri* mechanical adipose mimicry could induce adipocytic differentiation of mesenchymal stem cells. Indeed, it has been shown that *in vitro* recreation of adipose rigidity can stimulate adipogenesis of human adipose-derived mesenchymal stem cells without the use of chemical media additives [177]. *V. carteri* fully fits within the 2-4 kPa range of estimated optimal stiffness for adipogenesis mechanical induction [403]. Mesenchymal stem cells cultured on flexible substrate significantly reduce their cell surface area and aspect ratio as a result of low cytoskeleton contractility [407], influencing adipocyte differentiation via ERK signalling [408], promoting upregulation of gene expression of all three adipogenic markers (i.e., PPAR γ , CEBP α and aP2) and lipid accumulation [177]. The actin cytoskeleton reorganization dynamics also affect the roundness of the nucleus during adipocyte differentiation [409].

The relevance of *V. carteri* as a template for adipocytes expansion and differentiation is also highlighted by the fact that most engineered materials demonstrate Young modulus significantly higher ($E \approx 1$ MPa) than soft tissue they aim at reproducing (1-10 kPa). Indeed, Young's modulus of fibrillar proteins, which often make up these materials, is much greater than that of tissue component assemblies, which in turn are significantly stiffer than the elastic properties of bulk tissue samples [410]. As demonstrated in the case of obesity, ECM stiffness increase impaired adipogenesis, blunting the sensitivity to insulin and lipolytic cues, as well as the secretion of adipokines [411], stiffer biomaterials (> 4 kPa) are not suitable, failing to support adipogenesis.

In addition to adipocyte stiffness adequacy, *V. carteri* colonies sphericity could promote adipogenesis. Indeed, the cellular geometry driven by cellular contractility influences MSC differentiation, cells in rounder shapes that promote low contractility preferred to follow an adipocyte lineage, while elongated shapes promote increased myosin contractility which enhances pathways associated with osteogenesis [407]. The static strain imposed by adipocytes on neighboring preadipocytes promotes their differentiation [412]–[414].

An investigation by nanoindentation of the reconstructed tissue stiffness could be carried out during and at the end of the culture, to identify any modifications in Young's modulus of the *V. carteri* substrate and the formed preadipocytes *in situ* to fully evaluate the extent to which *V. carteri* mechanically influences adipogenesis. It would provide insights into the impact of both *in vitro* culture and compact stacking on *V. carteri* mechanical properties and the mechanical environment provided *in fine* to the cell at the cell level. Furthermore, it could enable to characterize the preadipocyte differentiation as adipocytes, and adipose tissues

soften with lipid accumulation, displaying Young's moduli of 3-4 kPa as mesenchymal stem cells versus 0-1kPa when differentiated into adipocytes [393].

C3.4.3 Potential impacts of *V. carteri* structural and molecular components

Adipogenesis is a central process involved in and reciprocally impacted by the regulation of many vital structural, mechanical, thermogenic, metabolic and endocrine functions. So far, *V. carteri* as a whole and evolved organism constitute a source of unexploited compounds for tissue engineering, regenerative medicine, and pharmaceutical purposes.

C3.4.3.1 Providing an ECM-like to basal membrane-like micro-environment

V. carteri represents a highly evolved and structured microorganism, constituting a study model of embryogenesis, morphogenesis and cellular differentiation extensively investigated. While *V. Carteri's* full genome has now been sequenced [26], only a subset of the proteins expressed by the organism has been experimentally described. Indeed, as a major structural constituent and glycoprotein of *V. carteri* cell wall and extracellular matrix, only 7 of the 49 pherophorins identified by gene analysis have been experimentally examined to determine their composition, localization, and function in the *V. carteri* colony [77], [88], [94], [95], [415], primarily for developmental biology purposes.

The Eukaryotic Orthologous Groups (KOG) annotation genome analysis (Fig. ??), which searches for protein analogies between *V. carteri*-predicted proteins and eukaryote proteins, revealed a variety of analogies, covering a broad range of essential organism processes classified in terms of functionality. As possible ligands diffusing or being exposed at the algal surface, predicted extracellular structures of interest were found within the cellular processes and signalling category. These proteins are involved in glycoprotein modification (e.g., exostosin 1 and 2), extracellular matrix building (e.g., collagen IV and XVIII and laminin alpha and gamma), cell adhesion (e.g., teneurin), or protein interactions (e.g., von Willebrand factor). Pherophorins were hypothesised to mediate cellular adhesion to *V. carteri* colonies in Chapter C1 due to their preponderance in the algal composition [76], [345], [346], their dense and fibrous nature, even on the outer surface of the algae [124], [416] and their functional equivalence to collagen in the development of extracellular structure [94], [174]. Interestingly, only three predicted proteins (i.e., Volca2_1|8156, Volca2_1|9651, Volca2_1|1961) enriched in proline amino acids demonstrated substantial homologies ($10^{-50} \leq E - value < 10^{-02}$) or identities ($E - value < 10^{-50}$) of sequences with pherophorins under BlastP sequence comparison. When the collagen IV and XIII functionally related predicted proteins were analysed against human collagen sequences, three protein sequences (i.e., Volca2_1|353, Volca2_1|10809, Volca2_1|14504) revealed high sequence homologies with a significant number of human collagens (e.g., COL I, COL II, COL IV, COL VI). These sequences contained hundreds of G-X-Y motifs, suggesting structural homology with collagen via a triple helix motif. This motif constitutes an highly conserved adhesion site for $\alpha 1\beta 1$ and $\alpha 2\beta 1$ integrins-mediating cell adhesion that allowed animal multicellularity and tissue

evolution [417]–[419]. The availability of an RGD motif as provided by Volca2_1 | 353 and Volca2_1 | 14504 would enable additional integrin binding opportunities (i.e., $\alpha 1\beta 1$, $\alpha 3\beta 1$, $\alpha 5\beta 1$, $\alpha V\beta 1$, $\alpha V\beta 3$, $\alpha V\beta 5$, $\alpha V\beta 6$, $\alpha V\beta 8$, $\alpha IIb\beta 3$ integrins) to enhance cell adhesion in the same way that fibronectin does [420], [421]. Furthermore, the six predicted laminin subunit-like proteins (e.g., Volca2_1 | 5511, Volca2_1 | 10243, Volca2_1 | 11791) confirmed sequence homologies to one or more human laminin subunits α , β or γ . Since many collagens and laminins are proteins formed by multiple subunits combination, these sequence homologies should be associated by conformations favourable for interaction with integrins to generate the integrin conformational switches that control its bidirectional outside-in and inside-out signalling. Given this, a laminin analogy could engage further additional interactions with integrins $\alpha 1\beta 1$, $\alpha 2\beta 1$, $\alpha 3\beta 1$, $\alpha 6\beta 1$, $\alpha 6\beta 4$, and $\alpha 7\beta 1$ [422].

Although the synthesis of such proteins has yet to be identified experimentally, it nevertheless highlights *V. carteri*'s potential for the development of a primitive and complex extracellular matrix within and on the colony's surface, structurally supported by a phosphorin-rich content and clustered with adhesive proteins. *V. carteri* may provide a basal membrane-like microenvironment (e.g., COL I, COL IV, COL V, COL VI, laminin, sulfated proteoglycans) with attachment points for integrins and other extracellular matrix receptors, influencing stem cell and preadipocyte differentiation via insulin sensitivity and systemic metabolism [423]–[425]. Indeed, the nature of the extracellular matrix influences adipogenesis initiation, progress and outcome via integrin-mediated signalling. ASCs dissociate integrin $\alpha 5$ and αV -mediated interactions with fibronectin RGD and LDV motifs to favour integrin $\alpha 6\beta 1$ and $\alpha 7$ -mediated interactions with laminins [426], [427] to engage in the adipocyte differentiation pathway. COLIII has been shown to be necessary for preadipocyte maturation into adipocytes influencing the ECM expression levels, particularly COL IV $\alpha 1$, COL VI $\alpha 1$, and fibronectin [428], [429]. Collagen VI, abundant in adipose tissue, inhibited ERK1/2 phosphorylation to enhance preadipocyte maturation by increasing the expression of adipocyte-specific factors such as SREBP-1c, PPAR γ , C/EBP α and β [430]. Mice with a null mutation in laminin 4 show a simultaneous reduction in COL I $\alpha 1$ and COL III $\alpha 1$ expression, as well as $\alpha 7$ and $\beta 1$ integrin expression, promoting adipocyte beiging and thermogenic capabilities [431]. The *V. carteri* adipose basal-membrane-like micro-environment should play a role in the mimicry of adipocyte and adipose tissue, driving adipogenesis. *V. carteri* adipose basal-membrane like micro-environment could participate in the mimicry of adipocyte and adipose tissue promoting adipogenesis by physical neighbouring strain. The white adipocyte phenotype could be particularly reproduced, as the highly conserved transmembrane proteins teneurin 2 and 4, showing homology to the predicted protein Volca2_1 | 7751, demonstrated high levels of expression in white adipocyte repressing the transcriptional activity of ZIC1 which is specific marker of brown adipose tissue [432], [433].

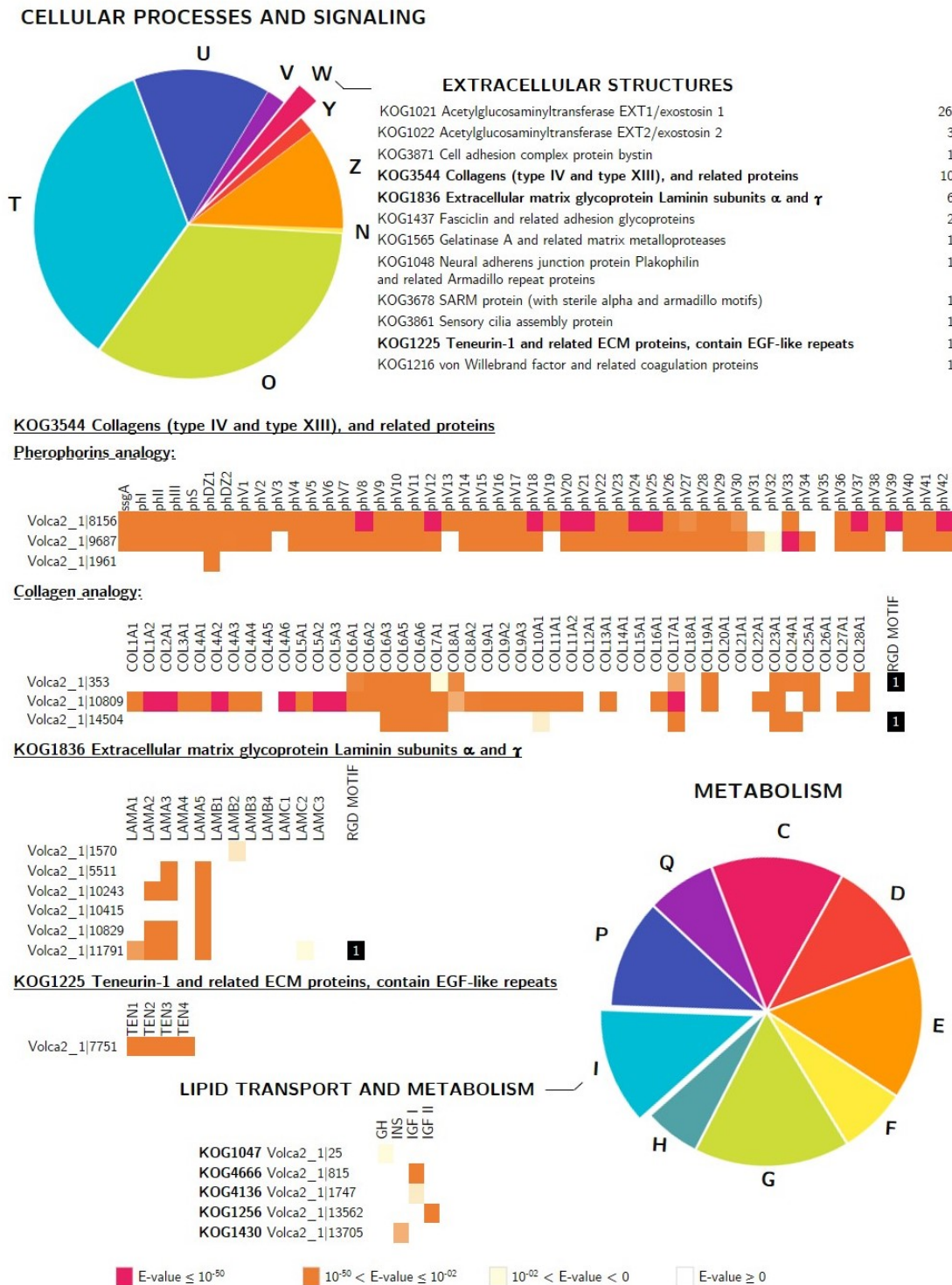


Figure C3.8: Sequence homology screening using BlastP [434], [435] based on EuKaryotic Orthologous Groups (KOG) annotation analysis of *V. carteri* [26] focusing on extracellular matrix and lipogenesis analogues. KOG classification and protein homologies heat map (C: Energy production and conversion, D: Cell cycle control, cell division, chromosome partitioning, E: Amino acid transport and metabolism, F: Nucleotide transport and metabolism, G: Carbohydrate transport and metabolism, H: Coenzyme transport and metabolism, I: Lipid transport and metabolism, P: Inorganic ion transport and metabolism, Q: Secondary metabolites biosynthesis, transport and catabolism, M: Cell wall, membrane, envelope biogenesis, N: Cell motility, O: Post-translational modification, protein turnover, chaperones, T: Signal transduction mechanisms, U: Intracellular trafficking, secretion, and vesicular transport, V: Defense mechanisms, W: Extracellular structures, Y: Nuclear structure, Z: Cytoskeleton, ph: Pherophorin, COL: Collagen, LAM: Laminin, TEN: Teneurin, GH: Growth hormone, INS: Insulin, IGF: Insulin growth factor).

C3.4.3.2 Stimulating adipogenesis hormonally

V. carteri possesses a primitive hormonal system comprising phytohormones (e.g., gibberellins, auxins, ethylene, and cytokinins), equivalent to many plants and microalgae and influencing their growth and development [436]. These mentioned phytohormones were identified by a functional study of the genome of *V. carteri* and are thought to be involved in the synthesis pathways of various amino acids and carotenoid biosynthesis [437]. The most studied hormone in *V. carteri* is the sex hormone secreted by male colonies inducing the formation of sexual embryos, while in the absence of the hormone only asexual embryos are formed [80]. Not being considered pheromones, pherophorins nevertheless contain a C-terminal pheromone-like Ph domain [346]. Sequence homologies for insulin and three related hormones (i.e., growth hormone, insulin-like growth factor I and II) were identified by matching protein sequences predicted to be associated with lipid metabolism and transport. Insulin-like growth factors I and II have a similar impact on the promotion of adipocyte differentiation and maturation to insulin as they share amino acid sequence homologies. IGF I demonstrate more than 60% homology with proinsulin [438]. IGF II presents about 67% homology with IGF I [439]. As a metabolic process, adipogenesis is subject to regulatory effects. While GH acts directly to reduce adipocyte size and enhance lipolysis through activation of the GH receptor, it also stimulates insulin-like growth factor IGF I synthesis, which in turn can stimulate cellular glucose uptake in preadipocytes and adipocytes via both the insulin receptor and the IGF I receptor [440], [441]. IGF II demonstrate similar combined effects as IGF I as it can bind insulin, IGF I, and IGF II receptors [442]. Insulin activates both PI 3-kinase and the prenylation pathways, triggering the induction of a series of adipogenic transcription factors that govern the differentiation of pre-adipocytes into mature adipocytes [443]. While further research into such analogous proteins is required, *V. carteri* may exhibit additional adipogenic endocrine and paracrine effects via insulin-like proteins.

C3.4.4 *V. carteri* promote tissue regeneration and adipogenesis *in vivo*

The *V. carteri* suspension implant displayed *in situ* soft tissue regeneration properties upon subcutaneous implantation, as endogenous cells were able to infiltrate the implant while developing a thick extracellular matrix. The malleability of *V. carteri* colonies' compact stacking and their surface cell adhesion capabilities allow for transitory anchoring and settling of cells, facilitating cellular migration, proliferation and matrix deposition. The heterogeneous outlines of the sphere-stacked suspension also enhance smooth fusion with the surrounding tissue [444]. While microspheres have been mainly incorporated in the past in the form of non-degradable polymeric nanoparticles and microparticles to improve the *in vivo* stability of collagen and hyaluronic acid filling for soft tissue augmentation of the lips, mouth and skull [215], [445], Zhang et al. [446] recently demonstrated that polymeric PLLA beads could stimulate endogenous collagen regeneration via long-term degradation (i.e., 13 months). Yet, to the best of our knowledge, this is the first application of natural acellularised individual degradable sphere packaging system for soft tissue regeneration purposes.

The suggested mechanism for *V. carteri* implant cell colonisation, tissue integration, and matrix remodelling is illustrated in Fig. C3.9. We hypothesize that *V. carteri* causes a mild local inflammatory response, as it must be targeted by the organism, showing the infiltration of inflammatory cells (i.e., monocytes, pro and anti-inflammatory macrophages), fibroblastic cells, mesenchymal stem cells and progenitor cells collectively mediating angiogenesis, inflammation reduction and tissue regeneration [447]. *V. carteri* colonies must be disrupted and eliminated by macrophage and fibroblast phagocytic mechanisms, as outlined in Chapter C2. Residual *V. carteri* material could facilitate the building up of neo extracellular matrix, both stabilizing cell anchorage and matrix deposition via protein-protein interactions, forming a remodelled homogeneous mesenchymal tissue.

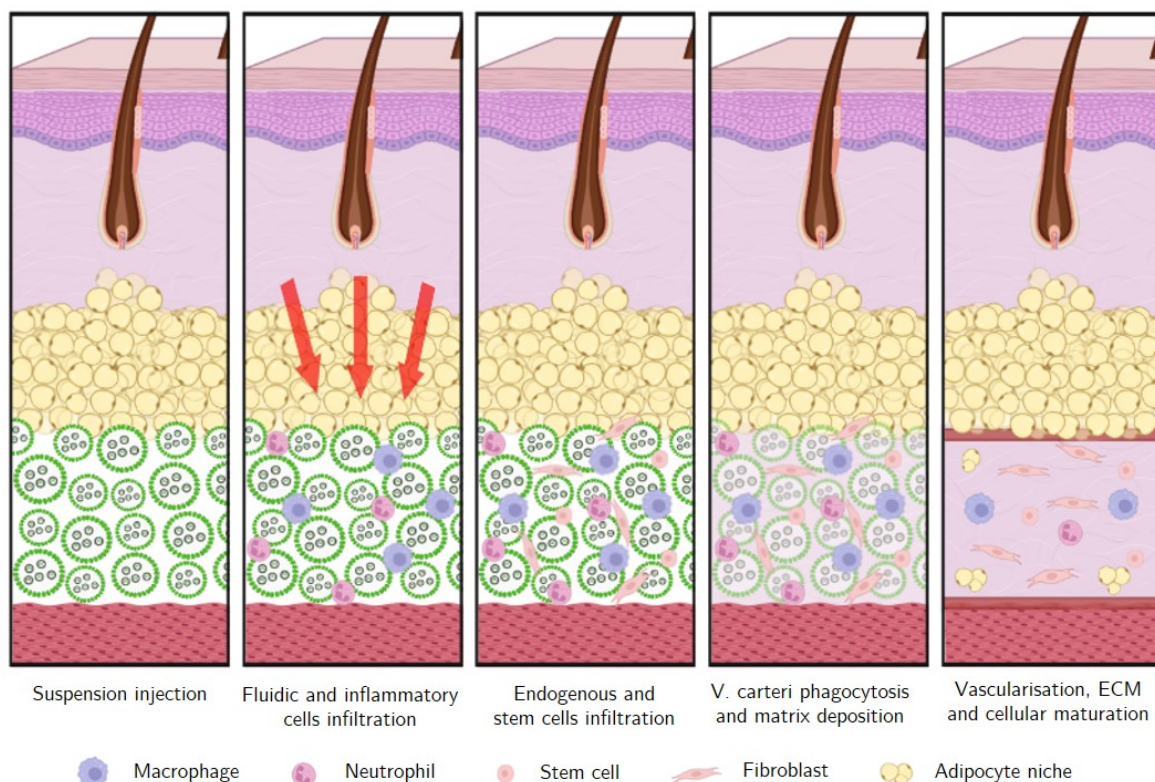


Figure C3.9: Suggested mechanism of *in situ* soft tissue regeneration mediated by *V. carteri* saturated suspension injection Created with BioRender.com.

While the mesenchymal tissue generated by *V. carteri* demonstrated tissular development to the degree observed upon 4-weeks implantation in collagen-based implants, including matured collagen bundles and neovascularisation on the implant's periphery [448], it also showed advanced adipose tissue niche development. *V. carteri* stiffness adequacy with adipose tissue stiffness must have promoted the adipocyte differentiation of infiltrated MSC and progenitor cells as mechanical and biochemical conditioning have been shown to be both equivalent and sufficient to drastically boost *in vivo* adipogenesis [449]. Indeed, *in vivo* ectopic adipogenesis have been previously successfully biochemically induced by triggering adipogenic genes activation mediated by PPAR- γ via material loading with rosiglitazone [449]), pioglitazone [450], [451] or insulin and IGF I [452]. Additionally, great enthusiasm

is also observed for decellularised dermis matrix [453], basal membrane [454] and adipose tissue [455] based-materials as these complex matrices that contain a wide variety of both structural (e.g., COL I, COL III) and adipogenic proteins (e.g., COL IV, COL VI, laminin) while additionally providing growth factor sourcing (e.g FGF2, VEGF-A, IGF I) have shown the capacity to efficiently support adipogenesis *in vitro* and *in vivo*. Yet, this type of induction often requires *in vitro* predifferentiation prior to implantation [456].

Our preliminary research has shown that *V. carteri* could rapidly induce adipogenic differentiation simultaneously with the inflammatory response, permitting the development of adipocyte niches. The simultaneity of such processes emphasizes how *V. carteri* may be a suitable compromise to promote healthy tissue regeneration by balancing the beneficial and negative impacts of the inflammatory response. Further research should be undertaken to precisely characterise the mechanism of *V. carteri* colony disruption in the early phase of implantation as well as to assess the maintenance and stability of long-term tissue regeneration (e.g., ECM maturation, adipose tissue expansion) via prolonged implantation. Delaying *V. carteri* disintegration or considering the simultaneous implantation of undifferentiated or pre-differentiated stem cells are levers that will allow initiating the differentiation of more stem cells and progenitor cells to expand the proportion of the adipose tissue into the formed mesenchymal tissue. In addition to subcutaneous implantation, a lumpectomy model should be considered to model the regenerative properties of *V. carteri* in a wound healing context restoring the structural and mechanical continuum required following tumour removal, as well as supporting the regeneration of a complex adipose tissue-based organisation as it exists in the breast environment.

C3.5 Conclusion

V. carteri is a biomaterial that promotes adipogenesis. Its adipogenic effects, demonstrated both *in vitro* and *in vivo*, are directly tied to its capability to mimic adipose tissue structurally, mechanically, and molecularly, as we suspect it to deliver primitive biochemical cues of extracellular matrix, cell adhesion, and lipid accumulation.

**Part D - *Volvox carteri* bioinspired
material, plant-based alternatives for
tissue engineering and regenerative
medicine**

Chapter D1

Cellulosic/Polyvinyl alcohol composite hydrogel: synthesis, characterization and applications in tissue engineering

*To counterbalance the structural and molecular complexity of *V. carteri*, we also engaged in the development of bioinspired materials from the algae for tissue engineering purposes that would be chemically and structurally fully characterised. As an analogy to *V. carteri* that we used as a structural block in our tissue development, we have produced here a composite hydrogel based on cellulose, the vegetal basic structural unit. This chapter corresponds to the published article: M. Stricher, C.-O. Sarde, E. Guénin, C. Egles, and F. Delbecq, "Cellulosic/polyvinyl alcohol composite hydrogel: Synthesis, characterization and applications in tissue engineering," *Polymers*, vol. 13, no. 20, p. 3598, Oct. 19, 2021, ISSN: 2073-4360. DOI: [10.3390/polym13203598](https://doi.org/10.3390/polym13203598).*

D1.1 Impact of the oxidation level on the DMCC particle size

Extra pure microcrystalline cellulose (MCC) was oxidised with 6.25, 12.5 or 25% w/w sodium periodate to obtain three different DMCC powders. Yields of 90-95% were obtained for DMCC 9% and 18%, while a loss in mass of 40% was observed for DMCC 36%.

These DMCC powders were observed by scanning electron microscopy and quantified by measuring the surface area. The aspects displayed by the cellulose particles show, in Fig. [D1.1](#), a significant fragmentation of the particles compared to the commercial microcrystalline cellulose. After oxidation, a global disappearance of $>50\,000\ \mu\text{m}^2$ particles, a 50% decrease of 5000 to $50\,000\ \mu\text{m}^2$ particles and a multiplication of 50 to $100\ \mu\text{m}^2$ particles going from 47% to 62-74% of total particles was observed. The presence of the generated dialdehyde groups and material crystallinity were also investigated later respectively by FTIR and XRD studies when DMCC powders were included in the composite hydrogels.

In parallel to the size and shape investigations, the number of aldehyde functions (CHO) was evaluated upon reaction with DNPH in acidic conditions. Indeed, aldehydes were converted to DNP through the formation of hydrazones. The quantification of the unreacted DNPH enabled the determination of the DNPH consumption which gave, in turn, an aldehyde content estimation. The tests were performed in triplicate to ensure the reproducibility

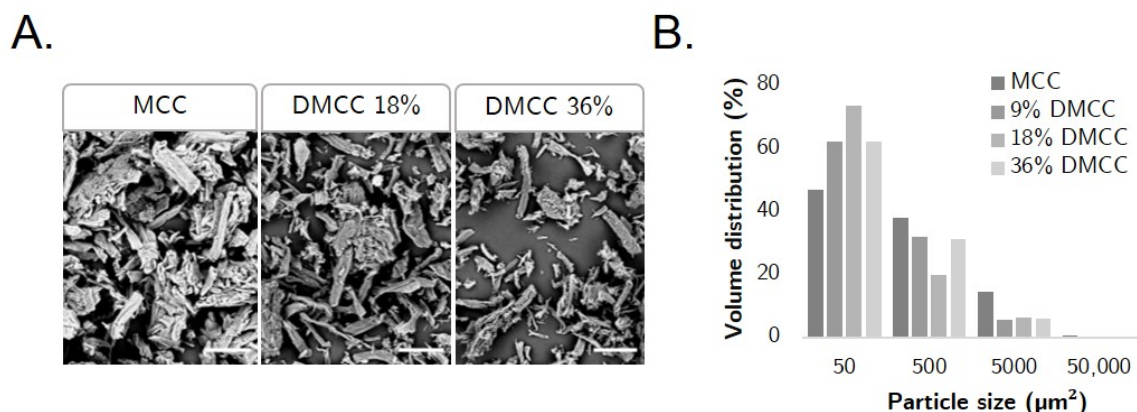


Figure D1.1: Morphological analysis of dialdehyde (DMCC) and non-oxidised micro-crystalline cellulose (MCC) particules. A. MEB visualisation (Scale bar: 100 µm), B. Granulometric distribution of cellulosic powders. Figure modified from [302].

of the method. Based on this principle, DNPH assays showed aldehyde levels of 5,3% and 11,3% in the DMCC 9% and 18% samples respectively. The precise determination of CHO contents was not possible for the 36% sample due to the variability in the UV measurement response. This result can be currently explained by the instability of the opened glucose ring in strongly oxidised DMCC, especially in presence of primary amines as for DNPH. The non-linearity of Schiff base formation for DMCC has already been demonstrated, lower levels of imine formation than the actual amount of CHO groups were observed [457]. On the other hand, the hydroxylamine hydrochloride reacted with aldehydes to form oximes and thus released hydrochloric acid (HCl) causing the pH drop of the medium. By titration of HCl with NaOH solution, it was possible to determine the molar number of aldehyde functions grafted on the surface of the polysaccharide backbone. Using this method, rates of 32,7%, 11,7% and 9% were obtained for DMCC 36%, 18% and 9% respectively.

Table D1.1: DNPH/Hydroxyproline CHO dosage. Table modified from [302].

Theoretical DMCC levels (%)	Experimental DMCC levels via DNPH method (%)	Experimental DMCC levels via Hydroxylamine method (%)
9	5,3 ± 0,6	9,0 ± 1,0
18	11,3 ± 0,6	11,7 ± 1,5
36	ND	32.7 ±

D1.2 Strategy for producing the DMCC/PVA scaffolds

The proposed protocol for the synthesis and shaping of cellulose/PVA scaffolds based on the functionalization of cellulose through aldehyde functions via classical sodium periodate oxidation was schematised in Fig. D1.2. For all DMCC/PVA formulations, the scaffold fabrication was allowed via a performant remodelling of both polymeric cellulose and PVA networks using a simple degeneration process in an NMP/LiCl system, followed by the regeneration of a dual robust composite in ethanol. A cohesive material can be obtained

starting from a 9% dialdehyde functionalization and a DMCC/PVA ratio of 1:2. Progressive heating of the polymer suspension led to complete dissolution of the powders between 30 and 50°C, gelation of the PVA around 70°C and finally to the formation of a smooth, viscous and homogeneous paste when the temperature of 90°C was reached. The gradual reconstitution of the networks in ethanol generated a hard and rigid hydrogel that became flexible once fully hydrated in water.

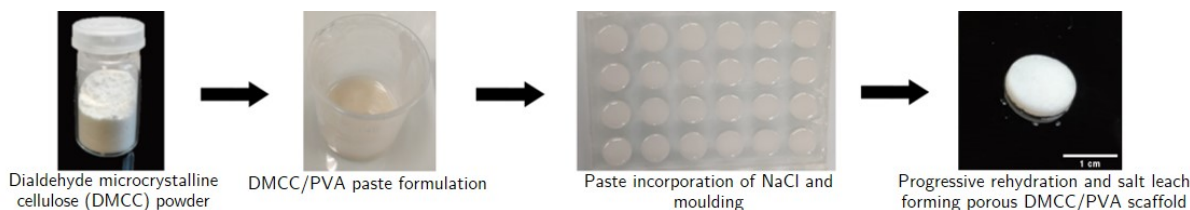


Figure D1.2: MCC hydrogel synthesis. Photographs of the moulding process and formulation of scaffolds based on partial dialdehyde cellulose (here, DMCC 9%/PVA (2:1) 0-500 μm NaCl). Figure modified from [302].

In Fig. D1.3, the XRD profiles of the cellulosic materials demonstrated a diffuse peak from 15° to 16° and 3 additional peaks at 20° , 22.5° and 40° respectively attributed to the (100), (110), (012), (200) and (004) and crystallographic planes. This type of profile was identical to what is commonly observed for type I microcrystalline cellulose [458]–[460]. Moreover, these profiles differed greatly from the PVA pattern. The crystallinity of the scaffolds was thus essentially related to their microcrystalline cellulose composition ($I = 68\%$) [461]. The crystallinity index of the cellulosic samples based on DMCC 9%, 18% and 36% were respectively 62.5, 62.3 and 51.0%. The crystallinity of the samples decreased progressively by oxidation with sodium periodate, demonstrating aldehyde functions formation starting from the furanose ring opening essentially localised at cellulose backbone extremities. The peak at 40° disappeared in the case of DMCC 36%, suggesting a slight modification of chains conformation. For DMCC 9% and 18%, as all the signals were observed, long domains of the cellulose backbone were assumed to remain unchanged.

The FTIR spectra logically displayed signature signals for PVA and cellulose, both basic constituents of the materials. For DMCC, a detailed description of the FT-IR spectrum can be found in the literature [462]. For PVA, at 3373 cm^{-1} the broadband (I) corresponds to hydroxyl OH groups involved in intermolecular and intramolecular hydrogen bonds. The 2918 cm^{-1} bands (II) and 1439 cm^{-1} bands represent CH polymer backbone stretching. The CH₂ from the long alkyl chain vibrations were observed at 2052 cm^{-1} . The 1728 cm^{-1} inflexion and $1097\text{--}1149\text{ cm}^{-1}$ multiple bands, in the fingerprint region (III), report C–O stretching. There, the 1145 cm^{-1} band is associated with PVA crystallinity nature (red) [463]–[466]. These peaks were found on the spectra of cellulosic materials attesting to the maintenance of the PVA structure.

As cellulose shares in common groups with PVA, many bands were in common (grey) especially in regions I, II and III. Cellulose specific vibrations (blue) related to C–O and OH

groups were respectively identified at 1057 cm^{-1} at 1650 cm^{-1} [467], [468]. These predominant hydroxyl groups in cellulose tend to adsorb moisture. Bound water is therefore most likely responsible for this last peak [469], [470]. Furthermore, the peaks at 1376 and 1021 cm^{-1} were attributed to CH_2 bending and C-O-C stretching vibration representative of a furanose ring or glucose subunit in the polysaccharide backbone. The characteristic signals of aldehyde groups currently found around 1730 cm^{-1} or 2700 cm^{-1} do not appear in FT-IR charts of the formed hydrogels [471]. The presence of C-O vibrations at 1057 cm^{-1} supported by those found at 1160 cm^{-1} as well as the band at $\text{OH } 890\text{ cm}^{-1}$ respectively were attributed to acetal and hemiacetal bonds [472].

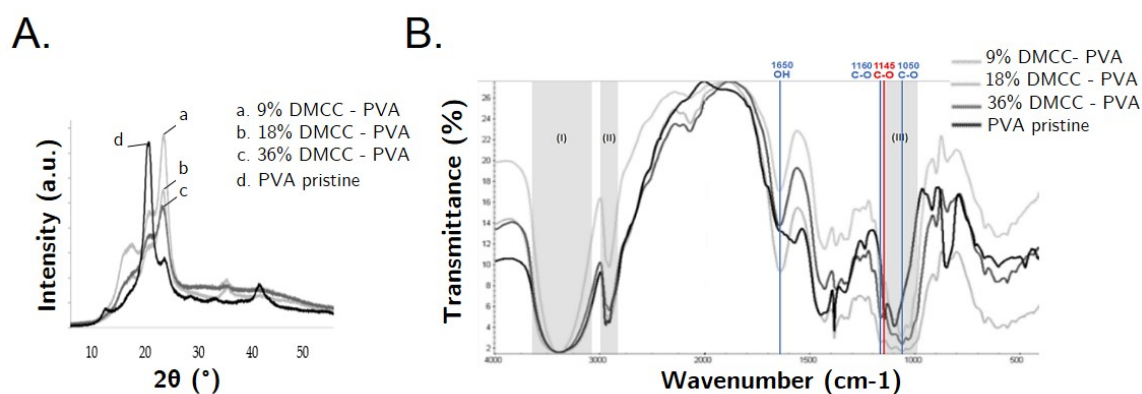


Figure D1.3: PVA and DMCC-based composite scaffolds physico-chemical analysis. A. XRD diffractograms, B. FT-IR spectra. Figure modified from [302]

D1.3 Structural characterization of the DMCC/PVA scaffolds

Cellulose/PVA composite hydrogels were produced controlling DMCC degree of oxidation, DMCC/PVA ratio and its porosity by the addition of porogen agents. Fluorescent blue staining of the cellulose with calcofluor white stain, that binds β -(1 \rightarrow 3) and β -(1 \rightarrow 4) polysaccharides, allows the observation of the macroscopic organisation of the polymeric network. In Fig. D1.4, the increasing cellulose ratio can be interpreted as 50-150 μm long microcrystals homogeneously distributed in a hydrogel loaded with DMCC fibres. This gel exhibits a micrometre-sized porosity attributable to its polymer network. Additional porosity was introduced through the solubilisation of NaCl salts of diameter calibrated between 0-500 μm or 50-100 μm demonstrating average diameters respectively of 305.4 ± 65.3 and $69.6 \pm 16.2\text{ }\mu\text{m}$.

Homogeneous distribution of porosity was obtained but the juxtaposition of the salts does not guarantee the interconnectivity of the pores required for biological applications. Indeed, the hydrogels present high-water contents (above 75% w/w) and an increasing porosity mediated by salt leaching. The degree of interconnectivity obtained by absorption of the free water contained in the hydrogel shows limited interconnectivity with the use of salts 0-500 μm . This was improved by the calibration of salts at 50-100 μm passing from 47.1

to 56.6%. To determine scaffolds potential applications in a biomedical context, we had to evaluate their swelling behaviour and mechanical properties. Dry materials showed similar rehydration profiles. After 1h, a maximum swelling was reached. The hydrogel retained 4 to 8 g of water per g of dried hydrogel, representing 42.6 to 80.0% of the initial average water/dry mass ratio. The deformation of hydrogel was observed for all samples except for the 9% DMCC/PVA (2:1) samples whose porosity was induced by salts of diameter 0-500 μm .

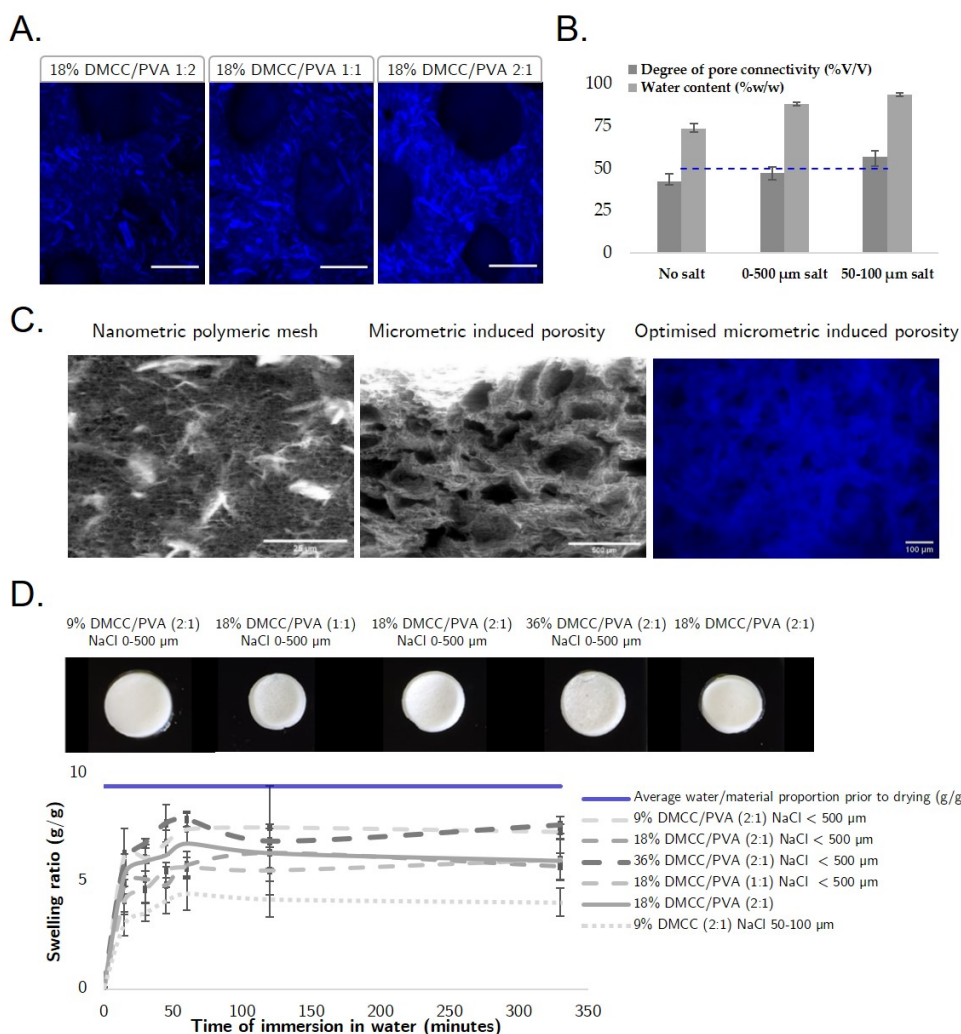


Figure D1.4: Structural analysis of MCC DMCC based scaffold. A. Calcofluor white stained DMCC 18%/PVA NaCl 0-500 μm scaffolds respectively at ratio 1:2, 1:1 and 2:1 showing cellulosic material (blue; scale bar : 250 μm); B. Degree of pore connectivity (%V/V) and water content (%w/w) quantifications modulating salt leaching induced porosity (n=5); C. MEB observation of nano and micro porosities of DMCC 18%/PVA (2:1) NaCl 0-500 μm scaffold; Calcofluor white stained DMCC 9%/PVA (2:1) NaCl 50-100 μm showing enhanced porosity; D. Swelling ratio study including photographs of rehydrated DMCC/PVA based scaffolds. Figure modified from [302].

In Fig. D1.5, the material mechanics was investigated through the estimation of Young's modulus at macroscopic and nanoscopic scales respectively by compression and nanoindentation. Macroscopically, a gradual increase in DMCC proportion significantly increased

the Young's modulus, as DMCC 18%/PVA ratio of (1:2), (1:1) and (2:1) respectively depict Young's moduli of 16.16, 24.25 and 57.21 kPa. The degree of oxidation of the cellulose dialdehyde also seemed to influence the mechanical properties of the hydrogels since Young's moduli of 42.81, 57.69, 20.9 kPa are obtained by compression for hydrogels respectively based on 9%, 18% and 36% DMCC. The introduction of salts leached porosity significantly increased the stiffness of the material moving from a modulus of 19.05 to 57.21 kPa for a DMCC 18%/PVA (2:1) hydrogels. At a nanometric level, when DMCC 9% materials demonstrated identical Young's moduli compared to the macro metric level of 42.86 kPa, DMCC 18% and 36% showed lower moduli respectively of 12.83 and 36.63 kPa.

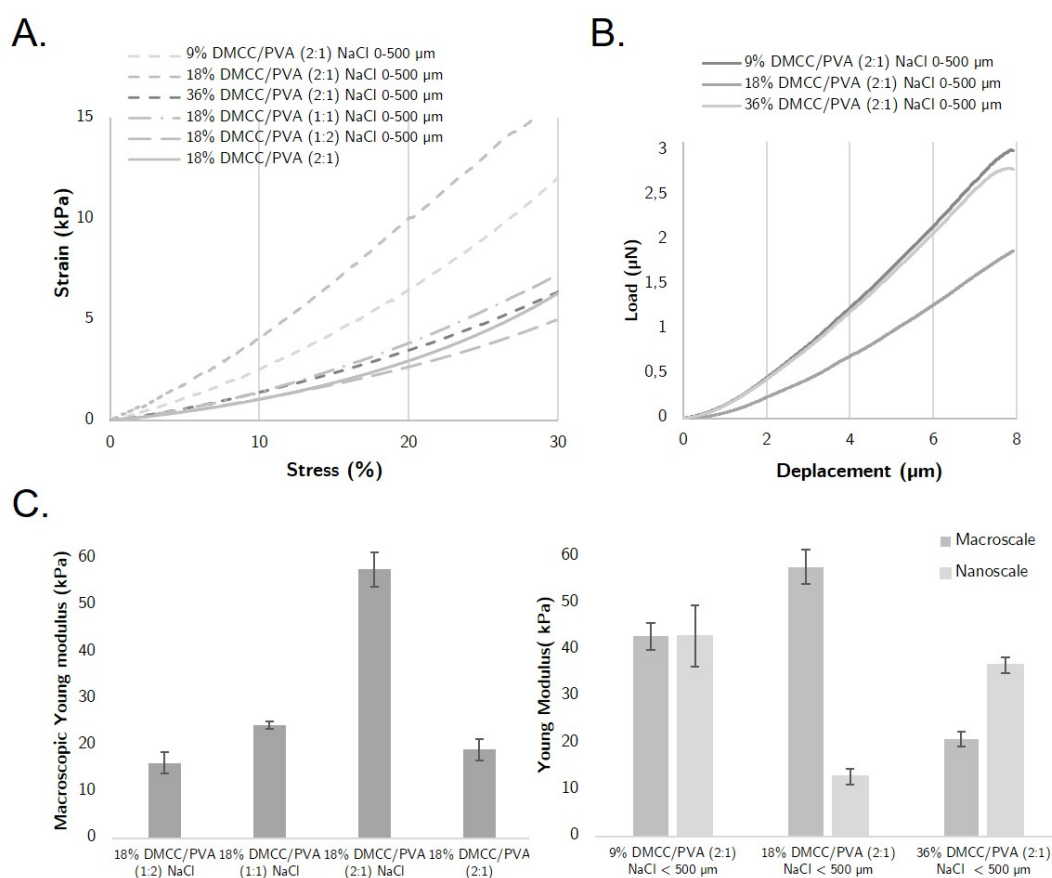


Figure D1.5: DMCC/PVA hydrogels mechanical properties A. Stress-strain curves obtained by compressive test. Compression up to 30%, speed: 0.01 mm/s, sensor: 22N (n=5); B. Load-displacement curves obtained upon 15,000 nm at 3 nm/s nanoindentation. Indenter diameter: 28.5 μm , stiffness: 0.47 N/m (n=3), C. Determination of macroscopic and nanoscopic Young's modulus. All conditions display *** significance except DMCC 9%/PVA (2:1) NaCl < 500 μm samples (***: p-values < 0.001 (ANOVA, Tukey test)). Figure modified from [302]

D1.4 Investigation of DMCC/PVA scaffold potential use for tissue engineering, implantable matrices

Firstly, indirect and direct cell viability were assessed in Fig. D1.6 using regulatory reference cell lineage L929 and for its intended use, primary neonatal human dermal fibroblasts

HDFn. Thus, L929 viabilities of 126.0, 89.4 and 79.9% were respectively obtained with 9%, 18%, 36% DMCC-based hydrogels relatively to an untreated control considered at 100%. The cytotoxic latex used as positive control showed drop-in viability down to 24.9%, while HDF viabilities of 99.7% and 92.8% were achieved with the 9% and 36% DMCC-based hydrogels.

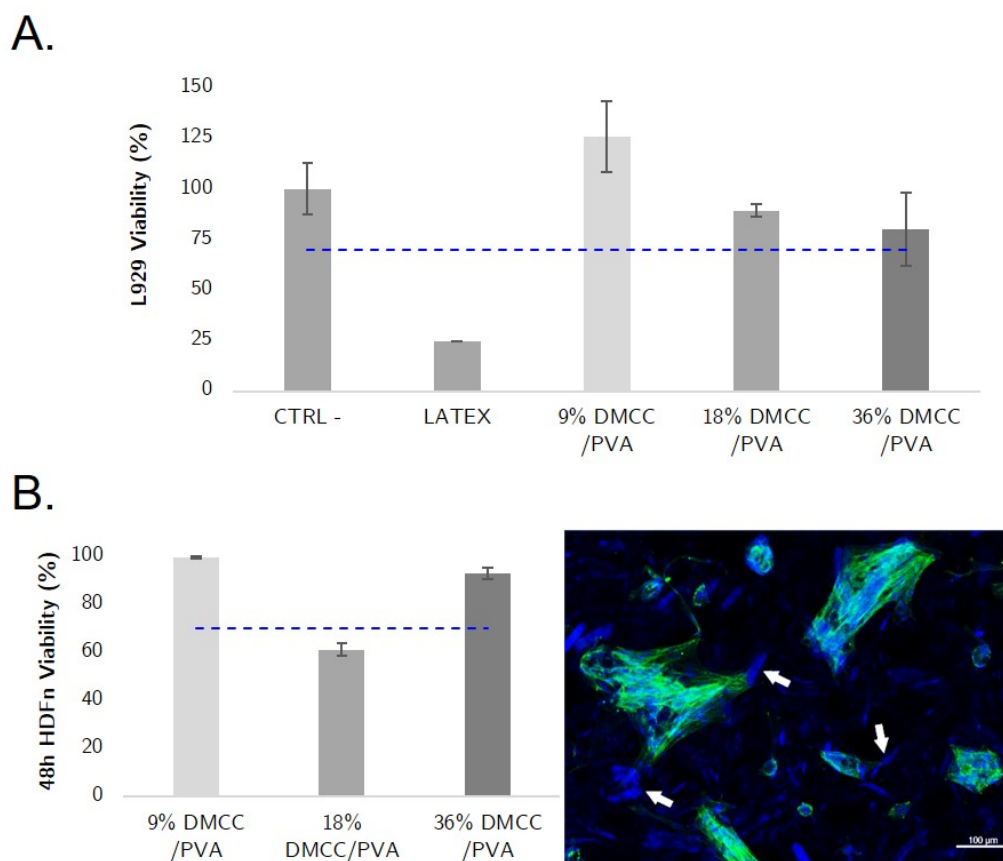


Figure D1.6: DMCC/PVA hydrogels cytocompatibility. A. DMCC/PVA (2:1) NaCl hydrogels cytocompatibility test following the ISO10993 standard protocol ($n = 3$), B. Neonatal human dermal fibroblast (HDFn) cultured on DMCC/PVA (2:1) NaCl hydrogels viability assay at 48 h ($n = 3$), C. Observation of adhered HDFn and spheroid-like structure on 9% DMCC/PVA (2:1) material (DAPI (blue): cell nucleus, Phalloidin(green): cell cytoskeleton, White arrow: cellulose). Figure modified from [302].

A low level of viability of 61.2% was reported for 18% oxidised cellulose-based hydrogel. HDF culture at the surface of porous materials showed good infiltration and pore occupation, with clusters of cells showing both a spread-out actin cytoskeleton that appears to anchor to nearby accessible cellulose particles (white arrows) as well as spheroid-like aggregations of cells.

One-month implantation of all materials in thymus-free nude mice showed no rejection of the implants, demonstrating their physical stability. As shown in Fig. D1.7, the material was completely recovered with no breakage, fragmentation or little to no sign of degradation for all porous and non-porous materials. The implanted area showed at the material interface

a thin fibrous capsule presenting mild to moderate neutrophilic and macrophages inflammatory infiltrates. The DMCC/PVA materials (2:1) of DMCC 9%, 18%, 36% displayed mean inflammatory scores of 3, 2.5 and 2.5 respectively (n=3). The addition of porosity increased the inflammation score to 3.3 for the DMCC 18%/PVA (2:1) material.

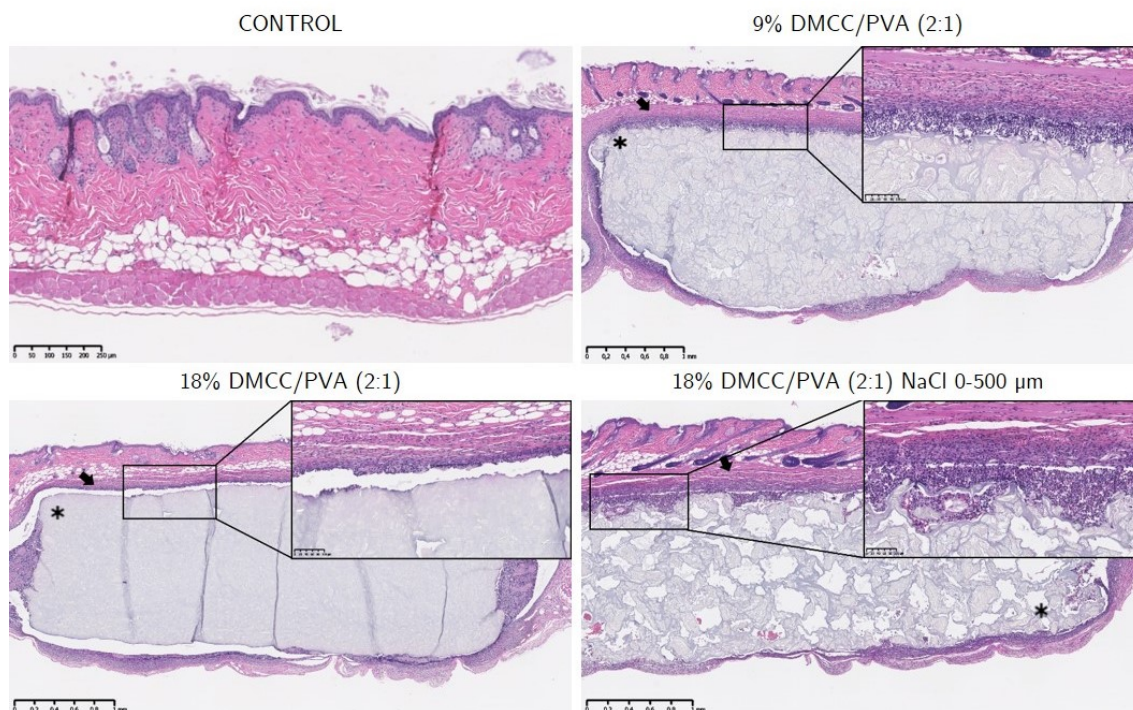


Figure D1.7: DMCC/PVA hydrogels biocompatibility Examination of *in vivo* biocompatibility and biostability of nanoporous and macroporous cellulosic materials in a nude mouse model through histological study upon 1-month subcutaneous implantation (n = 3). (*: cellulosic implant; black arrow: fibrous capsule). Figure modified from [302].

D1.5 Discussion

The loss of soft tissue, fatty, fibrous or muscular tissue, affects a wide spectrum of patients, as it is associated with multiple medical conditions related to trauma, burns, infections, tumour removals, degenerative diseases or autoimmune disorders. In addition to the physical impact of their tissue loss, patients encounter psychological cues linked to the loss of normal body contours that only can be remedied by filling in the affected area. Although common, autologous fat injection presents a need for repeated interventions questioning resulting viability as well as short term stability [473], [474]. Practitioners are still seeking an adequate methodology that can sustain stable volume and long-term tissue regeneration. Thus, biocompatible filling hydrogels such as our DMCC/PVA substitute are particularly promising for the filling of small to large tissue defects.

Our synthesis methodology allowed us to obtain a ready-to-use paste that can be declined in multiple forms, membrane, scaffold or beads completed by moulding, additive manufacturing, extrusion or electrospinning mainly for biomedical applications. Regarding

DMCC/PVA hydrogel synthesis, effective functionalisation of cellulose was obtained using the classical periodate sodium oxidation method. While FTIR and XDR proved the absence of aldehyde groups in our final cellulosic materials, those analyses provide insight into their formation mechanism, high reactivity and resulting bonding. Thus, FT-IR analysis highlighted the cellulose and PVA composition of the DMCC/PVA materials but did not distinguish the dialdehyde functions distinctly. Subsequent signals attributed to acetal and hemiacetal bonds were identified, demonstrating the effectiveness of the NMP/LiCl system for simultaneously strongly cross-link PVA and DMCC and engage electrostatic interactions to stabilise the hydrogels. XDR demonstrated a significant decrease of the crystallinity index linked to the cellulose increasing degree of oxidation [475]. This loss of crystallinity was considered to result from the opening of glucopyranose rings and the destruction of their ordered packing. This occurs mainly at the extremities of the accessible polymeric chains generating a fragmentation of the particles by disruption of the interchain hydrogen bonds [476]. As mentioned in the literature, the number average molecular weight (M_n) of biopolymers tends to be reduced as a result of oxidation [477].

Given the indirect evidence of aldehyde groups, further quantifications were undertaken with DNPH and hydroxylamine hydrochloride to characterise our DMCC powders. These methods have been widely used and prove to be very sensitive and accurate for the quantification of aldehyde content of polysaccharides [476], [478]. Lower rates of respectively 5-9%, 11-12% and 33% were thus obtained for the theoretically 9%, 18% and 36% DMCC powders. Cellulose and DMCC powders are difficult to solubilise. Indeed, DMCC is hardly soluble in water, even when heated, especially on dry or less than 75% oxidised products [479]. The aldehyde functionalities are present in a complex interconverting mixture of hydrates, intramolecular and intermolecular hemiacetals and acetals formed during reaction and drying and are therefore not in their free form to react [478], [480]. DMCC quantifications may be slightly underestimated by lack of accessibility and difficult reversibility of established bonds in water. Moreover, under our heating conditions in an acidic medium (post-reaction pH = 4) and especially in the presence of high concentrations of sodium periodate (36% mol/mol of cellulose), we observed significant hydrolysis of our product visualised through a very significant decrease in yield. Indeed, periodate oxidation is an incomplete reaction whose rate and yield depend on temperature, pH, reaction time and oxidant concentration. Higher temperature tends to produce better oxidation rates but lower yield, degrading both oxidant and DMCC through acid catalysed cleavage of the β -(1 \rightarrow 4) glycosidic bonds, fragmenting it in a heterogeneous manner [475]. The optimisation of sodium periodate oxidation relies on minimising the time and temperature of oxidation to limit cellulose hydrolysis. The addition of salts such as LiCl proves to be effective for that purpose in reducing inter and intrachain interactions, but LiCl-catalysed periodate degradation has also been observed [481].

During our studies, microwave heating has been considered and tested as a substitute for conventional heating for the reshaping and arrangement of cellulose and PVA polymers.

However, these devices are limited in terms of production scale, agitation quality and reaction observability. Moreover, the conventional heating reaction time has been reduced to approach the one used in microwave heating. For our application, this method has thus lost all interest.

Cellulose/PVA composite hydrogels can be synthesised controlling DMCC degree of oxidation, DMCC/PVA ratio and its porosity by the addition of poreforming agents. The physical characterization of our hydrogels reveals the homogeneity of the interconnected micrometric network, the incorporation of microcrystalline cellulose fibres, as well as the good integration of an additional porosity required for some biomedical applications. To reach sufficient interconnectivity of our additional porosity, a reduced granulometry of the salts was used to increase the surface area developed by these salts, thus favouring their juxtaposition and connection. Additional freezing-thawing was attempted to further connect the pores but the materials systematically returned to their initial shape, being very elastic. Their water absorption capacity was assessed to consider possible storage in a dry state and rehydration for use. However, only the 9% (2:1) NaCl 0-500 μm DMCC samples were able to regain a sufficiently high-water content and shape to be considered. Indeed, higher oxidation rates of 18% and 36% develop more cross-links and electrostatic interactions which are not fully recovered when broken by drying. In addition, hydrogels with large cavities hold more free water and thus rehydrate more efficiently.

By modulation of the DMCC/PVA ratio, we find that cellulose stiffens the hydrogel at the macro metric level, most likely through the crystalline micro cellulose fibres previously observed. Moreover, salts dissolution must generate irreversible dehydration of the material in the pore area, explaining the observed stiffening of porous hydrogels. The degree of oxidation of cellulose being largely related to the size of the particles, an impact on the mechanics of the hydrogel at the macroscopic level is observed when it varies. We assume that the higher stiffness observed for the 9% and 18% samples are certainly related to the presence of larger microcrystalline cellulose particles compared to the 36% DMCC particles which underwent more hydrolysis and fragmentation during oxidation. At the nanometric level, the 9% and 36% DMCC-based materials show a similar Young's modulus of about 40 kPa, while at 18% a significantly lower Young's modulus is obtained. These observations are most certainly linked to the organisation of the DMCC/PVA network, the nature and density of the associated interactions and bonds. Our hydrogels have mechanical properties similar to those of soft tissues whose Young's moduli range from 0.1kPa to 1MPa. By cellularisation, these matrices tend to stiffen as previously observed by deposition, remodelling and cross-linking of extracellular matrix protein notably collagen [482].

To consider any biomedical application, a rigorous study of the biological acceptability of this material has been undertaken. The release media of DMCC/PVA hydrogels show decreasing viability of L929 as the degree of oxidation of DMCC increases up to 18% DMCC oxidation, in conformity with the ISO 10993-5 standard. Since PVA is known to be fully

biocompatible, the indirect cytotoxicity observed on L929 is due to the release of cellulose dialdehyde particles. This same effect has already been observed on the NIH/3T3 fibroblast line where cell viability drops to 70% for 1.74 mmol/10 g PVA of CHO groups [483]. Despite being weakly oxidised, DMCC predominates in the composition of our hydrogel, reaching a minimum of 23.38 mmol/10 g PVA at 9%. The absence of toxicity observed below 18% reflects the full engagement of aldehyde groups in stable linkages non-deleterious at the cellular level. When seeded on the material surface, the cell-DMCC/PVA interaction shows a correlation between the cell viability of HDFs and the mechanical properties of the material at the nanometre level. Indeed, HDFs exhibit stronger cell viability for DMCC 9% and DMCC 36% than DMCC 18% material respectively showing Young Modulus of 23, 27 and 13 kPa. Although little data is available on DMCC/PVA hydrogels, numerous studies show the positive impact in 2D and 3D of matrix stiffness on fibroblast activity in terms of cell adhesion, proliferation and migration [484], [485]. The DMCC 9% /PVA (2:1) matrix appears to be the most suitable material for *in vitro* use.

Given that the DMCC/PVA materials have substantially identical microenvironments in their composition, very similar results are subsequently obtained for DMCC 9%, 18% and 36% material during long-term culture. As homogeneous and total infiltration of the porous material is achieved, the induction of porosity with controlled salt granularity proves to be effective and sufficient in our case. When cultured for 3 weeks, seeded fibroblasts organise themselves into spheroid-like cell aggregates. Indeed, as a biologically inert polymer, PVA shows an inability to engage interactions with ECM proteins such as fibronectin, collagen, laminin and thus associate with cellular integrin receptors. The incorporation of microcrystalline cellulose in our hydrogel offers anchorage points for these cellular aggregates. Indeed, on cellulose surfaces, HDFs can establish cell adhesions and develop filopodia as the numerous hydroxyl groups on the cellulose surface allow the protein adsorption required for cell adhesion by electrostatic interactions and hydrogen bonds [486], [487]. By chemical functionalization, oxidation, phosphorylation or specific chemical grafting, these interactions can be promoted to remedy growth factor or FBS supplementation [488]. Mechanically confined fibroblast has shown the ability to reprogram in stem-cell-like cells and rejuvenate [382], [383]. In the literature, PVA and bacterial cellulose also demonstrated spheroid formation and long-term stem-cell maintenance properties [489]–[491]. The potential of these spheroid-like structures at the surface of our DMCC/PVA material is very high, providing an environment recapitulating the *in vivo* complexity better than the traditional 2D or some 3D cultures. These cells functionality is more representative for pharmacological model predictivity and exhibit promising regeneration properties for tissue engineering and regenerative medicine applications.

Implanted DMCC/PVA hydrogels exhibit complete stability by a month of implantation, a mild inflammation characterised by extensive neutrophil and macrophage infiltration and the formation of a thin fibrous capsule at the periphery of the implant. By inducing porosity

in the implant, the contact surface is increased and cellular infiltration is facilitated, apparently increasing the inflammatory score. Such inflammation is indicative of a foreign body reaction (FBR), a key reaction in evaluating the safety of a scaffold in tissue engineering applications. Indeed, once implanted, our material interacts with its surroundings, through fluid, protein and cellular infiltration. Consisting of cellulose and PVA, the implant is recognised as non-self, and the body undertakes inflammatory processes aimed at its destruction or isolation from the rest of the body [492]. In the case of cellulose-based hydrogels, mild inflammation was also observed at 4 weeks and then disappeared at 8 weeks as the fibrous capsule surrounding the implant was refined [493], [494]. Lacking a cellulase equivalent to breaking β -(1 \rightarrow 4) glycosidic bond *in vivo*, cellulose demonstrates slow in situ degradation via particle macrophage phagocytosis. Cellulosic materials can persist in the crystalline form up to 5 months after implantation [495]. To overcome such *vivo* stability and to reinforce cellulose fibres usage as a biomaterial for tissue engineering, the degradation of cellulose may be modulated by incorporating cellulase into the material [496].

D1.6 Conclusion

We have developed and characterised a material based on cellulose dialdehyde and PVA, which has shown soft tissue-like mechanical properties, cytocompatibility, promising ability to form spheroidlike structures for the development of pharmacological models. Investigations should be conducted on different cell types to confirm and characterise these structures in terms of size, morphology, cell viability, metabolic activity and dedifferentiation/differentiation potential. The stability of this material *in vivo* also makes it a candidate for the development of raw, biochemically functionalised or cellularised implantable matrices. The synthesis path of our material also offers the possibility to produce innovative nanoscale culture substitutes for tissue engineering using nanocrystalline cellulose.

Chapter D2

The miniaturisation of a cellulose-based composite hydrogel for the production of *V. carteri* bio-inspired microspheres: proof of concept

*In the previous chapter, we were able to develop a cellulosic hydrogel with stiffness within a soft tissue matrix range, specifically matching fibrous tissue stiffness such as dermis, smooth muscle tissue, or breast tissue. The combination of the two polymers, cellulose and PVA, demonstrates our material's ability to sustain moderate cellular adhesion while promoting a spheroid-like cellular structure as *V. carteri* generates when in contact with various cell lineages such as human dermal fibroblasts or C3H/10T1/2 murine embryonic stem cells. We investigated here the potential of synthesizing microspheres based on this polymeric combination to pursue the replication of a material that structurally approximates *V. carteri* in its most basic structure, a deformable sphere.*

D2.1 Adaptation of the DMCC/PVA hydrogel synthesis process to nano-crystalline cellulose

Intending to finally form hydrogel microspheres, we had to modify the nature of the cellulose used by favouring the introduction of nanocrystalline cellulose. Indeed, upon granulometry analysis, both microcrystalline cellulose and oxidised dialdehyde microcrystalline cellulose showed isolated particles of greater than 100 μm long as well as polymeric bundled agglomerates that represented 40 to 50% of the particles, as shown in Chapter. [D1 Fig. D1.1](#). As 9% DMCC with a ratio of DMCC/PVA (2:1) displayed the best performance, mainly in terms of cytocompatibility, we first restricted ourselves to these formulation parameters for the production of DNCC/PVA materials, knowing that both the oxidation levels and polymer ratio could be adjusted later on. The oxidation conditions were not modified, but centrifugation and lyophilisation steps were introduced to assure the removal of residual reagents and co-products from the cellulosic suspension (i.e., sodium periodate, sodium iodate, sodium iodide) and the full drying of the polymer. Following those steps, a satisfactory reaction yield of $84.6 \pm 6.3\%$ was obtained, with the washings accounting for most of the polymer loss.

DNCC, like DMCC, was also subject to intramolecular and intermolecular hydrate, hemiacetal, and acetal formation upon oxidation reaction, washing, and lyophilization. In addition to reducing the number of functions accessible in their free form for the subsequent cross-linking reaction [478], [480], these intermolecular cross-links produced agglomerates, which then complicated the microsphere shaping. To break the intramolecular and intermolecular acetal and hemiacetal bonds, an acidification step in an aqueous phase at RT was added before proceeding to the DNCC/PVA cross-linking. The generated DNCC product was then, similarly to DMCC, cross-linked with PVA through degeneration in an NMP/LiCl system, regeneration and rehydration in absolute ethanol and subsequently water upon moulding, resulting in the cohesive white cylindrical hydrogel provided in Fig. D2.1 A. This DNCC/PVA hydrogel, showing more translucency and flexibility than the DMCC/PVA hydrogels, was formulated for the future physicochemical characterization of the material.

D2.2 Preliminary physico-chemical analysis of the DNCC/PVA hydrogel

In a first characterization effort, we determined the oxidation rate and crystallization of the DNCC and performed an FTIR analysis of the produced DNCC:PVA (2:1) hydrogel.

The anticipated DNCC oxidation rate of 9% was shown to finally reach 11.3% of dialdehyde functions, supporting the hydrolysis hypothesis already suspected in the case of DMCC in Chapter. As the decrease in the production yield of DNCC compared to DMCC (i.e., ~90-95% to ~85%) was thought to be partly attributable to the difficulty of handling NDCC, it could also result from more extensive hydrolysis. The higher functionality of the NCC causes it to be more prone to hydrolysis, especially under acidic conditions at high temperatures (i.e., 90°C, pH = 4), as sodium periodate targets the crystalline fraction [497]. Crystallinity analysis of DNCC revealed 15°, 16°, 20°, 22.5°, and 40° distinctive 2θ diffraction peaks corresponding to cellulose I diffraction planes (1 $\bar{1}$ 0), (110), (102), (200) and (004), respectively [498]–[500]. A crystallinity index of 76.6% was estimated here for DNCC. While this index is much superior to the 68% index commonly obtained for the MCC [501], it equals the NCC crystallinity index [502], confirming once again the absence of any influence of sodium periodate oxidation on the global crystal structure of NCC. Indeed, NCC itself has excellent crystallinity, and oxidation occurs only on the surface of the nanocrystal [497], [503].

The FTIR spectrum of the DNCC/PVA (2:1) material logically proves to be practically identical to the material reported in D1, as NCC and MCC show FTIR spectra identical in all respects [504]. As a result, the DNCC/PVA (2:1) material demonstrated typical signals of both PVA and cellulose. The band (I) corresponding to the OH hydroxyl groups engaged in intermolecular and intramolecular hydrogen bonding was detected at about 3373 cm⁻¹ for PVA. The bands at 2918 cm⁻¹ (II) and 1439 cm⁻¹ correspond to the CH stretching of the polymer backbone. The long alkyl chain's CH₂ vibrations were recorded at 2052 cm⁻¹.

In the footprint region (III), an inflexion of 1728 cm^{-1} , and numerous bands of $1097\text{--}1149\text{ cm}^{-1}$ denoting C–O stretching were obtained. Finally, the 1145 cm^{-1} band associated with the crystalline nature of PVA could be identified [463]–[466]. The PVA crystal structure was preserved in the DNCC/PVA material.

MCC and NCC, both cellulose materials, share functional groups with PVA. Indeed, several of the PVA bands also apply to NCC, notably in areas I, II, and III. The cellulose-specific peaks at 1376 and 1021 cm^{-1} were related to a furanose ring or a glucose subunit in the polysaccharide backbone's CH₂ bending and C–O–C stretching vibration. Peaks associated with C–O vibrations and, in particular, OH groups seemed to be more apparent than in the DMCC-based material, at 1060 cm^{-1} and 1650 cm^{-1} , respectively [467], [468]. As the NCC particles are entirely crystalline, they would absorb even more moisture than MCC, resulting in even more water molecules being bonded [469], [470]. Additionally, the typical signals of aldehyde groups, which are typically detected at 1730 cm^{-1} or 2700 cm^{-1} , were not observed [471]. However, the signal associated with the C–H of the aldehyde group, which is normally present at 790 cm^{-1} , appeared to be present at 810 cm^{-1} [505]. Moreover, signals corresponding to hemiacetal and acetal bonds in which the dialdehyde functions are anticipated to be prevalent were observed in the spectra at 1057 cm^{-1} and 1160 cm^{-1} (C–O vibrations) as well as 890 cm^{-1} (OH vibrations) [472], [497].

D2.3 DNCC/PVA hydrogel microsphere extrusion feasibility

To produce cellulosic microspheres, a jet of micro droplets of polymeric paste, DNCC/PVA degenerated in an NMP/LiCl system, must be generated. The material is therefore extruded through a needle and subjected to a coaxial airflow, which projects the microdroplets that instantly solidify into an ethanol solution via the regeneration of covalent bonds (i.e., acetal and hemiacetal linkages) and electrostatic forces (e.g., hydrogen bonds) between DNCC and PVA. The transfer of these microspheres into a water bath results in the formation of the final cellulosic hydrogel microspheres. As part of the establishment of this proof of concept, droplets ranging from $500\text{ }\mu\text{m}$ to 1 mm in diameter could be formulated by extrusion through a 24 gauge needle using a 5 mL syringe under an extrusion flow rate of 1.7 mL/min and a coaxial air flow rate of 3 L/min are shown in Fig. D2.2 A. The cellulosic content was revealed in Fig. D2.2 B, using the blue fluorescent Calcofluor white stain specifically binding β -(1→3) and β -(1→4) polysaccharides, showing the arrangement of nanocrystalline cellulose in the form of aggregates of 10 to $20\text{ }\mu\text{m}$ in diameter embedded in a PVA-based mesh.

D2.4 Discussion

In this proof of concept, we focused on establishing the feasibility of generating cellulosic microspheres. We synthesised here cohesive cellulose and PVA-based composite hydrogel by adapting the NMP/LiCl degeneration/regeneration technique described in Chapter D1

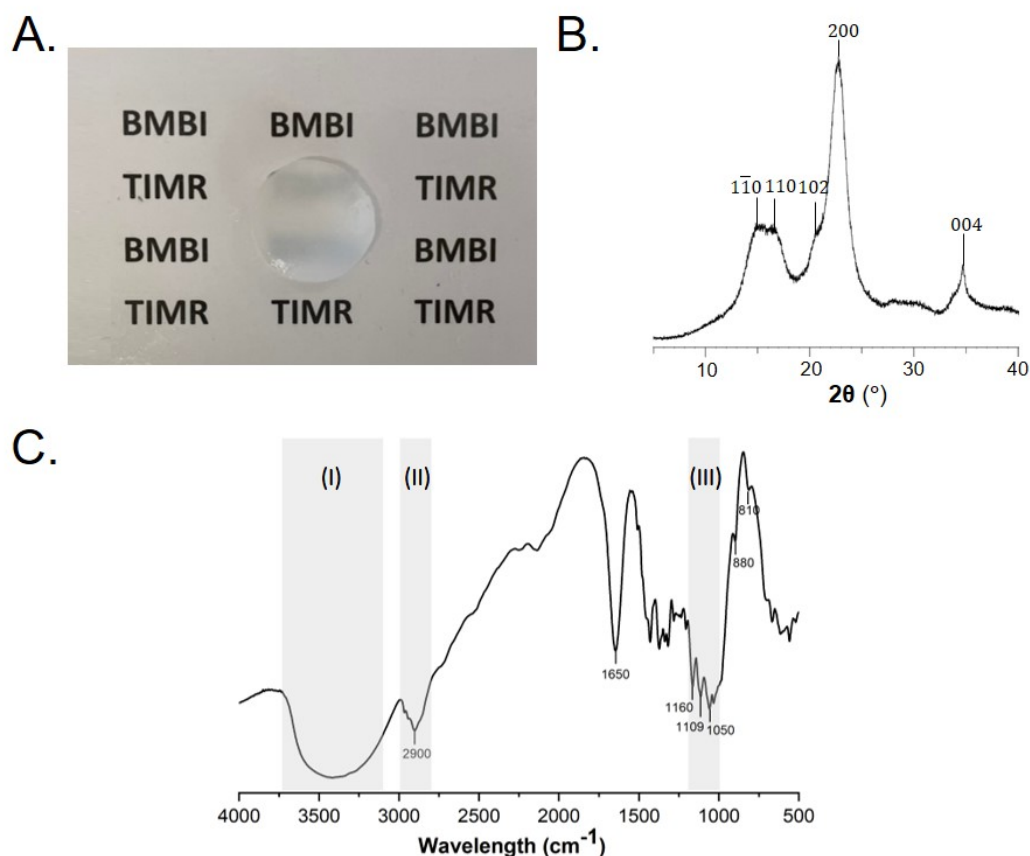


Figure D2.1: Physico-chemical characterisation of the DNCC/PVA hydrogels A. Photograph of the NCC/PVA-based hydrogel processed for further chemical investigation, B. XRD spectrum of DNCC, C. FTIR spectrum of the DNCC/PVA-based hydrogel

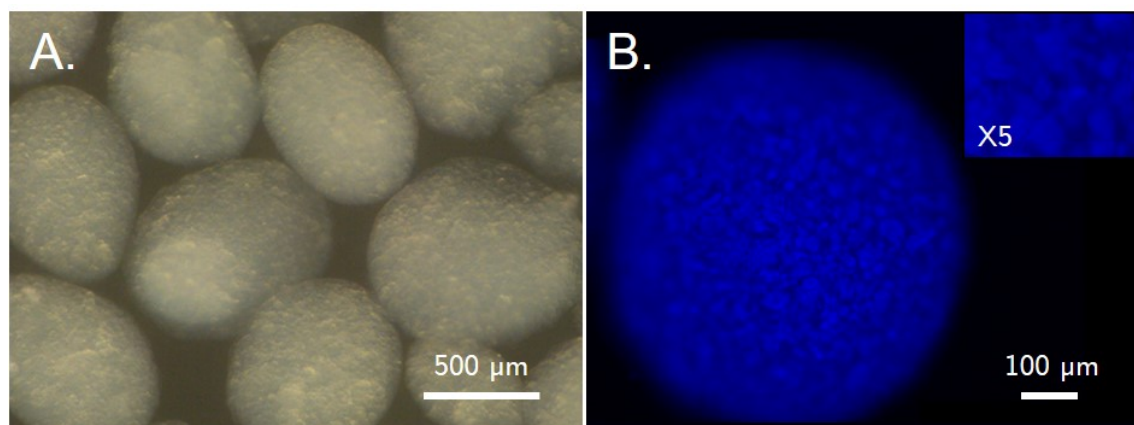


Figure D2.2: Production of NCC/PVA-based composite hydrogel microbeads A. Macroscopic photograph of synthesised microbeads composed of 9% dialdehyde cellulose nanoparticles. B. Calcofluor white stained 9% DNCC/PVA (2:1) showing nano cellulosic particles (blue)

to the use of nanocrystalline cellulose.

Specific staining demonstrated a significant decrease in the size of the cellulose particles present in this material in comparison to DMCC-based hydrogel. XDR did show an increase in the crystallinity of NCC compared to MCC, which is the consequence of the absence of

any amorphous content. This high crystallinity was preserved following oxidation, suggesting that the crystalline structure of the DNCC particles was maintained. Indeed, dialdehyde functions are added to the chain's extremities and, therefore, to the particles' periphery. The interactions and linkages stabilizing the DNCC/PVA polymeric network were confirmed (i.e., hydrogen, acetal, and hemiacetal bondings). However, further formulation adjusting would be needed as a first step to create a biomaterial that exhibits mechanical, protein adsorption, and cell adhesion properties comparable to *V. carteri*. While millimetric scale microspheres were produced, coaxial airflow extrusion parameters (i.e., increasing air flow rate, reducing polymer paste extrusion rate, or needle diameter) would need to be optimised to achieve an optimal microsphere diameter of 100 to 350 μm . Finally, additional structural, physicochemical, and mechanical characterization would be required to investigate the influence of the spherical shape and produce a final characterization of the material.

The emergence of NCC as promising green nanomaterials has sparked significant interest and research into their synthesis, surface functionalization, and various material developments. NCCs are rod-shaped particles formed by acid hydrolysis (e.g., in sulphuric acid, hydrochloric acid or phosphoric acid), isolating the cellulosic crystalline regions by removal of the structurally disordered amorphous region [506], [507]. NCC particles are thus inherently more crystalline than MCC, which have both crystalline and amorphous portions [508]. In addition to the negative surface charge provided by the abundance of -OH groups [509], the crystalline surface of NCCs has more hydrophobic edge planes (i.e., (200) planes) consisting of only -CH groups, giving them amphiphilic properties showing affinities for hydrophobic and aqueous phases [510], which improves water solubility and retention, as well as surface activity, functionalisation, and, as a result, copolymer cross-linking. While the stiffness of cellulosic fibres is undoubtedly affected by the origin of the wood and the manufacturing method, the Young's modulus increases dramatically as the crystalline proportion increases and the amorphous fraction is eliminated. Dried MCC, MFC, and NCC demonstrate Young's moduli of about 25, 100, and 130 GPa, respectively [511], [512]. NCC particles are generally implemented as a reinforcing agent in composite dry film compositions based on synthetic and natural polymers such as PVA [505], [513], alginate [514], chitosan [515]–[517] or gelatin [497]. Nevertheless, cellulosic fibres represent a mechanically versatile polymer as their water retention capacity, directly related to their high -OH content, causes a significant decrease in the cellulosic fibres' stiffness as the moisture level increases [518]. Cellulosic fibres in both MCC and NCC forms incorporated into the formulation of high water content hydrogels, such as PVA-based hydrogels, resulted in the production of relatively soft hydrogels with tunable Young's moduli ranging from 1 to 70 kPa [519]–[522]. Jayaramudu et al. [523] precisely reduced the Young's modulus of a PVA hydrogel from 82 kPa to 7 kPa by enhancing the hydrogel's water absorption capacity by increasing the CNC to PVA ratio. NCC demonstrates overall high biocompatibility, making it relevant for various biomedical applications, including wound dressings, implants, and drug delivery systems [504], [509], [524], [525].

We are therefore confident that a hydrogel with stiffness of about 2 kPa can be produced both as a flat cylindrical hydrogel and as microspheres using this polymer combination and cross-linking process. Such bio-inspired materials could first represent an alternative biomaterial for soft tissue replacement that would be more easily characterised and thus be more easily and rapidly marketable. Furthermore, this type of material would allow us to study the mechanisms of action of a sphere stacking model of the alga *V. carteri*, in particular the impact on cells of the sphere stacking itself, the influence of the surface curvature, and hydrogel rigidity.

D2.5 Conclusion

Using a co-axial airflow extrusion technique, we were capable of demonstrating the feasibility of synthesizing cellulosic beads based on NCC and PVA. As both highly functional polymers, NCC and PVA have been shown to form hydrogels with tunable stiffness, modulating the nature and strength of interaction or cross-linking involved in the polymeric network. Our final primary interest is in reproducing the mechanical properties of soft tissues like adipose tissue, mimicking *V. carteri* material. However, given the high strength and stiffness of NCC in a dry state, we could consider developing hard cellulosic analogues for bone reconstruction by limiting water swelling using oppositely charged NCC [526], additional functionalization, or heavy cross-linking [513].

Chapter D3

Production of *V. carteri*-like microspheres containing *V. carteri* content based on alginate cross-linked material: Proof of concept

To pursue our strategy of creating analogous models of *V. carteri* initiated in Chapter D2, ultimately intending to investigate the mechanisms involved in *V. carteri*'s biological properties (i. e. cell adhesion, proliferation, and adipogenesis), we planned to incorporate a molecular component directly from *V. carteri*. Considering our team's expertise in co-axial airflow extrusion and protein or peptide grafting of alginate, we chose to use this polymer to examine the feasibility of grafting *V. carteri* proteins. We could thus offer an all-algal alternative material that would structurally, mechanically, and molecularly replicate a *V. carteri* colony.

D3.1 *V. carteri* polymer separation from a raw extract

A freshly harvested saturated suspension of *V. carteri* was sonicated to produce a raw extract. Following brief and rapid centrifugation, four separate fractions (Fig. D3.1 A) were distinguished: a pellet (P) and three fractions numbered from 1 to 3 (F1 to F3). Electron microscopy was used to determine the composition of these fractions.

The pellet (Fig. D3.1 C) contained biflagellated somatic cells, as 1-2 μm spherical structures and mobile fresh under contrast-phase microscopy were observed. F1 (Fig. D3.1 D) also displayed spherical structures of comparable size that must correspond to somatic cell outer membrane debris and spheres of larger diameter, approximately 5 μm , corresponding to gonidia. F2 exhibited similar structures to F1 and colony membrane residues (Fig. D3.1 E). Finally, as the soluble fraction comprises *V. carteri* glycoproteins and polysaccharides, F3 residues could be found in all fractions. To remove any cellular and membrane residues, F3 was collected and filtered using a cellulose membrane with a porosity of 1 μm . When freeze-dried, F3 formed a sponge-like structure (Fig. D3.1 B) of auto-assembled *V. carteri* polymers and glycoproteins exhibiting very high porosity, as presented in Fig. D3.1 F.

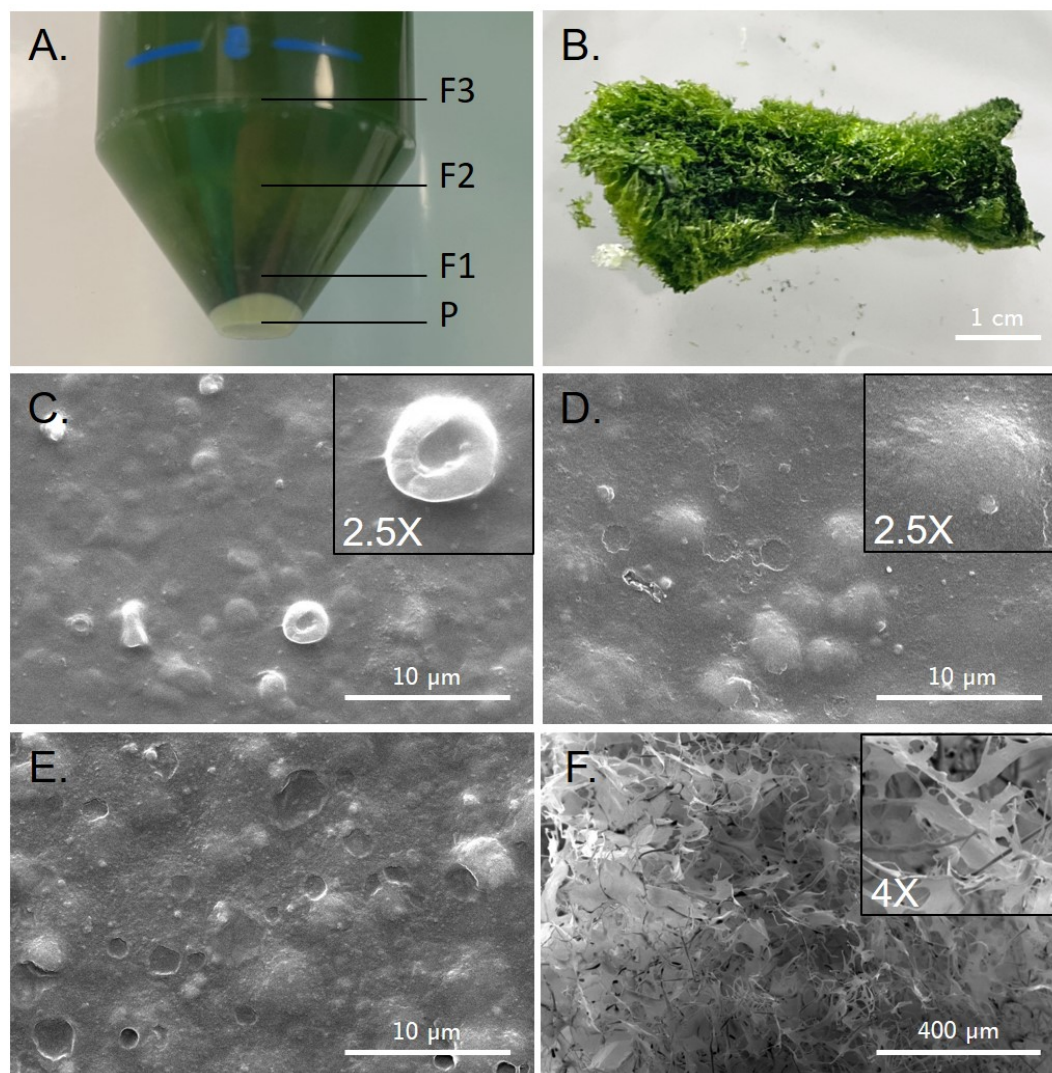


Figure D3.1: *V. carteri* extraction A. Photograph of 4 fractions separation upon quick *V. carteri* suspension sonication and centrifugation, B. Macroscopic observation of the freeze-dried F3 fraction, C-E. MEB observation of P to F2 fractions showing somatic cells, somatic cells surrounding membrane and gonidia, a few somatic cells surrounding membrane, gonidia and colonies membrane residues, respectively, F. MEB observation of the freeze-dried F3 fraction.

D3.2 *V. carteri* polymer and alginate cross-linking

The freeze-dried F3 fraction, referred to as *V. carteri* soluble extract hereafter, dissolved readily in water and was cross-linked through amination reactions using EDC/NHS in a 1.5%w/w alginate solution at a 15%w/w ratio. Dialysis was used to remove the non-cross-linked reagent residues and any small compounds (i.e., inferior to 12-14 kDa). The product was then freeze-dried and resolubilised to a concentration of 1.5%w/w alginate. A light brown viscous solution was obtained and filtered to 0.22 μm . The alginate solution was then extruded and subjected to a co-axial air flow which propels the alginate-micro droplets into the calcium-concentrated solution, causing the alginate to gel as white microspheres. The appearance of the alginate and alginate microspheres grafted to the *V. carteri* polymers is shown in Fig. D3.2. The speed and efficiency of the gelation did not seem to be affected

by the polymeric grafting.

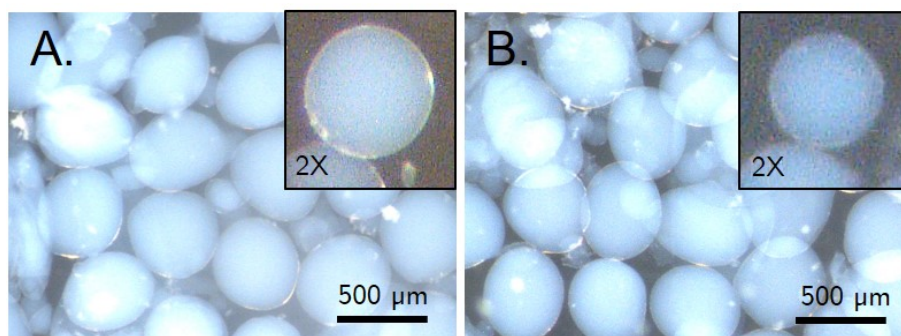


Figure D3.2: Production of *V. carteri*-like microbeads A. Macroscopic observation of alginate, B. Macroscopic observation of synthesised microbeads composed of alginate-*V. carteri* cross-linked material.

D3.3 Examining the efficacy of the cross-linking

Simultaneously to the microsphere fabrication, samples of the alginate extrusion solutions of pure and cross-linked *V. carteri* soluble extract were gelled to assess the cross-linking by FTIR analysis and protein quantification.

The spectra of alginate, *V. carteri* soluble extract, and alginate cross-linked to *V. carteri* soluble extract are shown in Fig. D3.3 A. The spectrum of sodium alginate in its pure form includes two signals at 890 and 950 cm^{-1} [527], representative of the carboxylic acid functions of the mannuronic and guluronic acid residues, respectively. At about 3389 cm^{-1} , the broad signal of the hydroxyl functions and the methylene elongation signals are found at 2928 cm^{-1} [528]. The spectra of *V. carteri* soluble extract display two bands at 1546 and 1654 cm^{-1} corresponding to the signals of amides I and II, which supports the peptide nature of the mixture [529]. At 3400 cm^{-1} , we observe a band of high amplitude for the hydroxyl signals, which could be associated with a large number of hydroxylated amino acids, particularly hydroxyproline (Hyp) [347] in the primary structure of the mixture proteins, but also non-negligible sugars and oligosaccharides covalently grafted onto these same proteins (i.e., Glucose, Mannose, Arabinose, Galactose) [77], [88], [94], [352]. The spectra of alginate material conjugated to *V. carteri* soluble extract revealed a signal at 3424 cm^{-1} corresponding to the hydroxyl function significantly stronger than in pure alginate, which might be attributed to the glycoprotein content of *V. carteri* soluble extract. The signals of the carbonyl groups of the alginate connected to those of the amide functions I and II of the *V. carteri* soluble extract overlap between 1550 and 1640 cm^{-1} . Alltogether, as repeated rinses were performed, these FTIR spectrum changes hinted at alginate modification, *V. carteri* entrapping and grafting with *V. carteri* material by strong interactions and probably covalent linkage through amination reaction with NHS/EDC.

To further confirm the proteic nature of the grafted *V. carteri* content, an empiric bicinchoninic acid assay (BCA) (Fig. D3.3 B) was performed on pure alginate and alginate-*V. carteri* cross-linked materials. The BCA protein assay is used routinely to quantify the total amount of protein in samples. The principle of this method revolves around the ability of proteins, via peptide bonds, to reduce Cu^{+2} to Cu^{+1} under alkaline conditions, resulting in a shift in the colouration of the solution from light green to violet. The solution turns increasingly purple as the protein content increases. Due to the extremely dark green colour of the pure *V. carteri* extract, the test could not be completed on the highly concentrated extracts. This method was nevertheless effective in determining the protein content of *V. carteri* extract produced with a lower concentrated algal suspension ($746.5 \pm 154.7 \mu\text{g}/50\text{K colonies}$). A bovine serum albumin solution was used as a positive control solution.

As anticipated, pure alginate didn't produce any colouring, reflecting the absence of protein content in the sample. On the other hand, alginate cross-linked with the *V. carteri* extracts exhibited a purple colour formation, proving the effectiveness of *V. carteri* protein coupling to alginate. Alginate *V. carteri* cross-linked solutions filtered at 0.8 and 0.45 μm prior to gelation display much paler purple BCA solutions. This reduced protein could reflect the potential removal of exceedingly large polymers before gelation that can either be extensively reticulated alginate polymer, excessively large cross-linked *V. carteri* glycoproteins, or polymer agglomerates related to the grafting reaction. Insofar as these filtrations are required to limit tubing obstruction during polymer extrusion under co-axial air flow, a pre-filtration of the alginate and protein extracts before the cross-linking reaction could be envisioned to pre-calibrate the polymeric suspension expected upon grafting.

D3.4 Discussion

The soluble components of *V. carteri* were separated from structural remains using rapid sonication, centrifugation, and filtration on a cellulose membrane with a porosity of 1 μm . The concentrated algal solution contained glycoproteins, polysaccharides, and smaller molecules such as pigments or active molecules. Interestingly, the soluble fraction showed self-assembly capabilities as a sponge-like material was formed upon freeze-drying, testifying to at least the involvement of weak electrostatic/bonding forces between *V. carteri* polymers. Indeed, some *V. carteri* glycoproteins (i.e., pheroporins DZ1 and DZ2) have already demonstrated autocatalytic self-assembly capabilities [94]. While this dried extract could be dissolved in an aqueous solution for further processing and cross-linking, we could stabilise this proteic reticulated material after cryostructuration through EDC cross-linking in ethanol to form a plant-based porous hydrogel [530].

Here we have demonstrated the feasibility of functionalizing alginate with *V. carteri* protein extracts, as both FTIR analysis and the BCA assay showed evidence of the grafting. Formulation adjustments will need to be made to determine the appropriate ratio of alginate to

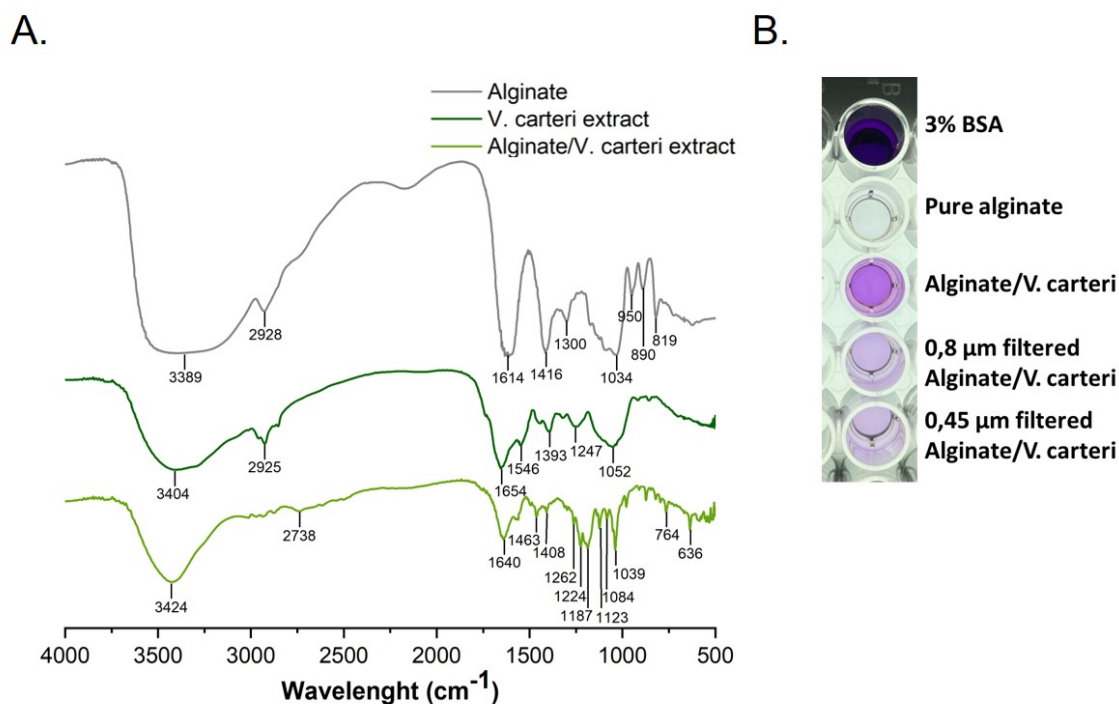


Figure D3.3: Alginate and *V. carteri* soluble extract cross-linking efficiency A. FTIR spectra of alginate, *V. carteri* extract, and *V. carteri* extract alginate cross-linked materials, B. Detection of proteic content in *V. carteri* extract alginate cross-linked materials: From top to bottom, post-reaction BCA assay solution of 3% bovine serum albumin (BSA, positive control), pure alginate, *V. carteri* extract alginate cross-linked material, 0.8 μm filtered *V. carteri* extract alginate cross-linked material, 0.45 μm *V. carteri* extract alginate cross-linked material.

V. carteri extracts to ensure proper alginate gelation and to confirm an observable beneficial effect of the inclusion of *V. carteri* proteins on cell adhesion.

The EDC/NHS cross-linking of soluble *V. carteri* extract and alginate is based on the association of the carboxylic functions of alginate with any compound having primary amines. This cross-linking therefore constitutes a coarse selection for *V. carteri*'s protein composition, namely its glycoproteins, while selecting against substances such as polysaccharides or pigments, as evidenced by the non-pigmentation of cross-linked alginate. The EDC/NHS or NHS-sulfo cross-linking process is one of the most widely used methods for the biological functionalisation of polymers and the conjugation of proteins onto polymeric materials. The strength of this system lies in its simplicity, efficiency, and versatility due to the ubiquity of carboxyl functions in many polymers and amine functions in protein sequences. This method was extensively used for the functionalization of natural polymers (e.g., collagen, gelatin, and alginate) as well as synthetic polymers (e.g., Polycaprolactone, Poly(L-lactide)) by grafting whole proteins (e.g., fibronectin, collagen) or peptides (e.g., fibronectin epitope, G₄RGDSP, laminin epitope, IKVAV, and adhesion peptide, YIGSR) mainly to improve cell adhesion, cell proliferation to promote cellular colonisation *in vitro*, tissue integration *in vivo*, and material biocompatibility [531]–[535]. This system has shown possibilities for stabilising collagen matrices, improving their physicochemical properties, including thermal and

enzymatic resistance, and modulating their rheological properties by either increasing their shear stress by homo cross-linking or decreasing them by the introduction of L-lysine[536], [537]. Other alternative polymers and proteins cross-linking, targeting specific amino acids such as lysine residues using 5,5'-bisvanillin cross-linker [538] or cysteine residues taking advantage of its thiol-reactivity to maleimide to generate a thiosuccinimide linkage [539]–[542]. *V. carteri* glycoproteins cross-linking and microsphere shaping enable us to assess the role of algal glycoproteins in *V. carteri* soluble extract capacities for cell adhesion, tissue development, and adipogenesis induction observed in Chapters C1, C2, and C3.

The implementation of *V. carteri* colonies' stiffening strategy could be considered by cross-linking their extracellular matrix to broaden its scope and better adapt to contractile cells (e.g., fibroblasts, myocytes). A *V. carteri*-based multi-mechanical environment model could be thus developed by combining a low stiffness of around 2 kPa for adipocyte differentiation and greater stiffness to be adjusted (10–50 kPa) for contractile cell expansion. Alternatively, such a model might be replicated by making use of alginate and *V. carteri* glycoproteins cross-linking, as the Young's modulus of an alginate hydrogel can vary from 1 to 500 kPa by modulating the proportion of β -d-mannuronic acid and α -l-guluronic acid, alginate concentration, and gelation parameters (e.g., cation nature and concentration, gelation speed and duration) [543]–[545].

D3.5 Conclusion

This chapter is a preliminary work towards the development of *V. carteri*-like microspheres to combine morphological, mechanical, and molecular components of *V. carteri* using alginate to better understand *V. carteri*-mediated cell adhesion mechanisms. However, this purely vegetal material also represents interest as an alternative bio-inspired material for tissue engineering.

Conclusion and perspectives

In the context of my thesis work, we were able to illustrate, through the biological capacities observed in our main study object, the micro-alga *V. carteri*, the interest in plant-based matrices and materials as alternatives to animal materials, which are still primarily employed in tissue engineering for the production of toxicological research models, pathology models for pharmacological screening purposes, or biomaterials for tissue regeneration.

We were able to identify and satisfy the production, sterility, and storage requirements for the use of partially deflagellated *V. carteri* in mammalian and human cell cultures. *In vitro*, *V. carteri* sphere-packing model proved stability and malleability. Indeed, the algal suspension's dimensional dispersion allows for the formation of a larger culture surface as well as an enhanced level of compaction, allowing for tissue cohesiveness. Both freshly harvested algal extract and ethanol-preserved colonies showed potential to enhance and support cell adhesion, respectively. The presence of adhesive glycoproteins specific to the Volvox algae, pherophorins in particular but possibly other collagen-like proteins (i.e., COL I, COL III, COL IV, and COL VI), and laminin-like proteins that could comprise RGD sequences as well as primitive equivalents of such adhesion sequences, are hypothesized to be the origin of these adhesion-promoting capacities. Indeed, early in the development of *V. carteri*, the responsibility for sustaining the cellular structures within the colony shifted from cell-cell interactions (i.e., algal-CAM) to the extracellular matrix. *V. carteri* glycoproteins must thus display motifs and structures capable of engaging affinities, possibly supported by N-glycosylations with cellular membrane structures involved in mammalian and human adhesion (i.e., cell adhesion molecules). Although the cell adhesion patterns differed depending on cell type (fibroblasts, endothelial cells, stem cells) and cell origin (murine and human), *V. carteri* suspension was able to support cell proliferation, extracellular matrix deposition, and tissue cohesion, demonstrating its interest as a matrix in tissue engineering. Such tissue development also exhibited *in vivo* better stability than collagen at 2 months post-implantation and the absence of exacerbated chronic inflammation, opening up the possibility of using *V. carteri* suspension as a matrix for soft tissue regeneration.

Furthermore, *V. carteri* suspension culture appeared to have the ability to influence and initiate certain cell fates. To begin, human dermal fibroblasts showed signs of dedifferentiation, showing an increased alkaline phosphatase activity typical of a stem cell phenotype. This effect is thought to be due to the development of cell aggregates during adhesion to algal colonies. Second, the *V. carteri* suspension induced adipogenesis in both adipose-derived stem cells and embryonic stem cells *in vitro*, as demonstrated by the significant accumulation of lipid droplets along the culture. Finally, injection of a *V. carteri* suspension alone

exhibited the capacity to create mesenchymal tissue at 1-month post-implantation, which included adipocyte islets, demonstrating *V. carteri*'s ability to support adipogenesis even *in situ*. The adipogenic capacities of *V. carteri* could be induced first and foremost by its low stiffness. Indeed, *V. carteri* colonies display an overall young modulus of about 2.8 kPa, thus in the range of the young moduli of mature adipocytes and adipose tissue. Molecular cues may also trigger adipogenesis. The surface of *V. carteri* colonies carries glycoproteins that could provide a basement membrane-like environment mimicking that of fat tissue. Also, the possibility of hormonal induction should not be neglected, as *V. carteri* exhibits lipid metabolism with phytohormones that may be analogous to insulin and insulin growth factors, which have been proven to stimulate adipogenesis. Because adipose tissue is the primary tissue used for soft tissue augmentation, this type of mesenchymal tissue development that promotes adipogenesis is promising and sought in tissue regeneration.

The hypothesis raised in this exploratory thesis work are proposed following essentially preliminary experiments that will require further investigations that will allow a better understanding and quantification of the phenomena observed and will enrich the knowledge of *V. carteri* microalga.

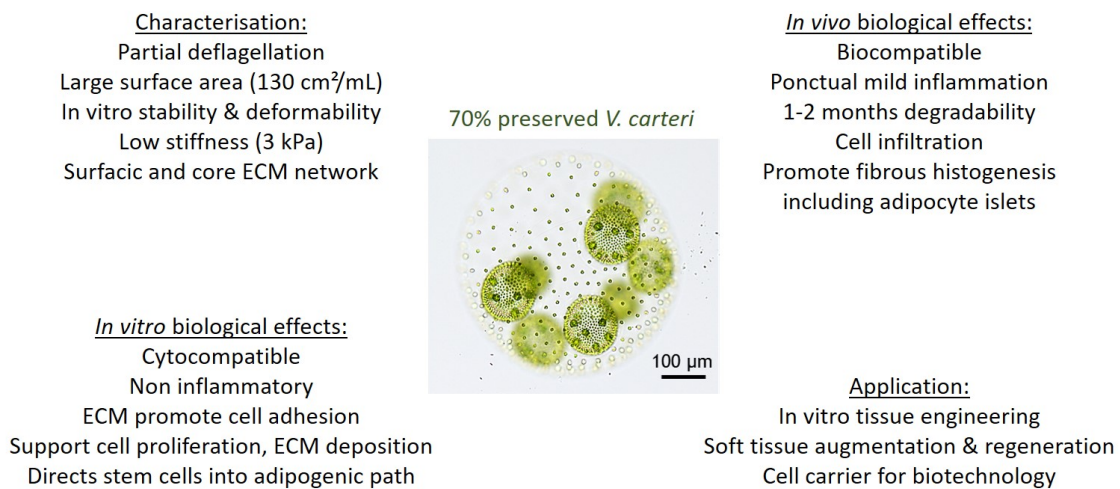


Figure D3.4: Knowledge provided by this thesis work for the use of *V. carteri* as a biomaterial for tissue engineering and application in regenerative medicine.

In this effort, we sought to produce plant-based alternatives that would allow us to eventually study *V. carteri* by reproducing their geometry and their stiffness or by incorporating molecular elements such as their glycoproteins. In an absolute sense, these materials, likewise of interest, could reasonably constitute potential therapeutic solutions that are more easily marketable as being less complex and more easily and less expensively characterized with respect to *V. carteri*.

We have therefore developed and characterized a cellulose and PVA-based composite hydrogel that is highly hydrophilic, globally biocompatible and with a stiffness approaching

that of fibrillar type soft tissue. As a result, we created and characterized a cellulose and PVA-based composite hydrogel that is highly hydrophilic, globally biocompatible, and has a stiffness similar to fibrillar soft tissue. This type of material, which generates spheroid-like cell aggregates due to PVA's anti-adhesivity, could allow us to determine whether the dedifferentiation of human dermal fibroblasts suspected by culture in a *V. carteri* suspension could be purely caused by weak cell adhesion or if molecular cues are involved. Such material may allow us to investigate, on a larger scale, the association between poor cell adhesiveness, spheroid formation, and cell reprogramming.

A miniaturization approach has been initiated to adapt this material into a weakly adhesive microsphere form similar in size to *V. carteri*. In the long run, it may be possible to determine the part attributable to sphericity or stiffness by modifying the mechanical characteristics of the material in both the *V. carteri* potential dedifferentiation and the adipogenesis induction processes.

In parallel, we have demonstrated the feasibility of cross-linking *V. carteri* glycoproteins on sodium alginate while guaranteeing the gelling capacity of the final *V. carteri* protein cross-linked alginate. Such a material could allow us to evaluate whether and if so, to identify which element(s) of *V. carteri* is responsible for the cell adhesion or adipogenic support capacities.

In this thesis work, we established the versatility of *V. carteri* as a matrix of interest for tissue engineering and tissue regeneration, highlighting its tissue-building capacities. These options represent only a fraction of what we could envision doing with *V. carteri* microalgae. We could consider broadening the spectrum of culturable cells to address different therapeutic issues by providing cell-carrying capacities or tissue development. By adapting the mechanical properties of the algae by seeking ways to soften or stiffen the colonies, we could envisage providing the biomechanical needs of cells ranging from neurons to muscular cells. The possible modulation of mechanical properties combined with the segmentation of *V. carteri* colonies by size could allow us to consider complexifying the sphere-stacking model to propose cocultures offering, for instance, stiffer smaller colonies (e.g., 100-150 μm) and softer bigger colonies (e.g., 200-300 μm) enabling the development of heterogeneous tissues whose microenvironment could be easily tracked with or without the use of cross-linked fluorescent molecules.

The potential of *V. carteri* extracts or specific compounds (i.e., pheroporins, collagen-like or laminin-like proteins) has only been hinted at here. These *V. carteri*-derived polymers could be used to promote cell adhesion to poorly bioactive surfaces or even to form basement membrane-like environments by chemical cross-linking or even electrospinning.

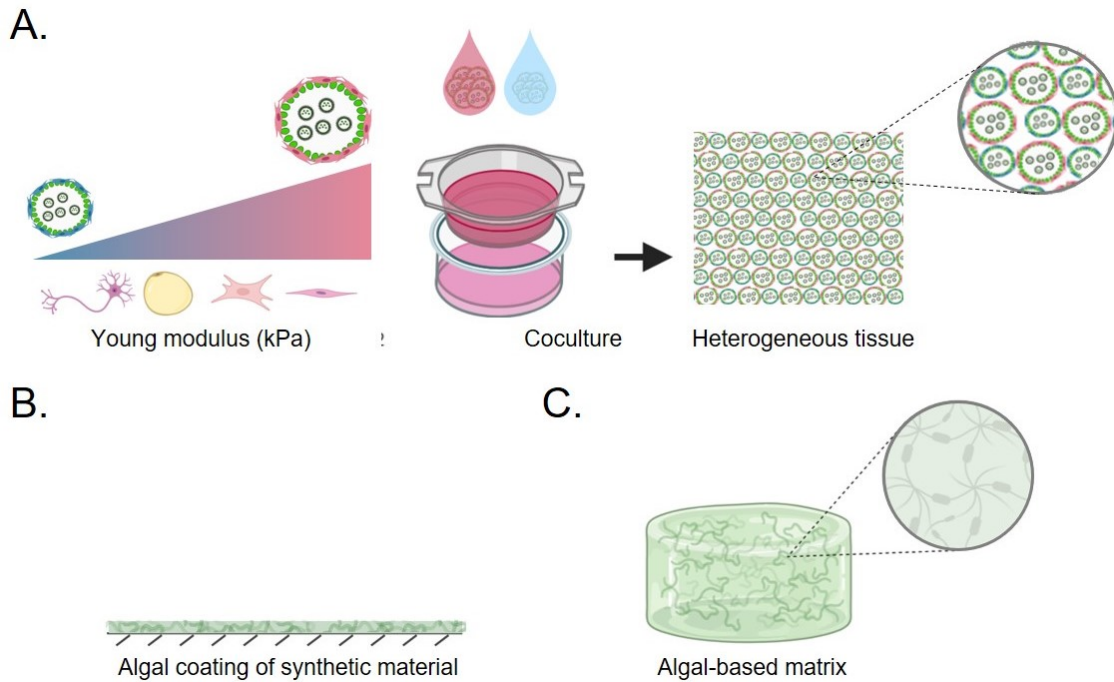


Figure D3.5: Development perspectives around *V. carteri* material. A. Heterogeneous coculture model based on sphere-stacking combining dimensional and mechanical segmentation by *V. carteri* colonies' softening or stiffening; B. Development of coating or porous matrix by stabilisation of glycoproteins extracted from *V. carteri*. Created with BioRender.com.

While sphere-packing is presumably not physiological in absolute terms for tissue development, *V. carteri* as a developmental model for multicellular acquisition and for the establishment of an ECM upon which everything stands inspired us to develop alternative scheme for tissue building. While a large number of uncertainties and unknowns remain around the mechanisms explaining *V. carteri*'s capabilities partly explored in this manuscript, *V. carteri* surely represents a high potential material for tissue engineering and regenerative medicine.

Bibliography

- [1] E. Szathmáry and J. M. Smith, "The major evolutionary transitions," *Nature*, vol. 374, no. 6519, pp. 227–232, Mar. 1995, ISSN: 0028-0836, 1476-4687. DOI: [10.1038/374227a0](https://doi.org/10.1038/374227a0).
- [2] M. D. Herron, "What are the major transitions?" *Biology & Philosophy*, vol. 36, no. 1, p. 2, Feb. 2021, ISSN: 0169-3867, 1572-8404. DOI: [10.1007/s10539-020-09773-z](https://doi.org/10.1007/s10539-020-09773-z).
- [3] Á. Kun, "The major evolutionary transitions and codes of life," *Biosystems*, vol. 210, p. 104548, Dec. 2021, ISSN: 03032647. DOI: [10.1016/j.biosystems.2021.104548](https://doi.org/10.1016/j.biosystems.2021.104548).
- [4] S. A. West, R. M. Fisher, A. Gardner, and E. T. Kiers, "Major evolutionary transitions in individuality," *Proceedings of the National Academy of Sciences*, vol. 112, no. 33, pp. 10112–10119, Aug. 18, 2015, ISSN: 0027-8424, 1091-6490. DOI: [10.1073/pnas.1421402112](https://doi.org/10.1073/pnas.1421402112).
- [5] J. T. Bonner, *On development: the biology of form*, 3. print, ser. A Commonwealth fund book. Cambridge, Mass.: Harvard Univ. Press, 1978, 282 pp., ISBN: 978-0-674-63412-1 978-0-674-63410-7.
- [6] L. W. Buss, *The evolution of individuality*. Princeton, N.J: Princeton Univ. Pr, 1987, 201 pp., ISBN: 978-0-691-60354-4 978-0-691-08468-8 978-0-691-08469-5.
- [7] E. Szathmáry, "Toward major evolutionary transitions theory 2.0," *Proceedings of the National Academy of Sciences*, vol. 112, no. 33, pp. 10104–10111, Aug. 18, 2015, ISSN: 0027-8424, 1091-6490. DOI: [10.1073/pnas.1421398112](https://doi.org/10.1073/pnas.1421398112).
- [8] G. Matt and J. Umen, "Volvox: A simple algal model for embryogenesis, morphogenesis and cellular differentiation," *Developmental Biology*, vol. 419, no. 1, pp. 99–113, Nov. 2016, ISSN: 00121606. DOI: [10.1016/j.ydbio.2016.07.014](https://doi.org/10.1016/j.ydbio.2016.07.014).
- [9] R. K. Grosberg and R. R. Strathmann, "The evolution of multicellularity: A minor major transition?" *Annual Review of Ecology, Evolution, and Systematics*, vol. 38, no. 1, pp. 621–654, Dec. 1, 2007, ISSN: 1543-592X, 1545-2069. DOI: [10.1146/annurev.ecolsys.36.102403.114735](https://doi.org/10.1146/annurev.ecolsys.36.102403.114735).
- [10] C. G. Ehrenberg, *[Vorträge in der Akademie der Wissenschaften zu Berlin im Jahre 1830 - 1836] / 2 Zur Erkenntniss der Organisation in der Richtung des kleinsten Raumes*. gedruckt in Druckerei der Königlichen Akademie der Wissenschaften, 1836, Medium: 154 S., 192 S., 30 S. : Ill. (4 Tafeln) ; 37 cm. DOI: [10.3931/E-RARA-12634](https://doi.org/10.3931/E-RARA-12634).
- [11] H. C. Bold, H. C. Bold, M. J. Wynne, and M. J. Wynne, *Introduction to the algae: structure and reproduction*, 2. ed. Englewood Cliffs, N. J: Prentice-Hall, 1985, 720 pp., ISBN: 978-0-13-477746-7.

- [12] M. D. Herron, "Origins of multicellular complexity: *Volvox* and the volvocine algae," *Molecular Ecology*, vol. 25, no. 6, pp. 1213–1223, Mar. 2016, ISSN: 0962-1083, 1365-294X. DOI: [10.1111/mec.13551](https://doi.org/10.1111/mec.13551).
- [13] D. L. Kirk, "A twelve-step program for evolving multicellularity and a division of labor," *BioEssays*, vol. 27, no. 3, pp. 299–310, Mar. 2005, ISSN: 0265-9247, 1521-1878. DOI: [10.1002/bies.20197](https://doi.org/10.1002/bies.20197).
- [14] M. D. Herron and R. E. Michod, "Evolution of complexity in the volvocine algae: Transitions in individuality through darwin's eye," *Evolution*, vol. 62, no. 2, pp. 436–451, Feb. 2008, ISSN: 0014-3820, 1558-5646. DOI: [10.1111/j.1558-5646.2007.00304.x](https://doi.org/10.1111/j.1558-5646.2007.00304.x).
- [15] E. R. Hanschen, M. D. Herron, J. J. Wiens, H. Nozaki, and R. E. Michod, "Multicellularity drives the evolution of sexual traits," *The American Naturalist*, vol. 192, no. 3, E93–E105, Sep. 2018, ISSN: 0003-0147, 1537-5323. DOI: [10.1086/698301](https://doi.org/10.1086/698301).
- [16] Y. Arakaki, H. Kawai-Toyooka, Y. Hamamura, *et al.*, "The simplest integrated multicellular organism unveiled," *PLoS ONE*, vol. 8, no. 12, E. Moreno, Ed., e81641, Dec. 11, 2013, ISSN: 1932-6203. DOI: [10.1371/journal.pone.0081641](https://doi.org/10.1371/journal.pone.0081641).
- [17] H. de Maleprade, F. Moisy, T. Ishikawa, and R. E. Goldstein, "Motility and phototaxis of *Gonium*, the simplest differentiated colonial alga," *Physical Review E*, vol. 101, no. 2, p. 022416, Feb. 24, 2020, ISSN: 2470-0045, 2470-0053. DOI: [10.1103/PhysRevE.101.022416](https://doi.org/10.1103/PhysRevE.101.022416).
- [18] S. Höhn and A. Hallmann, "Distinct shape-shifting regimes of bowl-shaped cell sheets – embryonic inversion in the multicellular green alga pleodorina," *BMC Developmental Biology*, vol. 16, no. 1, p. 35, Dec. 2016, ISSN: 1471-213X. DOI: [10.1186/s12861-016-0134-9](https://doi.org/10.1186/s12861-016-0134-9).
- [19] T. Hamaji, H. Kawai-Toyooka, H. Uchimura, *et al.*, "Anisogamy evolved with a reduced sex-determining region in volvocine green algae," *Communications Biology*, vol. 1, no. 1, p. 17, Dec. 2018, ISSN: 2399-3642. DOI: [10.1038/s42003-018-0019-5](https://doi.org/10.1038/s42003-018-0019-5).
- [20] M. D. Herron, J. D. Hackett, F. O. Aylward, and R. E. Michod, "Triassic origin and early radiation of multicellular volvocine algae," *Proceedings of the National Academy of Sciences*, vol. 106, no. 9, pp. 3254–3258, Mar. 3, 2009, ISSN: 0027-8424, 1091-6490. DOI: [10.1073/pnas.0811205106](https://doi.org/10.1073/pnas.0811205106).
- [21] J. J. Russell, J. A. Theriot, P. Sood, *et al.*, "Non-model model organisms," *BMC Biology*, vol. 15, no. 1, 55, s12915–017–0391–5, Dec. 2017, ISSN: 1741-7007. DOI: [10.1186/s12915-017-0391-5](https://doi.org/10.1186/s12915-017-0391-5).
- [22] J. G. Umen, "Volvox and volvocine green algae," *EvoDevo*, vol. 11, no. 1, p. 13, Dec. 2020, ISSN: 2041-9139. DOI: [10.1186/s13227-020-00158-7](https://doi.org/10.1186/s13227-020-00158-7).
- [23] E. H. Harris, Ed., *The Chlamydomonas sourcebook. 1: Introduction to chlamydomonas and its laboratory use / [editor-in-chief] Elizabeth H. Harris*, 2. ed, Amsterdam Heidelberg: Academic Press, 2009, 444 pp., ISBN: 978-0-12-370874-8.

- [24] presented at the, 5th International Volvox Conference, Tokyo, Japan.
- [25] presented at the, The 20th International Conference on the Cell and Molecular Biology of Chlamydomonas, Princeton University, New Jersey, USA, Jun. 4, 2023.
- [26] S. E. Prochnik, J. Umen, A. M. Nedelcu, *et al.*, "Genomic analysis of organismal complexity in the multicellular green alga *Volvox carteri*," *Science*, vol. 329, no. 5988, pp. 223–226, Jul. 9, 2010, ISSN: 0036-8075, 1095-9203. DOI: [10.1126/science.1188800](https://doi.org/10.1126/science.1188800).
- [27] H. Nozaki, F. Mori, Y. Tanaka, R. Matsuzaki, H. Yamaguchi, and M. Kawachi, "Cryopreservation of vegetative cells and zygotes of the multicellular volvocine green alga *gonium pectorale*," *BMC Microbiology*, vol. 22, no. 1, p. 103, Dec. 2022, ISSN: 1471-2180. DOI: [10.1186/s12866-022-02519-9](https://doi.org/10.1186/s12866-022-02519-9).
- [28] H. Nozaki, F. Mori, Y. Tanaka, *et al.*, "Cryopreservation of two species of the multicellular volvocine green algal genus *astrephomene*," In Review, preprint, Sep. 9, 2022. DOI: [10.21203/rs.3.rs-2016046/v1](https://doi.org/10.21203/rs.3.rs-2016046/v1).
- [29] A. Nakazawa and I. Nishii, "Amidic and acetonc cryoprotectants improve cryopreservation of volvocine green algae," *Cryo Letters*, vol. 33, no. 3, pp. 202–213, Jun. 2012, ISSN: 0143-2044.
- [30] W. H. Darden, "Sexual differentiation in *volvox aureus*," *The Journal of Protozoology*, vol. 13, no. 2, pp. 239–255, May 1966, ISSN: 00223921. DOI: [10.1111/j.1550-7408.1966.tb01901.x](https://doi.org/10.1111/j.1550-7408.1966.tb01901.x).
- [31] D. L. Kirk and M. M. Kirk, "Protein synthetic patterns during the asexual life cycle of *volvox carteri*," *Developmental Biology*, vol. 96, no. 2, pp. 493–506, Apr. 1983, ISSN: 00121606. DOI: [10.1016/0012-1606\(83\)90186-0](https://doi.org/10.1016/0012-1606(83)90186-0).
- [32] H. Nozaki, W. Mahakham, W. Heman, R. Matsuzaki, and M. Kawachi, "A new preferentially outcrossing monoicous species of *volvox* sect. *volvox* (chlorophyta) from thailand," *PLOS ONE*, vol. 15, no. 7, J. G. Umen, Ed., e0235622, Jul. 2, 2020, ISSN: 1932-6203. DOI: [10.1371/journal.pone.0235622](https://doi.org/10.1371/journal.pone.0235622).
- [33] K. Yamamoto, T. Hamaji, H. Kawai-Toyooka, *et al.*, "Three genomes in the algal genus *Volvox* reveal the fate of a haploid sex-determining region after a transition to homothallism," *Proceedings of the National Academy of Sciences*, vol. 118, no. 21, e2100712118, May 25, 2021, ISSN: 0027-8424, 1091-6490. DOI: [10.1073/pnas.2100712118](https://doi.org/10.1073/pnas.2100712118).
- [34] D. Smith and R. W. Lee, "The mitochondrial and plastid genomes of *volvox carteri*: Bloated molecules rich in repetitive DNA," *BMC Genomics*, vol. 10, no. 1, p. 132, 2009, ISSN: 1471-2164. DOI: [10.1186/1471-2164-10-132](https://doi.org/10.1186/1471-2164-10-132).
- [35] B. Klein, D. Wibberg, and A. Hallmann, "Whole transcriptome RNA-seq analysis reveals extensive cell type-specific compartmentalization in *volvox carteri*," *BMC Biology*, vol. 15, no. 1, p. 111, Dec. 2017, ISSN: 1741-7007. DOI: [10.1186/s12915-017-0450-y](https://doi.org/10.1186/s12915-017-0450-y).

- [36] B. Schiedlmeier, R. Schmitt, W. Müller, *et al.*, "Nuclear transformation of volvox carteri," *Proceedings of the National Academy of Sciences*, vol. 91, no. 11, pp. 5080–5084, May 24, 1994, ISSN: 0027-8424, 1091-6490. DOI: [10.1073/pnas.91.11.5080](https://doi.org/10.1073/pnas.91.11.5080).
- [37] S. Geng, P. De Hoff, and J. G. Umen, "Evolution of sexes from an ancestral mating-type specification pathway," *PLoS Biology*, vol. 12, no. 7, N. H. Barton, Ed., e1001904, Jul. 8, 2014, ISSN: 1545-7885. DOI: [10.1371/journal.pbio.1001904](https://doi.org/10.1371/journal.pbio.1001904).
- [38] J. A. Ortega-Escalante, R. Jasper, and S. M. Miller, "CRISPR /cas9 mutagenesis in *Volvox carteri*," *The Plant Journal*, vol. 97, no. 4, pp. 661–672, Feb. 2019, ISSN: 0960-7412, 1365-313X. DOI: [10.1111/tpj.14149](https://doi.org/10.1111/tpj.14149).
- [39] G. M. Smith, "A comparative study of the species of volvox," *Transactions of the American Microscopical Society*, vol. 63, no. 4, p. 265, Oct. 1944, ISSN: 00030023. DOI: [10.2307/3223302](https://doi.org/10.2307/3223302).
- [40] N. Halder, "Two algal species of volvox l. with their taxonomy and ecology from west bengal, india," *Songklanakarin Journal of Science and Technology*, vol. 38, no. 4, pp. 435–437, 2016.
- [41] D. L. Kirk, *Volvox: A Search for the Molecular and Genetic Origins of Multicellularity and Cellular Differentiation*, ser. Developmental and cell biology series. Cambridge, U.K: Cambridge University Press, 1998, ISBN: 978-0-521-45207-6.
- [42] L. Jaenicke and R. Gilles, "Differentiation and embryogenesis in volvox carteri," in *Biochemistry of Differentiation and Morphogenesis*, L. Jaenicke, Ed., Berlin, Heidelberg: Springer Berlin Heidelberg, 1982, pp. 288–294, ISBN: 978-3-642-68835-5 978-3-642-68833-1. DOI: [10.1007/978-3-642-68833-1_26](https://doi.org/10.1007/978-3-642-68833-1_26).
- [43] R. Starr, "Structure, reproduction and differentiation in volvox carteri f. nagariensis iyengar, strains HK 9 & 10," *Arch Protistenkunde*, pp. 204–222, 1969.
- [44] J. A. Zeikus and R. C. Starr, "The genetics and physiology of non-inducibility in volvox carteri f. nagariensis IYENGAR," *Archiv für Protistenkunde*, vol. 123, no. 2, pp. 127–161, Jan. 1980, ISSN: 00039365. DOI: [10.1016/S0003-9365\(80\)80001-7](https://doi.org/10.1016/S0003-9365(80)80001-7).
- [45] S. M. Miller, R. Schmitt, and D. L. Kirk, "Jordan, an active volvox transposable element similar to higher plant transposons," *The Plant Cell*, vol. 5, no. 9, pp. 1125–1138, Sep. 1993, ISSN: 1040-4651, 1532-298X. DOI: [10.1105/tpc.5.9.1125](https://doi.org/10.1105/tpc.5.9.1125).
- [46] M. O. P. Lyengar, "Contributions to our knowledge of the colonial volvocales of south india," *Botanical Journal of the Linnean Society*, vol. 49, no. 329, pp. 323–373, Jun. 1, 1933, ISSN: 1095-8339, 0024-4074. DOI: [10.1111/j.1095-8339.1933.tb00391.x](https://doi.org/10.1111/j.1095-8339.1933.tb00391.x).
- [47] C. R. Adams, K. A. Stamer, J. K. Miller, J. G. McNally, M. M. Kirk, and D. L. Kirk, "Patterns of organellar and nuclear inheritance among progeny of two geographically isolated strains of volvox carteri," *Current Genetics*, vol. 18, no. 2, pp. 141–153, Aug. 1990, ISSN: 0172-8083, 1432-0983. DOI: [10.1007/BF00312602](https://doi.org/10.1007/BF00312602).

- [48] M. Kirk, K. Stark, S. Miller, *et al.*, “regA, a volvox gene that plays a central role in germ-soma differentiation, encodes a novel regulatory protein,” *Development*, vol. 126, no. 4, pp. 639–647, Feb. 15, 1999, ISSN: 1477-9129, 0950-1991. DOI: [10.1242/dev.126.4.639](https://doi.org/10.1242/dev.126.4.639).
- [49] G. Kochert and I. Yates, “Purification and partial characterization of a glycoprotein sexual inducer from *Volvox carteri*,” *Proceedings of the National Academy of Sciences*, vol. 71, no. 4, pp. 1211–1214, Apr. 1974, ISSN: 0027-8424, 1091-6490. DOI: [10.1073/pnas.71.4.1211](https://doi.org/10.1073/pnas.71.4.1211).
- [50] S. Waffenschmidt, M. Knittler, and L. Jaenicke, “Characterization of a sperm lysin of volvox carteri,” *Sexual Plant Reproduction*, vol. 3, no. 1, Feb. 1990, ISSN: 0934-0882, 1432-2145. DOI: [10.1007/BF00189945](https://doi.org/10.1007/BF00189945).
- [51] D. R. Smith and R. W. Lee, “Low nucleotide diversity for the expanded organelle and nuclear genomes of volvox carteri supports the mutational-hazard hypothesis,” *Molecular Biology and Evolution*, vol. 27, no. 10, pp. 2244–2256, Oct. 1, 2010, ISSN: 0737-4038, 1537-1719. DOI: [10.1093/molbev/msq110](https://doi.org/10.1093/molbev/msq110).
- [52] M. Dauwalder, W. Whaley, and R. C. Starr, “Differentiation and secretion in volvox,” *Journal of Ultrastructure Research*, vol. 70, pp. 318–335, 1980.
- [53] A. H. Sessoms and R. J. Huskey, “Genetic control of development in *Volvox*: isolation and characterization of morphogenetic mutants,” *Proceedings of the National Academy of Sciences*, vol. 70, no. 5, pp. 1335–1338, May 1973, ISSN: 0027-8424, 1091-6490. DOI: [10.1073/pnas.70.5.1335](https://doi.org/10.1073/pnas.70.5.1335).
- [54] F. Mori, M. Erata, and M. Watanabe, “Cryopreservation of cyanobacteria and green algae in the NIES-collection,” *Microbiology and Culture Collections*, vol. 18, no. 1, pp. 45–55, 2002.
- [55] K. Kawafune, Y. Hongoh, T. Hamaji, *et al.*, “Two different rickettsial bacteria invading volvox carteri,” *PLOS ONE*, vol. 10, no. 2, R. E. Steele, Ed., e0116192, Feb. 11, 2015, ISSN: 1932-6203. DOI: [10.1371/journal.pone.0116192](https://doi.org/10.1371/journal.pone.0116192).
- [56] H. Nozaki, N. Ueki, M. Takusagawa, *et al.*, “Morphology, taxonomy and mating-type loci in natural populations of volvox carteri in taiwan,” *Botanical Studies*, vol. 59, no. 1, p. 10, Dec. 2018, ISSN: 1999-3110. DOI: [10.1186/s40529-018-0227-9](https://doi.org/10.1186/s40529-018-0227-9).
- [57] P. Ferris, B. J. S. C. Olson, P. L. De Hoff, *et al.*, “Evolution of an expanded sex-determining locus in *Volvox*,” *Science*, vol. 328, no. 5976, pp. 351–354, Apr. 16, 2010, ISSN: 0036-8075, 1095-9203. DOI: [10.1126/science.1186222](https://doi.org/10.1126/science.1186222).
- [58] R. Hiraide, H. Kawai-Toyooka, T. Hamaji, *et al.*, “The evolution of male–female sexual dimorphism predates the gender-based divergence of the mating locus gene MAT3/RB,” *Molecular Biology and Evolution*, vol. 30, no. 5, pp. 1038–1040, May 2013, ISSN: 1537-1719, 0737-4038. DOI: [10.1093/molbev/mst018](https://doi.org/10.1093/molbev/mst018).
- [59] H. Hoops, “Flagellar, cellular and organismal polarity in volvox carteri,” *Journal of Cell Science*, vol. 104, no. 1, pp. 105–117, Jan. 1, 1993, ISSN: 1477-9137, 0021-9533. DOI: [10.1242/jcs.104.1.105](https://doi.org/10.1242/jcs.104.1.105).

- [60] D. R. Brumley, M. Polin, T. J. Pedley, and R. E. Goldstein, "Metachronal waves in the flagellar beating of *Volvox* and their hydrodynamic origin," *Journal of The Royal Society Interface*, vol. 12, no. 108, p. 20141358, Jul. 2015, ISSN: 1742-5689, 1742-5662. DOI: [10.1098/rsif.2014.1358](https://doi.org/10.1098/rsif.2014.1358).
- [61] H. Sakaguchi and K. Iwasa, "Two photophobic responses in *volvox carteri*," *Plant and Cell Physiology*, Aug. 1979, ISSN: 1471-9053. DOI: [10.1093/oxfordjournals.pcp.a075885](https://doi.org/10.1093/oxfordjournals.pcp.a075885).
- [62] H. J. Hoops, I. Nishii, and D. L. Kirk, "Cytoplasmic bridges in *volvox* and its relatives," in *Cell-Cell Channels*, New York, NY: Springer New York, 2006, pp. 65–84, ISBN: 978-0-387-36058-4. DOI: [10.1007/978-0-387-46957-7_4](https://doi.org/10.1007/978-0-387-46957-7_4).
- [63] K. J. Green, G. I. Viamontes, and D. L. Kirk, "Mechanism of formation, ultrastructure, and function of the cytoplasmic bridge system during morphogenesis in *volvox*," *Journal of Cell Biology*, vol. 91, no. 3, pp. 756–769, Dec. 1, 1981, ISSN: 0021-9525, 1540-8140. DOI: [10.1083/jcb.91.3.756](https://doi.org/10.1083/jcb.91.3.756).
- [64] M. M. Kirk, A. Ransick, S. E. McRae, and D. L. Kirk, "The relationship between cell size and cell fate in *volvox carteri*," *Journal of Cell Biology*, vol. 123, no. 1, pp. 191–208, Oct. 1, 1993, ISSN: 0021-9525, 1540-8140. DOI: [10.1083/jcb.123.1.191](https://doi.org/10.1083/jcb.123.1.191).
- [65] D. L. Kirk, "The genetic program for germ-soma differentiation in *volvox*," *Annual Review of Genetics*, vol. 31, no. 1, pp. 359–380, Dec. 1997, ISSN: 0066-4197, 1545-2948. DOI: [10.1146/annurev.genet.31.1.359](https://doi.org/10.1146/annurev.genet.31.1.359).
- [66] —, "Germ-soma differentiation in *volvox*," *Developmental Biology*, vol. 238, no. 2, pp. 213–223, Oct. 2001, ISSN: 00121606. DOI: [10.1006/dbio.2001.0402](https://doi.org/10.1006/dbio.2001.0402).
- [67] —, "Germ cell specification in *volvox carteri*," in *Novartis Foundation Symposia*, J. Marsh and J. Goode, Eds., Chichester, UK: John Wiley & Sons, Ltd., Sep. 28, 2007, pp. 2–30, ISBN: 978-0-470-51457-3 978-0-471-94264-1. DOI: [10.1002/9780470514573.ch2](https://doi.org/10.1002/9780470514573.ch2).
- [68] Q. Cheng, V. Pappas, A. Hallmann, and S. M. Miller, "Hsp70a and GlcA interact as partner chaperones to regulate asymmetric division in *volvox*," *Developmental Biology*, vol. 286, no. 2, pp. 537–548, Oct. 2005, ISSN: 00121606. DOI: [10.1016/j.ydbio.2005.08.028](https://doi.org/10.1016/j.ydbio.2005.08.028).
- [69] G. I. Viamontes and D. L. Kirk, "Cell shape changes and the mechanism of inversion in *volvox*," *Journal of Cell Biology*, vol. 75, no. 3, pp. 719–730, Dec. 1, 1977, ISSN: 0021-9525, 1540-8140. DOI: [10.1083/jcb.75.3.719](https://doi.org/10.1083/jcb.75.3.719).
- [70] G. I. Viamontes, L. J. Fochtmann, and D. L. Kirk, "Morphogenesis in *volvox*: Analysis of critical variables," *Cell*, vol. 17, no. 3, pp. 537–550, Jul. 1979, ISSN: 00928674. DOI: [10.1016/0092-8674\(79\)90262-9](https://doi.org/10.1016/0092-8674(79)90262-9).
- [71] I. Nishii, S. Ogihara, and D. L. Kirk, "A kinesin, *InvA*, plays an essential role in *volvox* morphogenesis," *Cell*, vol. 113, no. 6, pp. 743–753, Jun. 2003, ISSN: 00928674. DOI: [10.1016/S0092-8674\(03\)00431-8](https://doi.org/10.1016/S0092-8674(03)00431-8).

- [72] A. Hallmann, "Morphogenesis in the family volvocaceae: Different tactics for turning an embryo right-side out," *Protist*, vol. 157, no. 4, pp. 445–461, Oct. 2006, ISSN: 14344610. DOI: [10.1016/j.protis.2006.05.010](https://doi.org/10.1016/j.protis.2006.05.010).
- [73] D. L. Kirk and I. Nishii, "Volvox carteri as a model for studying the genetic and cytological control of morphogenesis," *Development, Growth and Differentiation*, vol. 43, no. 6, pp. 621–631, Dec. 8, 2001, ISSN: 0012-1592, 1440-169X. DOI: [10.1046/j.1440-169X.2001.00612.x](https://doi.org/10.1046/j.1440-169X.2001.00612.x).
- [74] S. Höhn, A. R. Honerkamp-Smith, P. A. Haas, P. K. Trong, and R. E. Goldstein, "Dynamics of a Volvox embryo turning itself inside out," *Physical Review Letters*, vol. 114, no. 17, p. 178 101, Apr. 27, 2015, ISSN: 0031-9007, 1079-7114. DOI: [10.1103/PhysRevLett.114.178101](https://doi.org/10.1103/PhysRevLett.114.178101).
- [75] P. A. Haas and R. E. Goldstein, "Embryonic inversion in Volvox carteri : The flipping and peeling of elastic lips," *Physical Review E*, vol. 98, no. 5, p. 052 415, Nov. 30, 2018, ISSN: 2470-0045, 2470-0053. DOI: [10.1103/PhysRevE.98.052415](https://doi.org/10.1103/PhysRevE.98.052415).
- [76] G. Y. Matt and J. G. Umen, "Cell-type transcriptomes of the multicellular green alga Volvox carteri yield insights into the evolutionary origins of germ and somatic differentiation programs," *G3: Genes | Genomes | Genetics*, vol. 8, no. 2, pp. 531–550, Feb. 2018, ISSN: 2160-1836. DOI: [10.1534/g3.117.300253](https://doi.org/10.1534/g3.117.300253).
- [77] B. Heyde and A. Hallmann, "Targeted migration of pterophorin-s indicates extensive extracellular matrix dynamics in Volvox carteri," *The Plant Journal*, vol. 103, no. 6, pp. 2301–2317, Sep. 2020, ISSN: 0960-7412, 1365-313X. DOI: [10.1111/tpj.14901](https://doi.org/10.1111/tpj.14901).
- [78] D. L. Kirk and M. M. Kirk, "Heat shock elicits production of sexual inducer in Volvox," *Science*, vol. 231, no. 4733, pp. 51–54, Jan. 3, 1986, ISSN: 0036-8075, 1095-9203. DOI: [10.1126/science.3941891](https://doi.org/10.1126/science.3941891).
- [79] H. Tschochner, F. Lottspeich, and M. Sumper, "The sexual inducer of Volvox carteri : Purification, chemical characterization and identification of its gene," *The EMBO Journal*, vol. 6, no. 8, pp. 2203–2207, Aug. 1987, ISSN: 02614189. DOI: [10.1002/j.1460-2075.1987.tb02491.x](https://doi.org/10.1002/j.1460-2075.1987.tb02491.x).
- [80] R. C. Starr and L. Jaenicke, "Purification and characterization of the hormone initiating sexual morphogenesis in Volvox carteri f. nagariensis iyengar," *Proceedings of the National Academy of Sciences*, vol. 71, no. 4, pp. 1050–1054, Apr. 1974, ISSN: 0027-8424, 1091-6490. DOI: [10.1073/pnas.71.4.1050](https://doi.org/10.1073/pnas.71.4.1050).
- [81] H. Nozaki, "Morphology, sexual reproduction and taxonomy of volvox carteri f. kawasakiensis f. nov. (chlorophyta) from japan," *Phycologia*, vol. 27, no. 2, pp. 209–220, Jun. 1988, ISSN: 0031-8884, 2330-2968. DOI: [10.2216/i0031-8884-27-2-209.1](https://doi.org/10.2216/i0031-8884-27-2-209.1).
- [82] S. M. Coelho, J. Gueno, A. P. Lipinska, J. M. Cock, and J. G. Umen, "UV chromosomes and haploid sexual systems," *Trends in Plant Science*, vol. 23, no. 9, pp. 794–807, Sep. 2018, ISSN: 13601385. DOI: [10.1016/j.tplants.2018.06.005](https://doi.org/10.1016/j.tplants.2018.06.005).
- [83] R. Starr, "Meiosis in volvox carteri f. nagariensis," *Archiv für Protistenkunde*, no. 117, pp. 187–191, 1975.

- [84] J. Umen and S. Coelho, "Algal sex determination and the evolution of anisogamy," *Annual Review of Microbiology*, vol. 73, no. 1, pp. 267–291, Sep. 8, 2019, ISSN: 0066-4227, 1545-3251. DOI: [10.1146/annurev-micro-020518-120011](https://doi.org/10.1146/annurev-micro-020518-120011).
- [85] M. Kirk and D. Kirk, "Translational regulation of protein synthesis, in response to light, at a critical stage of volvox development," *Cell*, vol. 41, no. 2, pp. 419–428, Jun. 1985, ISSN: 00928674. DOI: [10.1016/S0092-8674\(85\)80015-5](https://doi.org/10.1016/S0092-8674(85)80015-5).
- [86] R. Gilles, C. Gilles, and L. Jaenicke, "Pheromone-binding and matrix-mediated events in sexual induction of volvox carteri," *Zeitschrift für Naturforschung C*, vol. 39, no. 6, pp. 584–592, Jun. 1, 1984, ISSN: 1865-7125, 0939-5075. DOI: [10.1515/znc-1984-0612](https://doi.org/10.1515/znc-1984-0612).
- [87] D. Kirk, R. Birchem, and N. King, "The extracellular matrix of volvox: A comparative study and proposed system of nomenclature," *Journal of Cell Science*, vol. 80, no. 1, pp. 207–231, Feb. 1, 1986, ISSN: 1477-9137, 0021-9533. DOI: [10.1242/jcs.80.1.207](https://doi.org/10.1242/jcs.80.1.207).
- [88] K. Godl, "Differential targeting of closely related ECM glycoproteins: The pherophorin family from volvox," *The EMBO Journal*, vol. 16, no. 1, pp. 25–34, Jan. 1, 1997, ISSN: 14602075. DOI: [10.1093/emboj/16.1.25](https://doi.org/10.1093/emboj/16.1.25).
- [89] A. Hallmann, P. Amon, K. Godl, M. Heitzer, and M. Sumper, "Transcriptional activation by the sexual pheromone and wounding: A new gene family from volvox encoding modular proteins with (hydroxy)proline-rich and metalloproteinase homology domains: VMPs: Inducible metalloproteinases from volvox," *The Plant Journal*, vol. 26, no. 6, pp. 583–593, Dec. 23, 2001, ISSN: 09607412. DOI: [10.1046/j.1365-313x.2001.01059.x](https://doi.org/10.1046/j.1365-313x.2001.01059.x).
- [90] M. Sumper, E. Berg, S. Wenzl, and K. Godl, "How a sex pheromone might act at a concentration below 10(16) m.," *The EMBO Journal*, vol. 12, no. 3, pp. 831–836, Mar. 1993, ISSN: 02614189. DOI: [10.1002/j.1460-2075.1993.tb05723.x](https://doi.org/10.1002/j.1460-2075.1993.tb05723.x).
- [91] H. Ertl, R. Mengele, S. Wenzl, J. Engel, and M. Sumper, "The extracellular matrix of volvox carteri: Molecular structure of the cellular compartment," *The Journal of Cell Biology*, vol. 109, no. 6, pp. 3493–3501, Dec. 1, 1989, ISSN: 0021-9525, 1540-8140. DOI: [10.1083/jcb.109.6.3493](https://doi.org/10.1083/jcb.109.6.3493).
- [92] H. Ertl, A. Hallmann, S. Wenzl, and M. Sumper, "A novel extensin that may organize extracellular matrix biogenesis in volvox carteri," *The EMBO Journal*, vol. 11, no. 6, pp. 2055–2062, Jun. 1992, ISSN: 02614189. DOI: [10.1002/j.1460-2075.1992.tb05263.x](https://doi.org/10.1002/j.1460-2075.1992.tb05263.x).
- [93] A. Hallmann and D. Kirk, "The developmentally regulated ECM glycoprotein ISG plays an essential role in organizing the ECM and orienting the cells of volvox," *Journal of Cell Science*, vol. 113, no. 24, pp. 4605–4617, Dec. 15, 2000, ISSN: 1477-9137, 0021-9533. DOI: [10.1242/jcs.113.24.4605](https://doi.org/10.1242/jcs.113.24.4605).
- [94] F. Ender, K. Godl, S. Wenzl, and M. Sumper, "Evidence for autocatalytic cross-linking of hydroxyproline-rich glycoproteins during extracellular matrix assembly in volvox," *The Plant Cell*, vol. 14, no. 5, pp. 1147–1160, May 2002, ISSN: 1040-4651, 1532-298X. DOI: [10.1105/tpc.000711](https://doi.org/10.1105/tpc.000711).

- [95] K. Godl, A. Hallmann, A. Rappel, and M. Sumper, "Pherophorins: A family of extracellular matrix glycoproteins from volvox structurally related to the sex-inducing pheromone," *Planta*, vol. 196, no. 4, Jul. 1995, ISSN: 0032-0935, 1432-2048. DOI: [10.1007/BF00197345](#).
- [96] F. Ender, A. Hallmann, P. Amon, and M. Sumper, "Response to the sexual pheromone and wounding in the green alga volvox: Induction of an extracellular glycoprotein consisting almost exclusively of hydroxyproline," *The Journal of Biological Chemistry*, vol. 274, no. 49, pp. 35 023–35 028, Dec. 3, 1999, ISSN: 0021-9258. DOI: [10.1074/jbc.274.49.35023](#).
- [97] C. A. Vacanti, "The history of tissue engineering," *Journal of Cellular and Molecular Medicine*, vol. 10, no. 3, pp. 569–576, Jul. 2006, ISSN: 1582-1838, 1582-4934. DOI: [10.1111/j.1582-4934.2006.tb00421.x](#).
- [98] R. Langer and J. P. Vacanti, "Tissue engineering," *Science*, vol. 260, no. 5110, pp. 920–926, May 14, 1993, ISSN: 0036-8075, 1095-9203. DOI: [10.1126/science.8493529](#).
- [99] A. Khademhosseini and R. Langer, "Microengineered hydrogels for tissue engineering," *Biomaterials*, vol. 28, no. 34, pp. 5087–5092, Dec. 2007, ISSN: 01429612. DOI: [10.1016/j.biomaterials.2007.07.021](#).
- [100] A. S. Daar and H. L. Greenwood, "A proposed definition of regenerative medicine," *Journal of Tissue Engineering and Regenerative Medicine*, vol. 1, no. 3, pp. 179–184, May 2007, ISSN: 19326254, 19327005. DOI: [10.1002/term.20](#).
- [101] C. Mason and P. Dunnill, "A brief definition of regenerative medicine," *Regenerative Medicine*, vol. 3, no. 1, pp. 1–5, Jan. 2008, ISSN: 1746-0751, 1746-076X. DOI: [10.2217/17460751.3.1.1](#).
- [102] L. Germain, F. A. Auger, E. Grandbois, *et al.*, "Reconstructed human cornea produced in vitro by tissue engineering," *Pathobiology*, vol. 67, no. 3, pp. 140–147, 1999, ISSN: 1015-2008, 1423-0291. DOI: [10.1159/000028064](#).
- [103] J. Liu, Z. Zhou, M. Zhang, F. Song, C. Feng, and H. Liu, "Simple and robust 3d bioprinting of full-thickness human skin tissue," *Bioengineered*, vol. 13, no. 4, pp. 10 090–10 100, Apr. 1, 2022, ISSN: 2165-5979, 2165-5987. DOI: [10.1080/21655979.2022.2063651](#).
- [104] M.-E. Han, S.-H. Kim, H. D. Kim, *et al.*, "Extracellular matrix-based cryogels for cartilage tissue engineering," *International Journal of Biological Macromolecules*, vol. 93, pp. 1410–1419, Dec. 2016, ISSN: 01418130. DOI: [10.1016/j.ijbiomac.2016.05.024](#).
- [105] T. Baudequin, C. Legallais, and F. Bedoui, "In vitro bone cell response to tensile mechanical solicitations: Is there an optimal protocol?" *Biotechnology Journal*, vol. 14, no. 1, p. 1 800 358, Jan. 2019, ISSN: 18606768. DOI: [10.1002/biot.201800358](#).
- [106] R. Tiruvannamalai-Annamalai, D. R. Armant, and H. W. T. Matthew, "A glycosaminoglycan based, modular tissue scaffold system for rapid assembly of perfusable, high cell density, engineered tissues," *PLoS ONE*, vol. 9, no. 1, C. Chan, Ed., e84287, Jan. 20, 2014, ISSN: 1932-6203. DOI: [10.1371/journal.pone.0084287](#).

- [107] C. A. Vacanti and J. Upton, "Tissue-engineered morphogenesis of cartilage and bone by means of cell transplantation using synthetic biodegradable polymer matrices," *Clinics in Plastic Surgery*, vol. 21, no. 3, pp. 445–462, Jul. 1994, ISSN: 0094-1298. DOI: [10.1016/S0094-1298\(20\)31022-1](https://doi.org/10.1016/S0094-1298(20)31022-1).
- [108] G. Lutzweiler, A. Ndreu Halili, and N. Engin Vrana, "The overview of porous, bioactive scaffolds as instructive biomaterials for tissue regeneration and their clinical translation," *Pharmaceutics*, vol. 12, no. 7, p. 602, Jun. 29, 2020, ISSN: 1999-4923. DOI: [10.3390/pharmaceutics12070602](https://doi.org/10.3390/pharmaceutics12070602).
- [109] R. O. Hynes, "The extracellular matrix: Not just pretty fibrils," *Science (New York, N.Y.)*, vol. 326, no. 5957, pp. 1216–1219, Nov. 27, 2009, ISSN: 1095-9203. DOI: [10.1126/science.1176009](https://doi.org/10.1126/science.1176009).
- [110] I. Jun, H.-S. Han, J. Edwards, and H. Jeon, "Electrospun fibrous scaffolds for tissue engineering: Viewpoints on architecture and fabrication," *International Journal of Molecular Sciences*, vol. 19, no. 3, p. 745, Mar. 6, 2018, ISSN: 1422-0067. DOI: [10.3390/ijms19030745](https://doi.org/10.3390/ijms19030745).
- [111] P. Yadav, G. Beniwal, and K. K. Saxena, "A review on pore and porosity in tissue engineering," *Materials Today: Proceedings*, vol. 44, pp. 2623–2628, 2021, ISSN: 22147853. DOI: [10.1016/j.matpr.2020.12.661](https://doi.org/10.1016/j.matpr.2020.12.661).
- [112] C. D. Spicer, "Hydrogel scaffolds for tissue engineering: The importance of polymer choice," *Polymer Chemistry*, vol. 11, no. 2, pp. 184–219, 2020, ISSN: 1759-9954, 1759-9962. DOI: [10.1039/C9PY01021A](https://doi.org/10.1039/C9PY01021A).
- [113] C. Liu, C. Zhu, J. Li, *et al.*, "The effect of the fibre orientation of electrospun scaffolds on the matrix production of rabbit annulus fibrosus-derived stem cells," *Bone Research*, vol. 3, no. 1, p. 15 012, Dec. 22, 2015, ISSN: 2095-6231. DOI: [10.1038/boneres.2015.12](https://doi.org/10.1038/boneres.2015.12).
- [114] G. Wei, Q. Jin, W. V. Giannobile, and P. X. Ma, "The enhancement of osteogenesis by nano-fibrous scaffolds incorporating rhBMP-7 nanospheres," *Biomaterials*, vol. 28, no. 12, pp. 2087–2096, Apr. 2007, ISSN: 01429612. DOI: [10.1016/j.biomaterials.2006.12.028](https://doi.org/10.1016/j.biomaterials.2006.12.028).
- [115] X. Sun, X. Zhao, L. Zhao, *et al.*, "Development of a hybrid gelatin hydrogel platform for tissue engineering and protein delivery applications," *Journal of Materials Chemistry B*, vol. 3, no. 30, pp. 6368–6376, 2015, ISSN: 2050-750X, 2050-7518. DOI: [10.1039/C5TB00645G](https://doi.org/10.1039/C5TB00645G).
- [116] P. F. Egan, S. J. Ferguson, and K. Shea, "Design of hierarchical three-dimensional printed scaffolds considering mechanical and biological factors for bone tissue engineering," *Journal of Mechanical Design*, vol. 139, no. 6, p. 061 401, Jun. 1, 2017, ISSN: 1050-0472, 1528-9001. DOI: [10.1115/1.4036396](https://doi.org/10.1115/1.4036396).

- [117] A. Kurzyk, B. Ostrowska, W. Świąszkowski, and Z. Pojda, "Characterization and optimization of the seeding process of adipose stem cells on the polycaprolactone scaffolds," *Stem Cells International*, vol. 2019, pp. 1–17, Feb. 20, 2019, ISSN: 1687-966X, 1687-9678. DOI: [10.1155/2019/1201927](https://doi.org/10.1155/2019/1201927).
- [118] M. Cámara-Torres, R. Sinha, C. Mota, and L. Moroni, "Improving cell distribution on 3d additive manufactured scaffolds through engineered seeding media density and viscosity," *Acta Biomaterialia*, vol. 101, pp. 183–195, Jan. 2020, ISSN: 17427061. DOI: [10.1016/j.actbio.2019.11.020](https://doi.org/10.1016/j.actbio.2019.11.020).
- [119] E. M. Bueno, G. Laevsky, and G. A. Barabino, "Enhancing cell seeding of scaffolds in tissue engineering through manipulation of hydrodynamic parameters," *Journal of Biotechnology*, vol. 129, no. 3, pp. 516–531, May 2007, ISSN: 01681656. DOI: [10.1016/j.jbiotec.2007.01.005](https://doi.org/10.1016/j.jbiotec.2007.01.005).
- [120] S. Lemonnier, T. Boudierlique, S. Naili, *et al.*, "Cell colonization ability of a commercialized large porous alveolar scaffold," *Applied Bionics and Biomechanics*, vol. 2017, pp. 1–10, 2017, ISSN: 1176-2322, 1754-2103. DOI: [10.1155/2017/8949264](https://doi.org/10.1155/2017/8949264).
- [121] P. Carmeliet and R. K. Jain, "Angiogenesis in cancer and other diseases," *Nature*, vol. 407, no. 6801, pp. 249–257, Sep. 2000, ISSN: 0028-0836, 1476-4687. DOI: [10.1038/35025220](https://doi.org/10.1038/35025220).
- [122] L. Ouyang, J. P. K. Armstrong, M. Salmeron-Sanchez, and M. M. Stevens, "Assembling living building blocks to engineer complex tissues," *Advanced Functional Materials*, vol. 30, no. 26, p. 1909009, Jun. 2020, ISSN: 1616-301X, 1616-3028. DOI: [10.1002/adfm.201909009](https://doi.org/10.1002/adfm.201909009).
- [123] M. Abedin and N. King, "Diverse evolutionary paths to cell adhesion," *Trends in Cell Biology*, vol. 20, no. 12, pp. 734–742, Dec. 2010, ISSN: 09628924. DOI: [10.1016/j.tcb.2010.08.002](https://doi.org/10.1016/j.tcb.2010.08.002).
- [124] W. S. Adair, S. A. Steinmetz, D. M. Mattson, U. W. Goodenough, and J. E. Heuser, "Nucleated assembly of chlamydomonas and volvox cell walls," *The Journal of Cell Biology*, vol. 105, no. 5, pp. 2373–2382, Nov. 1, 1987, ISSN: 0021-9525, 1540-8140. DOI: [10.1083/jcb.105.5.2373](https://doi.org/10.1083/jcb.105.5.2373).
- [125] Y. Arakaki, T. Fujiwara, H. Kawai-Toyooka, *et al.*, "Evolution of cytokinesis-related protein localization during the emergence of multicellularity in volvocine green algae," *BMC Evolutionary Biology*, vol. 17, no. 1, p. 243, Dec. 2017, ISSN: 1471-2148. DOI: [10.1186/s12862-017-1091-z](https://doi.org/10.1186/s12862-017-1091-z).
- [126] M. Pocock, "Volvox in south africa," *Annals of the South African Museum*, Annals of the South African Museum, vol. 16, pp. 473–521, 1933.
- [127] A. Meyer, "Die plasmaverbindung und die membranen von volvox," *Bot. Zeitg.*, vol. 54, pp. 187–217, 1986.
- [128] J. H. Shauky and L. A. Davidson, "Tissue mechanics and adhesion during embryo development," *Developmental Biology*, vol. 401, no. 1, pp. 152–164, May 2015, ISSN: 00121606. DOI: [10.1016/j.ydbio.2014.12.005](https://doi.org/10.1016/j.ydbio.2014.12.005).

- [129] G. Ruan, D. Wedlich, and A. Köhler, "How cell-cell adhesion contributes to early embryonic development," in *The Vertebrate Organizer*, H. Grunz, Ed., Berlin, Heidelberg: Springer Berlin Heidelberg, 2004, pp. 201–218, ISBN: 978-3-642-05732-8 978-3-662-10416-3. DOI: [10.1007/978-3-662-10416-3_13](https://doi.org/10.1007/978-3-662-10416-3_13).
- [130] O. Huber and M. Sumper, "Algal-CAMs: Isoforms of a cell adhesion molecule in embryos of the alga volvox with homology to drosophila fasciclin i.," *The EMBO Journal*, vol. 13, no. 18, pp. 4212–4222, Sep. 1994, ISSN: 02614189. DOI: [10.1002/j.1460-2075.1994.tb06741.x](https://doi.org/10.1002/j.1460-2075.1994.tb06741.x).
- [131] K. J. Green and D. L. Kirk, "Cleavage patterns, cell lineages, and development of a cytoplasmic bridge system in volvox embryos.," *Journal of Cell Biology*, vol. 91, no. 3, pp. 743–755, Dec. 1, 1981, ISSN: 0021-9525, 1540-8140. DOI: [10.1083/jcb.91.3.743](https://doi.org/10.1083/jcb.91.3.743).
- [132] H. Wang, T. Ding, N. Brown, *et al.*, "Zonula occludens-1 (ZO-1) is involved in morula to blastocyst transformation in the mouse," *Developmental Biology*, vol. 318, no. 1, pp. 112–125, Jun. 2008, ISSN: 00121606. DOI: [10.1016/j.ydbio.2008.03.008](https://doi.org/10.1016/j.ydbio.2008.03.008).
- [133] A. Albanese, J. M. Swaney, D. H. Yun, *et al.*, "Multiscale 3d phenotyping of human cerebral organoids," *Scientific Reports*, vol. 10, no. 1, p. 21 487, Dec. 2020, ISSN: 2045-2322. DOI: [10.1038/s41598-020-78130-7](https://doi.org/10.1038/s41598-020-78130-7).
- [134] A. A. Salahudeen, S. S. Choi, A. Rustagi, *et al.*, "Progenitor identification and SARS-CoV-2 infection in human distal lung organoids," *Nature*, vol. 588, no. 7839, pp. 670–675, Dec. 24, 2020, ISSN: 0028-0836, 1476-4687. DOI: [10.1038/s41586-020-3014-1](https://doi.org/10.1038/s41586-020-3014-1).
- [135] P. Hoang, A. Kowalczewski, S. Sun, *et al.*, "Engineering spatial-organized cardiac organoids for developmental toxicity testing," *Stem Cell Reports*, vol. 16, no. 5, pp. 1228–1244, May 2021, ISSN: 22136711. DOI: [10.1016/j.stemcr.2021.03.013](https://doi.org/10.1016/j.stemcr.2021.03.013).
- [136] H. Ahmed, H. Eslami Amirabadi, K. Toet, *et al.*, "Development of a diet-induced diseasemimicking in vitro model of non-alcoholic steatohepatitis / fibrosis," Poster, Poster, TNO Healthy Living, The Netherlands.
- [137] J. H. Low, P. Li, E. G. Y. Chew, *et al.*, "Generation of human PSC-derived kidney organoids with patterned nephron segments and a de novo vascular network," *Cell Stem Cell*, vol. 25, no. 3, 373–387.e9, Sep. 2019, ISSN: 19345909. DOI: [10.1016/j.stem.2019.06.009](https://doi.org/10.1016/j.stem.2019.06.009).
- [138] A. Lloyd, "Engineering surfaces to enhance cell adhesion," *Materials Today*, vol. 6, no. 11, p. 19, Nov. 2003, ISSN: 13697021. DOI: [10.1016/S1369-7021\(03\)01120-9](https://doi.org/10.1016/S1369-7021(03)01120-9).
- [139] M. Gupta, B. Doss, C. T. Lim, R. Voituriez, and B. Ladoux, "Single cell rigidity sensing: A complex relationship between focal adhesion dynamics and large-scale actin cytoskeleton remodeling," *Cell Adhesion & Migration*, vol. 10, no. 5, pp. 554–567, Sep. 2, 2016, ISSN: 1933-6918, 1933-6926. DOI: [10.1080/19336918.2016.1173800](https://doi.org/10.1080/19336918.2016.1173800).
- [140] N. Al-Azzam and A. Alazzam, "Micropatterning of cells via adjusting surface wettability using plasma treatment and graphene oxide deposition," *PLOS ONE*, vol. 17, no. 6, S. Honda, Ed., e0269914, Jun. 16, 2022, ISSN: 1932-6203. DOI: [10.1371/journal.pone.0269914](https://doi.org/10.1371/journal.pone.0269914).

- [141] C. J. Arias, R. L. Surmaitis, and J. B. Schlenoff, "Cell adhesion and proliferation on the "living" surface of a polyelectrolyte multilayer," *Langmuir*, vol. 32, no. 21, pp. 5412–5421, May 31, 2016, ISSN: 0743-7463, 1520-5827. DOI: [10.1021/acs.langmuir.6b00784](https://doi.org/10.1021/acs.langmuir.6b00784).
- [142] N. Baksh, N. D. Gallant, and R. G. Toomey, "Cell sheet engineering for integrating functional tissue in vivo: Successes and challenges," *MRS Bulletin*, vol. 42, no. 5, pp. 350–355, May 2017, ISSN: 0883-7694, 1938-1425. DOI: [10.1557/mrs.2017.91](https://doi.org/10.1557/mrs.2017.91).
- [143] K. Moschouris, N. Firoozi, and Y. Kang, "The application of cell sheet engineering in the vascularization of tissue regeneration," *Regenerative Medicine*, vol. 11, no. 6, pp. 559–570, Sep. 2016, ISSN: 1746-0751, 1746-076X. DOI: [10.2217/rme-2016-0059](https://doi.org/10.2217/rme-2016-0059).
- [144] D. Radke, L. Chen, S. Qi, and F. Zhao, "Prevascularized stem cell sheet for full-thickness skin wound repair," in *Vascular Surgery, Neurosurgery, Lower Extremity Ulcers, Antimicrobials, Wound Assessment, Care, Measurement and Repair*, M. A. Shiffman and M. Low, Eds., vol. 5, Series Title: Recent Clinical Techniques, Results, and Research in Wounds, Cham: Springer International Publishing, 2018, pp. 167–172, ISBN: 978-3-030-10715-4 978-3-030-10716-1. DOI: [10.1007/15695_2017_86](https://doi.org/10.1007/15695_2017_86).
- [145] P. P. Y. Lui, O. T. Wong, and Y. W. Lee, "Application of tendon-derived stem cell sheet for the promotion of graft healing in anterior cruciate ligament reconstruction," *The American Journal of Sports Medicine*, vol. 42, no. 3, pp. 681–689, Mar. 2014, ISSN: 0363-5465, 1552-3365. DOI: [10.1177/0363546513517539](https://doi.org/10.1177/0363546513517539).
- [146] C. J. Jackson, K. A. Tønseth, and T. P. Uthaim, "Cultured epidermal stem cells in regenerative medicine," *Stem Cell Research & Therapy*, vol. 8, no. 1, p. 155, Dec. 2017, ISSN: 1757-6512. DOI: [10.1186/s13287-017-0587-1](https://doi.org/10.1186/s13287-017-0587-1).
- [147] R. Guo, M. Morimatsu, T. Feng, *et al.*, "Stem cell-derived cell sheet transplantation for heart tissue repair in myocardial infarction," *Stem Cell Research & Therapy*, vol. 11, no. 1, p. 19, Dec. 2020, ISSN: 1757-6512. DOI: [10.1186/s13287-019-1536-y](https://doi.org/10.1186/s13287-019-1536-y).
- [148] S. Verpoorte and C. bibinitperiod B. M. Society, Eds., *14th International Conference on Miniaturized Systems for Chemistry and Life Sciences 2010, (MicroTAS 2010): Groningen, The Netherlands, 3 - 7 October 2010*, Red Hook, NY: Curran, 2011, ISBN: 978-1-61839-062-2.
- [149] A. R. Sousa, C. Martins-Cruz, M. B. Oliveira, and J. F. Mano, "One-step rapid fabrication of cell-only living fibers," *Advanced Materials*, vol. 32, no. 2, p. 1906305, Jan. 2020, ISSN: 0935-9648, 1521-4095. DOI: [10.1002/adma.201906305](https://doi.org/10.1002/adma.201906305).
- [150] Y. Jun, E. Kang, S. Chae, and S.-H. Lee, "Microfluidic spinning of micro- and nano-scale fibers for tissue engineering," *Lab Chip*, vol. 14, no. 13, pp. 2145–2160, 2014, ISSN: 1473-0197, 1473-0189. DOI: [10.1039/C3LC51414E](https://doi.org/10.1039/C3LC51414E).
- [151] M. C. McNamara, F. Sharifi, J. Okuzono, R. Montazami, and N. N. Hashemi, "Microfluidic manufacturing of alginate fibers with encapsulated astrocyte cells," *ACS Applied Bio Materials*, vol. 2, no. 4, pp. 1603–1613, Apr. 15, 2019, ISSN: 2576-6422, 2576-6422. DOI: [10.1021/acsabm.9b00022](https://doi.org/10.1021/acsabm.9b00022).

- [152] A. Shima, A. Itou, and S. Takeuchi, "Cell fibers promote proliferation of co-cultured cells on a dish," *Scientific Reports*, vol. 10, no. 1, p. 288, Dec. 2020, ISSN: 2045-2322. DOI: [10.1038/s41598-019-57213-0](https://doi.org/10.1038/s41598-019-57213-0).
- [153] K. Saeki, H. Hiramatsu, A. Hori, *et al.*, "Sacrificial alginate-assisted microfluidic engineering of cell-supportive protein microfibers for hydrogel-based cell encapsulation," *ACS Omega*, vol. 5, no. 34, pp. 21 641–21 650, Sep. 1, 2020, ISSN: 2470-1343, 2470-1343. DOI: [10.1021/acsomega.0c02385](https://doi.org/10.1021/acsomega.0c02385).
- [154] B. R. Lee, K. H. Lee, E. Kang, D.-S. Kim, and S.-H. Lee, "Microfluidic wet spinning of chitosan-alginate microfibers and encapsulation of HepG2 cells in fibers," *Biomicrofluidics*, vol. 5, no. 2, p. 022 208, Jun. 2011, ISSN: 1932-1058. DOI: [10.1063/1.3576903](https://doi.org/10.1063/1.3576903).
- [155] S. Nath and G. R. Devi, "Three-dimensional culture systems in cancer research: Focus on tumor spheroid model," *Pharmacology & Therapeutics*, vol. 163, pp. 94–108, Jul. 2016, ISSN: 01637258. DOI: [10.1016/j.pharmthera.2016.03.013](https://doi.org/10.1016/j.pharmthera.2016.03.013).
- [156] W. Kim, Y. Gwon, S. Park, H. Kim, and J. Kim, "Therapeutic strategies of three-dimensional stem cell spheroids and organoids for tissue repair and regeneration," *Bioactive Materials*, vol. 19, pp. 50–74, Jan. 2023, ISSN: 2452199X. DOI: [10.1016/j.bioactmat.2022.03.039](https://doi.org/10.1016/j.bioactmat.2022.03.039).
- [157] R. Foty, "A simple hanging drop cell culture protocol for generation of 3d spheroids," *Journal of Visualized Experiments*, no. 51, p. 2720, May 6, 2011, ISSN: 1940-087X. DOI: [10.3791/2720](https://doi.org/10.3791/2720).
- [158] J. M. Lee, D. Y. Park, L. Yang, *et al.*, "Generation of uniform-sized multicellular tumor spheroids using hydrogel microwells for advanced drug screening," *Scientific Reports*, vol. 8, no. 1, p. 17 145, Dec. 2018, ISSN: 2045-2322. DOI: [10.1038/s41598-018-35216-7](https://doi.org/10.1038/s41598-018-35216-7).
- [159] R.-Z. Lin, W.-C. Chu, C.-C. Chiang, C.-H. Lai, and H.-Y. Chang, "Magnetic reconstruction of three-dimensional tissues from multicellular spheroids," *Tissue Engineering Part C: Methods*, vol. 14, no. 3, pp. 197–205, Sep. 2008, ISSN: 1937-3384, 1937-3392. DOI: [10.1089/ten.tec.2008.0061](https://doi.org/10.1089/ten.tec.2008.0061).
- [160] S. Sart, R. F.-X. Tomasi, G. Amselem, and C. N. Baroud, "Multiscale cytometry and regulation of 3d cell cultures on a chip," *Nature Communications*, vol. 8, no. 1, p. 469, Dec. 2017, ISSN: 2041-1723. DOI: [10.1038/s41467-017-00475-x](https://doi.org/10.1038/s41467-017-00475-x).
- [161] P. Fattahi, A. Rahimian, M. Q. Slama, *et al.*, "Core-shell hydrogel microcapsules enable formation of human pluripotent stem cell spheroids and their cultivation in a stirred bioreactor," *Scientific Reports*, vol. 11, no. 1, p. 7177, Dec. 2021, ISSN: 2045-2322. DOI: [10.1038/s41598-021-85786-2](https://doi.org/10.1038/s41598-021-85786-2).
- [162] M. Ferrari, F. Cirisano, and M. C. Morán, "Mammalian cell spheroids on mixed organic-inorganic superhydrophobic coating," *Molecules*, vol. 27, no. 4, p. 1247, Feb. 12, 2022, ISSN: 1420-3049. DOI: [10.3390/molecules27041247](https://doi.org/10.3390/molecules27041247).

- [163] X. Dou, P. Li, and H. Schönherr, "Three-dimensional microstructured poly(vinyl alcohol) hydrogel platform for the controlled formation of multicellular cell spheroids," *Biomacromolecules*, vol. 19, no. 1, pp. 158–166, Jan. 8, 2018, ISSN: 1525-7797, 1526-4602. DOI: [10.1021/acs.biomac.7b01345](https://doi.org/10.1021/acs.biomac.7b01345).
- [164] D. Massai, G. Isu, D. Madeddu, *et al.*, "A versatile bioreactor for dynamic suspension cell culture. application to the culture of cancer cell spheroids," *PLOS ONE*, vol. 11, no. 5, M. Pesce, Ed., e0154610, May 4, 2016, ISSN: 1932-6203. DOI: [10.1371/journal.pone.0154610](https://doi.org/10.1371/journal.pone.0154610).
- [165] R.-Z. Lin and H.-Y. Chang, "Recent advances in three-dimensional multicellular spheroid culture for biomedical research," *Biotechnology Journal*, vol. 3, no. 9, pp. 1172–1184, Oct. 2008, ISSN: 18606768, 18607314. DOI: [10.1002/biot.200700228](https://doi.org/10.1002/biot.200700228).
- [166] X. Cui, Y. Hartanto, and H. Zhang, "Advances in multicellular spheroids formation," *Journal of The Royal Society Interface*, vol. 14, no. 127, p. 20160877, Feb. 2017, ISSN: 1742-5689, 1742-5662. DOI: [10.1098/rsif.2016.0877](https://doi.org/10.1098/rsif.2016.0877).
- [167] M. K. Han and J. de Rooij, "Converging and unique mechanisms of mechanotransduction at adhesion sites," *Trends in Cell Biology*, vol. 26, no. 8, pp. 612–623, Aug. 2016, ISSN: 09628924. DOI: [10.1016/j.tcb.2016.03.005](https://doi.org/10.1016/j.tcb.2016.03.005).
- [168] F. Martino, A. R. Perestrelo, V. Vinarský, S. Pagliari, and G. Forte, "Cellular mechanotransduction: From tension to function," *Frontiers in Physiology*, vol. 9, p. 824, Jul. 5, 2018, ISSN: 1664-042X. DOI: [10.3389/fphys.2018.00824](https://doi.org/10.3389/fphys.2018.00824).
- [169] P. Romani, L. Valcarcel-Jimenez, C. Frezza, and S. Dupont, "Crosstalk between mechanotransduction and metabolism," *Nature Reviews Molecular Cell Biology*, vol. 22, no. 1, pp. 22–38, Jan. 2021, ISSN: 1471-0072, 1471-0080. DOI: [10.1038/s41580-020-00306-w](https://doi.org/10.1038/s41580-020-00306-w).
- [170] C. F. Labuschagne, E. C. Cheung, J. Blagih, M.-C. Domart, and K. H. Vousden, "Cell clustering promotes a metabolic switch that supports metastatic colonization," *Cell Metabolism*, vol. 30, no. 4, 720–734.e5, Oct. 2019, ISSN: 15504131. DOI: [10.1016/j.cmet.2019.07.014](https://doi.org/10.1016/j.cmet.2019.07.014).
- [171] I. Smyrek, B. Mathew, S. C. Fischer, S. M. Lissek, S. Becker, and E. H. K. Stelzer, "E-cadherin, actin, microtubules and FAK dominate different spheroid formation phases and important elements of tissue integrity," *Biology Open*, bio.037051, Jan. 1, 2018, ISSN: 2046-6390. DOI: [10.1242/bio.037051](https://doi.org/10.1242/bio.037051).
- [172] Y. B. Lee, E. M. Kim, H. Byun, *et al.*, "Engineering spheroids potentiating cell-cell and cell-ECM interactions by self-assembly of stem cell microlayer," *Biomaterials*, vol. 165, pp. 105–120, May 2018, ISSN: 01429612. DOI: [10.1016/j.biomaterials.2018.02.049](https://doi.org/10.1016/j.biomaterials.2018.02.049).
- [173] A. Zuidema, W. Wang, and A. Sonnenberg, "Crosstalk between cell adhesion complexes in regulation of mechanotransduction," *BioEssays*, vol. 42, no. 11, p. 2000119, Nov. 2020, ISSN: 0265-9247, 1521-1878. DOI: [10.1002/bies.202000119](https://doi.org/10.1002/bies.202000119).

- [174] M. Kieliszewski and E. Shpak, "Synthetic genes for the elucidation of glycosylation codes for arabinogalactan-proteins and other hydroxyproline-rich glycoproteins:" *Cellular and Molecular Life Sciences*, vol. 58, no. 10, pp. 1386–1398, Sep. 2001, ISSN: 1420-682X. DOI: [10.1007/PL00000783](https://doi.org/10.1007/PL00000783).
- [175] N. A. Saffioti, E. A. Cavalcanti-Adam, and D. Pallarola, "Biosensors for studies on adhesion-mediated cellular responses to their microenvironment," *Frontiers in Bioengineering and Biotechnology*, vol. 8, p. 597950, Nov. 11, 2020, ISSN: 2296-4185. DOI: [10.3389/fbioe.2020.597950](https://doi.org/10.3389/fbioe.2020.597950).
- [176] A. J. Engler, S. Sen, H. L. Sweeney, and D. E. Discher, "Matrix elasticity directs stem cell lineage specification," *Cell*, vol. 126, no. 4, pp. 677–689, Aug. 2006, ISSN: 00928674. DOI: [10.1016/j.cell.2006.06.044](https://doi.org/10.1016/j.cell.2006.06.044).
- [177] D. A. Young, Y. S. Choi, A. J. Engler, and K. L. Christman, "Stimulation of adipogenesis of adult adipose-derived stem cells using substrates that mimic the stiffness of adipose tissue," *Biomaterials*, vol. 34, no. 34, pp. 8581–8588, Nov. 2013, ISSN: 01429612. DOI: [10.1016/j.biomaterials.2013.07.103](https://doi.org/10.1016/j.biomaterials.2013.07.103).
- [178] G. Chen, C. Dong, L. Yang, and Y. Lv, "3d scaffolds with different stiffness but the same microstructure for bone tissue engineering," *ACS Applied Materials & Interfaces*, vol. 7, no. 29, pp. 15790–15802, Jul. 29, 2015, ISSN: 1944-8244, 1944-8252. DOI: [10.1021/acsami.5b02662](https://doi.org/10.1021/acsami.5b02662).
- [179] R. Lev and D. Seliktar, "Hydrogel biomaterials and their therapeutic potential for muscle injuries and muscular dystrophies," *Journal of The Royal Society Interface*, vol. 15, no. 138, p. 20170380, Jan. 2018, ISSN: 1742-5689, 1742-5662. DOI: [10.1098/rsif.2017.0380](https://doi.org/10.1098/rsif.2017.0380).
- [180] J. Lee, A. A. Abdeen, D. Zhang, and K. A. Kilian, "Directing stem cell fate on hydrogel substrates by controlling cell geometry, matrix mechanics and adhesion ligand composition," *Biomaterials*, vol. 34, no. 33, pp. 8140–8148, Nov. 2013, ISSN: 01429612. DOI: [10.1016/j.biomaterials.2013.07.074](https://doi.org/10.1016/j.biomaterials.2013.07.074).
- [181] C. Argentati, F. Morena, I. Tortorella, *et al.*, "Insight into mechanobiology: How stem cells feel mechanical forces and orchestrate biological functions," *International Journal of Molecular Sciences*, vol. 20, no. 21, p. 5337, Oct. 26, 2019, ISSN: 1422-0067. DOI: [10.3390/ijms20215337](https://doi.org/10.3390/ijms20215337).
- [182] K. Takahashi and S. Yamanaka, "Induction of pluripotent stem cells from mouse embryonic and adult fibroblast cultures by defined factors," *Cell*, vol. 126, no. 4, pp. 663–676, Aug. 2006, ISSN: 00928674. DOI: [10.1016/j.cell.2006.07.024](https://doi.org/10.1016/j.cell.2006.07.024).
- [183] K. Takahashi, K. Tanabe, M. Ohnuki, *et al.*, "Induction of pluripotent stem cells from adult human fibroblasts by defined factors," *Cell*, vol. 131, no. 5, pp. 861–872, Nov. 2007, ISSN: 00928674. DOI: [10.1016/j.cell.2007.11.019](https://doi.org/10.1016/j.cell.2007.11.019).

- [184] F. Ruiz-Ojeda, A. Rupérez, C. Gomez-Llorente, A. Gil, and C. Aguilera, "Cell models and their application for studying adipogenic differentiation in relation to obesity: A review," *International Journal of Molecular Sciences*, vol. 17, no. 7, p. 1040, Jun. 30, 2016, ISSN: 1422-0067. DOI: [10.3390/ijms17071040](https://doi.org/10.3390/ijms17071040).
- [185] F. Martini, K. Welch, and M. Newsome, *Fundamentals of Anatomy and Physiology: Applications Manual*. Prentice Hall, 1998.
- [186] W. Li, "Damage models for soft tissues: A survey," *Journal of Medical and Biological Engineering*, vol. 36, no. 3, pp. 285–307, Jun. 2016, ISSN: 1609-0985, 2199-4757. DOI: [10.1007/s40846-016-0132-1](https://doi.org/10.1007/s40846-016-0132-1).
- [187] M. Sharabi, "Structural mechanisms in soft fibrous tissues: A review," *Frontiers in Materials*, vol. 8, p. 793 647, Jan. 5, 2022, ISSN: 2296-8016. DOI: [10.3389/fmats.2021.793647](https://doi.org/10.3389/fmats.2021.793647).
- [188] S. Budday, T. C. Ovaert, G. A. Holzapfel, P. Steinmann, and E. Kuhl, "Fifty shades of brain: A review on the mechanical testing and modeling of brain tissue," *Archives of Computational Methods in Engineering*, vol. 27, no. 4, pp. 1187–1230, Sep. 2020, ISSN: 1134-3060, 1886-1784. DOI: [10.1007/s11831-019-09352-w](https://doi.org/10.1007/s11831-019-09352-w).
- [189] J. L. Zitnay and J. A. Weiss, "Load transfer, damage, and failure in ligaments and tendons: DAMAGE IN LIGAMENTS AND TENDONS," *Journal of Orthopaedic Research®*, vol. 36, no. 12, pp. 3093–3104, Dec. 2018, ISSN: 07360266. DOI: [10.1002/jor.24134](https://doi.org/10.1002/jor.24134).
- [190] K. W. Jorgenson, S. M. Phillips, and T. A. Hornberger, "Identifying the structural adaptations that drive the mechanical load-induced growth of skeletal muscle: A scoping review," *Cells*, vol. 9, no. 7, p. 1658, Jul. 9, 2020, ISSN: 2073-4409. DOI: [10.3390/cells9071658](https://doi.org/10.3390/cells9071658).
- [191] L. D. Black, P. G. Allen, S. M. Morris, P. J. Stone, and B. Suki, "Mechanical and failure properties of extracellular matrix sheets as a function of structural protein composition," *Biophysical Journal*, vol. 94, no. 5, pp. 1916–1929, Mar. 2008, ISSN: 00063495. DOI: [10.1529/biophysj.107.107144](https://doi.org/10.1529/biophysj.107.107144).
- [192] P. Bhandari, A. Bath, L. Sadhotra, M. Singh, and M. Mukherjee, "Management of soft tissue defects of the ankle and foot," *Medical Journal Armed Forces India*, vol. 61, no. 3, pp. 253–255, Jul. 2005, ISSN: 03771237. DOI: [10.1016/S0377-1237\(05\)80167-4](https://doi.org/10.1016/S0377-1237(05)80167-4).
- [193] J. Sykes, "Management of soft tissue defect," *Journal of Trauma: Injury, Infection & Critical Care*, vol. 62, no. 6, S90, Jun. 2007, ISSN: 0022-5282. DOI: [10.1097/TA.0b013e318065b34a](https://doi.org/10.1097/TA.0b013e318065b34a).
- [194] F. Frizzera, G. J. P. L. d. Oliveira, J. A. Shibli, K. C. d. Moraes, E. B. Marcantonio, and E. Marcantonio Junior, "Treatment of peri-implant soft tissue defects: A narrative review," *Brazilian Oral Research*, vol. 33, e073, suppl 1 2019, ISSN: 1807-3107, 1806-8324. DOI: [10.1590/1807-3107bor-2019.vol33.0073](https://doi.org/10.1590/1807-3107bor-2019.vol33.0073).
- [195] L. B. Kaban, "Congenital abnormalities of the temporomandibular joint," in *Pediatric Oral and Maxillofacial Surgery*, Elsevier, 2004, pp. 302–339, ISBN: 978-0-7216-9691-1. DOI: [10.1016/B978-0-7216-9691-1.50024-7](https://doi.org/10.1016/B978-0-7216-9691-1.50024-7).

- [196] J. F. López, K. E. Hietanen, I. S. Kaartinen, *et al.*, "Primary flap reconstruction of tissue defects after sarcoma surgery enables curative treatment with acceptable functional results: A 7-year review," *BMC Surgery*, vol. 15, no. 1, p. 71, Dec. 2015, ISSN: 1471-2482. DOI: [10.1186/s12893-015-0060-y](https://doi.org/10.1186/s12893-015-0060-y).
- [197] X. Zhang, X. Yang, Y. Chen, *et al.*, "Clinical study on orthopaedic treatment of chronic osteomyelitis with soft tissue defect in adults," *International Wound Journal*, vol. 19, no. 6, pp. 1349–1356, Oct. 2022, ISSN: 1742-4801, 1742-481X. DOI: [10.1111/iwj.13729](https://doi.org/10.1111/iwj.13729).
- [198] S. Sharma, S. Muthu, M. Jeyaraman, R. Ranjan, and S. K. Jha, "Translational products of adipose tissue-derived mesenchymal stem cells: Bench to bedside applications," *World Journal of Stem Cells*, vol. 13, no. 10, pp. 1360–1381, Oct. 26, 2021, ISSN: 1948-0210. DOI: [10.4252/wjsc.v13.i10.1360](https://doi.org/10.4252/wjsc.v13.i10.1360).
- [199] P. A. De Lopes Sousa Martins, "Experimental and numerical studies of soft biological tissues," 2010, Publisher: Unpublished. DOI: [10.13140/RG.2.2.11437.74720](https://doi.org/10.13140/RG.2.2.11437.74720).
- [200] P. Zoio and A. Oliva, "Skin-on-a-chip technology: Microengineering physiologically relevant in vitro skin models," *Pharmaceutics*, vol. 14, no. 3, p. 682, Mar. 21, 2022, ISSN: 1999-4923. DOI: [10.3390/pharmaceutics14030682](https://doi.org/10.3390/pharmaceutics14030682).
- [201] D. Mertz, J. Sentosa, G. Luker, and S. Takayama, "Studying adipose tissue in the breast tumor microenvironment in vitro: Progress and opportunities," *Tissue Engineering and Regenerative Medicine*, vol. 17, no. 6, pp. 773–785, Dec. 2020, ISSN: 1738-2696, 2212-5469. DOI: [10.1007/s13770-020-00299-9](https://doi.org/10.1007/s13770-020-00299-9).
- [202] M. A. Teixeira, M. T. P. Amorim, and H. P. Felgueiras, "Poly(vinyl alcohol)-based nanofibrous electrospun scaffolds for tissue engineering applications," *Polymers*, vol. 12, no. 1, p. 7, Dec. 18, 2019, ISSN: 2073-4360. DOI: [10.3390/polym12010007](https://doi.org/10.3390/polym12010007).
- [203] D. S. Thoma, M. Zeltner, M. Hilbe, C. H. F. Hämmerle, J. Hüsler, and R. E. Jung, "Randomized controlled clinical study evaluating effectiveness and safety of a volume-stable collagen matrix compared to autogenous connective tissue grafts for soft tissue augmentation at implant sites," *Journal of Clinical Periodontology*, vol. 43, no. 10, pp. 874–885, Oct. 2016, ISSN: 0303-6979, 1600-051X. DOI: [10.1111/jcpe.12588](https://doi.org/10.1111/jcpe.12588).
- [204] "ISAPS international survey on aesthetic/cosmetic procedures performed in 2020," International Society of Aesthetic Plastic Surgery, 2020.
- [205] "Plastic surgery statistics report 2020," American Society of Plastic Surgeons, 2020.
- [206] M. Field, A. Splevins, P. Picaut, *et al.*, "AbobotulinumtoxinA (dysport®), OnabotulinumtoxinA (botox®), and IncobotulinumtoxinA (xeomin®) neurotoxin content and potential implications for duration of response in patients," *Toxins*, vol. 10, no. 12, p. 535, Dec. 13, 2018, ISSN: 2072-6651. DOI: [10.3390/toxins10120535](https://doi.org/10.3390/toxins10120535).
- [207] M. B. Gadarowski, R. I. Ghamrawi, S. L. Taylor, and S. R. Feldman, "PrabotulinumtoxinA-xvfs for the treatment of moderate-to-severe glabellar lines," *Annals of Pharmacotherapy*, vol. 55, no. 3, pp. 354–361, Mar. 2021, ISSN: 1060-0280, 1542-6270. DOI: [10.1177/1060028020943527](https://doi.org/10.1177/1060028020943527).

- [208] B. C. Patel, C. S. Wong, T. Wright, and A. D. Schaffner, "Breast implants," in *StatPearls*, Treasure Island (FL): StatPearls Publishing, 2022.
- [209] H. B. P. M. Dijkman, I. Slaats, and P. Bult, "Assessment of silicone particle migration among women undergoing removal or revision of silicone breast implants in the netherlands," *JAMA Network Open*, vol. 4, no. 9, e2125381, Sep. 20, 2021, ISSN: 2574-3805. DOI: [10.1001/jamanetworkopen.2021.25381](https://doi.org/10.1001/jamanetworkopen.2021.25381).
- [210] C. Hillard, J. D. Fowler, R. Barta, and B. Cunningham, "Silicone breast implant rupture: A review," *Gland Surgery*, vol. 6, no. 2, pp. 163–168, Apr. 2017, ISSN: 2227684X, 22278575. DOI: [10.21037/gs.2016.09.12](https://doi.org/10.21037/gs.2016.09.12).
- [211] D. Melita and A. Innocenti, "Surgical calf augmentation techniques: Personal experience, literature review and analysis of complications," *Aesthetic Plastic Surgery*, vol. 43, no. 4, pp. 973–979, Aug. 2019, ISSN: 0364-216X, 1432-5241. DOI: [10.1007/s00266-019-01347-z](https://doi.org/10.1007/s00266-019-01347-z).
- [212] J. Kaplan and R. Rohrich, "Breast implant illness: A topic in review," *Gland Surgery*, vol. 10, no. 1, pp. 430–443, Jan. 2021, ISSN: 2227684X, 22278575. DOI: [10.21037/gs-20-231](https://doi.org/10.21037/gs-20-231).
- [213] Q. Gao, L. Duan, X. Feng, and W. Xu, "Superiority of poly(l-lactic acid) microspheres as dermal fillers," *Chinese Chemical Letters*, vol. 32, no. 1, pp. 577–582, Jan. 2021, ISSN: 10018417. DOI: [10.1016/j.cclet.2020.03.071](https://doi.org/10.1016/j.cclet.2020.03.071).
- [214] Y. Zhang, Q. Luo, H. Liang, J. Chen, N. Zhao, and B. He, "In vivo neocollagenesis of injectable poly(l-lactic acid) microspheres," *Chinese Journal of Tissue Engineering Research*, vol. 26, no. 34, pp. 5448–5453, 2022. DOI: [10.12307/2022.454](https://doi.org/10.12307/2022.454).
- [215] D. R. Jordan, "Soft-tissue fillers for wrinkles, folds and volume augmentation," *Canadian Journal of Ophthalmology*, vol. 38, no. 4, pp. 285–288, Jun. 2003, ISSN: 00084182. DOI: [10.1016/S0008-4182\(03\)80093-5](https://doi.org/10.1016/S0008-4182(03)80093-5).
- [216] G. Lemperle, N. S. Sadick, T. R. Knapp, and S. M. Lemperle, "ArteFill® permanent injectable for soft tissue augmentation: II. indications and applications," *Aesthetic Plastic Surgery*, vol. 34, no. 3, pp. 273–286, Jun. 2010, ISSN: 0364-216X, 1432-5241. DOI: [10.1007/s00266-009-9414-0](https://doi.org/10.1007/s00266-009-9414-0).
- [217] S. R. Cohen, C. F. Berner, M. Busso, *et al.*, "ArteFill: A long-lasting injectable wrinkle filler material???-summary of the u.s. food and drug administration trials and a progress report on 4- to 5-year outcomes," *Plastic and Reconstructive Surgery*, vol. 118, 64S–76S, Suppl Sep. 2006, ISSN: 0032-1052. DOI: [10.1097/01.prs.0000234873.00905.a4](https://doi.org/10.1097/01.prs.0000234873.00905.a4).
- [218] J. H. Joseph, L. L. Eaton, and S. R. Cohen, "Current concepts in the use of bellafill," *Plastic and Reconstructive Surgery*, vol. 136, 171S–179S, Nov. 2015, ISSN: 0032-1052. DOI: [10.1097/PRS.0000000000001839](https://doi.org/10.1097/PRS.0000000000001839).

- [219] P. Solomon, C. L. Ng, J. Kerzner, and R. Rival, "Facial soft tissue augmentation with bellafill: A review of 4 years of clinical experience in 212 patients," *Plastic Surgery*, vol. 29, no. 2, pp. 98–102, May 2021, ISSN: 2292-5503, 2292-5511. DOI: [10.1177/2292550320933675](https://doi.org/10.1177/2292550320933675).
- [220] J. L. Deneve, K. K. Turaga, S. S. Marzban, *et al.*, "Single-institution outcome experience using AlloDerm® as temporary coverage or definitive reconstruction for cutaneous and soft tissue malignancy defects," *The American Surgeon*, vol. 79, no. 5, pp. 476–482, May 2013, ISSN: 1555-9823.
- [221] S. Becker, M. Saint-Cyr, C. Wong, *et al.*, "AlloDerm versus DermaMatrix in immediate expander-based breast reconstruction: A preliminary comparison of complication profiles and material compliance," *Plastic & Reconstructive Surgery*, vol. 123, no. 1, pp. 1–6, Jan. 2009, ISSN: 0032-1052. DOI: [10.1097/PRS.0b013e3181904bff](https://doi.org/10.1097/PRS.0b013e3181904bff).
- [222] J. M. Broyles, E. C. Liao, J. Kim, *et al.*, "Acellular dermal matrix-associated complications in implant-based breast reconstruction: A multicenter, prospective, randomized controlled clinical trial comparing two human tissues," *Plastic & Reconstructive Surgery*, vol. 148, no. 3, pp. 493–500, Sep. 2021, ISSN: 0032-1052. DOI: [10.1097/PRS.00000000000008194](https://doi.org/10.1097/PRS.00000000000008194).
- [223] J. Brosious, N. Wong, G. Fowler, *et al.*, "Evaluation of AlloMax acellular dermal matrix for objective collagen deposition," *Journal of Reconstructive Microsurgery*, vol. 30, no. 1, pp. 031–034, Jul. 17, 2013, ISSN: 0743-684X, 1098-8947. DOI: [10.1055/s-0033-1349721](https://doi.org/10.1055/s-0033-1349721).
- [224] T. B. Shahin, K. V. Vaishnav, M. Watchman, *et al.*, "Tissue augmentation with allograft adipose matrix for the diabetic foot in remission," *Plastic and Reconstructive Surgery - Global Open*, vol. 5, no. 10, e1555, Oct. 2017, ISSN: 2169-7574. DOI: [10.1097/GOX.0000000000001555](https://doi.org/10.1097/GOX.0000000000001555).
- [225] M. H. Gold, B. M. Kinney, M. S. Kaminer, R. J. Rohrich, and R. A. D'Amico, "A multi-center, open-label, pilot study of allograft adipose matrix for the correction of atrophic temples," *Journal of Cosmetic Dermatology*, vol. 19, no. 5, pp. 1044–1056, May 2020, ISSN: 1473-2130, 1473-2165. DOI: [10.1111/jocd.13363](https://doi.org/10.1111/jocd.13363).
- [226] L. Baumann, "Hyaluronic acid gel (juv™) preparations in the treatment of facial wrinkles and folds," *Clinical Interventions in Aging*, vol. Volume 3, pp. 629–634, Dec. 2008, ISSN: 1178-1998. DOI: [10.2147/CIA.S3118](https://doi.org/10.2147/CIA.S3118).
- [227] F. S. Brandt and A. Cazzaniga, "Hyaluronic acid fillers: Restylane and perlane," *Facial Plastic Surgery Clinics of North America*, vol. 15, no. 1, pp. 63–76, Feb. 2007, ISSN: 10647406. DOI: [10.1016/j.fsc.2006.11.002](https://doi.org/10.1016/j.fsc.2006.11.002).
- [228] G. Ducher, A. D. Prasetyo, M. G. Rubin, E. A. Moretti, A. Nikolis, and W. Prager, "Hyaluronic acid fillers with cohesive polydensified matrix for soft-tissue augmentation and rejuvenation: A literature review," *Clinical, Cosmetic and Investigational Dermatology*, vol. Volume 9, pp. 257–280, Sep. 2016, ISSN: 1178-7015. DOI: [10.2147/CCID.S106551](https://doi.org/10.2147/CCID.S106551).

- [229] P. Jacovella, "Use of calcium hydroxylapatite (radiess^e) for facial augmentation," *Clinical Interventions in Aging*, vol. Volume 3, pp. 161–174, Mar. 2008, ISSN: 1178-1998. DOI: [10.2147/CIA.S2065](https://doi.org/10.2147/CIA.S2065).
- [230] A. T. de Almeida, V. Figueredo, A. L. G. da Cunha, *et al.*, "Consensus recommendations for the use of hyperdiluted calcium hydroxyapatite (radiess^e) as a face and body biostimulatory agent," *Plastic and Reconstructive Surgery - Global Open*, vol. 7, no. 3, e2160, Mar. 2019, ISSN: 2169-7574. DOI: [10.1097/GOX.0000000000002160](https://doi.org/10.1097/GOX.0000000000002160).
- [231] M. Banihashemi, N. Zabolinejad, M. Salehi, D. Hamidi Alamdari, and S. Nakhaizadeh, "Platelet-rich plasma use for facial rejuvenation: A clinical trial and review of current literature," *Acta Biomedica Atenei Parmensis*, vol. 92, no. 2, e2021187, May 12, 2021, ISSN: 2531-6745, 0392-4203. DOI: [10.23750/abm.v92i2.9687](https://doi.org/10.23750/abm.v92i2.9687).
- [232] R. Alves and R. Grimalt, "A review of platelet-rich plasma: History, biology, mechanism of action, and classification," *Skin Appendage Disorders*, vol. 4, no. 1, pp. 18–24, 2018, ISSN: 2296-9195, 2296-9160. DOI: [10.1159/000477353](https://doi.org/10.1159/000477353).
- [233] J.-W. Groen, T. K. Krastev, J. Hommes, J. A. Wilschut, M. J. P. F. Ritt, and R. R. J. W. van der Hulst, "Autologous fat transfer for facial rejuvenation: A systematic review on technique, efficacy, and satisfaction," *Plastic and Reconstructive Surgery - Global Open*, vol. 5, no. 12, e1606, Dec. 2017, ISSN: 2169-7574. DOI: [10.1097/GOX.0000000000001606](https://doi.org/10.1097/GOX.0000000000001606).
- [234] C. Gretzer, L. Emanuelsson, E. Liljensten, and P. Thomsen, "The inflammatory cell influx and cytokines changes during transition from acute inflammation to fibrous repair around implanted materials," *Journal of Biomaterials Science, Polymer Edition*, vol. 17, no. 6, pp. 669–687, Jan. 2006, ISSN: 0920-5063, 1568-5624. DOI: [10.1163/156856206777346340](https://doi.org/10.1163/156856206777346340).
- [235] J. M. Anderson, "Biological responses to materials," *Annual Review of Materials Research*, vol. 31, no. 1, pp. 81–110, Aug. 2001, ISSN: 1531-7331, 1545-4118. DOI: [10.1146/annurev.matsci.31.1.81](https://doi.org/10.1146/annurev.matsci.31.1.81).
- [236] J. A. Jones, D. T. Chang, H. Meyerson, *et al.*, "Proteomic analysis and quantification of cytokines and chemokines from biomaterial surface-adherent macrophages and foreign body giant cells," *Journal of Biomedical Materials Research Part A*, vol. 83A, no. 3, pp. 585–596, Dec. 1, 2007, ISSN: 15493296, 15524965. DOI: [10.1002/jbm.a.31221](https://doi.org/10.1002/jbm.a.31221).
- [237] L. Mesure, G. De Visscher, I. Vranken, A. Lebacqz, and W. Flameng, "Gene expression study of monocytes/macrophages during early foreign body reaction and identification of potential precursors of myofibroblasts," *PLoS ONE*, vol. 5, no. 9, R. Gonçalves, Ed., e12949, Sep. 23, 2010, ISSN: 1932-6203. DOI: [10.1371/journal.pone.0012949](https://doi.org/10.1371/journal.pone.0012949).
- [238] K. L. Spiller, R. R. Anfang, K. J. Spiller, *et al.*, "The role of macrophage phenotype in vascularization of tissue engineering scaffolds," *Biomaterials*, vol. 35, no. 15, pp. 4477–4488, May 2014, ISSN: 01429612. DOI: [10.1016/j.biomaterials.2014.02.012](https://doi.org/10.1016/j.biomaterials.2014.02.012).

- [239] L. B. Moore and T. R. Kyriakides, "Molecular characterization of macrophage-biomaterial interactions," in *Immune Responses to Biosurfaces*, J. D. Lambris, K. N. Ekdahl, D. Ricklin, and B. Nilsson, Eds., vol. 865, Series Title: Advances in Experimental Medicine and Biology, Cham: Springer International Publishing, 2015, pp. 109–122, ISBN: 978-3-319-18602-3 978-3-319-18603-0. DOI: [10.1007/978-3-319-18603-0_7](https://doi.org/10.1007/978-3-319-18603-0_7).
- [240] K. E. Martin and A. J. García, "Macrophage phenotypes in tissue repair and the foreign body response: Implications for biomaterial-based regenerative medicine strategies," *Acta Biomaterialia*, vol. 133, pp. 4–16, Oct. 2021, ISSN: 17427061. DOI: [10.1016/j.actbio.2021.03.038](https://doi.org/10.1016/j.actbio.2021.03.038).
- [241] E. Dondossola, B. M. Holzapfel, S. Alexander, S. Filippini, D. W. Hutmacher, and P. Friedl, "Examination of the foreign body response to biomaterials by nonlinear intravital microscopy," *Nature Biomedical Engineering*, vol. 1, no. 1, p. 0007, Jan. 2017, ISSN: 2157-846X. DOI: [10.1038/s41551-016-0007](https://doi.org/10.1038/s41551-016-0007).
- [242] B. G. Keselowsky, A. W. Bridges, K. L. Burns, *et al.*, "Role of plasma fibronectin in the foreign body response to biomaterials," *Biomaterials*, vol. 28, no. 25, pp. 3626–3631, Sep. 2007, ISSN: 01429612. DOI: [10.1016/j.biomaterials.2007.04.035](https://doi.org/10.1016/j.biomaterials.2007.04.035).
- [243] S. Barr, E. Hill, and A. Bayat, "Functional biocompatibility testing of silicone breast implants and a novel classification system based on surface roughness," *Journal of the Mechanical Behavior of Biomedical Materials*, vol. 75, pp. 75–81, Nov. 2017, ISSN: 17516161. DOI: [10.1016/j.jmbbm.2017.06.030](https://doi.org/10.1016/j.jmbbm.2017.06.030).
- [244] A. Garcia Garcia, A. Hébraud, J.-L. Duval, *et al.*, "Poly(-caprolactone)/hydroxyapatite 3d honeycomb scaffolds for a cellular microenvironment adapted to maxillofacial bone reconstruction," *ACS Biomaterials Science & Engineering*, vol. 4, no. 9, pp. 3317–3326, Sep. 10, 2018, ISSN: 2373-9878, 2373-9878. DOI: [10.1021/acsbiomaterials.8b00521](https://doi.org/10.1021/acsbiomaterials.8b00521).
- [245] S. A. Munim and Z. A. Raza, "Poly(lactic acid) based hydrogels: Formation, characteristics and biomedical applications," *Journal of Porous Materials*, vol. 26, no. 3, pp. 881–901, Jun. 2019, ISSN: 1380-2224, 1573-4854. DOI: [10.1007/s10934-018-0687-z](https://doi.org/10.1007/s10934-018-0687-z).
- [246] S. Butylina, S. Geng, and K. Oksman, "Properties of as-prepared and freeze-dried hydrogels made from poly(vinyl alcohol) and cellulose nanocrystals using freeze-thaw technique," *European Polymer Journal*, vol. 81, pp. 386–396, Aug. 2016, ISSN: 00143057. DOI: [10.1016/j.eurpolymj.2016.06.028](https://doi.org/10.1016/j.eurpolymj.2016.06.028).
- [247] C. Li, C. Guo, V. Fitzpatrick, *et al.*, "Design of biodegradable, implantable devices towards clinical translation," *Nature Reviews Materials*, vol. 5, no. 1, pp. 61–81, Jan. 2020, ISSN: 2058-8437. DOI: [10.1038/s41578-019-0150-z](https://doi.org/10.1038/s41578-019-0150-z).
- [248] J. M. Morais, F. Papadimitrakopoulos, and D. J. Burgess, "Biomaterials/tissue interactions: Possible solutions to overcome foreign body response," *The AAPS Journal*, vol. 12, no. 2, pp. 188–196, Jun. 2010, ISSN: 1550-7416. DOI: [10.1208/s12248-010-9175-3](https://doi.org/10.1208/s12248-010-9175-3).

- [249] S. Michaelis, R. Robelek, and J. Wegener, "Studying cell–surface interactions in vitro: A survey of experimental approaches and techniques," in *Tissue Engineering III: Cell - Surface Interactions for Tissue Culture*, C. Kasper, F. Witte, and R. Pörtner, Eds., vol. 126, Series Title: Advances in Biochemical Engineering/Biotechnology, Berlin, Heidelberg: Springer Berlin Heidelberg, 2011, pp. 33–66, ISBN: 978-3-642-28281-2 978-3-642-28282-9. DOI: [10.1007/10_2011_112](https://doi.org/10.1007/10_2011_112).
- [250] J. Goddard and J. Hotchkiss, "Polymer surface modification for the attachment of bioactive compounds," *Progress in Polymer Science*, vol. 32, no. 7, pp. 698–725, Jul. 2007, ISSN: 00796700. DOI: [10.1016/j.progpolymsci.2007.04.002](https://doi.org/10.1016/j.progpolymsci.2007.04.002).
- [251] J.-P. Chen and C.-H. Su, "Surface modification of electrospun PLLA nanofibers by plasma treatment and cationized gelatin immobilization for cartilage tissue engineering," *Acta Biomaterialia*, vol. 7, no. 1, pp. 234–243, Jan. 2011, ISSN: 17427061. DOI: [10.1016/j.actbio.2010.08.015](https://doi.org/10.1016/j.actbio.2010.08.015).
- [252] T.-D. Zhang, X. Zhang, Key Laboratory for Space Bioscience and Biotechnology, Northwestern Polytechnical University, PR. China, X. Deng, and Key Laboratory for Space Bioscience and Biotechnology, Northwestern Polytechnical University, PR. China, "Applications of protein-resistant polymer and hydrogel coatings on biosensors and biomaterials," *Annals of Biotechnology*, vol. 1, no. 2, Apr. 23, 2018, ISSN: 26374927. DOI: [10.33582/2637-4927/1006](https://doi.org/10.33582/2637-4927/1006).
- [253] J. D. Friedl, V. Nele, G. De Rosa, and A. Bernkop-Schnürch, "Bioinert, stealth or interactive: How surface chemistry of nanocarriers determines their fate in vivo," *Advanced Functional Materials*, vol. 31, no. 34, p. 2103347, Aug. 2021, ISSN: 1616-301X, 1616-3028. DOI: [10.1002/adfm.202103347](https://doi.org/10.1002/adfm.202103347).
- [254] D. Zhang, Q. Chen, C. Shi, *et al.*, "Dealing with the foreign-body response to implanted biomaterials: Strategies and applications of new materials," *Advanced Functional Materials*, vol. 31, no. 6, p. 2007226, Feb. 2021, ISSN: 1616-301X, 1616-3028. DOI: [10.1002/adfm.202007226](https://doi.org/10.1002/adfm.202007226).
- [255] S. VandeVondele, J. Vörös, and J. A. Hubbell, "RGD-grafted poly-l-lysine-graft-(polyethylene glycol) copolymers block non-specific protein adsorption while promoting cell adhesion," *Biotechnology and Bioengineering*, vol. 82, no. 7, pp. 784–790, Jun. 30, 2003, ISSN: 00063592, 10970290. DOI: [10.1002/bit.10625](https://doi.org/10.1002/bit.10625).
- [256] L. Liu, G. Chen, T. Chao, B. D. Ratner, E. H. Sage, and S. Jiang, "Reduced foreign body reaction to implanted biomaterials by surface treatment with oriented osteopontin," *Journal of Biomaterials Science, Polymer Edition*, vol. 19, no. 6, pp. 821–835, Jan. 2008, ISSN: 0920-5063, 1568-5624. DOI: [10.1163/156856208784522083](https://doi.org/10.1163/156856208784522083).
- [257] S. J. Geelhood, T. A. Horbett, W. K. Ward, M. D. Wood, and M. J. Quinn, "Passivating protein coatings for implantable glucose sensors: Evaluation of protein retention," *Journal of Biomedical Materials Research Part B: Applied Biomaterials*, vol. 81B, no. 1, pp. 251–260, Apr. 2007, ISSN: 15524973, 15524981. DOI: [10.1002/jbm.b.30660](https://doi.org/10.1002/jbm.b.30660).

- [258] M. Gancedo, L. Ruiz-Corro, A. Salazar-Montes, A. R. Rincón, and J. Armendáriz-Borunda, "Pirfenidone prevents capsular contracture after mammary implantation," *Aesthetic Plastic Surgery*, vol. 32, no. 1, pp. 32–40, Jan. 2008, ISSN: 0364-216X, 1432-5241. DOI: [10.1007/s00266-007-9051-4](https://doi.org/10.1007/s00266-007-9051-4).
- [259] Y. Liao, L. Ouyang, L. Ci, *et al.*, "Pravastatin regulates host foreign-body reaction to polyetheretherketone implants via miR-29ab1-mediated SLIT3 upregulation," *Biomaterials*, vol. 203, pp. 12–22, May 2019, ISSN: 01429612. DOI: [10.1016/j.biomaterials.2019.02.027](https://doi.org/10.1016/j.biomaterials.2019.02.027).
- [260] N. De la Oliva, X. Navarro, and J. del Valle, "Dexamethasone reduces the foreign body reaction to intraneural electrode implants in the peripheral nerve of the rat: DEXAMETHASONE FOR FBR TO INTRANEURAL IMPLANTS," *The Anatomical Record*, vol. 301, no. 10, pp. 1722–1733, Oct. 2018, ISSN: 19328486. DOI: [10.1002/ar.23920](https://doi.org/10.1002/ar.23920).
- [261] Y. Chandorkar, N. Bhaskar, G. Madras, and B. Basu, "Long-term sustained release of salicylic acid from cross-linked biodegradable polyester induces a reduced foreign body response in mice," *Biomacromolecules*, vol. 16, no. 2, pp. 636–649, Feb. 9, 2015, ISSN: 1525-7797, 1526-4602. DOI: [10.1021/bm5017282](https://doi.org/10.1021/bm5017282).
- [262] H. M. Rostam, S. Singh, F. Salazar, *et al.*, "The impact of surface chemistry modification on macrophage polarisation," *Immunobiology*, vol. 221, no. 11, pp. 1237–1246, Nov. 2016, ISSN: 01712985. DOI: [10.1016/j.imbio.2016.06.010](https://doi.org/10.1016/j.imbio.2016.06.010).
- [263] H. M. Rostam, L. E. Fisher, A. L. Hook, *et al.*, "Immune-instructive polymers control macrophage phenotype and modulate the foreign body response in vivo," *Matter*, vol. 2, no. 6, pp. 1564–1581, Jun. 2020, ISSN: 25902385. DOI: [10.1016/j.matt.2020.03.018](https://doi.org/10.1016/j.matt.2020.03.018).
- [264] T. Kusaka, M. Nakayama, K. Nakamura, M. Ishimiya, E. Furusawa, and K. Ogasawara, "Effect of silica particle size on macrophage inflammatory responses," *PLoS ONE*, vol. 9, no. 3, H. Nakano, Ed., e92634, Mar. 28, 2014, ISSN: 1932-6203. DOI: [10.1371/journal.pone.0092634](https://doi.org/10.1371/journal.pone.0092634).
- [265] F. Lebre, C. H. Hearnden, and E. C. Lavelle, "Modulation of immune responses by particulate materials," *Advanced Materials*, vol. 28, no. 27, pp. 5525–5541, Jul. 2016, ISSN: 09359648. DOI: [10.1002/adma.201505395](https://doi.org/10.1002/adma.201505395).
- [266] J. L. Hernandez and K. A. Woodrow, "Medical applications of porous biomaterials: Features of porosity and tissue-specific implications for biocompatibility," *Advanced Healthcare Materials*, vol. 11, no. 9, p. 2102087, May 2022, ISSN: 2192-2640, 2192-2659. DOI: [10.1002/adhm.202102087](https://doi.org/10.1002/adhm.202102087).
- [267] H. Cao, K. Mchugh, S. Y. Chew, and J. M. Anderson, "The topographical effect of electrospun nanofibrous scaffolds on the *in vivo* and *in vitro* foreign body reaction," *Journal of Biomedical Materials Research Part A*, vol. 9999A, NA–NA, 2009, ISSN: 15493296, 15524965. DOI: [10.1002/jbm.a.32609](https://doi.org/10.1002/jbm.a.32609).

- [268] E. F. Irwin, K. Saha, M. Rosenbluth, L. J. Gamble, D. G. Castner, and K. E. Healy, "Modulus-dependent macrophage adhesion and behavior," *Journal of Biomaterials Science, Polymer Edition*, vol. 19, no. 10, pp. 1363–1382, Jan. 2008, ISSN: 0920-5063, 1568-5624. DOI: [10.1163/156856208786052407](https://doi.org/10.1163/156856208786052407).
- [269] F. Y. McWhorter, C. T. Davis, and W. F. Liu, "Physical and mechanical regulation of macrophage phenotype and function," *Cellular and Molecular Life Sciences*, vol. 72, no. 7, pp. 1303–1316, Apr. 2015, ISSN: 1420-682X, 1420-9071. DOI: [10.1007/s00018-014-1796-8](https://doi.org/10.1007/s00018-014-1796-8).
- [270] N. R. Patel, M. Bole, C. Chen, *et al.*, "Cell elasticity determines macrophage function," *PLoS ONE*, vol. 7, no. 9, L. L. Lenz, Ed., e41024, Sep. 18, 2012, ISSN: 1932-6203. DOI: [10.1371/journal.pone.0041024](https://doi.org/10.1371/journal.pone.0041024).
- [271] F. F. R. Damanik, T. C. Rothuizen, C. van Blitterswijk, J. I. Rotmans, and L. Moroni, "Towards an in vitro model mimicking the foreign body response: Tailoring the surface properties of biomaterials to modulate extracellular matrix," *Scientific Reports*, vol. 4, no. 1, p. 6325, May 2015, ISSN: 2045-2322. DOI: [10.1038/srep06325](https://doi.org/10.1038/srep06325).
- [272] F. Weber, H. Q. Quach, M. Reiersen, *et al.*, "Characterization of the foreign body response of titanium implants modified with polyphenolic coatings," *Journal of Biomedical Materials Research Part A*, vol. 110, no. 7, pp. 1341–1355, Jul. 2022, ISSN: 1549-3296, 1552-4965. DOI: [10.1002/jbm.a.37377](https://doi.org/10.1002/jbm.a.37377).
- [273] N. Söhling, M. Ondreka, K. Kontradowitz, T. Reichel, I. Marzi, and D. Henrich, "Early immune response in foreign body reaction is implant/material specific," *Materials*, vol. 15, no. 6, p. 2195, Mar. 16, 2022, ISSN: 1996-1944. DOI: [10.3390/ma15062195](https://doi.org/10.3390/ma15062195).
- [274] A. R. Costa-Pinto, A. M. Martins, M. J. Castelhana-Carlos, *et al.*, "In vitro degradation and in vivo biocompatibility of chitosan–poly(butylene succinate) fiber mesh scaffolds," *Journal of Bioactive and Compatible Polymers*, vol. 29, no. 2, pp. 137–151, Mar. 2014, ISSN: 0883-9115, 1530-8030. DOI: [10.1177/0883911514521919](https://doi.org/10.1177/0883911514521919).
- [275] L. S. Saleh and S. J. Bryant, "In vitro and in vivo models for assessing the host response to biomaterials," *Drug Discovery Today: Disease Models*, vol. 24, pp. 13–21, 2017, ISSN: 17406757. DOI: [10.1016/j.ddmod.2018.04.002](https://doi.org/10.1016/j.ddmod.2018.04.002).
- [276] A. Rodriguez, S. R. MacEwan, H. Meyerson, J. T. Kirk, and J. M. Anderson, "The foreign body reaction in t-cell-deficient mice," *Journal of Biomedical Materials Research Part A*, vol. 90A, no. 1, pp. 106–113, Jun. 2009, ISSN: 15493296, 15524965. DOI: [10.1002/jbm.a.32050](https://doi.org/10.1002/jbm.a.32050).
- [277] D. M. Higgins, R. J. Basaraba, A. C. Hohnbaum, E. J. Lee, D. W. Grainger, and M. Gonzalez-Juarrero, "Localized immunosuppressive environment in the foreign body response to implanted biomaterials," *The American Journal of Pathology*, vol. 175, no. 1, pp. 161–170, Jul. 2009, ISSN: 00029440. DOI: [10.2353/ajpath.2009.080962](https://doi.org/10.2353/ajpath.2009.080962).

- [278] A. H. Akbari Zahmati, R. Alipoor, A. Rezaei Shahmirzadi, V. Khor, and M. M. Abolhasani, "Chemical decellularization methods and its effects on extracellular matrix," *Internal Medicine and Medical Investigation Journal*, vol. 2, no. 3, p. 76, Sep. 11, 2017, ISSN: 2474-7750, 2474-7750. DOI: [10.24200/imminv.v2i3.63](https://doi.org/10.24200/imminv.v2i3.63).
- [279] U. Mendibil, R. Ruiz-Hernandez, S. Retegi-Carrion, N. Garcia-Urquia, B. Olalde-Graells, and A. Abarrategi, "Tissue-specific decellularization methods: Rationale and strategies to achieve regenerative compounds," *International Journal of Molecular Sciences*, vol. 21, no. 15, p. 5447, Jul. 30, 2020, ISSN: 1422-0067. DOI: [10.3390/ijms21155447](https://doi.org/10.3390/ijms21155447).
- [280] M. Karkanitsa, P. Fathi, T. Ngo, and K. Sadtler, "Mobilizing endogenous repair through understanding immune reaction with biomaterials," *Frontiers in Bioengineering and Biotechnology*, vol. 9, p. 730 938, Nov. 30, 2021, ISSN: 2296-4185. DOI: [10.3389/fbioe.2021.730938](https://doi.org/10.3389/fbioe.2021.730938).
- [281] J. L. Dziki, L. Huleihel, M. E. Scarritt, and S. F. Badylak, "Extracellular matrix bioscaffolds as immunomodulatory biomaterials <sup/>," *Tissue Engineering Part A*, vol. 23, no. 19, pp. 1152–1159, Oct. 2017, ISSN: 1937-3341, 1937-335X. DOI: [10.1089/ten.tea.2016.0538](https://doi.org/10.1089/ten.tea.2016.0538).
- [282] J. M. Aamodt and D. W. Grainger, "Extracellular matrix-based biomaterial scaffolds and the host response," *Biomaterials*, vol. 86, pp. 68–82, Apr. 2016, ISSN: 01429612. DOI: [10.1016/j.biomaterials.2016.02.003](https://doi.org/10.1016/j.biomaterials.2016.02.003).
- [283] A. Condé-Green, A. A. Marano, E. S. Lee, *et al.*, "Fat grafting and adipose-derived regenerative cells in burn wound healing and scarring: A systematic review of the literature," *Plastic and Reconstructive Surgery*, vol. 137, no. 1, pp. 302–312, Jan. 2016, ISSN: 0032-1052. DOI: [10.1097/PRS.0000000000001918](https://doi.org/10.1097/PRS.0000000000001918).
- [284] V. L. Negenborn, J.-W. Groen, J. M. Smit, F. B. Niessen, and M. G. Mullender, "The use of autologous fat grafting for treatment of scar tissue and scar-related conditions: A systematic review," *Plastic and Reconstructive Surgery*, vol. 137, no. 1, 31e–43e, Jan. 2016, ISSN: 0032-1052. DOI: [10.1097/PRS.0000000000001850](https://doi.org/10.1097/PRS.0000000000001850).
- [285] T. Saffari, S. Saffari, K. Vyas, S. Mardini, and A. Shin, "Role of adipose tissue grafting and adipose-derived stem cells in peripheral nerve surgery," *Neural Regeneration Research*, vol. 17, no. 10, p. 2179, 2022, ISSN: 1673-5374. DOI: [10.4103/1673-5374.336870](https://doi.org/10.4103/1673-5374.336870).
- [286] C. W. Patrick, "Adipose tissue engineering: The future of breast and soft tissue reconstruction following tumor resection," *Seminars in Surgical Oncology*, vol. 19, no. 3, pp. 302–311, Oct. 2000, ISSN: 8756-0437, 1098-2388. DOI: [10.1002/1098-2388\(200010/11\)19:3<302::AID-SSU12>3.0.CO;2-S](https://doi.org/10.1002/1098-2388(200010/11)19:3<302::AID-SSU12>3.0.CO;2-S).
- [287] R. Domenis, L. Lazzaro, S. Calabrese, *et al.*, "Adipose tissue derived stem cells: In vitro and in vivo analysis of a standard and three commercially available cell-assisted lipotransfer techniques," *Stem Cell Research & Therapy*, vol. 6, no. 1, p. 2, Dec. 2015, ISSN: 1757-6512. DOI: [10.1186/scrt536](https://doi.org/10.1186/scrt536).

- [288] E. Delay, R. Sinna, K. Chekaroua, T. Delaporte, S. Garson, and G. Toussoun, "Lipo-modeling of poland's syndrome: A new treatment of the thoracic deformity," *Aesthetic Plastic Surgery*, vol. 34, no. 2, pp. 218–225, Apr. 2010, ISSN: 0364-216X, 1432-5241. DOI: [10.1007/s00266-009-9428-7](https://doi.org/10.1007/s00266-009-9428-7).
- [289] A. Mojallal, M. Veber, C. Shipkov, N. Ghetu, J.-L. Foyatier, and F. Braye, "Analysis of a series of autologous fat tissue transfer for lower limb atrophies," *Annals of Plastic Surgery*, vol. 61, no. 5, pp. 537–543, Nov. 2008, ISSN: 0148-7043. DOI: [10.1097/SAP.0b013e318164088f](https://doi.org/10.1097/SAP.0b013e318164088f).
- [290] L. Shukla, Y. Yuan, R. Shayan, D. W. Greening, and T. Karnezis, "Fat therapeutics: The clinical capacity of adipose-derived stem cells and exosomes for human disease and tissue regeneration," *Frontiers in Pharmacology*, vol. 11, p. 158, Mar. 3, 2020, ISSN: 1663-9812. DOI: [10.3389/fphar.2020.00158](https://doi.org/10.3389/fphar.2020.00158).
- [291] T. M. Suszynski, D. A. Sieber, A. L. Van Beek, and B. L. Cunningham, "Characterization of adipose tissue for autologous fat grafting," *Aesthetic Surgery Journal*, vol. 35, no. 2, pp. 194–203, Feb. 2015, ISSN: 1527-330X, 1090-820X. DOI: [10.1093/asj/sju059](https://doi.org/10.1093/asj/sju059).
- [292] E. Bellini, M. P. Grieco, and E. Raposio, "The science behind autologous fat grafting," *Annals of Medicine and Surgery*, vol. 24, pp. 65–73, Dec. 2017, ISSN: 20490801. DOI: [10.1016/j.amsu.2017.11.001](https://doi.org/10.1016/j.amsu.2017.11.001).
- [293] P. A. Zuk, M. Zhu, P. Ashjian, *et al.*, "Human adipose tissue is a source of multipotent stem cells," *Molecular Biology of the Cell*, vol. 13, no. 12, M. Raff, Ed., pp. 4279–4295, Dec. 2002, ISSN: 1059-1524, 1939-4586. DOI: [10.1091/mbc.e02-02-0105](https://doi.org/10.1091/mbc.e02-02-0105).
- [294] P. Zuk, "Adipose-derived stem cells in tissue regeneration: A review," *ISRN Stem Cells*, vol. 2013, pp. 1–35, Feb. 14, 2013, ISSN: 2090-8792. DOI: [10.1155/2013/713959](https://doi.org/10.1155/2013/713959).
- [295] D. G. Phinney and D. J. Prockop, "Concise review: Mesenchymal stem/multipotent stromal cells: The state of transdifferentiation and modes of tissue repair—current views," *Stem Cells*, vol. 25, no. 11, pp. 2896–2902, Nov. 1, 2007, ISSN: 1066-5099, 1549-4918. DOI: [10.1634/stemcells.2007-0637](https://doi.org/10.1634/stemcells.2007-0637).
- [296] J. H. Choi, J. M. Gimble, K. Lee, *et al.*, "Adipose tissue engineering for soft tissue regeneration," *Tissue Engineering Part B: Reviews*, vol. 16, no. 4, pp. 413–426, Aug. 2010, ISSN: 1937-3368, 1937-3376. DOI: [10.1089/ten.teb.2009.0544](https://doi.org/10.1089/ten.teb.2009.0544).
- [297] L. Provasoli and I. J. Pintner, "Artificial media for fresh-water algae: Problems and suggestions.," in *Ecology of Algae*, ser. Pymatuning Special Publications 2, Tryon, C. A., Jr. & Hartmann R. T., University of Pittsburgh, Pittsburgh: Pymatuning Laboratory of Field Biology, 1959, pp. 84–96.
- [298] R. C. Starr, "Special methods-dry soil samples.," in *Handbook of phycological methods. 1: Culture methods and growth measurements / ed. by Janet R. Stein, J. R. Stein and J. A. Hellebust*, Eds., Cambridge: Univ.Pr, 1979, ISBN: 978-0-521-29747-9 978-0-521-20049-3.
- [299] Rasband W.S. and Eliceiri K.W., *Image j*, Bethesda, Maryland, USA, 1997.

- [300] G. B. Witman, K. Carlson, J. Berliner, and J. L. Rosenbaum, "CHLAMYDOMONAS FLAGELLA," *Journal of Cell Biology*, vol. 54, no. 3, pp. 507–539, Sep. 1, 1972, ISSN: 1540-8140, 0021-9525. DOI: [10.1083/jcb.54.3.507](https://doi.org/10.1083/jcb.54.3.507).
- [301] S. J. Coggin and G. Kochert, "FLAGELLAR DEVELOPMENT AND REGENERATION IN VOLVOX CARTERI (CHLOROPHYTA)," *Journal of Phycology*, vol. 22, no. 3, pp. 370–381, Sep. 1986, ISSN: 0022-3646, 1529-8817. DOI: [10.1111/j.1529-8817.1986.tb00038.x](https://doi.org/10.1111/j.1529-8817.1986.tb00038.x).
- [302] M. Stricher, C.-O. Sarde, E. Guénin, C. Egles, and F. Delbecq, "Cellulosic/polyvinyl alcohol composite hydrogel: Synthesis, characterization and applications in tissue engineering," *Polymers*, vol. 13, no. 20, p. 3598, Oct. 19, 2021, ISSN: 2073-4360. DOI: [10.3390/polym13203598](https://doi.org/10.3390/polym13203598).
- [303] A. Gautier, B. Carpentier, M. Dufresne, Q. Vu Dinh, P. Paullier, and C. Legallais, "Impact of alginate type and bead diameter on mass transfers and the metabolic activities of encapsulated c3a cells in bioartificial liver applications," *European Cells and Materials*, vol. 21, pp. 94–106, Jan. 25, 2011. DOI: [10.22203/eCM.v021a08](https://doi.org/10.22203/eCM.v021a08).
- [304] M. Pasqua, U. Pereira, C. Lartigue, *et al.*, "Preclinical characterization of alginate-poly-l-lysine encapsulated HepaRG for extracorporeal liver supply," *Biotechnology and Bioengineering*, vol. 118, no. 1, pp. 453–464, Jan. 2021, ISSN: 0006-3592, 1097-0290. DOI: [10.1002/bit.27583](https://doi.org/10.1002/bit.27583).
- [305] H. Zhao and N. D. Heindel, "Determination of degree of substitution of formyl groups in polyaldehyde dextran by the hydroxylamine hydrochloride method," *Pharmaceutical Research*, vol. 08, no. 3, pp. 400–402, 1991, ISSN: 07248741. DOI: [10.1023/A:1015866104055](https://doi.org/10.1023/A:1015866104055).
- [306] L. Segal, J. Creely, A. Martin, and C. Conrad, "An empirical method for estimating the degree of crystallinity of native cellulose using the x-ray diffractometer," *Textile Research Journal*, vol. 29, no. 10, pp. 786–794, Oct. 1959, ISSN: 0040-5175, 1746-7748. DOI: [10.1177/004051755902901003](https://doi.org/10.1177/004051755902901003).
- [307] *Anaconda software distribution*, Publication Title: Anaconda Documentation Version Number: Vers. 2-2.4.0, 2020.
- [308] H. Hertz, "On the contact of elastic solids," in *Miscellaneous Papers*, MacMillan, London, 1896.
- [309] —, "On the contact of rigid elastic solids and on hardness," in *Miscellaneous Papers*, MacMillan, London, 1896.
- [310] ISO, "Biological evaluation of medical devices — part 5: Tests for in vitro cytotoxicity," International Organization for Standardization, Geneva, Switzerland, ISO ISO 10993-5:2009, 2009.
- [311] N. Jaccard, L. D. Griffin, A. Keser, *et al.*, "Automated method for the rapid and precise estimation of adherent cell culture characteristics from phase contrast microscopy images," *Biotechnology and Bioengineering*, vol. 111, no. 3, pp. 504–517, Mar. 2014, ISSN: 0006-3592, 1097-0290. DOI: [10.1002/bit.25115](https://doi.org/10.1002/bit.25115).

- [312] Z. Pang, J. Chong, G. Zhou, *et al.*, "MetaboAnalyst 5.0: Narrowing the gap between raw spectra and functional insights," *Nucleic Acids Research*, vol. 49, W388–W396, W1 Jul. 2, 2021, ISSN: 0305-1048, 1362-4962. DOI: [10.1093/nar/gkab382](https://doi.org/10.1093/nar/gkab382).
- [313] R. Bansil and B. S. Turner, "The biology of mucus: Composition, synthesis and organization," *Advanced Drug Delivery Reviews*, vol. 124, pp. 3–15, Jan. 2018, ISSN: 0169409X. DOI: [10.1016/j.addr.2017.09.023](https://doi.org/10.1016/j.addr.2017.09.023).
- [314] P. Sharma and N. Sharma, "Industrial and biotechnological applications of algae: A review," *Journal of Advances in Plant Biology*, vol. 1, no. 1, C. Keskin, Ed., pp. 1–25, Aug. 10, 2017, ISSN: 2638-4469. DOI: [10.14302/issn.2638-4469.japb-17-1534](https://doi.org/10.14302/issn.2638-4469.japb-17-1534).
- [315] G. M. Figueroa-Torres, J. K. Pittman, and C. Theodoropoulos, "Optimisation of microalgal cultivation via nutrient-enhanced strategies: The biorefinery paradigm," *Biotechnology for Biofuels*, vol. 14, no. 1, p. 64, Dec. 2021, ISSN: 1754-6834. DOI: [10.1186/s13068-021-01912-2](https://doi.org/10.1186/s13068-021-01912-2).
- [316] M. A. Borowitzka and A. Vonshak, "Scaling up microalgal cultures to commercial scale," *European Journal of Phycology*, vol. 52, no. 4, pp. 407–418, Oct. 2, 2017, ISSN: 0967-0262, 1469-4433. DOI: [10.1080/09670262.2017.1365177](https://doi.org/10.1080/09670262.2017.1365177).
- [317] Q. Wang, H. Peng, and B. T. Higgins, "Cultivation of green microalgae in bubble column photobioreactors and an assay for neutral lipids," *Journal of Visualized Experiments*, no. 143, p. 59106, Jan. 7, 2019, ISSN: 1940-087X. DOI: [10.3791/59106](https://doi.org/10.3791/59106).
- [318] ISO, "Sterilization of health care products — moist heat — part 1: Requirements for the development, validation and routine control of a sterilization process for medical devices," International Organization for Standardization, Geneva, Switzerland, ISO 17665-1:2006, 2006.
- [319] —, "Sterilization of health care products — moist heat — part 2: Guidance on the application of ISO 17665-1," International Organization for Standardization, Geneva, Switzerland, ISO TS 17665-2:2009, 2009.
- [320] —, "Sterilization of health care products — moist heat — part 3: Guidance on the designation of a medical device to a product family and processing category for," International Organization for Standardization, Geneva, Switzerland, ISO TS 17665-3:2013, 2013.
- [321] —, "Sterilization of health care products — radiation — part 1: Requirements for development, validation and routine control of a sterilization process for medical devices," International Organization for Standardization, Geneva, Switzerland, ISO 11137-1:2006, 2006.
- [322] —, "Sterilization of health care products — radiation — part 2: Establishing the sterilization dose," International Organization for Standardization, Geneva, Switzerland, ISO 11137-2:2006, 2006.
- [323] —, "Sterilization of health care products — radiation — part 3: Guidance on dosimetric aspects of development, validation and routine control," International Organization for Standardization, Geneva, Switzerland, ISO 11137-3:2017, 2017.

- [324] —, “Sterilization of health-care products — ethylene oxide — requirements for the development, validation and routine control of a sterilization process for medical devices,” International Organization for Standardization, Geneva, Switzerland, ISO 11135:2014, 2014.
- [325] T. J. Pedley, D. R. Brumley, and R. E. Goldstein, “Squirmer with swirl: A model for *Volvox* swimming,” *Journal of Fluid Mechanics*, vol. 798, pp. 165–186, Jul. 10, 2016, ISSN: 0022-1120, 1469-7645. DOI: [10.1017/jfm.2016.306](https://doi.org/10.1017/jfm.2016.306).
- [326] K. Dunlap, “Localization of calcium channels in paramecium caudatum,” *The Journal of Physiology*, vol. 271, no. 1, pp. 119–133, Sep. 1, 1977, ISSN: 00223751. DOI: [10.1113/jphysiol.1977.sp011993](https://doi.org/10.1113/jphysiol.1977.sp011993).
- [327] P. Aiyar, D. Schaeme, M. García-Altares, *et al.*, “Antagonistic bacteria disrupt calcium homeostasis and immobilize algal cells,” *Nature Communications*, vol. 8, no. 1, p. 1756, Dec. 2017, ISSN: 2041-1723. DOI: [10.1038/s41467-017-01547-8](https://doi.org/10.1038/s41467-017-01547-8).
- [328] H. Fang, R. A. Pengal, X. Cao, *et al.*, “Lipopolysaccharide-induced macrophage inflammatory response is regulated by SHIP,” *The Journal of Immunology*, vol. 173, no. 1, pp. 360–366, Jul. 1, 2004, ISSN: 0022-1767, 1550-6606. DOI: [10.4049/jimmunol.173.1.360](https://doi.org/10.4049/jimmunol.173.1.360).
- [329] C. V. Rosadini and J. C. Kagan, “Early innate immune responses to bacterial LPS,” *Current Opinion in Immunology*, vol. 44, pp. 14–19, Feb. 2017, ISSN: 09527915. DOI: [10.1016/j.coi.2016.10.005](https://doi.org/10.1016/j.coi.2016.10.005).
- [330] J. D. Hasday, R. Bascom, J. J. Costa, T. Fitzgerald, and W. Dubin, “Bacterial endotoxin is an active component of cigarette smoke,” *Chest*, vol. 115, no. 3, pp. 829–835, Mar. 1999, ISSN: 00123692. DOI: [10.1378/chest.115.3.829](https://doi.org/10.1378/chest.115.3.829).
- [331] J. L. Stow, P. Ching Low, C. Offenhäuser, and D. Sangermani, “Cytokine secretion in macrophages and other cells: Pathways and mediators,” *Immunobiology*, vol. 214, no. 7, pp. 601–612, Jul. 2009, ISSN: 01712985. DOI: [10.1016/j.imbio.2008.11.005](https://doi.org/10.1016/j.imbio.2008.11.005).
- [332] M. E. Lund, J. To, B. A. O’Brien, and S. Donnelly, “The choice of phorbol 12-myristate 13-acetate differentiation protocol influences the response of THP-1 macrophages to a pro-inflammatory stimulus,” *Journal of Immunological Methods*, vol. 430, pp. 64–70, Mar. 2016, ISSN: 00221759. DOI: [10.1016/j.jim.2016.01.012](https://doi.org/10.1016/j.jim.2016.01.012).
- [333] M. Barbeck, M.-L. Schröder, S. Alkildani, O. Jung, and R. E. Unger, “Exploring the biomaterial-induced secretome: Physical bone substitute characteristics influence the cytokine expression of macrophages,” *International Journal of Molecular Sciences*, vol. 22, no. 9, p. 4442, Apr. 24, 2021, ISSN: 1422-0067. DOI: [10.3390/ijms22094442](https://doi.org/10.3390/ijms22094442).
- [334] K. M. Kopydlowski, C. A. Salkowski, M. J. Cody, *et al.*, “Regulation of macrophage chemokine expression by lipopolysaccharide in vitro and in vivo,” *Journal of Immunology (Baltimore, Md.: 1950)*, vol. 163, no. 3, pp. 1537–1544, Aug. 1, 1999, ISSN: 0022-1767.

- [335] T. Wohlschlager, A. Butschi, P. Grassi, *et al.*, "Methylated glycans as conserved targets of animal and fungal innate defense," *Proceedings of the National Academy of Sciences*, vol. 111, no. 27, Jul. 8, 2014, ISSN: 0027-8424, 1091-6490. DOI: [10.1073/pnas.1401176111](https://doi.org/10.1073/pnas.1401176111).
- [336] R. Mócsai, M. Blaukopf, E. Svehla, P. Kosma, and F. Altmann, "The n-glycans of *Chlorella sorokiniana* and a related strain contain arabinose but have strikingly different structures," *Glycobiology*, vol. 30, no. 8, pp. 663–676, Aug. 1, 2020, ISSN: 1460-2423. DOI: [10.1093/glycob/cwaa012](https://doi.org/10.1093/glycob/cwaa012).
- [337] E. A. Specht and S. P. Mayfield, "Algae-based oral recombinant vaccines," *Frontiers in Microbiology*, vol. 5, 2014, ISSN: 1664-302X. DOI: [10.3389/fmicb.2014.00060](https://doi.org/10.3389/fmicb.2014.00060).
- [338] T. L. Schenck, U. Hopfner, M. N. Chávez, *et al.*, "Photosynthetic biomaterials: A pathway towards autotrophic tissue engineering," *Acta Biomaterialia*, vol. 15, pp. 39–47, Mar. 2015, ISSN: 17427061. DOI: [10.1016/j.actbio.2014.12.012](https://doi.org/10.1016/j.actbio.2014.12.012).
- [339] M. L. Obaíd, J. P. Camacho, M. Brenet, *et al.*, "A first in human trial implanting microalgae shows safety of photosynthetic therapy for the effective treatment of full thickness skin wounds," *Frontiers in Medicine*, vol. 8, p. 772 324, Nov. 30, 2021, ISSN: 2296-858X. DOI: [10.3389/fmed.2021.772324](https://doi.org/10.3389/fmed.2021.772324).
- [340] J. Ávila-Román, E. Talero, A. Alcaide, *et al.*, "Preventive effect of the microalga *Chlamydomonas debaryana* on the acute phase of experimental colitis in rats," *British Journal of Nutrition*, vol. 112, no. 7, pp. 1055–1064, Oct. 14, 2014, ISSN: 0007-1145, 1475-2662. DOI: [10.1017/S0007114514001895](https://doi.org/10.1017/S0007114514001895).
- [341] L. Rahmawati, S. H. Park, D. S. Kim, *et al.*, "Anti-inflammatory activities of the ethanol extract of *Prasiola japonica*, an edible freshwater green algae, and its various solvent fractions in LPS-induced macrophages and carrageenan-induced paw edema via the AP-1 pathway," *Molecules*, vol. 27, no. 1, p. 194, Dec. 29, 2021, ISSN: 1420-3049. DOI: [10.3390/molecules27010194](https://doi.org/10.3390/molecules27010194).
- [342] Y. Manabe, Y. Takii, and T. Sugawara, "Siphonaxanthin, a carotenoid from green algae, suppresses advanced glycation end product-induced inflammatory responses," *Journal of Natural Medicines*, vol. 74, no. 1, pp. 127–134, Jan. 2020, ISSN: 1340-3443, 1861-0293. DOI: [10.1007/s11418-019-01354-z](https://doi.org/10.1007/s11418-019-01354-z).
- [343] S. Qiu, S. I. Khan, M. Wang, *et al.*, "Chemometrics-assisted identification of anti-inflammatory compounds from the green alga *Klebsormidium flaccidum* var. *zivo*," *Molecules*, vol. 25, no. 5, p. 1048, Feb. 26, 2020, ISSN: 1420-3049. DOI: [10.3390/molecules25051048](https://doi.org/10.3390/molecules25051048).
- [344] E. W. Craig, D. M. Mueller, M. Schaffer, B. D. Engel, and P. Avasthi, "The elusive actin cytoskeleton of a green alga expressing both conventional and divergent actins," *Cell Biology*, preprint, Feb. 18, 2019. DOI: [10.1101/554279](https://doi.org/10.1101/554279).
- [345] M. Sumper and A. Hallmann, "Biochemistry of the extracellular matrix of *Volvox*," in *International Review of Cytology*, vol. 180, Elsevier, 1998, pp. 51–85, ISBN: 978-0-12-364584-5. DOI: [10.1016/S0074-7696\(08\)61770-2](https://doi.org/10.1016/S0074-7696(08)61770-2).

- [346] A. Hallmann, "Extracellular matrix and sex-inducing pheromone in volvox," in *International Review of Cytology*, vol. 227, Elsevier, 2003, pp. 131–182, ISBN: 978-0-12-364631-6. DOI: [10.1016/S0074-7696\(03\)01009-X](https://doi.org/10.1016/S0074-7696(03)01009-X).
- [347] —, "The pherophorins: Common, versatile building blocks in the evolution of extracellular matrix architecture in volvocales," *The Plant Journal*, vol. 45, no. 2, pp. 292–307, 2005, ISSN: 09607412, 1365313X. DOI: [10.1111/j.1365-313X.2005.02627.x](https://doi.org/10.1111/j.1365-313X.2005.02627.x).
- [348] E. J. M. V. Damme, Ed., *Handbook of plant lectins: properties and biomedical applications*, Chichester ; New York: Wiley, 1998, 452 pp., ISBN: 978-0-471-96445-2.
- [349] E. Bause, T. Müller, and L. Jaenicke, "Synthesis and characterization of lipid-linked mannosyl oligosaccharides in volvox carteri f. nagariensis," *Archives of Biochemistry and Biophysics*, vol. 220, no. 1, pp. 200–207, Jan. 1983, ISSN: 00039861. DOI: [10.1016/0003-9861\(83\)90401-0](https://doi.org/10.1016/0003-9861(83)90401-0).
- [350] P. Chaturvedi, A. P. Singh, and S. K. Batra, "Structure, evolution, and biology of the MUC4 mucin," *The FASEB Journal*, vol. 22, no. 4, pp. 966–981, Apr. 2008, ISSN: 0892-6638, 1530-6860. DOI: [10.1096/fj.07-9673rev](https://doi.org/10.1096/fj.07-9673rev).
- [351] K. L. Johnson, A. M. Cassin, A. Lonsdale, A. Bacic, M. S. Doblin, and C. J. Schultz, "Pipeline to identify hydroxyproline-rich glycoproteins," *Plant Physiology*, vol. 174, no. 2, pp. 886–903, Jun. 2017, ISSN: 0032-0889, 1532-2548. DOI: [10.1104/pp.17.00294](https://doi.org/10.1104/pp.17.00294).
- [352] R. Schlipfenbacher, S. Wenzl, F. Lottspeich, and M. Sumper, "An extremely hydroxyproline-rich glycoprotein is expressed in inverting *Volvox* embryos," *FEBS Letters*, vol. 209, no. 1, pp. 57–62, Dec. 1, 1986, ISSN: 00145793. DOI: [10.1016/0014-5793\(86\)81084-5](https://doi.org/10.1016/0014-5793(86)81084-5).
- [353] A. Varki, J. Esko, and K. Colley, "Cellular organization of glycosylation," in *Essentials of Glycobiology*, ser. 2nd edition, The Consortium of Glycobiology Editors, Cold Spring Harbor (NY): Cold Spring Harbor Laboratory Press, 2009, ISBN: 978-0-87969-770-9.
- [354] E. Ruiz-May, I. Sørensen, Z. Fei, S. Zhang, D. Domozych, and J. Rose, "The secretome and n-glycosylation profiles of the charophycean green alga, *Penium margaritaceum*, resemble those of embryophytes," *Proteomes*, vol. 6, no. 2, p. 14, Mar. 21, 2018, ISSN: 2227-7382. DOI: [10.3390/proteomes6020014](https://doi.org/10.3390/proteomes6020014).
- [355] S. Sakakibara, K. Inouye, K. Shudo, Y. Kishida, Y. Kobayashi, and D. J. Prockop, "Synthesis of (pro-hyp-gly)_n of defined molecular weights evidence for the stabilization of collagen triple helix by hydroxyproline," *Biochimica et Biophysica Acta (BBA) - Protein Structure*, vol. 303, no. 1, pp. 198–202, Mar. 1973, ISSN: 00052795. DOI: [10.1016/0005-2795\(73\)90164-5](https://doi.org/10.1016/0005-2795(73)90164-5).
- [356] C. L. Jenkins, L. E. Bretscher, I. A. Guzei, and R. T. Raines, "Effect of 3-hydroxyproline residues on collagen stability," *Journal of the American Chemical Society*, vol. 125, no. 21, pp. 6422–6427, May 1, 2003, ISSN: 0002-7863, 1520-5126. DOI: [10.1021/ja034015j](https://doi.org/10.1021/ja034015j).

- [357] K. H. Sipilä, K. Drushinin, P. Rappu, *et al.*, "Proline hydroxylation in collagen supports integrin binding by two distinct mechanisms," *Journal of Biological Chemistry*, vol. 293, no. 20, pp. 7645–7658, May 2018, ISSN: 00219258. DOI: [10.1074/jbc.RA118.002200](https://doi.org/10.1074/jbc.RA118.002200).
- [358] M. A. McGuckin, S. K. Lindén, P. Sutton, and T. H. Florin, "Mucin dynamics and enteric pathogens," *Nature Reviews Microbiology*, vol. 9, no. 4, pp. 265–278, Apr. 2011, ISSN: 1740-1526, 1740-1534. DOI: [10.1038/nrmicro2538](https://doi.org/10.1038/nrmicro2538).
- [359] T. Crouzier, H. Jang, J. Ahn, R. Stocker, and K. Ribbeck, "Cell patterning with mucin biopolymers," *Biomacromolecules*, vol. 14, no. 9, pp. 3010–3016, Sep. 9, 2013, ISSN: 1525-7797, 1526-4602. DOI: [10.1021/bm400447z](https://doi.org/10.1021/bm400447z).
- [360] T. Hennet, "Collagen glycosylation," *Current Opinion in Structural Biology*, vol. 56, pp. 131–138, Jun. 2019, ISSN: 0959440X. DOI: [10.1016/j.sbi.2019.01.015](https://doi.org/10.1016/j.sbi.2019.01.015).
- [361] M. J. Stawikowski, B. Aukszi, R. Stawikowska, M. Cudic, and G. B. Fields, "Glycosylation modulates melanoma cell 21 and 31 integrin interactions with type IV collagen," *Journal of Biological Chemistry*, vol. 289, no. 31, pp. 21 591–21 604, Aug. 2014, ISSN: 00219258. DOI: [10.1074/jbc.M114.572073](https://doi.org/10.1074/jbc.M114.572073).
- [362] K. L. Reigle, G. Di Lullo, K. R. Turner, *et al.*, "Non-enzymatic glycation of type i collagen diminishes collagen-proteoglycan binding and weakens cell adhesion," *Journal of Cellular Biochemistry*, vol. 104, no. 5, pp. 1684–1698, Aug. 1, 2008, ISSN: 07302312, 10974644. DOI: [10.1002/jcb.21735](https://doi.org/10.1002/jcb.21735).
- [363] C. A. Miles and A. J. Bailey, "Thermal denaturation of collagen revisited," *Proceedings / Indian Academy of Sciences*, vol. 111, no. 1, pp. 71–80, Feb. 1999, ISSN: 0253-4134. DOI: [10.1007/BF02869897](https://doi.org/10.1007/BF02869897).
- [364] A. V. Taubenberger, M. A. Woodruff, H. Bai, D. J. Muller, and D. W. Hutmacher, "The effect of unlocking RGD-motifs in collagen i on pre-osteoblast adhesion and differentiation," *Biomaterials*, vol. 31, no. 10, pp. 2827–2835, Apr. 2010, ISSN: 01429612. DOI: [10.1016/j.biomaterials.2009.12.051](https://doi.org/10.1016/j.biomaterials.2009.12.051).
- [365] C.-T. Hsiao, H.-W. Cheng, C.-M. Huang, *et al.*, "Fibronectin in cell adhesion and migration via n-glycosylation," *Oncotarget*, vol. 8, no. 41, pp. 70 653–70 668, Sep. 19, 2017, ISSN: 1949-2553. DOI: [10.18632/oncotarget.19969](https://doi.org/10.18632/oncotarget.19969).
- [366] R. D. Cummings, "Stuck on sugars – how carbohydrates regulate cell adhesion, recognition, and signaling," *Glycoconjugate Journal*, vol. 36, no. 4, pp. 241–257, Aug. 2019, ISSN: 0282-0080, 1573-4986. DOI: [10.1007/s10719-019-09876-0](https://doi.org/10.1007/s10719-019-09876-0).
- [367] A. Varki, "Selectin ligands: Will the real ones please stand up?" *Journal of Clinical Investigation*, vol. 99, no. 2, pp. 158–162, Jan. 15, 1997, ISSN: 0021-9738. DOI: [10.1172/JCI119142](https://doi.org/10.1172/JCI119142).
- [368] N. Sasaki, Y. Itakura, and M. Toyoda, "Sialylation regulates myofibroblast differentiation of human skin fibroblasts," *Stem Cell Research & Therapy*, vol. 8, no. 1, p. 81, Dec. 2017, ISSN: 1757-6512. DOI: [10.1186/s13287-017-0534-1](https://doi.org/10.1186/s13287-017-0534-1).

- [369] Y.-C. Wang, S.-H. Kao, and H.-J. Hsieh, "A chemical surface modification of chitosan by glycoconjugates to enhance the cellbiomaterial interaction," *Biomacromolecules*, vol. 4, no. 2, pp. 224–231, Mar. 1, 2003, ISSN: 1525-7797, 1526-4602. DOI: [10.1021/bm0256294](https://doi.org/10.1021/bm0256294).
- [370] D. F. Williams, "Challenges with the development of biomaterials for sustainable tissue engineering," *Frontiers in Bioengineering and Biotechnology*, vol. 7, p. 127, May 31, 2019, ISSN: 2296-4185. DOI: [10.3389/fbioe.2019.00127](https://doi.org/10.3389/fbioe.2019.00127).
- [371] F. A. Müller, L. Müller, I. Hofmann, P. Greil, M. M. Wenzel, and R. Staudenmaier, "Cellulose-based scaffold materials for cartilage tissue engineering," *Biomaterials*, vol. 27, no. 21, pp. 3955–3963, Jul. 2006, ISSN: 01429612. DOI: [10.1016/j.biomaterials.2006.02.031](https://doi.org/10.1016/j.biomaterials.2006.02.031).
- [372] J. Namkaew, P. Laowpanitchakorn, N. Sawaddee, S. Jirajessada, S. Honsawek, and S. Yodmuang, "Carboxymethyl cellulose entrapped in a poly(vinyl) alcohol network: Plant-based scaffolds for cartilage tissue engineering," *Molecules*, vol. 26, no. 3, p. 578, Jan. 22, 2021, ISSN: 1420-3049. DOI: [10.3390/molecules26030578](https://doi.org/10.3390/molecules26030578).
- [373] C. Demitri, M. G. Raucci, A. Giuri, *et al.*, "Cellulose-based porous scaffold for bone tissue engineering applications: Assessment of hMSC proliferation and differentiation: Cellulose-based porous scaffold for bone tissue engineering applications," *Journal of Biomedical Materials Research Part A*, vol. 104, no. 3, pp. 726–733, Mar. 2016, ISSN: 15493296. DOI: [10.1002/jbm.a.35611](https://doi.org/10.1002/jbm.a.35611).
- [374] M. Janmohammadi, Z. Nazemi, A. O. M. Salehi, *et al.*, "Cellulose-based composite scaffolds for bone tissue engineering and localized drug delivery," *Bioactive Materials*, vol. 20, pp. 137–163, Feb. 2023, ISSN: 2452199X. DOI: [10.1016/j.bioactmat.2022.05.018](https://doi.org/10.1016/j.bioactmat.2022.05.018).
- [375] L. Diaz-Gomez, I. Gonzalez-Prada, R. Millan, *et al.*, "3d printed carboxymethyl cellulose scaffolds for autologous growth factors delivery in wound healing," *Carbohydrate Polymers*, vol. 278, p. 118924, Feb. 2022, ISSN: 01448617. DOI: [10.1016/j.carbpol.2021.118924](https://doi.org/10.1016/j.carbpol.2021.118924).
- [376] L. Zheng, S. Li, J. Luo, and X. Wang, "Latest advances on bacterial cellulose-based antibacterial materials as wound dressings," *Frontiers in Bioengineering and Biotechnology*, vol. 8, p. 593768, Nov. 23, 2020, ISSN: 2296-4185. DOI: [10.3389/fbioe.2020.593768](https://doi.org/10.3389/fbioe.2020.593768).
- [377] J. R. Gershlak, S. Hernandez, G. Fontana, *et al.*, "Crossing kingdoms: Using decellularized plants as perfusable tissue engineering scaffolds," *Biomaterials*, vol. 125, pp. 13–22, May 2017, ISSN: 01429612. DOI: [10.1016/j.biomaterials.2017.02.011](https://doi.org/10.1016/j.biomaterials.2017.02.011).
- [378] D. Steffens, M. Lersch, A. Rosa, *et al.*, "A new biomaterial of nanofibers with the microalga *Spirulina* scaffolds to cultivate with stem cells for use in tissue engineering," *Journal of Biomedical Nanotechnology*, vol. 9, no. 4, pp. 710–718, Apr. 1, 2013, ISSN: 15507033. DOI: [10.1166/jbn.2013.1571](https://doi.org/10.1166/jbn.2013.1571).

- [379] T. Fiedler, I. V. Belova, G. E. Murch, *et al.*, “A comparative study of oxygen diffusion in tissue engineering scaffolds,” *Journal of Materials Science: Materials in Medicine*, vol. 25, no. 11, pp. 2573–2578, Nov. 2014, ISSN: 0957-4530, 1573-4838. DOI: [10.1007/s10856-014-5264-7](https://doi.org/10.1007/s10856-014-5264-7).
- [380] D. Hlushkou, H. Liasneuski, U. Tallarek, and S. Torquato, “Effective diffusion coefficients in random packings of polydisperse hard spheres from two-point and three-point correlation functions,” *Journal of Applied Physics*, vol. 118, no. 12, p. 124 901, Sep. 28, 2015, ISSN: 0021-8979, 1089-7550. DOI: [10.1063/1.4931153](https://doi.org/10.1063/1.4931153).
- [381] K. Štefková, J. Procházková, and J. Pacherník, “Alkaline phosphatase in stem cells,” *Stem Cells International*, vol. 2015, pp. 1–11, 2015, ISSN: 1687-966X, 1687-9678. DOI: [10.1155/2015/628368](https://doi.org/10.1155/2015/628368).
- [382] B. Roy, L. Yuan, Y. Lee, A. Bharti, A. Mitra, and G. V. Shivashankar, “Fibroblast rejuvenation by mechanical reprogramming and redifferentiation,” *Proceedings of the National Academy of Sciences*, vol. 117, no. 19, pp. 10 131–10 141, May 12, 2020, ISSN: 0027-8424, 1091-6490. DOI: [10.1073/pnas.1911497117](https://doi.org/10.1073/pnas.1911497117).
- [383] B. Roy, S. Venkatachalapathy, P. Ratna, *et al.*, “Laterally confined growth of cells induces nuclear reprogramming in the absence of exogenous biochemical factors,” *Proceedings of the National Academy of Sciences*, vol. 115, no. 21, E4741–E4750, May 22, 2018, ISSN: 0027-8424, 1091-6490. DOI: [10.1073/pnas.1714770115](https://doi.org/10.1073/pnas.1714770115).
- [384] D. W. Moss, “Alkaline phosphatase isoenzymes,” *Clinical Chemistry*, vol. 28, no. 10, pp. 2007–2016, Oct. 1, 1982, ISSN: 0009-9147, 1530-8561. DOI: [10.1093/clinchem/28.10.2007](https://doi.org/10.1093/clinchem/28.10.2007).
- [385] “Soft tissue repair global market report 2022,” The Business Research Company, Market report, 2022, p. 175.
- [386] S. Ghanaati, M. Schlee, M. J. Webber, *et al.*, “Evaluation of the tissue reaction to a new bilayered collagen matrix *in vivo* and its translation to the clinic,” *Biomedical Materials*, vol. 6, no. 1, p. 015 010, Feb. 1, 2011, ISSN: 1748-6041, 1748-605X. DOI: [10.1088/1748-6041/6/1/015010](https://doi.org/10.1088/1748-6041/6/1/015010).
- [387] D. Rothamel, F. Schwarz, M. Sager, M. Hertel, A. Sculean, and J. Becker, “Biodegradation of differently cross-linked collagen membranes: An experimental study in the rat,” *Clinical Oral Implants Research*, vol. 16, no. 3, pp. 369–378, Jun. 2005, ISSN: 0905-7161, 1600-0501. DOI: [10.1111/j.1600-0501.2005.01108.x](https://doi.org/10.1111/j.1600-0501.2005.01108.x).
- [388] A. Atala, “From tissue to organ engineering,” in *Comprehensive Biomaterials*, Elsevier, 2011, pp. 547–562, ISBN: 978-0-08-055294-1. DOI: [10.1016/B978-0-08-055294-1.00191-4](https://doi.org/10.1016/B978-0-08-055294-1.00191-4).
- [389] K. Militzer, “Hair growth pattern in nude mice,” *Cells Tissues Organs*, vol. 168, no. 4, pp. 285–294, 2001, ISSN: 1422-6405, 1422-6421. DOI: [10.1159/000047845](https://doi.org/10.1159/000047845).

- [390] G. Lemperle, V. Morhenn, and U. Charrier, "Human histology and persistence of various injectable filler substances for soft tissue augmentation," *Aesthetic Plastic Surgery*, vol. 27, no. 5, pp. 354–366, Oct. 1, 2003, ISSN: 0364-216X, 1432-5241. DOI: [10.1007/s00266-003-3022-1](https://doi.org/10.1007/s00266-003-3022-1).
- [391] R. Pant, P. Firmal, V. K. Shah, A. Alam, and S. Chattopadhyay, "Epigenetic regulation of adipogenesis in development of metabolic syndrome," *Frontiers in Cell and Developmental Biology*, vol. 8, p. 619 888, Jan. 12, 2021, ISSN: 2296-634X. DOI: [10.3389/fcell.2020.619888](https://doi.org/10.3389/fcell.2020.619888).
- [392] J. Dufau, J. X. Shen, M. Couchet, *et al.*, "In vitro and ex vivo models of adipocytes," *American Journal of Physiology-Cell Physiology*, vol. 320, no. 5, pp. C822–C841, May 1, 2021, ISSN: 0363-6143, 1522-1563. DOI: [10.1152/ajpcell.00519.2020](https://doi.org/10.1152/ajpcell.00519.2020).
- [393] S. Abuhattum, P. Kotzbeck, R. Schlüßler, *et al.*, "Adipose cells and tissues soften with lipid accumulation while in diabetes adipose tissue stiffens," *Scientific Reports*, vol. 12, no. 1, p. 10 325, Dec. 2022, ISSN: 2045-2322. DOI: [10.1038/s41598-022-13324-9](https://doi.org/10.1038/s41598-022-13324-9).
- [394] A.-C. Pilkington, H. A. Paz, and U. D. Wankhade, "Beige adipose tissue identification and marker specificity—overview," *Frontiers in Endocrinology*, vol. 12, p. 599 134, Mar. 12, 2021, ISSN: 1664-2392. DOI: [10.3389/fendo.2021.599134](https://doi.org/10.3389/fendo.2021.599134).
- [395] A. Giordano, A. Smorlesi, A. Frontini, G. Barbatelli, and S. Cinti, "MECHANISMS IN ENDOCRINOLOGY: White, brown and pink adipocytes: The extraordinary plasticity of the adipose organ," *European Journal of Endocrinology*, vol. 170, no. 5, R159–R171, May 2014, ISSN: 0804-4643, 1479-683X. DOI: [10.1530/EJE-13-0945](https://doi.org/10.1530/EJE-13-0945).
- [396] H. Nobusue, N. Onishi, T. Shimizu, *et al.*, "Regulation of MKL1 via actin cytoskeleton dynamics drives adipocyte differentiation," *Nature Communications*, vol. 5, no. 1, p. 3368, May 2014, ISSN: 2041-1723. DOI: [10.1038/ncomms4368](https://doi.org/10.1038/ncomms4368).
- [397] I. Warnke, R. Goralczyk, E. Fuhrer, and J. Schwager, "Dietary constituents reduce lipid accumulation in murine c3h10 t1/2 adipocytes: A novel fluorescent method to quantify fat droplets," *Nutrition & Metabolism*, vol. 8, no. 1, p. 30, 2011, ISSN: 1743-7075. DOI: [10.1186/1743-7075-8-30](https://doi.org/10.1186/1743-7075-8-30).
- [398] G. Yu, X. Wu, M. A. Dietrich, *et al.*, "Yield and characterization of subcutaneous human adipose-derived stem cells by flow cytometric and adipogenic mRNA analyzes," *Cytotherapy*, vol. 12, no. 4, pp. 538–546, Jul. 2010, ISSN: 14653249. DOI: [10.3109/14653241003649528](https://doi.org/10.3109/14653241003649528).
- [399] B. Gustafson and U. Smith, "The WNT inhibitor dickkopf 1 and bone morphogenetic protein 4 rescue adipogenesis in hypertrophic obesity in humans," *Diabetes*, vol. 61, no. 5, pp. 1217–1224, May 1, 2012, ISSN: 0012-1797, 1939-327X. DOI: [10.2337/db11-1419](https://doi.org/10.2337/db11-1419).
- [400] J. Lindroos, J. Husa, G. Mitterer, *et al.*, "Human but not mouse adipogenesis is critically dependent on LMO3," *Cell Metabolism*, vol. 18, no. 1, pp. 62–74, Jul. 2013, ISSN: 15504131. DOI: [10.1016/j.cmet.2013.05.020](https://doi.org/10.1016/j.cmet.2013.05.020).

- [401] S. Gogg, A. Nerstedt, J. Boren, and U. Smith, "Human adipose tissue microvascular endothelial cells secrete PPAR ligands and regulate adipose tissue lipid uptake," *JCI Insight*, vol. 4, no. 5, e125914, Mar. 7, 2019, ISSN: 2379-3708. DOI: [10.1172/jci.insight.125914](https://doi.org/10.1172/jci.insight.125914).
- [402] J. R. Tse and A. J. Engler, "Stiffness gradients mimicking in vivo tissue variation regulate mesenchymal stem cell fate," *PLoS ONE*, vol. 6, no. 1, N. D. Leipzig, Ed., e15978, Jan. 5, 2011, ISSN: 1932-6203. DOI: [10.1371/journal.pone.0015978](https://doi.org/10.1371/journal.pone.0015978).
- [403] Y. Li, M. Wu, Z. Zhang, *et al.*, "Application of external force regulates the migration and differentiation of adipose-derived stem/progenitor cells by altering tissue stiffness," *Tissue Engineering Part A*, vol. 25, no. 23, pp. 1614–1622, Dec. 1, 2019, ISSN: 1937-3341, 1937-335X. DOI: [10.1089/ten.tea.2019.0046](https://doi.org/10.1089/ten.tea.2019.0046).
- [404] H. Yu, C. Y. Tay, W. S. Leong, S. C. W. Tan, K. Liao, and L. P. Tan, "Mechanical behavior of human mesenchymal stem cells during adipogenic and osteogenic differentiation," *Biochemical and Biophysical Research Communications*, vol. 393, no. 1, pp. 150–155, Feb. 2010, ISSN: 0006291X. DOI: [10.1016/j.bbrc.2010.01.107](https://doi.org/10.1016/j.bbrc.2010.01.107).
- [405] N. Alkhouli, J. Mansfield, E. Green, *et al.*, "The mechanical properties of human adipose tissues and their relationships to the structure and composition of the extracellular matrix," *American Journal of Physiology-Endocrinology and Metabolism*, vol. 305, no. 12, E1427–E1435, Dec. 15, 2013, ISSN: 0193-1849, 1522-1555. DOI: [10.1152/ajpendo.00111.2013](https://doi.org/10.1152/ajpendo.00111.2013).
- [406] L. Di Medio and M. L. Brandi, "Advances in bone turnover markers," in *Advances in Clinical Chemistry*, vol. 105, Elsevier, 2021, pp. 101–140, ISBN: 978-0-12-824627-6. DOI: [10.1016/bs.acc.2021.06.001](https://doi.org/10.1016/bs.acc.2021.06.001).
- [407] K. A. Kilian, B. Bugarija, B. T. Lahn, and M. Mrksich, "Geometric cues for directing the differentiation of mesenchymal stem cells," *Proceedings of the National Academy of Sciences*, vol. 107, no. 11, pp. 4872–4877, Mar. 16, 2010, ISSN: 0027-8424, 1091-6490. DOI: [10.1073/pnas.0903269107](https://doi.org/10.1073/pnas.0903269107).
- [408] L. Chen, H. Hu, W. Qiu, K. Shi, and M. Kassem, "Actin depolymerization enhances adipogenic differentiation in human stromal stem cells," *Stem Cell Research*, vol. 29, pp. 76–83, May 2018, ISSN: 18735061. DOI: [10.1016/j.scr.2018.03.010](https://doi.org/10.1016/j.scr.2018.03.010).
- [409] A. McColloch, M. Rabiei, P. Rabbani, A. Bowling, and M. Cho, "Correlation between nuclear morphology and adipogenic differentiation: Application of a combined experimental and computational modeling approach," *Scientific Reports*, vol. 9, no. 1, p. 16381, Dec. 2019, ISSN: 2045-2322. DOI: [10.1038/s41598-019-52926-8](https://doi.org/10.1038/s41598-019-52926-8).
- [410] R. Akhtar, M. J. Sherratt, J. K. Cruickshank, and B. Derby, "Characterizing the elastic properties of tissues," *Materials Today*, vol. 14, no. 3, pp. 96–105, Mar. 2011, ISSN: 13697021. DOI: [10.1016/S1369-7021\(11\)70059-1](https://doi.org/10.1016/S1369-7021(11)70059-1).

- [411] Y.-S. Tsai, A. Huang, Y.-S. Lin, L.-Z. Kao, M.-J. Tang, and P.-J. Tsai, "Adipose tissue stiffness in the development of metabolic diseases," *The FASEB Journal*, vol. 36, fasebj.2022.36.S1.R5289, S1 May 2022, ISSN: 0892-6638, 1530-6860. DOI: [10.1096/fasebj.2022.36.S1.R5289](https://doi.org/10.1096/fasebj.2022.36.S1.R5289).
- [412] N. Shoham, R. Gottlieb, O. Sharabani-Yosef, U. Zaretsky, D. Benayahu, and A. Gefen, "Static mechanical stretching accelerates lipid production in 3t3-l1 adipocytes by activating the MEK signaling pathway," *American Journal of Physiology-Cell Physiology*, vol. 302, no. 2, pp. C429–C441, Jan. 15, 2012, ISSN: 0363-6143, 1522-1563. DOI: [10.1152/ajpcell.00167.2011](https://doi.org/10.1152/ajpcell.00167.2011).
- [413] M. Ben-Or Frank, N. Shoham, D. Benayahu, and A. Gefen, "Effects of accumulation of lipid droplets on load transfer between and within adipocytes," *Biomechanics and Modeling in Mechanobiology*, vol. 14, no. 1, pp. 15–28, Jan. 2015, ISSN: 1617-7959, 1617-7940. DOI: [10.1007/s10237-014-0582-8](https://doi.org/10.1007/s10237-014-0582-8).
- [414] J. X. Shen, M. Couchet, J. Dufau, *et al.*, "3d adipose tissue culture links the organotypic microenvironment to improved adipogenesis," *Advanced Science*, vol. 8, no. 16, p. 2100106, Aug. 2021, ISSN: 2198-3844, 2198-3844. DOI: [10.1002/advs.202100106](https://doi.org/10.1002/advs.202100106).
- [415] S. Wenzl, D. Thym, and M. Sumper, "Development-dependent modification of the extracellular matrix by a sulphated glycoprotein in *Volvox carteri*," *The EMBO Journal*, vol. 3, no. 4, pp. 739–744, Apr. 1984, ISSN: 02614189. DOI: [10.1002/j.1460-2075.1984.tb01877.x](https://doi.org/10.1002/j.1460-2075.1984.tb01877.x).
- [416] K. Roberts, "Crystalline glycoprotein cell walls of algae: Their structure, composition and assembly," *Philosophical Transactions of the Royal Society of London. B, Biological Sciences*, vol. 268, no. 891, pp. 129–146, Jul. 25, 1974, ISSN: 0080-4622, 2054-0280. DOI: [10.1098/rstb.1974.0021](https://doi.org/10.1098/rstb.1974.0021).
- [417] A. L. Fidler, S. P. Boudko, A. Rokas, and B. G. Hudson, "The triple helix of collagens – an ancient protein structure that enabled animal multicellularity and tissue evolution," *Journal of Cell Science*, vol. 131, no. 7, jcs203950, Apr. 1, 2018, ISSN: 1477-9137, 0021-9533. DOI: [10.1242/jcs.203950](https://doi.org/10.1242/jcs.203950).
- [418] C. M. Yamazaki, Y. Kadoya, K. Hozumi, *et al.*, "A collagen-mimetic triple helical supramolecule that evokes integrin-dependent cell responses," *Biomaterials*, vol. 31, no. 7, pp. 1925–1934, Mar. 2010, ISSN: 01429612. DOI: [10.1016/j.biomaterials.2009.10.014](https://doi.org/10.1016/j.biomaterials.2009.10.014).
- [419] C. G. Knight, L. F. Morton, A. R. Peachey, D. S. Tuckwell, R. W. Farndale, and M. J. Barnes, "The collagen-binding α -domains of integrins 11 and 21 recognize the same specific amino acid sequence, GFOGER, in native (triple-helical) collagens," *Journal of Biological Chemistry*, vol. 275, no. 1, pp. 35–40, Jan. 2000, ISSN: 00219258. DOI: [10.1074/jbc.275.1.35](https://doi.org/10.1074/jbc.275.1.35).
- [420] Y. Takada, X. Ye, and S. Simon, "The integrins," *Genome Biology*, vol. 8, no. 5, p. 215, 2007, ISSN: 14656906. DOI: [10.1186/gb-2007-8-5-215](https://doi.org/10.1186/gb-2007-8-5-215).

- [421] H. Mao and Y. Ito, "4.19 growth factors and protein-modified surfaces and interfaces," in *Comprehensive Biomaterials II*, Elsevier, 2017, pp. 321–359, ISBN: 978-0-08-100692-4. DOI: [10.1016/B978-0-12-803581-8.10191-2](https://doi.org/10.1016/B978-0-12-803581-8.10191-2).
- [422] A. M. Belkin and M. A. Stepp, "Integrins as receptors for laminins," *Microscopy Research and Technique*, vol. 51, no. 3, pp. 280–301, Nov. 1, 2000, ISSN: 1059-910X, 1097-0029. DOI: [10.1002/1097-0029\(20001101\)51:3<280::AID-JEMT7>3.0.CO;2-O](https://doi.org/10.1002/1097-0029(20001101)51:3<280::AID-JEMT7>3.0.CO;2-O).
- [423] C. Bonnans, J. Chou, and Z. Werb, "Remodelling the extracellular matrix in development and disease," *Nature Reviews Molecular Cell Biology*, vol. 15, no. 12, pp. 786–801, Dec. 2014, ISSN: 1471-0072, 1471-0080. DOI: [10.1038/nrm3904](https://doi.org/10.1038/nrm3904).
- [424] I. Nakajima, S. Muroya, R.-I. Tanabe, and K. Chikuni, "Extracellular matrix development during differentiation into adipocytes with a unique increase in type v and VI collagen," *Biology of the Cell*, vol. 94, no. 3, pp. 197–203, Jun. 2002, ISSN: 02484900. DOI: [10.1016/S0248-4900\(02\)01189-9](https://doi.org/10.1016/S0248-4900(02)01189-9).
- [425] F. J. Ruiz-Ojeda, J. Wang, T. Bäcker, *et al.*, "Active integrins regulate white adipose tissue insulin sensitivity and brown fat thermogenesis," *Molecular Metabolism*, vol. 45, p. 101 147, Mar. 2021, ISSN: 22128778. DOI: [10.1016/j.molmet.2020.101147](https://doi.org/10.1016/j.molmet.2020.101147).
- [426] E. M. Morandi, R. Verstappen, M. E. Zwierzina, S. Geley, G. Pierer, and C. Ploner, "ITGAV and ITGA5 diversely regulate proliferation and adipogenic differentiation of human adipose derived stem cells," *Scientific Reports*, vol. 6, no. 1, p. 28 889, Sep. 2016, ISSN: 2045-2322. DOI: [10.1038/srep28889](https://doi.org/10.1038/srep28889).
- [427] A. Noro, T. Sillat, I. Virtanen, *et al.*, "Laminin production and basement membrane deposition by mesenchymal stem cells upon adipogenic differentiation," *Journal of Histochemistry & Cytochemistry*, vol. 61, no. 10, pp. 719–730, Oct. 2013, ISSN: 0022-1554, 1551-5044. DOI: [10.1369/0022155413502055](https://doi.org/10.1369/0022155413502055).
- [428] M. Al Hasan, P. E. Martin, X. Shu, S. Patterson, and C. Bartholomew, "Type III collagen is required for adipogenesis and actin stress fibre formation in 3t3-l1 preadipocytes," *Biomolecules*, vol. 11, no. 2, p. 156, Jan. 25, 2021, ISSN: 2218-273X. DOI: [10.3390/biom11020156](https://doi.org/10.3390/biom11020156).
- [429] T. Sillat, R. Saat, R. Pöllänen, M. Hukkanen, M. Takagi, and Y. T. Konttinen, "Basement membrane collagen type IV expression by human mesenchymal stem cells during adipogenic differentiation," *Journal of Cellular and Molecular Medicine*, vol. 16, no. 7, pp. 1485–1495, Jul. 2012, ISSN: 15821838. DOI: [10.1111/j.1582-4934.2011.01442.x](https://doi.org/10.1111/j.1582-4934.2011.01442.x).
- [430] C. Liu, K. Huang, G. Li, *et al.*, "Ascorbic acid promotes 3t3-l1 cells adipogenesis by attenuating ERK signaling to upregulate the collagen VI," *Nutrition & Metabolism*, vol. 14, no. 1, p. 79, Dec. 2017, ISSN: 1743-7075. DOI: [10.1186/s12986-017-0234-y](https://doi.org/10.1186/s12986-017-0234-y).
- [431] M. A. Gonzalez Porras, K. Stojkova, M. K. Vaicik, *et al.*, "Integrins and extracellular matrix proteins modulate adipocyte thermogenic capacity," *Scientific Reports*, vol. 11, no. 1, p. 5442, Dec. 2021, ISSN: 2045-2322. DOI: [10.1038/s41598-021-84828-z](https://doi.org/10.1038/s41598-021-84828-z).

- [432] D. Tews, V. Schwar, M. Scheithauer, *et al.*, "Comparative gene array analysis of progenitor cells from human paired deep neck and subcutaneous adipose tissue," *Molecular and Cellular Endocrinology*, vol. 395, no. 1, pp. 41–50, Sep. 2014, ISSN: 03037207. DOI: [10.1016/j.mce.2014.07.011](https://doi.org/10.1016/j.mce.2014.07.011).
- [433] D. Tews, T. Fromme, M. Keuper, *et al.*, "Teneurin-2 (TENM2) deficiency induces UCP1 expression in differentiating human fat cells," *Molecular and Cellular Endocrinology*, vol. 443, pp. 106–113, Mar. 2017, ISSN: 03037207. DOI: [10.1016/j.mce.2017.01.015](https://doi.org/10.1016/j.mce.2017.01.015).
- [434] S. Altschul, "Gapped BLAST and PSI-BLAST: A new generation of protein database search programs," *Nucleic Acids Research*, vol. 25, no. 17, pp. 3389–3402, Sep. 1, 1997, ISSN: 13624962. DOI: [10.1093/nar/25.17.3389](https://doi.org/10.1093/nar/25.17.3389).
- [435] S. F. Altschul, J. C. Wootton, E. M. Gertz, *et al.*, "Protein database searches using compositionally adjusted substitution matrices," *FEBS Journal*, vol. 272, no. 20, pp. 5101–5109, Oct. 2005, ISSN: 1742-464X, 1742-4658. DOI: [10.1111/j.1742-4658.2005.04945.x](https://doi.org/10.1111/j.1742-4658.2005.04945.x).
- [436] E. R. Tarakhovskaya, Y. I. Maslov, and M. F. Shishova, "Phytohormones in algae," *Russian Journal of Plant Physiology*, vol. 54, no. 2, pp. 163–170, Apr. 2007, ISSN: 1021-4437, 1608-3407. DOI: [10.1134/S1021443707020021](https://doi.org/10.1134/S1021443707020021).
- [437] M. Kanehisa, M. Furumichi, Y. Sato, M. Ishiguro-Watanabe, and M. Tanabe, "KEGG: Integrating viruses and cellular organisms," *Nucleic Acids Research*, vol. 49, pp. D545–D551, D1 Jan. 8, 2021, ISSN: 0305-1048, 1362-4962. DOI: [10.1093/nar/gkaa970](https://doi.org/10.1093/nar/gkaa970).
- [438] D. Le Roith, "Insulin-like growth factors," *New England Journal of Medicine*, vol. 336, no. 9, J. S. Flier and L. H. Underhill, Eds., pp. 633–640, Feb. 27, 1997, ISSN: 0028-4793, 1533-4406. DOI: [10.1056/NEJM199702273360907](https://doi.org/10.1056/NEJM199702273360907).
- [439] C. Livingstone and A. Borai, "Insulin-like growth factor-II: Its role in metabolic and endocrine disease," *Clinical Endocrinology*, vol. 80, no. 6, pp. 773–781, Jun. 2014, ISSN: 03000664. DOI: [10.1111/cen.12446](https://doi.org/10.1111/cen.12446).
- [440] A. Garten, S. Schuster, and W. Kiess, "The insulin-like growth factors in adipogenesis and obesity," *Endocrinology and Metabolism Clinics of North America*, vol. 41, no. 2, pp. 283–295, Jun. 2012, ISSN: 08898529. DOI: [10.1016/j.ec1.2012.04.011](https://doi.org/10.1016/j.ec1.2012.04.011).
- [441] M. Wabitsch, H. Hauner, E. Heinze, and W. M. Teller, "The role of growth hormone/insulin-like growth factors in adipocyte differentiation," *Metabolism*, vol. 44, pp. 45–49, Oct. 1995, ISSN: 00260495. DOI: [10.1016/0026-0495\(95\)90220-1](https://doi.org/10.1016/0026-0495(95)90220-1).
- [442] K. Zhang, F. Wang, J. Huang, *et al.*, "Insulin-like growth factor 2 promotes the adipogenesis of hemangioma-derived stem cells," *Experimental and Therapeutic Medicine*, Dec. 24, 2018, ISSN: 1792-0981, 1792-1015. DOI: [10.3892/etm.2018.7132](https://doi.org/10.3892/etm.2018.7132).
- [443] D. J. Klemm, J. W. Leitner, P. Watson, *et al.*, "Insulin-induced adipocyte differentiation," *Journal of Biological Chemistry*, vol. 276, no. 30, pp. 28 430–28 435, Jul. 2001, ISSN: 00219258. DOI: [10.1074/jbc.M103382200](https://doi.org/10.1074/jbc.M103382200).

- [444] S. Kim, J. Jang, S. Jung, *et al.*, "Chondrogenesis of rat bone marrow stromal cells in transforming growth factor-1 loaded alginate bead in in vivo," *Tissue Engineering and Regenerative Medicine*, vol. 5, pp. 650–659, Dec. 2008.
- [445] J.-B. Huh, J.-H. Kim, S. Kim, *et al.*, "Effects of PMMA and cross-linked dextran filler for soft tissue augmentation in rats," *International Journal of Molecular Sciences*, vol. 16, no. 12, pp. 28 523–28 533, Dec. 1, 2015, ISSN: 1422-0067. DOI: [10.3390/ijms161226112](https://doi.org/10.3390/ijms161226112).
- [446] Y. Zhang, H. Liang, Q. Luo, *et al.*, "In vivo inducing collagen regeneration of biodegradable polymer microspheres," *Regenerative Biomaterials*, vol. 8, no. 5, rbab042, Aug. 9, 2021, ISSN: 2056-3418, 2056-3426. DOI: [10.1093/rb/rbab042](https://doi.org/10.1093/rb/rbab042).
- [447] A. L. Mescher, "Macrophages and fibroblasts during inflammation and tissue repair in models of organ regeneration," *Regeneration*, vol. 4, no. 2, pp. 39–53, Apr. 2017, ISSN: 2052-4412, 2052-4412. DOI: [10.1002/reg2.77](https://doi.org/10.1002/reg2.77).
- [448] T. J. Puls, C. S. Fisher, A. Cox, *et al.*, "Regenerative tissue filler for breast conserving surgery and other soft tissue restoration and reconstruction needs," *Scientific Reports*, vol. 11, no. 1, p. 2711, Dec. 2021, ISSN: 2045-2322. DOI: [10.1038/s41598-021-81771-x](https://doi.org/10.1038/s41598-021-81771-x).
- [449] I. Gerges, M. Tamplenizza, F. Martello, *et al.*, "Conditioning the microenvironment for soft tissue regeneration in a cell free scaffold," *Scientific Reports*, vol. 11, no. 1, p. 13 310, Dec. 2021, ISSN: 2045-2322. DOI: [10.1038/s41598-021-92732-9](https://doi.org/10.1038/s41598-021-92732-9).
- [450] M. Kanemaru, J. Asai, J.-i. Jo, *et al.*, "Nanoparticle-mediated local delivery of pioglitazone attenuates bleomycin-induced skin fibrosis," *Journal of Dermatological Science*, vol. 93, no. 1, pp. 41–49, Jan. 2019, ISSN: 09231811. DOI: [10.1016/j.jdermsci.2018.11.012](https://doi.org/10.1016/j.jdermsci.2018.11.012).
- [451] A. Rojewska, A. Karewicz, K. Karnas, *et al.*, "Pioglitazone-loaded nanostructured hybrid material for skin ulcer treatment," *Materials*, vol. 13, no. 9, p. 2050, Apr. 28, 2020, ISSN: 1996-1944. DOI: [10.3390/ma13092050](https://doi.org/10.3390/ma13092050).
- [452] E. Yuksel, A. B. Weinfeld, R. Cleek, *et al.*, "De novo adipose tissue generation through long-term, local delivery of insulin and insulin-like growth factor-1 by PLGA/PEG microspheres in an in vivo rat model: A novel concept and capability," *Plastic and Reconstructive Surgery*, vol. 105, no. 5, pp. 1721–1729, Apr. 2000, ISSN: 0032-1052. DOI: [10.1097/00006534-200004050-00018](https://doi.org/10.1097/00006534-200004050-00018).
- [453] M.-H. Cheng, S. Uriel, M. L. Moya, *et al.*, "Dermis-derived hydrogels support adipogenesis in vivo," *Journal of Biomedical Materials Research Part A*, vol. 9999A, NA–NA, 2009, ISSN: 15493296, 15524965. DOI: [10.1002/jbm.a.32410](https://doi.org/10.1002/jbm.a.32410).
- [454] K. Abberton, S. Bortolotto, A. Woods, *et al.*, "Myogel, a novel, basement membrane-rich, extracellular matrix derived from skeletal muscle, is highly adipogenic in vivo and in vitro," *Cells Tissues Organs*, vol. 188, no. 4, pp. 347–358, 2008, ISSN: 1422-6405, 1422-6421. DOI: [10.1159/000121575](https://doi.org/10.1159/000121575).
- [455] I. Wu, Z. Nahas, K. A. Kimmerling, G. D. Rosson, and J. H. Elisseeff, "An injectable adipose matrix for soft-tissue reconstruction," *Plastic and Reconstructive Surgery*, vol. 129, no. 6, pp. 1247–1257, Jun. 2012, ISSN: 0032-1052. DOI: [10.1097/PRS.0b013e31824ec3dc](https://doi.org/10.1097/PRS.0b013e31824ec3dc).

- [456] B. M. Strem, K. C. Hicok, M. Zhu, *et al.*, "Multipotential differentiation of adipose tissue-derived stem cells," *The Keio Journal of Medicine*, vol. 54, no. 3, pp. 132–141, 2005, ISSN: 0022-9717, 1880-1293. DOI: [10.2302/kjm.54.132](https://doi.org/10.2302/kjm.54.132).
- [457] J. Leguy, "Periodate oxidation of cellulose for internal plasticization and materials design," Ph.D. dissertation, Université Grenoble Alpes, 2018.
- [458] A. R. A. Melo, J. C. D. Filho, R. P. C. Neto, *et al.*, "Effect of ultra-turrax on nanocellulose produced by acid hydrolysis and modified by nano ZnO by sol-gel method," *Materials Sciences and Applications*, vol. 11, no. 2, pp. 150–166, 2020, ISSN: 2153-117X, 2153-1188. DOI: [10.4236/msa.2020.112009](https://doi.org/10.4236/msa.2020.112009).
- [459] J. Wei, C. Du, H. Liu, Y. Chen, H. Yu, and Z. Zhou, "Preparation and characterization of aldehyde-functionalized cellulosic fibers through periodate oxidization of bamboo pulp," *BioResources*, vol. 11, no. 4, pp. 8386–8395, Aug. 12, 2016, ISSN: 1930-2126. DOI: [10.15376/biores.11.4.8386-8395](https://doi.org/10.15376/biores.11.4.8386-8395).
- [460] A. Mihranyan, A. P. Llagostera, R. Karmhag, M. Strømme, and R. Ek, "Moisture sorption by cellulose powders of varying crystallinity," *International Journal of Pharmaceutics*, vol. 269, no. 2, pp. 433–442, Jan. 2004, ISSN: 03785173. DOI: [10.1016/j.ijpharm.2003.09.030](https://doi.org/10.1016/j.ijpharm.2003.09.030).
- [461] X. Dang, P. Liu, M. Yang, H. Deng, Z. Shan, and W. Zhen, "Production and characterization of dialdehyde cellulose through green and sustainable approach," *Cellulose*, vol. 26, no. 18, pp. 9503–9515, Dec. 2019, ISSN: 0969-0239, 1572-882X. DOI: [10.1007/s10570-019-02747-9](https://doi.org/10.1007/s10570-019-02747-9).
- [462] M. Barghamadi, G. Barghamadi, M. Raouf, and A. Raouf, "Non-isothermal cure kinetics of diglycidyl ether of bisphenol-a with various aro-matic diamines," *Iranian Polymer Journal*, vol. 18, no. 431, 2009.
- [463] S. Suganthi, S. Vignesh, J. Kalyana Sundar, and V. Raj, "Fabrication of PVA polymer films with improved antibacterial activity by fine-tuning via organic acids for food packaging applications," *Applied Water Science*, vol. 10, no. 4, p. 100, Apr. 2020, ISSN: 2190-5487, 2190-5495. DOI: [10.1007/s13201-020-1162-y](https://doi.org/10.1007/s13201-020-1162-y).
- [464] T. Siddaiah, P. Ojha, N. O. G. V. R. Kumar, and C. Ramu, "Structural, optical and thermal characterizations of PVA/MAA:EA polyblend films," *Materials Research*, vol. 21, no. 5, Jul. 16, 2018, ISSN: 1980-5373, 1516-1439. DOI: [10.1590/1980-5373-mr-2017-0987](https://doi.org/10.1590/1980-5373-mr-2017-0987).
- [465] E. F. d. Reis, F. S. Campos, A. P. Lage, *et al.*, "Synthesis and characterization of poly (vinyl alcohol) hydrogels and hybrids for rMPB70 protein adsorption," *Materials Research*, vol. 9, no. 2, pp. 185–191, Jun. 2006, ISSN: 1516-1439. DOI: [10.1590/S1516-14392006000200014](https://doi.org/10.1590/S1516-14392006000200014).
- [466] H. S. Mansur, R. L. Oréfice, and A. A. Mansur, "Characterization of poly(vinyl alcohol)/poly(ethylene glycol) hydrogels and PVA-derived hybrids by small-angle x-ray scattering and FTIR spectroscopy," *Polymer*, vol. 45, no. 21, pp. 7193–7202, Sep. 2004, ISSN: 00323861. DOI: [10.1016/j.polymer.2004.08.036](https://doi.org/10.1016/j.polymer.2004.08.036).

- [467] H. Togrul, "Flow properties of sugar beet pulp cellulose and intrinsic viscosity–molecular weight relationship," *Carbohydrate Polymers*, vol. 54, no. 1, pp. 63–71, Oct. 1, 2003, ISSN: 01448617. DOI: [10.1016/S0144-8617\(03\)00146-2](https://doi.org/10.1016/S0144-8617(03)00146-2).
- [468] N. Jia, S.-M. Li, M.-G. Ma, and J. Zhu, "Synthesis and characterization of cellulose-silica composite fiber in ethanol/water mixed solvents," *BioResources*, vol. 6, no. 2, 2011. DOI: [10.15376/biores.6.2.1186-1195](https://doi.org/10.15376/biores.6.2.1186-1195).
- [469] P. Lv, G. Almeida, and P. Perré, "TGA-FTIR analysis of torrefaction of lignocellulosic components (cellulose, xylan, lignin) in isothermal conditions over a wide range of time durations," *BioResources*, vol. 10, no. 3, pp. 4239–4251, May 26, 2015, ISSN: 1930-2126. DOI: [10.15376/biores.10.3.4239-4251](https://doi.org/10.15376/biores.10.3.4239-4251).
- [470] J. Zhuang, M. Li, Y. Pu, A. Ragauskas, and C. Yoo, "Observation of potential contaminants in processed biomass using fourier transform infrared spectroscopy," *Applied Sciences*, vol. 10, no. 12, p. 4345, Jun. 24, 2020, ISSN: 2076-3417. DOI: [10.3390/app10124345](https://doi.org/10.3390/app10124345).
- [471] A. B. D. Nandiyanto, R. Oktiani, and R. Ragadhita, "How to read and interpret FTIR spectroscopy of organic material," *Indonesian Journal of Science and Technology*, vol. 4, no. 1, p. 97, Mar. 7, 2019, ISSN: 2527-8045, 2528-1410. DOI: [10.17509/ijost.v4i1.15806](https://doi.org/10.17509/ijost.v4i1.15806).
- [472] A. R. P. d. Silva, T. L. Macedo, D. J. Coletta, S. Feldman, and M. d. M. Pereira, "Synthesis, characterization and cytotoxicity of chitosan/polyvinyl alcohol/bioactive glass hybrid scaffolds obtained by lyophilization," *Matéria (Rio de Janeiro)*, vol. 21, no. 4, pp. 964–973, Dec. 2016, ISSN: 1517-7076. DOI: [10.1590/s1517-707620160004.0089](https://doi.org/10.1590/s1517-707620160004.0089).
- [473] E. Delay, S. Guerid, and A. C. Meruta, "Indications and controversies in lipofilling for partial breast reconstruction," *Clinics in Plastic Surgery*, vol. 45, no. 1, pp. 101–110, Jan. 2018, ISSN: 00941298. DOI: [10.1016/j.cps.2017.08.008](https://doi.org/10.1016/j.cps.2017.08.008).
- [474] F. Simonacci, N. Bertozzi, M. P. Grieco, E. Grignaffini, and E. Raposio, "Procedure, applications, and outcomes of autologous fat grafting," *Annals of Medicine and Surgery*, vol. 20, pp. 49–60, Aug. 2017, ISSN: 20490801. DOI: [10.1016/j.amsu.2017.06.059](https://doi.org/10.1016/j.amsu.2017.06.059).
- [475] H. Li, B. Wu, C. Mu, and W. Lin, "Concomitant degradation in periodate oxidation of carboxymethyl cellulose," *Carbohydrate Polymers*, vol. 84, no. 3, pp. 881–886, Mar. 2011, ISSN: 01448617. DOI: [10.1016/j.carbpol.2010.12.026](https://doi.org/10.1016/j.carbpol.2010.12.026).
- [476] U.-J. Kim, S. Kuga, M. Wada, T. Okano, and T. Kondo, "Periodate oxidation of crystalline cellulose," *Biomacromolecules*, vol. 1, no. 3, pp. 488–492, Sep. 1, 2000, ISSN: 1525-7797, 1526-4602. DOI: [10.1021/bm0000337](https://doi.org/10.1021/bm0000337).
- [477] S. F. Plappert, S. Quraishi, N. Pircher, *et al.*, "Transparent, flexible, and strong 2,3-dialdehyde cellulose films with high oxygen barrier properties," *Biomacromolecules*, vol. 19, no. 7, pp. 2969–2978, Jul. 9, 2018, ISSN: 1525-7797, 1526-4602. DOI: [10.1021/acs.biomac.8b00536](https://doi.org/10.1021/acs.biomac.8b00536).

- [478] M. Tummalapalli and B. Gupta, "A UV-vis spectrophotometric method for the estimation of aldehyde groups in periodate-oxidized polysaccharides using 2,4 -dinitrophenyl hydrazine," *Journal of Carbohydrate Chemistry*, vol. 34, no. 6, pp. 338–348, Jul. 24, 2015, ISSN: 0732-8303, 1532-2327. DOI: [10.1080/07328303.2015.1068793](https://doi.org/10.1080/07328303.2015.1068793).
- [479] U.-J. Kim, M. Wada, and S. Kuga, "Solubilization of dialdehyde cellulose by hot water," *Carbohydrate Polymers*, vol. 56, no. 1, pp. 7–10, May 2004, ISSN: 01448617. DOI: [10.1016/j.carbpol.2003.10.013](https://doi.org/10.1016/j.carbpol.2003.10.013).
- [480] M. Siller, H. Amer, M. Bacher, W. Roggenstein, T. Rosenau, and A. Potthast, "Effects of periodate oxidation on cellulose polymorphs," *Cellulose*, vol. 22, no. 4, pp. 2245–2261, Aug. 2015, ISSN: 0969-0239, 1572-882X. DOI: [10.1007/s10570-015-0648-5](https://doi.org/10.1007/s10570-015-0648-5).
- [481] J. Sirvio, U. Hyvakko, H. Liimatainen, J. Niinimäki, and O. Hormi, "Periodate oxidation of cellulose at elevated temperatures using metal salts as cellulose activators," *Carbohydrate Polymers*, vol. 83, no. 3, pp. 1293–1297, Jan. 30, 2011, ISSN: 01448617. DOI: [10.1016/j.carbpol.2010.09.036](https://doi.org/10.1016/j.carbpol.2010.09.036).
- [482] S. Tupin, J. Molimard, V. Cenizo, T. Hoc, B. Sohm, and H. Zahouani, "Multiscale approach to characterize mechanical properties of tissue engineered skin," *Annals of Biomedical Engineering*, vol. 44, no. 9, pp. 2851–2862, Sep. 2016, ISSN: 0090-6964, 1573-9686. DOI: [10.1007/s10439-016-1576-8](https://doi.org/10.1007/s10439-016-1576-8).
- [483] L. Münster, Z. Capáková, M. Fišera, I. Kuřitka, and J. Vícha, "Biocompatible dialdehyde cellulose/poly(vinyl alcohol) hydrogels with tunable properties," *Carbohydrate Polymers*, vol. 218, pp. 333–342, Aug. 2019, ISSN: 01448617. DOI: [10.1016/j.carbpol.2019.04.091](https://doi.org/10.1016/j.carbpol.2019.04.091).
- [484] S. Asano, S. Ito, K. Takahashi, *et al.*, "Matrix stiffness regulates migration of human lung fibroblasts," *Physiological Reports*, vol. 5, no. 9, e13281, May 2017, ISSN: 2051817X. DOI: [10.14814/phy2.13281](https://doi.org/10.14814/phy2.13281).
- [485] E. Hadjipanayi, V. Mudera, and R. A. Brown, "Close dependence of fibroblast proliferation on collagen scaffold matrix stiffness," *Journal of Tissue Engineering and Regenerative Medicine*, vol. 3, no. 2, pp. 77–84, Feb. 2009, ISSN: 19326254, 19327005. DOI: [10.1002/term.136](https://doi.org/10.1002/term.136).
- [486] S. Khan, M. Ul-Islam, M. W. Ullah, *et al.*, "Engineered regenerated bacterial cellulose scaffolds for application in in vitro tissue regeneration," *RSC Advances*, vol. 5, no. 103, pp. 84 565–84 573, 2015, ISSN: 2046-2069. DOI: [10.1039/C5RA16985B](https://doi.org/10.1039/C5RA16985B).
- [487] F. Mohammadi, M. Moeeni, C. Li, R. Boukherroub, and S. Szunerits, "Interaction of cellulose and nitrodopamine coated superparamagnetic iron oxide nanoparticles with alpha-lactalbumin," *RSC Advances*, vol. 10, no. 16, pp. 9704–9716, 2020, ISSN: 2046-2069. DOI: [10.1039/C9RA09045B](https://doi.org/10.1039/C9RA09045B).
- [488] H. Orelma, I. Filpponen, L.-S. Johansson, J. Laine, and O. J. Rojas, "Modification of cellulose films by adsorption of CMC and chitosan for controlled attachment of biomolecules," *Biomacromolecules*, vol. 12, no. 12, pp. 4311–4318, Dec. 12, 2011, ISSN: 1525-7797, 1526-4602. DOI: [10.1021/bm201236a](https://doi.org/10.1021/bm201236a).

- [489] K. Molyneaux, M. D. Wnek, S. E. Craig, *et al.*, "Physically-cross-linked poly(vinyl alcohol) cell culture plate coatings facilitate preservation of cell-cell interactions, spheroid formation, and stemness," *Journal of Biomedical Materials Research Part B: Applied Biomaterials*, jbm.b.34832, Apr. 13, 2021, ISSN: 1552-4973, 1552-4981. DOI: [10.1002/jbm.b.34832](https://doi.org/10.1002/jbm.b.34832).
- [490] T. Tronser, A. Laromaine, A. Roig, and P. A. Levkin, "Bacterial cellulose promotes long-term stemness of mESC," *ACS Applied Materials & Interfaces*, vol. 10, no. 19, pp. 16260–16269, May 16, 2018, ISSN: 1944-8244, 1944-8252. DOI: [10.1021/acsami.8b01992](https://doi.org/10.1021/acsami.8b01992).
- [491] Y. Okita, L. Zheng, K. Kawanishi, H. Miyoshi, K. Yanagihara, and M. Kato, "Polyvinyl alcohol scaffolds and supplementation support 3d and sphere culturing of human cancer cell lines by reducing apoptosis and promoting cellular proliferation," *Genes to Cells*, vol. 26, no. 5, pp. 336–343, May 2021, ISSN: 1356-9597, 1365-2443. DOI: [10.1111/gtc.12843](https://doi.org/10.1111/gtc.12843).
- [492] R. Klopfleisch and F. Jung, "The pathology of the foreign body reaction against biomaterials: Foreign body reaction to biomaterials," *Journal of Biomedical Materials Research Part A*, vol. 105, no. 3, pp. 927–940, Mar. 2017, ISSN: 15493296. DOI: [10.1002/jbm.a.35958](https://doi.org/10.1002/jbm.a.35958).
- [493] H. Ramphul, F. Gimié, J. Andries, D. Jhurry, and A. Bhaw-Luximon, "Sugar-cane bagasse cellulose-based scaffolds promote multi-cellular interactions, angiogenesis and reduce inflammation for skin tissue regeneration," *International Journal of Biological Macromolecules*, vol. 157, pp. 296–310, Aug. 2020, ISSN: 01418130. DOI: [10.1016/j.ijbiomac.2020.04.176](https://doi.org/10.1016/j.ijbiomac.2020.04.176).
- [494] D. J. Modulevsky, C. M. Cuerrier, and A. E. Pelling, "Biocompatibility of subcutaneously implanted plant-derived cellulose biomaterials," *PLOS ONE*, vol. 11, no. 6, F. Zhao, Ed., e0157894, Jun. 21, 2016, ISSN: 1932-6203. DOI: [10.1371/journal.pone.0157894](https://doi.org/10.1371/journal.pone.0157894).
- [495] M. Singh, A. R. Ray, P. V. K. Verma, and S. K. Guha, "Potential biosoluble carriers: Biocompatibility and biodegradability of oxidized cellulose," *Biomaterials, Medical Devices, and Artificial Organs*, vol. 7, no. 4, pp. 495–512, Jan. 1979, ISSN: 0090-5488. DOI: [10.3109/10731197909118964](https://doi.org/10.3109/10731197909118964).
- [496] A. Kamdem Tamo, I. Doench, A. Morales Helguera, D. Hoenders, A. Walther, and A. O. Madrazo, "Biodegradation of crystalline cellulose nanofibers by means of enzyme immobilized-alginate beads and microparticles," *Polymers*, vol. 12, no. 7, p. 1522, Jul. 9, 2020, ISSN: 2073-4360. DOI: [10.3390/polym12071522](https://doi.org/10.3390/polym12071522).
- [497] H. W. Kwak, H. Lee, S. Park, M. E. Lee, and H.-J. Jin, "Chemical and physical reinforcement of hydrophilic gelatin film with di-aldehyde nanocellulose," *International Journal of Biological Macromolecules*, vol. 146, pp. 332–342, Mar. 2020, ISSN: 01418130. DOI: [10.1016/j.ijbiomac.2019.12.254](https://doi.org/10.1016/j.ijbiomac.2019.12.254).

- [498] P. Bansal, M. Hall, M. J. Realff, J. H. Lee, and A. S. Bommarius, "Multivariate statistical analysis of x-ray data from cellulose: A new method to determine degree of crystallinity and predict hydrolysis rates," *Bioresource Technology*, vol. 101, no. 12, pp. 4461–4471, Jun. 2010, ISSN: 09608524. DOI: [10.1016/j.biortech.2010.01.068](https://doi.org/10.1016/j.biortech.2010.01.068).
- [499] J. Jonoobi, A. Harun, A. Shakeri, M. Misra, and K. Oksman, "Chemical composition, crystallinity, and thermal degradation of bleached and unbleached kenaf bast (*hibiscus cannabinus*) pulp and nanofibers," *Bioresources*, vol. 4, no. 2, pp. 626–639, 2009.
- [500] Q. Li and S. Renneckar, "Supramolecular structure characterization of molecularly thin cellulose i nanoparticles," *Biomacromolecules*, vol. 12, no. 3, pp. 650–659, Mar. 14, 2011, ISSN: 1525-7797, 1526-4602. DOI: [10.1021/bm101315y](https://doi.org/10.1021/bm101315y).
- [501] T. Suzuki and H. Nakagami, "Effect of crystallinity of microcrystalline cellulose on the compactability and dissolution of tablets," *European Journal of Pharmaceutics and Biopharmaceutics*, vol. 47, no. 3, pp. 225–230, May 1999, ISSN: 09396411. DOI: [10.1016/S0939-6411\(98\)00102-7](https://doi.org/10.1016/S0939-6411(98)00102-7).
- [502] F. Yudhanto, H. Sosiati, V. Yudha, and E. Syafri, "A preliminary study of isolation and characterization of nanocrystalline cellulose from microcrystalline cellulose by acid hydrolysis process," *Materials Science Forum*, vol. 1057, pp. 11–18, Mar. 31, 2022, ISSN: 1662-9752. DOI: [10.4028/p-45x464](https://doi.org/10.4028/p-45x464).
- [503] H. Luo, H. Lan, R. Cha, *et al.*, "Dialdehyde nanocrystalline cellulose as antibiotic substitutes against multidrug-resistant bacteria," *ACS Applied Materials & Interfaces*, vol. 13, no. 29, pp. 33 802–33 811, Jul. 28, 2021, ISSN: 1944-8244, 1944-8252. DOI: [10.1021/acsami.1c06308](https://doi.org/10.1021/acsami.1c06308).
- [504] M. H. Sainorudin, N. A. Abdullah, M. S. Asmal Rani, *et al.*, "Structural characterization of microcrystalline and nanocrystalline cellulose from *Ananas comosus* l. leaves: Cytocompatibility and molecular docking studies," *Nanotechnology Reviews*, vol. 10, no. 1, pp. 793–806, Aug. 9, 2021, ISSN: 2191-9097. DOI: [10.1515/ntrev-2021-0053](https://doi.org/10.1515/ntrev-2021-0053).
- [505] H. Lee, J. You, H.-J. Jin, and H. W. Kwak, "Chemical and physical reinforcement behavior of dialdehyde nanocellulose in PVA composite film: A comparison of nanofiber and nanocrystal," *Carbohydrate Polymers*, vol. 232, p. 115 771, Mar. 2020, ISSN: 01448617. DOI: [10.1016/j.carbpol.2019.115771](https://doi.org/10.1016/j.carbpol.2019.115771).
- [506] S. Mondal, "Preparation, properties and applications of nanocellulosic materials," *Carbohydrate Polymers*, vol. 163, pp. 301–316, May 2017, ISSN: 01448617. DOI: [10.1016/j.carbpol.2016.12.050](https://doi.org/10.1016/j.carbpol.2016.12.050).
- [507] A. Khan, M. Jawaid, L. K. Kian, A. A. P. Khan, and A. M. Asiri, "Isolation and production of nanocrystalline cellulose from conocarpus fiber," *Polymers*, vol. 13, no. 11, p. 1835, Jun. 1, 2021, ISSN: 2073-4360. DOI: [10.3390/polym13111835](https://doi.org/10.3390/polym13111835).
- [508] C. P. Azubuike and A. O. Okhamafe, "Physicochemical, spectroscopic and thermal properties of microcrystalline cellulose derived from corn cobs," *International Journal Of Recycling of Organic Waste in Agriculture*, vol. 1, no. 1, p. 9, 2012, ISSN: 2251-7715. DOI: [10.1186/2251-7715-1-9](https://doi.org/10.1186/2251-7715-1-9).

- [509] Z. Hosseinidoust, M. N. Alam, G. Sim, N. Tufenkji, and T. G. M. van de Ven, "Cellulose nanocrystals with tunable surface charge for nanomedicine," *Nanoscale*, vol. 7, no. 40, pp. 16 647–16 657, 2015, ISSN: 2040-3364, 2040-3372. DOI: [10.1039/C5NR02506K](https://doi.org/10.1039/C5NR02506K).
- [510] C. Bruel, J. R. Tavares, P. J. Carreau, and M.-C. Heuzey, "The structural amphiphilicity of cellulose nanocrystals characterized from their cohesion parameters," *Carbohydrate Polymers*, vol. 205, pp. 184–191, Feb. 2019, ISSN: 01448617. DOI: [10.1016/j.carbpol.2018.10.026](https://doi.org/10.1016/j.carbpol.2018.10.026).
- [511] W. J. Lee, A. J. Clancy, E. Kontturi, A. Bismarck, and M. S. P. Shaffer, "Strong and stiff: High-performance cellulose nanocrystal/poly(vinyl alcohol) composite fibers," *ACS Applied Materials & Interfaces*, vol. 8, no. 46, pp. 31 500–31 504, Nov. 23, 2016, ISSN: 1944-8244, 1944-8252. DOI: [10.1021/acsami.6b11578](https://doi.org/10.1021/acsami.6b11578).
- [512] S. Eichhorn and R. Young, "The young's modulus of a microcrystalline cellulose," *Cellulose*, vol. 8, no. 3, pp. 197–207, 2001, ISSN: 09690239. DOI: [10.1023/A:1013181804540](https://doi.org/10.1023/A:1013181804540).
- [513] J. A. Sirviö, S. Honkaniemi, M. Visanko, and H. Liimatainen, "Composite films of poly(vinyl alcohol) and bifunctional cross-linking cellulose nanocrystals," *ACS Applied Materials & Interfaces*, vol. 7, no. 35, pp. 19 691–19 699, Sep. 9, 2015, ISSN: 1944-8244, 1944-8252. DOI: [10.1021/acsami.5b04879](https://doi.org/10.1021/acsami.5b04879).
- [514] T. Huq, S. Salmieri, A. Khan, *et al.*, "Nanocrystalline cellulose (NCC) reinforced alginate based biodegradable nanocomposite film," *Carbohydrate Polymers*, vol. 90, no. 4, pp. 1757–1763, Nov. 2012, ISSN: 01448617. DOI: [10.1016/j.carbpol.2012.07.065](https://doi.org/10.1016/j.carbpol.2012.07.065).
- [515] A. Khan, R. A. Khan, S. Salmieri, *et al.*, "Mechanical and barrier properties of nanocrystalline cellulose reinforced chitosan based nanocomposite films," *Carbohydrate Polymers*, vol. 90, no. 4, pp. 1601–1608, Nov. 2012, ISSN: 01448617. DOI: [10.1016/j.carbpol.2012.07.037](https://doi.org/10.1016/j.carbpol.2012.07.037).
- [516] Q. Xu, Y. Ji, Q. Sun, Y. Fu, Y. Xu, and L. Jin, "Fabrication of cellulose nanocrystal/chitosan hydrogel for controlled drug release," *Nanomaterials*, vol. 9, no. 2, p. 253, Feb. 13, 2019, ISSN: 2079-4991. DOI: [10.3390/nano9020253](https://doi.org/10.3390/nano9020253).
- [517] M. Bansal, G. S. Chauhan, A. Kaushik, and A. Sharma, "Extraction and functionalization of bagasse cellulose nanofibres to schiff-base based antimicrobial membranes," *International Journal of Biological Macromolecules*, vol. 91, pp. 887–894, Oct. 2016, ISSN: 01418130. DOI: [10.1016/j.ijbiomac.2016.06.045](https://doi.org/10.1016/j.ijbiomac.2016.06.045).
- [518] I. H. Sahputra, A. Alexiadis, and M. J. Adams, "Effects of moisture on the mechanical properties of microcrystalline cellulose and the mobility of the water molecules as studied by the hybrid molecular mechanics-molecular dynamics simulation method," *Journal of Polymer Science Part B: Polymer Physics*, vol. 57, no. 8, pp. 454–464, Apr. 15, 2019, ISSN: 08876266. DOI: [10.1002/polb.24801](https://doi.org/10.1002/polb.24801).
- [519] T. Xia, R. Zhao, F. Feng, and L. Yang, "The effect of matrix stiffness on human hepatocyte migration and function—an in vitro research," *Polymers*, vol. 12, no. 9, p. 1903, Aug. 24, 2020, ISSN: 2073-4360. DOI: [10.3390/polym12091903](https://doi.org/10.3390/polym12091903).

- [520] R.-s. Dong, F. Lu, P.-d. Liu, *et al.*, "Preparation of nanocellulose-polyvinyl alcohol composite hydrogels from *desmodium intortum* (mill.) urb.: Chemical property characterization," *Industrial Crops and Products*, vol. 176, p. 114371, Feb. 2022, ISSN: 09266690. DOI: [10.1016/j.indcrop.2021.114371](https://doi.org/10.1016/j.indcrop.2021.114371).
- [521] R. Kummala, W. Xu, C. Xu, and M. Toivakka, "Stiffness and swelling characteristics of nanocellulose films in cell culture media," *Cellulose*, vol. 25, no. 9, pp. 4969–4978, Sep. 2018, ISSN: 0969-0239, 1572-882X. DOI: [10.1007/s10570-018-1940-y](https://doi.org/10.1007/s10570-018-1940-y).
- [522] G. K. Tummala, T. Joffre, V. R. Lopes, *et al.*, "Hyperelastic nanocellulose-reinforced hydrogel of high water content for ophthalmic applications," *ACS Biomaterials Science & Engineering*, vol. 2, no. 11, pp. 2072–2079, Nov. 14, 2016, ISSN: 2373-9878, 2373-9878. DOI: [10.1021/acsbiomaterials.6b00484](https://doi.org/10.1021/acsbiomaterials.6b00484).
- [523] T. Jayaramudu, H.-U. Ko, H. Kim, J. Kim, R. Muthoka, and J. Kim, "Electroactive hydrogels made with polyvinyl alcohol/cellulose nanocrystals," *Materials*, vol. 11, no. 9, p. 1615, Sep. 4, 2018, ISSN: 1996-1944. DOI: [10.3390/ma11091615](https://doi.org/10.3390/ma11091615).
- [524] N. Karimi Dehkordi, M. Minaian, A. Talebi, V. Akbari, and A. Taheri, "Nanocrystalline cellulose–hyaluronic acid composite enriched with GM-CSF loaded chitosan nanoparticles for enhanced wound healing," *Biomedical Materials*, vol. 14, no. 3, p. 035003, Mar. 7, 2019, ISSN: 1748-605X. DOI: [10.1088/1748-605X/ab026c](https://doi.org/10.1088/1748-605X/ab026c).
- [525] N. I. S. Murizan, N. S. Mustafa, N. H. A. Ngadiman, N. Mohd Yusof, and A. Idris, "Review on nanocrystalline cellulose in bone tissue engineering applications," *Polymers*, vol. 12, no. 12, p. 2818, Nov. 27, 2020, ISSN: 2073-4360. DOI: [10.3390/polym12122818](https://doi.org/10.3390/polym12122818).
- [526] K. Zhang, M. Y. Ismail, and H. Liimatainen, "Water-resistant nanopaper with tunable water barrier and mechanical properties from assembled complexes of oppositely charged cellulosic nanomaterials," *Food Hydrocolloids*, vol. 120, p. 106983, Nov. 2021, ISSN: 0268005X. DOI: [10.1016/j.foodhyd.2021.106983](https://doi.org/10.1016/j.foodhyd.2021.106983).
- [527] K. Sakugawa, A. Ikeda, A. Takemura, and H. Ono, "Simplified method for estimation of composition of alginates by FTIR," *Journal of Applied Polymer Science*, vol. 93, no. 3, pp. 1372–1377, 2004, eprint: <https://onlinelibrary.wiley.com/doi/pdf/10.1002/app.20589>. DOI: <https://doi.org/10.1002/app.20589>.
- [528] H. Daemi and M. Barikani, "Synthesis and characterization of calcium alginate nanoparticles, sodium homopolymannuronate salt and its calcium nanoparticles," *Scientia Iranica*, vol. 19, no. 6, pp. 2023–2028, Dec. 2012, ISSN: 10263098. DOI: [10.1016/j.scient.2012.10.005](https://doi.org/10.1016/j.scient.2012.10.005).
- [529] Y. Ji, X. Yang, Z. Ji, *et al.*, "DFT-calculated IR spectrum amide I, II, and III band contributions of *N*-methylacetamide fine components," *ACS Omega*, vol. 5, no. 15, pp. 8572–8578, Apr. 21, 2020, ISSN: 2470-1343, 2470-1343. DOI: [10.1021/acsomega.9b04421](https://doi.org/10.1021/acsomega.9b04421).

- [530] I. A. Rodionov, N. V. Grinberg, T. V. Burova, V. Y. Grinberg, T. I. Shabatina, and V. I. Lozinsky, "Cryostructuring of polymer systems. 44. freeze-dried and then chemically cross-linked wide porous cryostructurates based on serum albumin," *e-Polymers*, vol. 17, no. 4, pp. 263–274, Jun. 27, 2017, ISSN: 1618-7229, 2197-4586. DOI: [10.1515/epoly-2016-0317](https://doi.org/10.1515/epoly-2016-0317).
- [531] M. Wissink, R. Beernink, J. Pieper, *et al.*, "Immobilization of heparin to EDC/NHS-crosslinked collagen. characterization and in vitro evaluation," *Biomaterials*, vol. 22, no. 2, pp. 151–163, Jan. 2001, ISSN: 01429612. DOI: [10.1016/S0142-9612\(00\)00164-2](https://doi.org/10.1016/S0142-9612(00)00164-2).
- [532] A. J. Kuijpers, G. H. M. Engbers, J. Krijgsveld, S. A. J. Zaat, J. Dankert, and J. Feijen, "Cross-linking and characterisation of gelatin matrices for biomedical applications," *Journal of Biomaterials Science, Polymer Edition*, vol. 11, no. 3, pp. 225–243, Jan. 2000, ISSN: 0920-5063, 1568-5624. DOI: [10.1163/156856200743670](https://doi.org/10.1163/156856200743670).
- [533] L. Boulais, R. Jellali, U. Pereira, E. Leclerc, S. A. Bencherif, and C. Legallais, "Cryogel-integrated biochip for liver tissue engineering," *SSRN Electronic Journal*, 2020, ISSN: 1556-5068. DOI: [10.2139/ssrn.3757905](https://doi.org/10.2139/ssrn.3757905).
- [534] C. S. Silva, R. D. Pinto, S. Amorim, *et al.*, "Fibronectin-functionalized fibrous meshes as a substrate to support cultures of thymic epithelial cells," *Biomacromolecules*, vol. 21, no. 12, pp. 4771–4780, Dec. 14, 2020, ISSN: 1525-7797, 1526-4602. DOI: [10.1021/acs.biomac.0c00933](https://doi.org/10.1021/acs.biomac.0c00933).
- [535] L. Koh, M. Islam, D. Mitra, *et al.*, "Epoxy cross-linked collagen and collagen-laminin peptide hydrogels as corneal substitutes," *Journal of Functional Biomaterials*, vol. 4, no. 3, pp. 162–177, Aug. 28, 2013, ISSN: 2079-4983. DOI: [10.3390/jfb4030162](https://doi.org/10.3390/jfb4030162).
- [536] C. Yang, "Enhanced physicochemical properties of collagen by using EDC/NHS-crosslinking," *Bulletin of Materials Science*, vol. 35, no. 5, pp. 913–918, Oct. 2012, ISSN: 0250-4707, 0973-7669. DOI: [10.1007/s12034-012-0376-5](https://doi.org/10.1007/s12034-012-0376-5).
- [537] R. Usha, K. Sreeram, and A. Rajaram, "Stabilization of collagen with EDC/NHS in the presence of l-lysine: A comprehensive study," *Colloids and Surfaces B: Biointerfaces*, vol. 90, pp. 83–90, Feb. 2012, ISSN: 09277765. DOI: [10.1016/j.colsurfb.2011.10.002](https://doi.org/10.1016/j.colsurfb.2011.10.002).
- [538] Z. Li, Y. Jiang, K. Wüst, M. Callari, and M. H. Stenzel, "Crosslinking of self-assembled protein–polymer conjugates with divanillin," *Australian Journal of Chemistry*, 2020, ISSN: 0004-9425. DOI: [10.1071/CH19617](https://doi.org/10.1071/CH19617).
- [539] A. Cox, D. Vinciguerra, F. Re, *et al.*, "Protein-functionalized nanoparticles derived from end-functional polymers and polymer prodrugs for crossing the blood-brain barrier," *European Journal of Pharmaceutics and Biopharmaceutics*, vol. 142, pp. 70–82, Sep. 2019, ISSN: 09396411. DOI: [10.1016/j.ejpb.2019.06.004](https://doi.org/10.1016/j.ejpb.2019.06.004).
- [540] M. E. B. Smith, F. F. Schumacher, C. P. Ryan, *et al.*, "Protein modification, bioconjugation, and disulfide bridging using bromomaleimides," *Journal of the American Chemical Society*, vol. 132, no. 6, pp. 1960–1965, Feb. 17, 2010, ISSN: 0002-7863, 1520-5126. DOI: [10.1021/ja908610s](https://doi.org/10.1021/ja908610s).

-
- [541] S. Ravi, V. R. Krishnamurthy, J. M. Caves, C. A. Haller, and E. L. Chaikof, "Maleimide–thiol coupling of a bioactive peptide to an elastin-like protein polymer," *Acta Biomaterialia*, vol. 8, no. 2, pp. 627–635, Feb. 2012, ISSN: 17427061. DOI: [10.1016/j.actbio.2011.10.027](https://doi.org/10.1016/j.actbio.2011.10.027).
- [542] J. L. Vanderhooft, B. K. Mann, and G. D. Prestwich, "Synthesis and characterization of novel thiol-reactive poly(ethylene glycol) cross-linkers for extracellular-matrix-mimetic biomaterials," *Biomacromolecules*, vol. 8, no. 9, pp. 2883–2889, Sep. 1, 2007, ISSN: 1525-7797, 1526-4602. DOI: [10.1021/bm0703564](https://doi.org/10.1021/bm0703564).
- [543] J. L. Drury, R. G. Dennis, and D. J. Mooney, "The tensile properties of alginate hydrogels," *Biomaterials*, vol. 25, no. 16, pp. 3187–3199, Jul. 2004, ISSN: 01429612. DOI: [10.1016/j.biomaterials.2003.10.002](https://doi.org/10.1016/j.biomaterials.2003.10.002).
- [544] C. K. Kuo and P. X. Ma, "Ionically crosslinked alginate hydrogels as scaffolds for tissue engineering: Part 1. structure, gelation rate and mechanical properties," *Biomaterials*, vol. 22, no. 6, pp. 511–521, Mar. 2001, ISSN: 01429612. DOI: [10.1016/S0142-9612\(00\)00201-5](https://doi.org/10.1016/S0142-9612(00)00201-5).
- [545] D. Seth, H. N. Mishra, and S. C. Deka, "Effect of microencapsulation using extrusion technique on viability of bacterial cells during spray drying of sweetened yoghurt," *International Journal of Biological Macromolecules*, vol. 103, pp. 802–807, Oct. 2017, ISSN: 01418130. DOI: [10.1016/j.ijbiomac.2017.05.099](https://doi.org/10.1016/j.ijbiomac.2017.05.099).

Appendix

Article

Cellulosic/Polyvinyl Alcohol Composite Hydrogel: Synthesis, Characterization and Applications in Tissue Engineering

Mathilde Stricher ¹ , Claude-Olivier Sarde ², Erwann Guénin ² , Christophe Egles ¹  and Frédéric Delbecq ^{2,*}

¹ Université de Technologie de Compiègne, CNRS, Biomechanics and Bioengineering, Centre de Recherche Royallieu, CEDEX CS 60 319, 60 203 Compiègne, France; mathilde.stricher@utc.fr (M.S.); christophe.egles@utc.fr (C.E.)

² Université de Technologie de Compiègne, ESCOM, TIMR (Integrated Transformations of Renewable Matter), Centre de Recherche Royallieu, CEDEX CS 60 319, 60 203 Compiègne, France; claude-olivier.sarde@utc.fr (C.-O.S.); erwann.guenin@utc.fr (E.G.)

* Correspondence: f.delbecq@escom.fr

Abstract: The biomedical field still requires composite materials for medical devices and tissue engineering model design. As part of the pursuit of non-animal and non-proteic scaffolds, we propose here a cellulose-based material. In this study, 9%, 18% and 36% dialdehyde-functionalized microcrystalline celluloses (DAC) were synthesized by sodium periodate oxidation. The latter was subsequently coupled to PVA at ratios 1:2, 1:1 and 2:1 by dissolving in N-methyl pyrrolidone and lithium chloride. Moulding and successive rehydration in ethanol and water baths formed soft hydrogels. While oxidation effectiveness was confirmed by dialdehyde content determination for all DAC, we observed increasing hydrolysis associated with particle fragmentation. Imaging, FTIR and XDR analysis highlighted an intertwined DAC/PVA network mainly supported by electrostatic interactions, hemiacetal and acetal linkage. To meet tissue engineering requirements, an interconnected porosity was optimized using 0–50 µm salts. While the role of DAC in strengthening the hydrogel was identified, the oxidation ratio of DAC showed no distinct trend. DAC 9% material exhibited the highest indirect and direct cytocompatibility creating spheroid-like structures. DAC/PVA hydrogels showed physical stability and acceptability *in vivo* that led us to propose our DAC 9%/PVA based material for soft tissue graft application.

Keywords: cellulose dialdehyde; PVA; regeneration process; porous three-dimensional scaffold; biomedical use



Citation: Stricher, M.; Sarde, C.-O.; Guénin, E.; Egles, C.; Delbecq, F. Cellulosic/Polyvinyl Alcohol Composite Hydrogel: Synthesis, Characterization and Applications in Tissue Engineering. *Polymers* **2021**, *13*, 3598. <https://doi.org/10.3390/polym13203598>

Academic Editor: Marek Kowalczyk

Received: 22 September 2021

Accepted: 16 October 2021

Published: 19 October 2021

Publisher's Note: MDPI stays neutral with regard to jurisdictional claims in published maps and institutional affiliations.



Copyright: © 2021 by the authors. Licensee MDPI, Basel, Switzerland. This article is an open access article distributed under the terms and conditions of the Creative Commons Attribution (CC BY) license (<https://creativecommons.org/licenses/by/4.0/>).

1. Introduction

Among recent technologies deployed in tissue engineering or regenerative medicine, scaffold creation is a major strategy for the replacement or repair of soft tissues such as skin, nerves, tendons, ligaments, and cartilage. Clinicians need ready-to-use and easy-to-handle devices to replace the traditionally preferred grafts which are, however, limited in terms of availability, compatibility and rejection. The overall goal of a biocompatible scaffold is to promote and drive the cell regenerative response which supports cell signalling toward adhesion, proliferation and extracellular matrix (ECM) deposition while the material degrades in a controllable and non-toxic manner.

Hydrogels are water-swollen macromolecular networks of hydrophilic polymers that can be formed either by physical gelation through variations of temperature, pH, ionic content or freeze-thaw method, or through chemical gelation under covalent cross-linking via chemical conjugation or polymerization generating nanosized pores [1]. Unfortunately, most of the time, these chemical reactions require toxic or harmful reagents such as carbodiimides or dialdehydes (mainly glutaraldehyde). For tissue engineering applications, hydrogels should exhibit high porosity, tissue-like water content, injectability; and tunable permeability, degradability and mechanical property. However, their nanosized mesh limits nutrients and cellular wastes diffusion, drastically inhibiting cell settlement, attachment

and proliferation, as well as neo-tissue formation [2]. Thus, additional macro-porosity is often provided through particle leaching, freeze-drying, gas foaming or electrospinning [3].

Natural biomaterials such as proteins or polysaccharides exhibit biocompatibility and degradability due to their resemblance to tissue extracellular matrix [4]. However, they often demonstrate poor mechanical properties. Therefore, combining them with synthetic polymers such as polyvinylpyrrolidone (PVP), polycaprolactone (PCL), poly-ethylene-glycol (PEG), poly-L-lactic acid (PLA), composite hydrogel design tends to enhance their high stretchability and soft tissue-like stiffness [5]. The benefits of composite materials are thus widely recognized and actively investigated [6]. A particular impulse is emerging for the development of cellulosic materials combined with other natural polymers including chitosan, starch, alginates, collagen and hyaluronic acid [7].

Cellulose, the main constituent of higher plants cell walls, is the Earth's most abundant organic biopolymer. It can be easily extracted as microcrystals, nanocrystals and nanofibrils from rice husk, raw cotton sliver and sisal, as well as from waste paper and agricultural by-products using usual chemical procedures such as acid hydrolysis, chlorination, alkaline extraction, and bleaching [8–12]. Made up of O glycosidic β -(1→4) linked polymer of D-glucose sub-units, cellulose is a hydrophilic fibrous biopolymer featuring both amorphous and crystalline zones held together by Van der Waals forces and hydrogen bonds. The cellulose hydrophobic sheet association and all interchained hydrogen bonding networks stabilize a crystal-like structure limiting its solubility in water and organic solvents that complicates its handling [13]. Recently, some progress was made for dissolving polysaccharides such as starch or cellulose by using ionic liquids or LiCl dissolved in organic solvents such as DMF [14,15]. To date, cellulosic based materials in development take numerous forms: hydrogel films, three-dimensional scaffolds or drug delivery systems (DDS), mainly for their great mechanical strengthening properties and well-known biocompatibility and biodegradability [16,17]. For these purposes, cellulose derivatives could be functionalised via silyl groups, carboxylic acid or aldehydes functions to engage physical and chemical interactions with various other polymers [18–20].

Among all chemically modified cellulose, one of the most promising candidates remains the dialdehyde cellulose (DAC) that expresses a reduced number of hydrogen bonds and weakened inter-chains interactions due to the controlled level of oxidation for the glucose subunits. When oxidized, a glucose sub-unit is currently cleaved between two neighbouring carbons holding the $-OH$ functions, this leads to the formation of two distinct aldehyde functions. Thus, the material is expected to become easily soluble in an amide-type solvent such as *N*-methyl pyrrolidone (NMP) or *N,N*-dimethylacetamide (DMAc) containing a slight amount of LiCl [21]. For our experiments, we focused exclusively on NMP in regards to its relatively good biological tolerance and its ability to form an organogel when filled with PVA before to the solubilisation of cellulose at an elevated temperature [22].

Polyvinyl alcohol (PVA) is one of the synthetic polymers that can be sustainably produced by the successive conversion of bio-based ethanol to ethylene, forming the vinyl acetate monomers polymerized to produce bio-sourced PVA, followed by subsequent cleavage of the successive acetyl groups [23–25]. PVA is a synthetic polymer presenting hydrogel self-assembling abilities under repeated freeze-thaw cycles through physical crosslinking of side hydroxyl groups offering tunable mechanical properties [26]. Its high hydrophilicity without functional groups such as $COOH$ or NH_2 makes the PVA inherently non-adhesive to proteins but also to cells unable to engage binding surface receptors, favouring cell-cell interactions [27,28]. PVA-coated surfaces have allowed for the formation of reproducible sized spheroids for glioma, dental pulp or hair follicle cells showing excellent cell activity, migration and regenerative potential [29–31]. Interestingly, the poor bioactivity of PVA can be balanced through combination with polymers of higher adhesive properties or conjugation with adhesive proteins [32–34].

In this work, we aimed at developing and characterizing a cellulose/PVA material modulating DAC oxidation degree and DAC/PVA ratio, for versatile uses as implantable

matrices for soft tissue filling or innovative tissue engineering initiatives. Through the meticulous selection of the components (MCC, PVA) and solvents (NMP, ethanol and water), the limitation of the number and duration of reactions, we offer an eco-friendly, economical and easy-to-scale solution for the development of cellulose-based materials.

2. Materials and Methods

All chemicals were purchased from ACROS Organics, Carlsbad, CA, USA unless otherwise stated.

2.1. Cellulosic Scaffold Fabrication

The chemical reactions corresponding to the protocol are shown in Figure 1. Extra pure microcrystalline cellulose (mean particles size: 90 μm) was suspended with 6.25, 12.5 or 25% *w/w* sodium periodate in water for 4 h reaction at 90°C under conventional thermal heating with stirring and reflux. Dried DAC powders with theoretical molar dialdehyde content of 9, 18 and 36% were stored at room temperature (RT). Reaction yield is determined from the dried product mass. For the formulation of DAC/PVA (2:1), 3.2 g of DAC and 1.6 g of fully hydrolysed PVA (Sigma Aldrich) were suspended in 20 mL of concentrated 1-Methyl-2-pyrrolidone (NMP; 99.5% Extra Dry) at 12% *w/w* Lithium chloride (LiCl; 99%) for 20 min reaction at 90°C under conventional thermal heating with constant stirring. The resulting paste was deposited in pre-made PDMS moulds forming cylindrical samples 16 mm in diameter and 3 mm thick following successive immersion in absolute ethanol (Fisher Bioreagents, Waltham, MA, USA) and ultra-pure water (Millipore, Burlington, MA, USA).

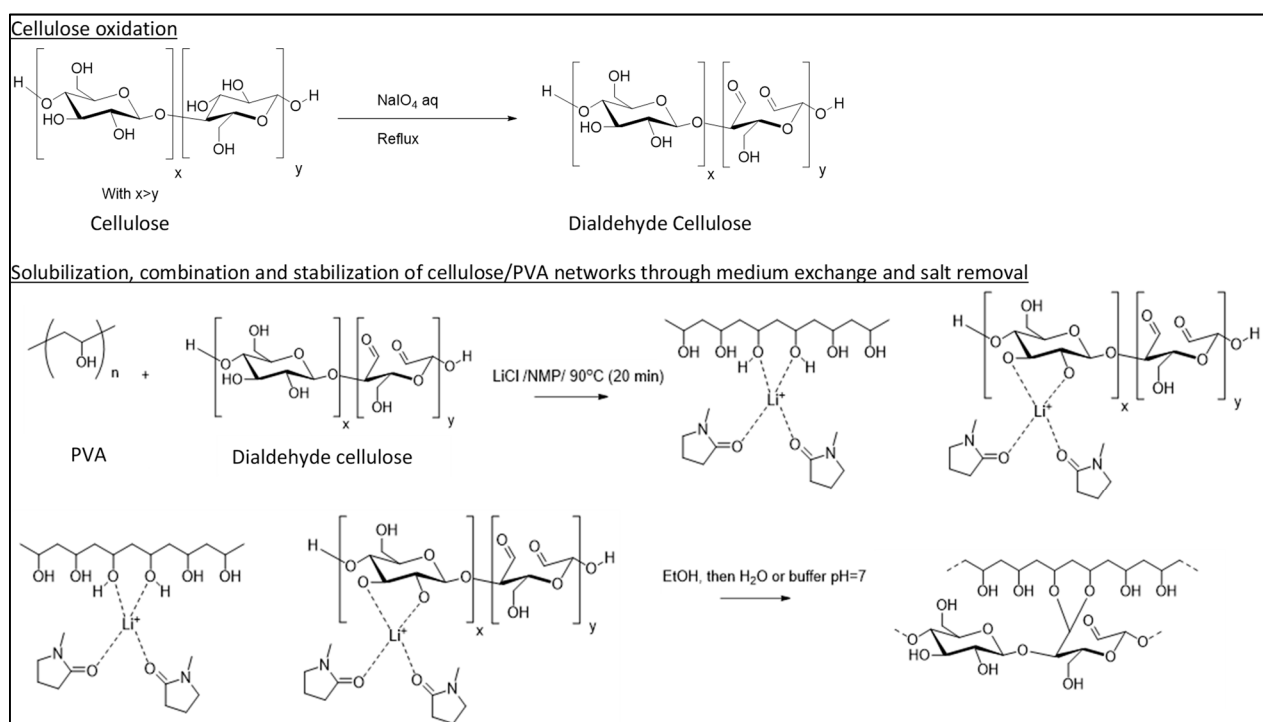


Figure 1. Reaction mechanisms of cellulose dialdehyde oxidation and formulation of cellulosic/PVA scaffolds.

DAC/PVA ratio was also modulated to 1:1 and 1:2. Macro-porosity is promoted by 1 g/mL NaCl (0–500 μm and 50–100 μm ; VWR Chemicals; Radnor, PA, USA) addition before casting. Long-term storage of the resulted DAC/PVA scaffolds was ensured in absolute ethanol at 4 °C.

2.2. Characterisation of Dialdehyde Celluloses (DACs)

2.2.1. FE-SEM Observations of DACs Morphology

Each set of oxidised cellulose powder was observed using scanning electron microscopy (XL 30-ESEM FEG, Philips, Amsterdam, The Netherlands). The surface of cellulose particles was quantified using Image J software [35].

2.2.2. Quantification of the Aldehyde Content (DC %)

For each DAC sample, the degree of oxidation was estimated following 2 distinct methods: 2,4-dinitrophenylhydrazine (DNPH) and hydroxylamine hydrochloride. For the DNPH method using each sample, 0.1 g of DAC to be tested were dissolved under stirring at room temperature (RT) for 4 h in 30 mL of 16.77 mM DNPH in acidified methanol solution. The reacted yellowed cellulose was filtered, washed with acetone before being dried and weighed. The filtrate was diluted in 400 mL of distilled water. Non-reacted DPNH solution absorbances were measured by UV spectroscopy at 350 nm. The dialdehyde content was thus determined using a calibration curve prepared with DNPH acidified methanol solutions varying from 2.0 to 17 mM. For the hydroxylamine method [36] and each sample, 0.1 g of DAC to be tested were dissolved under stirring at RT for 3 h in 25 mL of 25 mM hydroxylamine hydrochloride ($\text{NH}_2\text{OH}\cdot\text{HCl}$) at initial pH of 3.4. Released hydrochloric acid acidifying the solution were then dosed back raising the pH to the initial one via a NaOH solution (0.1 M) under stirring and measurement with a pH meter. The dialdehyde content was thus determined as:

$$\text{DC}(\%) = \frac{V_{\text{NaOH}} \times C_{\text{NaOH}}}{m_{\text{sample}} \times M_w} \times \frac{1}{2} \times 100 \quad (1)$$

where M_w represents the molar weight of the dialdehyde cellulose unit ($160 \text{ g}\cdot\text{mol}^{-1}$).

2.3. Physico-Chemical Characterisations of DAC/PVA Scaffolds

2.3.1. Fourier-Transform Infrared Spectroscopy (FT-IR)

FTIR spectra of dried materials of PVA, 9%, 18% or 36% DAC/PVA (2:1) were recorded with an FT-IR 4000 (Jasco, Tsukuba, Japan) in a range of 400 to 4000 cm^{-1} operated at 4 cm^{-1} resolution using KBr method.

2.3.2. X-ray Diffraction Analysis (XDR)

XDR was recorded on an X'pert MRD diffractometer (Pan Analytic/Philips, Eindhoven, The Netherlands; 40 Kv, 30 mA) using $\text{Cu K}\alpha$ ($\lambda = 0.151418 \text{ nm}$) radiation. Scans were performed over a 2θ range from 0 to 55° , with a step size of 0.018° with a counting time per step of 5 s. The crystallinity index of the cellulosic samples was calculated based on equation (1), where the crystalline I_{Cr} and the amorphous I_{am} components are both defined as the peak intensity at 2θ of 22.7° and the minimum intensity around 2θ of 18° [37]:

$$I = \frac{(I_{Cr} - I_{am})}{I_{Cr}} \times 100 \quad (2)$$

2.3.3. Structure Observations

The microstructure and nanostructure of the DAC/PVA composite scaffolds were evaluated using scanning electron microscopy (XL 30-ESEM FEG, Philips, Amsterdam, The Netherlands) using ethanol dehydrated and dried samples. Rehydrated samples were stained for 15 min with a drop of Calcofluor White Stain and a drop of 10% potassium hydroxide then rinsed in large amounts of water. Cellulose contents of the scaffolds were observed at 433 nm using epifluorescence microscopy (Leica DMI6000 B, Leica Microsystems, Wetzlar, Germany).

2.3.4. Degree of Pore Connectivity, Total Water Content and Swelling Ratio Evaluations

DAC/PVA composites pastilles were weighted at several stages: hydrated (m_h), dehydrated (m_w) gently wicked on absorbent paper to remove water entrapped into scaffold cavities and dried (m_d) under laboratory hood for 24 h. The swelling ratio of the scaffold was recorded via mass measurement (m_s) upon rehydration into ultrapure water every 15 min for one hour and then regularly until no further mass fluctuations were observed. The degree of pore connectivity (PC), total water content (Q_w) and Swelling ratio (α) were calculated as:

$$PC = \frac{(m_h - m_w)}{m_h} \times 100 \quad (3)$$

$$Q_W = \frac{(m_h - m_d)}{m_h} \quad (4)$$

$$\alpha = \frac{m_s}{m_d} \quad (5)$$

2.4. Mechanical Characterization of Cellulosic Scaffold

2.4.1. Uniaxial Compressive Test

Uniaxial compression tests were conducted on overnight rehydrated cylindrical cellulosic hydrogels (16 mm diameter, 3 mm thick). The wet samples were compressed with a 22 N load cell at a rate of 0.6 mm/min to 35% strain using a Synergie 400 mechanical testing system (MTS system, Eden Prairie, MN, USA). The Young's modulus was obtained as the slope of the stress-strain curve between 10–20% deformation, avoiding any surface detection bias.

2.4.2. Nanoindentation

Cellulosic hydrogel Young's moduli were estimated using a PIUMA CHIARO nanoindentation system (Optics11, Amsterdam, The Netherlands). A colloidal probe with a cantilever stiffness of 0.47 N/m and a diameter of 28.5 μm was used. For each hydrogel formulation, three separate samples were tested at five locations by indentation of 15,000 nm at 3 nm/s. Before testing, calibration of the cantilever sensitivity was performed by indenting a hard surface (e.g., Petri dish).

2.5. Biological Characterisation of Cellulosic Scaffold

Unless otherwise specified, all reagents were purchased from Gibco, Grand Island, NE, USA. The experiments were performed on DAC/PVA scaffolds (2:1) with 9%, 18% and 36% DAC.

2.5.1. Cytotoxicity Testing

Extracts of sterile materials were formulated following the ISO 10993-5 standards. As a positive control, latex was extracted at 6 cm^2/mL and test cellulosic materials at 1.25 cm^2/mL for 24 h at 37 °C on stirring in DMEM medium supplemented with 10% SVF, PenStrep (100 U/mL, 100 $\mu\text{g}/\text{mL}$) and L-glutamine 2 mM. 100 μL of extracts were deposited on L929 mice fibroblast cell monolayers (ATCC-CCL-1, ATCC, Manassas, VA, USA) pre-cultured for 24 h in 96-well plates and incubated for an additional 24 h at 37 °C in the presence of 5% CO₂. The medium was then substituted with 120 μL of MTS solution (1:5; Promega, Madison, WI, USA) in a complete medium for 2 h at 37 °C. The absorbance was read at 490 nm. The viability percentage for each material was determined as the absorbance ratio to the untreated control. According to the standards, an extract inducing over 70% viability was considered non-toxic.

2.5.2. HDF Cell Adhesion, Viability, Proliferation and In Vitro Tissue Building Assessments

Neonatal human dermal fibroblasts (HDFn, C-004-5C, Thermo Fisher Scientific, Waltham, MA, USA) were grown in DMEM medium supplemented with 10% FCS (Hyclone, Logan,

UT, USA), 2 mM L-glutamine, 100 U/mL penicillin and 100 µg/mL streptomycin at 37 °C with 5% CO₂. For all experiments, cellulosic materials were seeded with 250,000 HDFn cells. Cell adhesion was examined at 48 h of culture on samples fixed for 15 min with 4% PFA, permeabilized for 5 min with 0.1% Triton X-100, saturated for 10 min with 1% BSA and stained for 30 min with phalloidin/DAPI (1/1000; 1/200) at room temperature in the dark. The nucleus and the actin cytoskeleton were respectively revealed by DAPI and Phalloidin (Ex/Em: 493/517 nm; Ex/Em: 340/488 nm) using confocal microscopy (Zeiss LSM 710, Oberkochen, Germany). Cell viability was also checked at 48 h of culture by 30 min treatment with Fixable Dead Cell Stain, followed by DAPI/Phalloidin staining. To visualise long term cell organisation within the matrix, seeded DAC/PVA scaffolds were maintained in culture for 3 weeks and then stained for DAPI/Phalloidin

2.5.3. Implantation in an Athymic Mice Model

Pathogen-free 5-week-old male athymic mice (Rj: NMRI-Foxn1 nu/nu, JANVIER LABS, Le Genest-Saint-Isle, France; 30 g) were housed in polycarbonate cages, in a temperature and humidity-controlled room, and had free access to food and water *ad libitum*. All the in-vivo experiments were approved by the “Comité Régional d’Ethique en Matière d’Expérimentation Animale de Picardie” (CREMEAP; C2EA-96) and were done in compliance with European directive 2010-EU63. Ethanol sterilized DAC/PVA scaffolds were implanted subcutaneously on the backs of athymic mice. The animals were sacrificed after one month and their skins at implantation point were harvested, observed under a microscope and processed under classical histology procedures (Althisia, Troyes, France). An anatomopathological study of the haematoxylin eosin-stained sections was performed by a veterinary pathologist and ranked as follow (SCIEMPATH BIO, Larcay, Belgium). Local inflammation scores at the implantation site were calculated ranging from 0 (absent) to 4 (severe) following the ISO10993-6 considering the infiltration of cellular inflammation at the interface of the material, the presence of fibrosis/fibrous capsule surrounding the injected filler, necrosis and tissue degeneration. A score of 0 designates that the absence of inflammatory reaction as the cellularity at the interface is similar to the non-injected adjacent dermis. Scores of 1 to 4 were respectively attributed when no inflammatory reaction, low focal to multifocal inflammatory reaction, moderate multifocal to diffuse inflammatory and severe inflammatory reaction showing extensive infiltrates, necrosis or fibrosis were observed at the implant interface.

2.6. Statistics

Data are shown as mean ± standard deviations (SD). To determine significant statistical differences, the one-way ANOVA tests and Tukey test were used. Statistical significance was represented as *p*-values < 0.05 (*), *p*-values < 0.01 (**) and *p*-values < 0.001 (***).

3. Results

3.1. Impact of the Oxidation Level on the DAC Particle Size

Extra pure microcrystalline cellulose was oxidised with 6.25, 12.5 or 25% *w/w* sodium periodate to obtain three different DAC powders. Yields of 90–95% were obtained for DAC 9% and 18%, while a loss in mass of 40% was observed for DAC 36%. These DAC powders were observed by scanning electron microscopy and quantified by measuring the surface area, the aspects displayed by the cellulose particles show, in Figure 2, a significant fragmentation of the particles compared to the commercial microcrystalline cellulose. After oxidation, a global disappearance of >50,000 µm² particles, a 50% decrease of 5000 to 50,000 µm² particles and a multiplication of 50 to 100 µm² particles going from 47% to 62–74% of total particles were observed. The presence of the generated dialdehyde groups and material crystallinity were also investigated later, respectively, by FTIR and XRD studies when DAC powders were included in the composite hydrogels.

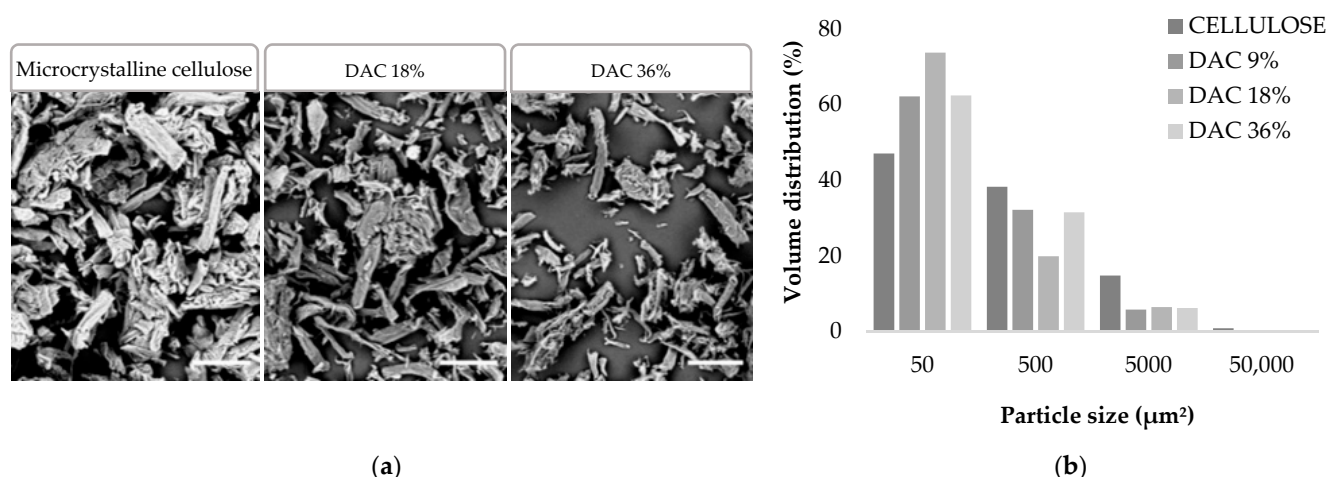


Figure 2. (a) MEB visualisation (Scale bar = 100 µm) and (b) Granulometric distribution of cellulosic powders.

In parallel to the size and shape investigations, the number of aldehyde functions (CHO) was evaluated upon reaction with DNPH in acidic conditions. Indeed, aldehydes were converted to DNP through the formation of hydrazones. The quantification of the unreacted DNPH enabled the determination of the DNPH consumption which gave an aldehyde content estimation in Table 1. The tests were performed in triplicate to ensure the reproducibility of the method. Based on this principle, DNPH assays showed aldehyde levels of 5.3% and 11.3% in the DAC 9% and 18% samples respectively. The precise determination of CHO contents was not possible for the 36% sample due to the variability in the UV measurement response. This result can be currently explained by the instability of the opened glucose ring in strongly oxidized DAC, especially in presence of primary amines as for DNPH. The non-linearity of Schiff base formation for DAC has already been demonstrated, lower levels of imine formation than the actual amount of CHO groups were observed [38]. On the other hand, the hydroxylamine hydrochloride reacted with aldehydes to form oximes and thus released hydrochloric acid (HCl) causing the pH drop of the medium. By titration of HCl with NaOH solution, it was possible to determine the molar number of aldehyde functions grafted on the surface of the polysaccharide backbone. Using this method, rates of 32.7%, 11.7% and 9% were obtained for DAC 36%, 18% and 9% respectively.

Table 1. DNPH/Hydroxylamine CHO dosage (n = 3).

Theoretical DAC Levels (%)	Experimental DAC Levels Obtained via DNPH Method (%)	Experimental DAC Levels Obtained via Hydroxylamine Method (%)
9	5.3 ± 0.6	9.0 ± 1.0
18	11.3 ± 0.6	11.7 ± 1.5
36	ND	32.7 ± 0.6

3.2. Strategy for Producing the DAC/PVA Scaffolds

The proposed protocol for the synthesis and shaping of cellulose/PVA scaffolds based on the functionalization of cellulose through aldehyde functions via classical sodium periodate oxidation was schematized in Figure 3. For all DAC/PVA formulations, the scaffold fabrication was allowed via a performant remodelling of both polymeric cellulose and PVA networks using a simple degeneration process in an NMP/LiCl system, followed by the regeneration of a dual robust composite in ethanol. A cohesive material can be obtained starting from a 9% dialdehyde functionalization and a DAC/PVA ratio of 1:2. Progressive heating of the polymer suspension led to complete dissolution of the powders between 30 and 50 °C, gelation of the PVA around 70 °C and finally to the formation of a

smooth, viscous and homogeneous paste when the temperature of 90 °C was reached. The gradual reconstitution of the networks in ethanol generated a hard and rigid hydrogel that became flexible once fully hydrated in water.

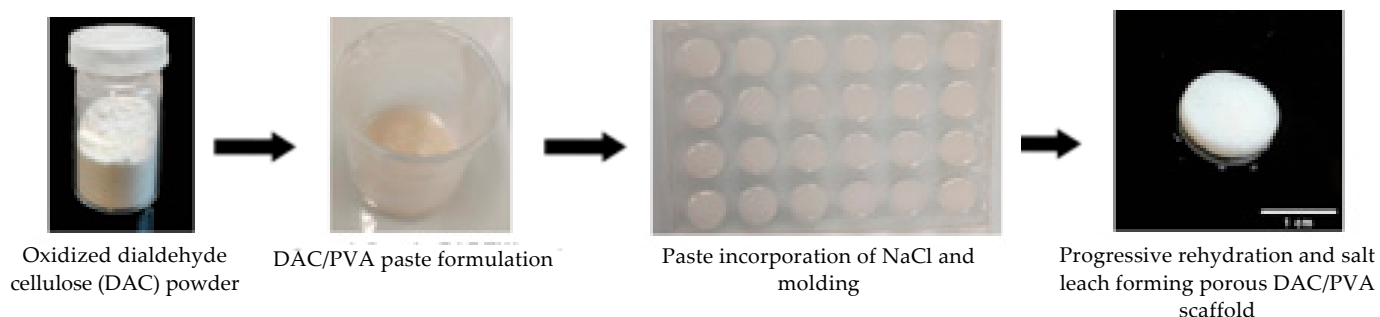


Figure 3. Photographs of the moulding process and formulation of scaffolds based on partial dialdehyde cellulose (here, DAC 9%/PVA (2:1) 0–500 μm NaCl).

In Figure 4, the XRD profiles of the cellulosic materials demonstrated a diffuse peak from 15° to 16° and 3 additional peaks at 20 °C, 22.5° and 40° respectively attributed to the (100), (1 $\bar{1}$ 0), (012), (200) and (004) crystallographic planes. This type of profile was identical to what is commonly observed for type I microcrystalline cellulose [39–41]. Moreover, these profiles differed greatly from the PVA pattern. The crystallinity of the scaffolds was thus essentially related to their microcrystalline cellulose composition ($I = 68\%$) [42]. The crystallinity index of the cellulosic samples based on DAC 9%, 18% and 36% were, respectively, 62.5, 62.3 and 51.0%. The crystallinity of the samples decreased progressively by oxidation with sodium periodate, demonstrating aldehyde functions formation starting from the furanose ring opening essentially localized at cellulose backbone extremities. The peak at 40° disappeared in the case of DAC 36%, suggesting a slight modification of chains conformation. For DAC 9% and 18%, as all the signals were observed, long domains of the cellulose backbone were assumed to remain unchanged.

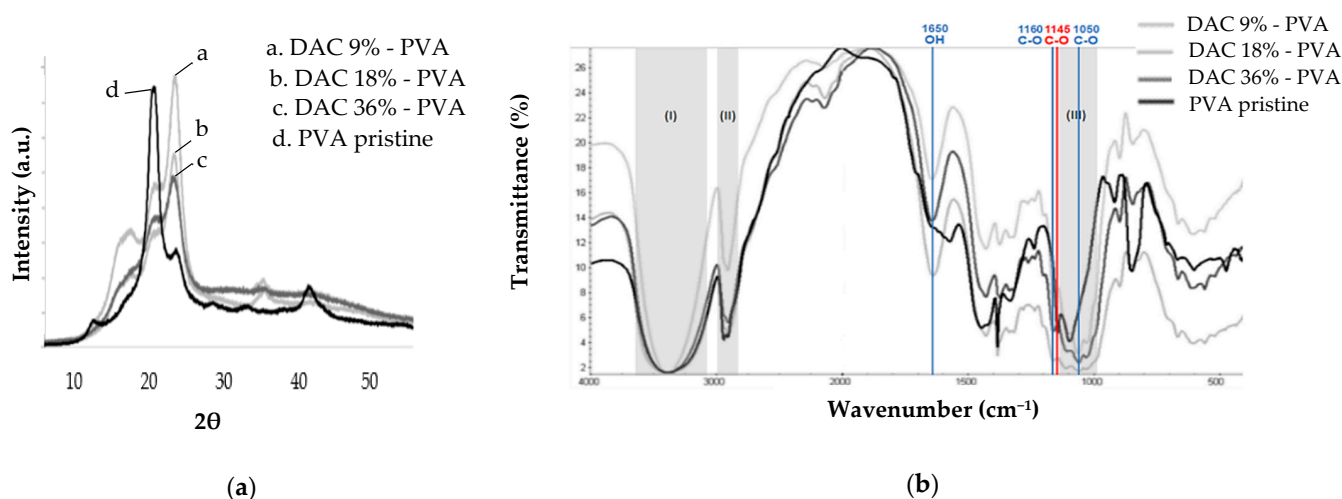


Figure 4. PVA and DAC-based composite scaffolds (a) XRD diffractograms; (b) FT-IR spectra.

The FTIR spectra logically displayed signature signals for PVA and cellulose, both basic constituents of the materials. For DAC, a detailed description of the FT-IR spectrum can be found in the literature [43]. For PVA, at 3373 cm^{-1} the broadband (I) corresponds to hydroxyl OH groups involved in intermolecular and intramolecular hydrogen bonds. The 2918 cm^{-1} bands (II) and 1439 cm^{-1} bands represent CH polymer backbone stretching. The CH_2 from the long alkyl chain vibrations were observed at 2052 cm^{-1} . The 1728 cm^{-1}

inflexion and 1097–1149 cm^{-1} multiple bands, in the fingerprint region (III), report C–O stretching. There, the 1145 cm^{-1} band is associated with PVA crystallinity nature (red) [44–47]. These peaks were found on the spectra of cellulosic materials, attesting to the maintenance of the PVA structure.

As cellulose shares groups in common with PVA, many bands were found to be in common (grey) especially in regions I, II and III. For better visualization of the fingerprint region, the FTIR spectra limited to region 1800 cm^{-1} to 700 cm^{-1} was provided in Supplementary Materials, Figure S1. Cellulose specific vibrations (blue) related to C–O and OH groups were, respectively, identified at 1057 cm^{-1} at 1650 cm^{-1} [48,49]. These predominant hydroxyl groups in cellulose tend to adsorb moisture. Bound water is therefore most likely responsible for this last peak [50,51]. Furthermore, the peaks at 1376 and 1021 cm^{-1} were attributed to CH₂ bending and C–O–C stretching vibration representative of a furanose ring or glucose sub-unit in the polysaccharide backbone. The characteristic signals of aldehyde groups currently found that around 1730 cm^{-1} or 2700 cm^{-1} do not appear in FT-IR charts of the formed hydrogels [52]. The presence of C–O vibrations at 1057 cm^{-1} supported by those found at 1160 cm^{-1} as well as the band at OH 890 cm^{-1} , respectively, were attributed to acetal and hemiacetal bonds [53].

3.3. Structural Characterization of the DAC/PVA Scaffolds

Cellulose/PVA composite hydrogels were produced, controlling DAC degree of oxidation, DAC/PVA ratio and its porosity by the addition of porogen agents. Blue staining of the cellulose with calcofluor white stain allows for the observation of the macroscopic organisation of the polymeric network. In Figure 5, the increasing cellulose ratio can be interpreted as 50–150 μm long microcrystals homogeneously distributed in a hydrogel loaded with DAC fibres. This gel exhibits a micrometre-sized porosity attributable to its polymer network. Additional porosity was introduced through the solubilisation of NaCl salts of diameter calibrated between 0–500 μm or 50–100 μm demonstrating average diameters respectively of 305.4 ± 65.3 and 69.6 ± 16.2 μm . Homogeneous distribution of porosity was obtained, but the juxtaposition of the salts does not guarantee the interconnectivity of the pores required for biological applications. Indeed, the hydrogels present high-water contents (above 75% *w/w*) and an increasing porosity mediated by salt leaching. The degree of interconnectivity obtained by absorption of the free water contained in the hydrogel shows limited interconnectivity with the use of salts 0–500 μm . This was improved by the calibration of salts at 50–100 μm passing from 47.1 to 56.6%. To determine scaffolds potential applications in a biomedical context, we had to evaluate their swelling behaviour and mechanical properties. Dry materials showed similar rehydration profiles. After 1 h, a maximum swelling was reached. The hydrogel retained 4 to 8 g of water per g of dried hydrogel, representing 42.6 to 80.0% of the initial average water/dry mass ratio. The deformation of hydrogel was observed for all samples except for the 9% DAC/PVA (2:1) samples whose porosity was induced by salts of diameter 0–500 μm .

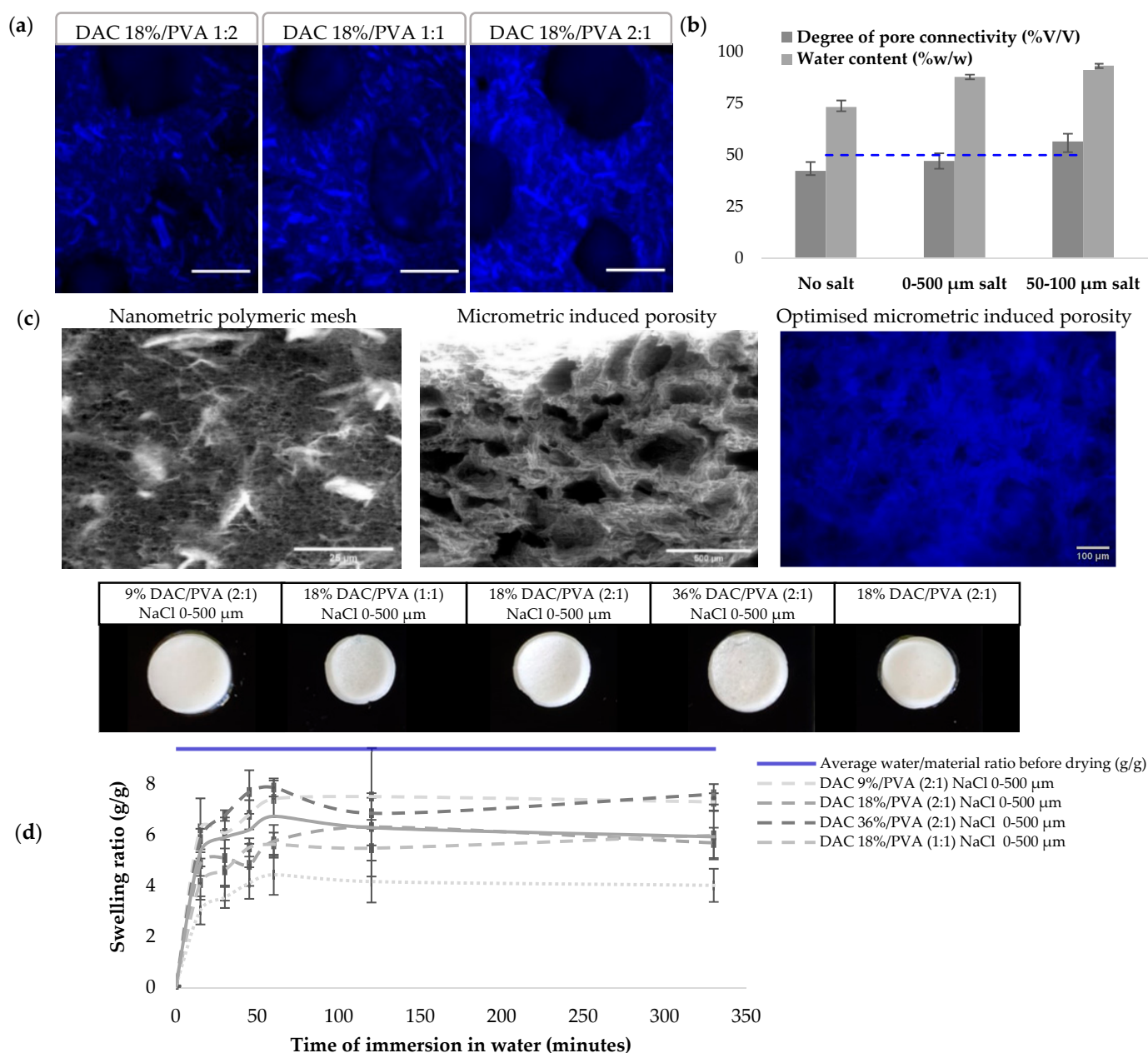


Figure 5. (a) Calcofluor white stained DAC 18%/PVA NaCl 0–500 μm scaffolds respectively at ratio 1:2, 1:1 and 2:1 showing cellulosic material (blue; scale bar: 250 μm); (b) Degree of pore connectivity (%v/v) and water content (%w/w) quantifications modulating salt leaching induced porosity ($n = 5$); (c) MEB observation of nano and micro porosities of DAC 18%/PVA (2:1) NaCl 0–500 μm scaffold; Calcofluor white stained DAC 9%/PVA (2:1) NaCl 50–100 μm showing enhanced porosity; (d) Swelling ratio study including photographs of rehydrated DAC/PVA based scaffolds.

In Figure 6, the material mechanics were investigated through the estimation of Young's modulus at macroscopic and nanoscopic scales respectively by compression and nanoindentation. Macroscopically, a gradual increase in DAC proportion significantly increased the Young's modulus, as DAC 18%/PVA ratio of (1:2), (1:1) and (2:1) respectively depict Young's moduli of 16.16, 24.25 and 57.21 kPa. The degree of oxidation of the cellulose dialdehyde also seemed to influence the mechanical properties of the hydrogels since Young's moduli of 42.81, 57.69, 20.9 kPa are obtained by compression for hydrogels respectively based on 9%, 18% and 36% DAC. The introduction of salt-leached porosity significantly increased the stiffness of the material moving from a modulus of 19.05 to 57.21 kPa for a DAC 18%/PVA (2:1) hydrogels. At a nanometric level, when DAC 9% based

materials demonstrated identical Young's moduli compared to the macro metric level of 42.86 kPa, DAC 18% and 36% based materials showed lower moduli, respectively, of 12.83 and 36.63 kPa.

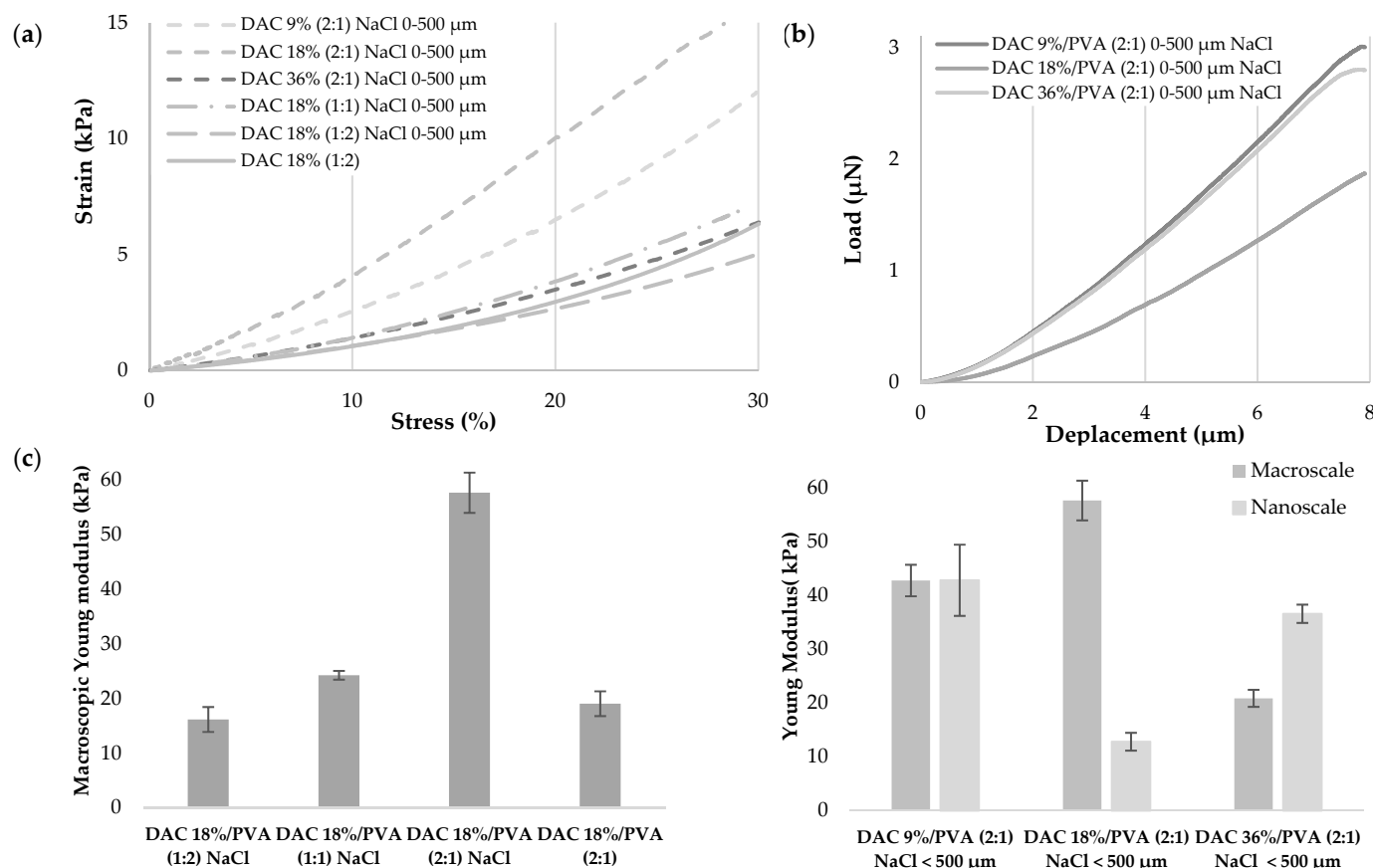


Figure 6. DAC/PVA hydrogels mechanical properties (a) Stress-strain curves obtained by compressive test. Compression up to 30%, speed: 0.01 mm/s, sensor: 22N ($n = 5$); (b) Load-displacement curves obtained upon 15,000 nm at 3 nm/s nanoindentation. Indenter diameter: 28.5 μm , stiffness: 0.47 N/m ($n = 3$) (c) Determination of macroscopic and nanoscopic Young's modulus. All conditions display *** significance except DAC 9%/PVA (2:1) NaCl < 500 μm samples (***) p -values < 0.001 (ANOVA, Tukey test).

3.4. Investigation of DAC/PVA Scaffold Potential Use for Tissue Engineering, Implantable Matrices

Firstly, indirect and direct cell viability were assessed in Figure 7 using regulatory reference cell lineage L929 and for its intended use, primary neonatal dermal fibroblasts HDFn. Thus, L929 viabilities of 126.0, 89.4 and 79.9% were, respectively, obtained with 9%, 18%, 36% DAC-based hydrogels to a relatively untreated control considered at 100%. The cytotoxic latex used as positive control showed drop-in viability down to 24.9%, while HDF viabilities of 99.7% and 92.8% were achieved with the 9% and 36% DAC-based hydrogels.

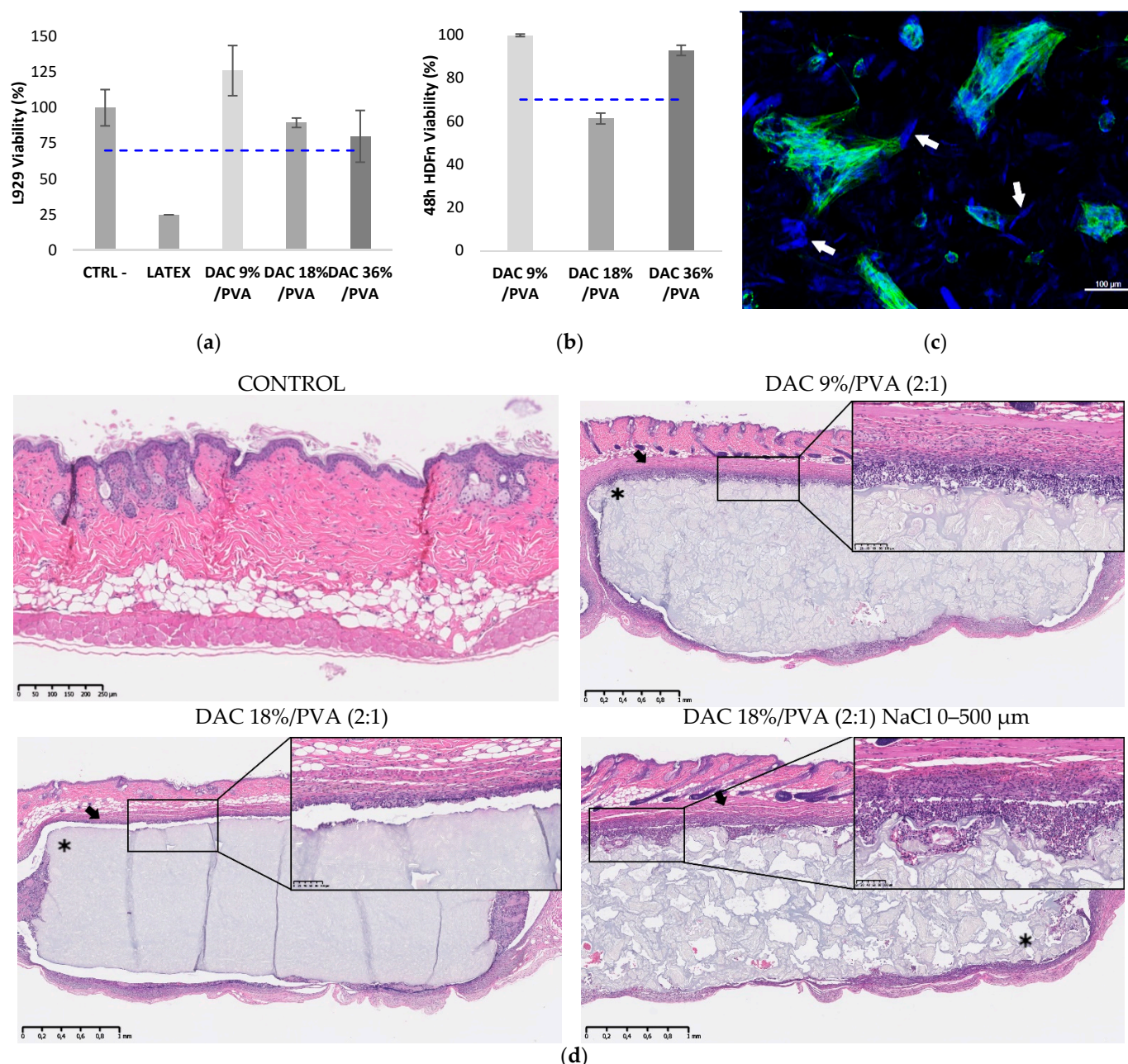


Figure 7. (a) DAC/PVA (2:1) NaCl hydrogels cytocompatibility test following the ISO10993 standard protocol (n = 3); (b) Neonatal human dermal fibroblast (HDFn) cultured on DAC/PVA (2:1) NaCl hydrogels viability assay at 48 h (n = 3); (c) Observation of adhered HDFn and spheroid-like structure on 9% DAC/PVA (2:1) material. DAPI: cell nucleus (blue); Phalloidin: cell cytoskeleton (green); White arrow: cellulose. (d) Examination of *in vivo* biocompatibility and biostability of nanporous and macroporous cellulosic materials in a nude mouse model through histological study upon 1-month subcutaneous implantation (n = 3). *: cellulosic implant; arrow: fibrous capsule.

A low level of viability of 61.2% was reported for 18% oxidized cellulose-based hydrogel. HDF culture at the surface of porous materials showed good infiltration and pore occupation, with clusters of cells showing both a spread-out actin cytoskeleton that appears to anchor to nearby accessible cellulose particles (white arrows), as well as spheroid-like aggregations of cells.

One-month implantation of all materials in thymus-free nude mice showed no rejection of the implants, demonstrating their physical stability. As shown in Figure 7d, the material was completely recovered with no breakage, fragmentation or little to no sign

of degradation for all porous and non-porous materials. The implanted area showed at the material interface a thin fibrous capsule presenting mild to moderate neutrophilic and macrophages inflammatory infiltrates. The DAC/PVA materials (2:1) of DAC 9%, 18%, 36% displayed mean inflammatory scores of 3, 2.5 and 2.5, respectively ($n = 3$). The addition of porosity increased the inflammation score to 3.3 for the DAC 18%/PVA (2:1) material.

4. Discussion

The loss of soft tissue, fatty, fibrous or muscular tissue affects a wide spectrum of patients, as it is associated with multiple medical conditions related to trauma, burns, infections, tumour removals, degenerative diseases or autoimmune disorders. In addition to the physical impact of their tissue loss, patients encounter psychological cues linked to the loss of normal body contours that only can be remedied by filling in the affected area. Although common, autologous fat injection presents a need for repeated intervention questioning resulting viability and short term stability [54,55]. Practitioners are still seeking an adequate methodology that can sustain stable volume and long-term tissue regeneration. Thus, biocompatible filling hydrogels such as our DAC/PVA substitute are particularly promising for the filling of small to large tissue defects.

Our synthesis methodology allowed us to obtain a ready-to-use paste that can be declined in multiple forms, membrane, scaffold or beads completed by moulding, additive manufacturing, extrusion or electrospinning mainly for biomedical applications. Regarding DAC/PVA hydrogel synthesis, effective functionalisation of cellulose was obtained using the classical periodate sodium oxidation method. While FTIR and XDR proved the absence of aldehyde groups in our final cellulosic materials, those analyses provide insight into their formation mechanism, high reactivity and resulting bonding. Thus, FT-IR analysis highlighted the cellulose and PVA composition of the DAC/PVA materials but did not distinguish the dialdehyde functions distinctly. Subsequent signals attributed to acetal and hemiacetal bonds were identified, demonstrating the effectiveness of the NMP/LiCl system for simultaneously strongly cross-link PVA and DAC and engage electrostatic interactions to stabilise the hydrogels. XDR demonstrated a significant decrease of the crystallinity index linked to the cellulose increasing degree of oxidation [56]. This loss of crystallinity was considered to result from the opening of glucopyranose rings and the destruction of their ordered packing. This occurs mainly at the extremities of the accessible polymeric chains generating a fragmentation of the particles by disruption of the interchain hydrogen bonds [57]. As mentioned in the literature, the number average molecular weight (M_n) of biopolymers tends to be reduced as a result of oxidation [58]. Given the indirect evidence of aldehyde groups, further quantifications were undertaken with DNPH and hydroxylamine hydrochloride to characterise our DAC powders. These methods have been widely used and prove to be very sensitive and accurate for the quantification of aldehyde content of polysaccharides [57,59]. Lower rates of respectively 5–9%, 11–12% and 33% were thus obtained for the theoretically 9%, 18% and 36% DAC powders. Cellulose and DAC powders are difficult to solubilise. Indeed, DAC is hardly soluble in water, even when heated, especially on dry or less than 75% oxidized products [60]. The aldehyde functionalities are present in a complex interconverting mixture of hydrates, intramolecular and intermolecular hemiacetals and acetals formed during reaction and drying and are therefore not in their free form to react [59,61]. DAC quantifications may be slightly underestimated by lack of accessibility and difficult reversibility of established bonds in water. Moreover, under our heating conditions in an acidic medium (post-reaction pH = 4) and especially in the presence of high concentrations of sodium periodate (36% mol/mol of cellulose), we observed significant hydrolysis of our product visualized through a very significant decrease in yield. Indeed, periodate oxidation is an incomplete reaction whose rate and yield depend on temperature, pH, reaction time and oxidant concentration. Higher temperature tends to produce better oxidation rates but lower yield, degrading both oxidant and DAC through acid catalysed cleavage of the β -(1 \rightarrow 4) glycosidic bonds, fragmenting it in a heterogeneous manner [56]. The optimisation of sodium periodate

oxidation relies on minimising the time and temperature of oxidation to limit cellulose hydrolysis. The addition of salts such as LiCl proves to be effective for that purpose in reducing inter and intrachain interactions, but LiCl-catalysed periodate degradation has also been observed [62]. During our studies, microwave heating has been considered and tested as a substitute for conventional heating for the reshaping and arrangement of cellulose and PVA polymers. However, these devices are limited in terms of production scale, agitation quality and reaction observability. Moreover, the conventional heating reaction time has been reduced to approach the one used in microwave heating. For our application, this method has thus lost all interest.

Cellulose/PVA composite hydrogels can be synthesized controlling DAC degree of oxidation, DAC/PVA ratio and its porosity by the addition of pore-forming agents. The physical characterization of our hydrogels reveals the homogeneity of the interconnected micrometric network and the incorporation of microcrystalline cellulose fibres, as well as the good integration of an additional porosity required for some biomedical applications. To reach sufficient interconnectivity of our additional porosity, a reduced granulometry of the salts was used to increase the surface area developed by these salts, thus favouring their juxtaposition and connection. Additional freezing-thawing was attempted to further connect the pores but the materials systematically returned to their initial shape, being very elastic. Their water absorption capacity was assessed to consider possible storage in a dry state and rehydration for use. However, only the 9% (2:1) NaCl 0–500 μm DAC samples were able to regain a sufficiently high-water content and shape to be considered. Indeed, higher oxidation rates of 18% and 36% develop more cross-links and electrostatic interactions which are not fully recovered when broken by drying. In addition, hydrogels with large cavities hold more free water and thus rehydrate more efficiently. By modulation of the DAC/PVA ratio, we find that cellulose stiffens the hydrogel at the macro metric level, most likely through the crystalline micro cellulose fibres previously observed. Moreover, salts dissolution must generate irreversible dehydration of the material in the pore area, explaining the observed stiffening of porous hydrogels. The degree of oxidation of cellulose being largely related to the size of the particles, an impact on the mechanics of the hydrogel at the macroscopic level is observed when it varies. We assume that the higher stiffness observed for the 9% and 18% samples are certainly related to the presence of larger microcrystalline cellulose particles compared to the 36% DAC particles which underwent more hydrolysis and fragmentation during oxidation. At the nanometric level, the 9% and 36% DAC-based materials show a similar Young's modulus of about 40 kPa, while at 18% a significantly lower Young's modulus is obtained. These observations are most certainly linked to the organisation of the DAC/PVA network, as well as the nature and density of the associated interactions and bonds. Our hydrogels have mechanical properties similar to those of soft tissues whose Young's moduli range from 0.1 kPa to 1 MPa. By cellularisation, these matrices tend to stiffen as previously observed by deposition, remodelling and crosslinking of extracellular matrix protein notably collagen [63].

To consider any biomedical application, a rigorous study of the biological acceptability of this material has been undertaken. The release media of DAC/PVA hydrogels show decreasing viability of L929 as the degree of oxidation of DAC increases up to 18% DAC oxidation, in conformity with the ISO 10993-5 standard. Since PVA is known to be fully biocompatible, the indirect cytotoxicity observed on L929 is due to the release of cellulose dialdehyde particles. This same effect has already been observed on the NIH/3T3 fibroblast line where cell viability drops to 70% for 1.74 mmol/10 g PVA of CHO groups [64]. Despite being weakly oxidised, DAC predominates in the composition of our hydrogel, reaching a minimum of 23.38 mmol/10 g PVA at 9%. The absence of toxicity observed below 18% reflects the full engagement of aldehyde groups in stable linkages non-deleterious at the cellular level. When seeded on the material surface, the cell-DAC/PVA interaction shows a correlation between the cell viability of HDFs and the mechanical properties of the material at the nanometre level. Indeed, HDFs exhibit stronger cell viability for DAC 9% and DAC 36% than DAC 18% material respectively showing Young Modulus of around 37, 13 and

43 kPa. Although little data is available on DAC/PVA hydrogels, numerous studies show the positive impact in 2D and 3D of matrix stiffness on fibroblast activity in terms of cell adhesion, proliferation and migration [65,66]. The DAC 9% /PVA (2:1) matrix appears to be the most suitable material for *in vitro* use.

Given that the DAC/PVA materials have substantially identical microenvironments in their composition, very similar results are subsequently obtained for DAC 9%, 18% and 36% material during long-term cultivation. As homogeneous and total infiltration of the porous material is achieved, the induction of porosity with controlled salt granularity proves to be effective and sufficient in our case. When cultured for 3 weeks, seeded fibroblasts organise themselves into spheroid-like cell aggregates. Indeed, as a biologically inert polymer, PVA shows an inability to engage interactions with ECM proteins such as fibronectin, collagen, laminin and thus associate with cellular integrin receptors. The incorporation of micro-crystalline cellulose in our hydrogel offers anchorage points for these cellular aggregates. Indeed, on cellulose surfaces, HDFs can establish cell adhesions and develop filopodia as the numerous hydroxyl groups on the cellulose surface allow the protein adsorption required for cell adhesion by electrostatic interactions and hydrogen bonds [67–69]. By chemical functionalization, oxidation, phosphorylation or specific chemical grafting, these interactions can be promoted to remedy growth factor or FBS supplementation [70]. Mechanically confined fibroblast has shown the ability to reprogram in stem-cell-like cells and rejuvenate [71,72]. In the literature, PVA and bacterial cellulose also demonstrated spheroid formation and long-term stem-cell maintenance properties [29,73,74]. The potential of these spheroid-like structures at the surface of our DAC/PVA material is very high, providing an environment recapitulating the *in-vivo* complexity better than the traditional 2D or some 3D cultures. These cells functionality is more representative for pharmacological model predictivity and exhibit promising regeneration properties for tissue engineering and regenerative medicine applications.

Implanted DAC/PVA hydrogels exhibit complete stability by a month of implantation, a mild inflammation characterised by extensive neutrophil and macrophage infiltration and the formation of a thin fibrous capsule at the periphery of the implant. By inducing porosity in the implant, the contact surface is increased and cellular infiltration is facilitated, apparently increasing the inflammatory score. Such inflammation is indicative of a foreign body reaction (FBR), a key reaction in evaluating the safety of a scaffold in tissue engineering applications. Indeed, once implanted, our material interacts with its surroundings, through fluid, protein and cellular infiltration. Consisting of cellulose and PVA, the implant was recognised as non-self, and the body undertakes inflammatory processes aimed at its destruction or isolation from the rest of the body [75]. In the case of cellulose-based hydrogels, mild inflammation was also observed at 4 weeks and then disappeared at 8 weeks as the fibrous capsule surrounding the implant was refined [76,77]. Lacking a cellulase equivalent to breaking β 1-4 glycosidic bond *in vivo*, cellulose demonstrates slow *in situ* degradation via particle macrophage phagocytosis. Cellulosic materials can persist in the crystalline form up to 5 months after implantation [78]. To overcome such *vivo* stability and to reinforce cellulose fibres usage as a biomaterial for tissue engineering, the degradation of cellulose may be modulated by incorporating cellulase into the material [79].

5. Conclusions

We have developed and characterised a material based on cellulose dialdehyde and PVA, which has shown soft tissue-like mechanical properties, cytocompatibility and the promising ability to form spheroid-like structures for the development of pharmacological models. Investigations should be conducted on different cell types to confirm and characterise these structures in terms of size, morphology, cell viability, metabolic activity and dedifferentiation/differentiation potential. The stability of this material *in vivo* also makes it a candidate for the development of raw, biochemically functionalized or cellularized implantable matrices. The synthesis path of our material also offers the possibility to pro-

duce innovative nanoscale culture substitutes for tissue engineering using nanocrystalline cellulose.

Supplementary Materials: The following are available online at <https://www.mdpi.com/article/10.3390/polym13203598/s1>, Figure S1: Zoom of PVA and DAC-based composite scaffolds FT-IR spectra.

Author Contributions: M.S.: methodology, formal analysis, investigation, writing—original draft preparation. C.-O.S. and E.G.: methodology. C.E.: conceptualization, supervision, writing—review and editing. F.D.: conceptualization, supervision, formal analysis, investigation, writing—review and editing. All authors have read and agreed to the published version of the manuscript.

Funding: This research was supported by a PhD student fellowship from the French higher education and research ministry (MESR).

Institutional Review Board Statement: The study was conducted according to the guidelines of the Declaration of Helsinki, the European directive 2010-EU63. and approved by the “Comité Régional d’Ethique en Matière d’Expérimentation Animale de Picardie” (CREMEA, C2EA-96, APAFIS#15099-2019030814383996 v1, 2 April 2019).

Data Availability Statement: Data Availability Statement Raw data are stored in-house at UTC and can be made available upon request.

Acknowledgments: We would like to thank Franco Otaola and Cristina Belda Marin for sharing their mould casting methodology, Frédéric Nadaud for collecting all the electron microscopy material and Vanessa Bleicher for her high-quality technical support.

Conflicts of Interest: The authors declare no conflict of interest. The funders had no role in the design of the study; in the collection, analyses, or interpretation of data; in the writing of the manuscript, or in the decision to publish the results.

References

1. Zhu, J.; Marchant, R.E. Design properties of hydrogel tissue-engineering scaffolds. *Expert Rev. Med. Devices* **2011**, *8*, 607–626. [CrossRef]
2. Fan, C.; Wang, D.-A. Macroporous Hydrogel Scaffolds for Three-Dimensional Cell Culture and Tissue Engineering. *Tissue Eng. Part B Rev.* **2017**, *23*, 451–461. [CrossRef] [PubMed]
3. Annabi, N.; Nichol, J.W.; Zhong, X.; Ji, C.; Koshy, S.; Khademhosseini, A.; Dehghani, F. Controlling the Porosity and Microarchitecture of Hydrogels for Tissue Engineering. *Tissue Eng. Part B Rev.* **2010**, *16*, 371–383. [CrossRef] [PubMed]
4. Troy, E.; Tilbury, M.A.; Power, A.M.; Wall, J.G. Nature-Based Biomaterials and Their Application in Biomedicine. *Polymers* **2021**, *13*, 3321. [CrossRef] [PubMed]
5. Chaudhari, A.; Vig, K.; Baganizi, D.; Sahu, R.; Dixit, S.; Dennis, V.; Singh, S.; Pillai, S. Future Prospects for Scaffolding Methods and Biomaterials in Skin Tissue Engineering: A Review. *Int. J. Mol. Sci.* **2016**, *17*, 1974. [CrossRef] [PubMed]
6. Gsib, O.; Duval, J.-L.; Goczkowski, M.; Deneufchatel, M.; Fichet, O.; Larreta-Garde, V.; Bencherif, S.; Egles, C. Evaluation of Fibrin-Based Interpenetrating Polymer Networks as Potential Biomaterials for Tissue Engineering. *Nanomaterials* **2017**, *7*, 436. [CrossRef] [PubMed]
7. Dutta, S.D.; Patel, D.K.; Lim, K.-T. Functional cellulose-based hydrogels as extracellular matrices for tissue engineering. *J. Biol. Eng.* **2019**, *13*, 55. [CrossRef] [PubMed]
8. Kale, R.D.; Bansal, P.S.; Gorade, V.G. Extraction of Microcrystalline Cellulose from Cotton Sliver and Its Comparison with Commercial Microcrystalline Cellulose. *J. Polym. Environ.* **2018**, *26*, 355–364. [CrossRef]
9. Ludueña, L.N.; Vecchio, A.; Stefani, P.M.; Alvarez, V.A. Extraction of cellulose nanowhiskers from natural fibers and agricultural byproducts. *Fibers Polym.* **2013**, *14*, 1118–1127. [CrossRef]
10. Rosa, S.M.L.; Rehman, N.; de Miranda, M.I.G.; Nachtigall, S.M.B.; Bica, C.I.D. Chlorine-free extraction of cellulose from rice husk and whisker isolation. *Carbohydr. Polym.* **2012**, *87*, 1131–1138. [CrossRef]
11. Pirani, S.; Hashaikh, R. Nanocrystalline cellulose extraction process and utilization of the byproduct for biofuels production. *Carbohydr. Polym.* **2013**, *93*, 357–363. [CrossRef] [PubMed]
12. Danial, W.H.; Abdul Majid, Z.; Mohd Muhid, M.N.; Triwahyono, S.; Bakar, M.B.; Ramli, Z. The reuse of wastepaper for the extraction of cellulose nanocrystals. *Carbohydr. Polym.* **2015**, *118*, 165–169. [CrossRef] [PubMed]
13. Bergensträhle, M.; Wohler, J.; Himmel, M.E.; Brady, J.W. Simulation studies of the insolubility of cellulose. *Carbohydr. Res.* **2010**, *345*, 2060–2066. [CrossRef] [PubMed]
14. Zhang, C.; Liu, R.; Xiang, J.; Kang, H.; Liu, Z.; Huang, Y. Dissolution Mechanism of Cellulose in N, N-Dimethylacetamide/Lithium Chloride: Revisiting through Molecular Interactions. *J. Phys. Chem. B* **2014**, *118*, 9507–9514. [CrossRef] [PubMed]




15. Peng, H.; Wang, S.; Xu, H.; Hao, X. Preparation, properties and formation mechanism of cellulose/polyvinyl alcohol bio-composite hydrogel membranes. *New J. Chem.* **2017**, *41*, 6564–6573. [\[CrossRef\]](#)
16. Maharjan, B.; Park, J.; Kaliannagounder, V.K.; Awasthi, G.P.; Joshi, M.K.; Park, C.H.; Kim, C.S. Regenerated cellulose nanofiber reinforced chitosan hydrogel scaffolds for bone tissue engineering. *Carbohydr. Polym.* **2021**, *251*, 117023. [\[CrossRef\]](#) [\[PubMed\]](#)
17. Krüger, M.; Oosterhoff, L.A.; van Wolferen, M.E.; Schiele, S.A.; Walther, A.; Geijssen, N.; De Laporte, L.; van der Laan, L.J.W.; Kock, L.M.; Spee, B. Cellulose Nanofibril Hydrogel Promotes Hepatic Differentiation of Human Liver Organoids. *Adv. Healthc. Mater.* **2020**, *9*, 1901658. [\[CrossRef\]](#) [\[PubMed\]](#)
18. Kumar, A.; Lee, Y.; Kim, D.; Rao, K.M.; Kim, J.; Park, S.; Haider, A.; Lee, D.H.; Han, S.S. Effect of crosslinking functionality on microstructure, mechanical properties, and in vitro cytocompatibility of cellulose nanocrystals reinforced poly (vinyl alcohol)/sodium alginate hybrid scaffolds. *Int. J. Biol. Macromol.* **2017**, *95*, 962–973. [\[CrossRef\]](#)
19. Du, H.; Liu, W.; Zhang, M.; Si, C.; Zhang, X.; Li, B. Cellulose nanocrystals and cellulose nanofibrils based hydrogels for biomedical applications. *Carbohydr. Polym.* **2019**, *209*, 130–144. [\[CrossRef\]](#) [\[PubMed\]](#)
20. Kumar, A.; Matari, I.A.I.; Han, S.S. 3D printable carboxylated cellulose nanocrystal-reinforced hydrogel inks for tissue engineering. *Biofabrication* **2020**, *12*, 025029. [\[CrossRef\]](#)
21. Jayaramudu, T.; Ko, H.-U.; Zhai, L.; Li, Y.; Kim, J. Preparation and characterization of hydrogels from polyvinyl alcohol and cellulose and their electroactive behavior. *Soft Mater.* **2017**, *15*, 64–72. [\[CrossRef\]](#)
22. Jayaramudu, T.; Hyun-U, K.; Xiaoyuan, G.; Yaguang, L.; Sang Youn, K.; Jaehwan, K. *Cellulose/Polyvinyl Alcohol-Based Hydrogels for Reconfigurable Lens*; Varadan, V.K., Ed.; International Society for Optics and Photonics: Las Vegas, NV, USA, 2016; p. 980212.
23. Zhang, M.; Dong, X.; Ouyang, Y.; Li, Y.; Liu, T.; Cheng, T.; Minli, H.; Ma, J.; Li, G. Vapor-Phase Oxidation of Ethylene to Produce Vinyl Acetate. Chinese Patent CN102936198, 25 May 2016.
24. Liu, Y.; Hu, H.; Yang, X.; Lv, J.; Zhou, L.; Luo, Z. Hydrophilic modification on polyvinyl alcohol membrane by hyaluronic acid. *Biomed. Mater.* **2019**, *14*, 055009. [\[CrossRef\]](#) [\[PubMed\]](#)
25. Cooper, T.A. 5-Developments in bioplastic materials for packaging food, beverages and other fast-moving consumer goods. In *Trends in Packaging of Food, Beverages and Other Fast-Moving Consumer Goods (FMCG)*; Farmer, N., Ed.; Woodhead Publishing: Cambridge, UK, 2013; pp. 108–152. ISBN 978-0-85709-503-9.
26. Gupta, S.; Goswami, S.; Sinha, A. A combined effect of freeze–thaw cycles and polymer concentration on the structure and mechanical properties of transparent PVA gels. *Biomed. Mater.* **2012**, *7*, 015006. [\[CrossRef\]](#) [\[PubMed\]](#)
27. Schmedlen, R.H.; Masters, K.S.; West, J.L. Photocrosslinkable polyvinyl alcohol hydrogels that can be modified with cell adhesion peptides for use in tissue engineering. *Biomaterials* **2002**, *23*, 4325–4332. [\[CrossRef\]](#)
28. Zajackowski, M.B.; Cukierman, E.; Galbraith, C.G.; Yamada, K.M. Cell–Matrix Adhesions on Poly(vinyl alcohol) Hydrogels. *Tissue Eng.* **2003**, *9*, 525–533. [\[CrossRef\]](#)
29. Molyneaux, K.; Wnek, M.D.; Craig, S.E.L.; Vincent, J.; Rucker, I.; Wnek, G.E.; Brady-Kalnay, S.M. Physically-cross-linked poly(vinyl alcohol) cell culture plate coatings facilitate preservation of cell–cell interactions, spheroid formation, and stemness. *J. Biomed. Mater. Res. B Appl. Biomater.* **2021**, *109*, 1744–1753. [\[CrossRef\]](#) [\[PubMed\]](#)
30. Hsieh, H.-Y.; Young, T.-H.; Yao, C.-C.; Chen, Y.-J. Aggregation of human dental pulp cells into 3D spheroids enhances their migration ability after reseeding. *J. Cell. Physiol.* **2019**, *234*, 976–986. [\[CrossRef\]](#) [\[PubMed\]](#)
31. Huang, Y.-C.; Chan, C.-C.; Lin, W.-T.; Chiu, H.-Y.; Tsai, R.-Y.; Tsai, T.-H.; Chan, J.-Y.; Lin, S.-J. Scalable production of controllable dermal papilla spheroids on PVA surfaces and the effects of spheroid size on hair follicle regeneration. *Biomaterials* **2013**, *34*, 442–451. [\[CrossRef\]](#) [\[PubMed\]](#)
32. Nittelman, C.R.; Mortisen, D.J.; Henry, S.M.; Anseth, K.S. Attachment of fibronectin to poly(vinyl alcohol) hydrogels promotes NIH3T3 cell adhesion, proliferation, and migration. *J. Biomed. Mater. Res.* **2001**, *57*, 217–223. [\[CrossRef\]](#)
33. Peng, L.; Zhou, Y.; Lu, W.; Zhu, W.; Li, Y.; Chen, K.; Zhang, G.; Xu, J.; Deng, Z.; Wang, D. Characterization of a novel polyvinyl alcohol/chitosan porous hydrogel combined with bone marrow mesenchymal stem cells and its application in articular cartilage repair. *BMC Musculoskelet. Disord.* **2019**, *20*, 257. [\[CrossRef\]](#)
34. Pan, Z.; Yin, H.; Wang, S.; Xiong, G.; Yin, Z. Potential In Vitro Tissue-Engineered Anterior Cruciate Ligament by Copolymerization of Polyvinyl Alcohol and Collagen. *J. Craniofac. Surg.* **2021**, *32*, 799–803. [\[CrossRef\]](#)
35. Rasband, W.S.; Eliceiri, K.W. *Image J*; U.S. National Institutes of Health: Bethesda, MD, USA, 1997.
36. Zhao, H.; Heindel, N.D. Determination of Degree of Substitution of Formyl Groups in Polyaldehyde Dextran by the Hydroxylamine Hydrochloride Method. *Pharm. Res.* **1991**, *8*, 400–402. [\[CrossRef\]](#) [\[PubMed\]](#)
37. Segal, L.; Creely, J.J.; Martin, A.E.; Conrad, C.M. An Empirical Method for Estimating the Degree of Crystallinity of Native Cellulose Using the X-Ray Diffractometer. *Text. Res. J.* **1959**, *29*, 786–794. [\[CrossRef\]](#)
38. Leguy, J. *Periodate Oxidation of Cellulose for Internal Plasticization and Materials Design*; Université Grenoble Alpes: Grenoble, France, 2018.
39. Melo, A.R.A.; Filho, J.C.D.; Neto, R.P.C.; Ferreira, W.S.; Archanjo, B.S.; Curti, R.V.; Tavares, M.I.B. Effect of Ultra-Turrax on Nanocellulose Produced by Acid Hydrolysis and Modified by Nano ZnO by Sol-Gel Method. *Mater. Sci. Appl.* **2020**, *11*, 150–166. [\[CrossRef\]](#)
40. Wei, J.; Du, C.; Liu, H.; Chen, Y.; Yu, H.; Zhou, Z. Preparation and Characterization of Aldehyde-Functionalized Cellulosic Fibers through Periodate Oxidization of Bamboo Pulp. *BioResources* **2016**, *11*, 8386–8395. [\[CrossRef\]](#)

41. Mihranyan, A.; Llagostera, A.P.; Karmhag, R.; Strømme, M.; Ek, R. Moisture sorption by cellulose powders of varying crystallinity. *Int. J. Pharm.* **2004**, *269*, 433–442. [\[CrossRef\]](#)
42. Dang, X.; Liu, P.; Yang, M.; Deng, H.; Shan, Z.; Zhen, W. Production and characterization of dialdehyde cellulose through green and sustainable approach. *Cellulose* **2019**, *26*, 9503–9515. [\[CrossRef\]](#)
43. Barghamadi, M.; Barghamadi, G.; Raouf, M.; Raouf, A. Non-isothermal Cure Kinetics of Diglycidyl Ether of Bisphenol-A with Various Aromatic Diamines. *Iran. Polym. J.* **2009**, *18*, 431–443.
44. Suganthi, S.; Vignesh, S.; Kalyana Sundar, J.; Raj, V. Fabrication of PVA polymer films with improved antibacterial activity by fine-tuning via organic acids for food packaging applications. *Appl. Water Sci.* **2020**, *10*, 100. [\[CrossRef\]](#)
45. Siddaiah, T.; Ojha, P.; Kumar, N.O.G.V.R.; Ramu, C. Structural, Optical and Thermal Characterizations of PVA/MAA:EA Polyblend Films. *Mater. Res.* **2018**, *21*. [\[CrossRef\]](#)
46. dos Reis, E.F.; Campos, F.S.; Lage, A.P.; Leite, R.C.; Heneine, L.G.; Vasconcelos, W.L.; Lobato, Z.I.P.; Mansur, H.S. Synthesis and characterization of poly (vinyl alcohol) hydrogels and hybrids for rMPB70 protein adsorption. *Mater. Res.* **2006**, *9*, 185–191. [\[CrossRef\]](#)
47. Mansur, H.S.; Oréface, R.L.; Mansur, A.A.P. Characterization of poly(vinyl alcohol)/poly(ethylene glycol) hydrogels and PVA-derived hybrids by small-angle X-ray scattering and FTIR spectroscopy. *Polymer* **2004**, *45*, 7193–7202. [\[CrossRef\]](#)
48. Togrul, H. Flow properties of sugar beet pulp cellulose and intrinsic viscosity–molecular weight relationship. *Carbohydr. Polym.* **2003**, *54*, 63–71. [\[CrossRef\]](#)
49. Jia, N.; Li, S.-M.; Ma, M.-G.; Zhu, J. Synthesis and characterization of cellulose-silica composite fiber in ethanol/water mixed solvents. *BioResources* **2011**, *6*, 1186–1195.
50. Lv, P.; Almeida, G.; Perré, P. TGA-FTIR Analysis of Torrefaction of Lignocellulosic Components (cellulose, xylan, lignin) in Isothermal Conditions over a Wide Range of Time Durations. *BioResources* **2015**, *10*, 4239–4251. [\[CrossRef\]](#)
51. Zhuang, J.; Li, M.; Pu, Y.; Ragauskas, A.; Yoo, C. Observation of Potential Contaminants in Processed Biomass Using Fourier Transform Infrared Spectroscopy. *Appl. Sci.* **2020**, *10*, 4345. [\[CrossRef\]](#)
52. Nandiyanto, A.B.D.; Oktiani, R.; Ragadhita, R. How to Read and Interpret FTIR Spectroscopy of Organic Material. *Indones. J. Sci. Technol.* **2019**, *4*, 97. [\[CrossRef\]](#)
53. da Silva, A.R.P.; Macedo, T.L.; Coletta, D.J.; Feldman, S.; Pereira, M.d.M. Synthesis, characterization and cytotoxicity of Chitosan/Polyvinyl Alcohol/Bioactive Glass hybrid scaffolds obtained by lyophilization. *Matér. Rio Jan.* **2016**, *21*, 964–973. [\[CrossRef\]](#)
54. Delay, E.; Guerid, S.; Meruta, A.C. Indications and Controversies in Lipofilling for Partial Breast Reconstruction. *Clin. Plast. Surg.* **2018**, *45*, 101–110. [\[CrossRef\]](#)
55. Simonacci, F.; Bertozzi, N.; Grieco, M.P.; Grignaffini, E.; Raposio, E. Procedure, applications, and outcomes of autologous fat grafting. *Ann. Med. Surg.* **2017**, *20*, 49–60. [\[CrossRef\]](#)
56. Li, H.; Wu, B.; Mu, C.; Lin, W. Concomitant degradation in periodate oxidation of carboxymethyl cellulose. *Carbohydr. Polym.* **2011**, *84*, 881–886. [\[CrossRef\]](#)
57. Kim, U.-J.; Kuga, S.; Wada, M.; Okano, T.; Kondo, T. Periodate Oxidation of Crystalline Cellulose. *Biomacromolecules* **2000**, *1*, 488–492. [\[CrossRef\]](#) [\[PubMed\]](#)
58. Plappert, S.F.; Quraishi, S.; Pircher, N.; Mikkonen, K.S.; Veigel, S.; Klinger, K.M.; Potthast, A.; Rosenau, T.; Liebner, F.W. Transparent, Flexible, and Strong 2,3-Dialdehyde Cellulose Films with High Oxygen Barrier Properties. *Biomacromolecules* **2018**, *19*, 2969–2978. [\[CrossRef\]](#)
59. Tummalapalli, M.; Gupta, B. A UV-Vis Spectrophotometric Method for the Estimation of Aldehyde Groups in Periodate-Oxidized Polysaccharides Using 2,4-Dinitrophenyl Hydrazine. *J. Carbohydr. Chem.* **2015**, *34*, 338–348. [\[CrossRef\]](#)
60. Kim, U.-J.; Wada, M.; Kuga, S. Solubilization of dialdehyde cellulose by hot water. *Carbohydr. Polym.* **2004**, *56*, 7–10. [\[CrossRef\]](#)
61. Siller, M.; Amer, H.; Bacher, M.; Roggenstein, W.; Rosenau, T.; Potthast, A. Effects of periodate oxidation on cellulose polymorphs. *Cellulose* **2015**, *22*, 2245–2261. [\[CrossRef\]](#)
62. Sirvio, J.; Hyvakkö, U.; Liimatainen, H.; Niinimäki, J.; Hormi, O. Periodate oxidation of cellulose at elevated temperatures using metal salts as cellulose activators. *Carbohydr. Polym.* **2011**, *83*, 1293–1297. [\[CrossRef\]](#)
63. Tupin, S.; Molimard, J.; Cenizo, V.; Hoc, T.; Sohm, B.; Zahouani, H. Multiscale Approach to Characterize Mechanical Properties of Tissue Engineered Skin. *Ann. Biomed. Eng.* **2016**, *44*, 2851–2862. [\[CrossRef\]](#)
64. Münster, L.; Capáková, Z.; Fišera, M.; Kuřitka, I.; Vícha, J. Biocompatible dialdehyde cellulose/poly(vinyl alcohol) hydrogels with tunable properties. *Carbohydr. Polym.* **2019**, *218*, 333–342. [\[CrossRef\]](#) [\[PubMed\]](#)
65. Asano, S.; Ito, S.; Takahashi, K.; Furuya, K.; Kondo, M.; Sokabe, M.; Hasegawa, Y. Matrix stiffness regulates migration of human lung fibroblasts. *Physiol. Rep.* **2017**, *5*, e13281. [\[CrossRef\]](#)
66. Hadjipanayi, E.; Mudera, V.; Brown, R.A. Close dependence of fibroblast proliferation on collagen scaffold matrix stiffness. *J. Tissue Eng. Regen. Med.* **2009**, *3*, 77–84. [\[CrossRef\]](#)
67. Khan, S.; Ul-Islam, M.; Ullah, M.W.; Ikram, M.; Subhan, F.; Kim, Y.; Jang, J.H.; Yoon, S.; Park, J.K. Engineered regenerated bacterial cellulose scaffolds for application in in vitro tissue regeneration. *RSC Adv.* **2015**, *5*, 84565–84573. [\[CrossRef\]](#)
68. Mohammadi, F.; Moeni, M.; Li, C.; Boukherroub, R.; Szunerits, S. Interaction of cellulose and nitrodopamine coated superparamagnetic iron oxide nanoparticles with alpha-lactalbumin. *RSC Adv.* **2020**, *10*, 9704–9716. [\[CrossRef\]](#)

69. Orelma, H.; Filpponen, I.; Johansson, L.-S.; Laine, J.; Rojas, O.J. Modification of Cellulose Films by Adsorption of CMC and Chitosan for Controlled Attachment of Biomolecules. *Biomacromolecules* **2011**, *12*, 4311–4318. [[CrossRef](#)] [[PubMed](#)]
70. Courtenay, J.; Sharma, R.; Scott, J. Recent Advances in Modified Cellulose for Tissue Culture Applications. *Molecules* **2018**, *23*, 654. [[CrossRef](#)]
71. Roy, B.; Venkatachalapathy, S.; Ratna, P.; Wang, Y.; Jokhun, D.S.; Nagarajan, M.; Shivashankar, G.V. Laterally confined growth of cells induces nuclear reprogramming in the absence of exogenous biochemical factors. *Proc. Natl. Acad. Sci. USA* **2018**, *115*, E4741–E4750. [[CrossRef](#)]
72. Roy, B.; Yuan, L.; Lee, Y.; Bharti, A.; Mitra, A.; Shivashankar, G.V. Fibroblast rejuvenation by mechanical reprogramming and redifferentiation. *Proc. Natl. Acad. Sci. USA* **2020**, *117*, 10131–10141. [[CrossRef](#)]
73. Tronser, T.; Laromaine, A.; Roig, A.; Levkin, P.A. Bacterial Cellulose Promotes Long-Term Stemness of mESC. *ACS Appl. Mater. Interfaces* **2018**, *10*, 16260–16269. [[CrossRef](#)] [[PubMed](#)]
74. Okita, Y.; Zheng, L.; Kawanishi, K.; Miyoshi, H.; Yanagihara, K.; Kato, M. Polyvinyl alcohol scaffolds and supplementation support 3D and sphere culturing of human cancer cell lines by reducing apoptosis and promoting cellular proliferation. *Genes Cells* **2021**, *26*, 336–343. [[CrossRef](#)] [[PubMed](#)]
75. Klopffleisch, R.; Jung, F. The pathology of the foreign body reaction against biomaterials: Foreign Body Reaction to Biomaterials. *J. Biomed. Mater. Res. A* **2017**, *105*, 927–940. [[CrossRef](#)] [[PubMed](#)]
76. Ramphul, H.; Gimié, F.; Andries, J.; Jhurry, D.; Bhaw-Luximon, A. Sugar-cane bagasse cellulose-based scaffolds promote multi-cellular interactions, angiogenesis and reduce inflammation for skin tissue regeneration. *Int. J. Biol. Macromol.* **2020**, *157*, 296–310. [[CrossRef](#)] [[PubMed](#)]
77. Modulevsky, D.J.; Cuerrier, C.M.; Pelling, A.E. Biocompatibility of Subcutaneously Implanted Plant-Derived Cellulose Biomaterials. *PLoS ONE* **2016**, *11*, e0157894. [[CrossRef](#)]
78. Singh, M.; Ray, A.R.; Verma, P.V.K.; Guha, S.K. Potential Biosoluble Carriers: Biocompatibility and Biodegradability of Oxidized Cellulose. *Biomater. Med. Devices Artif. Organs* **1979**, *7*, 495–512. [[CrossRef](#)] [[PubMed](#)]
79. Kamdem Tamo, A.; Doench, I.; Morales Helguera, A.; Hoenders, D.; Walther, A.; Madrazo, A.O. Biodegradation of Crystalline Cellulose Nanofibers by Means of Enzyme Immobilized-Alginate Beads and Microparticles. *Polymers* **2020**, *12*, 1522. [[CrossRef](#)] [[PubMed](#)]

Article

Solvent-Free Production by Extrusion of Bio-Based Poly(glycerol-co-diacids) Sheets for the Development of Biocompatible and Electroconductive Elastomer Composites

Shengzhi Ji ¹, Mathilde Stricher ^{1,2} , Frédéric Nadaud ³, Erwann Guenin ¹ , Christophe Egles ^{2,†,‡} 
and Frédéric Delbecq ^{1,*,†}

¹ Université de Technologie de Compiègne, ESCOM, TIMR (Integrated Transformations of Renewable Matter), Centre de Recherche Royallieu, CS 60 319, CEDEX, 60 203 Compiègne, France

² Université de Technologie de Compiègne, CNRS, BMBI (Biomechanics and Bioengineering), Centre de Recherche Royallieu, CS 60 319, CEDEX, 60 203 Compiègne, France

³ UTC-SAPC, Rue du Docteur Schweitzer, CS 60319, CEDEX, 60 203 Compiègne, France

* Correspondence: f.delbecq@escom.fr

† These authors contributed equally to this work.

‡ Current address: Normandie Université, UNIROUEN, INSA Rouen, CNRS, PBS (UMR 6270), 55 Rue Saint-Germain, 27 000 Évreux, France.



Citation: Ji, S.; Stricher, M.; Nadaud, F.; Guenin, E.; Egles, C.; Delbecq, F. Solvent-Free Production by Extrusion of Bio-Based Poly(glycerol-co-diacids) Sheets for the Development of Biocompatible and Electroconductive Elastomer Composites. *Polymers* **2022**, *14*, 3829. <https://doi.org/10.3390/polym14183829>

Academic Editor: Shazed Aziz

Received: 18 July 2022

Accepted: 31 August 2022

Published: 13 September 2022

Publisher's Note: MDPI stays neutral with regard to jurisdictional claims in published maps and institutional affiliations.



Copyright: © 2022 by the authors. Licensee MDPI, Basel, Switzerland. This article is an open access article distributed under the terms and conditions of the Creative Commons Attribution (CC BY) license (<https://creativecommons.org/licenses/by/4.0/>).

Abstract: Faced with growing global demand for new potent, bio-based, biocompatible elastomers, the present study reports the solvent-free production of 13 pure and derived poly(glycerol-co-diacid) composite sheets exclusively using itaconic acid, sebacic acid, and 2,5-furandicarboxylic acid (FDCA) with glycerol. Herein, modified melt polycondensation and Co(II)-catalyzed polytransesterification were employed to produce all exploitable prepolymers, enabling the easy and rapid manufacturing of elastomer sheets by extrusion. Most of our samples were loaded with 4 wt% of various additives such as natural polysaccharides, synthetic polymers, and/or 25 wt% sodium chloride as porogen agents. The removal of unreacted monomers and acidic short oligomers was carried out by means of washing with NaHCO₃ aqueous solution, and pH monitoring was conducted until efficient sheet surface neutralization. For each sheet, their surface morphologies were observed by Field-emission microscopy, and DSC was used to confirm their amorphous nature and the impact of the introduction of every additive. The chemical constitution of the materials was monitored by FTIR. Then, cytotoxicity tests were performed for six of our most promising candidates. Finally, we achieved the production of two different types of extrusion-made PGS elastomers loaded with 10 wt% PANI particulates and 4 wt% microcrystalline cellulose for adding potential electroconductivity and stability to the material, respectively. In a preliminary experiment, we showed the effectiveness of these materials as performant, time-dependent electric pH sensors when immersed in a persistent HCl atmosphere.

Keywords: bio-based elastomers; twin-screw extrusion; composite bioplastic; high processability; flexible atmospheric pH sensor

1. Introduction

Today, a great number of biodegradable poly(glycerol-co-diacids) are synthesized for various applications, especially in the biomedical fields, e.g., as cellular scaffolds to rebuild damaged tissues (e.g., cartilage, bone, nerve, or epithelial tissue), or as wound dressings [1,2]. These properties are enabled by biological recognition, enhanced cell adhesion, suitable mechanical properties, and tailored degradation kinetics. These polymers are generally formed through a typical melt polycondensation method involving the hydroxyl groups of glycerol subunits that can react with the carboxylic acid groups of diacid monomers to form successive and stable ester functions along the polymer backbone.

Thus, a large variety of commercially available diacids contribute to the production of many polyesters, such as saturated or unsaturated aliphatic diacids (e.g., succinic acid, maleic acid, dodecanoic acid [3], etc.), petro-sourced terephthalic acid, and its bio-based counterpart FDCA [4].

Among these poly(glycerol-co-diacid) elastomers, poly(glycerol sebacate) (PGS) is now recognized for its remarkable cytocompatibility (in the myocardium [5], arteries [6], bone [7], and cartilage [8]) and physicochemical properties [9]. It has been studied as a surgical sealant and tissue adhesive, useful to promote the regeneration of blood vessels, retinas, and nervous tissues [10]. It can be also employed as a drug delivery system (DDS) or surgical sealant when loaded with bioactive compounds [11] or various chemicals [12]. Compared to other poly(glycerol-co-diacids), PGS expresses a shorter *in vivo* degradation period of up to 60 days. Furthermore, PGS composites with the addition of various fillers, such as proteins (e.g., gelatin [13], zein [14], silk [15], elastin [16]), polysaccharides (e.g., chitosan [17], cellulose [18]), synthetic polymers (e.g., polycaprolactone [19], polyvinylpyrrolidone [20], polyethylene oxide [21]), and inorganic species (e.g., TiO₂ [22], β -tricalcium phosphate [23], Bioglass® [24], SiO₂ NPs [25], CaTiO₃ ceramic [26], nano-hydroxyapatite [27], halloysite nanotubes [28], carbon nanotubes [29]), show enhanced performances, including better mechanical properties, hydrophilicity, adhesiveness, and biocompatibility. Many works have even reported the use of electrospinning to organize biocompatible scaffolds of PGS composites for tissue engineering or other applications in the field of biomedicine [30,31]. As a second challenge, rapid production of PGS-based flexible sensors has begun to receive considerable attention [32–34]. In fact, to ensure continuous monitoring of human health, for various purposes, it is important to furnish wearable electronics, such as electronic skin and neuronal implants, made of inert biocompatible polyesters [35] coupled with an electroconductive polymer such as polypyrrole [36] to avoid undesired inflammation in living organisms.

To obtain PGS scaffolds, two distinct stages are usually required: first the preparation of prepolymers, followed by thermal curing to provide a crosslinked insoluble polymer. Many studies report that a melted homogeneous solution of sebacic acid (SA) and glycerol must be stirred under an inert atmosphere in a temperature range between 120 and 140 °C for a maximum period of four days [37–41]. Recently, some studies have shown the influence of the atmosphere of the prepolymerization on the overall properties of the resulting PGS [42]. It has also been proven that the reaction time can be shortened down to few minutes when the mixture is heated under microwave irradiation [43–45]. This step affords a stable prepolymer as a brittle opaque wax that is very soluble in polar solvents with low boiling points such as tetrahydrofuran (THF), acetone, or methanol, which can be stored in a refrigerator to prevent their slow degradation. The next steps of polyester synthesis include, first, the introduction of an organic solution of the prepolymer in a mold, followed by the removal of the solvent in a vacuum before proceeding to the thermal curing. Finally, PGS is obtained as a stretchable and adhesive elastomer, sometimes displaying shape-memory ability. These properties are directly connected to the creation of internal hydrogen bond networks by the remaining free hydroxyl groups of the glycerol subunits, along with its relative high temperature sensitivity.

In this work, our strategy initially focused on the development of new and well-known pure biosourced poly(glycerol-co-diacids) and their composite materials. As illustrated in Figure 1, the initial pathway involved the preparation of each prepolymer under heating (conventional or microwave) prior to treatment in a twin-screw extruder. To the best of our knowledge, only one article has previously reported the successful use of a twin-screw extruder to produce PGS composite sheets that display shape-memory potential [23].

All elastomers and PGS composites were obtained as quite transparent or almost translucent sheets, and were studied for their physicochemical properties, pH profiles in aqueous solutions, and biocompatibility. PGS loaded with a slight amount of an electroconductive system (polystyrene sulfonate-poly (3,4-ethylenedioxythiophene) (PSSNa-PEDOT)) or a single polymer (polyaniline (PANI)) were also produced in the same manner. In sum-

mary, we intended to develop new and remarkable stimulus-sensitive electroconductive bio-based sensors with improved performance over time.

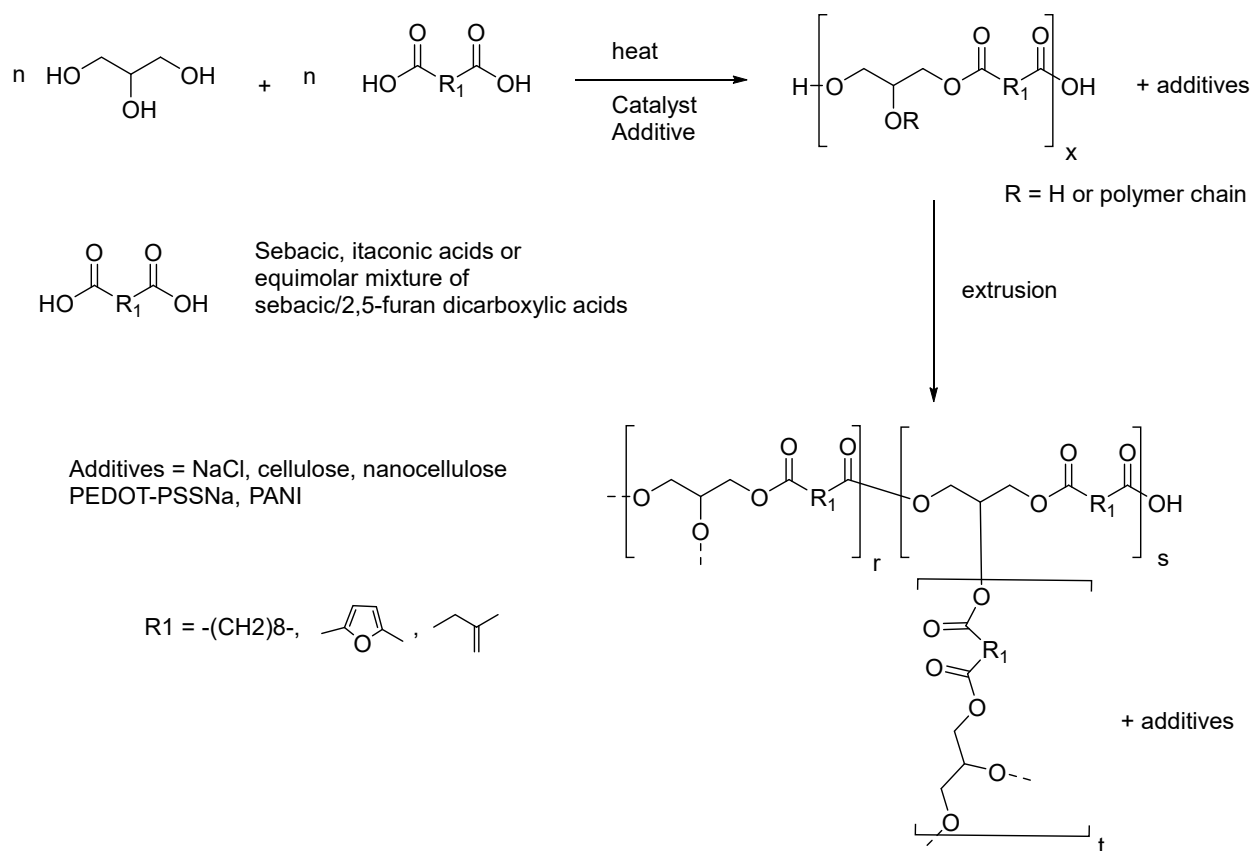


Figure 1. General procedure for the production of all composite elastomers.

2. Materials and Methods

2.1. Materials

All chemicals were used as received, without further purification. Itaconic acid (99%) (IA), sodium chloride (NaCl), potassium persulfate (KPS or $\text{K}_2\text{S}_2\text{O}_8$), extra-pure aniline (99.5%), cobalt(II) acetate tetrahydrate ($\text{Co}(\text{Ac})_2 \cdot 4 \text{H}_2\text{O}$ (98%), poly(sodium-p-styrenesulfonate) (PSSNa) with a molecular weight of 70,000, and 3,4-ethylenedioxythiophene (97%) (EDOT) were purchased from Acros Organics (Geel, Belgium). Sebacic acid (98+%), microcrystalline cellulose, Pluronic[®] F-127, furan-2,5-dicarboxylic acid (FDCA 98%), p-toluene sulfonic acid monohydrate (p-tsOH or PTSA), glycerol (reagent plus >99% GC), and lithium perchlorate ($\text{LiClO}_4 \geq 95\%$) were obtained from Alfa Aesar (Tewksbury, MA, USA) and Sigma-Aldrich (St. Louis, MO, USA). The water used in all experiments was Millipore Milli-Q grade (Burlington, MA, USA).

2.2. Preparation of Polyester-Based Elastomers

All elastomeric extrudable materials were synthesized according to the following method: Equimolar amounts of a chosen diacid (I: itaconic or S: sebacic acids) or a mixture of two different diacids (FS: equimolar mixture of furan dicarboxylic and sebacic acids) were introduced to a 100 mL flask (total = 60.0 mmol) in the presence of 5.6 g (60.0 mmol) of glycerol. In some cases, glycerol could be loaded with 4 wt% of a selected additive and/or 25 wt% NaCl. After the addition of 0.01 g (0.05 mmol) of PTSA, the resulting dispersion was heated under an inert atmosphere in a range of temperatures from 150 to 160 °C until the mixture turned into a homogeneous solution. The stirring continued for up to three hours until a crosslinked elastomer was formed.

In the case of prepolymer synthesis assisted by microwave irradiation, all materials were introduced in the same quantities in a dedicated 30 mL vial closed with a septum. The reaction was conducted by using a microwave heating apparatus (Anton Paar Monowave 300, Anton Paar, Graz, Austria) under magnetic stirring (600 rpm) for the desired conditions of time and temperature, usually heated at 160 °C for 5–15 min.

Melt polytransesterification was carried out by means of conventional heating [46]. To obtain a robust elastomer, 5.6 g (60 mmol) of glycerol or a 4–10 wt% glycerol dispersion of one or two additives was first heated up in the presence of 1 equivalent of a dimethyl diacid ester obtained by esterification of their corresponding acids, as reported in the literature [47–49]. Then, 0.6 g of $\text{Co}(\text{Ac})_2 \cdot 4 \text{H}_2\text{O}$ was added to the melted solution, and the solvent-free mixture was stirred in neat condition at 160 °C for a minimum of three hours under an inert gas stream. The reaction was stopped when the agitation started to become difficult, leading to the formation of a crosslinked and colored elastomer ready for the extrusion process.

The progress of these above procedures was monitored by nuclear magnetic resonance (^1H NMR) spectra recorded on a Bruker Avance III 400 spectrometer (Bruker, Billerica, MA, USA), using DMSO-d_6 as solvent. Only prepolymers of Poly(glycerol-co-itaconate) (PGI) and Poly(glycerol-co-2,5-furandicarboxylate-co-sebacate) (PGFS) were studied, and their chemical shifts (δ) are quoted in parts per million (ppm). The coupling constants are quoted in Hz. For the PGS prepolymers, their ^1H NMR spectra corroborate those found in the literature [50].

2.3. Extrusion of PGI, PGS, PGFS, and PGS Composites

A lab-scaled HAAKE MiniLab 3 (Thermo Scientific, Waltham, MA, USA) twin-screw extruder was employed to obtain molded elastomer sheets of 80 mm length, 20 mm width, and 1.5 mm thickness. The samples were obtained through a recirculation of the prepolymer inside the apparatus. The screw length of the extruder was 110 mm, and for each experiment, 4–5 g of a chosen prepolymer was extruded as follows: The extruder chamber was filled partwise with small fractions cut from each prepolymer as a starting material. Controlling the torque and the inner pressure, the feeding of the extruder took 5 min on average, and the chamber temperature set points ranged from 50 °C to the final temperature of 180 °C. The screw speed was also set to a maximum value of 200 rpm, and the extrusion took about 20 min to be achieved.

2.4. Removal of Unreacted Monomers and Surface pH Monitoring

In order to remove unreacted acidic monomers and short oligomers, and also to neutralize the surface of the bioplastic sheets, each sample was introduced to 100 mL of a saturated sodium hydrogen carbonate (NaHCO_3) aqueous solution for a period of 24–48 h. Then, the samples were transferred into deionized water to ensure the constant pH neutrality of the surrounding medium, and dried in vacuum prior to the subsequent analysis.

2.5. Fourier-Transform Infrared (FTIR)

The FTIR (ATR) spectra of the pure and composite polyesters were recorded on a Nicolet iS5 FTIR (Thermo Scientific) spectrometer in the range of 400 to 4000 cm^{-1} , operated at 4 cm^{-1} resolution and equipped with an ATR plate including a ZnSe crystal.

2.6. Field-Emission Scanning Electron Microscopy (FE-SEM)

The observations of the elastomer surfaces were conducted using a Quanta FEG 250 (FEI, Hillsboro, OR, USA) microscope with a small fragment of each elastomer deposited on a carbon-coated Pd-Pt grid and dried for 1 h under reduced pressure. The SEM micrographs were acquired in secondary electron mode, and were obtained under a low vacuum, 15 kV accelerating voltage, and 10 mm working distance.

2.7. Differential Scanning Calorimetry (DSC)

Experiments were conducted on a DSC 8 MC (Mettler Toledo, Giessen, Germany) using aluminum pans. Scans were conducted under nitrogen at a heating rate of 10 °C/min, in a temperature range varying between 0 and 250 °C.

2.8. Production of Electroconductive Polymer Glycerol Solutions

For PSSNa-PEDOT, 0.32 g of PSSNa and 0.48 g (3.36 mmol) of EDOT were added successively to 5.6 g (60.0 mmol) of glycerol. Under an inert atmosphere, a slight amount of KPS (0.04 g; 0.25 mmol) was added to the clear solution, and the resulting mixture was stirred for 1 h at 130 °C until the mixture turned dark blue. The procedure was scalable and employed without further purification in the preparation of the prepolymers by polycondensation, as described in Section 2.2. Then, the resulting composite material was loaded with PSSNa-PEDOT at a concentration near to 4 wt%.

For the 4 wt% PANI glycerol solution, we employed a modified procedure [51]. In 5.6 g of glycerol, 0.31 g (3.38 mmol) of aniline dispersion was vigorously stirred during the addition of 0.04 g (0.15 mmol) of KPS. Then, the mixture was also stirred at 130 °C for 4 h to afford a dark brown solution of PANI particles. A 10 wt% PANI solution was obtained by the same manner. On the other hand, a 10 wt% emeraldine PANI glycerol dispersion with better electroconductive performance was prepared as follows: 2.5 g (9.25 mmol) of KPS dissolved in 100 mL of distilled water was added dropwise to 100 mL of 1.0 M HCl aqueous solution containing 2.5 mL (2.55 g; 27.4 mmol) of fresh aniline, under stirring at room temperature. On the next day, the dark blue/green dispersion was filtered to remove short, water-soluble oligomers of PANI, washed with clean water, and the desired emeraldine PANI was recovered as a green solid. The material was then dried in vacuum, and 0.56 g of the solid was introduced to 5.1 g of glycerol to obtain a 10 wt% PANI dispersion that could provide a solution at temperatures above 150 °C, especially in the presence of a diacid monomer.

2.9. Electroconductivity and pH Sensitivity Study of PANI Conductive Polymer Blends

Two kinds of PGS–10 wt% PANI composite sheets (PGS8 and 9) were successively tested for their conductivity and pH sensitivity according this two-step procedure: First, a selected polymer sheet was connected by both of its extremities in series between a generator and a potentiometer (Leybold®, Hurth, Germany). Rapidly, the elastomer band was introduced to a beaker filled with 20 mL of 37% HCl aqueous solution and closed with aluminum foil. During the measurement, all direct contact with the acidic solution was strictly avoided. The generator delivered a current at a voltage between 15 and 20 volts, and the evolution of the current circulating in the plastic sheet was read directly on the screen of the potentiometer as a function of time.

In parallel, to corroborate our results, cyclic voltammetry (CV) measurements were also conducted after having performed the above pH sensitivity study using a three-electrode system on Metrohm Autolab PGSTAT101 (Metrohm Autolab, Utrecht, Netherlands) monitored using the NOVA software (Chongqing, China). This procedure involved a platinum wire as the counter electrode, a saturated calomel electrode (SCE) as the reference electrode, and PANI elastomer blend PGS8 or 9 as the working electrode. A 0.1 M LiClO₄ aqueous solution was used as the electrolyte, and the CV curves were recorded at scan rates of 100 mV·s^{−1} for a variation of potential found between −2.0 and +2.0 V.

3. Results and Discussion

3.1. Optimization of Prepolymer Synthesis and Extrusion Process

Prepolymers were prepared by mixing diacids with glycerol in the presence of a catalytic amount of paratoluene sulfonic acid (p-TSA). Adding a slight amount of PTSA to the mixture of monomers increased the polycondensation rate and, under conventional heating at 150–160 °C, the reaction time was reduced to a few hours, without apparent degradation of the material. The polycondensation procedure led to the formation of

linear or branched polymer backbones (Figure 2) due to the branching unit nature (B3) of glycerol compared to the linear structure (A2) of the diacids. In the A2 + B3 system, usually performed in bulk conditions for greater conversion of all monomers engaged in the reaction, the thermoset behavior of the material evolved closely with the increasing number of the ester functions.

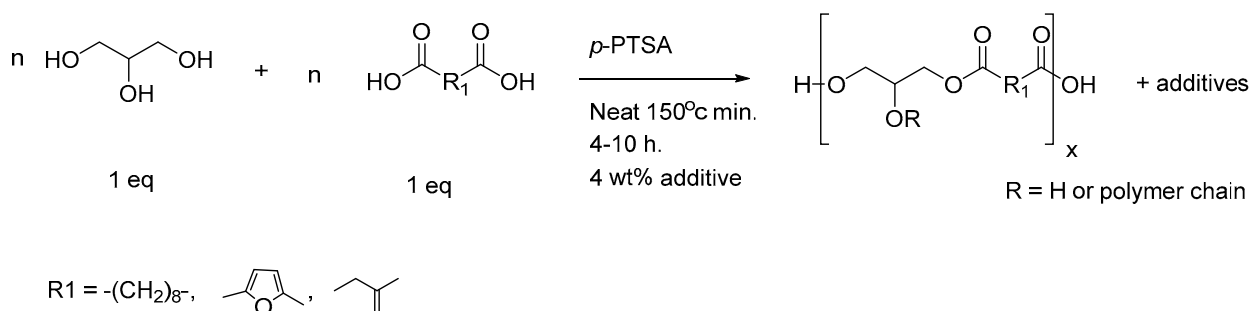


Figure 2. Modified synthetic pathway for producing poly(glycerol-co-diacids) composites (R = hydrogen or polymer chain).

Several prepolymers were produced under conventional heating. For pre-PGI and pre-PGS, glycerol and diacid monomers were mixed at a ratio of 1:1; in the case of pre-PGFS, the ratio was set up at 1:0.5:0.5. To form prepolymers with additives, prior to the polycondensation process, 4 wt% of a selected polysaccharide (e.g., flaxseed gum, micro/nanocellulose, almond gum) in a defined volume of glycerol (results not shown here) was added to the formulation. At this concentration, each biopolymer was almost soluble in the hot liquid.

According to the SEM observations of the surfaces' morphologies, each additive showed a particular influence on the reticulated networks of the materials, which were often covered with holes and fractures (Figure S1, see Supplementary Materials).

Then, the same process was repeated for inorganic species such as graphene oxide (GO) or NaCl; the solids remained dispersed in the glycerol itself prior to the prepolymer synthesis. The synthesis of the electroconductive additives PSSNa:PEDOT and PANI is described in the Materials and Methods, and the preparation of the prepolymers was performed in the same manner as that of the other additives. The different prepared samples are listed in Table 1.

Table 1. List of prepolymers, describing their appearances and modes of production.

Entry	Additive (4 wt%)	Temp (°C)	Original Characteristics
Pre-PGI1	-	160	Not sticky, elastic
Pre-PGI2	-	150	Not sticky, elastic, translucent
Pre-PGS1	-	160	Sticky, soft, translucent
Pre-PGS2	NaCl ¹	160	Sticky, brown, soft, translucent
Pre-PGS3	Microcrystalline cellulose	150	Not sticky, soft, translucent
Pre-PGS4	Nanocellulose	150	Sticky, soft, translucent
Pre-PGS5	Pluronic® F127	150	Sticky, soft, translucent
Pre-PGS6	PSSNa-PEDOT ²	150	Sticky, rigid, dark blue
Pre-PGS7	PANI ²	150	Sticky, dark brown
Pre-PGFS1	-	150	Sticky, elastic, white
Pre-PGFS1	NaCl ¹	150	Sticky, elastic, cream

¹ NaCl added to the bulk as a porogen agent at 25 wt% concentration. ² Electroconductive polymers synthesized from their respective monomers (EDOT or aniline) in glycerol, in the presence of KPS, prior to polycondensation.

For all of the prepolymers, the control of the temperature was necessary. For example, for pre-PGI1, the mixture was initially heated at 160 °C, and the reaction required 4 h to produce the desired prepolymer. For the pre-PGI2 prepolymer, by reducing the temperature to 150 °C, the reaction rate was reduced, requiring 10 h on average to form a material similar to pre-PGI1. Compared to SA, itaconic acid (IA) could provide the elastomer with some additional properties, especially due to the existence of a double bond suitable to create an anchor point that could allow post-functionalizations such as grafting of biomolecules. Secondly, to date, there is no example in the literature of poly(glycerol-co-diacids) involving IA as a co-monomer subunit, although other types of polyesters have been prepared [52–54].

For pre-PGS 1–6, when 4 wt% of an external component was added to the bulk reaction, each polycondensation needed a minimum of 8 h to produce a robust prepolymer. Moreover, the pre-PGS7 prepolymer loaded with 4 wt% nitrogen-rich PANI could generate interactions between nitrogen atoms and the carboxylic acid functions of the monomers, reducing the total amount of protons available for the polycondensation mechanism.

A series of terpolymers or poly(glycerol-2,5-furan dicarboxylate-co-sebacate) (PGFS) was also developed. PGFS is an elastomer made of glycerol, SA, and FDCA mixed at various ratios. By gradually replacing a percentage of SA with its FDCA counterpart in the polymer backbone, new and interesting material properties appeared, evolving from a soft and weak elastomer to a more elastic and sticky material (Figure S2, see Supplementary Materials). For our extrusion procedure, we focused on prepolymers at a ratio of 1:05:05 (pre-PGFS1), forming a very sticky and white paste. A second prepolymer—pre-PGFS2, loaded with 25 wt% NaCl—was also produced.

As has already been proven, that reaction time could be shortened down to a few minutes when microwave irradiation was used as a heating source [42,44,45]; the same prepolymer preparations were thus conducted under microwave irradiation. The production of poly(glycerol itaconate) (pre-PGI) prepolymers was carried out under microwave heating using an equimolar mixture of glycerol and IA stirred at 160 °C in the presence of traces of PTSA. Even by shortening the reaction time from 15 to 5 min, the transparent, originally liquid prepolymer quickly became rigid, rubbery, and difficult to recover from the glassware, and could not be used for the next step of the extrusion. On the other hand, using the same above conditions, with a slight amount of PTSA, under microwave irradiation, PGS prepolymers (pre-PGS) were formed as the typical white wax currently described in the literature (Figure S3, see Supplementary Materials).

3.2. Extrusion of PGI, PGS, PGFS, and PGS Composites

In the next stage of our study, all previous prepolymers produced by conventional heating and reported in Table 1 were extruded. A lab-scaled twin-screw extruder was employed to obtain molded elastomer sheets by adding the prepolymers to the chamber. The chamber temperature increased from 50 to 180 °C. The mixture was recirculated in the extruder chamber, and stable sheets were isolated. The results are shown in Figure 3:

As depicted in Figure 3, depending on the nature of each additive, clear variations in the sheet translucency and color were noticed. For PGI1 and 2, both materials were not sticky, but only PGI1 was almost translucent. However, except for PGS3, which contained 4 wt% microcrystalline cellulose, all elastomers were able to adhere to glassware or other types of smooth surface. Prepolymers of PGS heated at 150 °C during their synthesis generated slightly colored and translucent materials. Some degree of translucency was observed with Pluronic® F-127 for PGS2 and PGFS2. The addition of NaCl seriously affected the structure of the isolated sheets. Conversely, once inert additives were replaced with 4 wt% of very colorful components such as the electroconductive polymers PEDOT or PANI, the resulting samples of PGS6 and 7 turned into deep blue and dark brown sheets, respectively. The color was uniformly dispersed in the network.

On the other hand, when using prepolymers prepared by microwave irradiation, despite our efforts, the pre-PGS wax only melted in the recirculating extruder chamber, and never produced the desired PGS sheets after 2 h of circulation time.



Figure 3. Photographs of elastomer sheets obtained by extrusion of their prepolymers when driven by the twin screws at a speed of 200 rpm and heated at 180 °C.

3.3. FE-SEM Observations and Spectroscopic Analysis

As depicted in Figure 4, each sheet showed a specific and different surface based on the nature and amount of the additives included over the entire thickness of their networks. PGI1's surface was not regular, showing a lot of deformations and short fractures. The result was similar for PGI2. PGS1 showed a sharper microrelief. PGS2 demonstrated small and visible geometric cavities purposely generated by the addition of NaCl as a porogen agent. For PGS3 and PGS4, the addition of any kind of cellulose had a good impact on the surface homogeneity, due to the additional ester functions created between the hydroxyl groups of the polysaccharides and the carboxylic acid groups of SA [55]. Interestingly, for PGS5, the same phenomenon occurred. By adding 4 wt% Pluronic® to the prepolymer, even with an enlarged view (Figure S4, see Supplementary Materials), neither fractures nor defects were detected on the surface of the elastomer. According to its polyether nature, it was also possible to stabilize the inner polymer matrix by means of a successive and strong hydrogen bond network promoted by the Pluronic's ether functions and accessible hydroxyl groups.

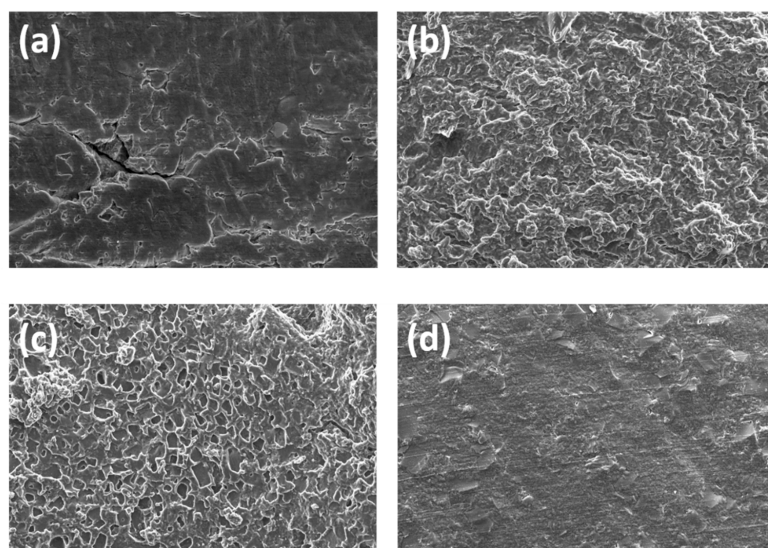


Figure 4. Photographs of elastomer sheets' surfaces by FE-SEM observations: (a) PGI1; (b) PGS1; (c) PGS2; (d) PGS3. Scale bars = 400 μm .

PGS6 and 7, with the incorporation of a slight amount of PSSNa/PEDOT or PANI, respectively, showed a clear impact on their surface morphologies. PGS6 was layered, displaying some parallel arrays, while PGS7 showed a much more wrinkled and sinuous aspect. In the zoomed view shown in Figure 5a, the PGS7 sheet surface displays deep cavities that should be interconnected without the use of a leachable porogen agent such as NaCl. The shape of the surface is influenced by the multiple evident ionic interactions permitted by the nitrogen-rich nature of PANI and the carboxylic acid functions of the oligomers contained within the elastomer.

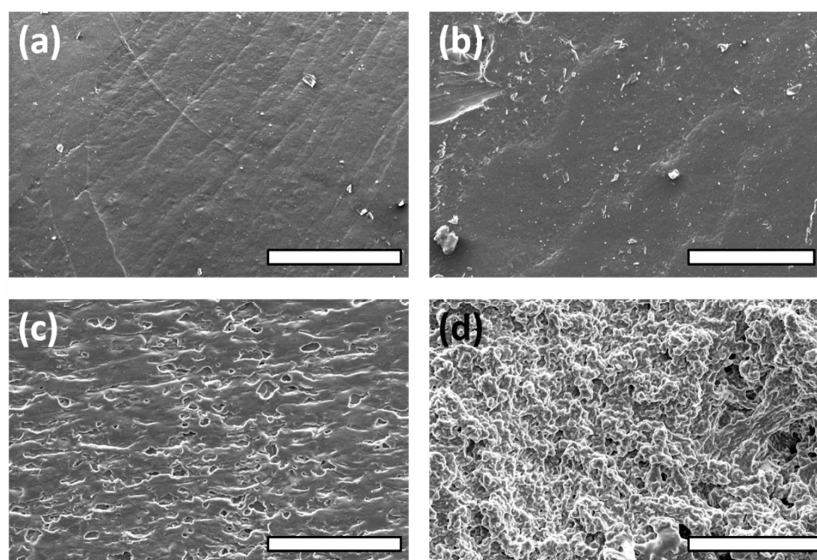


Figure 5. Photographs of elastomer sheets' surfaces by FE-SEM observations: (a) PGS4; (b) PGS5; (c) PGS6; (d) PGS7. Scale bars = 400 μm .

In Figure 6, PGFS1 shows a smooth surface. As we suspected, the extrusion of PGFS2 loaded with NaCl as a porogen failed to produce a porous surface like that of PGS2, due to its excessive plasticity.

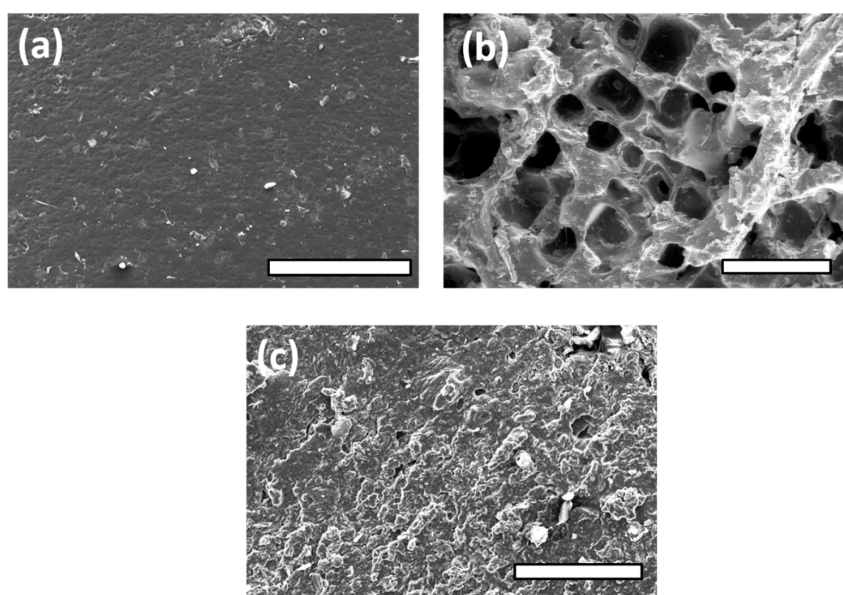


Figure 6. Photographs of elastomer sheets' surfaces by FE-SEM observations: (a) PGFS1; (b) PGFS2 (prepolymer after leaching of NaCl in deionized water); (c) PGFS2 (after extrusion process). Scale bars = 400 μm for (a,c), and 1 mm for (b).

From a molecular point of view, the FTIR analyses provided in Figures 7 and 8 constitute an important source of information about the overall integrity and crosslinking mechanisms involved in the synthesized materials—especially following the extrusion treatment. In Figure 7, both PGI1 and 2 show four characteristic bands at 3300, 2900, 1740, and 1150 cm^{-1} , representative of -OH stretching, alkane or CH_2 moieties, C=O stretching, and C-O of ester function, respectively. Two additional signals corresponding to CH=CH_2 stretching appeared at 819 and 1638 cm^{-1} . Furthermore, a medium band located at 3400 cm^{-1} suggested moderate hydrogen bond networks between free hydroxyl groups of the materials. PGFS1 and 2 demonstrated the persistence of bands from carboxylic groups currently observed at 1410 cm^{-1} —a situation that could explain the subsequent strong acidic nature of the material. In these spectra, three bands found at 764, 832, and 963 cm^{-1} were observed, corresponding to mono- and disubstituted furan rings. In addition, the ^1H NMR chart of the prepolymers of pre-PGFS showed too much variety of signals found between 7 and 8 ppm, which could represent the imperfect involvement of FDCA in the polymer backbone [46].

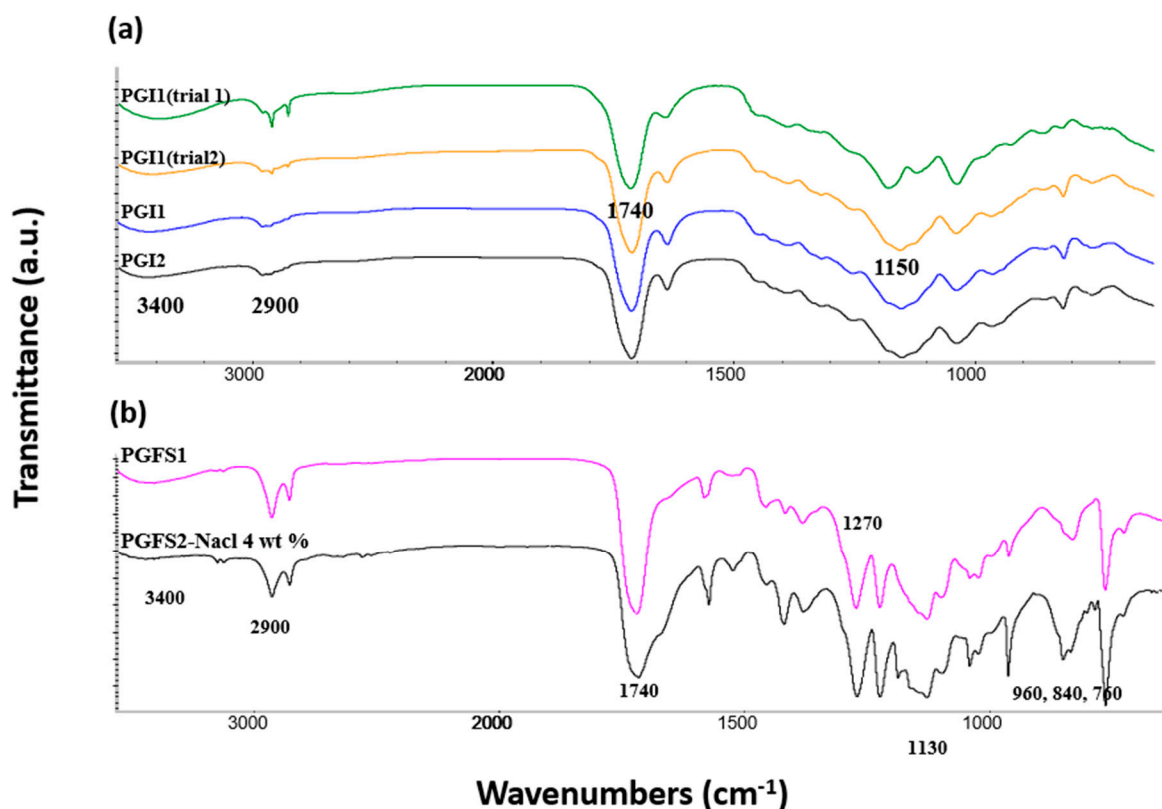


Figure 7. Infrared spectra of elastomer sheets: (a) for PGI 1 and 2 (and from prepolymers obtained under microwave irradiation); (b) for PGFS1 and 2.

In Figure 8, PGS1–7 demonstrate two distinct bands attributed to alkane groups and located in the range between 2850 and 2920 cm^{-1} . Except for PGS6, all ester functions appeared as a single vibration band. Compared to these bands, the weakness of the -OH band is a consequence of a high esterification degree (ED), which must have been reinforced during the extrusion process. Moreover, at 4 wt% concentration of all additives, the FTIR detector was not sensitive enough to detect their presence through their characteristic peaks. We must note that the extrusion process is perfectly repeatable, as the FTIR signals emitted by different samples extruded from the same prepolymers were perfectly identical.

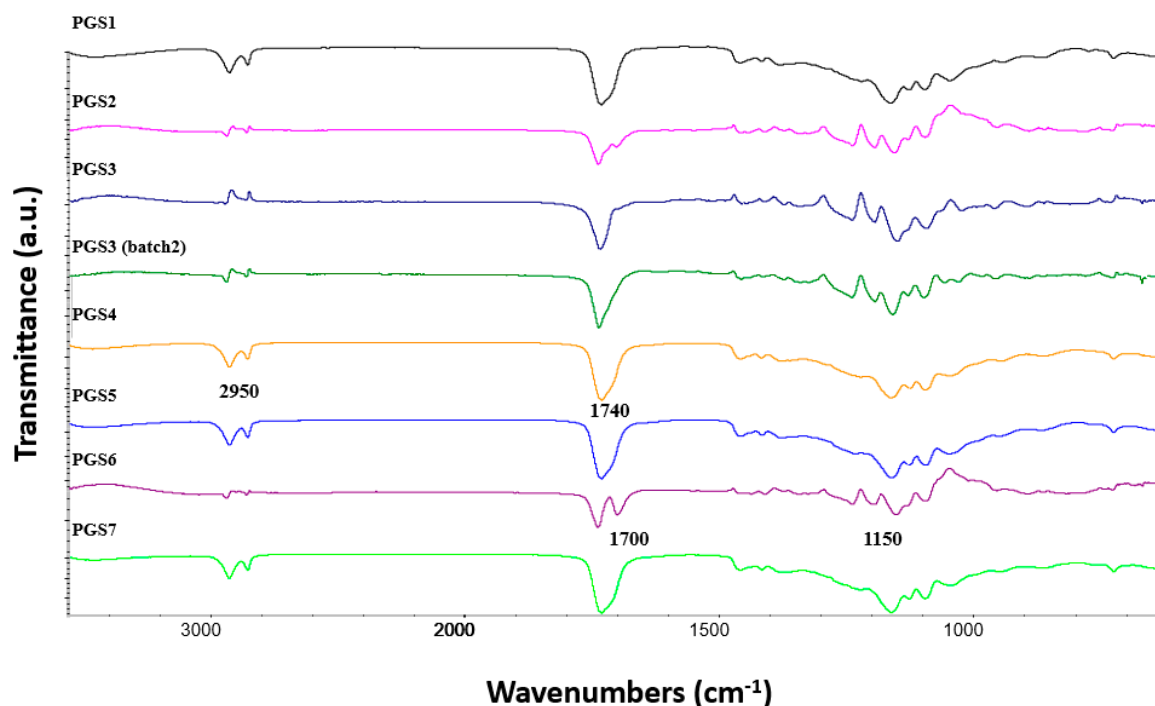


Figure 8. Infrared spectra of elastomer sheets from PGS1 to PGS7.

3.4. Calorimetry and pH Monitoring of the Materials

All results of the DSC analysis of each elastomer sheet produced by extrusion are reported in Table 2. For the most representative samples, the results of the measurements were all reported in the Figures S7–S9 (see Supplementary Materials).

Table 2. DSC results of PGI1 and 2, PGFS1 and 2, and PGS1–7.

Event (°C)	PGI1	PGI2	PGFS1	PGFS2	PGS1	PGS2	PGS3	PGS4	PGS5	PGS6	PGS7
Tm1		55			37		16	35	9	6	11
Tm2		83						74	38	36	
Ttc	177	136	190	56	141	124	128	130	183	241	

With Tm1 and Tm2 as melting temperatures; Ttc as temperature of thermal crosslinking.

For the PGI1 sheet, due to the higher temperature of 160 °C employed for the preparation of its corresponding prepolymer precursor, only a crystallization exotherm was recorded at 177 °C, corroborating its supposed advanced level of reticulation compared to PGI2. Thus, PGI2 is clearly more amorphous than PGI1, with two successive melting bands of Tm found at 55 and 83 °C. More specifically, Tm1 corresponds to the departure of entrapped molecules of water, while Tm2 is representative of the internal hydrogen bond networks inside the elastomer sheets. The lower Ttc of 136 °C could also confirm the lower ED, explained by the lower temperature applied during the prepolymer preparation, despite the superior temperature of 180 °C that is usually necessary for generating the elastomer sheets. For PGFS1, only a superior Ttc of 190 °C was detected, and its value was seriously reduced to 56 °C due to the presence of a great amount of NaCl inside the network of PGFS2. We can assume that when NaCl is added to a solid polymer, the salt can act as a nucleating agent, reducing the normal value of Ttc. On the other hand, PGS1 gave typical values of both Tm and Ttc, found at 37 and 141 °C, respectively. In PGS2, the presence of the NaCl once again had the same effect already observed for PGFS2, reducing the initial value of Ttc to 124 °C. The addition of 4 wt% microcellulose in PGS3 allowed the temperature of both events to be reduced by 10 °C. With nanocellulose, we did not observe

exactly the same incidence, and compared to PGS1 another T_m was detected at 74 °C. PGS4, 5, and 6 showed three distinct events, including two T_m s and one T_{tc} . All materials showed a principal value of T_m varying around 38 °C. For PGS5 and 6, T_m values lower than 10 °C could correspond to the cleavage of weak interactions between the polymeric additives and the polymer covalent network. Furthermore, the introduction of a slight amount of Pluronic or PSSNa/PEDOT to the elastomer delayed the reticulation phenomenon of the material at higher temperatures. For PGS7, the presence of a nitrogen-rich polymer prevented possible undesired degradation at working temperatures between 140 and 250 °C.

3.5. Alternative Polytransesterification for the Production of Non-Acidic Sheets

For the purpose of biological studies, sheets with neutral surfaces were needed. Therefore, the materials were neutralized while removing entrapped and unreacted acidic monomers by immersing each elastomer sheet in a saturated NaHCO_3 water bath. Unfortunately, PGI1 and 2 were subject to rapid degradation. On the other hand, PGFS1 and 2 continued to express corrosive behavior by releasing acidic monomers or shorter water-soluble oligomers, despite repeated washing. PGS1–7 released their remaining acidic fragments after a period of 8 days when immersed in pure water. In all cases, no swelling phenomena were observed.

Thus, to solve the degradation problems encountered with PGI1 and 2 during the monomer extraction in a basic medium, and to suppress the excessive acidity of PGFS1 and 2, another method was developed to produce these materials. Our group has already developed a mild method for producing poly(glycerol-co-diacids) directly from a mixture of glycerol and a dimethyl ester by melt polytransesterification in the presence of a cobalt(II) salt [46]. Therefore, exploitable prepolymers decorated only with ester functions were prepared, as depicted in the Figure 9. Simultaneously, we intended to evaluate the real impact of the introduction of 4 wt% PANI in the PGS sheets—especially on their surface morphology.

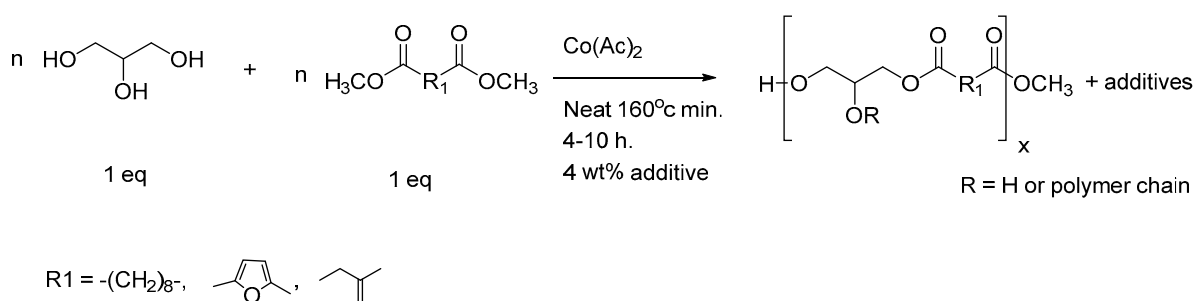


Figure 9. Alternative pathway to access to ester-functionalized prepolymers.

Thus, three further sheets were produced from dimethyl itaconate, 2,5-furandicarboxylate, and sebacate, listed as PGI-Co and PGS7-Co when containing 4 wt% PANI, and PGFS-Co when loaded with 25 wt% NaCl. All prepolymers were extruded using the unchanged previous conditions of a final temperature of 180 °C and a screw rotation speed of 200 rpm. As illustrated in Figure 10, except for PGFS-Co, two sturdy and purple sheets were easily recovered from the apparatus and immersed in deionized water. A rapid discoloration of the sheets was observed, as depicted in Figure 10.

For PGI-Co and PGS7-Co, because the pH of their washing water remained neutral, PGI-Co was subjected to some swelling despite the supposed pronounced hydrophobic character of the ester-functionalized sheet. For PGFS-Co, the material remained strongly acidic. The SEM observations shown in Figure 10 indicate the good homogeneity of the surfaces but, once again, the strong sticky character of PGFS prevented the creation of holes in the network. To confirm the potential of our polytransesterification process, the FTIR results were compared with those of the elastomer counterparts obtained via melt polycondensation (Figure 10b), and showed no clear differences in their global composition.

These materials seemed to be suitable for use in the next stage, i.e., the cytotoxicity tests. For further details of the procedure, see the ESI results.

As shown in Figure 10d, only elastomers produced by the classic melt polycondensation method expressed good cytocompatibility. Details of the cytotoxicity tests can be found in the ESI results. It is easy to imagine that cobalt traces could demonstrate toxicity against L929 cell lines under the ISO10993 standard protocol. On the other hand, the neutral polymer sheets of PGS3, 6, and 7, as expected, showed better cytocompatibility. The presence of 4 wt% of an electroconductive polymer caused moderate cytotoxicity and a bad impact on the general biocompatibility of these materials [56].

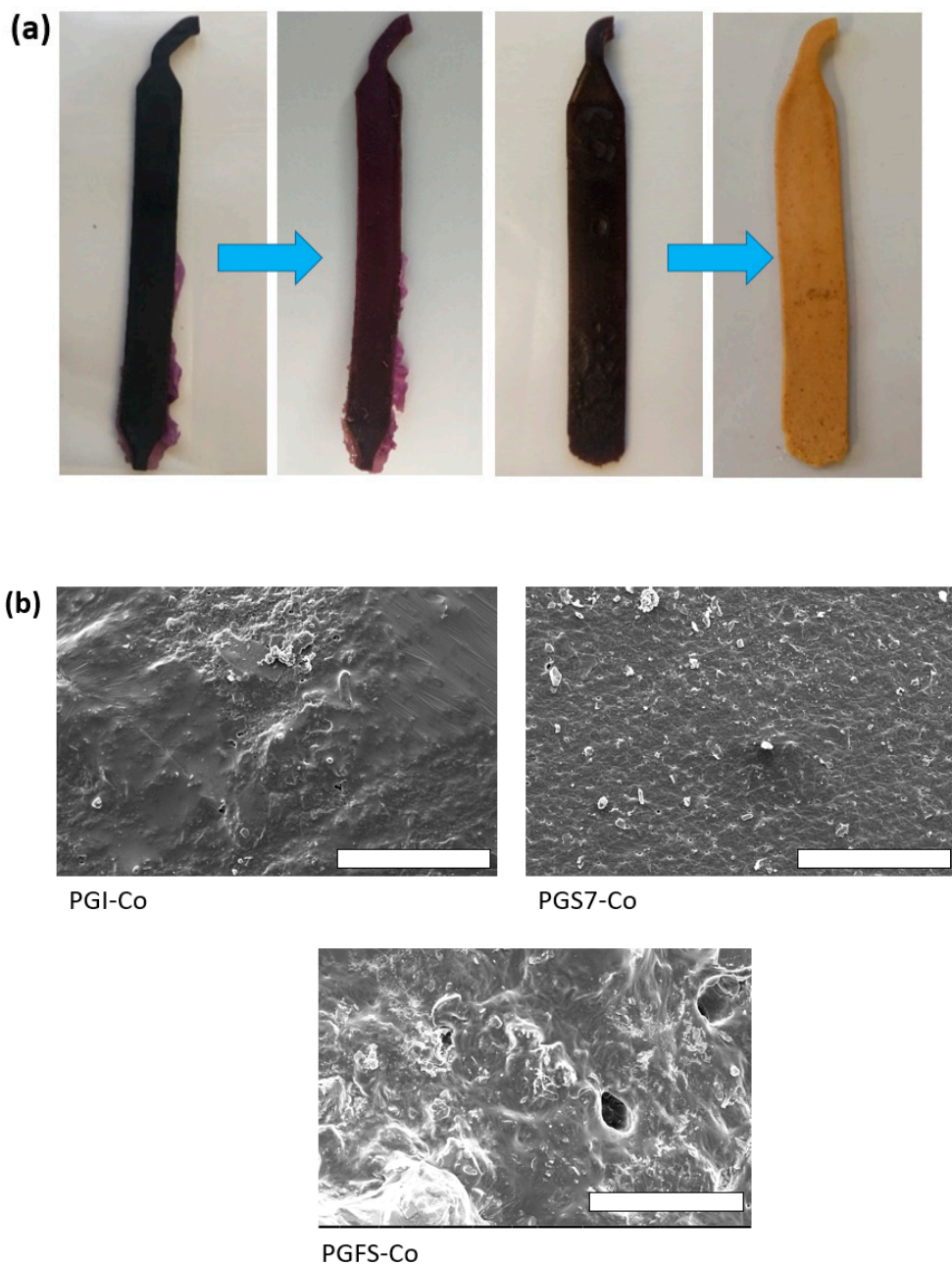


Figure 10. Cont.

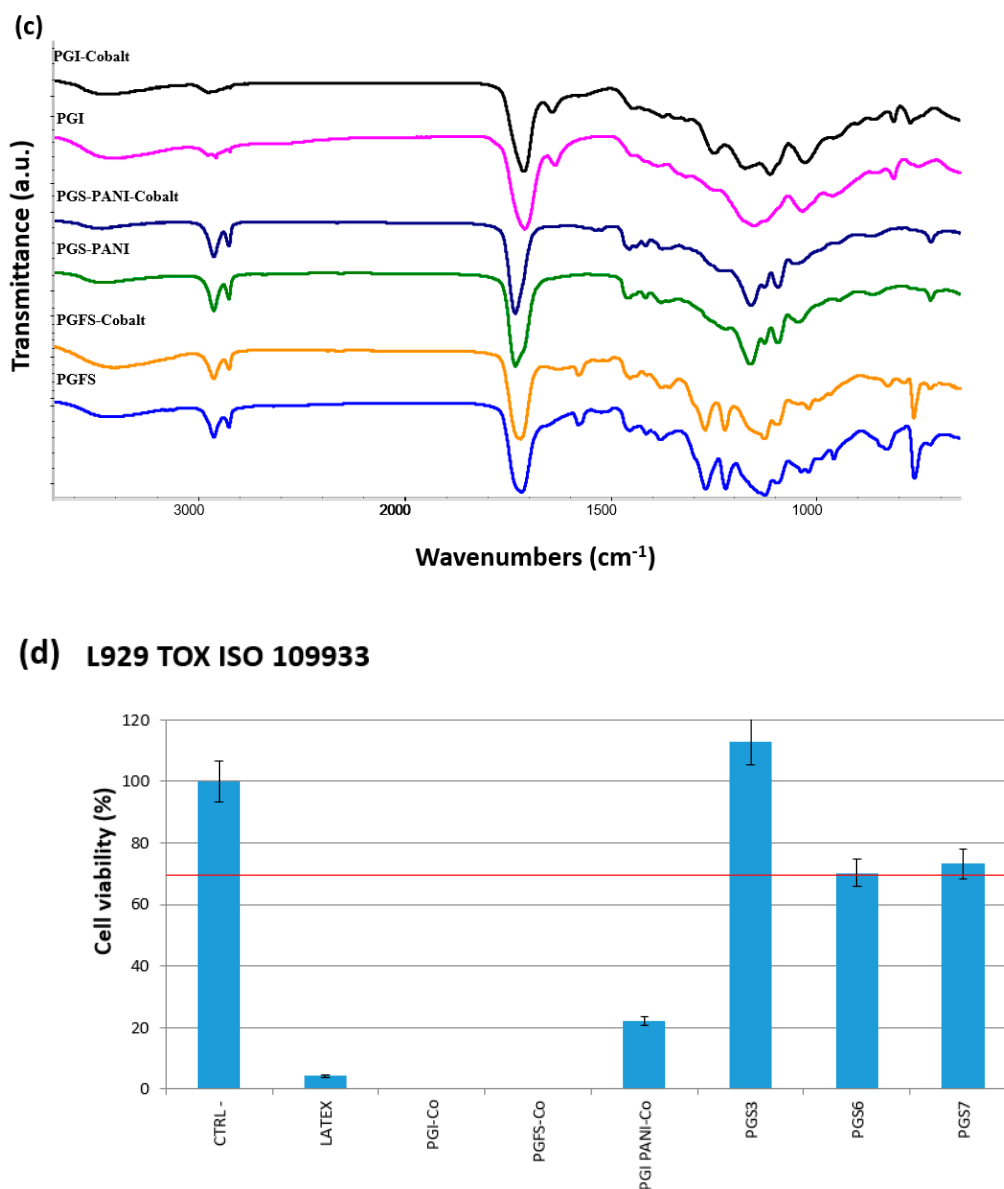


Figure 10. (a) Evolution of PGS7-Co and PGI-Co after immersion in a deionized water bath. (b) Comparison between infrared spectra of elastomer sheets from PGI-Co, PGS7-Co, and PGFS-Co, along with their classic melt-polycondensation-produced counterparts. (c) Photographs of FE-SEM observations of PGI-Co, PGS7-Co, and PGFS-Co surfaces (scale bars = 400 μm). (d) Cytocompatibility tests following the ISO10993 standard protocol and performed with PGI-Co, PGFS-Co, PGS7-Co, PGS3, PGS6, and PGS7.

3.6. Study of a PGS Sheet Doped with 10 wt% PANI as a pH Sensor

Compared to PGS6, PGS7 was better tolerated, and we decided to focus only on PGS doped with PANI to develop an effective pH sensor sheet obtained through active extrusion.

In view of its “insulator character”, the charge of PANI in the PGS sheet was enhanced for further investigations. As shown in Figure 11, the material PGS8—containing both 4 wt% microcellulose and 10 wt% PANI—was first produced as a dark brown, flexible, sticky sheet. When the sheet was immersed in 50 mL of deionized water, the pH of the liquid never went below 7. On the basis of preliminary electric tests, the electrical conductivity of the sheet gave an estimated value of $1.66 \cdot 10^{-8} \text{ S} \cdot \text{cm}^{-1}$.

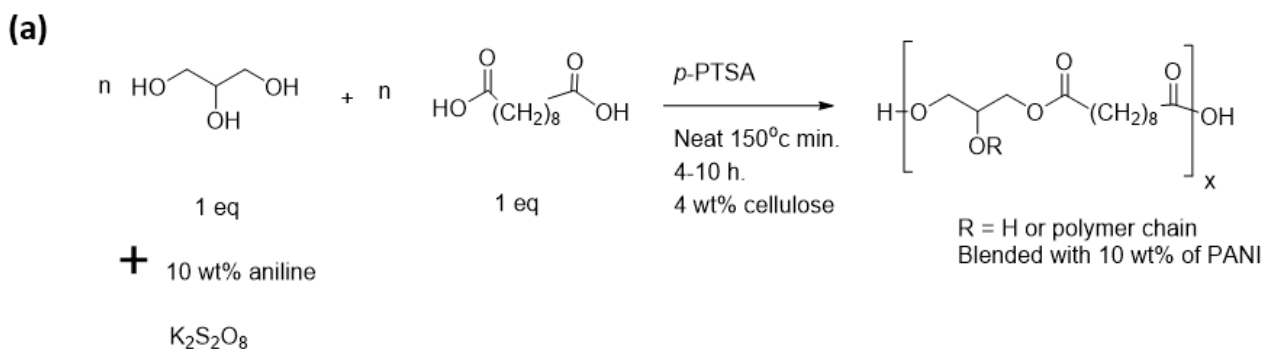
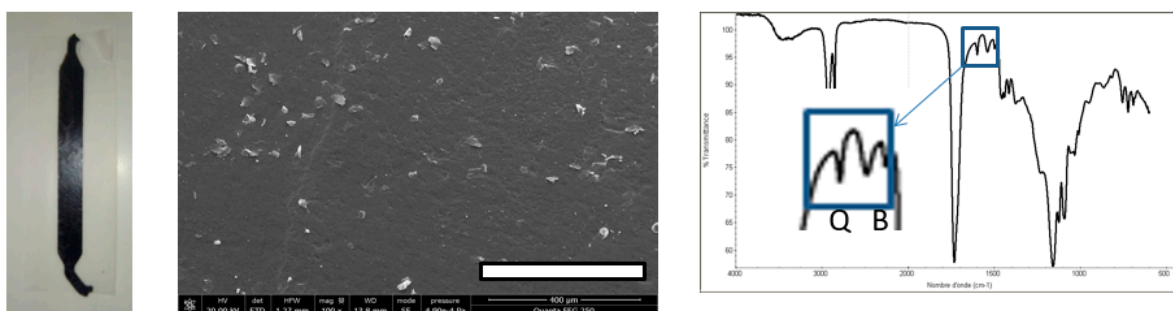
**(b)**

Figure 11. (a) Scheme for the production of the PGS8 prepolymer. (b) from left to right: image of the bioplastic composite sheet of PGS8; photograph of the FE-SEM observation of the PGS8 surface (scale bar = 400 μm); and its corresponding FTIR spectrum. R—H or polymer chain; Q—Quinoid units; B—Benzoid units.

In the FTIR spectrum of PGS8, compared to the charts of PGS7, the characteristic bands of the emeraldine PANI corresponding to C—H bonding were clearly observed at 1034 and 821 cm^{-1} , as well as bands corresponding to C—C benzenoid stretching at 1504 cm^{-1} and, finally, to C=N quinoid stretching at 1599 cm^{-1} [57]. Because the electrical conductivity of PGS8 was close to the limit of the operating zone area [32], another pathway was employed to produce a second type of PGS loaded with emeraldine PANI, as detailed in Figure 12 [57].

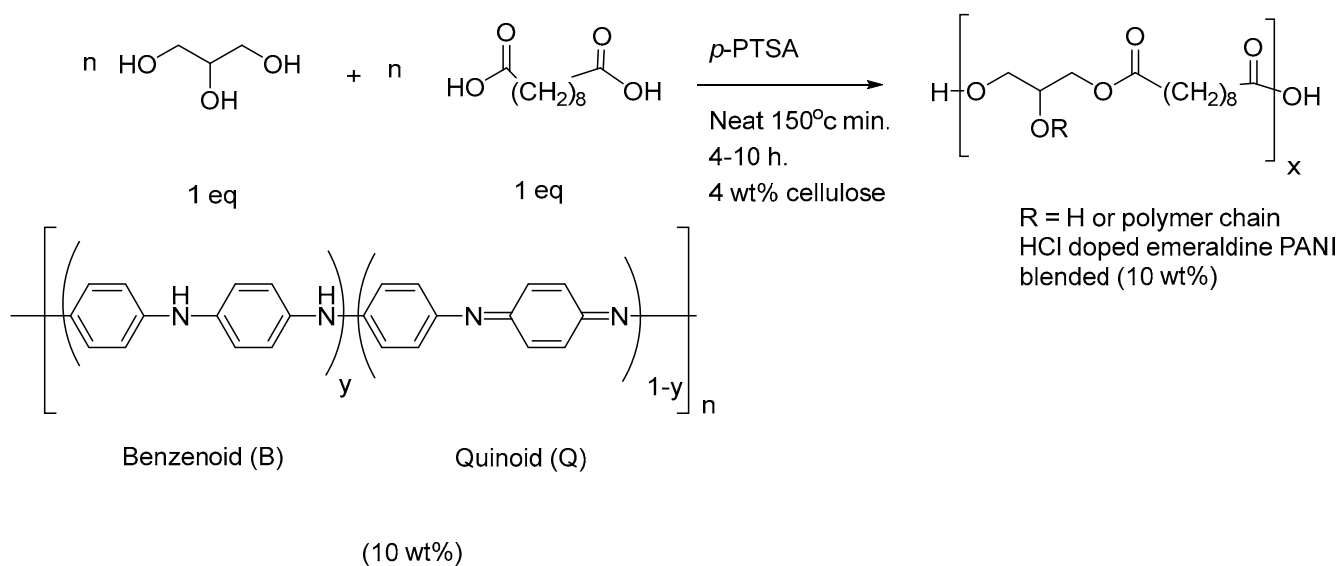


Figure 12. Global procedure for the production of robust PGS9 sheets containing 10 wt% emeraldine PANI.

A final material containing 10 wt% emeraldine PANI was produced, listed as PGS9. Herein, a desired amount of the dried green solid in its protonated form was simply dispersed in glycerol prior to the melt polycondensation and, finally, a second type of elastomer candidate was also generated by extrusion. Unfortunately, this time, when immersed in a water bath, the pH value decreased to below 4. As with PGS8, similar characteristic signals were observed in its FTIR spectrum (Figure S5, see Supplementary Materials). During the preliminary electroconduction test, no improvement of the electrical conductivity was observed for PGS9. In parallel, to measure the impact of both the amount and nature of PANI introduced, images of FE-SEM observation were also taken for a deep comprehensive study of the phenomena reported below, as shown in Figure 13.

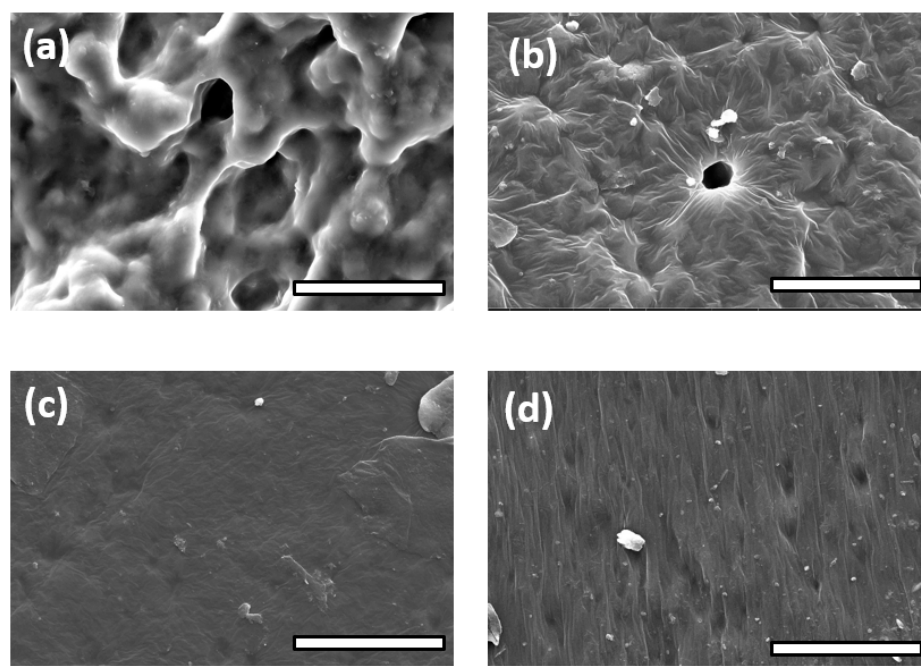


Figure 13. Images of FE-SEM observations from (a) PGS7, (b) PGS7-Co, (c) PGS8, and (d) PGS9. Scale bars = 40 μm .

In these images, it is possible to see four distinct and different morphologies of the surface, according to the difference in polarity between PGS7 and its PGS7-Co counterparts, for the same 4 wt% concentration of loaded PANI. However, the most important difference lies in the fact that once the PANI concentration reached a value of 10 wt%, for both PGS8 and 9, their surfaces became more flat, with the appearance of twisted bands aligned along their lengths with the PANI fibers, which could improve the electroconductivity of the material.

Some recent papers encouraged us to determine the electroconductivity of our elastomer sheets when doped with a strong acid [58,59]. Nevertheless, we carried out further investigation by measuring the response of our pH sensor candidates when placed in a closed and acidic atmosphere of HCl. These results are shown in Figure 14.

For PGS8, the circulating voltage started at 750 mV, and 60 min later, the voltage reached a maximum value of 2500 mV. The discharge was very rapid after the return of the sheet to a normal atmosphere, and took only 10 min to approach a final value of 1200 mV. Surprisingly, PGS9 needed more time to increase the voltage from 1130 to 3750 mV, and the inverse decrease time in the normal atmosphere followed the same pattern as for PGS8, with a period of 25 min to fall from 4110 mV back to its initial voltage value. During our experiments, we also noticed that direct finger-skin contact could increase the value of the measured voltage by 10 mV. In fact, emeraldine PANI is known as a material that can be doped via electrochemical oxidation or direct protonation. The increase in H^+ along the

macromolecule backbone changes its spin pairing, and produces a new global state without variation in the number of electrons available. After performing the tests, the sheets were dried in a vacuum, and we controlled the electroconductivity of both PGS8 and 9 sheets via cyclic voltammetry (Figure S6, see Supplementary Materials). Their relative behaviors were also demonstrated on their cyclic voltammograms (CV) conducted in aqueous 0.1 M LiClO₄ solution. Indeed, PGS9 did not show any powerful resistance that could correspond with the rapid increase of voltage, while for PGS8 between -2000 and 400 mV a reversible redox phenomenon occurred due to the possible partial oxidation state of PANI contained in the PGS8.

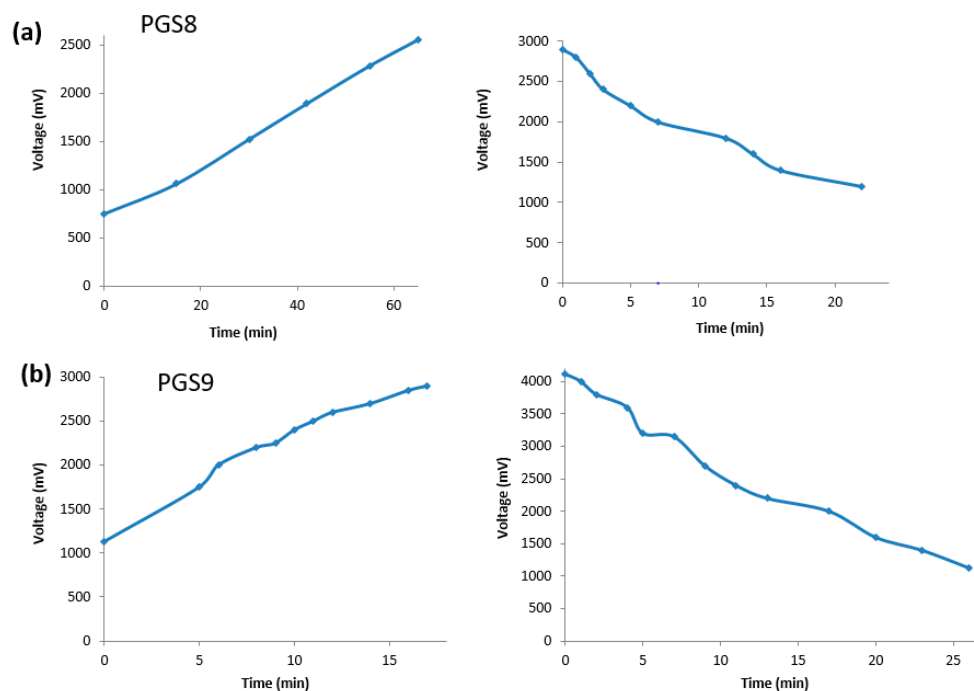


Figure 14. Plots of the dynamic responses of PGS8 and 9 pH sensor candidates versus time and their respective inverse decrease time: charge and discharge for (a) PGS8 and (b) PGS9. The sheets were powered by a constant current of 20 V.

4. Conclusions

In this work, PGS was shown to be the best bio-based elastomer in the field of tissue engineering and biomedicine, with a strong potential for producing hybrid and composite materials—especially compared to PGI. As an A2 monomer subunit, compared to SA, FDCA did not integrate properly in the terpolymer backbone of PGFS—especially when employed in a typical melt polycondensation. An alternative polytransesterification method catalyzed by a Co(II) salt did not solve these problems. However, starting from an improved method for producing biocompatible PGS composite elastomers using recirculating extrusion, this study achieved the rapid development of two different kinds of performant PGS sheets blended with 10 wt% PANI as time-dependent electric pH sensors. In the near future, our intention is to exploit our concept by incorporating small fractions of these materials in more complicated devices, such as microelectromechanical systems (MEMSs) [60] or supercapacitors [61].

Supplementary Materials: The following supporting information can be downloaded at: <https://www.mdpi.com/article/10.3390/polym14183829/s1>, Figure S1: FE-SEM micrographs of various poly(glycerol-co-diacids) blended composites. The scale bars were set up at 400 μm ; Figure S2: Evolution of PGFS aspect function of their SA and FDCA contents; Figure S3: Pictures of: (a) PGI prepolymer formed under micro-wave heating (from left to right: 15 min without *p*TSA; 5 min with *p*TSA; 15 min with *p*TSA); (b) PGS prepolymer produced after 15 min of MW irradiation in presence of *p*TSA catalyst; Figure S4: Picture of enlargement from PGS5 FE-SEM observation enlargement; Figure S5: FT-IR spectrum of PGS9; Figure S6: Cyclic voltammograms (CV) obtained from measurements conducted in 0.1 M LiClO_4 aqueous solution using PGS8 and PGS9 as working electrodes; Figure S7: DSC thermograms of: (a) PGS1; (b) PGS2; (c) PGS3; (d) PGS4; Figure S8: DSC thermograms of: (a) PGS5; (b) PGS6; (c) PGS7; Figure S9: DSC thermograms of: (a) PGI2; (b) PGFS1; (c) PGFS2.

Author Contributions: Conceptualization, F.D.; methodology, S.J. and E.G.; formal analysis, F.D.; investigation, S.J., F.N. and F.D.; writing—original draft preparation, F.D.; writing—review and editing, M.S., C.E. and E.G.; supervision, F.D. and C.E.; project administration, F.D. All authors have read and agreed to the published version of the manuscript.

Funding: This research was supported by a PhD student fellowship from the French Higher Education and Research Ministry (MESR).

Institutional Review Board Statement: Not applicable.

Informed Consent Statement: Not applicable.

Data Availability Statement: Raw data are stored in-house at UTC, and can be made available upon request.

Acknowledgments: We would like to thank La Région Haut-de-France for financing the acquisition of the extrusion apparatus employed in this work. S. Ji wishes to thank UTC for the funding of her internship.

Conflicts of Interest: The authors declare no conflict of interest.

References

- Valerio, O.; Misra, M.; Mohanty, A.K. Poly(glycerol-co-diacids) polyesters: From Glycerol Biorefinery to Sustainable Engineering Applications, A review. *ACS Sustain. Chem. Eng.* **2018**, *6*, 5681–5693. [\[CrossRef\]](#)
- Tham, W.H.; Wahit, M.U.; Kadir, M.R.A.; Wong, T.W.; Hassan, O. Polyol-based biodegradable polyesters: A short review. *Rev. Chem. Eng.* **2016**, *32*, 201–221. [\[CrossRef\]](#)
- Zhang, T.; Howell, B.A.; Dumitrascu, A.; Martin, S.J.; Smith, P.B. Synthesis and characterization of glycerol adipic acid hyper-branched polyesters. *Polymer* **2014**, *55*, 5065–5072. [\[CrossRef\]](#)
- Amarasekera, A.S.; Razzaq, A.; Bonham, P. Synthesis and characterization of all renewable resources based branched polyesters: Poly(2,5-furandicarboxylic acid-co-glycerol). *Polym. Sci.* **2013**, *2013*, 645169. [\[CrossRef\]](#)
- Neal, R.A.; Jean, A.; Park, H.; Wu, P.B.; Hsiao, J.; Engalmayr, G.C., Jr.; Langer, R.; Freed, L.E. Three-Dimensional Elastomeric Scaffolds Designed with Cardiac-Mimetic Structural and Mechanical Features. *Tissue Eng. Part A* **2013**, *19*, 793–807. [\[CrossRef\]](#)
- Crapo, P.M.; Wang, Y. Physiologic compliance in engineered small-diameter arterial constructs based on an elastomeric substrate. *Biomaterials* **2010**, *31*, 1626–1635. [\[CrossRef\]](#)
- Zaky, S.H.; Lee, K.-W.; Gao, J.; Jensen, A.; Close, J.; Wang, Y.; Almarza, A.J.; Sfeir, C. Poly(glycerol Sebacate) Elastomer: A novel Material for Mechanically Loaded Bone Regeneration. *Tissue Eng. Part A* **2014**, *20*, 45–53. [\[CrossRef\]](#)
- Kemppainen, J.M.; Hollister, S.J. Tailoring the Mechanical properties of 3D-designed poly(glycerol sebacate) scaffolds for cartilage applications. *J. Biomed. Mater. Res. Part A* **2010**, *94*, 9–18. [\[CrossRef\]](#)
- Loh, X.J.; Karim, A.A.; Owh, C. Poly(glycerol sebacate) biomaterial: Synthesis and biomedical applications. *J. Mater. Chem. B* **2015**, *3*, 7641–7652. [\[CrossRef\]](#)
- Sundback, C.A.; Shyu, J.Y.; Wang, Y.; Faquin, W.C.; Langer, R.S.; Vacanti, J.P.; Hadlock, T.A. Biocompatibility analysis of poly(glycerol sebacate) as a nerve guide material. *Biomaterials* **2005**, *26*, 5454–5464. [\[CrossRef\]](#)
- Louage, B.; Tack, L.; Wang, Y.; De Geest, B.G. Poly(glycerol Sebacate) nanoparticles for encapsulation of hydrophobic anti-cancer drugs. *Polym. Chem.* **2017**, *8*, 5033–5038. [\[CrossRef\]](#)
- Chen, Q.; Liang, S.; Thouas, G.A. Synthesis and characterization of poly(glycerol sebacate)-co-lactic acid as surgical sealants. *Soft Matter* **2011**, *7*, 6484–6492. [\[CrossRef\]](#)
- Shirazaki, P.; Varshosaz, J.; Kharazi, A.Z. Electrospun gelatin/poly(Glycerol Sebacate) Membrane with Controlled Release of antibiotics for wound dressing. *Adv. Biomed. Res.* **2007**, *6*, 205.

14. Vogt, L.; Liverani, L.; Roether, J.A.; Boccaccini, A.R. Electrospun Zein Fibers Incorporating Poly(Glycerol Sebacate) for soft Tissue Engineering. *Nanomaterials* **2018**, *8*, 150. [\[CrossRef\]](#)
15. Zhang, X.; Jia, C.; Qiao, X.; Liu, T.; Sun, K. Silk fibroin microfibers and chitosan modified poly(glycerol sebacate) composite scaffolds for skin tissue engineering. *Polym. Test.* **2017**, *62*, 88–95. [\[CrossRef\]](#)
16. Lee, K.-W.; Stolz, D.B.; Wang, Y. Substantial expression of mature elastin in arterial constructs. *Proc. Natl. Acad. Sci. USA* **2011**, *108*, 2705–2710. [\[CrossRef\]](#)
17. Savarani, S.; Ebrahimian-Hoseinabadi, M.; Mohebbi-Kalhor, D. Polyglycerol sebacate/chitosan/gelatin nano-composite scaffolds for engineering neural construct. *Mater. Chem. Phys.* **2019**, *222*, 147–151. [\[CrossRef\]](#)
18. Zhou, L.; He, H.; Jiang, C.; He, S. Preparation and Characterization of poly(glycerol sebacate)/cellulose nanocrystals elastomeric composites. *J. Appl. Polym. Sci.* **2015**, *132*, 42196. [\[CrossRef\]](#)
19. Gaharwar, A.K.; Nikkhah, M.; Sant, S.; Khademhosseini, A. Anisotropic poly(glycerol sebacate)-poly(ϵ -caprolactone) electrospun fibers promote endothelial cell guidance. *Biofabrication* **2015**, *5*, 015001.
20. Keirouz, A.; Fortunato, G.; Zhang, M.; Callanan, A.; Radacs, N. Nozzle-free electrospinning of polyvinylpyrrolidone/poly(glycerol sebacate) fibrous scaffolds for skin tissue engineering applications. *Med. Eng. Phys.* **2019**, *71*, 56–67. [\[CrossRef\]](#)
21. O'Brien, D.; Hankins, A.; Golestaneh, N.; Paranjape, M. Highly aligned and geometrically structured poly(glycerol sebacate)-polyethylene oxide composite fiber matrices towards bioscaffolding applications. *Biomed. Microdevices* **2019**, *21*, 53. [\[CrossRef\]](#) [\[PubMed\]](#)
22. Roether, J.A.; Rai, R.; Wolf, R.; Tallawi, M.; Boccaccini, A.R. Biodegradable poly(glycerol sebacate)/poly(3-hydroxybutyrate)-TiO₂ nanocomposites: Fabrication and characterization. *Mater. Sci. Technol.* **2014**, *30*, 574–581. [\[CrossRef\]](#)
23. Tevlek, A.; Agacik, D.T.; Aydin, H.M. Stretchable poly(glycerol-sebacate)/ β tricalcium phosphate composites with shape recovery feature by extrusion. *J. Appl. Polym. Sci.* **2020**, *137*, 48689. [\[CrossRef\]](#)
24. Liang, S.; Cook, W.D.; Chen, Q. Physical Characterization of poly(glycerol sebacate)/Bioglass[®] composites. *Polym. Int.* **2012**, *61*, 17–22. [\[CrossRef\]](#)
25. Ferrer, C.T.; Vilarino-Feltrer, G.; Rizk, M.; Sydow, H.G.; Valles-Liunch, A. Nanocomposites based on poly(glycerol sebacate) with silica nanoparticles with potential application in dental tissue engineering. *Int. J. Polym. Mater. Polym. Biomater.* **2019**, *69*, 761–772. [\[CrossRef\]](#)
26. Naser, R.; Khrazi, A.Z.; Dini, G. Fabrication of PGS/CaTiO₃ Nano-Composite for Biomedical Application. *Int. J. Nanosci. Nanotechnol.* **2016**, *12*, 103–108.
27. Rosenbalm, T.N.; Teruel, H.; Day, C.S.; Donati, G.L.; Morykwas, M.; Argenta, L.; Kuthirummal, N.; Palyachenko, N.L. Structural and Mechanical Characterization of bioresorbable, elastomeric nanocomposites from poly(glycerol sebacate)/nano hydroxyl apatite for tissue transport applications. *J. Biomed. Mater. Res. B* **2016**, *104*, 1366–1373. [\[CrossRef\]](#)
28. Chen, Q.-Z.; Liang, S.-L.; Wang, J.; Simon, G.P. Manipulation of Mechanical compliance of elastomeric PGS by incorporation of halloysite nanotubes for tissue engineering applications. *J. Mech. Behav. Biomed. Mater.* **2011**, *4*, 1805–1818. [\[CrossRef\]](#)
29. Gaharwar, A.K.; Patel, A.; Dolatshahi-Pirouz, A.; Zhang, H.; Rangarajan, K.; Iviglia, G.; Shin, S.-R.; Hussein, H.A.; Khademhosseini, A. Elastomeric nanocomposite scaffolds made from PGS chemically crosslinked with CNT. *Biomater. Sci.* **2015**, *3*, 45–68. [\[CrossRef\]](#)
30. Li, C.-Y.; Hu, M.-H.; Hu, J.-J. Use of Aligned Microscale of Sacrificial fibers in Creating Biomimetic, Anisotropic Poly(glycerol sebacate) Scaffolds. *Polymers* **2019**, *11*, 1492. [\[CrossRef\]](#)
31. Wu, H.-J.; Hu, M.-H.; Tuan-Mu, H.-Y.; Hu, J.-J. Preparation of aligned poly(glycerol sebacate) fibrous membranes for anisotropic tissue engineering. *Mater. Sci. Eng. C* **2019**, *100*, 30–37. [\[CrossRef\]](#) [\[PubMed\]](#)
32. Solazzo, M.; O'Brien, F.J.; Nicolosi, V.; Monaghan, M.G. The rationale and emergence of electroconductive biomaterials scaffolds in cardiac tissue engineering. *APL Bioeng.* **2019**, *3*, 041501. [\[CrossRef\]](#) [\[PubMed\]](#)
33. Qazi, T.H.; Rai, R.; Dippold, D.; Roether, J.E.; Shubert, D.W.; Rosellini, E.; Barbani, N.; Boccaccini, A.R. Development and characterization of novel electrically conductive PANI-PGS composite for cardiac tissue engineering applications. *Acta Biomater.* **2014**, *10*, 2434–2445. [\[CrossRef\]](#)
34. Hu, T.; Wu, Y.; Zhao, X.; Wang, L.; Bi, L.; Ma, P.X.; Guo, B. Micropatterned, electroactive, and biodegradable poly(glycerol sebacate)-aniline trimer elastomer for tissue engineering. *Chem. Eng. Technol.* **2019**, *366*, 208–222. [\[CrossRef\]](#)
35. Cao, Y.; Smith, P.; Heeger, A.J. Counter-ion induced processability of conducting polyaniline and of conducting polyblends of polyaniline in bulk polymers. *Synth. Met.* **1992**, *48*, 91–97. [\[CrossRef\]](#)
36. Ezazi, N.Z.; Adjary, R.; Correia, A.; Makila, E.; Salonen, J.; Kemell, M.; Hirvonen, J.; Rojas, O.J.; Ruskoaho, H.J.; Santos, H.A. Fabrication and Characterization of Drug Loaded Conductive Poly(glycerol Sebacate)/Nanoparticle-Based Composite Patch for Myocardial Infarctus Applications. *ACS Appl. Mater. Interfaces* **2020**, *12*, 6899–6909. [\[CrossRef\]](#)
37. Gadomska-Gajadur, A.; Wrzecionek, H.; Matyszczyk, G.; Pietowski, P.; Wieclaw, M.; Ruskowski, P. Optimization of Poly(Glycerol sebacate) Synthesis for Biomedical Purposes with the Design Experiments. *Org. Process Res. Dev.* **2018**, *22*, 1793–1800. [\[CrossRef\]](#)
38. Li, X.; Hong, A.T.-L.; Naskar, N.; Chung, H.-J. Criteria for quick and Consistent Synthesis of Poly(glycerol Sebacate) for Tailored Mechanical Properties. *Biomacromolecules* **2015**, *16*, 1525–1533. [\[CrossRef\]](#)
39. Harris, J.J.; Lu, S.; Gabriele, P. Commercial Challenges in Developing Biomaterials for Medical Device Development. *Polym. Int.* **2018**, *67*, 969–974. [\[CrossRef\]](#)

40. Kafouris, D.; Kossiras, F.; Constantinides, C.; Nguyen, N.Q.; Wesdemiotis, C.; Patrickios, C.S. Biosourced Amphiphilic Degradable Elastomers of Poly(glycerol Sebacate): Synthesis network and Oligomer Characterization. *Macromolecules* **2013**, *46*, 622–630. [[CrossRef](#)]
41. Liu, Q.; Tian, H.; Ding, T.; Shi, R.; Feng, Y.; Zhang, L.; Chen, D.; Tian, W. Preparation and Characterization of a Thermoplastic Poly(glycerol Sebacate) Elastomer by Two-Step Method. *J. Appl. Polym. Sci.* **2007**, *103*, 1412–1419. [[CrossRef](#)]
42. Martin-Cabezuelo, R.; Vilariño-Feltrer, G.; Valles-Lluch, A. Influence of prepolymerization atmosphere on the properties of pure and poly(glycerol sebacate). *Mater. Sci. Eng. C* **2021**, *119*, 111429. [[CrossRef](#)] [[PubMed](#)]
43. Lee, S.H.; Lee, K.-W.; Gade, P.S.; Robertson, A.M.; Wang, Y. Microwave assisted Facile Fabrication of porous poly(glycerol sebacate) scaffolds. *J. Biomater. Sci. Polym. Ed.* **2018**, *29*, 907–916. [[CrossRef](#)] [[PubMed](#)]
44. Aydin, H.H.; Salimi, K.; Rzaev, Z.M.O.; Piskin, E. Microwave-assisted rapid synthesis of poly(glycerol sebacate) elastomers. *Biomater. Sci.* **2013**, *1*, 503–509. [[CrossRef](#)]
45. Lau, C.C.; Bayazit, H.K.; Knowles, J.C.; Tang, J. Tailoring degree of esterification and branching of poly(glycerol sebacate) by energy efficient microwave irradiation. *Polym. Chem.* **2017**, *8*, 3937–3947. [[CrossRef](#)]
46. Zhao, D.; Delbecq, F.; Len, C. One-pot FDCA diesters synthesis from mucic acid and their solvent-free regioselective polytransesterification for production of glycerol-based furanic polyesters. *Molecules* **2019**, *24*, 1030. [[CrossRef](#)]
47. Wuang, S.; Dupin, L.; Noel, H.; Carroux, C.J.; Renaud, L.; Gehin, T.; Meyer, A.; Souteyrand, E.; Vasseur, J.J.; Vergoten, G.; et al. Toward the Rational Design of Galactosylated Glycoclusters That Target *Pseudomonas aeruginosa* Lectin A (Lec A): Influence of a Linker Arms That lead to Low-Nanomolar Multivalent Ligands. *Chem. Eur. J.* **2016**, *22*, 11785–11794. [[CrossRef](#)]
48. Kunkuma, V.L.; Kaki, S.S.; Rao, B.V.S.K.; Prasad, R.B.N.; Prabhavathi Devi, B.L.A. A simple and facile method for the synthesis of 1-Octosanol. *Eur. J. Lipid Sci. Technol.* **2013**, *115*, 921–927. [[CrossRef](#)]
49. Malferrari, D.; Armenise, N.; Decesari, S.; Galletti, P.; Tagliavini, E. Surfactants from Itaconic acids Physicochemical Properties and Assessments of the Synthetic Strategies. *ACS Sustain. Chem. Eng.* **2015**, *3*, 1579–1588. [[CrossRef](#)]
50. Nijst, C.L.E.; Bruggeman, J.P.; Karp, J.M.; Ferreira, L.; Zumbuehl, A.; Bettinger, C.J.; Langer, R. Synthesis and Characterization of Photocurable Elastomers from Poly(Glycerol-co-Sebacate). *Biomacromolecules* **2007**, *10*, 3067–3073. [[CrossRef](#)]
51. Konyushenko, E.N.; Reynaud, S.; Pellerin, V.; Trchova, M.; Stejskal, J.; Sapurina, I. Polyaniline prepared in ethylene glycol or glycerol. *Polymer* **2021**, *52*, 1900–1907. [[CrossRef](#)]
52. Dai, J.; Ma, S.; Wu, Y.; Han, L.; Zhang, L.; Zhu, J.; Liu, X. Polyesters derived from itaconic acid for the properties and bio-based contact enhancement of soybean-oil thermosets. *Green Chem.* **2015**, *17*, 2383–2392. [[CrossRef](#)]
53. Chanda, S.; Ramakrishnan, S. Poly(alkylene itaconate)s—an interesting class of polyesters with periodically located exo-chains double bonds susceptible to Michael addition. *Polym. Chem.* **2015**, *6*, 2108–2114. [[CrossRef](#)]
54. Moore, O.B.; Hanson, P.-A.; Comerford, J.W.; Pellis, A.; Farmer, T.J. Improving the Post-Polymerization Modification of Biobased Itaconate Unsaturated Polyesters; Catalyzing Aza-Michael Additions with Reusable iodine on acidic Alumina. *Front. Chem.* **2019**, *7*, 501. [[CrossRef](#)] [[PubMed](#)]
55. Hua, S.; Chen, F.; Liu, Z.-Y.; Yang, W.; Yang, M. Preparation of cellulose-graft-poly(lactic acid) via melt polycondensation for use in poly(lactic acid) based composites: Synthesis, characterization and properties. *RSC Adv.* **2016**, *6*, 1973–1983. [[CrossRef](#)]
56. Humpolicek, P.; Kasparkova, V.; Saha, P.; Stejskal, J. Biocompatibility of polyaniline. *Synth. Met.* **2012**, *162*, 722–727. [[CrossRef](#)]
57. Neelakandan, R.; Giridev, V.R.; Murugesan, M.; Madhusoothanan, M. Surface Resistivity and Shear Characteristics of Polyaniline Coated Polyester Fabric. *J. Ind. Text.* **2009**, *39*, 175–185. [[CrossRef](#)]
58. Zhao, Z.; Zhou, J.; Xiao, H.; Lu, Y.; Lu, M. Creation of polyaniline-coated polyester fabrics with conductive, electrothermal and energy-storage properties via micro-dissolution method. *Mater. Today Commun.* **2020**, *24*, 101042. [[CrossRef](#)]
59. Li, Y.; Mao, Y.; Xiao, C.; Xu, X.; Li, X. Flexible pH sensor based on a conductive PANI membrane for pH monitoring. *RSC Adv.* **2021**, *10*, 21–28. [[CrossRef](#)]
60. Dejeu, J.; Cot, A.; Rougeot, P.; Lakard, B.; Lakard, S.; Gauthier, M. Development of new sticky and conducting polymer surfaces for MEMS applications. *Synth. Met.* **2021**, *276*, 116757. [[CrossRef](#)]
61. Ba, Y.; Zhou, S.; Jiao, S.; Pan, W. Fabrication of polyaniline/copper sulfide/polyethylene (terephthalate) thread electrode for flexible fiber-shaped supercapacitors. *J. Appl. Polym. Sci.* **2018**, *135*, 46769. [[CrossRef](#)]

MINI-REVIEW ARTICLE

Dermatokinetics: Advances and Experimental Models, Focus on Skin Metabolism

Paul Quantin¹, Mathilde Stricher¹, Sophie Catoire², Hervé Ficheux¹ and Christophe Egles^{1,*}¹BioMécanique et BioIngénierie, Université de Technologie de Compiègne, UMR 7338 UTC-CNRS, France; ²Department of Cell Culture, Laboratory of Cell Alternative, Trosly Breuil, France

Abstract: Numerous dermal contact products, such as drugs or cosmetics, are applied on the skin, the first protective barrier to their entrance into the organism. These products contain various xenobiotic molecules that can penetrate the viable epidermis. Many studies have shown that keratinocyte metabolism could affect their behavior by biotransformation. While aiming for detoxification, toxic metabolites can be produced. These metabolites may react with biological macromolecules often leading to sensitization reactions. After passing through the epidermis, xenobiotics can reach the vascularized dermis and therefore, be bioavailable and distributed into the entire organism.

To highlight these mechanisms, dermatokinetics, based on the concept of pharmacokinetics, has been developed recently. It provides information on the action of xenobiotics that penetrate the organism through the dermal route.

The purpose of this review is first to describe and synthesize the dermatokinetics mechanisms to consider when assessing the absorption of a xenobiotic through the skin. We focus on skin absorption and specifically on skin metabolism, the two main processes involved in dermatokinetics. In addition, experimental models and methods to assess dermatokinetics are described and discussed to select the most relevant method when evaluating, in a specific context, dermatokinetics parameters of a xenobiotic. We also discuss the limits of this approach as it is notably used for risk assessment in the industry where scenario studies generally focus only on one xenobiotic and do not consider interactions with the rest of the exposome. The hypothesis of adverse effects due to the combination of chemical substances in contact with individuals and not to a single molecule, is being increasingly studied and embraced in the scientific community.

ARTICLE HISTORY

Received: October 30, 2021

Revised: January 24, 2022

Accepted: February 09, 2022

DOI:

10.2174/1389200223666220517114004

Keywords: *In vitro* models, toxicity, metabolism, drugs, xenobiotics, dermatokinetics.

1. INTRODUCTION

Pharmacokinetics describes the fate and behavior of a xenobiotic at pharmacological doses in a living organism or *in vitro* system over time. Often designated by the acronym ADME, it involves absorption, distribution, metabolism, and elimination mechanisms (Fig. 1) [1]. The aim is to define the amount of substance that can potentially reach a target in the body and have a desired or adverse biological effect. Data on the substance-target interaction and possible toxic effects are obtained from pharmacotoxicology studies. Pharmacokinetics should also specify the form of the xenobiotic over time, as it is likely to be converted, through metabolism, into other substances whose fate must also be studied. Finally, pharmacokinetics should enable us to anticipate and predict the exposure of a molecule in an organism, particularly in the case of the appearance of a toxic metabolite. During risk assessment, pharmacokinetics provides information on systemic and target organ levels of exposure and thus allows any risk characterization.

Human organisms are daily exposed to numerous xenobiotics from drugs, cosmetics, or other chemical substances and may be absorbed by three main routes: respiratory, oral, and dermal.

In the skin, pharmacokinetics could depend on specific mechanisms linked to the dermal route. In this perspective, dermatokinetics defines the behavior of a xenobiotic that is absorbed into the body through the epidermis, by specifying quantitative (tissue concentration and bioavailability) and qualitative (possible metabolites) factors. The aim is also to specify the temporal aspect of the xenobiotic's fate, as its duration of presence in the tissues can strongly impact the potential effects.

For the preparation of this general review, several databases were used, mainly Scopus and PubMed. The study was performed using various search terms and keywords such as: xenobiotic metabolism enzyme, skin metabolism, skin biotransformation, pharmacokinetic, dermatokinetic, skin absorption, skin toxicity, dermal risk assessment, and skin metabolism bioactivation. Selected studies were compared and summarized based on existing theories and mechanistic models, in addition to the experience of the authors in the industrial sector of dermal products and academic research in skin bioengineering.

2. DESCRIPTION OF ADME PHARMACOKINETICS STEPS

2.1. Absorption

When a molecule interacts with an organism, absorption is the first limiting step in the entry of the substance into the internal environment [1]. Depending on its physicochemical properties (molecular weight, ionization state and solubility) and the source of exposure, xenobiotics can be absorbed through different routes (primarily dermal, oral, or respiratory). Whether through the skin or the intestinal wall, absorption differs by the constitution and the thickness of the membrane to be cross. Also, depending on the size of the molecule, absorption will be more or less important, the smaller ones being more easily absorbed passively. The lipophilic character of the molecule is also important to facilitate absorption because the membranes are mainly made up of lipids; ionized substances will be weakly absorbed, except at membrane pores.

After absorption into the body, the molecule will be distributed to the organs and tissues through the blood system. In pharmacokinetics, it is considered that the level of absorption of a substance is the parameter that most affects the difference between the external and internal dose [2].

*Address correspondence to this author at the BioMécanique et BioIngénierie, Université de Technologie de Compiègne, UMR 7338 UTC-CNRS, France; E-mail: christophe.egles@utc.fr

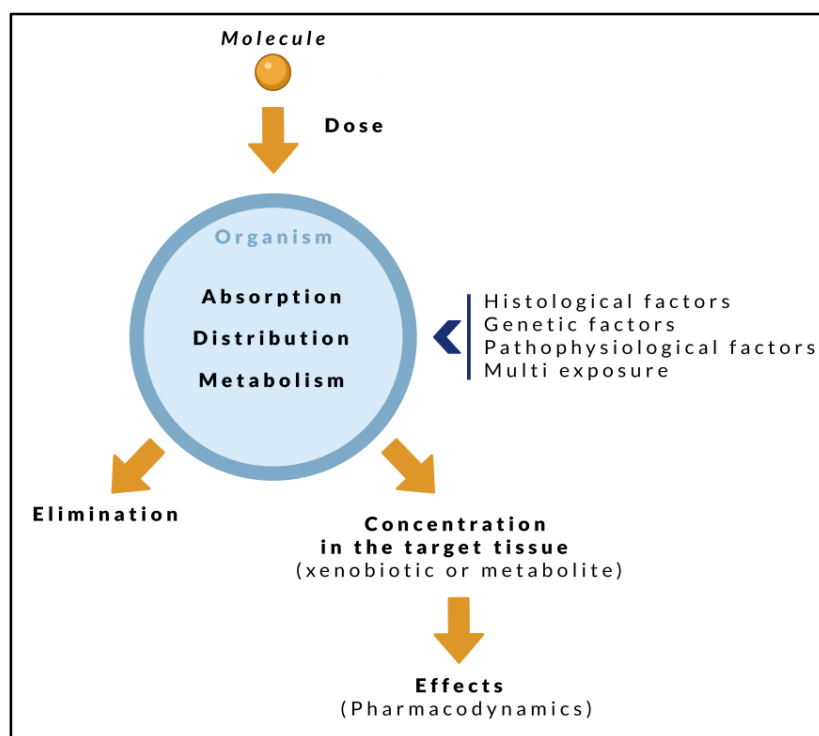


Fig. (1). Description of the main steps in pharmacokinetics. Absorption into the internal environment leads to the distribution of the molecule into the tissues where it can be metabolized before being eliminated into the external environment. Pharmacodynamics follows pharmacokinetics and relates to the effects of the substance in the target tissues. (A higher resolution / colour version of this figure is available in the electronic copy of the article).

2.2. Distribution

As for absorption, during distribution in the organism, the affinity of the molecule for the different organs and tissues depends on its physicochemical properties [3]. The main factor modifying the distribution is plasma protein binding which can impact the bioavailability.

Plasma proteins are present in large quantities in the bloodstream (about 60 g/L) and can potentially bind any circulating molecule. When the molecule is distributed through the bloodstream, a certain fraction of the dose may bind to proteins, mostly albumin. Only the free form can diffuse to tissues and have biological activity. This plasma protein binding must therefore be evaluated as it allows the exposure to be interpreted in terms of the active fraction [4].

2.3. Metabolism and Elimination

2.3.1. Definition

To eliminate a molecule absorbed by the body, various metabolic processes may be involved. The term metabolism refers to the biotransformation by an enzymatic reaction of a substrate into products or metabolites. The primary function of this process is to facilitate the elimination step. The ultimate goal is to decrease the substance lipophilicity and increase its water-solubility to allow its elimination in physiological excreta mainly urine, faeces, and bile [5].

This process is present in various tissues such as skin, lungs, and kidneys [6], but the liver because of its blood flow (1500 mL/min), its mass (about 2% of body weight) and its high enzymatic content is the primary detoxification organ [7]. The transformation process is performed by hepatocytes and cholangiocytes *via* enzyme functionalization and substrate conjugation reactions. The abundant iso-enzymes of the cytochrome P450 family (CYP) provide

vide the fundamental metabolizing enzyme system. However, other distinct, parallel, or complementary metabolic pathways may play an important role.

At the intracellular level, enzymes of the CYP family are expressed in the membranes of the smooth endoplasmic reticulum while others are soluble in the cytoplasm. This distinction is important and must be considered when attempting to isolate enzymes by subcellular fractionation techniques [8].

Briefly, two phases of metabolism can be distinguished according to the transformation processes induced by these enzymes: Phase I and Phase II reactions (summarized in Fig. 2).

During Phase I metabolism, the molecule to be eliminated is functionalized lead to derivatives whose functional groups are most often hydroxyl (-OH), amines (-NH₂), or carboxyl (-COOH). During Phase II metabolism, the new function on the substrate is used to conjugate highly water-soluble entities, thus facilitating excretion. Phase I enzymes are mainly represented by CYP isoforms but other Phase I enzymes such as Alcohol Dehydrogenases, Monooxygenases or Peroxidases are also present. On the other hand, Glutathione S-Transferase (GST), Glucuronosyltransferase (UGT), Sulfotransferase (SULT) are phase II enzymes capable of conjugating water-soluble compounds such as glutathione, glucuronic acid, or sulfate derivatives, respectively.

Enzymes for xenobiotic metabolism have multiple substrate specificities as an enzyme can use and metabolize various substrates [9].

Metabolism generally leads to less toxic molecules. However, it may also generate more toxic metabolites than the initial molecule [10].

Phase 0 and phase III steps involve transporters of influx and efflux, playing a central role in delivering substrates and excretion of metabolites.

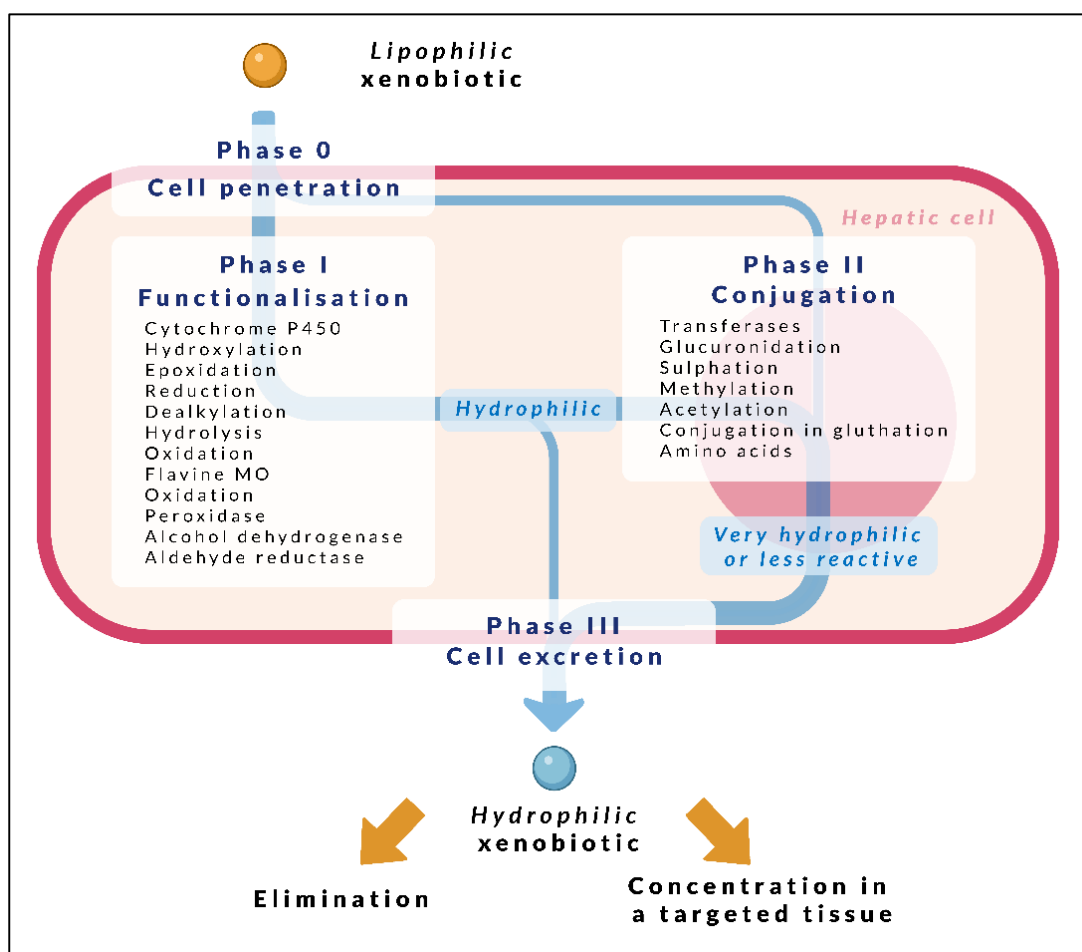


Fig. (2). Steps of xenobiotic metabolism at the cellular level. The exogenous molecule enters the cell through the plasma membrane using phase 0 influx transporters and is then transformed by phase I and then phase II enzyme complexes that render it water-soluble for excretion. The xenobiotic is excreted from the cell by efflux transporters during phase III. (A higher resolution / colour version of this figure is available in the electronic copy of the article).

2.3.2. Metabolic Variability

Different endogenous (*e.g.* genetic) and exogenous/environmental factors (exposure to a specific substance) can affect the metabolism and thus modulate the biological response. From a quantitative point of view, the activities of enzymes can be induced or inhibited. On the other hand, from a qualitative point of view, certain pathways will be favored and others inhibited [7].

2.3.2.1. Species

Qualitative and quantitative variations may exist, with the presence of different isoforms in diverse species or different levels of the same isoform in two different species. This may result in the creation of distinct metabolites between the study species and the target species and may lead to biases in the extrapolation and interpretation of data [11].

2.3.2.2. Age

As with interspecies variation, quantitative and qualitative variations in metabolic capacity, especially for CYPs, have been shown in the newborn [12, 13] and the elderly [14].

2.3.2.3. Diseases State

A pathological situation (*e.g.*, hepatic impairment, cardiac insufficiency) may have an impact on the metabolic capacities and

thus modify the pharmacokinetic parameters of a xenobiotic [15, 16].

2.3.2.4. Genetic Polymorphism

Different variants of the same isoform may exist in the population, as the metabolic capacity of each variant is not the same.

Their presence is explained by genetic mutation mechanisms (substitution/insertion, deletion of bases, or splicing defects) and can lead to a truncated protein, decreased activity, or even inactive.

Two typical profiles are found in the population: slow metabolizers with two mutated alleles and fast metabolizers with at least one wild-type allele [17].

A well-known example concerns the metabolism of ethanol in the East Asian population [18]. They have an inactive aldehyde dehydrogenase that prevents them from properly metabolizing acetaldehyde (from the dehydrogenation of ethanol) to acetate. When consuming ethyl alcohol, carriers of this variant show signs of intolerance much more rapidly than the rest of the population. In addition, they are also exposed to serious toxic risks due to the accumulation of aldehyde, which has carcinogenic properties.

2.3.2.5. Environment

Xenobiotics present in environmental pollution, food or even drugs may interfere with the enzymatic activities that normally

metabolize them, in terms of induction and inhibition. Inhibition is faster than induction because an inhibitor acts directly on the enzyme and does not require any transcriptional regulation step [19].

2.3.3. Metabolism Induction Mechanisms

Xenobiotics can play a ligand role by binding and activating transcription factors, increasing the gene expression coding for xenobiotic metabolism enzymes. The implementation of transcriptional regulatory mechanisms leads to an increase in the synthesis of the corresponding enzymes. These processes are slow, around 24 to 48 hours to observe an increase in protein synthesis and may require chronic exposure to the inducer to reveal a phenomenon, involving deleterious processes absent in basal conditions. Yet, not all enzymes are inducible. Drugs such as phenobarbital or omeprazole, ethanol from alcohol consumption or combustion products such as Polycyclic Aromatic Hydrocarbons (PAHs) can induce enzymes for xenobiotic metabolism.

Most of the transcription factors are nuclear receptors present in the cytoplasm and their activation and translocation to the nucleus play their role in activating transcription [20]. The most known and characterized transcription factors are the Pregnane X Receptors (PXR), Peroxisome Proliferators-Activated Receptor (PPAR), Constitutive Androstane Receptor (CAR), and Aromatic hydrocarbon Receptors (AhR). AhR does not belong to the family of nuclear receptors because, unlike the previous one, it is not involved in hormonal regulation [21].

Different mechanisms can lead to the activation of transcription. Xenobiotics internalized in the cell can directly activate receptors in the cytoplasm before being transposed to the nucleus; this is the case for CAR after xenobiotic-induced phosphorylation. PXR and PPAR are located directly in the nucleus and the fixation of the xenobiotic in their hydrophobic pocket would lead to their dimerization with another indispensable actor, Retinoic Acid Receptor (RXR) for the activating effect on detoxification gene promoter sequences [22]. CAR activity also depends on RXR. The mechanisms of the AhR receptor pathway involve the release of the receptor that is bound to chaperone proteins in the cytoplasm under basal conditions. The binding of a xenobiotic ligand will allow this release and then its translocation to the nucleus *via* the partner Arnt (AhR nuclear translocator). The dimer is then bound to XRE (xenobiotic response element) promoter sequences to induce transcription mechanisms.

The mechanisms described above have been identified primarily at the hepatic level and the literature on the molecular signaling pathways involved being limited to this organ. However, some molecular partners have been identified in other organs, such as the skin [23], and are described shortly later in a specific paragraph.

2.4. Bioavailability

The concept of bioavailability was originally developed for the drugs, it refers to the fraction of the dose which reaches the systemic circulation as an intact molecule [16, 24]. It is summarized as *F*, bioavailability factor and is assessed by the ratio of the dose or fraction that reached the circulation by a given route of administration divided by a reference dose, administered intravenously, thus directly available in the circulation and considered equal to 100%. This parameter is very important because it reflects both the behavior of a substance during its absorption and its first pass through an organ.

Depending on the route of administration, the absorption variables will significantly influence the kinetic profile (Fig. 3) which may affect the biological effects induced by the substance of interest.

3. DERMATOKINETICS

Dermatokinetics designates the entry into the body and the pathway of a substance administered dermally. The main mechanisms involved are described in this section.

3.1. Specificity of Skin Structure

The skin is an organ that covers almost the total body and whose surface varies from 1.5 to 2 m² for an adult, *i.e.* approximately 15% of the total weight. It represents a significant interface with the external environment, constituting of a physical and vital barrier for the organism [25]. However, this protective barrier is not totally impermeable and allows the passing of many substances to varying degrees.

The skin consists of three layers: the epidermis, the dermis, and the hypodermis. The outermost layer of the epidermis is called the Stratum Corneum (SC) and is considered to be the major barrier to skin penetration. The stratum corneum is a 10 to 20 µm thick structure composed of multiple layers of corneocytes, which are anucleated cells filled with hydrophilic keratin and firmly attached to each other by junctions, corneodesmosomes. The structure of the stratum corneum is schematically described as a brick and mortar wall with cells loaded with hydrophilic proteins and surrounded by lipids acting as cement, bound to cell membrane proteins by covalent bonds [26]. The stratum corneum is also known for its function as a reservoir of topically applied substances [27] and is involved in skin hydration [28]. Keratinocytes are the main cells of the epidermis, but other cell populations perform sensory, immune, and photoprotection processes. The dermal-epidermal junction separates the epidermis from the underlying dermis. It is permeable to the molecules which have penetrated the epidermis that may reach the vascularized dermis. In the opposite direction, it is permeable to nutrients and cells involved in immunological reactions.

3.2. Skin Penetration of Xenobiotics in Humans

3.2.1. Cutaneous Absorption Pathways

Dermal absorption is defined as the transfer of a xenobiotic through the skin from the external environment to the bloodstream. Penetration is the first step in absorption and consists of the entry of a substance into a layer of the skin [29]. A molecule with the ability to penetrate the epidermis will be able to reach the systemic circulation *via* numerous dermal peripheral blood vessels connected to the general circulation.

When a substance is applied to the skin, it first interacts with the stratum corneum. There are three pathways (Fig. 4) by which the substance can penetrate the skin:

- (1) The intracellular route: the substance moves alternately into keratin-filled hydrophilic corneocytes and then into the lipid-rich intercellular hydrophobic spaces.
- (2) The intercellular pathway: the substance goes around the corneocytes in the intercellular cement consisting of aqueous and lipid phases.
- (3) Intrafollicular route: the substance bypasses corneocytes and intercellular cement by entering hair follicles, sweat or sebaceous glands.

These three routes play a role in cutaneous absorption, with a predominance of intercellular passage (90-99%), which allows the diffusion of both lipophilic and hydrophilic molecules.

Intercellular passage involves diffusion around cells and allows penetration according to its affinity for hydrophilic or lipophilic intercellular components. This is a longer but more efficient path for compounds to be absorbed. Intracellular passing is shorter,

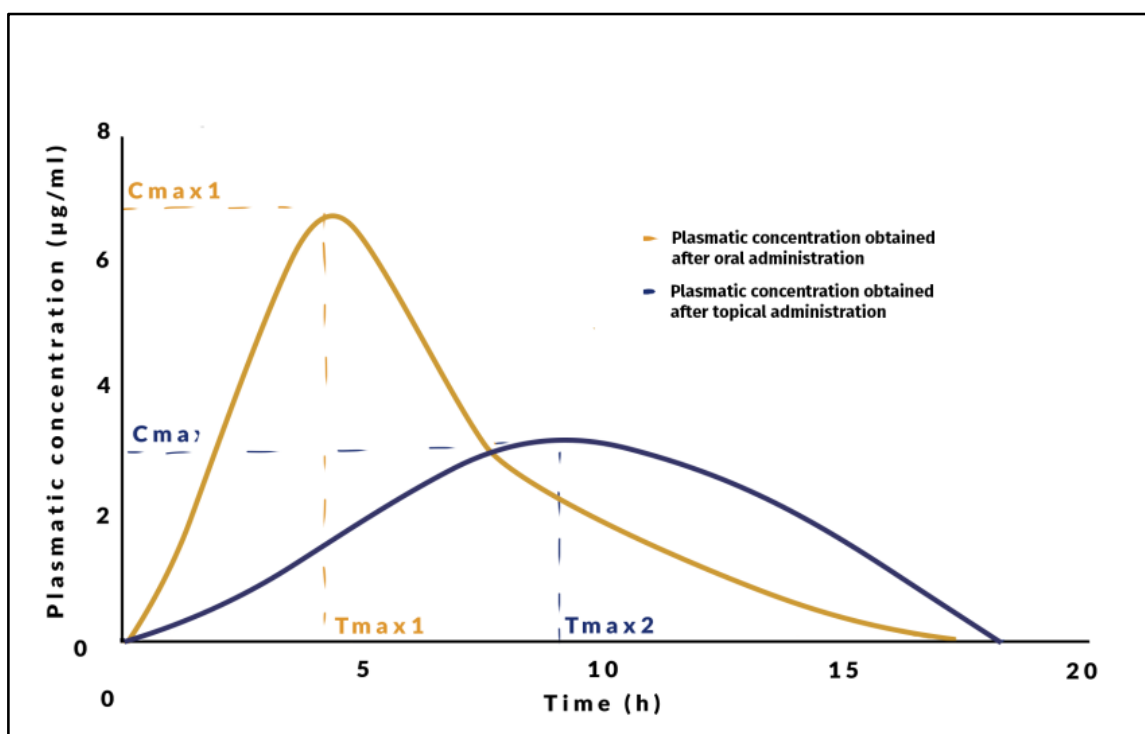


Fig. (3). Comparison of systemic bioavailability after oral and dermal administration. The yellow curve shows a dosage obtained after oral administration, the blue curve after topical administration. The bioavailability parameters are different in the two situations; the respective effects will also be distinct. (A higher resolution / colour version of this figure is available in the electronic copy of the article).

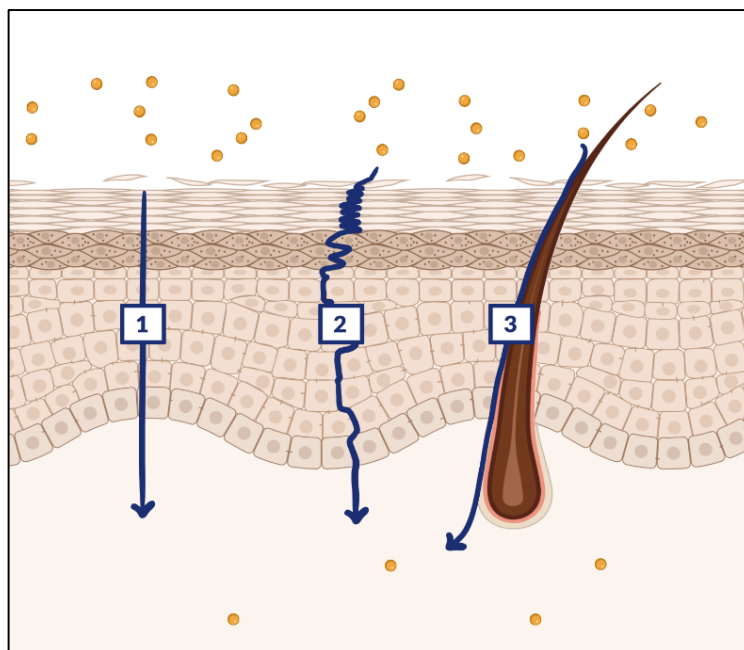


Fig. (4). Absorption pathways of a xenobiotic through the skin. Intracellular (1), Inter cellular (2) and Intrafollicular (3) Pathways allow lipophilic substances to enter the body upon topical application. (A higher resolution / colour version of this figure is available in the electronic copy of the article).

25 μm , compared to 350 μm for the intercellular path but requires the molecule to pass through hydrophilic and lipophilic compartments [30, 31]. Similarly, the intrafollicular passage is negligible since the total surface area covered by hair on the human body is less than 1%. One can note that intrafollicular passing is typically absent in *in vitro* models and therefore is less studied.

3.2.2. Parameters Affecting Skin Absorption

Dermal absorption is modulated by various factors related to:

- The active ingredient (molecular weight [32], octanol/water partition coefficient [33], formulation, volatility, etc.).

- The vehicle (hydrophilicity/lipophilicity, penetration enhancer effect).
- The conditions of application of the substance (dose, site, surface area, frequency, and duration of application).
- The individual (age, skin condition, skin hydration, occlusion, skin flora) [34].

For a given molecule it's possible to predict its behavior regarding its permeability through skin membranes. As mentioned above, some criteria are important and will be detailed here below:

- Molecular weight should be less than 500; of course, this is not a strict cut-off value as other properties may modulate this value.
- Log P, which represents the Octanol/Water partition coefficient, needs to be kept in the range 1-2
- The environment of the molecule should be adapted to keep the molecule under a non-ionized form. In consequence, pKa plays an important role.
- A polar or non-polar environments will act differently on penetration. A non-polar environment will tend to increase penetration.

Experimentally, two parameters are considered to classify dermal penetration:

The measured steady-state penetration rate, J_{ss} expressed as $\mu\text{g}/\text{cm}^2/\text{h}$ and the permeability coefficient K_p expressed as cm/h . Both parameters are useful to compare and predict the behavior of a molecule regarding its permeability.

With the use of enhancers, skin penetration may dramatically be increased by physical methods (iontophoresis, electroporation, and ultrasound) or chemical methods (compound increasing the skin penetration of another substance in co-formulation) [35]. Such methods could impact the organization of lipid layers, the interaction with intracellular proteins of corneocytes, the distribution of the ingredient in the stratum corneum, and the hydration of the stratum corneum to form polar channels conducive to the diffusion of hydrophilic substances, *etc.* This "enhancer" effect is to be considered in so far as it increases the bioavailability of a substance, which must be considered in the risk assessment. This effect can be sought in the case of therapeutic molecules that have difficulty passing through the cutaneous barrier but needs to be avoided in the case of a substance with toxic potential.

3.3. Metabolism in the Epidermis

As seen before, substances with specific physicochemical properties, including lipophilic characteristics can be passively absorbed through human skin.

Yet, the skin is more than a simple physical barrier; it also has an endogenous enzymatic activity [36] capable of interacting with absorbed xenobiotics with the ultimate aim of facilitating their elimination from the body. On the body scale, skin metabolism has a lesser impact in comparison to the hepatic metabolism [29] responsible for handling all molecules, endogenous and xenobiotics, present in the systemic. However, skin metabolism mechanisms may have consequences on local or systemic toxicity. Skin metabolism investigation appears to be crucial as it will allow the development of predictive models of the metabolic profile of a substance absorbed through the skin.

3.3.1. Metabolic Pathways in the Skin

Most hepatic detoxification enzymes are present in the skin and are active through enzyme activity located in the epidermis [37-41]. Some authors have attempted to compare liver and skin activities, and have considered that 0.1-28% of Phase I and 0.6-50% of Phase

II liver activities are found in the skin [29]. The large variability in the published data makes the interpretation very hard and the conclusion uncertain.

An extensive review of the literature on enzymes for xenobiotic metabolism in the skin [42] concluded that more research is needed to understand the mechanisms found in human skin when a xenobiotic is absorbed and metabolized. Numerous criticisms were expressed on the quantitative data from studies that have attempted to determine the expression and activity levels of enzymes for xenobiotic metabolism in the skin. The main problem relates to experimental and technical points, as the lack of standardization prevents the studies' comparison.

However, it is well established that even if a significant variability is evidenced, the published data depict similar tendencies. Detoxification activities are indeed present in the skin and the experimental models used.

3.3.1.1. Phase I Enzymes

Represented mainly by enzymes of the cytochrome P 450 family, the associated mechanisms involve oxidation and/or reduction reactions on different substrates.

3.3.1.1.1. The Cytochrome P450

Since the late 1980s, this family had its own nomenclature [43]. The genes coding for enzymes of the Cytochrome P450 family and the enzymes themselves are referred to as CYP. This is followed by a number indicating the family, a capital letter indicating the sub-family and another number for the isoform. CYPs are responsible for the metabolism of many endogenous substrates such as prostaglandins, leukotrienes, vitamin D, corticosteroids, testosterone, and certain fatty acids. These enzymes are involved most of the time, in the elimination and detoxification of xenobiotics. However, in some cases, CYPs activate toxic chemicals such as pro-carcinogens [44] or drug metabolism [45] leading to metabolites more active than the parent drug. The most caricatural case is that an inactive prodrug could be activated by metabolic transformation.

The typical CYP-catalyzed reaction involves the incorporation of an oxygen atom into a substrate. In addition to the intervention of molecular oxygen, a cofactor, nicotinamide adenine phosphate (NADPH), is necessary for the reaction to take place, bringing two electrons. NADPH is regenerated by another enzyme: NADPH P450 reductase, which allows the recycling of the cofactor in each reaction cycle.

CYPs in the skin are by far, less abundant than in the liver. However, a large number of studies have identified, located, and measured their activity in the skin. The presence of CYP messenger RNAs in healthy and untreated human skin has been demonstrated, but in terms of enzyme activity, some authors consider these enzymes as not active in the skin [46].

On the other hand, enzyme activities corresponding to CYPs involved in the metabolism of procarcinogens and drugs (CYP1A1, CYP1A2, CYP1B1, CYP2A6, CYP2E1, CYP2D6, and CYP3A4/5) have been identified in the skin [47].

The CYP1A family, known and documented for its strong inducibility in the liver by polycyclic aromatic hydrocarbons (PAHs), is used as a biomarker of exposure to environmental pollutants [37, 48]. The ability of the skin to respond to PAH exposure in terms of induction in skin models has been studied [49], however, the impact of this modulation has never been correlated with a change in the dermal bioavailability of a substance absorbed through the skin, as the assessment of induction is used as a marker of functionality.

3.3.1.1.2. Enzymes Other than CYP

Flavin Mono-Oxygenase (FMO) also uses molecular oxygen to oxidize nitrogen, sulfur, or phosphorus compounds. NADPH is also

needed for facilitating the catalysis of this reaction. Present in the epidermis and skin appendages such as the sebaceous glands and hair follicles at levels comparable to CYP, these enzymes may compete with CYP for the same substrates [40, 50].

Alcohols and aldehyde dehydrogenases (ADH and ALDH) catalyze the oxidation of alcoholic derivatives to aldehyde and then to carboxylic acid. Unlike CYP and FMO, the source of oxidant is not molecular oxygen but a nicotinamide adenine dinucleotide (NAD) molecule. Alcohol dehydrogenase is present in human skin, and its involvement in the generation of aldehyde sensitizing derivatives is strongly suspected [51, 52].

Monoamine oxidases (MAOs) can also be found in the skin [53] and differ from those in the liver. They allow the oxidative deamination of primary amines into aldehydes.

Esterases identified in human skin are significantly involved in the hydrolysis of ester functions of certain xenobiotics and their biotransformation into the corresponding alcohol and acid [54]. Represented mainly by enzymes of the cytochrome P 450 family, the associated mechanisms involve oxidation and/or reduction reactions on different substrates.

3.3.1.2. Phase II Enzymes

Phase II metabolism aims to transform previously functionalized molecules during Phase I into conjugated hydrophilic substrates to facilitate solubilization in excreta and therefore eliminated. At the level of enzymatic catalysis, these are essentially conjugation reactions by transferases between an electrophilic function of the phase I metabolite and a nucleophilic substrate. Human skin expressed a broad range of phase II enzymes, they are more abundant than phase I compared to liver levels [55].

UDP glucuronyltransferases (UGTs) catalyze the formation of glucuronide conjugates by adding glucuronic acid to the oxygen, nitrogen, or sulfur functions of a molecule. Like CYPs, UGTs are expressed in the membrane of the endoplasmic reticulum. UGT activity is well observed in human skin, epidermis, and even in the stratum corneum [56, 57].

Sulfotransferases are involved in sulfate group conjugation mechanisms on a substrate previously activated in phase I. Sulfonconjugation reactions of endogenous steroids and xenobiotics can

be carried out in the skin. Phase II is generally considered to be a mechanism leading to the deactivation of xenobiotics, but it has been shown that sulfotransferases can also transform and activate substances. Minoxidil is activated in human skin by sulfotransferases to the active metabolite, minoxidil sulfate [58].

N-acetyl transferases are present in the skin and their activity is selective towards certain xenobiotics such as aromatic amines. This pathway represents a detoxification mechanism for p-aminobenzoic acid [59, 60].

Finally, glutathiones transferases (GST) are functional in human skin. GSTs transfer reduced glutathione to electrophilic metabolites because this group is highly nucleophilic. The isoform π of GST is the one most present in the skin [42, 61] unlike the liver where the other forms are mainly found (α , μ , θ , and α).

3.3.2. Importance of Skin Metabolism and Toxic Reactions

In general, Phase I metabolism is associated with the formation of reactive and potentially toxic derivatives when Phase II metabolism reduces the reactivity of metabolites by conjugation. The term bioactivation is used to describe the results of a metabolic step that generates a form that is more reactive than the parent molecule and possibly toxic. It is recognized that skin metabolism can contribute to the initiation of pathological events (Fig. 5). This mainly concerns the activation of small absorbable molecules in the skin that can trigger a sensitization reaction, the first stage of allergic contact dermatitis [62]. Other toxic effects such as genotoxicity [63] or induction of carcinogenesis [64] could be triggered by skin metabolites but are less common than sensitization-related problems.

Skin sensitization is the first step in allergic contact dermatitis. The mechanism relies on the ability of a hapten, a low molecular weight substance with antigenic properties, to reach the epidermis and bind to skin proteins to form an immunogenic complex [65]. This binding occurs between an electrophilic and nucleophilic structure (amino acids rich in sulfur and nitrogen) such as lysine and cysteine [66]. The role of cutaneous metabolism is of prime importance here because it enables the activation of prohaptens, which cannot bind skin proteins due to lack of adequate chemical groups, into competent haptens [39, 67, 68]. Following the formation of the immunogenic complex, a cascade of reactions leads to the proliferation of antigen-specific T cells. A second exposure to

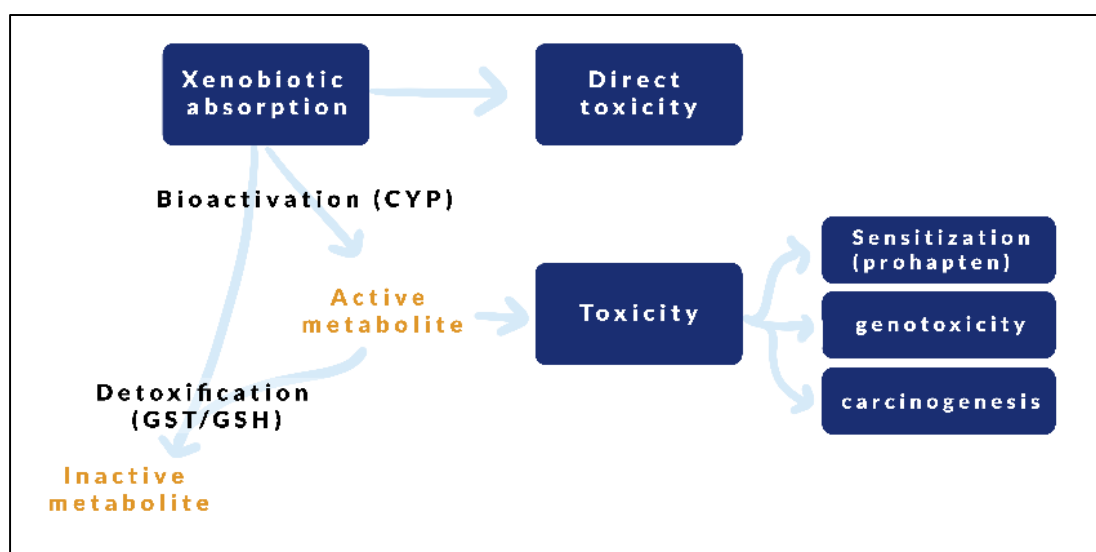


Fig. (5). The balance between activation and detoxification by xenobiotic metabolism. The importance of skin metabolism is demonstrated during the bioactivation of substances absorbed in the epidermis into toxic metabolites and/or during detoxification into inactive metabolites. (A higher resolution / colour version of this figure is available in the electronic copy of the article).

the antigen is then sufficient to generate the second stage of the pathology, the elucidation phase, which results in an inflammatory reaction.

The biotransformation mechanisms allowing hapten activation described above appear to be a widely accepted hypothesis by the scientific community [69, 70]. Eugenol and its derivatives, such as aromatic compounds found in perfumery, constitute a model for prohaptens and have been identified as substrates for CYP [71]. Other alcoholic, unsaturated derivatives, such as geraniol or cinnamic alcohol, can be oxidized to corresponding aldehydes capable of forming an immunogenic complex with skin proteins [51]. The importance of knowing the metabolic fate of an absorbed substance makes sense to predict any reactive behavior that could activate the mechanisms and cause toxic inflammatory reactions.

Polycyclic Aromatic Hydrocarbons (PAHs) are found in the environment and are a growing concern in terms of pollution. PAHs acquire their carcinogenic potential after activation by enzymes for xenobiotic metabolism. The metabolic pathway of Benzo [a] Pyrene (B[a]p) is well documented and is a good illustration of CYPs activation.

The full activation requires both CYP 1A1 and CYP 1B1 to lead to an epoxide intermediate, which is second step converted with an epoxide hydrolase into diol epoxides, more active, and responsible for DNA interaction leading to a genotoxic effect.

This example holds also for many other PAH structures, such as 7, 12-dimethylbenz[a] anthracene, as demonstrated by T Shimada et Fujii-Kuriyama [44].

4. EXPERIMENTAL MODELING IN DERMATOKINETICS

In the context of human risk assessment, the role of pharmacokinetics is to describe the behavior of an exogenous molecule that interacts with a human organism. In the majority of cases, the issue

is to predict this behavior using different models because, for obvious ethical reasons, experimentation on humans is not conceivable for fundamental or applied research and is very rarely used for regulatory purposes in toxicology. The development of relevant models to reproduce physiological and/or pathological functions of the human organism is therefore essential for their use in the perspective of a robust methodology.

4.1. Experimental Skin Models Used in Research and Toxicology

The definition of the concept of the model is very broad. In biomedical research and toxicology, the assessor is limited to so-called experimental models that enable the reproduction of functions of interest to predict human reactivity and sensitivity to a chemical substance, the understanding of a disease or homeostasis of organisms. Historically, toxicology research has used animals for experimental models.

Table 1 presents the main advantages and drawbacks of each skin model used in research.

4.1.1. Animal Models

For centuries, animal models have been used as a reference to study the impact of a molecule on a living organism extrapolating it to humans [72-74]. The use of animals to investigate potential adverse effects on humans is widely developed. Today, the use of animals as experimental models is controlled by strict ethical regulations [75].

Rodent skin is the *in vivo* skin model recommended by the OECD [76] and the FDA [77] for skin pharmacokinetic data acquisition. The most commonly used animal is the rat due to its ease of use and a large amount of data available on this model. However, despite these recommendations and advantages, a major disadvantage persists and reduces the quality of extrapolation to humans.

Table 1. Summary of models available for dermatokinetic research.

Model	Benefits	Disadvantages
Animal skin <i>in vivo</i>	Opportunity for integrated organization-wide studies Preservation of metabolic capacity Maintenance of physiological regulations	Not compatible with high throughput screening Complex use Quantitative and qualitative interspecies variability in absorption and metabolism Testing for cosmetics prohibited
Human skin <i>in vivo</i>	Gold standard model	Very strong limitation of use because of ethical issues
Animal skin <i>ex vivo</i>	Morphology and structure of preserved <i>in situ</i> skin Compatible with cosmetic tests	Difficulty of supply
Human skin <i>ex vivo</i>	Compatible with cosmetic tests	Decreased metabolic capacity Supply difficulties
Reconstructed epidermis	Animal alternative closest to human skin Compatible with cosmetic test Suitable reproducibility	Decreased metabolic capacity Complex manufacturing
Primary keratinocytes	Compatible with cosmetic tests Physiological properties close to <i>in vivo</i>	No information on absorption Decreased metabolic capacity
Keratinocyte line	Compatible with cosmetic tests Easy to use Excellent reproducibility and homogeneity	No information on absorption Removal from <i>in vivo</i> Loss of physiological properties
Intracellular fraction	Compatible with cosmetic tests High metabolic activity	No information on absorption
Artificial membranes	Compatible with cosmetic tests Excellent reproducibility	No metabolic properties

Morphological disparities, particularly in terms of epidermal thickness, result in an overestimation of absorption. Variations as big as 10-fold have also been observed between rat and human skin [78]. Concerning metabolism, even if the enzymatic material is mostly similar, significant quantitative and qualitative differences exist [40]. These differences must therefore be considered when analyzing the data generated with this model to avoid misinterpretation.

Mice can also be used. Its small size is a limitation but its widespread use and characterization make it an affordable model. For example, athymic "nude" mice with a deficient immune system can be grafted with human skin [79-81].

Similarly, pig skin has strong structural homology for the human epidermis, and studies have shown that its use can generate results extrapolated to humans in terms of skin absorption but also metabolic capacities [82]. Once again, logistical and regulatory constraints limit its use. The skin of other animals may also be used. Monkey' skin (rhesus macaque) has been the most studied because of its close human phylogenetic and therefore morphological relationship [83]. However, the high cost, the difficulty of supply and ethical issues often prohibit its use in research.

4.1.2. Alternative Models for Animal Experimentation

From a regulatory point of view, the evolution of European laws has resulted in a reduction in the number of animals used in research work. According to the European Commission Regulation animal testing and the marketing of finished cosmetic products and cosmetic ingredients are prohibited. The REACH regulation (namely «Registration, Evaluation, and Authorization of Chemicals»), which concerns all industrial chemicals, goes in the same direction by recommending to limit the number of animals. Therefore, this regulatory framework was accelerated and allowed the development of alternative models for animals.

From a scientific point of view, the main difficulty with non-animal tests is to reproduce all the events involved in biological effects on an organism [84]. It is recognized by the scientific community that animal models do not fully reflect human physiology, in particular the kinetic and dynamic phenomena of the human organism, leading to uncertainties in extrapolating animal data to humans [85, 86].

4.1.2.1. In vitro Skin Models

Monolayer cell cultures from primary cultures (keratinocytes or other cells from human skin samples) or cell lines (the HaCaT keratinocyte line or other immortalized lines) are good models for assessing metabolism by studying molecular mechanisms [59, 87, 88]. Therefore, their uses are widespread in basic skin biology research but do not allow the study of the diffusion of a substance and cannot be used in applied models for predicting skin absorption and metabolism.

To overcome this defect and approximate human skin, three-dimensional reconstructed skin models have been developed over the last decade. First developed for transplants of burned patients, those constructs are now widely used by the cosmetic and pharmaceutical industry to test substances [89-91]. A distinction is made between epidermis models reconstructed on an inert matrix and "whole skin" models containing an epidermis reconstructed on a dermis equivalent containing fibroblasts [92]. The epidermis may be composed of keratinocytes alone or co-cultured with melanocytes and skin immune cells [93]. Studies have shown their relevance and similarity to the structure and enzymatic equipment of the human epidermis [94-97].

There are many advantages to using skin equivalents *in vitro*: good measurement repeatability (intra-model), no supply problems, and no ethical issues. Those models provide the same permeability

characteristics as skin *ex vivo* when comparing several substances to different physicochemical properties. Even if good repeatability for a model can be achieved, there is great variability between models. In addition, inadequate barrier function in current models is due to altered desquamation, non-keratinized microscopic foci, and differences in lipid composition and organization. Also, the permeability of these models can vary from 5 to 50 times greater than *ex vivo* skin [98, 99].

4.1.2.2. Ex vivo Models

Human skin can be removed by surgery and by biopsy, to obtain viable explants maintained in culture in a nutrient medium. Explants are the closest model to *in vivo* human skin. Work has focused on their metabolic capacities in comparison to other skin models [40] and their use as predictive tools [100]. The structure and morphology of the epidermis are preserved while a decrease in metabolic capacities can be observed through time. Difficult in supply, conservation, transport, or cost are the main disadvantages.

4.1.2.3. Synthetic Membranes

New approaches have led to the development of synthetic membranes that mimic skin structure. Composed of different classes of lipids mimicking human epidermis composition, their multi-layer structure creates a morphological homology with the epidermis. Several artificial systems have been developed; among which Stratum Corneum substitutes [101], STRAT-M[®] membranes [102], or Parallel Artificial Membrane Permeability Assays (PAMPA) [103].

Synthetic membranes are used today as a screening tool to predict skin absorption, and studies are ongoing to validate them as alternatives to human skin.

Several authors have shown a good correlation with human skin for a limited range of chemicals [104]. In contrast, synthetic membranes are very sensitive to changes in experimental conditions and formulations [105].

The undeniable advantage of these models is that they have a very high degree of reproducibility in data generation. Despite this, their use remains limited due to the lack of metabolic activity.

4.1.2.4. Isolated Fractions

These models provide samples with varying levels of enzyme enrichment and allow the mechanisms of metabolism to be studied exclusively [106]. They include subcellular fractions from human or animal skins (S9 fraction and microsomes), purified enzymes, and enzymes recombined in expression vectors [107].

Fractions must be precisely selected as different enzymatic materials are been measured. Microsomes are endoplasmic reticulum vesicles and therefore will only contain CYP and FMO expressed in the organelle membrane. All families of enzymes are present in the S9 fraction which corresponds to a supernatant obtained after centrifugation at 9,000 g of a cell homogenate. Some authors have pointed out the advantages of such subcellular fractions derived from human skin and highlighted that inter-individual variability in Phase II enzymes should be considered to improve and implement the mathematic model used in risk assessment [108].

Interestingly, other authors [109] use S9 of hepatic origin to simulate the metabolic activity of the skin, but this approach is criticized because of the qualitative and quantitative differences between the two organs. Due to the low concentration of enzymes in the skin, the production of such a fraction of skin origin is complex and requires large amounts of samples at baseline. Purification from the latter appears to be very difficult from a technical point of view [110].

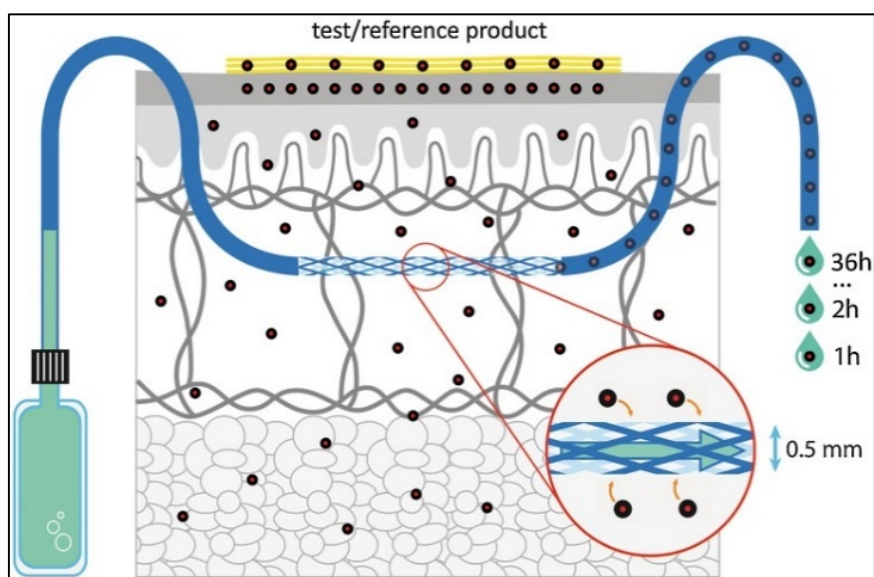


Fig. (6). Schematic representation of open flow dermal microdialysis. (A higher resolution / colour version of this figure is available in the electronic copy of the article).

4.2. Dermal Bioavailability Study Methods

4.2.1. *In vivo* Studies

Animals are exposed to the topically administered molecule, placed in metabolism cages, and sacrificed at the end of the study to determine the quantity of the interesting substance absorbed and present in excreta, tissues, and biological fluids [111]. For this type of *in vivo* study, radiolabelled molecules are often used to allow the entire pathway to be monitored, including parent molecules, and metabolites. The choice of the radioactive isotope and a relevant position of the labelled atom within the molecule are essential to follow the metabolic fate of substances [112].

Exposure should mimic the physiological conditions to which a human subject could be exposed: limited deposition zone, exposure time of 6-24 h in general, and occlusions of the administration site if any. Studies in humans, which are highly regulated, are also possible, reserved for products that have previously demonstrated their innocuousness. The quantity of product absorbed in the subject will be measured in samples of plasma, excreta, exhaled air, or in the superficial layers of the epidermis by tape stripping [113] layers of stratum corneum being successively removed from the exposed skin area using adhesive films.

4.2.2. Membrane Studies in an *In vitro* System

These percutaneous penetration studies are primarily conducted with a diffusion cell system also known as the Franz cell [114, 115]. A membrane, explant of human, or animal skin, reconstructed skin or synthetic membrane, is used in an air/liquid interface system.

The test substance shall be applied to the membrane for a given duration based on appropriate human exposure. Samples of the receiving fluid are collected at different times to determine the amount (and rate) of the test substance that has penetrated the membrane. At the end of the study, the total absorption of the test substance through the skin is estimated. It may be expressed as a percentage, amount, or ratio of absorption per unit time, or, in the case of an infinite dose, as permeability constant.

4.2.3. Cutaneous Microdialysis

The microdialysis (or microperfusion) method can be applied to dermatokinetic studies to measure the cutaneous penetration of a

substance on a whole skin explant *ex vivo* (including epidermis, dermis, and hypodermis) or *in vivo* [116, 117]. Microdialysis was initially developed for brain research but its application in the field of dermatokinetics is increasingly used. It is an invasive technique based on the principle of inserting a thin catheter into the tissue to be studied to sample analytes by concentration gradient (see schematic Fig. 6). Also called a probe, the catheter consists of a tube with a hollow fiber made of a semi-permeable membrane (allowing water and low molecular weight compounds to pass through). A circuit connected to a pump allows the catheter to be infused with a liquid of a composition homologous to that of the extracellular medium of the tissue. A concentration gradient exchange occurs when the liquid is infused into the tissue, with the desired substance moving from the most concentrated to the least concentrated medium. This process is used to sample and quantify metabolites produced from a parent substance that is absorbed after application to the skin surface of a subject. Although there are definite advantages, ethical constraints limit the use of this technique due to its invasive nature. Technical disadvantages have also been identified such as low spatial (applicable to only a small skin surface) and temporal (for short time exposure) resolution.

4.2.4. Innovative Bioreactor System

The diffusion cell system, allowing to evaluate the penetration of a substance through a membrane, can be adapted by "adding" the missing property of biotransformation by including functional enzymes. To mimic the two major skin functions, absorption, and metabolism, a biomimetic bioreactor model has been developed (Fig. 7). The work focused on the development of a method for immobilizing enzymes to re-create the skin's metabolism [107]. This study required the use of membrane fractions containing CYPs [118] and the use of suitable assembly methods to preserve the structural and catalytic properties of these entities. Several physico-chemical techniques were used to characterize the different immobilization steps. To reproduce a biological system, enzyme immobilization can be used. It can be defined as the attachment of an enzyme to a phase such as a carrier or a matrix. The use of this technique enables to create biomimetic systems and to exploit enzymes outside their original medium. Attachment to a carrier protects the enzymes from denaturing conditions to which they may be exposed outside their normal environment, pH, temperature, or ionic forces are factors that can degrade the tertiary structure of proteins that

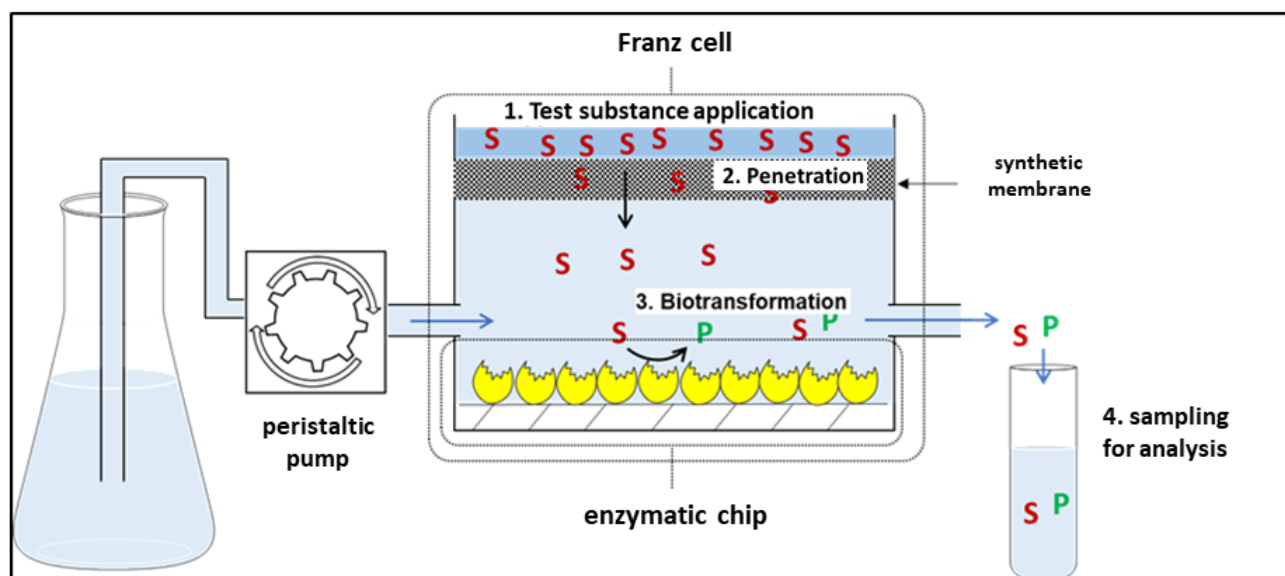


Fig. (7). Schematic description of the bioreactor. A diffusion cell, connected to a peristaltic pump generating a flow in the receiving chamber is used. The enzyme chip on which the membrane fractions will be immobilized is included in the bottom. A test substance can therefore be applied to the outside surface of the synthetic membrane used, penetrate through it, be absorbed into the receiving chamber, and then bio-transformed on contact with the enzymes. Samples are taken to measure the absorbed parent substance and the metabolites produced over time. (A higher resolution / colour version of this figure is available in the electronic copy of the article).

confer enzyme functionality. Another aspect that could be explored is the adsorption of human skin microsomes. Microsomes can be prepared from cultures of keratinocytes treated with known inducers, before being adsorbed with the layer-by-layer method.

CONCLUSION

Dermatokinetics is a relevant tool to picture the fate and the behavior of a xenobiotic that crosses the cutaneous barrier. Regarding skin bioavailability assessment, only skin absorption is documented by regulatory procedures when other influencing parameters such as skin metabolism are not systematically assessed. It is becoming increasingly recognized that skin metabolism may play a relevant role in the biotransformation of molecules able to cross the stratum corneum. Regarding the experimental part, assessors have a wide choice of models and methods to evaluate these parameters. The choice of model should be adjusted according to criteria of biological significance in humans or to meet official recommendations.

However, risk assessment of cutaneous products still raises questions about the representativity of the existing models compared to *in vivo* skin metabolisms. When the precise determination of toxic molecule's effects is complex on its own, it is of major importance to establish a consensus when facing complex situations created by mixtures of molecules coming in contact with human skin. Risk assessment in the industry, as asked by regulations, is generally performed realized a priori on raw materials in a context that is far from its final use. Consumers are daily exposed to a broad range of substances that can cause biological effects as is well described by exposure studies [119]. This results in complexity for the risk assessment process. These difficulties may be related to simultaneous exposure to different molecules or with risks of interactions between the molecules or between induced biological mechanisms. The type of population or sub-population must also be considered due to different sensitivities and sensibilities (children, adults, seniors.). It is therefore essential to integrate this systemic notion of combined exposures when the safety of a chemical ingredient must be assessed.

We have studied this problem to explain the undesirable and unexpected effects of cosmetic products. By analogy to the analysis of pharmacovigilance data in pharmacovigilance for pharmaceuti-

cals [120], the hypothesis of an interaction with another molecule has been put forward. This theory is based on the problems of drug interactions [121] in which the concurrent use of two drugs, generally absorbed orally, can cause toxic effects that are not present if the molecules are not administered at the same time. We focused on the dermatokinetics phase and more precisely on skin metabolism that could be subject to interaction. Our hypothesis targeted induction phenomena of skin metabolism that could be caused by chemicals found in the systemic blood circulation. We have studied the hypothesis of CYP induction phenomena of the epidermis *in vivo* in a subject exposed in a systemic way [48]. The results suggested that the expression of enzymes in the human epidermis can be regulated by chemical factors present in the bloodstream. This shows that more studies should focus on skin metabolism induction by exposure substances and those multi-exposures are a challenge for risk assessment.

CONSENT FOR PUBLICATION

Not applicable.

FUNDING

None.

CONFLICT OF INTEREST

The authors declare no conflicts of interest, financial or otherwise.

ACKNOWLEDGEMENTS

Declared none.

REFERENCES

- [1] Kwon, Y. *Handbook of Essential Pharmacokinetics, Pharmacodynamics and Drug Metabolism for Industrial Scientists*; Springer: Amsterdam, Netherlands, 2001.
- [2] Abuhelwa, A.Y.; Williams, D.B.; Upton, R.N.; Foster, D.J.R. Food, gastrointestinal pH, and models of oral drug absorption. *Eur. J. Pharm. Biopharm.*, 2017, 112, 234-248.

- <http://dx.doi.org/10.1016/j.ejpb.2016.11.034> PMID: 27914234
- [3] Toutain, P.L.; Bousquet-Mélou, A. Bioavailability and its assessment. *J. Vet. Pharmacol. Ther.*, **2004**, 27(6), 455-466. <http://dx.doi.org/10.1111/j.1365-2885.2004.00604.x> PMID: 15601440
 - [4] Damre, A.A.; Iyer, K.R. The significance and determination of plasma protein binding. In: *Encyclopedia of Drug Metabolism and Interactions*; Lyubimov, A.V., Ed.; American Cancer Society: Atlanta, Georgia, **2012**; pp. 1-18. <http://dx.doi.org/10.1002/9780470921920.edm032>
 - [5] Anzenbacher, P.; Anzenbacherová, E. Drug-metabolizing enzymes—an overview. In: *Metabolism of Drugs and Other Xenobiotics*; Anzenbacher, P.; Zanger, U.M., Eds.; Wiley-VCH Verlag GmbH & Co. KGaA, **2012**; pp. 1-25. <http://dx.doi.org/10.1002/9783527630905.ch1>
 - [6] Krishna, D.R.; Klotz, U. Extrahepatic metabolism of drugs in humans. *Clin. Pharmacokinet.*, **1994**, 26(2), 144-160. <http://dx.doi.org/10.2165/00003088-199426020-00007> PMID: 8162658
 - [7] Zanger, U.M.; Schwab, M. Cytochrome P450 enzymes in drug metabolism: Regulation of gene expression, enzyme activities, and impact of genetic variation. *Pharmacol. Ther.*, **2013**, 138, 103-141.
 - [8] Zhang, D.; Luo, G.; Ding, X.; Lu, C. Preclinical experimental models of drug metabolism and disposition in drug discovery and development. *Acta Pharm. Sin. B*, **2012**, 2(6), 549-561. <http://dx.doi.org/10.1016/j.apsb.2012.10.004>
 - [9] Iyanagi, T. Molecular mechanism of phase I and phase II drug-metabolizing enzymes: Implications for detoxification. *Int. Rev. Cytol.*, **2007**, 260, 35-112. [http://dx.doi.org/10.1016/S0074-7696\(06\)60002-8](http://dx.doi.org/10.1016/S0074-7696(06)60002-8) PMID: 17482904
 - [10] Jancova, P.; Anzenbacher, P.; Anzenbacherová, E. Phase II Drug Metabolizing Enzymes. *Biomed. Pap.*, **2010**, 154, 103-116.
 - [11] Calabrese, E.J. *Principles of Animal Extrapolation*; CRC Press: Boca Raton, FL, USA, **1991**.
 - [12] Björkman, S. Prediction of cytochrome p450-mediated hepatic drug clearance in neonates, infants and children: How accurate are available scaling methods? *Clin. Pharmacokinet.*, **2006**, 45(1), 1-11. <http://dx.doi.org/10.2165/00003088-200645010-00001> PMID: 16430308
 - [13] Renwick, A.G. Toxicokinetics in infants and children in relation to the ADI and TDI. *Food Addit. Contam.*, **1998**, 15(Suppl 1), 17-35. <http://dx.doi.org/10.1080/02652039809374612>
 - [14] Kinirons, M.T.; O'Mahony, M.S. Drug metabolism and ageing. *Br. J. Clin. Pharmacol.*, **2004**, 57(5), 540-544. <http://dx.doi.org/10.1111/j.1365-2125.2004.02096.x> PMID: 15089805
 - [15] Morgan, E.T. Impact of infectious and inflammatory disease on cytochrome P450-mediated drug metabolism and pharmacokinetics. *Clin. Pharmacol. Ther.*, **2009**, 85(4), 434-438. <http://dx.doi.org/10.1038/clpt.2008.302> PMID: 19212314
 - [16] Rowland, M.; Tozer, T.N. *Clinical Pharmacokinetics: Concepts and Applications*; Lea & Febiger: Philadelphia, **1989**.
 - [17] Belle, D.J.; Singh, H. Genetic factors in drug metabolism. *Am. Fam. Physician*, **2008**, 77(11), 1553-1560. PMID: 18581835
 - [18] Hurley, T.D.; Edenberg, H.J. Genes encoding enzymes involved in ethanol metabolism. *Alcohol Res.*, **2012**, 34(3), 339-344. PMID: 23134050
 - [19] Niedzwiecki, M.M.; Walker, D.I.; Vermeulen, R.; Chadeau-Hyam, M.; Jones, D.P.; Miller, G.W. The exposome: Molecules to populations. *Annu. Rev. Pharmacol. Toxicol.*, **2019**, 59(1), 107-127. <http://dx.doi.org/10.1146/annurev-pharmtox-010818-021315> PMID: 30095351
 - [20] Honkakoski, P.; Negishi, M. Regulation of cytochrome P450 (CYP) genes by nuclear receptors. *Biochem. J.*, **2000**, 347(Pt 2), 321-337. <http://dx.doi.org/10.1042/bj3470321> PMID: 10749660
 - [21] Kawajiri, K.; Fujii-Kuriyama, Y. The aryl hydrocarbon receptor: A multifunctional chemical sensor for host defense and homeostatic maintenance. *Exp. Anim.*, **2017**, 66(2), 75-89. <http://dx.doi.org/10.1538/expanim.16-0092> PMID: 27980293
 - [22] Kliever, S.A.; Goodwin, B.; Willson, T.M. The nuclear pregnane X receptor: A key regulator of xenobiotic metabolism. *Endocr. Rev.*, **2002**, 23(5), 687-702. <http://dx.doi.org/10.1210/er.2001-0038> PMID: 12372848
 - [23] Pavék, P.; Dvorák, Z. Xenobiotic-induced transcriptional regulation of xenobiotic metabolizing enzymes of the cytochrome P450 superfamily in human extrahepatic tissues. *Curr. Drug Metab.*, **2008**, 9(2), 129-143. <http://dx.doi.org/10.2174/138920008783571774> PMID: 18288955
 - [24] Dumont, C.; Prieto, P.; Asturiol, D.; Worth, A. Review of the availability of *in vitro* and *in silico* methods for assessing dermal bioavailability. *Appl. in vitro Toxicol.*, **2015**, 1(2), 147-164. <http://dx.doi.org/10.1089/aivt.2015.0003>
 - [25] Elias, P.M. The skin barrier as an innate immune element. *Semin. Immunopathol.*, **2007**, 29(1), 3-14. <http://dx.doi.org/10.1007/s00281-007-0060-9> PMID: 17621950
 - [26] Elias, P.M. Epidermal lipids, barrier function, and desquamation. *J. Invest. Dermatol.*, **1983**, 80(1), 44s-49s. <http://dx.doi.org/10.1038/jid.1983.12>
 - [27] Vickers, C.F. Existence of reservoir in the stratum corneum: Experimental proof. *Arch. Dermatol.*, **1963**, 88(1), 20-23. <http://dx.doi.org/10.1001/archderm.1963.01590190026002> PMID: 14042657
 - [28] Warner, R.R.; Stone, K.J.; Boissy, Y.L. Hydration disrupts human stratum corneum ultrastructure. *J. Invest. Dermatol.*, **2003**, 120(2), 275-284. <http://dx.doi.org/10.1046/j.1523-1747.2003.12046.x> PMID: 12542533
 - [29] Roberts, M.S.; Walters, K.A. *Dermal Absorption and Toxicity Assessment*, 2nd Ed.; CRC Press: Boca Raton, FL, USA, **2007**. <http://dx.doi.org/10.3109/9780849375927>
 - [30] Bolzinger, M.-A.; Briançon, S.; Pelletier, J.; Chevalier, Y. Penetration of drugs through skin, a complex rate-controlling membrane. *Curr. Opin. Colloid Interface Sci.*, **2012**, 17(3), 156-165. <http://dx.doi.org/10.1016/j.cocis.2012.02.001>
 - [31] Smith, C.; Hotchkiss, S. *Allergic Contact Dermatitis: Chemical and Metabolic Mechanisms*; Taylor & Francis: Oxfordshire, **2001**.
 - [32] Roberts, D.W.; Mekenyan, O.G.; Dimitrov, S.D.; Dimitrova, G.D. What determines skin sensitization potency-myths, maybes and realities. Part 1. The 500 molecular weight cut-off. *Contact Dermat.*, **2013**, 68(1), 32-41. <http://dx.doi.org/10.1111/j.1600-0536.2012.02160.x> PMID: 22924443
 - [33] Alkilani, A.Z.; McCrudden, M.T.C.; Donnelly, R.F. Transdermal drug delivery: Innovative pharmaceutical developments based on disruption of the barrier properties of the stratum corneum. *Pharmaceutics*, **2015**, 7(4), 438-470. <http://dx.doi.org/10.3390/pharmaceutics7040438> PMID: 26506371
 - [34] SCCS. SCCS notes of guidance for the testing of cosmetic ingredients and their safety evaluation 9th revision. **2015**. Available from: https://ec.europa.eu/health/scientific_committees/consumer_safety/docs/sccs_o_190.pdf
 - [35] Lane, M.E. Skin penetration enhancers. *Int. J. Pharm.*, **2013**, 447(1-2), 12-21. <http://dx.doi.org/10.1016/j.ijpharm.2013.02.040> PMID: 23462366
 - [36] Pannatier, A.; Jenner, P.; Testa, B.; Etter, J.C. The skin as a drug-metabolizing organ. *Drug Metab. Rev.*, **1978**, 8(2), 319-343. <http://dx.doi.org/10.3109/03602537808993791> PMID: 363387
 - [37] Baron, J.M.; Merk, H.F. Drug metabolism in the skin. *Curr. Opin. Allergy Clin. Immunol.*, **2001**, 1(4), 287-291. <http://dx.doi.org/10.1097/01.all.0000011028.08297.b3> PMID: 11964702
 - [38] Hewitt, N.J.; Edwards, R.J.; Fritsche, E.; Goebel, C.; Aeby, P.; Scheel, J.; Reisinger, K.; Ouédraogo, G.; Duche, D.; Eilstein, J.; Latil, A.; Kenny, J.; Moore, C.; Kuehn, J.; Barroso, J.; Fautz, R.; Pfuhrer, S. Use of human *in vitro* skin models for accurate and ethical risk assessment: Metabolic considerations. *Toxicol. Sci.*, **2013**, 133(2), 209-217. <http://dx.doi.org/10.1093/toxsci/kft080> PMID: 23539547
 - [39] Lepoittevin, P. La peau: Acteur majeur du métabolisme. *Prog. En Derm.-Allergol. Lille*, **2004**, 10, 153.
 - [40] Oesch, F.; Fabian, E.; Guth, K.; Landsiedel, R. Xenobiotic-metabolizing enzymes in the skin of rat, mouse, pig, guinea pig, man, and in human skin models. *Arch. Toxicol.*, **2014**, 88(12), 2135-2190. <http://dx.doi.org/10.1007/s00204-014-1382-8> PMID: 25370008

- [41] Pyo, S.M.; Maibach, H.I. Skin metabolism: Relevance of skin enzymes for rational drug design. *Skin Pharmacol. Physiol.*, **2019**, *32*(5), 283-294.
http://dx.doi.org/10.1159/000501732 PMID: 31357203
- [42] Oesch, F.; Fabian, E.; Landsiedel, R. Xenobiotica-metabolizing enzymes in the skin of rat, mouse, pig, guinea pig, man, and in human skin models. *Arch. Toxicol.*, **2018**, *92*(8), 2411-2456.
http://dx.doi.org/10.1007/s00204-018-2232-x PMID: 29916051
- [43] Nebert, D.W.; Nelson, D.R.; Coon, M.J.; Estabrook, R.W.; Feyereisen, R.; Fujii-Kuriyama, Y.; Gonzalez, F.J.; Guengerich, F.P.; Gunsalus, I.C.; Johnson, E.F.; Loper, J.C.; Sato, R.; Waterman, M.R.; Waxman, D.J. The P450 superfamily: Update on new sequences, gene mapping, and recommended nomenclature. *DNA Cell Biol.*, **1991**, *10*(1), 1-14.
http://dx.doi.org/10.1089/dna.1991.10.1 PMID: 1991046
- [44] Shimada, T.; Fujii-Kuriyama, Y. Metabolic activation of polycyclic aromatic hydrocarbons to carcinogens by cytochromes P450 1A1 and 1B1. *Cancer Sci.*, **2004**, *95*(1), 1-6.
http://dx.doi.org/10.1111/j.1349-7006.2004.tb03162.x PMID: 14720319
- [45] Ortiz de Montellano, P.R. Cytochrome P450-activated prodrugs. *Future Med. Chem.*, **2013**, *5*(2), 213-228.
http://dx.doi.org/10.4155/fmc.12.197 PMID: 23360144
- [46] van Eijl, S.; Zhu, Z.; Cupitt, J.; Gierula, M.; Götz, C.; Fritsche, E.; Edwards, R.J. Elucidation of xenobiotic metabolism pathways in human skin and human skin models by proteomic profiling. *PLoS One*, **2012**, *7*(7), e41721.
http://dx.doi.org/10.1371/journal.pone.0041721 PMID: 22848577
- [47] Ahmad, N.; Mukhtar, H. Cytochrome p450: A target for drug development for skin diseases. *J. Invest. Dermatol.*, **2004**, *123*(3), 417-425.
http://dx.doi.org/10.1111/j.0022-202X.2004.23307.x PMID: 15304077
- [48] Quantin, P.; Patatian, A.; Floreani, M.; Egles, C.; Benech, P.; Ficheux, H. Temporal transcriptomic analysis of human primary keratinocytes exposed to β -naphthoflavone highlights the protective efficacy of skin to environmental pollutants. *Toxicol. In vitro*, **2020**, *65*, 104822.
http://dx.doi.org/10.1016/j.tiv.2020.104822 PMID: 32151702
- [49] Neis, M.M.; Wendel, A.; Wiederholt, T.; Marquardt, Y.; Jousen, S.; Baron, J.M.; Merk, H.F. Expression and induction of cytochrome p450 isoenzymes in human skin equivalents. *Skin Pharmacol. Physiol.*, **2010**, *23*(1), 29-39.
http://dx.doi.org/10.1159/000257261 PMID: 20090406
- [50] Janmohamed, A.; Dolphin, C.T.; Phillips, I.R.; Shephard, E.A. Quantification and cellular localization of expression in human skin of genes encoding flavin-containing monooxygenases and cytochromes P450. *Biochem. Pharmacol.*, **2001**, *62*(6), 777-786.
http://dx.doi.org/10.1016/S0006-2952(01)00718-3 PMID: 11551524
- [51] Cheung, C.; Hotchkiss, S.A.M.; Pease, C.K.S. Cinnamic compound metabolism in human skin and the role metabolism may play in determining relative sensitisation potency. *J. Dermatol. Sci.*, **2003**, *31*(1), 9-19.
http://dx.doi.org/10.1016/S0923-1811(02)00139-1 PMID: 12615359
- [52] Lockley, D.J.; Howes, D.; Williams, F.M. Cutaneous metabolism of glycol ethers. *Arch. Toxicol.*, **2005**, *79*(3), 160-168.
http://dx.doi.org/10.1007/s00204-004-0619-3 PMID: 15551062
- [53] Yasuda, K.; Montagna, W. Histology and cytochemistry of human skin. 20. The distribution of monoamine oxidase. *J. Histochem. Cytochem.*, **1960**, *8*(5), 356-366.
http://dx.doi.org/10.1177/8.5.356 PMID: 13846477
- [54] McCracken, N.W.; Blain, P.G.; Williams, F.M. Nature and role of xenobiotic metabolizing esterases in rat liver, lung, skin and blood. *Biochem. Pharmacol.*, **1993**, *45*(1), 31-36.
http://dx.doi.org/10.1016/0006-2952(93)90373-5 PMID: 8424820
- [55] Kazem, S.; Linssen, E.C.; Gibbs, S. Skin metabolism phase I and phase II enzymes in native and reconstructed human skin: A short review. *Drug Discov. Today*, **2019**, *24*(9), 1899-1910.
http://dx.doi.org/10.1016/j.drudis.2019.06.002 PMID: 31176740
- [56] Krien, P.M.; Kermici, M. Evidence for the existence of a self-regulated enzymatic process within the human stratum corneum -an unexpected role for urocanic acid. *J. Invest. Dermatol.*, **2000**, *115*(3), 414-420.
http://dx.doi.org/10.1046/j.1523-1747.2000.00083.x PMID: 10951277
- [57] Moss, T.; Howes, D.; Williams, F.M. Percutaneous penetration and dermal metabolism of triclosan (2,4, 4'-trichloro-2'-hydroxydiphenyl ether). *Food Chem. Toxicol.*, **2000**, *38*(4), 361-370.
http://dx.doi.org/10.1016/S0278-6915(99)00164-7 PMID: 10722890
- [58] Buhl, A.E.; Waldon, D.J.; Baker, C.A.; Johnson, G.A. Minoxidil sulfate is the active metabolite that stimulates hair follicles. *J. Invest. Dermatol.*, **1990**, *95*(5), 553-557.
http://dx.doi.org/10.1111/1523-1747.ep12504905 PMID: 2230218
- [59] Goebel, C.; Hewitt, N.J.; Kunze, G.; Wenker, M.; Hein, D.W.; Beck, H.; Skare, J. Skin metabolism of aminophenols: Human keratinocytes as a suitable *in vitro* model to qualitatively predict the dermal transformation of 4-amino-2-hydroxytoluene *in vivo*. *Toxicol. Appl. Pharmacol.*, **2009**, *235*(1), 114-123.
http://dx.doi.org/10.1016/j.taap.2008.11.014 PMID: 19100279
- [60] Luu-The, V.; Duche, D.; Ferraris, C.; Meunier, J.-R.; Leclaire, J.; Labrie, F. Expression profiles of phases 1 and 2 metabolizing enzymes in human skin and the reconstructed skin models Episkin and full thickness model from Episkin. *J. Steroid Biochem. Mol. Biol.*, **2009**, *116*(3-5), 178-186.
http://dx.doi.org/10.1016/j.jsmb.2009.05.011 PMID: 19482084
- [61] Habig, W.H.; Pabst, M.J.; Jakoby, W.B. Glutathione S-transferases. The first enzymatic step in mercapturic acid formation. *J. Biol. Chem.*, **1974**, *249*(22), 7130-7139.
http://dx.doi.org/10.1016/S0021-9258(19)42083-8 PMID: 4436300
- [62] Smith Pease, C.K.; Basketter, D.A.; Patlewicz, G.Y. Contact allergy: The role of skin chemistry and metabolism. *Clin. Exp. Dermatol.*, **2003**, *28*(2), 177-183.
http://dx.doi.org/10.1046/j.1365-2230.2003.01239.x PMID: 12653709
- [63] Brinkmann, J.; Stolpmann, K.; Trappe, S.; Otter, T.; Genkinger, D.; Bock, U.; Liebsch, M.; Henkler, F.; Hutzler, C.; Luch, A. Metabolically competent human skin models: Activation and genotoxicity of benzo[a]pyrene. *Toxicol. Sci.*, **2013**, *131*(2), 351-359.
http://dx.doi.org/10.1093/toxsci/kfs316 PMID: 23148024
- [64] Wiebel, F.J.; Gelboin, H.V. Cutaneous carcinogenesis: Metabolic interaction of chemical carcinogens with skin. In: *Comprehensive Physiology*; John Wiley & Sons, Inc., **2010**.
- [65] Peiser, M.; Tralau, T.; Heidler, J.; Api, A.M.; Arts, J.H.E.; Basketter, D.A.; English, J.; Diepgen, T.L.; Fuhlbrigge, R.C.; Gaspari, A.A.; Johansen, J.D.; Karlberg, A.T.; Kimber, I.; Lepoittevin, J.P.; Liebsch, M.; Maibach, H.I.; Martin, S.F.; Merk, H.F.; Platzeck, T.; Rustemeyer, T.; Schnuch, A.; Vandebriel, R.J.; White, I.R.; Luch, A. Allergic contact dermatitis: Epidemiology, molecular mechanisms, *in vitro* methods and regulatory aspects. Current knowledge assembled at an international workshop at BfR, Germany. *Cell. Mol. Life Sci.*, **2012**, *69*(5), 763-781.
http://dx.doi.org/10.1007/s00018-011-0846-8 PMID: 21997384
- [66] Ahlfors, S.R.; Sterner, O.; Hansson, C. Reactivity of contact allergenic haptens to amino acid residues in a model carrier peptide, and characterization of formed peptide-hapten adducts. *Skin Pharmacol. Appl. Skin Physiol.*, **2003**, *16*(1), 59-68.
http://dx.doi.org/10.1159/000068288 PMID: 12566830
- [67] Barratt, M.D.; Basketter, D.A. Possible origin of the skin sensitization potential of isoeugenol and related compounds. (I). Preliminary studies of potential reaction mechanisms. *Contact Dermatitis*, **1992**, *27*, 98-104.
- [68] Karlberg, A.-T.; Bergström, M.A.; Börje, A.; Luthman, K.; Nilsson, J.L.G. Allergic contact dermatitis--formation, structural requirements, and reactivity of skin sensitizers. *Chem. Res. Toxicol.*, **2008**, *21*(1), 53-69.
http://dx.doi.org/10.1021/tx7002239 PMID: 18052130
- [69] Natsch, A. The Nrf2-Keap1-ARE toxicity pathway as a cellular sensor for skin sensitizers--functional relevance and a hypothesis on innate reactions to skin sensitizers. *Toxicol. Sci.*, **2010**, *113*(2), 284-292.
http://dx.doi.org/10.1093/toxsci/kfp228 PMID: 19767620
- [70] Urbisch, D.; Becker, M.; Honarvar, N.; Kolle, S.N.; Mehling, A.; Teubner, W.; Wareing, B.; Landsiedel, R. Assessment of pre- and

- pro-haptens using nonanimal test methods for skin sensitization. *Chem. Res. Toxicol.*, **2016**, 29(5), 901-913.
<http://dx.doi.org/10.1021/acs.chemrestox.6b00055> PMID: 27070937
- [71] Thompson, D.; Constantin-Teodosiu, D.; Egestad, B.; Mickos, H.; Moldéus, P. Formation of glutathione conjugates during oxidation of eugenol by microsomal fractions of rat liver and lung. *Biochem. Pharmacol.*, **1990**, 39(10), 1587-1595.
[http://dx.doi.org/10.1016/0006-2952\(90\)90525-P](http://dx.doi.org/10.1016/0006-2952(90)90525-P) PMID: 2337416
- [72] Ewald, B.H.; Gregg, D.A. Animal research for animals. *Ann. N. Y. Acad. Sci.*, **1983**, 406, 48-58.
<http://dx.doi.org/10.1111/j.1749-6632.1983.tb53484.x> PMID: 6349465
- [73] Orfila, M.-J.-B. *Treatise on Toxicology*; Fortin, Masson: Paris, **1843**.
- [74] Priestley, J.; Hey, W. Observations on different kinds of air. *Philos. Trans. R. Soc.*, **1772**, 62, 147-264.
<http://dx.doi.org/10.1098/rstl.1772.0021>
- [75] Allen, D.; Waters, M.D. *Reducing, Refining and Replacing the Use of Animals in Toxicity Testing*; Royal Society of Chemistry: London, **2013**.
<http://dx.doi.org/10.1039/9781849737920>
- [76] OECD. *Test No. 427: Skin Absorption: In vivo Method*; Organisation for Economic Co-operation and Development: Paris, **2004**. Available from: https://read.oecd-ilibrary.org/environment/test-no-427-skin-absorption-in-vivo-method_9789264071063-en#page1
- [77] FDA. *Topical Dermatological Drug Product NDAs and ANDAs -In vivo Bioavailability, Bioequivalence, in vitro Release, and Associated Studies*; Food and Drug Agency: Rockville, MD, **1998**.
- [78] Rougier, A.; Lotte, C.; Maibach, H.I. *In vivo* percutaneous penetration of some organic compounds related to anatomic site in humans: Predictive assessment by the stripping method. *J. Pharm. Sci.*, **1987**, 76(6), 451-454.
<http://dx.doi.org/10.1002/jps.2600760608> PMID: 3625489
- [79] Abd, E.; Yousef, S.A.; Pastore, M.N.; Telaprolu, K.; Mohammed, Y.H.; Namjoshi, S.; Grice, J.E.; Roberts, M.S. Skin models for the testing of transdermal drugs. *Clin. Pharmacol.*, **2016**, 8, 163-176.
<http://dx.doi.org/10.2147/CPAA.S64788> PMID: 27799831
- [80] Quantin, P.; Ghazi, K.; Pereira, U.; Smith, A.; Degardin, L.; Vigneron, P.; Fichoux, H.; Garlick, J.; Rapetti, L.; Egles, C. Utilization of a mouse/human chimeric model for long term metabolic testing of human skin. *J. Pharmacol. Toxicol. Methods*, **2020**, 102, 106663.
<http://dx.doi.org/10.1016/j.vascn.2019.106663> PMID: 31837436
- [81] Reifenrath, W.G.; Chellquist, E.M.; Shipwash, E.A.; Jederberg, W.W.; Krueger, G.G. Percutaneous penetration in the hairless dog, weanling pig and grafted athymic nude mouse: Evaluation of models for predicting skin penetration in man. *Br. J. Dermatol.*, **1984**, 111(s27)(Suppl. 27), 123-135.
<http://dx.doi.org/10.1111/j.1365-2133.1984.tb15590.x> PMID: 6204672
- [82] Jacques, C. Study of the diffusion and cutaneous metabolism of xenobiotics on preserved pig ear skin in comparison with the liver, Doctoral Thesis, Université de Toulouse, **2010**.
- [83] Bronaugh, R.L.; Stewart, R.F.; Wester, R.C.; Bucks, D.; Maibach, H.I.; Anderson, J. Comparison of percutaneous absorption of fragrances by humans and monkeys. *Food Chem. Toxicol.*, **1985**, 23(1), 111-114.
[http://dx.doi.org/10.1016/0278-6915\(85\)90228-5](http://dx.doi.org/10.1016/0278-6915(85)90228-5) PMID: 4038674
- [84] Wilkinson, G.R. *Prediction of In vivo Parameters of Drug Metabolism and Distribution from In vitro Studies*; National Academies Press: US, **1987**.
- [85] Saraf, S.K.; Kumaraswamy, V. Basic research: Issues with animal experimentations. *Indian J. Orthop.*, **2013**, 47(1), 6-9.
<http://dx.doi.org/10.4103/0019-5413.106882> PMID: 23532705
- [86] Shanks, N.; Greek, R.; Greek, J. Are animal models predictive for humans? *Philos. Ethics Humanit. Med.*, **2009**, 4(1), 2.
<http://dx.doi.org/10.1186/1747-5341-4-2> PMID: 19146696
- [87] Götz, C.; Pfeiffer, R.; Tigges, J.; Blatz, V.; Jäckh, C.; Freytag, E.-M.; Fabian, E.; Landsiedel, R.; Merk, H.F.; Krutmann, J.; Edwards, R.J.; Pease, C.; Goebel, C.; Hewitt, N.; Fritsche, E. Xenobiotic metabolism capacities of human skin in comparison with a 3D epidermis model and keratinocyte-based cell culture as *in vitro* alternatives for chemical testing: Activating enzymes (Phase I). *Exp. Dermatol.*, **2012**, 21(5), 358-363.
<http://dx.doi.org/10.1111/j.1600-0625.2012.01486.x> PMID: 22509833
- [88] Götz, C.; Pfeiffer, R.; Tigges, J.; Ruwiedel, K.; Hübenthal, U.; Merk, H.F.; Krutmann, J.; Edwards, R.J.; Abel, J.; Pease, C.; Goebel, C.; Hewitt, N.; Fritsche, E. Xenobiotic metabolism capacities of human skin in comparison with a 3D-epidermis model and keratinocyte-based cell culture as *in vitro* alternatives for chemical testing: Phase II enzymes. *Exp. Dermatol.*, **2012**, 21(5), 364-369.
<http://dx.doi.org/10.1111/j.1600-0625.2012.01478.x> PMID: 22509834
- [89] MacNeil, S. Progress and opportunities for tissue-engineered skin. *Nature*, **2007**, 445(7130), 874-880.
<http://dx.doi.org/10.1038/nature05664> PMID: 17314974
- [90] Poncet, M. Skin constructs for replacement of skin tissues for *in vitro* testing. *Adv. Drug Deliv. Rev.*, **2002**, 54(Suppl. 1), S19-S30.
[http://dx.doi.org/10.1016/S0169-409X\(02\)00112-6](http://dx.doi.org/10.1016/S0169-409X(02)00112-6) PMID: 12460713
- [91] Poumay, Y.; Dupont, F.; Marcoux, S.; Leclercq-Smekens, M.; Héryn, M.; Coquette, A. A simple reconstructed human epidermis: Preparation of the culture model and utilization in *in vitro* studies. *Arch. Dermatol. Res.*, **2004**, 296(5), 203-211.
<http://dx.doi.org/10.1007/s00403-004-0507-y> PMID: 15349789
- [92] Schäfer-Korting, M.; Mahmoud, A.; Lombardi Borgia, S.; Brügener, B.; Kleuser, B.; Schreiber, S.; Mehnert, W. Reconstructed epidermis and full-thickness skin for absorption testing: Influence of the vehicles used on steroid permeation. *Altern. Lab. Anim.*, **2008**, 36(4), 441-452.
<http://dx.doi.org/10.1177/026119290803600405> PMID: 18826333
- [93] Régnier, M.; Patwardhan, A.; Scheynius, A.; Schmidt, R. Reconstructed human epidermis composed of keratinocytes, melanocytes and Langerhans cells. *Med. Biol. Eng. Comput.*, **1998**, 36(6), 821-824.
<http://dx.doi.org/10.1007/BF02518889> PMID: 10367476
- [94] Eilstein, J.; Léreaux, G.; Budimir, N.; Hussler, G.; Wilkinson, S.; Duché, D. Comparison of xenobiotic metabolizing enzyme activities in *ex vivo* human skin and reconstructed human skin models from SkinEthic. *Arch. Toxicol.*, **2014**, 88(9), 1681-1694.
<http://dx.doi.org/10.1007/s00204-014-1218-6> PMID: 24658324
- [95] Hu, T.; Bailey, R.E.; Morrall, S.W.; Aardema, M.J.; Stanley, L.A.; Skare, J.A. Dermal penetration and metabolism of p-aminophenol and p-phenylenediamine: Application of the EpiDerm human reconstructed epidermis model. *Toxicol. Lett.*, **2009**, 188(2), 119-129.
<http://dx.doi.org/10.1016/j.toxlet.2009.03.019> PMID: 19446244
- [96] Hu, T.; Khambatta, Z.S.; Hayden, P.J.; Bolmarich, J.; Binder, R.L.; Robinson, M.K.; Carr, G.J.; Tiesman, J.P.; Jarrold, B.B.; Osborne, R.; Reichling, T.D.; Nemeth, S.T.; Aardema, M.J. Xenobiotic metabolism gene expression in the EpiDerm *in vitro* 3D human epidermis model compared to human skin. *Toxicol. Vitro Int. J. Publ. Assoc. BIBRA*, **2010**, 24(5), 1450-1463.
<http://dx.doi.org/10.1016/j.tiv.2010.03.013> PMID: 20350595
- [97] Schreiber, S.; Mahmoud, A.; Vuia, A.; Rübelke, M.K.; Schmidt, E.; Schaller, M.; Kandárová, H.; Haberland, A.; Schäfer, U.F.; Bock, U.; Korting, H.C.; Liebsch, M.; Schäfer-Korting, M. Reconstructed epidermis versus human and animal skin in skin absorption studies. *Toxicol. In vitro*, **2005**, 19(6), 813-822.
<http://dx.doi.org/10.1016/j.tiv.2005.04.004> PMID: 15913948
- [98] Lotte, C.; Patouillet, C.; Zanini, M.; Messenger, A.; Roguet, R. Permeation and skin absorption: Reproducibility of various industrial reconstructed human skin models. *Skin Pharmacol. Appl. Skin Physiol.*, **2002**, 15(Suppl. 1), 18-30.
<http://dx.doi.org/10.1159/000066679> PMID: 12476006
- [99] Poncet, M.; Gibbs, S.; Pilgram, G.; Boelsma, E.; Koerten, H.; Bouwstra, J.; Mommaas, M. Barrier function in reconstructed epidermis and its resemblance to native human skin. *Skin Pharmacol. Appl. Skin Physiol.*, **2001**, 14(Suppl. 1), 63-71.
<http://dx.doi.org/10.1159/000056392> PMID: 11509909
- [100] Antille, C.; Tran, C.; Sorg, O.; Saurat, J.-H. Penetration and metabolism of topical retinoids in *ex vivo* organ-cultured full-thickness human skin explants. *Skin Pharmacol. Physiol.*, **2004**, 17(3), 124-128.
<http://dx.doi.org/10.1159/000077238> PMID: 15087591
- [101] de Jager, M.; Groenink, W.; Bielsa i Guivernau, R.; Andersson, E.; Angelova, N.; Poncet, M.; Bouwstra, J. A novel *in vitro* percutaneous penetration model: Evaluation of barrier properties with p-

- aminobenzoic acid and two of its derivatives. *Pharm. Res.*, **2006**, 23(5), 951-960.
<http://dx.doi.org/10.1007/s11095-006-9909-1> PMID: 16715385
- [102] Uchida, T.; Kadhum, W.R.; Kanai, S.; Todo, H.; Oshizaka, T.; Sugibayashi, K. Prediction of skin permeation by chemical compounds using the artificial membrane, Strat-M™. *Eur. J. Pharm. Sci.*, **2015**, 67, 113-118.
<http://dx.doi.org/10.1016/j.ejps.2014.11.002> PMID: 25447745
- [103] Sinkó, B.; Garrigues, T.M.; Balogh, G.T.; Nagy, Z.K.; Tsinman, O.; Avdeef, A.; Takács-Novák, K. Skin-PAMPA: A new method for fast prediction of skin penetration. *Eur. J. Pharm. Sci. Off. J. Eur. Fed. Pharm. Sci.*, **2012**, 45(5), 698-707.
<http://dx.doi.org/10.1016/j.ejps.2012.01.011> PMID: 22326705
- [104] Ng, S-F.; Rouse, J.; Sanderson, D.; Eccleston, G. A comparative study of transmembrane diffusion and permeation of ibuprofen across synthetic membranes using franz diffusion cells. *Pharmaceutics*, **2010**, 2(2), 209-223.
<http://dx.doi.org/10.3390/pharmaceutics2020209> PMID: 27721352
- [105] Herkenne, C.; Naik, A.; Kalia, Y.N.; Hadgraft, J.; Guy, R.H. Ibuprofen transport into and through skin from topical formulations: *In vitro-in vivo* comparison. *J. Invest. Dermatol.*, **2007**, 127(1), 135-142.
<http://dx.doi.org/10.1038/sj.jid.5700491> PMID: 16858418
- [106] Jia, L.; Liu, X. The conduct of drug metabolism studies considered good practice (II): *In vitro* experiments. *Curr. Drug Metab.*, **2007**, 8(8), 822-829.
<http://dx.doi.org/10.2174/138920007782798207> PMID: 18220563
- [107] Quantin, P.; Colaço, E.; El Kirat, K.; Egles, C.; Fichoux, H.; Landoulsi, J. Layer-by-layer assembly of nanosized membrane fractions for the assessment of cytochrome P450 xenobiotic metabolism. *ACS Omega*, **2018**, 3(10), 12535-12544.
<http://dx.doi.org/10.1021/acsomega.8b01738> PMID: 31457987
- [108] Spriggs, S.; Cubberley, R.; Loadman, P.; Sheffield, D.; Wierzbicki, A. A study of inter-individual variability in the Phase II metabolism of xenobiotics in human skin. *Toxicol. Lett.*, **2018**, 292, 63-72.
<http://dx.doi.org/10.1016/j.toxlet.2018.04.011> PMID: 29709425
- [109] Natsch, A.; Haupt, T. Utility of rat liver S9 fractions to study skin-sensitizing prohaptenes in a modified KeratinoSens assay. *Toxicol. Sci.*, **2013**, 135(2), 356-368.
<http://dx.doi.org/10.1093/toxsci/kft160> PMID: 23872582
- [110] Chun, H.S.; Kuzmicky, P.A.; Rucoba, L.; Kado, N.Y.; Rice, R.H. Cytotoxicity and keratinocyte microsome-mediated mutagenic activation of carcinogens in cultured epidermal cells. *Toxicol. Lett.*, **2000**, 115(2), 165-172.
[http://dx.doi.org/10.1016/S0378-4274\(00\)00190-9](http://dx.doi.org/10.1016/S0378-4274(00)00190-9) PMID: 10802392
- [111] Reifenrath, W.G.; Hawkins, G.S.; Kurtz, M.S. Percutaneous penetration and skin retention of topically applied compounds: An *in vitro-in vivo* study. *J. Pharm. Sci.*, **1991**, 80(6), 526-532.
<http://dx.doi.org/10.1002/jps.2600800605> PMID: 1941541
- [112] Krone, V. Absorption: *In vivo* tests (radiolabeled). In: *Drug Discovery and Evaluation: Safety and Pharmacokinetic Assays*; Vogel, H.G.; Maas, J.; Hock, F.J.; Mayer, D., Eds.; Springer: Berlin, Heidelberg, **2013**; pp. 799-834.
http://dx.doi.org/10.1007/978-3-642-25240-2_33
- [113] Herkenne, C.; Alberti, I.; Naik, A.; Kalia, Y.N.; Mathy, F-X.; Pr  at, V.; Guy, R.H. *In vivo* methods for the assessment of topical drug bioavailability. *Pharm. Res.*, **2008**, 25(1), 87-103.
<http://dx.doi.org/10.1007/s11095-007-9429-7> PMID: 17985216
- [114] Bartosova, L.; Bajgar, J. Transdermal drug delivery *in vitro* using diffusion cells. *Curr. Med. Chem.*, **2012**, 19(27), 4671-4677.
<http://dx.doi.org/10.2174/092986712803306358> PMID: 22934776
- [115] Pineau, A.; Guillard, O.; Favreau, F.; Marraud, A.; Fauconneau, B.; Gaudin, A.; Vincent, C.M.; Marraud, A.; Marty, J.-P. *In vitro* study of percutaneous absorption of aluminum from antiperspirants through human skin in the Franz™ diffusion cell. *J. Inorg. Biochem.*, **2012**, 110, 21-26.
<http://dx.doi.org/10.1016/j.jinorgbio.2012.02.013> PMID: 22459170
- [116] Bodenlenz, M.; Tiffner, K.I.; Raml, R.; Augustin, T.; Dragatin, C.; Birngruber, T.; Schimek, D.; Schwagerle, G.; Pieber, T.R.; Raney, S.G.; Kanfer, I.; Sinner, F. Open flow microperfusion as a dermal pharmacokinetic approach to evaluate topical bioequivalence. *Clin. Pharmacokinet.*, **2017**, 56(1), 91-98.
<http://dx.doi.org/10.1007/s40262-016-0442-z> PMID: 27539717
- [117] Holmgaard, R.; Nielsen, J.B.; Benfeldt, E. Microdialysis sampling for investigations of bioavailability and bioequivalence of topically administered drugs: Current state and future perspectives. *Skin Pharmacol. Physiol.*, **2010**, 23(5), 225-243.
<http://dx.doi.org/10.1159/000314698> PMID: 20484965
- [118] McGinnity, D.F.; Griffin, S.J.; Moody, G.C.; Voice, M.; Hanlon, S.; Friedberg, T.; Riley, R.J. Rapid characterization of the major drug-metabolizing human hepatic cytochrome P-450 enzymes expressed in *Escherichia coli*. *Drug Metab. Dispos.*, **1999**, 27(9), 1017-1023.
 PMID: 10460801
- [119] Dennis, K.K.; Auerbach, S.S.; Balshaw, D.M.; Cui, Y.; Fallin, M.D.; Smith, M.T.; Spira, A.; Sumner, S.; Miller, G.W. The importance of the biological impact of exposure to the concept of the exposome. *Environ. Health Perspect.*, **2016**, 124(10), 1504-1510.
<http://dx.doi.org/10.1289/EHP140> PMID: 27258438
- [120] Guerriaud, M. *Droit pharmaceutique*; Elsevier Masson, **2016**.
- [121] Palleria, C.; Di Paolo, A.; Giofr  , C.; Caglioti, C.; Leuzzi, G.; Siniscalchi, A.; De Sarro, G.; Gallelli, L. Pharmacokinetic drug-drug interaction and their implication in clinical management. *J. Res. Med. Sci.*, **2013**, 18(7), 601-610.
 PMID: 24516494

DISCLAIMER: The above article has been published, as is, ahead-of-print, to provide early visibility but is not the final version. Major publication processes like copyediting, proofing, typesetting and further review are still to be done and may lead to changes in the final published version, if it is eventually published. All legal disclaimers that apply to the final published article also apply to this ahead-of-print version.